

**Zein-Eddine's edits in green** including

section "1 Executive Summary..." in exesum/exesum.tex

**Thia's edit in red** including

section "1 Executive Summary..." in exesum/exesum.tex

section "2.1 SoLID Project Introduction/Overview" in intro/intro.tex

**Zhiwen's edit in magenta** including

section "2.1.4 Baseline and Enhanced Baseline configuration" in intro/intro.tex

section "2.2.7 SIDIS with Baseline and Enhanced Baseline configuration" in intro/intro\_sidis.tex

section "7.4 GEM with Baseline and Enhanced Baseline configuration" in gem\_us/gem\_stage.tex

section "10.10 EC with Baseline and Enhanced Baseline configuration" in calorimeter/calor\_stage.tex

section "9 Heavy Gas Cherenkov" in cerenkov\_hg/cerenkov\_hg.tex

**Seamus and Ole's edits in magenta**

section "Appendix C Software Development Effort Estimate" in appendix/software\_manpower.tex

**JP's edit in blue** including

section "1 Executive Summary..." in exesum/exesum.tex

section "2.1 SoLID Project Introduction/Overview" in intro/intro.tex

section "Appendix A Summary of Recommendations..." in appendix/original\_recommendations.tex

section "Appendix D Cost Estimations 2018" in appendix/cost\_2018/cost\_2018.tex

**SAW's edit in magenta**

section "14.4 Data rates, event size..." in daq/daq.tex

**Xiaochao's edit in cyan**

section "10.9 EC Collaboration Status and Construction Outlook" in calorimeter/calor\_construction.tex

section "10.10 EC with Baseline and Enhanced Baseline configuration" in calorimeter/calor\_stage.tex

**Whit's edit in cyan**

section "4.2 SoLID magnet" in magnet/magnet.tex

section "18.3 Support Structure for Equipment Located Inside Cryostat Bore" in support/support.tex

section "19 Installation" in installation/installation.tex

**Michael's edit in Orange**

section "8.1.2: Light Gas Cherenkov, Design, Mirrors" in cerenkov\_lg/cerenkov\_lg.tex

**SoLID (Solenoidal Large Intensity Device)  
Updated Preliminary Conceptual Design Report**

The SoLID Collaboration

December 15, 2018



# 1 Contents

2	<b>1 Executive Summary of the Responses to Recommendations from the Jefferson Lab</b>	
3	<b>Director’s Review Committee</b>	<b>1</b>
4	1.1 Overview	1
5	1.2 Physics Program	2
6	1.2.1 SIDIS Production of Charged Pions	2
7	1.2.2 PVDIS	2
8	1.2.3 $J/\psi$ Production	3
9	1.3 Possible Expansions in the Physics Reach of SoLID	4
10	1.3.1 Generalized Parton Distributions (GPD)	4
11	1.3.2 SIDIS Production of Charged Kaons	5
12	1.4 Experimental Design, Simulation and Feasibility	6
13	1.4.1 Solenoidal Magnet	6
14	1.4.2 Acceptance, Efficiency and Systematics	7
15	1.4.3 Rates and Data Acquisition	8
16	1.5 Summary	8
17	<b>2 Introduction and Overview of SoLID Experimental Programs</b>	<b>10</b>
18	2.1 SoLID Project Introduction/Overview	10
19	2.1.1 Base Equipment Description	10
20	2.1.2 Dependencies to Base Equipment	10
21	2.1.3 Experiment-specific Dependencies	11
22	2.1.4 Baseline and Enhanced Baseline Configurations	12
23	2.1.5 Research Program	12
24	2.2 SIDIS Program	13
25	2.2.1 Introduction	13
26	2.2.2 Transverse Structure and Semi-Inclusive Deep Inelastic Scattering	14
27	2.2.3 The Phenomenology TSSAs and TMDs	16
28	2.2.4 Overview of SIDIS program	17
29	2.2.5 Beam Time and Projections	18
30	2.2.6 Comparisons with SBS and CLAS12 SIDIS programs	20
31	2.2.7 SIDIS with Baseline and Enhanced Baseline Configurations	22
32	2.3 PVDIS Program	31
33	2.3.1 Motivation for PVDIS	31
34	2.3.2 Review of the Theory	31
35	2.3.3 Charge Symmetry Violation	33
36	2.3.4 Higher Twist	35
37	2.3.5 Data Sample and analysis	36
38	2.3.6 Beam Time and Projections	37
39	2.4 $J/\psi$ Program	39
40	2.4.1 Motivation	39
41	2.4.2 Program Overview	43
42	2.4.3 Beam Time and Projection	44
43	2.5 Possible Expansion in Physics Reach	46
44	2.5.1 GPD Program	46
45	2.5.2 SIDIS Production of Charged Kaons	47

46	<b>3</b>	<b>Technical Requirements and Experimental Setup</b>	<b>49</b>
47	3.1	Summary of Requirements . . . . .	49
48	3.2	SIDIS- <sup>3</sup> He Experiments . . . . .	54
49	3.3	SIDIS-proton Experiment . . . . .	57
50	3.4	PVDIS Experiment . . . . .	59
51	3.5	$J/\psi$ Experiment . . . . .	61
52	<b>4</b>	<b>Magnet</b>	<b>65</b>
53	4.1	Requirements . . . . .	65
54	4.2	SoLID magnet . . . . .	65
55	4.3	Planned Modifications . . . . .	66
56	4.4	Current Status and Planned Test . . . . .	68
57	<b>5</b>	<b>Targets</b>	<b>71</b>
58	5.1	Polarized <sup>3</sup> He Target . . . . .	71
59	5.2	Transversely Polarized Proton Target . . . . .	71
60	5.3	Cryogenic Target for PVDIS . . . . .	74
61	<b>6</b>	<b>Baffles</b>	<b>77</b>
62	<b>7</b>	<b>GEM Tracker</b>	<b>83</b>
63	7.1	Design . . . . .	83
64	7.2	GEM tracker R&D . . . . .	87
65	7.2.1	GEM chamber R&D program in UVa . . . . .	87
66	7.2.2	GEM chamber R&D programs in China . . . . .	90
67	7.3	Collaboration Status and Construction Outlook . . . . .	93
68	7.4	GEM with Baseline and Enhanced Baseline Configurations . . . . .	94
69	<b>8</b>	<b>Light Gas Cherenkov</b>	<b>96</b>
70	8.1	Design . . . . .	96
71	8.1.1	Tank and Cherenkov Gas . . . . .	96
72	8.1.2	Mirrors . . . . .	96
73	8.1.3	PMTs . . . . .	97
74	8.1.4	Magnetic Shielding and Winston Cones . . . . .	97
75	8.2	Tank Support . . . . .	99
76	8.3	Simulations . . . . .	99
77	8.3.1	Collection Efficiencies . . . . .	100
78	8.3.2	Background Rates . . . . .	100
79	8.3.3	Pion Rejection . . . . .	100
80	<b>9</b>	<b>Heavy Gas Cherenkov</b>	<b>105</b>
81	9.1	Optical System Design . . . . .	105
82	9.2	Simulation . . . . .	106
83	9.2.1	Photoelectron Yield . . . . .	106
84	9.2.2	Pion Detection Efficiency and Kaon Rejection Factor . . . . .	106
85	9.3	Performance of the PMTs in Magnetic Field . . . . .	107
86	9.4	Engineering Design . . . . .	108
87	9.5	Gas and Gas System . . . . .	108

88	<b>10 Electromagnetic Calorimeter</b>	<b>112</b>
89	10.1 Overview . . . . .	112
90	10.2 Shower Detector Design Considerations . . . . .	114
91	10.2.1 Total Length of the Calorimeter . . . . .	114
92	10.2.2 Sampling Ratio of the Shower Detector . . . . .	115
93	10.2.3 Lateral Size of the Calorimeter Module . . . . .	116
94	10.3 Preshower Detector . . . . .	117
95	10.4 Layout and Support . . . . .	119
96	10.5 Light Readout . . . . .	119
97	10.6 Radiation Effects . . . . .	121
98	10.7 Performance . . . . .	121
99	10.7.1 Intrinsic electron-pion separation . . . . .	121
100	10.7.2 PID performance under realistic background simulation . . . . .	124
101	10.7.3 Trigger capability . . . . .	126
102	10.7.4 Shower Position Measurement . . . . .	130
103	10.7.5 Supplemental Information: PID Selection Cuts . . . . .	130
104	10.8 Scintillator Pad Detector for SIDIS Experiments . . . . .	132
105	10.9 EC Collaboration Status and Construction Outlook . . . . .	134
106	10.10 EC with Baseline and Enhanced Baseline Configurations . . . . .	135
107	<b>11 MRPC</b>	<b>136</b>
108	11.1 Overview . . . . .	136
109	11.2 Structure of the MRPC Prototype . . . . .	136
110	11.3 Gas system . . . . .	137
111	11.4 Cosmic Ray Test . . . . .	137
112	11.5 Beam Test at Hall A . . . . .	138
113	11.5.1 Test Setup . . . . .	138
114	11.5.2 HV Scan Result . . . . .	139
115	11.5.3 Rate Scan Result . . . . .	139
116	11.6 Radiation hardness and aging . . . . .	139
117	11.7 Conclusions . . . . .	140
118	11.8 R&D Plan for Better Time Resolution . . . . .	140
119	<b>12 Simulation and Reconstruction</b>	<b>148</b>
120	12.1 End-to-End Software Framework . . . . .	148
121	12.2 Simulation . . . . .	149
122	12.2.1 Simulation Software . . . . .	149
123	12.2.2 Simulation Status . . . . .	151
124	12.2.3 Physics Event Generators . . . . .	152
125	12.2.4 GEM Digitization . . . . .	153
126	12.3 Reconstruction . . . . .	156
127	12.3.1 Tracking . . . . .	156
128	12.3.2 Additional Reconstruction Algorithms . . . . .	158
129	<b>13 Integration and Expected Performance</b>	<b>159</b>
130	13.1 Overview . . . . .	159
131	13.2 SIDIS Program . . . . .	159
132	13.3 PVDIS Program . . . . .	163

133	13.3.1	Acceptances, efficiencies, and systematic uncertainties for PVDIS . . . . .	163
134	13.3.2	Kinematics, Resolution and Calibration for PVDIS . . . . .	165
135	13.4	$J/\psi$ Program . . . . .	169
136	<b>14</b>	<b>Data Acquisition</b>	<b>172</b>
137	14.1	Introduction and Requirements . . . . .	172
138	14.1.1	SIDIS Trigger and Rate Estimate . . . . .	173
139	14.1.2	$J/\psi$ Trigger and Rate Estimate . . . . .	173
140	14.1.3	PVDIS Trigger and Rate Estimate . . . . .	173
141	14.2	DAQ Hardware and Trigger . . . . .	174
142	14.2.1	GEM readout . . . . .	174
143	14.2.2	SIDIS Configuration . . . . .	176
144	14.2.3	PVDIS Configuration . . . . .	177
145	14.3	Event size from FADC . . . . .	179
146	14.4	Data rates, event size, and tape storage . . . . .	180
147	14.5	Hall DAQ installation . . . . .	181
148	14.5.1	Experiment switch over . . . . .	181
149	14.6	Managing data rates . . . . .	181
150	14.7	Summary and Pre R&D plans . . . . .	182
151	<b>15</b>	<b>Radiation damage estimates and Activation</b>	<b>187</b>
152	15.1	Radiation damage to GEM electronics . . . . .	187
153	15.2	Power deposited . . . . .	188
154	15.2.1	Power in 1st baffle (due to Möllers), (Cooling, activation) . . . . .	189
155	15.2.2	Power in exit hole in magnet (elastics) (Cooling, activation) . . . . .	189
156	15.2.3	Power in the entrance surface of the magnet (Cooling, activation) (external target configurations) . . . . .	190
157	15.2.4	Heat load in magnet cryostat . . . . .	191
158	15.3	Estimates for radiation damage in the Hall . . . . .	192
159	15.3.1	Radiation damage to electronics in Hall . . . . .	192
160	15.3.2	Radiation from beam pipe . . . . .	193
161	15.3.3	Radiation with external targets . . . . .	194
162			
163	<b>16</b>	<b>Slow Controls</b>	<b>201</b>
164	16.1	General Requirements . . . . .	201
165	16.2	Frontend GUIs . . . . .	201
166	16.3	High/Low Voltage Controls . . . . .	202
167	16.4	DAQ Crate Control . . . . .	202
168	16.5	Gas Systems Requirements . . . . .	202
169	16.6	Detector Systems . . . . .	202
170	<b>17</b>	<b>Electron Beam Polarimetry</b>	<b>203</b>
171	17.1	Compton Polarimetry . . . . .	203
172	17.2	The Hall A Compton Polarimeter Baseline Upgrade . . . . .	203
173	17.3	Upgrades Beyond the Baseline . . . . .	205
174	17.3.1	Laser System and Luminosity . . . . .	206
175	17.3.2	Alternative Laser System . . . . .	208
176	17.3.3	Chicane Magnet Modification . . . . .	210

177	17.3.4 Photon Detection . . . . .	210
178	17.4 Systematic Uncertainties . . . . .	211
179	17.4.1 Sources of Correlated Error . . . . .	211
180	17.4.2 Systematic Errors for the Electron Detector . . . . .	211
181	17.4.3 Systematic Errors for the Photon Detector . . . . .	214
182	17.5 Summary of Compton Polarimetry . . . . .	215
183	17.6 Møller Polarimetry . . . . .	215
184	17.7 The Hall A Upgrade: “High Field” Iron Foil Targets . . . . .	216
185	17.7.1 Ferromagnetic Foil Targets . . . . .	217
186	17.7.2 Simplified Møller Scattering Target Assembly . . . . .	219
187	<b>18 Supports and Infrastructure</b>	<b>221</b>
188	18.1 Magnet Support . . . . .	221
189	18.2 Endcap Support Structure and Motion Mechanism . . . . .	221
190	18.3 Support Structure for Equipment Located Inside Cryostat Bore . . . . .	221
191	18.4 Power Requirements . . . . .	221
192	<b>19 Installation</b>	<b>223</b>
193	19.1 Experimental Layout . . . . .	223
194	19.2 Magnet Moving and Placement . . . . .	223
195	19.3 Helium Dewar Support and Upper Access Platform . . . . .	227
196	19.4 Endcap Forward Angle Detector Package Installation Structure . . . . .	227
197	19.5 Large Angle Detector and Baffle Installation Mechanism . . . . .	227
198	19.6 Light Gas Cherenkov Installation Structure . . . . .	228
199	<b>20 Project Status and Proposed Management Organization</b>	<b>229</b>
200	20.1 Collaboration and Organization . . . . .	229
201	20.2 Cost estimation . . . . .	231
202	<b>Bibliography</b>	<b>232</b>
203	<b>Appendices</b>	<b>248</b>
204	<b>Appendix A Summary of Recommendations from the 2015 SoLID Director’s Review and</b>	
205	<b>the Responses</b>	<b>248</b>
206	A.1 On the physics relevance and risks . . . . .	248
207	A.2 On the viability of approach and the experimental technique . . . . .	249
208	A.3 On the understanding, completeness, and credibility of the resources needed for the	
209	SoLID project. . . . .	251
210	<b>Appendix B Summary of Subsystems</b>	<b>253</b>
211	B.1 Magnet . . . . .	253
212	B.2 GEM . . . . .	253
213	B.3 Light Gas Cherenkov . . . . .	254
214	B.4 Heavy Gas Cherenkov . . . . .	254
215	B.5 Electromagnetic Calorimeter and Scintillator-Pad Detector . . . . .	254
216	B.6 MRPC . . . . .	255
217	B.7 DAQ . . . . .	255

218	<b>Appendix C Software Development Effort Estimate</b>	<b>257</b>
219	C.1 Effort Estimate . . . . .	257
220	C.2 Comparison with GlueX . . . . .	257
221	C.3 Simulations Required for Project Goals . . . . .	259
222	<b>Appendix D Cost Estimations 2018</b>	<b>260</b>
223	D.1 Summary of SoLID overall cost estimation 2018 . . . . .	260
224	<b>Appendix E Cost Estimations</b>	<b>263</b>
225	E.1 Summary of SoLID overall cost estimation . . . . .	263
226	E.2 Estimation of Cost Request for Subsystems . . . . .	266
227	E.2.1 Cost of Electromagnetic Calorimeters . . . . .	266
228	E.2.2 Cost of the Light-Gas Cherenkov Counters . . . . .	267
229	E.2.3 Cost of Heavy-Gas Cherenkov Detectors . . . . .	267
230	E.2.4 Cost of GEM detectors . . . . .	268
231	E.2.5 Cost of MRPC . . . . .	268
232	E.2.6 Cost of DAQ Electronics and High Voltage Power Supplies . . . . .	269
233	E.2.7 Cost of Magnet Modification and Refurbishing . . . . .	270
234	E.2.8 Cost of Detector Support, Hall Infrastructure Upgarde and Installation . . . . .	271
235	<b>Appendix F Basis for Cost Estimates</b>	<b>272</b>
236	F.1 Cost of Electromagnetic Calorimeters . . . . .	272
237	F.1.1 Cost Estimation: 1st iteration . . . . .	272
238	F.1.2 Cost Estimation: 2nd iteration, breakdown by the year . . . . .	272
239	F.2 Cost of the Light-Gas Cherenkov Counters . . . . .	274
240	F.2.1 Cost Estimation: 1st iteration . . . . .	274
241	F.2.2 Cost Estimation: 2nd iteration, breakdown by the year . . . . .	274
242	F.3 Cost of Heavy-Gas Cherenkov Detectors . . . . .	275
243	F.3.1 Cost Estimation: 1st iteration . . . . .	275
244	F.3.2 Cost Estimation: 2nd iteration, breakdown by the year . . . . .	275
245	F.4 Cost of GEM Detectors . . . . .	278
246	F.4.1 Cost Estimation: 1st iteration . . . . .	278
247	F.4.2 Cost Estimation: 2nd iteration, breakdown by the year . . . . .	278
248	F.5 Cost of MRPC . . . . .	280
249	F.5.1 Cost Estimation: 1st iteration . . . . .	280
250	F.5.2 Cost Estimation: 2nd iteration, breakdown by the year . . . . .	280
251	F.6 Cost of DAQ Electronics and High Voltage Power Supplies . . . . .	282
252	F.6.1 Cost Estimation: 1st iteration . . . . .	282
253	F.6.2 Cost Estimation: 2nd iteration, breakdown by the year . . . . .	282
254	F.7 Cost of Magnet Modification and Refurbishing . . . . .	285
255	F.7.1 Cost Estimation: 1st iteration . . . . .	285
256	F.7.2 Cost Estimation: 2nd iteration, breakdown by the year . . . . .	285
257	F.8 Cost of Detector Support, Hall Infrastructure Upgarde and Installation . . . . .	286
258	F.8.1 Cost Estimation: 1st iteration . . . . .	286
259	F.8.2 Cost Estimation of Baffles: 1st iteration . . . . .	286
260	F.8.3 Cost Estimation: 2nd iteration, breakdown by the year . . . . .	286
261	F.9 Oversight Manpower . . . . .	286
262	F.9.1 Cost Estimation: 1st iteration . . . . .	286

263	F.9.2 Cost Estimation: 2nd iteration, breakdown by the year . . . . .	286
264	F.10 JLab Overhead . . . . .	286
265	F.10.1 Cost Estimation: 1st iteration . . . . .	286
266	F.10.2 Cost Estimation: 2nd iteration, breakdown by the year . . . . .	287

# 1 Executive Summary of the Responses to Recommendations from the Jefferson Lab Director’s Review Committee

## 1.1 Overview

To exploit the full potential of the Jefferson Lab (JLab) 12 GeV energy upgrade, a large acceptance high luminosity device, SoLID (Solenoidal Large Intensity Detector), was proposed for a rich and vibrant science program. Five SoLID experiments, one PVDIS, three SIDIS and one  $J/\psi$  production, were approved with high ratings in 2010–2012 by the JLab Program Advisory Committee. After years of work by the collaboration, a robust, low risk and flexible design concept, capable of accomplishing this broad and varied physics program, was determined. A preliminary conceptual design report (pCDR) for SoLID was submitted to the JLab Director in 2014.

A JLab Director’s Review for SoLID was held in February 2015. The review committee felt that SoLID was in a good state to move forward, but also identified a number of areas where additional work would be needed. Thirty-six recommendations were made in total (see Appendix A), with some aiming at longer term efforts required by any project of similar magnitude, and others more specifically relevant for the nearer term. After discussions with the Physics Division and JLab management, the collaboration aimed at the first step to address recommendations that are necessary to proceed with a Science Review as required for the DOE Critical Decision CD-0, while continuing to also address the longer term recommendations to the extent possible with available resources. The collaboration completed this effort, which culminated in a revised version of this pCDR document. The revised document was submitted, along with a change summary, to the review committee, who accepted it in October 2017, stating that the collaboration did “...an excellent job in addressing those recommendations in their updated Pre-CDR.” and “...the Committee believes that the SoLID Experiment is ready for its DOE Critical Decision Zero (CD0) Review.” To follow up regarding possibilities for the latter, a meeting was held in July 2018 at the DOE to discuss the SoLID plans and progress. All present at that meeting agreed that a cost update would be beneficial, and this pCDR document was updated once more accordingly.

This chapter summarizes the preparatory work to reach the milestone of the DOE Science Review. It includes the experiment specific recommendations related to the three core measurements (SIDIS, PVDIS and  $J/\psi$  production), as well as ones related to the general performance of the instrumentation to reach the scientific goals. For PVDIS, the viability of the calibration procedure to determine  $Q^2$  was studied including realistic misalignments of the detectors. The design of the baffles was re-examined including the choice of materials. For SIDIS, careful studies were performed to show the impact of SoLID compared to world data and other programs, including comparisons to projected data from JLab CLAS12 and SBS programs. Examples of physics reach, such as measurements of the transversity distribution and tensor charge, were simulated and are presented. For  $J/\psi$ , bin migration effects and trigger rates were simulated. Additional science topics that can be facilitated by SoLID, such as Generalized Parton Distributions and kaon identification in SIDIS, recommended in the review, were also considered and presented here.

Realistic simulations, as well as tracking and data acquisition development, have shown that the performance of the instrumentation will allow realization of SoLID scientific goals with the proposed design. The acceptances, efficiencies and systematic uncertainties were simulated in detail for each of the three core measurements. Meticulous magnet field modeling confirmed that the forces are tolerable and the fringe field at the polarized target location can be controlled to the desired level. Effects of possible radiation damage were carefully evaluated. Significant progress has also been made in the development of a full analysis simulation and software framework.

Beyond the items listed above which were deemed critical to the near term path to a Science



313 Review, work is continuing on the many recommended fronts. The coils, coil collars, and cryostat of  
314 the CLEO-II magnet arrived at JLab in 2016, **and work on magnet instrumentation and controls has**  
315 **begun**. Other activities include the development of GEM foil production in China and assessment  
316 of the risk factor, communication with expert groups in calorimeter design and R&D, and stability  
317 testing of the conductivity of MRPC glass. An initial study of the slow control system has been  
318 performed. A pre-R&D plan including a cost estimation was developed with inputs from the JLab  
319 management and has been submitted to DOE. Meanwhile, detector pre-R&D activities for some  
320 sub-systems are continuing and are supported by international collaborations (China and Canada),  
321 such as the calorimeter and the MRPC, and the heavy gas Cherenkov systems.

322 **Our answers to all thirty-six recommendations from the Director’s Review Panel are summa-**  
323 **rized in the next few subsections, or merged into the original pCDR. These recommendations and a**  
324 **brief answer to each recommendation are in Appendix A.**

325 As a whole, the collaboration considers the progress on SoLID to be adequately substantial and  
326 positive to enable the next phase to begin, in particular a DOE Science Review. **We therefore submit**  
327 **this recently revised pCDR, and look forward to subsequent guidance from the laboratory.**

## 328 **1.2 Physics Program**

### 329 **1.2.1 SIDIS Production of Charged Pions**

330 The SoLID SIDIS program includes three approved experiments using transversely and longitudi-  
331 nally polarized  $^3\text{He}$  targets and a transversely polarized proton ( $\text{NH}_3$ ) target, respectively. With the  
332 combination of the high luminosity and the large acceptance with a full azimuthal coverage, the  
333 SoLID SIDIS experiments will allow measurements in 4-dimensional bins with high statistics and  
334 well controlled systematics. Compared to CLAS12 and SBS SIDIS programs, SoLID has better  
335 FOM and thus higher statistics in the region  $x = (0.05, 0.55)$ , as shown in Figure 1. To demon-  
336 strate the physics impact of the SoLID SIDIS program, we performed the transversity extraction  
337 based on [1, 2] with simulated data of CLAS12, SBS and SoLID, and compare their results in Fig-  
338 ure 2. SoLID can improve the transversity uncertainty for  $u$  ( $d$ ) quark by a factor of 3 (7) over  
339 CLAS12, and by a factor of 5 (10) compared to SBS. The tensor charge determination will have  
340 similar improvements which together with neutron EDM measurements will provide constraints on  
341 quark EDMs and thus new physics beyond the Standard Model. It is also evident that the pro-  
342 jected high precision results from SoLID will provide powerful tests of Lattice QCD and much  
343 more quantitative information about TMDs and quark OAMs inside the nucleon. **In the baseline**  
344 **configuration where the international contributions are not counted, the pion PID will be limited to**  
345 **momentum above 2.5 GeV/c. The impact of the SIDIS program is still very significant as shown**  
346 **in Figure 20 and Figure 21. The international contributions with addition of MRPC detectors will**  
347 **enhance the pion PID to the full capability for momentum above 1.0 GeV/c. The enhanced baseline**  
348 **configuration will enable the full impact as shown in Figure 20 and Figure 21.**

### 349 **1.2.2 PVDIS**

350 The unique feature of SoLID, combining high luminosity and large acceptance, makes it possible  
351 to achieve the high precision needed to reach a high physics impact: using PVDIS to probe physics  
352 beyond the Standard Model (SM). Measurements of PVDIS on a deuterium target will determine the  
353 effective electron-quark neutral-weak coupling constants  $2C_{2u} - C_{2d}$  that is inaccessible with other  
354 means. PVDIS measurements can also access a number of topics in hadronic physics, including  
355 searching for charge symmetry violation in the parton distribution functions, determining the  $d/u$   
356 ratio in the proton without nuclear effects, and a clean extraction of higher-twist effects caused by

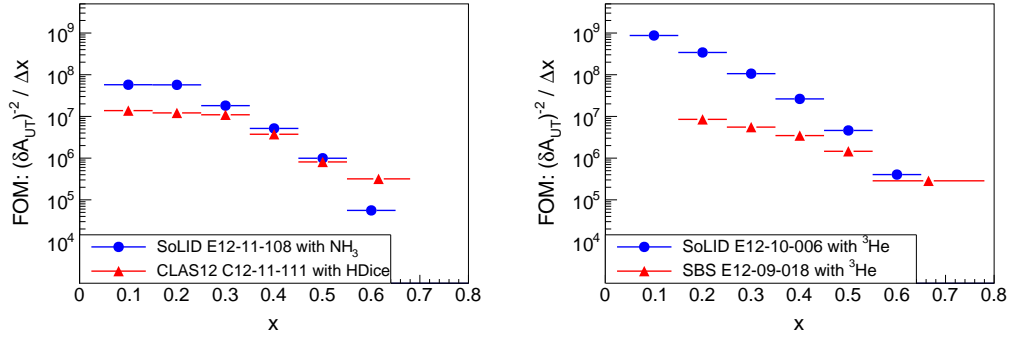


Figure 1: Comparisons of the FOM, defined as the sum of the inverse square of the statistical uncertainties of the single spin asymmetry (roughly proportional to statistics). The SoLID SIDIS experiment with the polarized  $\text{NH}_3$  target is compared with the CLAS12 experiment in the left panel. The SoLID SIDIS experiments with polarized  $^3\text{He}$  targets are compared with the SBS experiment in the right panel. In both comparisons, kinematic cuts of  $W > 2.3 \text{ GeV}$  and  $0.3 < z < 0.7$  are applied.

357 quark-quark correlations. The 6-GeV PVDIS collaboration [3] has published in a paper in Nature  
 358 with the result  $2C_{2u} - C_{2d} = -0.145 \pm 0.068$ . This is the first measurement sufficiently sensitive  
 359 to show that the  $C_{2q}$  are non-zero as predicted by the SM. One way to quantify the reach of various  
 360 experiments is to quote mass limits suitable for composite models [4], where the couplings are on  
 361 the order of  $4\pi/\Lambda^2$  where  $\Lambda$  is the compositeness mass scale. Such limits for the 6-GeV PVDIS  
 362 collaboration and the SoLID PVDIS experiment [5] are shown in Figure 3. The sensitivity to be  
 363 reached by SoLID is at the same level as LHC's for non-parity-violating couplings.

### 364 1.2.3 $J/\psi$ Production

365 Hadrons, the emergent phenomena of QCD, are in the realm of the strong interaction regime where  
 366 much of its dynamics remains to be understood. While significant progress has been achieved in  
 367 exploring QCD in its asymptotically free regime, the theory in the strong coupling regime is hardly  
 368 tractable without numerical techniques. For example, an impressive success was achieved with the  
 369 recent lattice QCD determination of the low-lying levels of the baryon spectrum [6] but there is a  
 370 long road ahead to fully grasp the implications of QCD in this regime, for example, to understand  
 371 the origin of the nucleon mass.

372 The impressive luminosity offered by SoLID combined with the large acceptance detection  
 373 opens new opportunities for measurements of rare processes with unprecedented precision. In par-  
 374 ticular, measurement of the elastic production of  $J/\psi$  on the proton near threshold could provide  
 375 unique and much needed information on the pure gluonic component of the QCD interaction, as  
 376 well as to verify the nature of the charmed “pentaquark” states recently observed at LHCb [7]. A  
 377 measurement very close to the threshold (Figure 4) where the cross section drops rapidly can pro-  
 378 vide important information on the trace anomaly, which is responsible for a large fraction of the  
 379 proton mass, and will possibly impact our understanding of QCD in the strong-coupling regime.

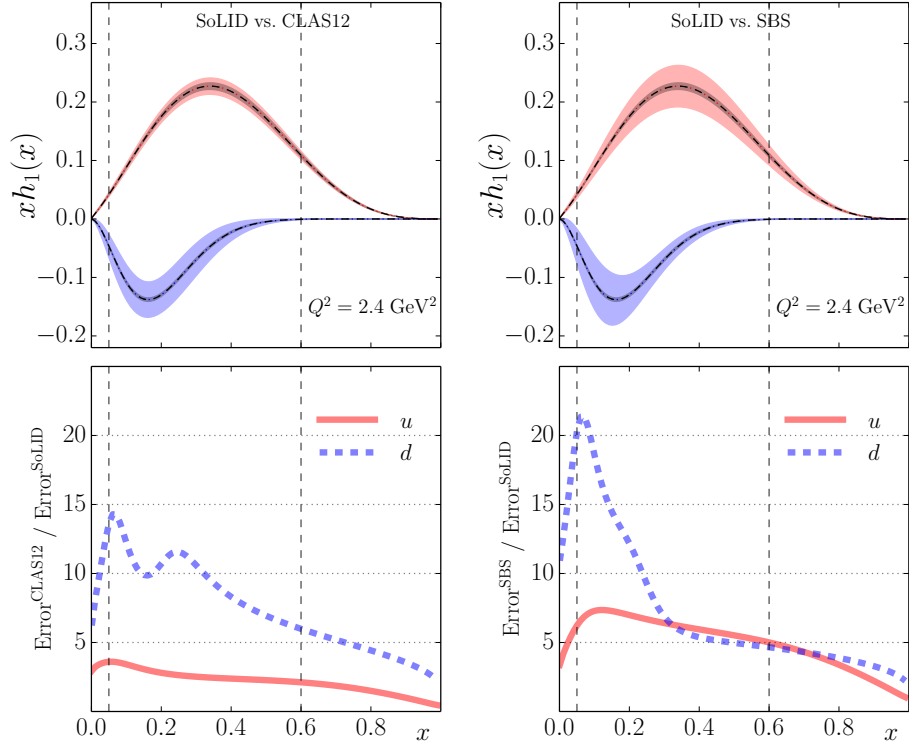


Figure 2: Comparisons of the impact on transversity extractions for up (red) and the down (blue) quarks, as the extension of published works [1, 2]. The left column shows the comparison between SoLID and CLAS12, and the right column shows the comparison between SoLID and SBS. In the upper panels, the light shaded bands show the uncertainties of the transversity function  $h_1(x)$  expected from SBS or CLAS12, and the dark shaded bands show the uncertainties expected from SoLID. The ratio of CLAS12 or SBS expected results to those from SoLID are shown in the lower panels. All results are plotted at a typical JLab12 scale  $Q^2 = 2.4 \text{ GeV}^2$ .

### 380 1.3 Possible Expansions in the Physics Reach of SoLID

#### 381 1.3.1 Generalized Parton Distributions (GPD)

382 The unique features of SoLID's large acceptance and high luminosity make it an attractive device  
 383 for the experimental study of GPDs. A number of groups have been working on developing a  
 384 SoLID-GPD program. There are several GPD experiments in different stages of study/approval. A  
 385 proposal of Time-like Compton Scattering (TCS) from an unpolarized liquid hydrogen has  
 386 been approved as a run-group experiment to test the universality of GPD, explore the underlying  
 387 principles of factorization, and quantify the importance of higher twist effects. Double Deeply  
 388 Virtual Compton Scattering (DDVCS) in the di-lepton channel on an unpolarized liquid hydrogen  
 389 target was reviewed by the JLab PAC as a Letter-Of-Intent and the collaboration was encouraged  
 390 to develop it into a two-stage program with an initial focus to have a first significant DDVCS mea-  
 391 surement (over a limited kinematic region) using the baseline SoLID setup. The Deep Exclusive  
 392 Meson Production (DEMP) with the transversely polarized  $^3\text{He}$  target has also been approved as a  
 393 run-group experiment. A measurement of DVCS on polarized  $^3\text{He}$  is under development. These  
 394 measurements, together with the planned CLAS12 and Hall A/C GPD experiments, will make a  
 395 significant contributions in disentangling different GPDs in the JLab 12-GeV kinematic region.

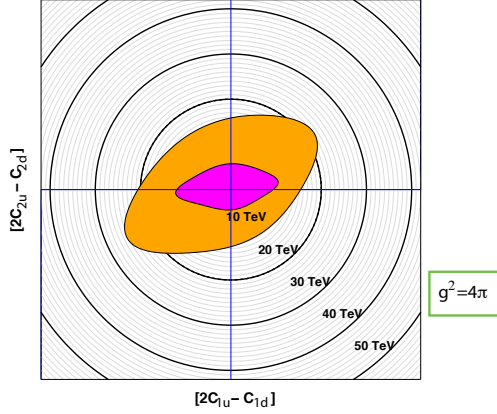


Figure 3: Projected mass limits for composite models from PVDIS. Purple region is excluded by published 6 GeV data and the orange region is the projected reach with SoLID and the final Qweak result.

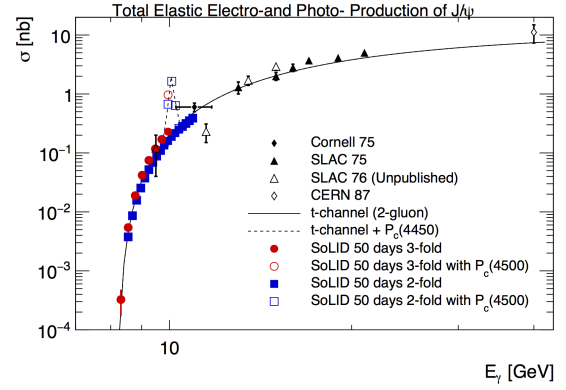


Figure 4: Projected uncertainties of total elastic  $J/\psi$  electro- and photo-production cross sections based on a 2-gluon exchange model including a projection of the LHCb pentaquark production assuming a coupling of 5%.

### 396 1.3.2 SIDIS Production of Charged Kaons

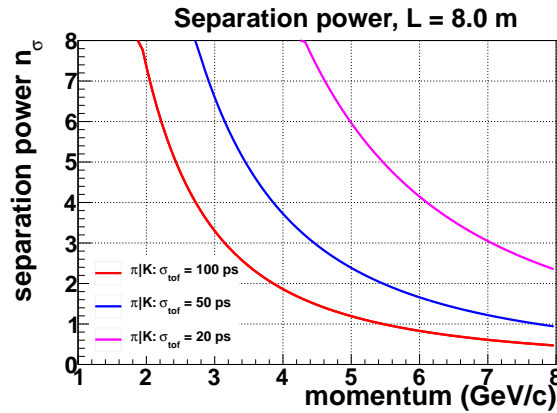


Figure 5: Kaon identification by TOF.

397 We have studied kaon identification for SoLID to potentially extend its physics programs. This  
 398 science is achievable via an enhancement from the effort of our international collaborators. A  
 399 planned R&D effort by a Chinese collaboration (Tsinghua University and USTC) on next generation  
 400 MRPC technology for SoLID, sPHENIX and EIC is being pursued, aiming for a 20 ps resolution  
 401 in a high-rate environment. While a full RICH detector for kaon detection is an alternate solution  
 402 technically, a high resolution TOF is a practical solution given the cost of the former. SoLID needs  
 403 kaon identification over a momentum range of 1 GeV/c to 7 GeV/c. Given the  $\sim 8$  meter flight  
 404 distance, a TOF time resolution of 20 ps is required to obtain a 3 sigma separation between pions  
 405 and kaons as shown in Figure 5. A promising avenue is to improve the timing of the planned SoLID  
 406 TOF-MRPC detector. Bench tests of thin-gap MRPC prototype detectors have demonstrated the  
 407 potential to reach a resolution of sub-20 ps [8, 9], while 80 ps is the current standard.. The plan

408 is to develop a prototype and readout electronics system next year. Beam test and finalizing of the  
409 detector and electronics design will be done in the following year.

## 410 **1.4 Experimental Design, Simulation and Feasibility**

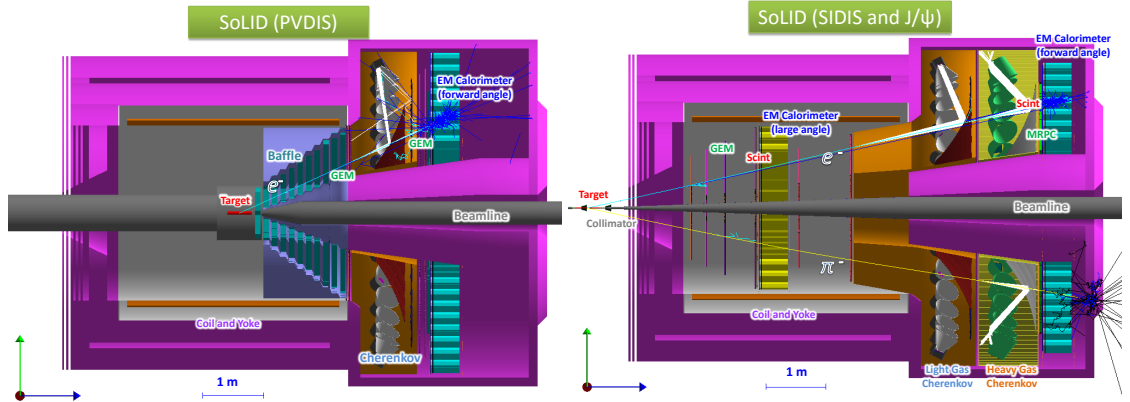
411 While SoLID is a large and complex device, composed of many elements working in concert, no  
412 single element is high risk. Novel additions to the baseline SoLID detector configuration are being  
413 considered by our international collaborators as noted, but we stress that the SoLID basic design  
414 approach relies on existing, proven detector and magnet technology to achieve the science of the  
415 core program.

### 416 **1.4.1 Solenoidal Magnet**

417 The CLEO II magnet was removed from the CESR beamline by Cornell University and JLab per-  
418 sonnel during the 2016 summer down. All ancillary power, cryogenic and control services were  
419 disconnected from the magnet in preparation for iron removal. The iron was removed layer by layer  
420 and stored at Cornell's laydown yard. **Note! I took out "until 2017 when it will be shipped to JLab"**.  
421 With the cryostat exposed, the axial transport brackets were installed and the cryostat moved to the  
422 transport frame. The service turret and neck were removed to reduce the height of the cryostat for  
423 safe highway transit. The entire unit was wrapped in marine grade shrink wrap to provide a weather  
424 barrier for the trip to JLab. Three-axis accelerometers were mounted to the cryostat to monitor loads  
425 during the road trip. All loads remained under allowable thresholds specified in the Oxford CLEO  
426 II Operating Manual. Upon arrival at JLab in November 2016, the magnet was rolled into the Test  
427 Lab for climate controlled storage, as shown in Figure 6. **Note! Also took out "We are making plans  
428 for testing the magnet with a new power supply and in-situ mapping."**



Figure 6: CLEO II magnet at JLab.

Figure 7: Left: SoLID PVDIS setup. Right: SoLID SIDIS and  $J/\psi$  setup.

430 The SoLID setups for the PVDIS and the SIDIS and  $J/\psi$  configurations are shown in Figure 7.  
 431 Substantial progress has been made in developing a SoLID simulation package with realistic sub-  
 432 system responses that includes all elements of the apparatus: EM showers in the electromagnetic  
 433 calorimeter, optical processes in the two Cherenkov detectors, energy deposition in the GEMs and  
 434 MRPC and their digitizations. A new event generator has been used for the estimation of hadron  
 435 background rates. The simulation package allowed detailed simulations of the performance and  
 436 feasibility of all core measurements, namely the PVDIS, SIDIS and  $J/\psi$  measurements.

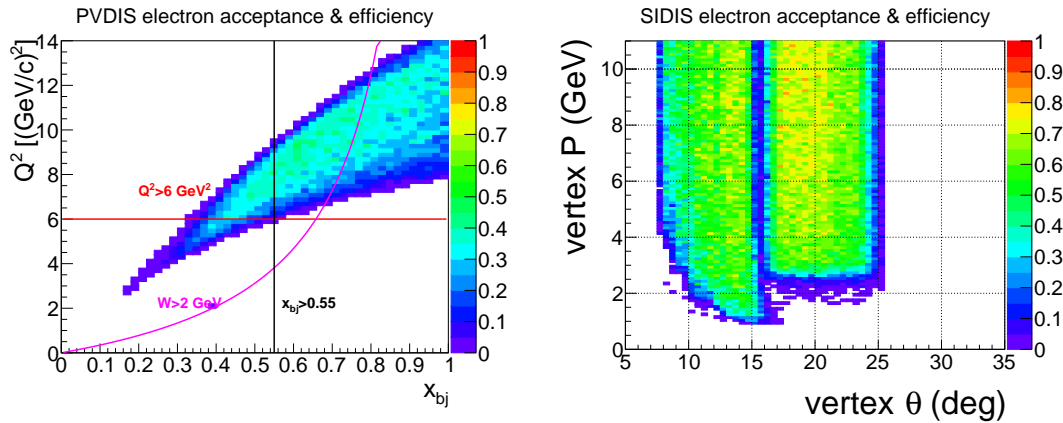


Figure 8: Left panel: electron acceptance and efficiency (except tracking) of SoLID PVDIS with the 40 cm LD2 target and the baffle. Curves show bounds of the kinematic range with  $Q^2 > 6 \text{ GeV}^2$ ,  $W > 2 \text{ GeV}$ , and  $x_{bj} > 0.55$ . Right panel: electron acceptance and efficiency (except tracking) of SoLID SIDIS with the 40 cm  $^3\text{He}$  target and two target window collimators. The result for  $J/\psi$  has a similar shape, but higher values because it has a 15 cm long target and no collimator.

437 A Kalman Filter based track finding and fitting algorithm is being developed and tested with  
 438 digitized GEM simulation data. Tracking resolution from the simulated tracking fitting results in-  
 439 cluding all material effects was studied. With background taken into account, tracking efficiency



Table 1: Average electron detection efficiencies of all SoLID sub-detectors and the total SoLID efficiency.

Detector	EC	Cerenkov	Scintillator pad and MRPC	GEM tracking	Total
average efficiency	95%	95%	98%	90%	80%

440 was obtained with the simulation. We have good electron detection efficiency from all sub-detectors.  
 441 They vary slightly across the phase space and the average efficiency values are shown in Table 1.  
 442 The PVDIS setup with its 40 cm long LD2 target has an  $\approx 0.35$  acceptance due to the baffle and  
 443 the SIDIS setup with its 40 cm long  $^3\text{He}$  target has an  $\approx 0.7$  acceptance due to the two target win-  
 444 dows collimators. Figure 8 shows the combined effect of acceptance and efficiency (except tracking)  
 445 for the two configurations. Systematic uncertainties for PVDIS and SIDIS are summarized in Ta-  
 446 ble 2. The total systematic uncertainty for  $J/\psi$  is about 11%, dominated by acceptance, and the  
 447 bin-migration effect is expected to be small. These results were used as inputs to the physics pro-  
 448 jections.

Table 2: The systematic uncertainties on the asymmetry measurements of PVDIS and SIDIS.

PVDIS Systematic (rel.)		SIDIS Systematic (abs.)		SIDIS Systematic (rel.)	
Polarimetry	0.4%	Raw asymmetry	0.0014	Target polarization	3%
$Q^2$	0.2%	Detector resolution	< 0.0001	Nuclear effect	(4 – 5)%
Radiative corrections	0.2%			Random coincidence	0.2%
Reconstruction errors	0.2%			Radiative correction	(2 – 3)%
				Diffractive meson	3%
Total	0.6%	Total	0.0014	Total	(6 – 7)%

### 449 1.4.3 Rates and Data Acquisition

450 The trigger rates were simulated with the full background, see Table 3. The SIDIS configuration,  
 451 with an expected trigger rate of 100 kHz and total data rate of over 3 GB/s, represents the greatest  
 452 challenge for SoLID data acquisition. Recent performance of GlueX and HPS DAQs with extrap-  
 453 olations by the JLab data acquisition and fast electronics groups give confidence that trigger rates  
 454 of 100 kHz and above are achievable. Data for each of the 30 sectors of SoLID will pass through  
 455 two readout controllers (ROCs), a PC based ROC for GEM data, and a VME ROC for all other  
 456 detectors. The portion of the total data rate for non-GEM detectors, about 400 MB/s, is less than 15  
 457 MB/s per VME crate, so will not limit the trigger rate at 100 kHz. GEM detector trigger rates of 50  
 458 kHz have been achieved by HPS using an APV25 sample size of six. With a planned sample size of  
 459 one for SIDIS, the GEM readout will not be limited to 100 kHz. The overall data rate required by  
 460 SIDIS, which exceeds the rate currently achieved by GlueX, can be recorded by multiplexing data  
 461 from the readout controllers to multiple event-building computers. Designing a DAQ system with  
 462 60 ROCs that can handle data rates of several GB/s will require some R&D, including firmware and  
 463 software improvements, but is feasible using technology currently in use at JLab.

## 464 1.5 Summary

465 The strong and unique physics program of SoLID, consisting of PVDIS, SIDIS and  $J/\psi$  production,  
 466 was presented in the context of the worldwide effort. The science related recommendations from

Table 3: Rates, run times and data total estimates for PVDIS, SIDIS and  $J/\Psi$  experiments. For PVDIS, there are 30 sectors each of which has a separate DAQ.

Experiment	PVDIS	SIDIS $^3\text{He}$	$J/\psi$
Trigger rate (expected) (kHz)	$15 \times 30$	100	30
Data rate (GB/s)	$0.2 \times 30$	3.2	2.5
Running time (days)	169	125	60
Total data (PB)	175	70	25

467 the Director’s Review committee have been addressed. **The device, while complex, is low risk with**  
 468 **a high potential to deliver the proposed strong and varied physics program.** The scientific reach,  
 469 unique strength and feasibility of the SoLID program demonstrate that we are ready **to proceed to**  
 470 **the** next step: the anticipated Science Review by DOE.



## 2 Introduction and Overview of SoLID Experimental Programs

### 2.1 SoLID Project Introduction/Overview

#### 2.1.1 Base Equipment Description

The SoLID (Solenoidal Large Intensity Device) project will develop a large acceptance spectrometer/detector system capable of handling very high rates. It is designed to satisfy the requirements of five approved high-scientific rated experiments, four A and one A-, as well as to become base equipment for a continued program of physics in the 12 GeV era at Jefferson Lab that requires both high luminosity and large acceptance. The base equipment composing the SoLID project includes two configurations: the “SIDIS” (Semi-Inclusive Deep Inelastic Scattering) configuration and the “PVDIS” (Parity-Violating Deep Inelastic Scattering) configuration. Although the geometrical layouts for the detectors are not the same in the two configurations, most of the following items are common:

1. A solenoidal magnet with a power supply and cryogenic system, identified as the CLEO-II magnet. With some modifications as described in the magnet section, this magnet meets the experimental requirements. The coils, coil collars, and cryostat of the CLEO-II magnet have arrived at JLab in 2016.
2. An electromagnetic calorimeter for electron identification. (In the SIDIS configuration, it is separated into two sectors, a forward sector and a large-angle sector).
3. A light gas Cherenkov detector for electron identification.
4. A heavy gas Cherenkov detector for pion (hadron) identification. This is for the SIDIS configuration only.
5. Forward-angle and a large-angle scintillator-pad detectors for time-of-flight and for photon rejection. These are for the SIDIS configuration only.
6. **GEM detectors for tracking: These are planned to be provided primarily by the UVa (Nilanga Liyanage group) as part of the SoLID project, with some potential, additional enhancement of science reach provided by our international collaboration.**
7. A data acquisition system (DAQ). Part of the DAQ electronics, mainly FADCs, will be from the JLab Physics Division Shared Electronics Pool (see next section on Dependencies to Base Equipment).
8. Supporting structures for the magnet and the detectors.
9. Requisite Hall A infrastructure to accommodate the functioning of the above — cooling, cabling, and the like.

#### 2.1.2 Dependencies to Base Equipment

The following items are requisite outside contributions to the SoLID base equipment:

1. **Enhancement of GEM detectors for tracking: A collaboration of five Chinese institutions (USTC, CIAE, Tsinghua, Lanzhou and IMP) have committed to performing R&D and applying for support from the Chinese funding agencies to construct an additional plane of GEMs and an upgrade of readout electronics for the SoLID project.**

- 509 2. A MRPC (Multi-Gap Resistive Plate Chamber) detector serving as a time-of-flight (TOF)  
 510 detector **to extend the base science reach of SoLID via enhancement of pion (hadron) and**  
 511 **the addition of kaon identification:** Two Chinese groups (Tsinghua University and USTC)  
 512 have committed to perform R&D and apply for full funding to construct the required MRPC  
 513 detector for the SoLID project. The Chinese groups, in collaboration with US institutions,  
 514 will also apply for separate funding for MRPC electronics.
- 515 3. DAQ electronics: JLab intends to have an electronics pool to share basic DAQ electronics  
 516 among the four experimental halls. Some of these electronics, mainly FADCs, will be utilized  
 517 by SoLID.
- 518 4. Magnet: JLab formally requested the CLEO-II magnet and received a positive response from  
 519 Cornell University. JLab, in coordination with Cornell, had the magnet coils, coil collars and  
 520 cryostat transported to JLab in the fall of 2016.
- 521 5. Beamline: The Hall A beam line with standard instrumentation is assumed to be in operational  
 522 condition and is not included in the SoLID base equipment.

### 523 2.1.3 Experiment-specific Dependencies

524 The five approved experiments in the SoLID research program would require the SoLID base equip-  
 525 ment, as well as the development of components outside the base equipment of the SoLID project.  
 526 The following lists such additional equipment that is either standard and existing at JLab or that will  
 527 be available for experiments planned before the SoLID experiments:

- 528 1. For SIDIS transverse  $^3\text{He}$  and longitudinal  $^3\text{He}$ : The existing polarized  $^3\text{He}$  target with per-  
 529 formance already achieved from the 6 GeV transversity (E06-010) experiment is required.  
 530 However, modifications to the stand, supports, and service may be required to accommodate  
 531 integration into SoLID.
- 532 2. For  $J/\Psi$  the standard cryogenic LH2 target system is assumed. This is standard Hall A  
 533 equipment, however the SoLID SIDIS configuration will require re-arrangement of the de-  
 534 tector system for the target and there may be significant modifications required for both to  
 535 accommodate integration into SoLID.
- 536 3. For PVDIS: A Compton polarimeter and a super-conducting Moller polarimeter (both also  
 537 required by MOLLER and to be employed for PREX also) are assumed to be available.
- 538 4. **A set of baffles. This is for the PVDIS configuration only, and may actually be made base**  
 539 **equipment as noted later via scope contingency.**

540 For completeness, though not as general dependencies for SoLID base equipment, the following  
 541 experiment-specific items which will require additional resource/funding are listed:

- 542 1. For PVDIS: a custom, high-power cryotarget is required. ESR2 is assumed to be available  
 543 (required by the Moller project).
- 544 2. For SIDIS transverse proton: a transversely polarized proton target will need development.  
 545 An initial study has been performed by Oxford which concluded that such a target is feasible.

#### 546 **2.1.4 Baseline and Enhanced Baseline Configurations**

547 The SoLID spectrometer will be a large-acceptance, high-luminosity device designed to fully exploit  
548 the discovery potential of the 12 GeV CEBAF upgrade at JLab. The proposed SoLID Spectrometer  
549 has a baseline configuration and an enhanced baseline configuration. The baseline configuration  
550 allows for the collection of a large amount of precise data that will have a significant impact on  
551 our understanding of the nucleon structure and the QCD dynamics. With additional funding for the  
552 enhanced baseline configuration, SoLID will reach its full design goals to have better efficiency,  
553 resolution and kinematic coverage to achieve the full scientific goals and maximize the 12-GeV  
554 scientific discovery potential as promised. The changes from the baseline to enhanced baseline con-  
555 figuration include tripling the number of EC shower readout channels, adding one additional GEM  
556 plane covering both forward and large angles, and placing an MRPC detector at the forward angle  
557 for improved particle identification. The rest of the document focuses on the enhanced baseline  
558 configuration, including the proposed measurements and their physics impact. In sections 2.2.7, 7.4,  
559 and 10.10, we describe in detail the changes between the two configurations and show how these  
560 changes will improve our physics results based on the studies we have carried out.

#### 561 **2.1.5 Research Program**

562 The five currently-approved, high-impact experiments approved for the SoLID project are as fol-  
563 lows:

- 564 1. SIDIS-transverse  $^3\text{He}$ : Semi-inclusive deep-inelastic-scattering of electron beam on a trans-  
565 versely polarized  $^3\text{He}$  target. It is focusing on charged pion production to study transverse  
566 spin (transversity) and other transverse momentum dependent parton distributions (TMDs). It  
567 will provide a 4-d  $(x, z, P_T, Q^2)$  mapping of the Collins, Sivers and pretzelosity asymmetries  
568 of the neutron in the valance quark region with high precision. Combined with the SIDIS  
569 measurement on the proton and the world  $e^+e^-$  data, the Collins asymmetries will allow for  
570 an extraction of one of the fundamental properties of the nucleon, the tensor charge of the  
571 u and d quarks to better than 10%, providing a benchmark test of lattice QCD. The Sivers  
572 and Pretzelosity asymmetries will allow an extraction of the Sivers function and pretzelosity  
573 function, providing crucial information on the quark orbital motion.
- 574 2. SIDIS-longitudinal  $^3\text{He}$ : Semi-inclusive deep-inelastic-scattering of electron beam on a lon-  
575 gitudinally polarized  $^3\text{He}$  target. It is focusing on charged pion production to study TMDs.  
576 Combined with transversely polarized  $^3\text{He}$  target experiment, it will provide a precision 4-d  
577  $(x, z, P_T, Q^2)$  mapping of the two worm-gear asymmetries of the neutron in the valence quark  
578 region, allowing an extraction of the two so-called worm-gear TMDs ( $g_{1T}$ , longi-transversity  
579 and  $h_{1L}^\perp$ , trans-helicity) with high precision, providing crucial information on the quark orbital  
580 motion and the spin-orbital correlations.
- 581 3. SIDIS-transverse proton: Same as in 1) but on the proton.
- 582 4. PVDIS on the deuteron and the proton: PVDIS on the deuteron will provide a precision test  
583 of the Standard Model. It provides the best measurement of the  $C_2$  coupling and also provides  
584 a precision measurement of  $\sin^2 \theta_W$  at an intermediate value of  $Q^2$ . The broad kinematical  
585 range enables the separation of the testing of the Standard Model and the study of fundamental  
586 hadron properties, including a precision measurement of possible charge symmetry violation  
587 at the partonic level and a unique measurement of the higher-twist effect (twist-4 term). The

588 proton measurement provides a clean measurement of the d-quark over u-quark ratio in the  
589 high- $x$  region without nuclear effects.

590 5.  $J/\Psi$  production near threshold: This fully exclusive measurement of the electroproduction  
591 of  $J/\Psi$  mesons from protons near threshold will be sensitive to the non-perturbative gluonic  
592 interaction between the  $J/\psi$  and nucleon, and might reveal an enhancement of the cross  
593 section just above the production threshold. This in turn could be a manifestation of the  
594 important role of the conformal anomaly. A further consequence is whether or not  $J/\psi$ -  
595 nuclear bound states would exist in nature. This experiment could open a new window to  
596 study QCD in the non-perturbative region using charmonium in a multi-phase program.

597 All proposals are available at

598 [http://www.jlab.org/exp\\_prog/generated/12GeV/halla.html](http://www.jlab.org/exp_prog/generated/12GeV/halla.html)

## 599 **2.2 SIDIS Program**

### 600 **2.2.1 Introduction**

601 Deep inelastic lepton-nucleon scattering (DIS) experiments have played a fundamental role in de-  
602 scribing the partonic momentum structure of hadrons. The unpolarized parton distribution functions  
603 (PDF) have been extracted with excellent precision over a large range of  $x$  and  $Q^2$  from DIS, Drell-  
604 Yan and other processes after several decades of experimental and theoretical efforts. The compari-  
605 son of the structure functions in the large  $Q^2$  range with QCD evolution equations has provided one  
606 of the best tests of QCD.

607 When the target and/or beam are polarized the essential properties of spin-angular momentum  
608 structure of hadrons is probed. Three decades of intensive experimental and theoretical investiga-  
609 tion have resulted in a great deal of knowledge on the partonic origin of the nucleon spin structure.  
610 Motivated by the “spin crisis” from the European Muon Collaboration experiment in the 1980s [11],  
611 the longitudinal polarized parton distribution functions have been determined with significantly im-  
612 proved precision over a large region of  $x$  and  $Q^2$  from polarized deep-inelastic (DIS) experiments  
613 carried out at CERN, SLAC, DESY in the last two decades, and more recently at JLab and at RHIC  
614 from polarized proton-proton scattering (see [12, 13] for reviews and compilation of references).  
615 In particular, considerable knowledge has been gained from inclusive DIS experiments on the lon-  
616 gitudinal structure – the  $x$ -dependence and the helicity distributions – in terms of the unpolarized  
617 (denoted  $q^a(x)$  or  $f_1^a(x)$ ) and helicity (denoted  $\Delta q^a(x)$  or  $g_1^a(x)$ ) parton distribution functions for  
618 the various flavors (indicated by  $a$ ).

619 In more recent experimental and theoretical studies, it has become evident that precise knowl-  
620 edge of the transverse structure of partons is essential to unfold the full momentum and spin  
621 structure of the nucleon. This concerns in particular the investigations of the chiral-odd trans-  
622 versely polarized quark distribution function or transversity [14] (denoted as  $\delta q(x)$ ,  $h_1(x)$  or also  
623  $\Delta_T q(x)$ ) which is probed in transverse spin polarization experiments. Like the axial charge  $\Delta q^a =$   
624  $\int_0^1 dx (g_1^a(x) + g_1^{\bar{a}}(x))$ , the tensor charge  $\delta q^a = \int_0^1 dx (h_1^a(x) - h_1^{\bar{a}}(x))$  is a basic property of the  
625 nucleon. The essential role of the transversity distribution function emerges from a systematic ex-  
626 tension of the QCD parton model to include transverse momentum and spin degrees of freedom.  
627 In this context, semi-inclusive deep-inelastic lepton nucleon scattering (SIDIS) has emerged as an  
628 essential tool to probe both the longitudinal and transverse momentum and spin structure of the nu-  
629 cleon. The azimuthal dependence in the scattering of leptons off transversely polarized nucleons is  
630 explored through the analysis of transverse single spin asymmetries (TSSAs). Recent work [15–17]  
631 predicts that these observables are factorized convolutions of leading-twist transverse momentum

632 dependent parton distributions (TMDs) and fragmentation functions (FFs) at low transverse momen-  
 633 tum. These functions provide *essential non-perturbative* information on the partonic sub-structure  
 634 of the nucleon; they offer a rich understanding of the motion of partons inside the nucleon, of the  
 635 quark orbital properties, and of spin-orbit correlations. They also provide essential information on  
 636 multi-parton correlations at leading-twist, allowing us to explore and uncover the dynamics of the  
 637 quark-gluon structure of the nucleon.

638 At leading twist if we integrate over the transverse momenta of quarks, the three quark distri-  
 639 bution functions remain: the unpolarized parton distribution  $f_1$ , the longitudinal polarized parton  
 640 distribution  $g_1$ , and the quark transversity distribution  $h_1$ . Besides  $f_1$ ,  $g_1$  and  $h_1$ , there are five  
 641 more transverse momentum dependent distribution functions [15, 16]. Fig. 9 tabulates all these  
 642 eight TMDs according to the polarizations of the quark (f, g, h) and nucleon (U, L, T). Since these  
 643 TMDs provide the description of the parton distributions beyond the collinear approximation, they  
 644 depend not only on the longitudinal momentum fraction  $x$ , but also on the transverse momentum,  
 645  $k_T$ . An intuitive interpretation of the  $k_T$  dependent transversity distribution,  $h_1$ , is that it gives the  
 646 probability of finding a transversely polarized parton inside a transversely polarized nucleon with  
 647 certain longitudinal momentum fraction  $x$  and transverse momentum  $k_T$ . The JLab 12 GeV up-  
 648 grade provides a unique opportunity to extend our understanding of nucleon spin and momentum  
 649 structure by carrying out multi-dimensional precision studies of longitudinal and transverse spin  
 650 and momentum degrees of freedom from SIDIS experiments with high luminosity in combination  
 651 with large acceptance detectors. Such a program will provide the much needed kinematic reach to  
 652 unfold the momentum and flavor structure of the nucleon. In the next section, we summarize the  
 653 essential role that transverse polarization studies play in unfolding this structure in SIDIS.

### 654 2.2.2 Transverse Structure and Semi-Inclusive Deep Inelastic Scattering

655 The transverse spin and momentum structure of the nucleon was first discussed in 1970s [18, 19]  
 656 followed by renewed interest in late 1980s [14, 20]. The transversity function is a chirally odd quark  
 657 distribution function, and the least known among the three leading twist parton distribution func-  
 658 tions. It describes the net quark transverse polarization in a transversely polarized nucleon [20]. In  
 659 the non-relativistic limit, the transversity distribution function  $h_1(x, Q^2)$  is the same as the longi-  
 660 tudinal quark polarization distribution function,  $g_1(x, Q^2)$ . Therefore, the transversity distribution  
 661 function probes the relativistic nature of the quarks inside the nucleon.

662 There are several interesting properties of the quark transversity distribution. First it does not  
 663 mix with gluons; that is, it evolves as a non-singlet distribution [21] and doesn't mix with gluons  
 664 under evolution and thus has valence-like behavior [22]. Secondly in the context of the parton model  
 665 it satisfies the Soffer bound [23], which is an inequality among the three leading twist distributions,  
 666  $|h_1^q| \leq \frac{1}{2}(f_1^q + g_1^q)$ , based on unitarity and parity conservation. QCD evolution of transversity was  
 667 studied in Ref. [24], where it was shown that Soffer's inequality holds up to next to leading order  
 668 (NLO) QCD corrections. In the past [25] and more recently [26], studies have been performed that  
 669 consider the violation of this bound. Therefore, it is interesting to experimentally test the Soffer's  
 670 inequality as a function of  $Q^2$ . Lastly, the lowest moment of  $h_1^q$  is the tensor charge, which has been  
 671 calculated from lattice QCD [27] and various models [28–33]. Due to the valence-like nature of the  
 672 transversity distribution, measuring transversity in the high- $x$  region (JLab kinematics) is crucial to  
 673 determine tensor charge of quarks. The experimental determination of the transversity function is  
 674 challenging - it is not accessible in polarized inclusive DIS measurements when neglecting quark  
 675 masses -  $h_1$  decouples at leading twist in an expansion of inverse powers of the hard scale in in-  
 676 clusive deep-inelastic scattering due to the helicity conserving property of the QCD interactions.  
 677 However, paired with another hadron in the initial state *e.g.* double polarized Drell-Yan processes

678 (two transversity distributions) [19], or in the final state, *e.g.* semi-inclusive deep-inelastic [34] scat-  
 679 tering (transversity and Collins fragmentation function), leading twist  $h_1$  can be accessed without  
 680 suppression by a hard scale.

681 The most feasible way to access the transversity distribution function is via an azimuthal sin-  
 682 gle spin asymmetry, in semi-inclusive deep-inelastic lepto-production of mesons on a transversely  
 683 polarized nucleon target,  $e N^\uparrow \rightarrow e \pi X$ . In this case the chiral-odd partner is the Collins frag-  
 684 mentation function,  $H_1^\perp$  [34], which has been extracted from charged pion pair production from  
 685  $e^+e^-$  annihilation [35]. Assuming factorization, schematically this transverse single spin asymme-  
 686 try (TSSA) contains  $h_1$  and  $H_1^\perp$ ,  $A_{UT} \sim h_1 \otimes H_1^\perp$  ( $U \equiv$  unpolarized lepton beam,  $T \equiv$  transversely  
 687 polarized target) [16].

688 The first evidence of non-trivial transverse spin effects in SIDIS has been observed in the trans-  
 689 verse single spin asymmetries measured by the HERMES [36–38], and the COMPASS [39, 40]  
 690 experiments from a transversely polarized proton or deuteron target, where an unpolarized lepton  
 691 beam is scattered off  $l p^\uparrow \rightarrow l' h X$ . Besides the non-zero Collins asymmetry, which contains  $h_1$   
 692 and  $H_1^\perp$  discussed previously, another non-zero asymmetry (Sivers asymmetry), was also observed.  
 693 The Sivers asymmetry is associated with a naive T-odd transverse momentum dependent (TMD)  
 694 parton distribution function [41]. More recently, results on Collins and Sivers asymmetries on neu-  
 695 tron were reported for the first time using a polarized  $^3\text{He}$  target at Jefferson Lab [42]. In contrast  
 696 to inclusive deep-inelastic lepton-nucleon scattering where transverse momentum is integrated out,  
 697 these processes are sensitive to the transverse-momentum scale,  $P_T$ , which is on the order of the  
 698 intrinsic quark momentum,  $k_T$ ; that is  $P_T \sim k_T$ . This is evident by considering the generic struc-  
 699 ture of the TSSA for a transversely polarized nucleon target which is characterized by interference  
 700 between helicity flip and helicity non-flip amplitudes  $A_{UT} \sim \text{Im}(f^{*+} f^-)$ . In the collinear limit of  
 701 QCD, partonic processes conserve helicity and Born amplitudes are real [43]. For this structure to  
 702 be non-zero at leading twist we must go beyond the collinear limit where such a reaction mechanism  
 703 requires a recoil scale sensitive to the intrinsic quark transverse momentum. This is roughly set by  
 704 the confinement scale  $k_T \sim \Lambda_{\text{QCD}}$  [44]. Because strongly interacting processes conserve parity  
 705 transverse spin asymmetries are described by T-odd correlations between transverse spin  $\mathcal{S}_T$ , longi-  
 706 tudinal momentum  $\mathbf{P}$  and intrinsic quark momentum  $\mathbf{k}_T$  [34, 41], which are depicted by the generic  
 707 vector product  $i\mathcal{S}_T \cdot (\mathbf{P} \times \mathbf{k}_\perp)$ . These correlations imply a leading twist reaction mechanism which  
 708 is associated with a naive T-odd transverse momentum dependent (TMD) parton distribution [41]  
 709 and fragmentation [34] function (PDF & FF).

710 A crucial theoretical breakthrough [45–47] was that the reaction mechanism is due to non-trivial  
 711 phases arising from the color gauge invariant property of QCD. This leads to the picture that TSSAs  
 712 arise from initial and final state interactions [48–50] (ISI/FSI) of the active quark with the soft  
 713 distribution or fragmentation remnant in SIDIS, which manifests itself as a gauge link that links  
 714 the bilocal quark configuration. This gauge link gives rise to the final state gluonic interactions  
 715 between the active quark and target remnant. Thus, T-odd TMDs are of crucial importance because  
 716 they possess transverse spin polarization structure as well as the necessary phases to account for  
 717 TSSAs at leading twist. Further work on factorization theorems for SIDIS indicate that there are two  
 718 leading twist T-odd TMDs; the Sivers function, denoted as  $f_{1T}^\perp$ , describing the probability density  
 719 of finding unpolarized partons inside a transversely polarized proton, is one of these functions. All  
 720 these aforementioned ingredients (TMD, FF, gauge link) enter the factorized [17] hadronic tensor  
 721 for semi-inclusive deep-inelastic scattering.

722 Exploring the transverse spin structure of the TMD PDFs reveals evidence of a rich spin-orbit  
 723 structure of the nucleon. When the transverse spin and momentum correlations are associated with  
 724 the nucleon, where the quark remains *unpolarized*, the Sivers function [41] describes the helicity  
 725 flip of the nucleon target in a helicity basis. Since the quark is unpolarized in the Sivers func-



tion, the orbital angular momentum of the quarks must come into play to conserve overall angular momentum in the process [51, 52]. Indeed a partonic description of the Sivers and Boer-Mulders functions requires wave function components with nonzero orbital angular momentum and thus provides information about the correlation between the quark orbital angular momentum (OAM) and the nucleon/quark spin, respectively [48, 53].

Unlike the Sivers function, which provides a clean probe of the QCD FSI, the functions  $g_{1T}$  and  $h_{1L}^\perp$  are (naive) T-even, and thus do not require FSI to be nonzero. Nevertheless, they also require interference between wave function components that differ by one unit of OAM and thus require OAM to be nonzero. Recently, a first ever determination of  $g_{1T}$  was reported [54] using a polarized  $^3\text{He}$  target at Jefferson Lab, in which a positive azimuthal asymmetry for  $\pi^-$  production on  $^3\text{He}$  and the neutron was observed, while the  $\pi^+$  asymmetries are consistent with zero. Finally, the pretzelosity  $h_{1T}^\perp$  requires interference between wave function components that differ by two units of OAM (e.g. p-p or s-d interference). Combining the wealth of information from all these functions could be invaluable for disentangling the spin orbit correlations in the nucleon wave function, thus providing important information about the quark orbital angular momentum.

Complementary to Generalized Parton distributions (or Impact Parameter Dependent distributions), which describe the probability of finding a parton with certain longitudinal momentum fraction and at certain transverse position  $b$  (1-D momentum space and 2-D coordinate space), TMDs give a description of the nucleon structure in 3-D momentum space. Furthermore, by including the transverse momentum of the quark, the TMDs reveal important information about the nucleon/parton spin-orbital angular momentum correlations.

### 2.2.3 The Phenomenology TSSAs and TMDs

All eight leading twist TMDs can be accessed in SIDIS. The transversity, Sivers, and pretzelosity TMDs can be accessed through a transversely polarized target. There are three mechanisms which can lead to the single (transversely polarized target) spin azimuthal asymmetries, which are the Collins asymmetry, the Sivers asymmetry, and the pretzelosity asymmetry. As mentioned previously, the quark transversity function in combination with the chiral-odd Collins fragmentation function [34] gives rise to an azimuthal (Collins) asymmetry in  $\sin(\phi_h + \phi_S)$ , where azimuthal angles of both the hadron (pion) ( $\phi_h$ ) and the target spin ( $\phi_S$ ) are with respect to the virtual photon axis and relative to the lepton scattering plane. The Sivers asymmetry [41, 55, 56] refers to the azimuthal asymmetry in  $\sin(\phi_h - \phi_S)$  due to the correlation between the transverse target polarization of the nucleon and the transverse momentum of the quarks, which involves the orbital angular momentum of the unpolarized quarks [48, 51]. The pretzelosity asymmetry is similar to Collins asymmetry except it is due to quarks polarized perpendicularly to the nucleon spin direction in the transverse plane in a transversely polarized nucleon. It has an azimuthal angular dependence of  $\sin(3\phi_h - \phi_S)$ . One can disentangle these angular distributions by taking the azimuthal moments of the asymmetries as has been done by the HERMES Collaboration [38], the COMPASS Collaboration [40], and most recently by the Jefferson Lab E06-010 collaboration [42]. With a longitudinally polarized lepton beam, and a transversely polarized target, the double spin asymmetry from SIDIS has an azimuthal angular dependence of  $\cos(\phi_h - \phi_S)$  that allows for the determination of the  $g_{1T}$  TMD as was done in [54]. With a longitudinally polarized target, the single target spin asymmetry with an azimuthal angular dependence of  $\sin(2\phi_h)$  is sensitive to  $h_{1L}^\perp$ , while the double spin asymmetry allows for the determination of the helicity TMD,  $g_1$ .

In recent years a great deal of understanding of transverse spin effects, final state interactions, and the spin orbit structure of partonic-hadronic interactions has been gained from model calculations of the TMDs and fragmentation functions. In particular the final state interactions in TSSAs

772 through the Sivers function has been studied in spectator models and the light-cone wave func-  
 773 tion approach [48–50, 57–61] as well as the bag model [62] and the NJL jet model [66]. The  
 774 Collins function has been calculated in [63–65] while studies of the universality of T-odd fragmen-  
 775 tation functions have been carried out in [67–69]. The Boer-Mulders function has been calculated  
 776 in [50, 59, 61, 70, 71] and the spin orbit effects of the pretzelosity function have been studied in both  
 777 light-cone constituent quarks models [72–75], while model predictions of azimuthal and transverse  
 778 spin asymmetries have been predicted in [59, 76, 77].

779 The first model dependent extractions of the transversity distribution have been carried out [78]  
 780 by combining SIDIS [37, 38, 79, 80] data with  $e^+e^-$  data [35] on the Collins function. Within  
 781 the uncertainties, the Soffer bound is respected. In addition, the extraction of the Sivers func-  
 782 tion [81–85] has been performed by combining SIDIS data from the HERMES [38] on the proton  
 783 and COMPASS data [40] on the deuteron. Complementing the data from the HERMES [37, 38],  
 784 COMPASS [80], and BELLE [35] experiments, the recent results from the Jefferson Lab Hall A  
 785 experiment E06-010 [42] on the neutron (with polarized  $^3\text{He}$ ) will facilitate a flavor decomposition  
 786 of the transversity distribution function,  $h_1$  [20, 86] and the Sivers distribution function  $f_{1T}^\perp$  [41]  
 787 in the overlapping kinematic regime. However a model-independent determination of these leading  
 788 twist functions requires data in a wider kinematic range with high precision in *four dimensions* of  
 789 ( $Q^2, x, z, P_T$ ).

#### 790 2.2.4 Overview of SIDIS program

791 The 12-GeV energy upgrade at CEBAF together with the newly proposed SoLID opens a great new  
 792 window to perform precision studies of the transverse spin and transverse-momentum-dependent  
 793 structure in the valence quark region for both the proton and the neutron. The experimental program  
 794 on TMDs is one of the main thrusts of the 12-GeV physics program at Jefferson Lab.

795 Currently, there are three A rated SoLID experiments (E12-10-006 [87], E12-11-007 [88], and  
 796 E12-11-108 [89]) on TMD physics with two involving a transversely (longitudinally) polarized  
 797  $^3\text{He}$  (neutron) target, and one employing a transversely polarized  $\text{NH}_3$  (proton) target. To extract  
 798 TMDs with precisions from single and double spin asymmetry measurements, the detection system  
 799 should have the capability to handle large luminosities, a full azimuthal angular coverage, good  
 800 kinematic coverage in terms of  $Q^2, x, z, P_T$  for SIDIS, and good particle identification for electrons  
 801 and charged pions. Further, the influence due to the residual magnetic field of the spectrometer  
 802 magnet needs to be negligible for polarized targets. SoLID is such a device that has been proposed  
 803 and designed for these newly approved SIDIS experiments.

804 These new SIDIS experiments employ a superconducting solenoid magnet, a detector system  
 805 consisting of forward-angle detectors and large-angle detectors, and a high-pressure polarized  $^3\text{He}$   
 806 target or a polarized  $\text{NH}_3$  target positioned upstream of the magnet. The polarized  $^3\text{He}$  target is  
 807 based on the technique of spin-exchange optical pumping of hybrid Rb-K alkali atoms. Such a  
 808 target was used successfully in the recently completed SSA experiment [42, 54] with a 6-GeV  
 809 electron beam at JLab and an in-beam polarization of 55-60% was achieved. For the polarized  
 810 proton experiment E12-11-108, an upgraded version of the JLab/UVa/SLAC polarized  $\text{NH}_3$  target  
 811 will be used. The main upgrade will involve using a new magnet to replace the aging Helmholtz-  
 812 coil magnet and to have fast spin-flip capability with the Adiabatic Fast Passage (AFP) technique.  
 813 Preliminary design study has been carried out for such a magnet with a vertical opening angle of  $\pm$   
 814  $25^\circ$  to satisfy the requirement of the experiment. The target is based on the principle of dynamic  
 815 nuclear polarization (DNP) by using microwave pumping to reach high proton polarizations [90,  
 816 91]. The CLEO-II magnet with new end caps and modification of the yolks has been identified  
 817 as the magnet of the choice for SoLID based on both the requirements of the experiments and the



818 availability of the magnet. Six layers of GEM detectors will be placed inside the coils as tracking  
 819 detectors. A combination of an electromagnetic calorimeter, gas Cherenkov counters, a layer of  
 820 Multi-gap Resistive Plate Chamber (MRPC) and a thin layer of scintillator will be used for particle  
 821 identification in the forward-angle region. As only electrons will be identified in the large-angle  
 822 region, a shashlyk-type [92, 93] electromagnetic calorimeter will be sufficient to provide the pion  
 823 rejection. More details about SoLID experimental setup, kinematic coverage, particle identification,  
 824 and other important considerations for SIDIS can be found in Section 3.2 and 3.3.

## 825 2.2.5 Beam Time and Projections

826 **E12-10-006** Experiment E12-10-006 was approved 90 days of total beam time with 15  $\mu\text{A}$ , 11/8.8  
 827 GeV electron beams on a 40-cm long, 10 amgs transversely polarized  $^3\text{He}$  target. 69 days is for  
 828 beam on the polarized  $^3\text{He}$  target, and 10 days for a dedicated study of the  $x - z$  factorization with  
 829 Hydrogen and Deuterium gas using a reference target cell. Additional 3.0 days is requested with  
 830 a longitudinal target polarization to study the systematics of potential  $A_{UL}$  contamination, where  
 831  $U$  stands for an unpolarized beam and  $L$  for a longitudinally polarized target. A total overhead  
 832 time of 8 days is requested. This overhead time will be shared among activities such as unpolarized  
 833 target runs, target spin flip and target polarization measurements, as has been done in the past during  
 834 other Hall A polarized  $^3\text{He}$  target experiments. Although beam polarization is not required for the  
 835 proposed SSA measurements, polarized beam with polarization of 85% or higher will be used for  
 836 for parasitic measurements of  $A_{LT}$ , which can be used to access  $g_{1T}$  as demonstrated in [54].



837 Projected data from E12-10-006 are binned into 4-dimensional  $(x, P_h, z, Q^2)$  bins. For a typical  
 838  $z$  and  $Q^2$  bin ( $0.40 < z < 0.45$ ,  $2 \text{ GeV}^2 < Q^2 < 3 \text{ GeV}^2$ ), data projections for Siverts asymmetry  
 839 measurements, left panel for  $\pi^+$  and right panel for  $\pi^-$ , are shown in Fig. 10 as examples. Also  
 840 shown are results from the 6-GeV experiment E06-010 [42], and predictions of Siverts asymmetries  
 841 from Anselmino *et al.* [94] with model uncertainties. For complete projections which consist of  
 842 1400 data points, we refer to the proposal [87].

843 **E12-11-007** Experiment E12-11-007 was approved 35 days of total beam time with 15  $\mu\text{A}$ , 11/8.8  
 844 GeV electron beams on a 40-cm long, 10 amgs longitudinally polarized  $^3\text{He}$  target to match about  
 845 50% statistics of experiment E12-10-006. When combined with experiment E12-10-006, this exper-  
 846 iment will not require any beam time for calibration data, including reference cell runs and detector  
 847 calibrations.

848 A maximum likelihood method [95] was used to extract angular modulations with combined,  
 849 projected data sets from both E12-11-007 and E12-10-006. Projected data are binned into 4-  
 850 dimensional  $(x, P_h, z, Q^2)$  bins. For a typical  $z$  and  $Q^2$  bin ( $0.40 < z < 0.45$ ,  $2 \text{ GeV}^2 < Q^2 <$   
 851  $3 \text{ GeV}^2$ , one of the total 48  $z - Q^2$  bins), data projections are shown in Fig. 11 as examples. For  
 852 complete projections, we refer to the proposal [88].

853 **E12-11-108** Experiment E12-11-108 was approved 94 days of total beam time with 100 nA,  
 854 11/8.8 GeV electron beams on a 3-cm long, polarized  $\text{NH}_3$  target. The 8.8 GeV beam energy will  
 855 provide precision data on the radiative corrections along with the increased  $Q^2$  coverage. 90 days  
 856 are for beam on a transversely polarized  $\text{NH}_3$  target including 7.5 days for dilution measurements,  
 857 optics, and detector calibrations. Also 4 days are requested with a longitudinal target polarization to  
 858 study the systematics of potential  $A_{UL}$  contamination. Although beam polarization is not required  
 859 for the proposed SSA measurements, a longitudinally polarized beam will be used for a parasitic  
 860 measurement of the  $A_{LT}$ , which can be used to access  $g_{1T}$ . In addition, there will be an overhead  
 861 time of 26 days for regular target annealing which does not need an electron beam.

## Leading Twist TMDs

 : Nucleon Spin    
  : Quark Spin

		Quark polarization		
		Un-Polarized (U)	Longitudinally Polarized (L)	Transversely Polarized (T)
Nucleon Polarization	U	$f_1 = \text{circle with red dot}$		$h_1^\perp = \text{circle with red dot} - \text{circle with red dot}$ Boer-Mulder
	L		$g_1 = \text{circle with red arrow} - \text{circle with red arrow}$ Helicity	$h_{1L}^\perp = \text{circle with red arrow} - \text{circle with red arrow}$
	T	$f_{1T}^\perp = \text{circle with red dot} - \text{circle with red dot}$ Sivers	$g_{1T}^\perp = \text{circle with red arrow} - \text{circle with red arrow}$	$h_{1T}^\perp = \text{circle with red dot} - \text{circle with red dot}$ Transversity $h_{1T}^\perp = \text{circle with red arrow} - \text{circle with red arrow}$

Figure 9: Leading twist TMDs classified according to the polarizations of the quark (f, g, h) and nucleon (U, L, T).

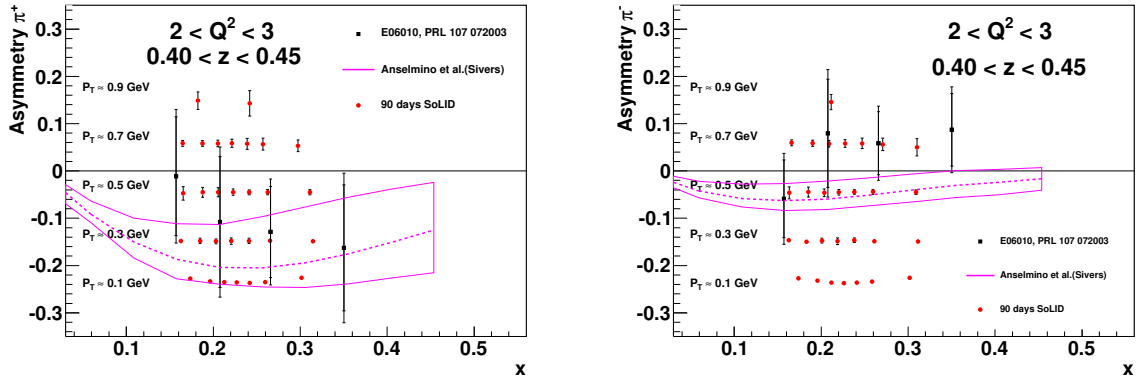


Figure 10: The left panel shows the projected Sivers asymmetry measurement for  $\pi^+$  for a typical  $z$  and  $Q^2$  bin ( $0.40 < z < 0.45$ ,  $2 \text{ GeV}^2 < Q^2 < 3 \text{ GeV}^2$ ) as a function of  $x$  with different ranges of the hadron transverse momentum labeled. The right panel shows the projection for the corresponding  $\pi^-$  Sivers asymmetry measurement. Also shown are the results from the 6-GeV experiment E06-010 [42].

862 Projected data from E12-11-108 are binned into 4-dimensional  $(x, P_h, z, Q^2)$  bins. For a typical  
863  $z$  and  $Q^2$  bin ( $0.40 < z < 0.45, 2 \text{ GeV}^2 < Q^2 < 3 \text{ GeV}^2$ ), data projections for Collins asymmetry  
864 measurements, left panel for  $\pi^+$  and right panel for  $\pi^-$ , are shown in Fig. 12 as examples. Also  
865 shown are predictions of Collins asymmetries from Anselmino *et al.* [94] with model uncertainties.  
866 For complete projections of E12-11-108, we refer to the proposal [89].

867 The combination of these three experiments will allow for accessing important information  
868 about TMDs from proton and neutron, and the flavor separation of the TMDs (transversity, Sivers,  
869 pretzelosity, and  $g_{1T}$ ) for u and d quark. A good example based on a study in Ref. [96] to demon-  
870 strate the impact of this program is shown in Fig. 13 in which the projected transversity distributions  
871 for u and d quarks are shown at a typical  $Q^2 = 2.4 \text{ GeV}^2$  based on the up-to-date knowledge of  
872 evolution of the transverse momentum dependent distribution and fragmentation functions. The ex-  
873 pected improvement in the knowledge of the transversity distribution is enormous: from the wide  
874 error bands based on the current knowledge to the narrow bands from the SoLID program, and the  
875 access to the valence quark region, which has been essentially unexplored as of now. In fact the  
876 proposed SoLID SIDIS program will allow for studies of the  $k_T$  dependence, and the  $Q^2$  evolution  
877 of the TMDs also. Furthermore, the SoLID SIDIS program will provide precise information on the  
878 tensor charge of the nucleon, an important property of the nucleon like spin or magnetic moment,  
879 and is determined by the valence quarks inside the nucleon. A quantitative study [96] demonstrates  
880 that the SoLID SIDIS program will improve the accuracy of the tensor charge determination by one  
881 order of magnitude, and allows for benchmark tests of lattice QCD predictions. The high impact of  
882 these data on the extraction of the tensor charge of the u and d quark is shown in Fig. 14.

### 883 2.2.6 Comparisons with SBS and CLAS12 SIDIS programs

884 In Table 4, we compare the experimental conditions of the SIDIS experiments with SoLID, SBS  
885 and CLAS12. The values of solid angle coverage in the table are simplified descriptions. A more  
886 realistic acceptance from GEMC is used for the estimation of the physics impact. Compared with  
887 SBS, the statistics of SIDIS events with SoLID are much better due to the large acceptance. This  
888 will allow us to have 4-dimensional bins with SoLID, while SBS will only have 3-dimensional bins.

	SoLID	SBS	SoLID	CLAS12
Experiment	E12-10-006 Approved (A)	E12-09-018 Approved (A-)	E12-11-108 Approved (A)	C12-11-111 Conditional
Targets	$^3\text{He}$ (“n”)	$^3\text{He}$ (“n”)	$\text{NH}_3$ (“p”)	HDice (“p”)
Polarization ( $P$ )	65% (60% in beam)	65% (<60% in beam)	70%	60%
Dilution ( $f$ )	0.15~0.3	0.15~0.3	0.13	0.33×80%
Luminosity ( $L \text{ cm}^{-2} \text{ s}^{-1}$ )	$1.0 \times 10^{36}$	$2.7 \times 10^{36}$	$1.0 \times 10^{35}$	$1.4 \times 10^{33}$
Solid angle ( $\Omega_e \times \Omega_h \text{ sr}^2$ )	$0.482 \times 0.139$	$0.044 \times 0.063$	$0.482 \times 0.139$	$1.14 \times 1.16$

Table 4: Comparison of the experimental conditions of SoLID, SBS, and CLAS12.

889 A comparison of the Figure of Merit (FOM), which is calculated by the sum of the inverse  
890 square of the statistical uncertainties of the SSA, is shown in Figure 15 and Figure 16. In these

891 comparisons, we applied the same kinematic cuts of  $W > 2.3$  GeV and  $0.3 < z < 0.7$ . Compared  
 892 with CLAS12, SoLID has higher statistics in smaller  $x$  region and has comparable (or slightly lower)  
 893 statistics in larger  $x$  region. Compared with SBS, SoLID has higher statistics up to about  $x \sim 0.55$ ,  
 894 while SBS has more coverage in large  $x$  region.

895 The physics impact of SoLID is the precise measurement of the TMD's in the valance region.  
 896 One highlight is the Collins SSA, which is related to the transversity distribution, which in turn is  
 897 dominated by the valance quark distribution. It is related to quark transversity distribution, which  
 898 is valance quark dominant. To compare the improvement on the determination of transversity, we  
 899 model the transversity distributions with the recent global fit of [1], which includes the TMD evo-  
 900 lution effect. We estimate the errors with the standard Hessian method [286]. The Hessian is the  
 901 second derivatives of the  $\chi^2$  with respect to the parameters at the least  $\chi^2$  point. It reflects not  
 902 only the uncertainties of the parameters but also the correlations of the parameters. The Hessian of  
 903 the world data is obtained from the covariant matrix of the global fit [1]. The Hessians of SoLID,  
 904 CLAS12, and SBS are calculated with the simulated data. To ensure that the SIDIS events are in the  
 905 current fragmentation region, which can be described by TMD factorization, we adopt the recent  
 906 theoretical study on the criteria of the current fragmentation kinematics [10] and only use the bins in  
 907 the current fragmentation region to study the physics impact. The impacts on the transversity extrac-  
 908 tions are compared in Figure 17 and Figure 18. In the comparison, only statistical uncertainties are  
 909 used to compare with CLAS12 and SBS. The improvement from SoLID data including systematic  
 910 errors is also shown in Figure 18. To remove the model dependence as much as possible, we take  
 911 the ratio between the prior uncertainties and the post uncertainties to show the improvements from  
 912 the SoLID, CLAS12, and SBS SIDIS experiments. SoLID can improve the transversity uncertainty  
 913 for  $u$  ( $d$ ) quark by a factor of 3 (7) over CLAS12, and by a factor of 5 (10) compared to SBS.

914 The tensor charge, which is the integral of transversity distributions, is a fundamental quantity  
 915 in QCD. It describes the coupling between a nucleon and a tensor current. Note that in QCD, this  
 916 correlation is different from the correlation between the longitudinal quark spin with the longitudinal  
 917 spin of the nucleon which is measured by the structure function  $g_1$ . The impact of the determination  
 918 of the tensor charge from SoLID, CLAS12, and SBS are compared in Table 5. The improvements  
 919 are shown in two ways, the typical measured  $x$  region by JLab-12 experiments and the full  $x$  region.

	World vs. SBS+CLAS12	World vs. SoLID	SBS+CLAS12 vs. SoLID	World vs. SoLID including systematics
$\delta u^{\text{measured}}$	6.1	16	2.8	6.7
$\delta d^{\text{measured}}$	1.9	17	9.3	11
$\delta u^{\text{full}}$	5.4	16	3.0	5.9
$\delta d^{\text{full}}$	1.8	17	10	10

Table 5: Comparison of improvements to tensor charge extractions. “World” represents all world available data by 2015. In the first three comparisons, only statistical errors are used, while in the last comparison both statistical and systematic errors are included. The values in the table give the ratio between the prior error and the post error. The measured region is the integral over  $x$  from 0.05 to 0.6, and the full region is the integral over  $x$  from 0 to 1.

920 One of the advantages of SoLID SIDIS experiments is that the high statistics allows us to have  
 921 four-dimensional bins. This will help study TMDs, which are three dimensional distributions. To  
 922 show the impact of SoLID on TMD measurements, we take the Siverson function as an example. In  
 923 the analysis, we do a global fit with both unpolarized multiplicity data and Siverson asymmetry data.

924 The fitting result is used as the input model for future SoLID, CLAS12, and SBS pseudo-data. The  
925 uncertainties from the world data and from inclusion of SoLID, CLAS12, and SBS are estimated in  
926 the same framework. Similar to the case of transversity extraction, we only select the bins that pass  
927 the kinematic cuts of the current fragmentation criteria. In Figure 19, we show the improvement  
928 from SoLID on the extraction of the Sivers function, and compare it with CLAS12 and SBS.

### 929 **2.2.7 SIDIS with Baseline and Enhanced Baseline Configurations**

930 The results shown in the previous sections are for the enhanced baseline configuration. Combining  
931 both the EC (Section 10.10) and GEM (Section 7.4) changes from the baseline to enhanced baseline  
932 configuration, we can increase the detection efficiency of the SIDIS events with electrons for the  
933 large-angle kinematics and pions for the forward angular range by 12%, and with electrons at the  
934 forward angle and pions at the forward angle by 2%. On average, the total SIDIS events collected  
935 will increase by 5%. For the baseline configuration, the SIDIS program is already projected to have  
936 a major impact on improving the precision of various TMDs and related physics. As an example,  
937 we present the improvement of the transversity and tensor charge uncertainties in Figure 20, and  
938 Sivers uncertainties in Figure 21. On average, a factor of 3 for u quark and 10 for d quark over  
939 the current world data can be achieved. However, we still miss low momentum pion data at the  
940 forward angle, and the corresponding low transverse momentum coverage is not ideal. The planned  
941 change from the baseline to enhanced baseline configuration by adding a plane of MRPC detectors  
942 at the forward angle will fill this gap. The ability to achieve a timing resolution of 100 ps in the  
943 high rate environment of SoLID will enable us to identify pions below 2.5 GeV by using time-of-  
944 flight. This enhanced kinematic coverage of the SIDIS program will greatly improve the data at  
945 the low transverse momentum region and a moderate  $z$  region. We also show in Figure 20 and  
946 Figure 21 that the transversity, tensor charge, and Sivers uncertainties from the enhanced baseline  
947 configuration measurement will be further reduced on average by a factor of 1.5 for both u and d  
948 quark compared with those from the baseline configuration.

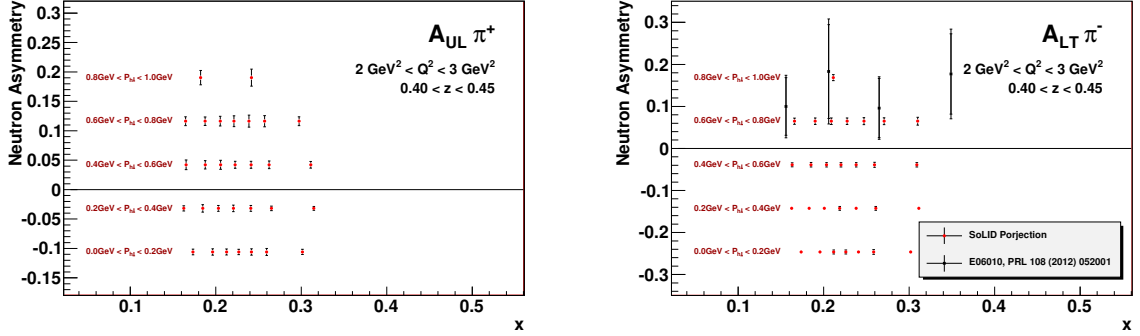


Figure 11: The left panel shows the projection for a typical  $z$  and  $Q^2$  bin ( $0.40 < z < 0.45$ ,  $2 \text{ GeV}^2 < Q^2 < 3 \text{ GeV}^2$ , one of the total 48  $z - Q^2$  bins) for the  $\pi^+$  single target spin asymmetry  $A_{UL}^{\sin(2\Phi_h)}$  measurement as a function of  $x$  with different ranges of the hadron transverse momentum labeled. The right panel shows the projection for the corresponding  $z - Q^2$  bin for the  $\pi^-$  double spin asymmetry  $A_{LT}^{\cos(\Phi_h - \Phi_S)}$  measurement. Also shown are the results from the 6-GeV experiment E06-010 [54].

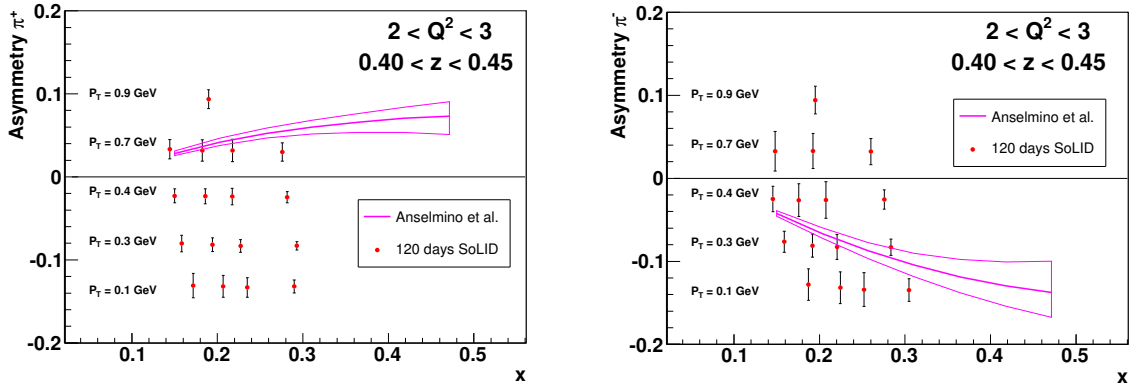


Figure 12: The left panel shows the projection for a typical  $z$  and  $Q^2$  bin ( $0.40 < z < 0.45$ ,  $2 \text{ GeV}^2 < Q^2 < 3 \text{ GeV}^2$ ) for the  $\pi^+$  Collins asymmetry measurement as a function of  $x$  with different ranges of the hadron transverse momentum labeled. The right panel shows the projection for the corresponding  $z - Q^2$  bin for the  $\pi^-$  measurement. Also shown are predictions of Collins asymmetries from Anselmino *et al.* [94] with model uncertainties.

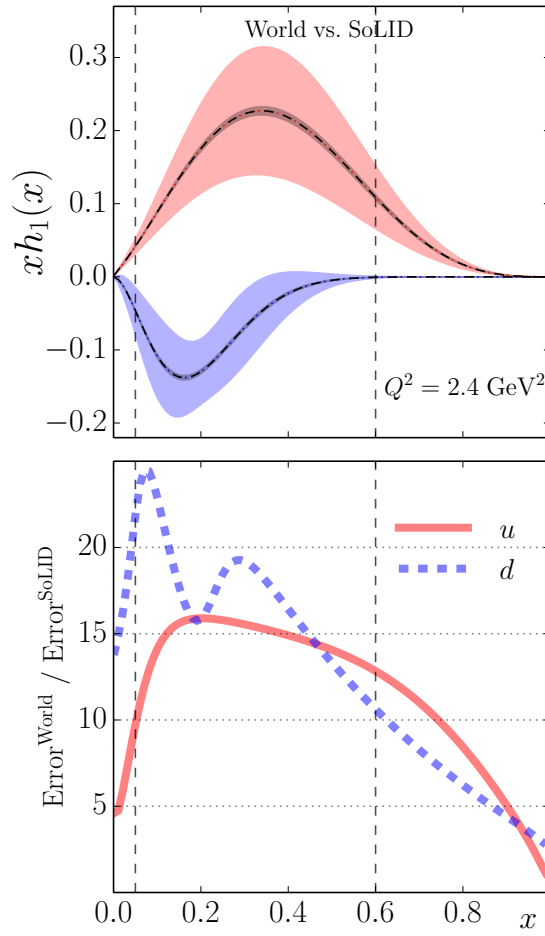


Figure 13: The impact on  $u$  and  $d$  quark transversity distributions by the SIDIS program using SoLID. The wide error bands show the current knowledge from the global analysis of the world data, and the narrow error bands show the SoLID projections. The lower panel shows the improvements, which are the ratios between the current errors and the projected errors.

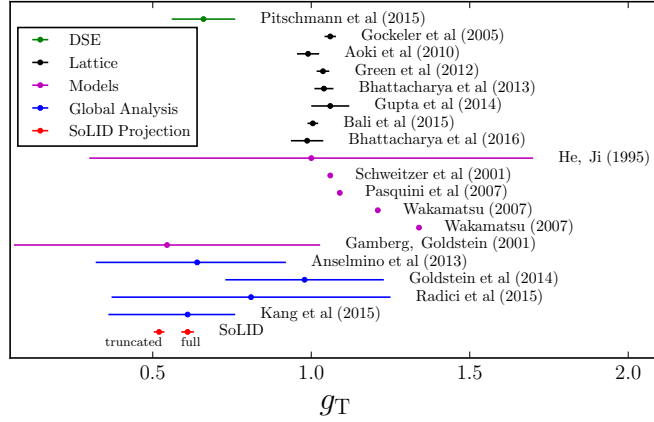


Figure 14: The impact of the projected SoLID measurement of the tensor charge together with current knowledge from models, Dyson-Schwinger equations, global analyses, and lattice QCD simulations.

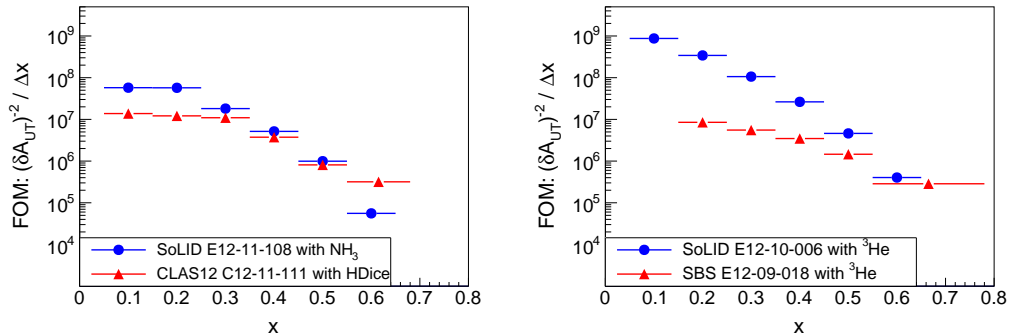


Figure 15: Comparison of the FOM at different  $x$  regions. SoLID SIDIS experiment with the proton target is compared with CLAS12 in the left panel. SoLID SIDIS experiments with the neutron target are compared to the SBS experiment in the right panel. In both comparisons, the same kinematic cuts of  $W > 2.3$  GeV and  $0.3 < z < 0.7$  are applied.



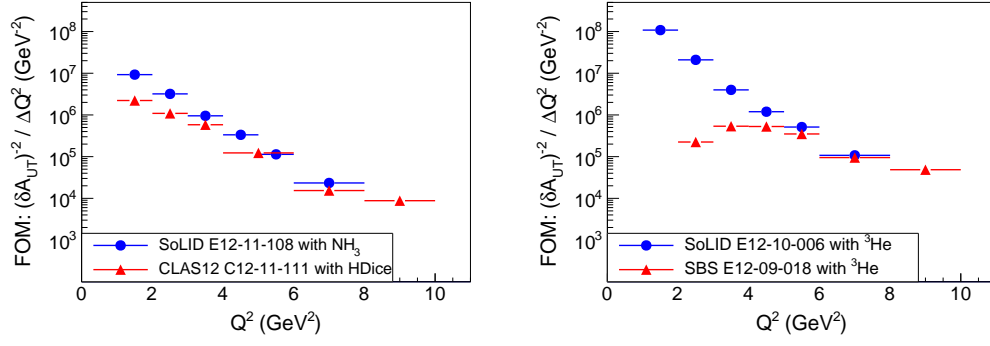


Figure 16: Comparison of the FOM at different  $Q^2$  regions. SoLID SIDIS experiment with the proton target is compared with CLAS12 in the left panel. SoLID SIDIS experiments with the neutron target are compared to the SBS experiment in the right panel. In both comparisons, the same kinematic cuts of  $W > 2.3$  GeV and  $0.3 < z < 0.7$  are applied.

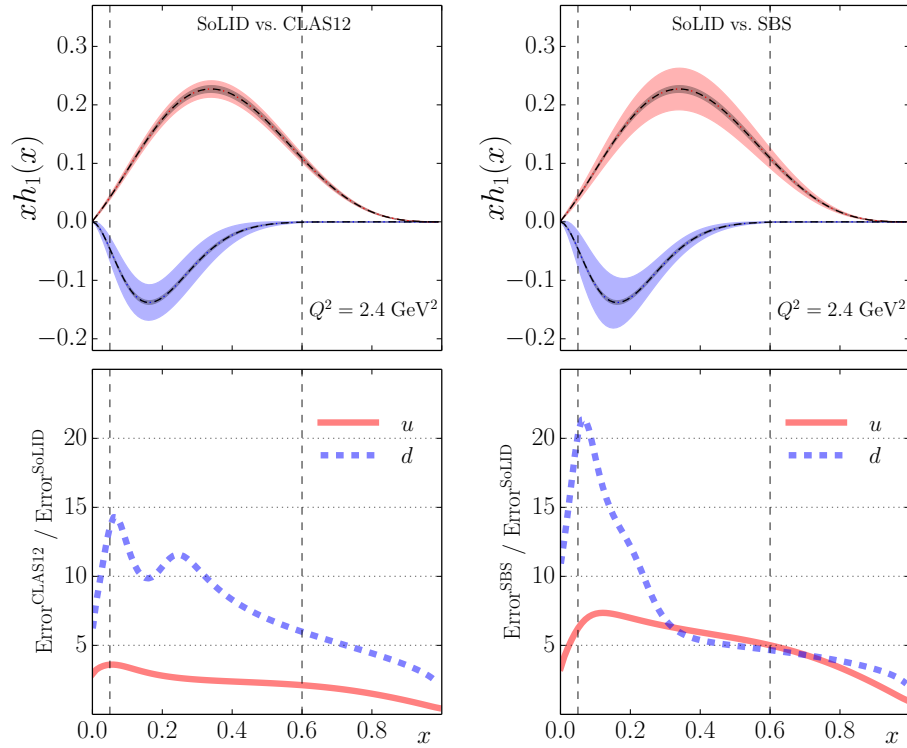


Figure 17: Comparisons of the impact on transversity extractions for up (red) and the down (blue) quarks, as the extension of published works [1, 2]. The left column shows the comparison between SoLID and CLAS12, and the right column shows the comparison between SoLID and SBS. In the upper panels, the light shaded bands show the uncertainties of the transversity function  $h_1(x)$  expected from SBS or CLAS12, and the dark shaded bands show the uncertainties expected from SoLID. The ratio of CLAS12 or SBS expected results to those from SoLID are shown in the lower panels. All results are plotted at a typical JLab12 scale  $Q^2 = 2.4$  GeV<sup>2</sup>.

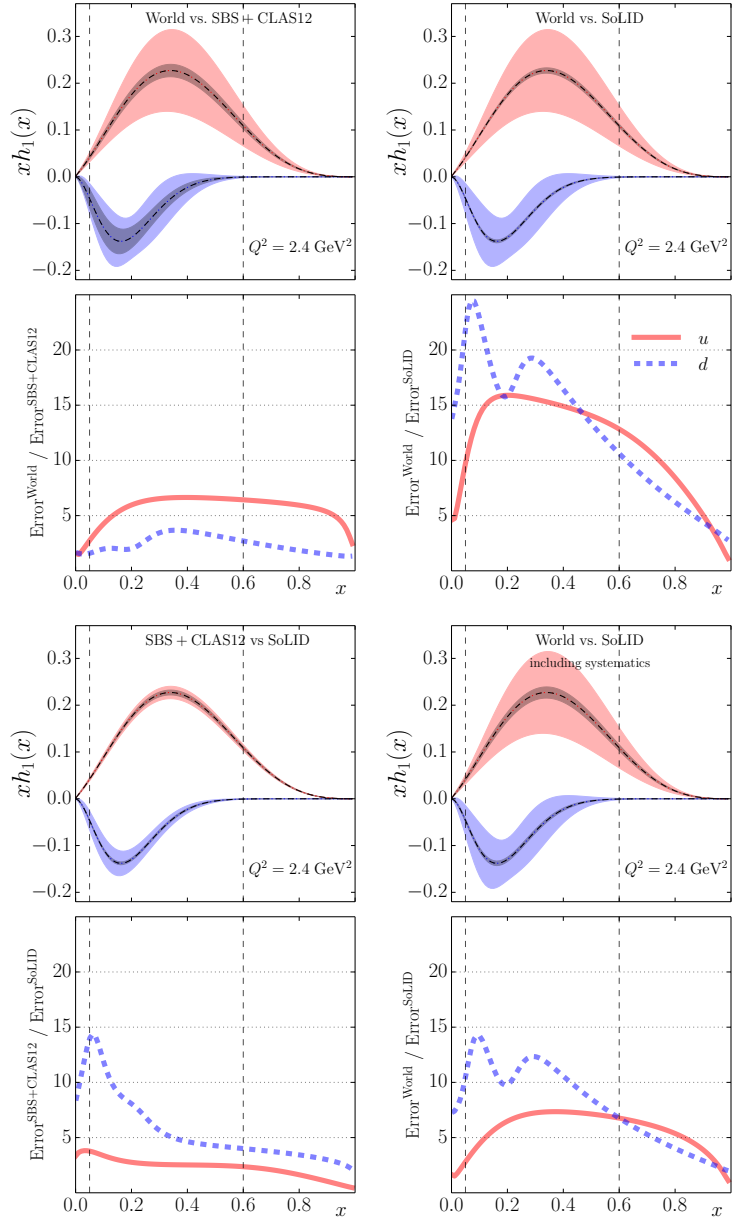


Figure 18: Comparison of the impact on the transversity extractions. The “World” represents all world available data by 2015. The upper left panel shows the improvement from future JLab12 data, i.e. SBS and CLAS12, before SoLID on the base of world available data by 2015. The upper right panel shows the improvements from SoLID data. The lower left panel shows the further improvement from SoLID data after the expected SBS and CLAS12 data. The lower right panel shows the improvements from SoLID data including the systematic uncertainties. The current uncertainties are from the global fit [1], and the future uncertainties are obtained by including the pseudo-data from these experiments with only statistical errors for the first three, and with both statistical and systematic errors for the last one. The curves in the lower panels show the improvement, which is the ratio between the prior uncertainties and the post uncertainties. The  $x$ -range between the two vertical dashed lines is directly measured by SoLID.

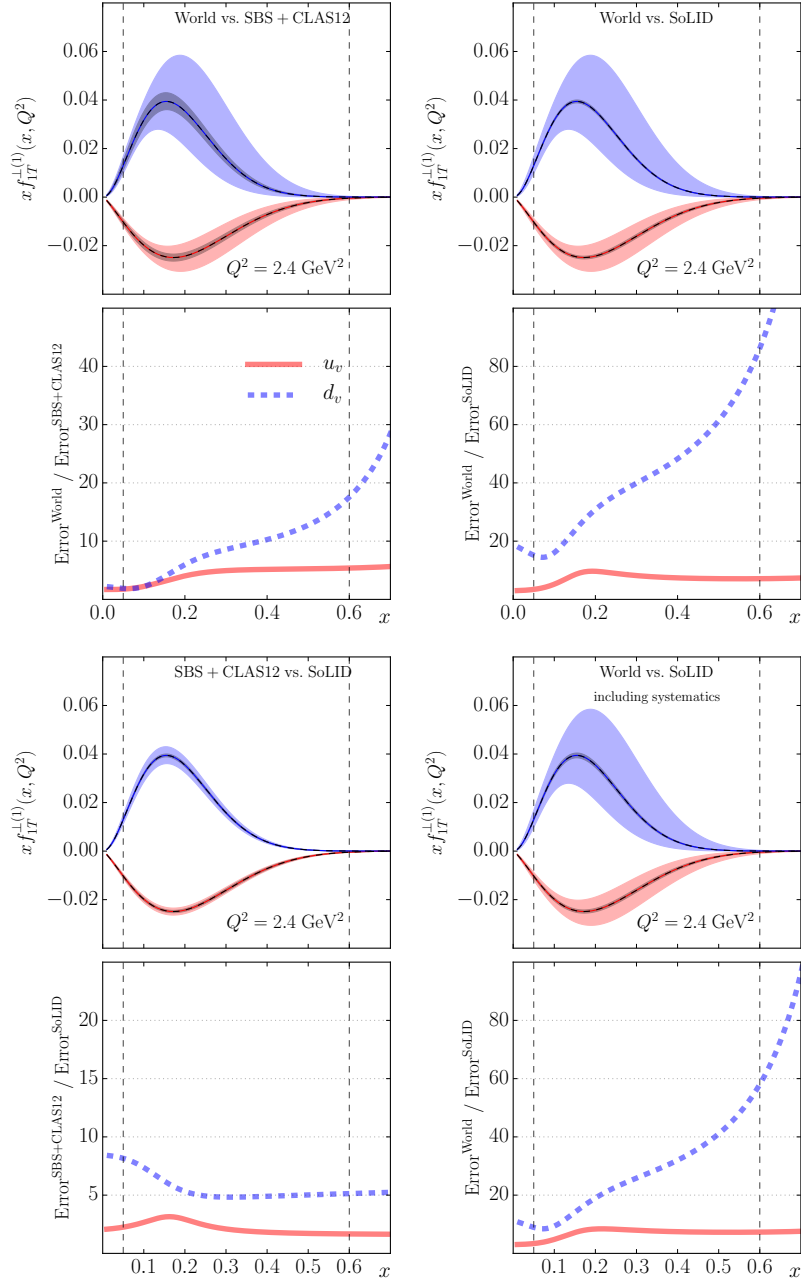


Figure 19: Comparison of the impact on the first transverse moment of the Siverts function. Labels are the same as those in Figure 18.

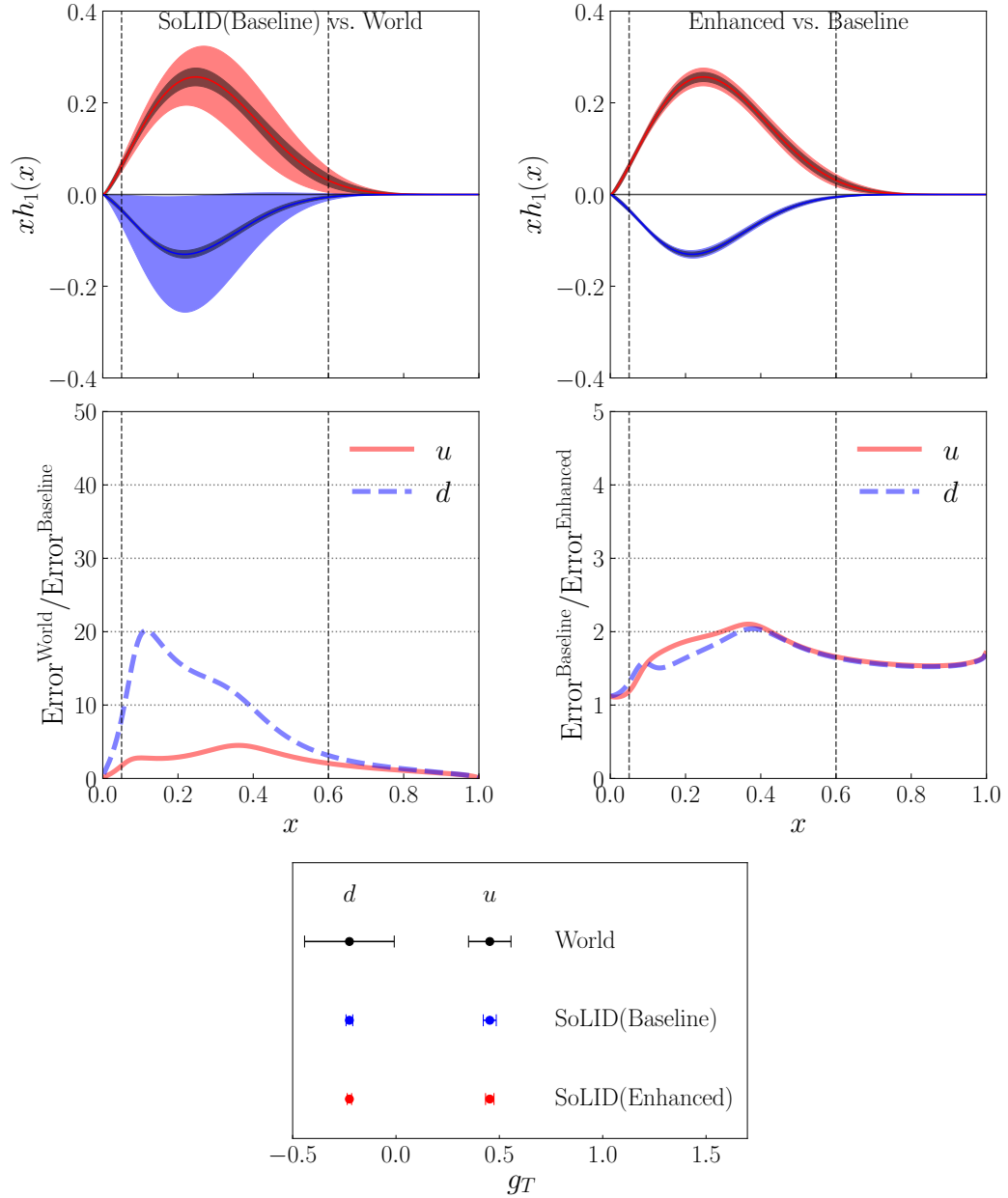


Figure 20: Upper left panel: the impact on transversity extractions for up (red) and the down (blue) quarks by SoLID baseline configuration; the outer light shaded bands show the uncertainties from the world data, and the inner dark shaded bands show the uncertainties expected from SoLID baseline configuration. Upper right panel: the comparison of the impacts between the baseline and enhanced baseline configurations; the outer light shaded bands show the uncertainties expected from the baseline configuration, and the dark shaded bands show the uncertainties expected from the enhanced baseline configuration. The uncertainty ratios curves are shown in bottom plots. Lower panel: the tensor charge extraction uncertainty from the current world data (black), SoLID with the baseline configuration (blue), and SoLID with the enhanced baseline configuration (red). All results are plotted at a typical JLab 12 GeV scale  $Q^2 = 2.4 \text{ GeV}^2$ .

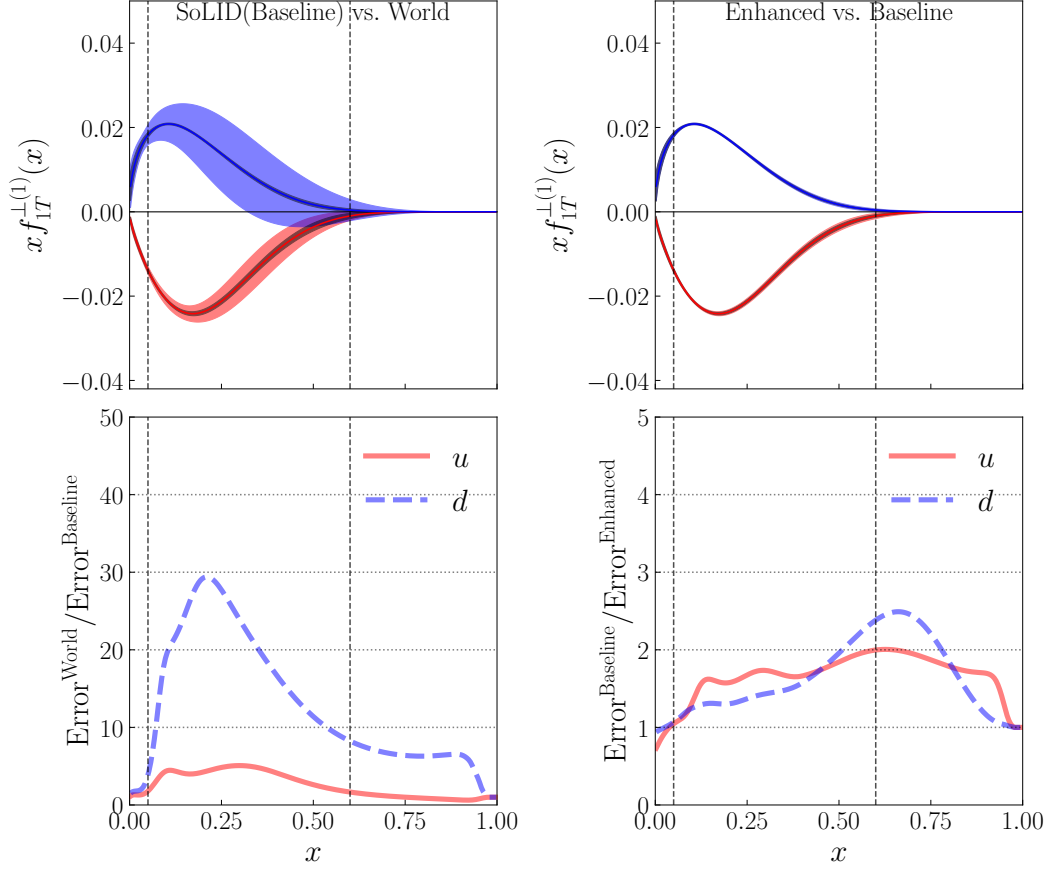


Figure 21: Left panel: the impact on Sivers extractions for up (red) and the down (blue) quarks by SoLID baseline configuration; the outer light shaded bands show the uncertainties from the world data, and the inner dark shaded bands show the uncertainties expected from SoLID baseline configuration. Right panel: the comparison of the impacts between the baseline and enhanced baseline configurations; the outer light shaded bands show the uncertainties expected from the baseline configuration, and the dark shaded bands show the uncertainties expected from the enhanced baseline configuration. The uncertainty ratios curves are shown in bottom plots. All results are plotted at a typical JLab 12 GeV scale  $Q^2 = 2.4 \text{ GeV}^2$ .

949 **2.3 PVDIS Program**

950 **2.3.1 Motivation for PVDIS**

951 The unique opportunities for experiments on parity violation at JLab with the 12 GeV upgrade were  
 952 recognized in the NSAC long-range planning exercises. The experiment was approved by PAC 35.  
 953 Quoting the PAC 35 report, “the PAC believes the mission of this and future experiments using  
 954 SoLID are sufficiently important that the Laboratory should make every effort to assist in securing  
 955 the necessary funding.”

956 We reiterate here the physics topics that become accessible with the advent of a longitudinally  
 957 polarized 11 GeV electron beam via measurements of the parity-violating asymmetry  $A_{PV}$  in deep  
 958 inelastic scattering (DIS) in the kinematic region of large Bjorken  $x = Q^2/2M\nu$ .  $A_{PV}$  is defined  
 959 to be:

$$A_{PV} = \frac{\sigma_R - \sigma_L}{\sigma_R + \sigma_L} \quad (1)$$

960 where  $\sigma_R(\sigma_L)$  is the cross section for incident right-(left-) handed electrons.

961 The primary motivation of PVDIS is to search for new interactions beyond the Standard Model  
 962 (SM). PVDIS is unique in that it is sensitive to fundamental axial-hadronic currents but does not have  
 963 large radiative corrections that involve soft hadronic physics and are impossible to make reliably.

964 We propose to obtain data over a broad kinematic range, with  $x > 0.2$ ,  $2 < Q^2 < 10$ . With a  
 965 deuterium target, the asymmetry is approximately independent of kinematics and insensitive to the  
 966 structure function. However, it is possible that the following physics could be observed in our data:

- 967 1. Charge Symmetry violation (CSV) at the quark level.
- 968 2. Higher-twist effects in the parity-violating asymmetry. Significant higher-twist effects are  
 969 observed in DIS cross sections, but in PVDIS large higher-twist contributions can only be  
 970 due to quark-quark correlations.

971 If these effects are large, they will constitute an important discovery. If they are small, our test of  
 972 the SM will be quite reliable.

973 It has been suggested that there is additional CSV in heavier nuclei. By obtaining data with a  
 974 lead target, we could test this hypothesis. Such an effect would have profound implications for our  
 975 understanding of the EMC effect.

976 By switching the target to hydrogen, we can also measure the  $d/u$  ratio in the proton, without  
 977 requiring any nuclear corrections.

978 **2.3.2 Review of the Theory**

979 The general expression for  $A_{PV}$  for  $Q^2 \ll M_Z^2$  is [97]

$$A^{PV} = - \left( \frac{G_F Q^2}{4\sqrt{2}\pi\alpha} \right) \left[ g_A^e Y_1 \frac{F_1^{\gamma Z}}{F_1^\gamma} + \frac{g_V^e}{2} Y_3 \frac{F_3^{\gamma Z}}{F_1^\gamma} \right] = - \left( \frac{G_F Q^2}{4\sqrt{2}\pi\alpha} \right) (Y_1 a_1 + Y_3 a_3). \quad (2)$$

980 Here the  $F_i^\gamma$  are the electromagnetic structure functions and the  $F_i^{\gamma Z}$  are structure functions for the  
 981 parity-violating interference term. The  $Y_i$  are functions of the kinematic variable  $y = \nu/E$  and the  
 982 ratios of structure functions  $R^j(x, Q^2)$ :

$$Y_1(x, y, Q^2) = \frac{1 + (1-y)^2 - y^2(1-r^2/(1+R^{\gamma Z})) - 2xyM/E}{1 + (1-y)^2 - y^2(1-r^2/(1+R^\gamma)) - 2xyM/E} \left( \frac{1 + R^{\gamma Z}}{1 + R^\gamma} \right) \quad (3)$$

$$Y_3(x, y, Q^2) = \frac{1 - (1 - y)^2}{1 + (1 - y)^2 - y^2(1 - r^2/(1 + R^\gamma)) - 2xyM/E} \left( \frac{r^2}{1 + R^\gamma} \right) \quad (4)$$

983 The above expressions are quite general.

984 In order to account for possible violations of the Standard Model, it is essential to express the  
985 parity-violating part of the electron-hadron interaction in terms of general phenomenological four-  
986 fermion contact interactions

$$\mathcal{L}^{PV} = \frac{G_F}{\sqrt{2}} [\bar{e}\gamma^\mu\gamma_5 e (C_{1u}\bar{u}\gamma_\mu u + C_{1d}\bar{d}\gamma_\mu d) + \bar{e}\gamma^\mu e (C_{2u}\bar{u}\gamma_\mu\gamma_5 u + C_{2d}\bar{d}\gamma_\mu\gamma_5 d)]$$

987 with additional terms as required for the heavy quarks. Here  $C_{1j}$  ( $C_{2j}$ ) gives the vector (axial-  
988 vector) coupling to the  $j^{\text{th}}$  quark. For the Standard Model:

$$C_{1u} = g_A^e g_V^u \approx -\frac{1}{2} + \frac{4}{3} \sin^2 \theta_W \approx -0.19 \quad (5)$$

$$C_{1d} = g_A^e g_V^d \approx \frac{1}{2} - \frac{2}{3} \sin^2 \theta_W \approx 0.34 \quad (6)$$

$$C_{2u} = g_V^e g_A^u \approx -\frac{1}{2} + 2 \sin^2 \theta_W \approx -0.030 \quad (7)$$

$$C_{2d} = g_V^e g_A^d \approx \frac{1}{2} - 2 \sin^2 \theta_W \approx 0.025 \quad (8)$$

989 The numerical values include electroweak radiative corrections. The key point is that the  $C_{1i}$  are  
990 about an order of magnitude larger than the  $C_{2i}$ , which makes the  $a_1$  term dominant. Recently, the  
991 JLab PVDIS collaboration published in the journal Nature[98] the result that the  $C_{2i}$ 's are indeed  
992 nonzero. The results are shown in Figure 22.

993 As recently pointed out by Mantry, et al., [99] for the deuteron where  $I = 0$ ,  $Y_1 = 1$  and

$$a_1^D(x) = g_A^e \frac{F_1^{D\gamma Z}}{F_1^{D\gamma}} = a_1^D(x) = \frac{6}{5} (2C_{1u} - C_{1d}) \left( 1 + \frac{2s^+}{u^+ + d^+} \right)$$

994 The only corrections to these formulae are physics beyond the Standard Model, CSV and quark-  
995 quark correlations, which form the motivation for the experiment, and known corrections including  
996 strange quarks and target mass corrections.

997 For the  $a_3$  term, we use the quark-parton model (QPM), which describes the structure functions  
998 in terms of parton distribution functions (PDF's) functions  $f_i(x)$  ( $\bar{f}_i(x)$ ), which are the probabilities  
999 that the  $i^{\text{th}}$  quark (antiquark) carries a fraction  $x$  of the nucleon momentum. With the definitions  
1000  $f_i^\pm = f_i \pm \bar{f}_i$ ,  $y = \nu/E$ , the structure functions are given by

$$F_1^\gamma = \frac{1}{2} \sum_i e_i^2 (f_i(x) + \bar{f}_i(x))$$

$$F_1^{\gamma Z} = \sum_i e_i g_V^i (f_i(x) + \bar{f}_i(x))$$

$$F_3^{\gamma Z} = 2 \sum_i e_i g_A^i (f_i(x) - \bar{f}_i(x)),$$

1003 where  $e_i$  is the electromagnetic charge of the  $i^{\text{th}}$  quark. Then

$$a_3^D(x) = \frac{g_V^e F_3^{\gamma Z}}{2 F_1^\gamma} = 2 \frac{\sum_i C_{2i} e_i f_i^-(x)}{\sum_i e_i^2 f_i^+(x)} = \frac{6}{5} (2C_{2u} - C_{2d}) \left( \frac{u^+ - d^+}{u^+ + d^+} \right) + \dots$$



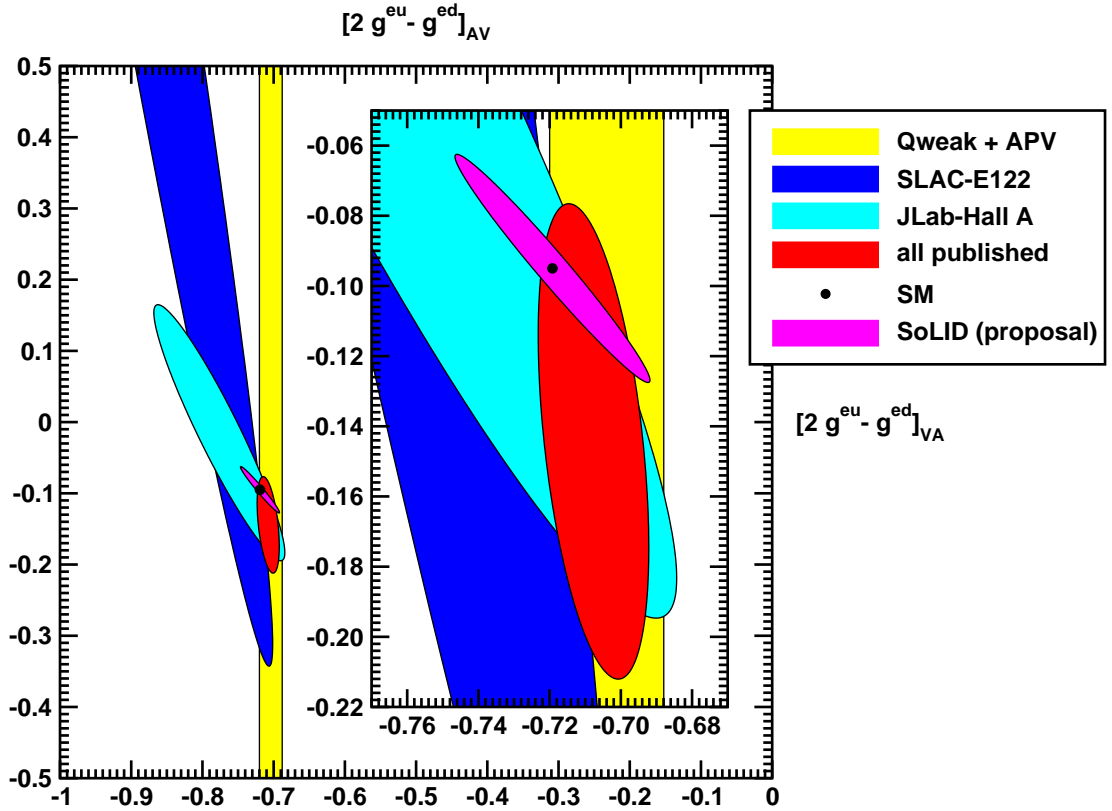


Figure 22: Results from the JLab PVDIS collaboration together with the projected results from the SoLID PVDIS experiment.

1004 Contributions due to higher twist to this term can be obtained from neutrino scattering. The contri-  
 1005 bution of  $R^\gamma$  to  $A_{PV}$  is given in the  $Y_3$  factor.

1006 The key is that since  $(2C_{2u} - C_{2d})$  is small, there is less sensitivity to the hadronic physics,  
 1007 whereas  $(u^+ - d^-)(u^+ + d^+) \sim 1$  so that we are sensitive to new physics contributions to the  $C_{2i}$ .

1008 The main goal of the experiment is to place a narrow error band on the  $C_{2i}$  plots of Figures  
 1009 23 and 22. An example of new physics that can contribute to the  $C_{2i}$  but not to the  $C_{1i}$  that have  
 1010 been precisely measured by Qweak and atomic parity violation in Cs, is a leptophobic  $Z'$  [100] as  
 1011 illustrated in Fig. 24. At the LHC, such a particle would be swamped by background. The proposed  
 1012 data will also improve the mass limits for generic models for composite for quarks and leptons [101]  
 1013 as shown in Figure 25.

### 1014 2.3.3 Charge Symmetry Violation

1015 The subtle violation of fundamental symmetries in hadronic systems can often provide important  
 1016 insights into the dynamics at work in those systems. The famous Nolen-Schiffer anomaly has  
 1017 played a significant role in nuclear structure for decades. When it comes to hadron structure charge  
 1018 symmetry violation is of great interest because of its link to the role of di-quarks in non-perturbative  
 1019 parton distribution functions [102–104].

1020 The NuTeV experiment published a discrepancy with the Standard Model [105] with a signifi-  
 1021 cance of about three sigma. The result stirred a lot of controversy, resulting in a serious re-evaluation

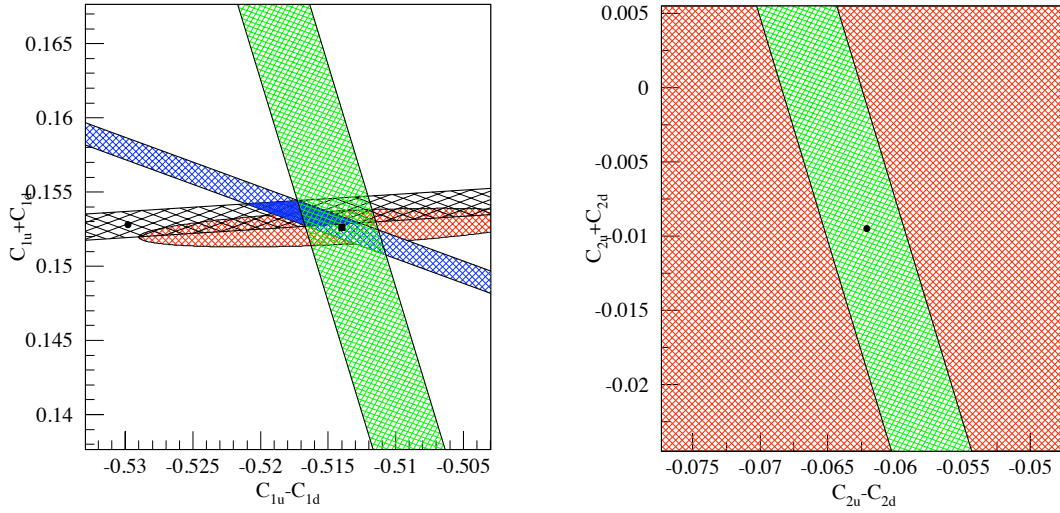


Figure 23: Green band: limits projected for this experiment. The blue band is the Qweak experiment and the black is the Cs APV.

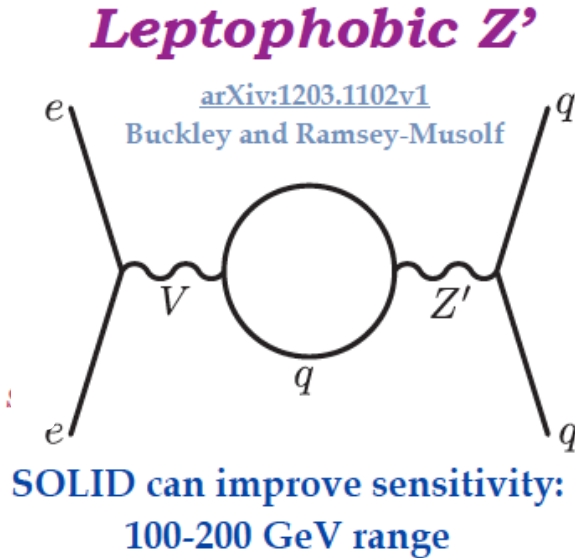


Figure 24: Diagram of a leptophobic  $Z'$  that can contribute to the  $C_{2i}$  and few other observables.

1022 of the work. Additional corrections, including changes in the Cabibbo angle, strange sea, and im-  
 1023 proved radiative corrections, have recently been made, but have changed the result very little.

1024 One possible explanation of the NuTeV result is charge symmetry violation (CSV) in the PDF's.  
 1025 This was overlooked in the NuTeV analysis, even though estimates which suggested how important  
 1026 it could be had existed in the literature for almost a decade [103, 104]. Various authors [106–108]  
 1027 have also presented the case that this is a reasonable explanation.

1028 Our experiment is also sensitive to CSV. If the  $x$ -dependence of the CSV falls slower than the

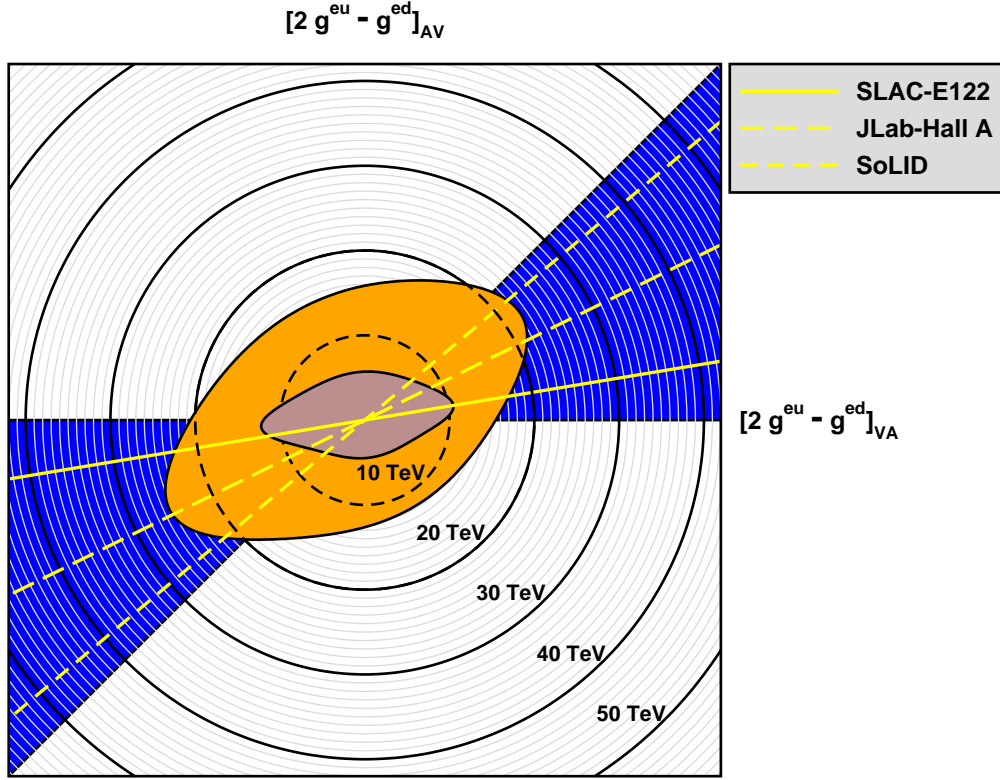


Figure 25: Polar plot for limits on composite models. The gray ellipse includes the published results from the PVDIS and Qweak collaborations. The orange ellipse gives the projected limits with the full Qweak statistics and the SoLID data.

1029 PDF's as suggested by the curves in Figure 26 our asymmetry should display a clear  $x$ -dependence.  
 1030 Moreover, these results will provide an important test of the CSV explanation for NuTeV.

1031 Another interesting possible contribution to the NuTeV anomaly is the isovector EMC ef-  
 1032 fect [109], which occurs for heavy nuclei. Measuring PVDIS in a target such as Pb would be  
 1033 able to demonstrate this effect.

### 1034 2.3.4 Higher Twist

1035 A recent paper has examined the contribution of higher twist (HT) effects to the dominant  $Y_1 a_1$   
 1036 term in  $A_{PV}$ . [99] The correction can be parameterized as a fractional contribution  $R_1(HT)$  by

$$Y_1 a_1 \approx Y_1 a_1 (1 + R_1(HT) + \dots)$$

1037 where the ellipsis refers to other corrections including CSV. It turns out that the only contribution  
 1038 comes from the operator

$$\mathcal{O}_{ud}^{\mu\nu} = \frac{1}{2} [\bar{u}(x) \gamma^\mu u(x) d(0) \gamma^\nu d(0) + (u \leftrightarrow d)]$$

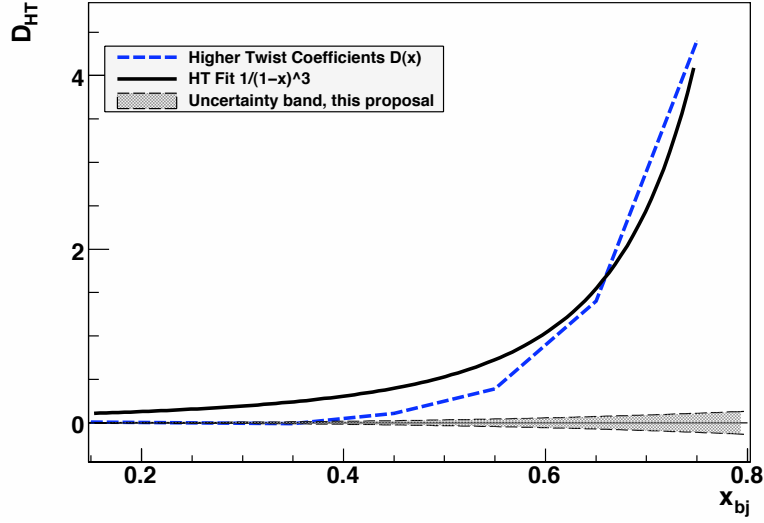


Figure 26: Possible contribution to  $A_{PV}$  due to CSV

1039 which arises only from quark-quark correlations, or in other words, di-quarks in the nucleon. Higher  
 1040 twist contributions involving gluons cancel in the ratio. The special feature of  $A_{PV}$  is that it is the  
 1041 only practical experiment that can isolate higher twist due to four quarks.

1042 The result is

$$R_1(HT) = -\frac{4}{5} \frac{[(9 - 20 \sin^2 \theta_W) F_1^{\gamma;4q} - 5 F_1^{\gamma Z;4q}]}{(1 - \frac{20}{9} \sin^2 \theta_W)[u_p(x) + d_p(x)]}$$

1043 where  $F_1^{\gamma;4q}$  and  $F_1^{\gamma Z;4q}$  are the four-quark higher twist contributions to the structure functions.

### 1044 2.3.5 Data Sample and analysis

1045 The observation of CSV is possible with our apparatus only if the effect varies with  $x$ . An  $x$ -  
 1046 independent CSV effect would be indistinguishable from a change in the  $C_{1q}$ 's. It is quite natural,  
 1047 however, to expect that the  $x$ -dependence is similar to that shown in Figure 26, and we will make that  
 1048 assumption in our further discussion. From observations of higher-twist contributions to DIS cross  
 1049 sections, it is also natural to assume that  $Q^2$ -dependent effects will also increase with increasing  $x$ .

1050 If indeed either higher twist effects or CSV are clearly seen, the experiment will be a success.  
 1051 If they are absent, we plan to untangle the effects of hadronic and electroweak physics by fitting the  
 1052 asymmetries to a function of the form

$$A_{PV}^D = A_{PV}^{EW} \left( 1 + \beta_{HT} \frac{1}{(1-x)^3 Q^2} + \beta_{CSV} x^2 \right) \quad (9)$$

1053 Since the size of the hadronic effects is small, the sensitivity to the exact form is not important. The  
 1054 resulting statistical errors on the fit parameters are:

$$\delta A_{PV}^{EW} / A_{PV}^{EW} = 0.3\%; \quad \delta \beta_{HT} = 0.0026; \quad \delta \beta_{CSV} = 0.017$$

1055 With this method, we use the full statistical power of the data set. However, the result has some  
 1056 sensitivity to the exact form of the chosen fitting functions. Under the scenario where the hadronic

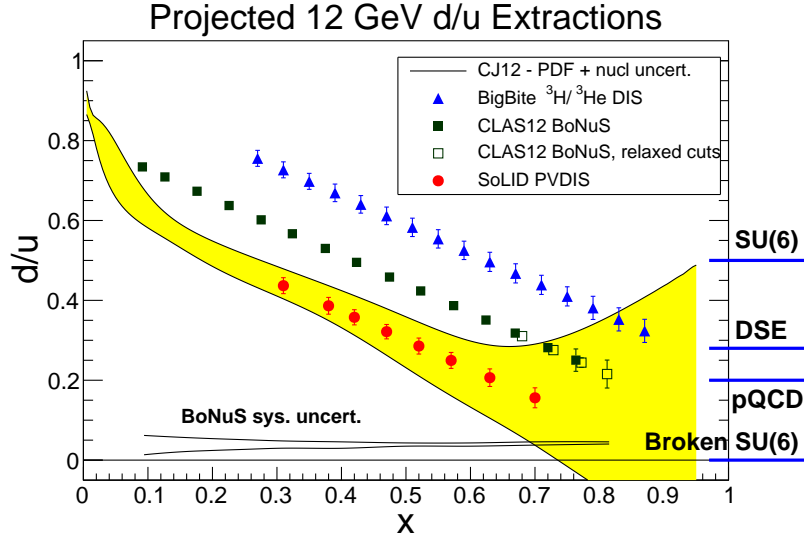


Figure 27: Anticipated precision for  $d/u$  measurement with SoLID as well as other proposed experiments.

1057 effects are small, these errors are negligible as long as we assume that CSV and higher twist effects  
 1058 depend strongly on  $x$ , as expected. The one-sigma band for the CSV term is plotted in Figure 26.

1059 If the pattern of higher twist effects is the same for  $A_{PV}$  as it is for the cross sections, then at  
 1060  $x = 0.6$  the asymmetries at the different  $Q^2$  values will differ by 15%. In that scenario, the rapid  
 1061  $x$ -dependence of the higher-twist coefficients for the cross section would imply that higher twist  
 1062 effects would still be negligible at  $x = 0.4$ . With a comparable  $x$ -dependence, a  $Q^2$ -dependent  
 1063 effect as small as  $\sim 3\%$  of the effect seen in cross-section measurements would be easily identifiable  
 1064 given our statistical precision.

1065 **Measuring  $d/u$  at high  $x$**  Hydrogen is another useful target. Since it is not isoscalar, the structure  
 1066 functions do not cancel in the expression for  $a(x)$ . In particular,

$$a(x) \approx \frac{3}{4} \left[ \frac{6C_{1u}u(x) - 3C_{1d}d(x)}{u(x) + \frac{1}{4}d(x)} \right] \sim \left[ \frac{u(x) + 0.912d(x)}{u(x) + 0.25d(x)} \right]$$

1067 and we see that  $a(x)$  is sensitive to the ratio  $d/u$ . The determination of this for the proton is a topic  
 1068 of considerable interest at large values of  $x$  [110–113]. The ratio is difficult to determine from cross  
 1069 section data because at large  $x$  complicated nuclear physics effects become important for deuterium  
 1070 targets. Alternative methods include comparing  $^3\text{He}$  and tritium or detecting the recoil proton from  
 1071 deuteron. Projected errors for all three approaches are shown in Fig. 27.

### 1072 2.3.6 Beam Time and Projections

1073 For the deuterium data, we have based our sensitivity on 180 days of production running at  $50 \mu\text{A}$ ,  
 1074 with  $1/3$  of the data at 6.6 GeV and the rest at 11 GeV. Approximately 27 additional days, run  
 1075 at various currents, will be required for checkout and calibrations. An additional 18 days will be  
 1076 required at 4.4 GeV and  $50 \mu\text{A}$  for radiative correction measurements. The total beam request at

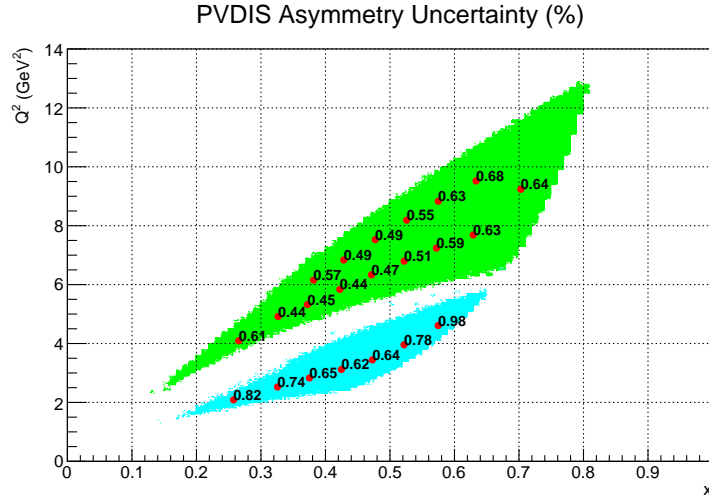


Figure 28: Anticipated statistical precision for  $A_{PV}$  in percent versus  $Q^2$  and  $x$ . 11 GeV data (green region) are based on a simulation including the electron calorimeter trigger. For the 6.6 GeV data the effect of the trigger is estimated.

1077 all energies for the deuterium measurement is 225 days, with about 25 of those days run mostly at  
 1078 reduced beam currents. Projected statistical uncertainties in  $A_{PV}$  are shown in Fig. 28.

1079 For the hydrogen measurement, 90 days are needed for production data at 11 GeV, about 9 days  
 1080 are required at 4.4 GeV to control radiative corrections and another 14 days will be required for  
 1081 calibration. The running time requested for hydrogen totals to 113 days. We have been approved  
 1082 for 180 days total. The plan is to first take half the deuterium data. If nothing exciting appears, we  
 1083 will switch to hydrogen.

1084 In the future, we would also anticipate requesting an additional comparable run for a heavy  
 1085 nucleus such as Pb.

## 1086 **2.4 $J/\psi$ Program**

### 1087 **2.4.1 Motivation**

1088 One of the fundamental goals of modern nuclear physics is to understand hadrons and nuclei starting  
1089 with the basic ingredients of QCD namely quarks and gluons and their interactions. While signifi-  
1090 cant progress has been made in exploring the theory in its perturbative region much remains to be  
1091 understood in the strong region, particularly where gluonic exchanges dominate. Strong gluonic  
1092 field configurations and interactions are responsible for most of the mass of nucleons and nuclei.  
1093 Fundamental approaches such as lattice QCD, effective field theories or dual string theories (that  
1094 would match QCD) could in principle shed light on confinement of hadrons and perhaps make  
1095 predictions of novel phenomena of strong interactions.

1096 We plan to explore this strong interaction using a particular system that emphasizes the multi-  
1097 gluon exchange between two color neutral particles which do not share a common valence quark,  
1098 namely nucleons/nuclei and charmonia. It has long been argued that the force acting between nu-  
1099 cleon/nucleus and  $J/\psi$  is an attractive force, which has negligible mesonic ( $D\bar{D}$ ) or multi-mesonic  
1100 ( $\rho\pi$ ) exchange contribution at low energies [114]. Since the nucleon/nucleus and  $J/\psi$  are color  
1101 neutral, this force is dubbed as color Van der Waals force in analogy with the atomic-molecular  
1102 physics case. This situation is unique in nuclear physics where a force exchanged between nucleons  
1103 or hadrons is purely gluonic especially at low energy. A direct consequence of such an attractive  
1104 force is the possible existence of a nuclear bound quarkonium state which was proposed more than  
1105 20 years ago by Brodsky, Schmidt and de Teramond [115] but has yet to be observed. A calculation  
1106 using the operator product expansion (OPE) [116] to describe the low energy interaction of quarko-  
1107 nium with nuclei, in the limit where the mass of the charm quark is infinite, found that the  $J/\psi$   
1108 binds in nuclear matter with about 10 MeV but the authors caution about possible large corrections  
1109 due to confinement effects.

1110 Due to the lack of experimental data, a timid but sustained theoretical activity on the subject fol-  
1111 lowed over the past twenty years. For example, Kaidalov and Volkovitsky [117] argued that S-wave  
1112 quarkonia can be found in nuclei with  $A \geq 10$  and with binding energy of few MeV, while de Tera-  
1113 mond et al. [118] in an update to his original paper with Brodsky [115] estimated a binding energy  
1114 of 2 MeV in  $^{12}\text{C}$  and 10 MeV in  $^{208}\text{Pb}$ , while Shevchenko [119] pointed in a later work that the  
1115 interaction of charmonium-nucleon is so small that the potential depth for nuclear bound state may  
1116 only be possible for nuclei with  $A > 200$ . Applying QCD sum rules Hayashigaki [120] finds a 4 to  
1117 7 MeV binding of the  $J/\psi$  in nuclear matter. Yokokawa, Sasaki, Hatsuda and Hayashigaki [121]  
1118 performed a first lattice study in the quenched approximation of low energy charmonium-hadron  
1119 interaction to determine the scattering length. But more recently Kawanai and Sasaki [122] calcu-  
1120 lated the charmonium-nucleon potential from the equal-time Bethe-Salpeter amplitude through the  
1121 effective Schrödinger equation and found that the charmonium-nucleon potential is weakly attrac-  
1122 tive at short distances and exponentially screened at large distances. Finally, Tsushima, Lu, Krein  
1123 and Thomas [123, 124] have recently explored the  $J/\psi$ -nuclear bound states and found that the  
1124 attractive potential that originate from the  $D$  and  $D^*$  meson loops in the  $J/\psi$  in nuclear medium  
1125 should produce bound states.

1126 Many of the  $J/\psi$  photoproduction experiments that have been performed at high photon ener-  
1127 gies and low  $t$  or in the case of electroproduction at large center of mass energy  $s$  and low  $t$  (see  
1128 Refs. [125–132]) are usually considered as a diffractive production. Experiments in the thresh-  
1129 old region are few and were performed soon after the discovery of the  $J/\psi$  particle more than 35  
1130 years ago [133–136]. In particular, the measurements of Cornell [134] and SLAC [136] show large  
1131 discrepancies at photon energy around 10 GeV.



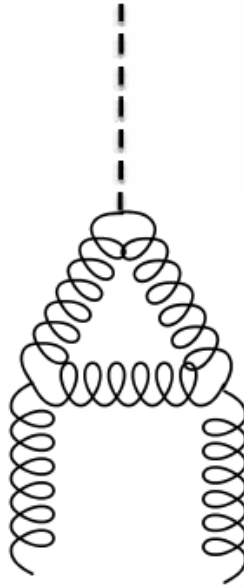


Figure 29: Anomaly diagram which dominate the cross section interaction at threshold.

1132 It is fair to say that not much is known in the region where the energy of the photon is just  
 1133 above 8.2 GeV and where  $t$  is about 2 GeV, namely the threshold region. With Jefferson Lab at  
 1134 12 GeV, we enter a new kinematic domain where the electro/photo-production of charmed hadrons  
 1135 near threshold becomes possible. It is precisely a region well suited for the investigation of the  
 1136 QCD Van der Waals interaction, since as we approach the threshold and due to the conformal scale  
 1137 anomaly of the low energy  $J/\psi$ -nucleon interaction [137, 138] the non-perturbative part of the  
 1138 interaction vanishes more slowly than the perturbative part. In his paper of 1998 [138], Kharzeev  
 1139 considered explicitly the possible enhancement of the threshold cross section due to this conformal  
 1140 scale anomaly which corresponds to a diagram where the coupling of the quarkonium to the nucleon  
 1141 occurs through triangle gluonic lines (see Fig. 29). As shown in Fig. 30, the scattering amplitude in  
 1142 the threshold region is also dominated by its real part in contrast to the case of high energy.

1143 Later Brodsky, Chudakov, Hoyer and Laget [139] discussed the photoproduction of charm near  
 1144 threshold and invoked the two-gluon exchange mechanism in the production. These authors also  
 1145 considered the possible enhancement of the cross section at threshold due to a strong interaction  
 1146 beyond two-gluon exchanges as shown in Fig. 31. Whereas Sibirtsev, Krewald and Thomas [140]  
 1147 attributed the mechanism of the  $J/\psi$  photoproduction at low energies and large  $t$  to a mechanism  
 1148 different from pomeron or two-gluon exchange. They considered the possibility of the exchange  
 1149 of an axial vector trajectory that couples with the axial form factor of the nucleon in this case also  
 1150 enhancing the cross section at threshold.

1151 At first, the charmonium production near the threshold region would not seem to lend itself to  
 1152 calculations using pQCD similar to the case of deep inelastic scattering at large  $Q^2$ . However, a  
 1153 closer look reveals a new scale at play, namely the mass of heavy quarks, which when compared to  
 1154  $\Lambda_{QCD}$  enables a perturbative approach to evaluate the scattering amplitude of the process. This fact  
 1155 was used a while ago to derive charm photoproduction sum rules in a way similar to deep inelastic  
 1156 scattering [141–143].

1157 In the reaction  $\gamma^* + N \rightarrow J/\psi + N$ , the production mechanism at threshold can be viewed in a

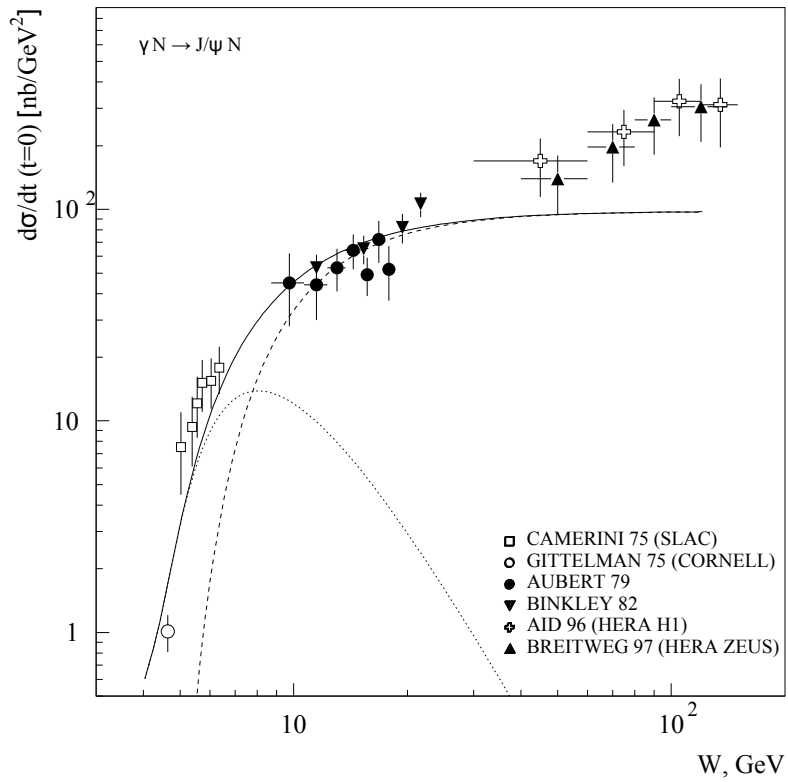


Figure 30: Forward  $J/\psi$  photoproduction data compared to the results of [138] with (solid line) and without (dashed line) the real part of the amplitude.

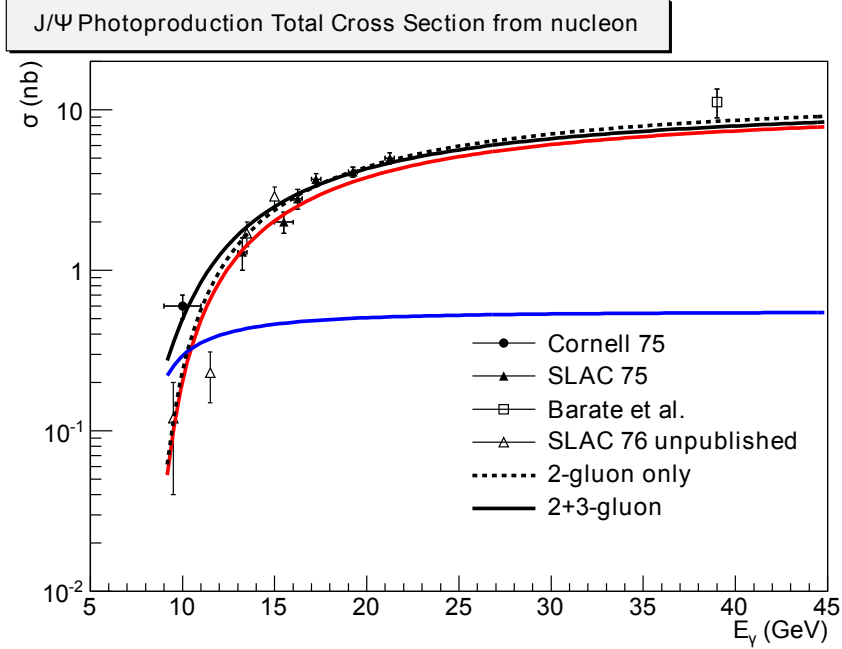


Figure 31: The 2-gluon model is shown as dotted black line. The (2+3)-gluon model is shown as solid black line. Furthermore, the 2-gluon contribution and 3-gluon contribution in the (2+3)-gluon model are shown as red and blue lines as well. Data are from “Cornell 75” [134], “SLAC 75” [133], “SLAC 76” [136] and “Barate et al.” [128].

1158 way similar to the  $J/\psi$  elastic scattering off a nucleon at small relative velocity. The coupling of the  
 1159 soft gluonic fields to the nucleon, at low  $Q^2$  is determined by the low-energy theorem in QCD based  
 1160 on the anomaly in the trace of the energy-momentum tensor. The  $J/\psi$ -nucleon scattering amplitude  
 1161 is proportional to the nucleon matrix element of the following gluon operator [144]:

$$\langle N | \frac{1}{2} \vec{E}^a \cdot \vec{E}^a | N \rangle = \frac{4\pi^2}{b} \langle N | \theta_\mu^\mu | N \rangle + 2\pi\alpha_s \langle N | \theta_G^{00} | N \rangle, \quad (10)$$

1162 where  $\vec{E}^a$  represents the chromo-electric field,  $\theta_G^{\mu\nu}$  is the energy-momentum tensor of the gluon  
 1163 field,  $\theta_\mu^\mu$  is the anomalous trace of the full energy-momentum tensor in QCD in the chiral limit,  $b$  is  
 1164 the coefficient in the QCD beta function with three light (massless in the chiral limit) quarks and  $\alpha_s$   
 1165 is the QCD coupling.

1166 It is argued [144] that this matrix element is bound by

$$\langle N | \frac{1}{2} \vec{E}^a \cdot \vec{E}^a | N \rangle \geq \frac{4\pi^2}{b} 2m_N^2 \quad (11)$$

1167 In a measurement of electroproduction close to the threshold region, and unlike at high energy,  
 1168 the real part of the scattering amplitude contribution dominates compared to the imaginary part  
 1169 even though the allowed exchanges are purely gluonic. This contribution probes the matrix element  
 1170 represented by  $\langle N | \theta_\mu^\mu | N \rangle = 2m_N^2$ . Hence, in a threshold measurement we probe the conformal  
 1171 anomaly contribution to the low energy  $J/\psi - N$  interaction comparable to a Higgs-like coupling<sup>1</sup>.

<sup>1</sup>The coupling of the contact term is sensitive to the entire mass of nucleon, and as such is similar to the Higgs coupling.

1172 Furthermore, the determination of an upper limit of the strength of this interaction will help de-  
1173 termine whether or not a nucleon- $J/\psi$  bound state due to the Van der Waals color forces would  
1174 exist.

## 1175 2.4.2 Program Overview

1176 The high luminosity and large solid angle offered by the Jefferson Lab 12 GeV energy upgrade  
1177 combined with the SoLID detector in Hall A is a unique tool to start an investigation program of the  
1178  $J/\psi$ -nucleon interaction.

1179 In a first phase, measurements of the cross section of electro- and photo-production of  $J/\psi$  on a  
1180 nucleon near threshold will take place with experiment E12-12-006[151] using SoLID. These mea-  
1181 surements at threshold have not been revisited since the 70s. The precision and energy range close to  
1182 threshold of the proposed measurements will best probe the possible enhancement of the cross sec-  
1183 tion due to the contribution of the conformal anomaly very close to the threshold photon energy of  
1184  $J/\psi$  production. Threshold enhancements due to on-shell rescattering or quasi-bound states around  
1185 threshold have been observed in several processes such as  $e^+e^- \rightarrow p\bar{p}, \Lambda\bar{\Lambda}, \Sigma^0\bar{\Sigma}_0, \Lambda\bar{\Sigma}_0$  [145] as  
1186 well as in the  $J/\psi$  radiative decays, e.g.  $J/\psi \rightarrow p\bar{p}\gamma$  [146]. The experiment E12-12-006 aims  
1187 at observing such enhancement in the  $J/\psi$ -proton system and offers the capability to explore the  
1188 region below threshold if there are hints of an enhancement of the cross section just above thresh-  
1189 old. Furthermore, the proposed cross section measurement could also shed light on the existence of  
1190 predicted super-heavy  $N^*$  with hidden charm with a mass around 4.3 GeV [148].

1191 In a second phase we shall explore the interference of the Bethe-Heitler amplitude with that  
1192 of the  $J/\psi$  electroproduction to attempt a determination of the relative contribution of the real  
1193 and the imaginary part of the scattering amplitude. Moreover, a study of the angular distribution  
1194 of the  $J/\psi$  decay can reveal whether the  $J/\psi$  was originally produced from an octet or singlet  
1195 state. Recently a phenomenological analysis of the forward  $J/\psi - p$  scattering amplitude within a  
1196 dispersive framework [147] resulted in a  $\psi$  binding energy in nuclear matter of  $2.7 \pm 0.3$  MeV. The  
1197 latter number uncertainty would be dramatically improved with more accurate cross section data in  
1198 the threshold region. Furthermore, in the same reference a path towards unraveling the ratio of real  
1199 to imaginary part of the  $J/\psi$ -nucleon scattering amplitude is described through the measurement of  
1200 the  $\gamma p \rightarrow e^+e^-p$  forward-backward asymmetry in the vicinity of the  $J/\psi$  resonant amplitude. This  
1201 forward-backward asymmetry is sizable due to the interference of the Bethe-Heitler amplitude with  
1202 the  $J/\psi$  production amplitude.

1203 Finally, studies of  $J/\psi$  production and propagation in the nuclear medium is the natural exten-  
1204 sion of the proposed measurements on a nucleon. The study of multi-gluon QCD Van der Waals  
1205 forces in nuclei is believed to shed new light on their possible role in  $J/\psi$ -nuclear bound states  
1206 [115, 115–122]. Another related challenge is the in-medium properties of charmonia as well as the  
1207 possible restoration of the chiral symmetry in the nuclear medium, which is closely connected to the  
1208 modifications of masses and widths of mesons when embedded in the nuclear environment [123].  
1209 For these studies, it is important to find the appropriate kinematical conditions to produce  $J/\psi$  near  
1210 rest, or with small momentum relative to the nucleus. Therefore, measurements near threshold and  
1211 even sub-threshold look promising [149].

1212 At JLab Hall C, a photoproduction experiment (E03-008) was performed in the *subthreshold*  
1213 regime using the CEBAF at 6 GeV. Unfortunately no signal was observed after one week of beam  
1214 on a  $^{12}\text{C}$  target [149]. This experiment allowed to set a limit on the cross section, which was found to  
1215 be consistent with the quasi-free production. The experiment used a bremsstrahlung beam produced  
1216 on a copper radiator by the 6 GeV incident electron beam. The pair of spectrometers (HMS and  
1217 SOS) of Hall C were used to detect the pair of leptons resulting from the decay of the  $J/\psi$ . A

1218 proposal "A-dependence of  $J/\psi$  photoproduction near threshold" [150] for the 12 GeV upgrade  
1219 of Hall C was also considered by the PAC32 and conditionally approved. The authors proposed  
1220 the use of bremsstrahlung photon beam created in a radiator to look at the photoproduction near  
1221 threshold in a series of nuclei. The physics goal was to measure the photoproduction cross section  
1222 on hydrogen and then investigate the A dependence of the propagation of the  $J/\psi$  in the nuclear  
1223 medium. In this proposal, only the  $J/\psi$  is detected through the detection of the decay leptonic pair.  
1224 The experiment E12-12-006[151] as the first phase of the program, will utilize the SoLID spec-  
1225 trometer to measure the cross section of the full exclusive electro- and photo-production of  $J/\psi$   
1226 near threshold ( $4.05 \text{ GeV} < W < 4.45 \text{ GeV}$  and  $|t - t_{min}| < 2.5 \text{ GeV}^2$ ) to study QCD in the  
1227 non-perturbative regime with luminosity of  $10^{37} \text{ cm}^{-2} \text{ s}^{-1}$ .

### 1228 **2.4.3 Beam Time and Projection**

1229 The experiment E12-12-006 was approved by Jefferson Lab PAC39 with total 60 PAC days[151].  
1230 Among them, 50 days will be used for production run with  $3 \mu\text{A}$ , and 11 GeV electron beam on a 15  
1231 cm long liquid hydrogen target. The other 10 days will be shared among activities, such as detector  
1232 calibration, data taking with Al dummy target, and special low luminosity running for understanding  
1233 the trigger efficiency and normalization for the cross section measurement.

1234 Our projections for the total elastic cross sections of electro- and photo-production are plotted  
1235 against the effective photon energy in Fig. 32. Together, we have also plotted the world data of  
1236  $J/\psi$  photoproduction near threshold. The fit of 2-gluon exchange only model is shown as well with  
1237 a solid line. In our projections we also included the possible photoproduction of the LHCb "pen-  
1238 taquark" [160]. It is clear that the proposed measurements will significantly advance our knowledge  
1239 of electroproduction of  $J/\psi$  near the threshold region.

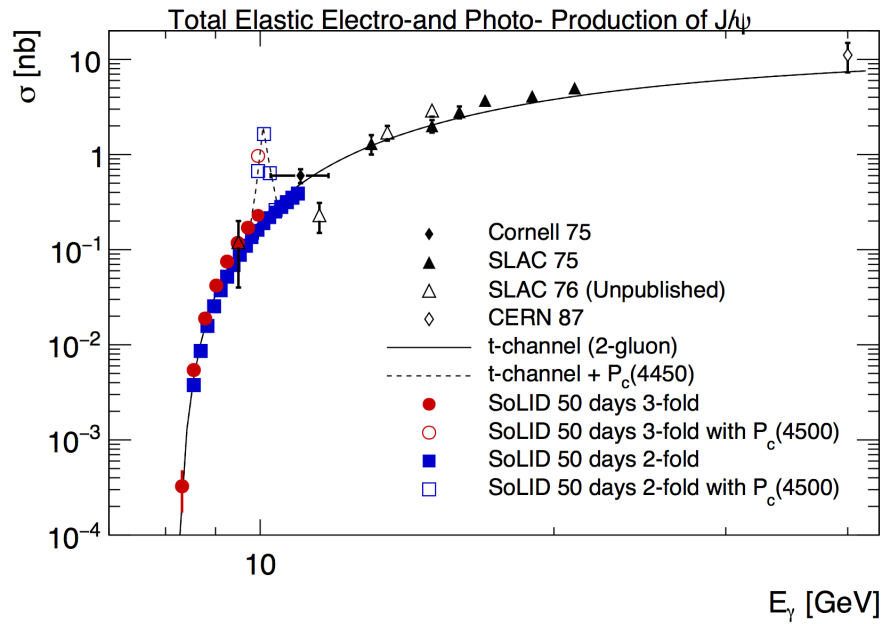


Figure 32: Projected uncertainties on the total elastic  $J/\psi$  electro-and photo-production cross sections. Our projections are based on the 2-gluon exchange model. The central values of our projections are positioned at 1.2 times or 0.8 times of the predicted total cross section of the 2-gluon exchange model in order to differentiate our projections from SLAC76 [136] points. The electro-production data is plotted against effective photon energy. We have also included the projection of the LHCb pentaquark photoproduction with a 5% coupling according to [7]

1240 **2.5 Possible Expansion in Physics Reach**

1241 **2.5.1 GPD Program**

1242 There are several GPD experiments in different stages of study/approval. As has been remarked  
 1243 elsewhere, a variety of hard exclusive measurements are needed to disentangle the contributions of  
 1244 the different GPDs, with the general Compton processes (DVCS, TCS, DDVCS) sensitive to various  
 1245 real and imaginary combinations of all four leading twist GPDs (Fig. 33), vector-meson Deep Ex-  
 1246 clusive Meson Production (DEMP) sensitive to the spin-average  $H$  and  $E$  GPDs and pseudoscalar-  
 1247 meson DEMP sensitive to the spin-difference  $\tilde{H}$  and  $\tilde{E}$  GPDs. The SoLID GPD program under  
 1248 investigation includes many of these reactions, and has the potential to improve greatly our under-  
 1249 standing of nucleon structure.

**General Compton Processes  
Accessing GPDs**

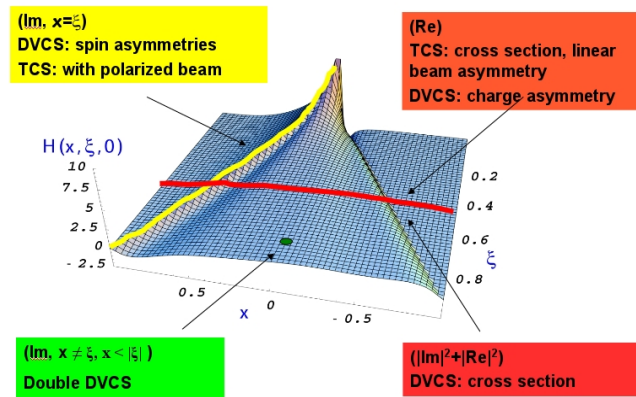


Figure 33: General Compton processes accessing GPDs.

1250 Timelike Compton Scattering (TCS) from an unpolarized  $\text{LH}_2$  target can provide information  
 1251 on the real (imaginary) parts of the Compton amplitude using unpolarized (circularly polarized)  
 1252 photons. In this case, the produced lepton pair sets the hard scale ( $Q^2 > 4 \text{ GeV}^2$ ) and the az-  
 1253 imuthal asymmetry of the  $\ell^+\ell^-$  plane with respect to the  $q$ -vector allows the separation of the GPD  
 1254 and Bethe-Heitler contributions. This has been approved as a run group experiment with the  $J/\psi$   
 1255 experiment (E12-12-006A).

1256 Double Deeply Virtual Compton Scattering (DDVCS) in the di-lepton channel on an unpolar-  
 1257 ized  $\text{LH}_2$  target has been reviewed by PAC43 as LOI12-12-005. The solenoidal configuration is  
 1258 ideal for high luminosity, with a fully parasitic proposal (as part of the  $J/\psi$  run group) for the  $e^+e^-$   
 1259 channel under preparation. Once this experiment has run, a later phase of measurements might  
 1260 include the  $\mu^+\mu^-$  channel. A workshop at ECT Trento to refine the TCS and DDVCS physics  
 1261 program was held for October 24-28, 2016.

1262 A possible Deeply Virtual Compton Scattering (DVCS) experiment on polarized  $^3\text{He}$  is also  
 1263 under study. The 12 GeV polarized DVCS experiments to date utilize longitudinally (E12-06-119)  
 1264 and transversely (C12-12-010) polarized proton targets. No polarized neutron-DVCS experiment  
 1265 has been proposed at JLab to date, and SoLID could make a unique contribution here once the



1266 reaction exclusivity requirements and possible backgrounds are better understood. A complete set of  
1267 SoLID DVCS data with both proton and neutron targets at varied polarization would be essential to  
1268 control systematic uncertainties, perform flavor decomposition, and disentangle the different GPDs.

1269 Deep Exclusive Meson ( $\pi^-$ ) Production (DEMP) using a transversely polarized  $^3\text{He}$  (neutron)  
1270 target looks very promising. The transverse single-spin asymmetry in exclusive charged  $\pi$  pro-  
1271 duction has been identified as the most sensitive observable to probe  $\tilde{E}$ . In this case, one fits the  
1272  $\sin(\phi - \phi_S)$  dependence, where  $(\phi - \phi_S)$  is the azimuthal difference between the  $\pi^-$  reaction plane  
1273 and the polarized target. Theoretical calculations suggest higher twist corrections likely cancel in  
1274 the asymmetry, allowing access to GPDs at much lower value of  $Q^2$  than typically required  
1275 in DEMP reactions. This measurement has been approved as a run group experiment with the  
1276 transversely polarized  $^3\text{He}$  SIDIS experiment (E12-10-006B), and detailed studies on the expected  
1277 uncertainties are underway.

1278 This summary makes clear that the SoLID-SIDIS setup is indeed very attractive in terms of  
1279 acceptance and luminosity, and will allow a Phase 1 GPD program to be initiated with minimal  
1280 impact on the approved SoLID program. Once this has been executed, one could envision a later  
1281 Phase 2 suite of GPD experiments with additional recoil detectors near the target (such as low  
1282 momentum proton tagging for DEMP), dedicated configurations (for DDVCS), or improved EC  
1283 resolution (to allow exclusive vector meson and  $\pi^0$  measurements). These would require much  
1284 more study, and are clearly beyond the scope of the present proposals.

## 1285 2.5.2 SIDIS Production of Charged Kaons

1286 The extension of the SIDIS production of charged pion to the SIDIS production of charged kaons is  
1287 under study. Because the kaon contains a valence strange/antistrange quark, the SIDIS production  
1288 of charged kaons is more sensitive to the strange distributions. Compared to the pion data, the kaon  
1289 data are very limited. Lacking the knowledge of the strange quark distributions will prevent us from  
1290 fully understanding the spin structures of the nucleon. Taking advantage of high luminosities and  
1291 large acceptance, SoLID could be ideal to measure the SIDIS production of charged kaons with  
1292 high statistics. The combination of the proton and the neutron ( $^3\text{He}$ ) targets, and the detection of  
1293 charged pions and charged kaons in a similar kinematic region helps us to have flavor separations of  
1294 all light quark distributions, *i.e.*,  $u$ ,  $\bar{u}$ ,  $d$ ,  $\bar{d}$ ,  $s$ , and  $\bar{s}$ . As kaon is heavier than pion, the SoLID kine-  
1295 matics covers a intermediate region from target-fragmentation to current-fragmentation. A precise  
1296 measurement in this region will allow us to understand how the factorization breaks down.

1297 A full RICH detector for kaon detection is likely to be too costly to consider. A high resolution  
1298 TOF is a more practical solution. SoLID needs to do kaon identification over a momentum range  
1299 of 1 GeV/c to 7 GeV/c. Given the 8 m flight distance, a TOF time resolution of 20 ps is required  
1300 to obtain a 3-sigma separation between pions and kaons, as shown in Figure 34. Two detector  
1301 technologies that could give high resolution TOF are being investigated.

1302 The Large Area Picosecond Photodetector (LAPPD) collaboration [178] is developing large area  
1303 detectors capable of time resolutions in the picosecond range. Such detectors use Micro Channel  
1304 Plate photomultipliers, which have small paths for electrons, achieving better timing resolution than  
1305 traditional PMTs. Resolutions of 20 ps for a single photoelectron have been achieved and resolutions  
1306 of under 10 ps could be obtained for multiple photoelectrons. The main drawback of Micro Channel  
1307 Plate PMTs is the high cost per area. The LAPPD project is aiming to producing large area MCP  
1308 PMTs with a cheaper microchannel plate, significantly reducing the cost for large area of detectors.  
1309 Depending on the ultimate costs, this could be an option for SoLID.

1310 A second TOF option is improving the timing performance of the MRPC detector in SoLID.  
1311 The baseline MRPC is designed to reach 80 ps. Improvement of the MRPC timing resolution would

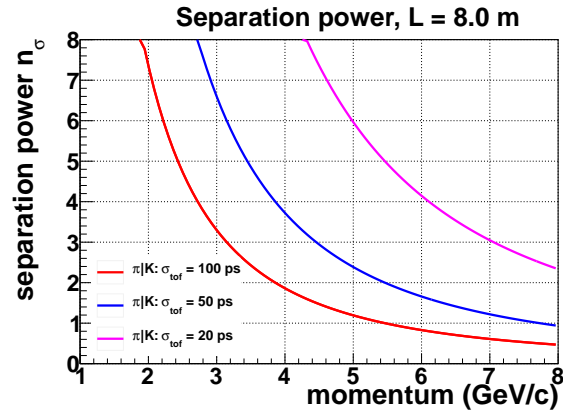


Figure 34: Kaon identification by TOF.

1312 extend the momentum range of  $\pi/K$  identification to the full momentum range. Beam tests showed  
 1313 that current MRPC designs can reach 50 ps with test beam and 80 ps in high background area.  
 1314 There is ongoing EIC R&D [179] on Multi Gap Resistive Plate to improve the timing resolution. A  
 1315 thin gap MRPC prototype has been built and tested by BNL and University of Illinois, achieving a  
 1316 resolution of 20 ps. The R&D plan is described in the MRPC section.

## 1317 3 Technical Requirements and Experimental Setup

### 1318 3.1 Summary of Requirements

1319 The minimum requirements of the base equipment for SoLID are summarized below and also listed  
1320 in Table 6,

- 1321 • Magnet: Outer diameter is 3 meters (to fit in Hall A), inner diameter is 1 meter and length is  
1322 greater than 3 meters. Field strength is greater than 1.35 tesla and integrated BdL is 5 tesla-  
1323 meters. Acceptance in azimuthal angle ( $\phi$ ) is  $2\pi$ , in polar angle ( $\theta$ ) is  $8^\circ$  to  $24^\circ$  for the SIDIS  
1324 configuration and  $22^\circ$  to  $35^\circ$  for the PVDIS configuration. Momentum range is 1–7 GeV, and  
1325 momentum resolution (combined with 100-micron tracking resolution) is 2%. Fringe field at  
1326 the front end after endcap (shielding) is less than 5 gauss (for polarized target operation).
- 1327 • GEM Tracking Chambers: Six planes for SIDIS and five for PVDIS. Total area is  $37\text{ m}^2$ , total  
1328 number of channels 165K. Tracking efficiency is greater than 90%. Radial position resolution  
1329 reaches 0.1 mm. Works in high rate environment.
- 1330 • EM Calorimeter: Shashlyk sampling (lead-scintillator/fiber) calorimeter. Total 1800 modules  
1331 of shower (18 radiation length) and 1800 pre-shower (2 radiation length), with an area of  $100$   
1332  $\text{cm}^2$  for each module. Energy resolution is  $10\%/\sqrt{E}$ . Reaches  $50 : 1$   $\pi$  suppression with  
1333 electron efficiency better than 90%. Reaches  $5 : 1$  photon suppression. Radiation hard (gain  
1334 decreasing less than 20% after 400 KRad). Combined EC and Cherenkov for PVDIS trigger  
1335 rate to be below 600 KHz (20 KHz/sector). In front of the EM Calorimeter, there are 300  
1336 pieces of scintillator pad detectors (SPDs) with thickness of 5 mm or 20 mm to help with  
1337 photon rejection.
- 1338 • Light Gas Cherenkov: 2 meters long with 1 atm  $\text{CO}_2$  gas for SIDIS and 1 meter long with  
1339 1 atm  $\text{CO}_2$  for PVDIS. Contains 60 mirrors and 270 PMTs. The total area is  $20\text{ m}^2$ . Pro-  
1340 vides number of photo-electrons larger than 10 and electron efficiency greater than 90%.  $\pi$   
1341 suppression is greater than 500 for momentum less than 4 GeV (SIDIS) or less than 3.2 GeV  
1342 (PVDIS). Works in moderate field up to 200 gauss ( $< 100$  gauss after mu-metal shielding).  
1343 Combined EC and Cherenkov for PVDIS trigger rate to be below 600 kHz (20 KHz/sector).
- 1344 • Heavy Gas Cherenkov: 1 meter long 1.5-atm  $\text{C}_4\text{F}_8\text{O}/\text{C}_4\text{F}_{10}$  gas, with 30 mirrors and 480  
1345 PMTs. Total area is  $20\text{ m}^2$  (active  $8.5\text{ m}^2$ ) and the number of photo-electrons is greater than  
1346 10. With an efficiency for  $\pi$  better than 90%, kaon suppression is greater than 10:1, from 2.5  
1347 to 7.5 GeV. Works in moderate field up to 200 gauss ( $< 100$  gauss after mu-metal shielding)
- 1348 • MRPC: 50 super-modules, each of which contains 3 MRPC modules. There are totally 1650  
1349 strips and 3300 readout channels, covering an area of  $10\text{ m}^2$ . Timing resolution is better than  
1350 100 ps. Kaon suppression is about 20:1 for momentum  $> 2.5$  GeV and photon suppression is  
1351 as high as 10:1. Works at a high rate up to  $10\text{ KHz}/\text{cm}^2$ .
- 1352 • DAQ: 282 FADC sampling at 250 MHz. 32 high-speed pipeline VME switched Series (VXS)  
1353 system. 30 GEM Scalable-read-out system (SRS). Can handle trigger rate of 100 KHz for  
1354 SIDIS with event size of 2.6 KBytes and trigger rate of 600 KHz (20 KHz per sector) for  
1355 PVDIS with event size of 48 KBytes
- 1356 • Baffles: Eleven planes of lead blocks, 30 sectors in each plane, thickness of 9 cm, with az-  
1357 imuthal angle opening for each block to be more than  $4^\circ$  out of  $12^\circ$  ( $360^\circ/30$ ). One additional

1358 plane of lead blocks with thickness of 5 cm is placed in front of the EM Calorimeter at the  
1359 small radius region ( $110 \text{ cm} < r < 200 \text{ cm}$ ). The design is optimized to block low energy  
1360 particle, photon and hadron backgrounds to an acceptable level (total trigger rate below 600  
1361 kHz (20 KHz/sector) for the PVDIS configuration).

1362 A summary of the detector requirements of all approved experimental programs is given in  
1363 Table 7. The key parameters of the approved programs are in Table 8. The experimental setup of  
1364 PVDIS, SIDIS- $^3\text{He}$ , SIDIS-proton and  $J/\psi$  are shown in the next few subsections.

Table 6: Summary of Minimum Requirements of SoLID Base Equipment. Items listed in brackets are particularly for SoLID-PVDIS requirements.

Equipment	dimension/description	description	performance, eff	performance, rej	conditions
Magnet	OD 3m, ID 1m, L > 3m	B > 1.35 T, BDL > 5 T-m	2 $\pi$ , 8 to 24° (22 to 35°)	P: 1-7 GeV, Res 2%	Fringe field < 5 G
GEMs	6 planes (5 planes)	Total 37 m <sup>2</sup> , Chan 165K	Track Eff > 90%	Posi res 100 $\mu$ m	high rate
EM Calorimeter	1800 $\times$ 100 cm <sup>2</sup>	18 RL + 2 RL + 1 cm SPD	E res 10%, eff > 90%	50:1 $\pi$ , 5:1 $\gamma$	rad hard
Light Cherenkov	2m CO2 (1m CO2)	60 mirr, 270 PMTs, 20 m <sup>2</sup>	$\gamma$ -e > 10, Eff > 90%	$\pi$ 500:1 < 4.5(3.2) GeV	150 G field
Heavy Cherenkov	1m 1.5 atm C4F8O/C4F10	30 mirr, 480 PMTs, 20 m <sup>2</sup>	$\gamma$ -e > 10, Eff > 90%	K 10:1 2.5-7 GeV	150 G field
MRPC	50 $\times$ 3 modules, 10 m <sup>2</sup>	1650 strips, 3300 chan.	Time res < 100 ps	K 20:1 < 2.5 GeV, $\gamma$ 10:1	high rate
DAQ	282 FADC @ 250 MHz	32 pipeline VXS, 30 SRS	Trig 100 KHz $\times$ 2.6 KB	Trig 30 $\times$ 20 KHz $\times$ 48 KB	high noise
Baffle	11 $\times$ 30 blocks, 9 cm	5 cm, r 110-200 cm	area open $\phi$ > 4° / 12°	reduce background	

Table 7: Detector Summary for Approved Experiments

Experiments	PVDIS	SIDIS- $^3\text{He}$	SIDIS-Proton	$J/\psi$
Target Length	LH <sub>2</sub> /LD <sub>2</sub> 40 cm	$^3\text{He}$ 40 cm	NH <sub>3</sub> 3 cm	LH <sub>2</sub> 15 cm
Target Polarization	N/A	$\sim 60\%$	$\sim 70\%$	N/A
Target Spin Flip	N/A	$\leq 20$ mins	$\leq 4$ hours	N/A
GEM Tracking Chambers	5 chambers	6 chambers	6 chambers	6 chambers
E&M Calorimeter	Forward angle	Forward + Large angle	Forward + Large angle	Forward + Large angle
Light Gas Cherenkov	1 m long	2 m long	2 m long	2 m long
Baffles	Yes	N/A	N/A	N/A
Heavy Gas Cherenkov	N/A	1 m long	1 m long	N/A
MRPC (TOF)	N/A	100 ps resolution	100 ps resolution	100 ps resolution
Beam Polarimetry	0.4% determination	$< 3\%$	$< 3\%$	N/A
Target Polarimetry	N/A	$\sim 3\%$	$\sim 3\%$	N/A
DAQ	Single trigger	Coincidence trigger	Coincidence trigger	Coincidence trigger

Table 8: Summary of Key Parameters for Approved Programs

Experiments	PVDIS	SIDIS- $^3\text{He}$	SIDIS-Proton	$J/\psi$
Reaction channel	$p(\vec{e}, e')X$	$(e, e'\pi^\pm)$	$(e, e'\pi^\pm)$	$e + p \rightarrow e' + J/\Psi(e^-, e^+) + p$
Approved number of days	169	125	120	60
Target	LH <sub>2</sub> /LD <sub>2</sub>	$^3\text{He}$	NH <sub>3</sub>	LH <sub>2</sub>
Unpolarized luminosity ( $\text{cm}^{-2}\text{s}^{-1}$ )	$0.5 \times 10^{39} / 1.3 \times 10^{39}$	$\sim 10^{37}$	$\sim 10^{36}$	$\sim 10^{37}$
Momentum coverage (GeV/c)	2.3-5.0	0.8-7.0	0.8-7.0	0.6-7.0
Momentum resolution	$\sim 2\%$	$\sim 2\%$	$\sim 2\%$	$\sim 2\%$
Polar angle coverage (degrees)	22-35	8-24	8-24	8-24
Polar angle resolution	1 mr	0.6 mr	0.6 mr	0.6 mr
Azimuthal angle resolution	-	5 mr	5 mr	5 mr
Trigger type	Single $e^-$	Coincidence $e^- + \pi^\pm$	Coincidence $e^- + \pi^\pm$	Triple coincidence $e^- e^- e^+$
Expected DAQ rates	$< 20 \text{ kHz} \times 30$	$< 100 \text{ kHz}$	$< 100 \text{ kHz}$	$< 30 \text{ kHz}$
Backgrounds	Negative pions, photons	$(e, \pi^- \pi^\pm)$ $(e, e' K^\pm)$	$(e, \pi^- \pi^\pm)$ $(e, e' K^\pm)$	BH process Random coincidence
Major requirements	Radiation hardness 0.4% Polarimetry $\pi^-$ contamination $Q^2$ calibration	Radiation hardness Detector resolution Kaon contamination DAQ	Shielding of <i>sheet-of-flame</i> Target spin flip Kaon contamination	Radiation hardness Detector resolution

## 1365 3.2 SIDIS-<sup>3</sup>He Experiments

1366 The E12-10-006 [181] (E12-11-007 [182]) is designed to measure the single/double spin asymme-  
1367 tries through the semi-inclusive deep-inelastic scattering (SIDIS) ( $e, e'\pi^\pm$ ) with the SoLID spec-  
1368 trometer and the transversely (longitudinally) polarized <sup>3</sup>He target. The layout of the experiment is  
1369 shown in Fig. 35 and Fig. 36. The entire detector system consists of two parts: the forward-angle  
1370 detectors and the large-angle detectors.

1371 At forward angle, there are five layers of GEM detectors inside the coils to provide the forward-  
1372 angle tracking, and the first three of them are shared with the large-angle detectors. A 2 m long  
1373 light gas Cherenkov counter is installed after the GEM detectors to discriminate the scattered elec-  
1374 trons from the produced pions. A 1 m long heavy gas Cherenkov counter right after the light gas  
1375 Cherenkov counter can separate kaons and protons from the pions at momenta larger than 2.5 GeV/c.  
1376 One layer of Multi-gap Resistive Plate Chamber (MRPC) is placed after the heavy gas Cherenkov  
1377 counter to provide timing information and particle identification of hadrons at low momentum ( $<$   
1378 2.5 GeV/c), as well as to suppress photon background. A “Shashlyk”-type forward-angle Electro-  
1379 magnetic calorimeter (FAEC) will be used for electron/pion separation. One layer of scintillator pad  
1380 detector (SPD) is placed in front of the FAEC to reject photons and reduce the calorimeter-based  
1381 trigger rates. The polar angular coverage for the forward-angle detectors ranges from 8° to 14.8°  
1382 and the momentum coverage extends from 0.8 GeV/c to 7.0 GeV/c. A combination of the FAEC,  
1383 the gas Cherenkov counter, and the MRPC will be used for electron and pion identifications.

1384 To cover the large electron scattering angles, there are four layers of GEM detectors placed  
1385 inside the coils, with the last three layers shared with the forward angle detectors. Following a layer  
1386 of SPD, another “Shashlyk”-type large-angle Electromagnetic calorimeter (LAEC) will be placed  
1387 inside the coils to separate electrons and hadrons. The large-angle detectors are mainly used for  
1388 electron detection in a momentum range of 3.5-6.0 GeV/c where the expected  $\pi^-/e$  ratio smaller  
1389 than 1.5. The polar angle coverage ranges from 15.7° to 24°.

1390 The standard Hall A polarized <sup>3</sup>He target will be used in its transverse mode. A higher than  
1391 60% target polarization with a faster than 20 minutes target spin flip is expected at the full polarized  
1392 luminosity of  $10^{36}$  N cm<sup>-2</sup> s<sup>-1</sup>, which is corresponding to the unpolarized luminosity of  $10^{37}$  N  
1393 cm<sup>-2</sup> s<sup>-1</sup>. The target polarization is expected to be limited by the magnetic field gradient in the  
1394 target region, which is dominated by the leakage field from the SoLID magnet. Therefore, the  
1395 design of the magnet yokes is important to achieve the required target polarization. As shown  
1396 in Fig. 35 and Fig. 36, the target will be located about 70 cm upstream of the front yoke. Two  
1397 target collimators will be placed close to two windows of the 40 cm long target in order to reduce  
1398 backgrounds generated from both windows. The expected kinematic coverage includes: i)  $0.05$   
1399  $< x < 0.6$  which comprises the majority of the valence quark region; ii)  $0.3 < z < 0.7$  in which the  
1400 leading order  $x - z$  factorization is expected to hold; iii) maximum pion transverse momentum  $P_T$   
1401 up to 1 GeV/c, where the TMD framework is valid; and iv)  $1 \text{ GeV}^2 < Q^2 < 8 \text{ GeV}^2$  with about 2  
1402  $\text{GeV}^2$  coverage in  $\Delta Q^2$  at fixed  $x$ . These kinematic coverages can be achieved by combining data  
1403 with incident electron energies of 11 and 8.8 GeV.

1404 In order to achieve the proposed precision in asymmetries, the negative pion contamination in  
1405 the electron sample needs to be controlled to below 1%. At forward angle, it is achieved by a  
1406 combination of the FAEC and the light gas Cherenkov detector. At large angle, the LAEC alone  
1407 will be enough to provide the required pion rejection, since the expected pion to electron ratio is  
1408 small. Furthermore, the coincidence detection of electron and leading pion in the SIDIS kinematics  
1409 would further reduce the pion contamination in the electron sample.

1410 The particle identification of the leading pion (forward angle detector only) will be achieved by  
1411 a combination of time-of-flight (TOF) from the MRPC and the heavy gas Cherenkov detector. The



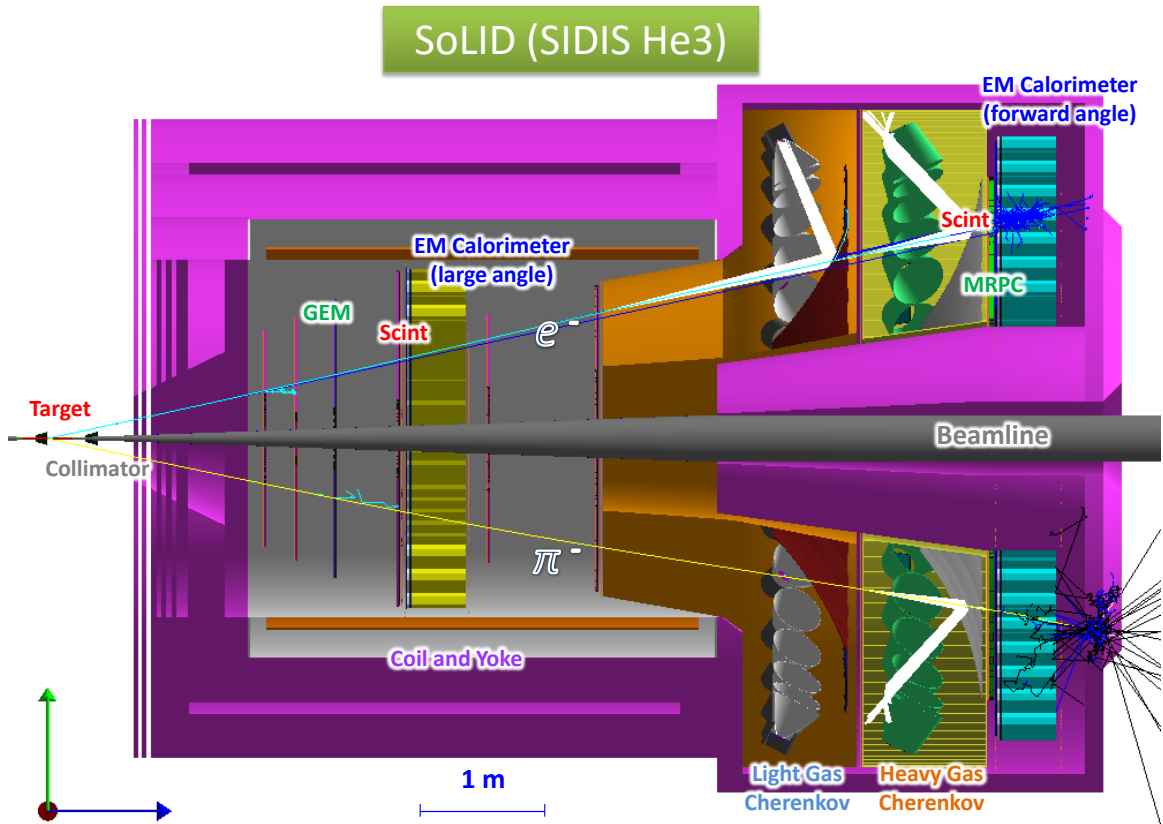


Figure 35: The experimental layout of the SoLID SIDIS- $^3\text{He}$  setup based on the CLEO magnet. The scattered electrons are detected by both forward-angle and large-angle detectors. The leading pions are detected by the forward-angle detector only. The polarized  $^3\text{He}$  target will be placed upstream in front of the spectrometer entrance.

1412 electron, kaon, and proton contaminations in the pion samples are all required to be kept below the  
 1413 1% level. The electron rejection will be achieved by the combination of the FAEC and the light  
 1414 gas Cherenkov counter. With the expected  $100\text{ps}$  TOF resolution from the MRPC, a separation of  
 1415 3 standard deviations (6 standard deviations from peak to peak) between pions and protons can be  
 1416 achieved for momenta up to  $4\text{ GeV}/c$ . Pions with momenta higher than  $2.5\text{ GeV}/c$  will trigger the  
 1417 heavy gas Cherenkov detector, while the momentum threshold for kaons to trigger the same detector  
 1418 is  $7.6\text{ GeV}/c$ . Therefore, the heavy gas Cherenkov detector would provide additional rejection  
 1419 of protons when the pion momenta are larger than  $2.5\text{ GeV}/c$ . For pions with momenta below  $2.5$   
 1420  $\text{GeV}/c$ , the TOF would provide a separation better than 2 standard deviations (4 standard deviations  
 1421 from peak to peak) between pions and kaons. Since the kaon to pion ratio is expected to be  
 1422 about 0.1, a combination of the TOF and the heavy gas Cherenkov detector would easily satisfy the  
 1423 requirement of below 1% kaons contamination.

1424 The extraction of various TMD asymmetries relies on the  $\phi_S$  and  $\phi_h$  angular dependence of  
 1425 the measured single/double spin azimuthal asymmetries in each kinematic bin of the 4-D ( $x$ ,  $Q^2$ ,  
 1426  $z$ , and  $P_T$ ) phase space. Since the kinematics of interests are in the deep-inelastic-scattering (DIS)  
 1427 region, the requirements on the resolution of the reconstructed kinematic variables are modest. For

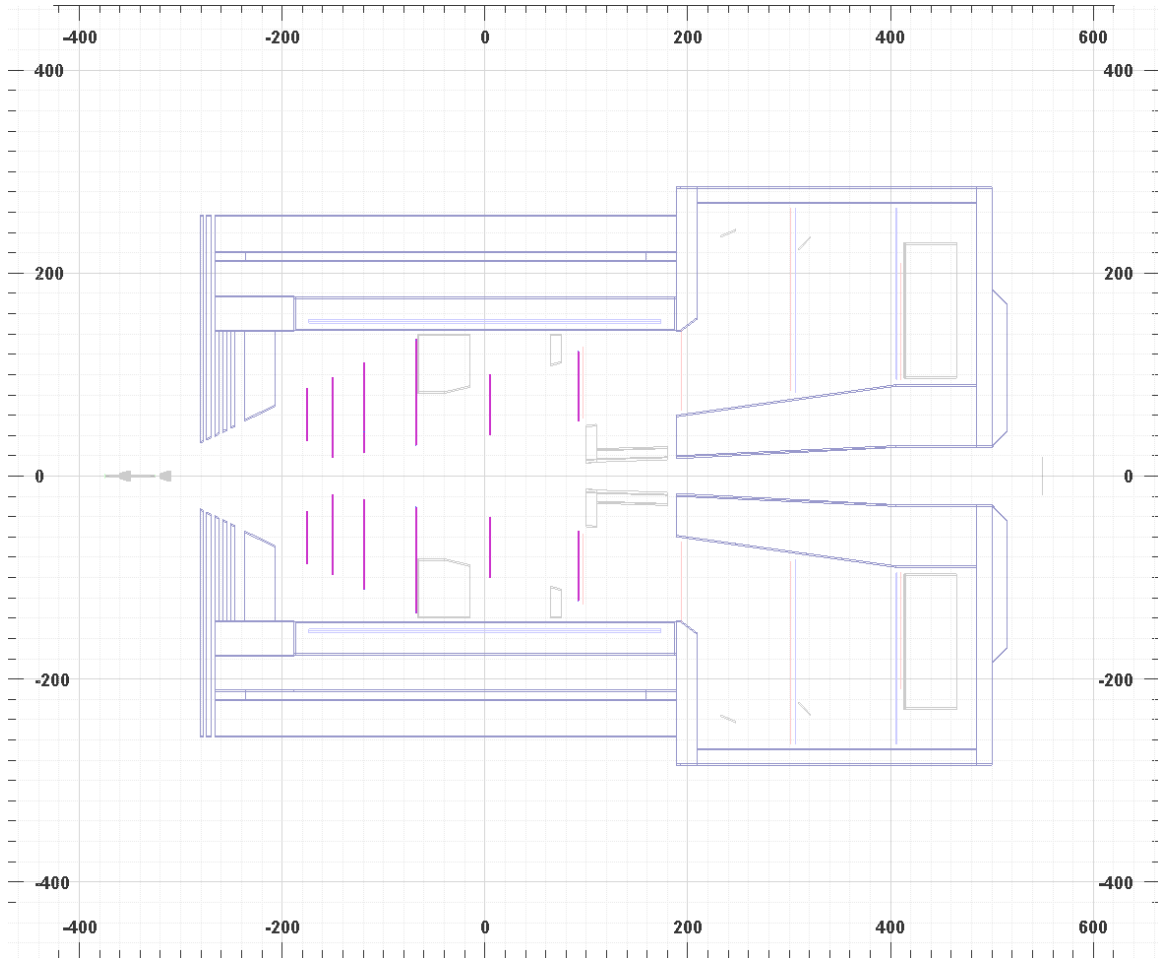


Figure 36: A 2D representation of the experimental layout of SoLID SIDIS- $^3\text{He}$  setup based on the CLEO magnet.

1428 example, a better than a few percent momentum resolution, a better than a few mrad polar angular  
 1429 resolution, a better than 10 mrad azimuthal angular resolution, and a 1-2 cm reconstructed vertex  
 1430 resolution would satisfy the needs of these experiments.

1431 With similar reaction channels, E12-10-006 [181], E12-11-007 [182], and E12-11-108 [183]  
 1432 (see next section) will share the same design of the DAQ system. The required overall luminosity  
 1433 of E12-10-006 and E12-11-007 is  $10^{37} \text{ N/cm}^2\text{s}^{-1}$ , which is an order of magnitude higher than that  
 1434 of E12-11-108. The goal of the SIDIS DAQ is to satisfy the requirement of  $\sim 100 \text{ kHz}$  trigger rate.

1435 The SIDIS process requires the detection of both the scattered electron and the leading pion.  
 1436 Therefore, a single electron trigger or a coincidence trigger of electron and hadron would satisfy  
 1437 this need. The electron trigger at the large-angle detectors will be provided by the LAEC at an  
 1438 energy threshold of about 3 GeV. Such a trigger would be sensitive to both high energy electrons  
 1439 and high energy photons (mostly from the  $\pi^0$  decay). With the large angle SPD being incorporated  
 1440 into the trigger, the electron-like triggers can be significantly suppressed. The electron trigger at the  
 1441 forward angle detector will be formed by a coincidence between the light gas Cherenkov detector,  
 1442 the FAEC, the SPD and the MRPC. Considering the kinematic information of the scattered electrons  
 1443 from the DIS process (e.g.  $Q^2 > 1 \text{ GeV}^2$ ), a position dependent energy threshold with a low limit

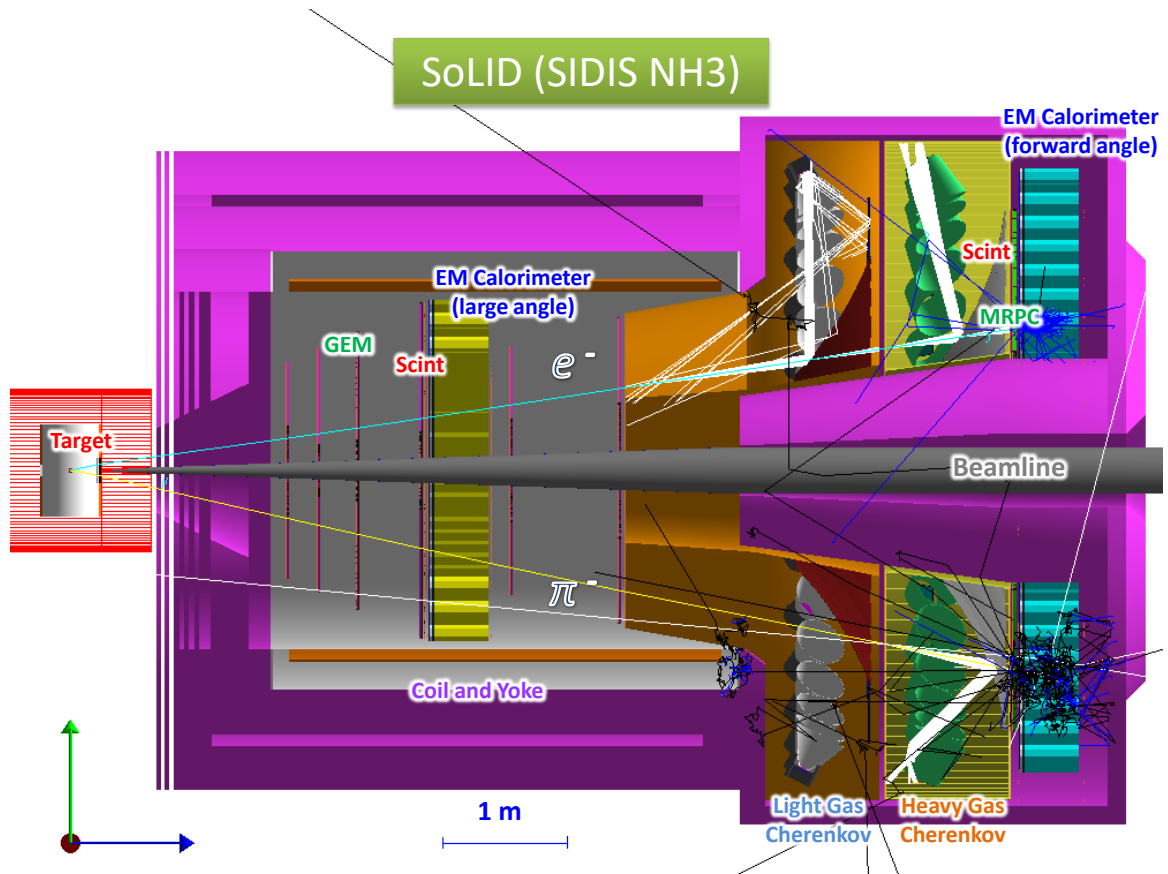


Figure 37: The experimental layout of the SoLID SIDIS-proton setup based on the CLEO magnet. It's the same like SIDIS- $^3\text{He}$  setup, except the  $^3\text{He}$  target is replaced by transversely polarized  $\text{NH}_3$  target upstream in front of the spectrometer entrance. The scattered electrons are detected by both forward-angle and large-angle detectors. The leading pions are detected by the forward-angle detector only.

1444 at 0.8 GeV in FAEC could significantly reduce the trigger rate. The charged hadron trigger at the  
 1445 forward angle will be formed with a coincidence between the FAEC, the SPD and the MRPC. The  
 1446 coincidence trigger is given by overlapping the electron trigger and the hadron trigger within a  
 1447 narrow time window. If the single electron trigger can not satisfy the requirement of  $\sim 100$  kHz  
 1448 trigger rate, the coincidence trigger could retain more SIDIS events. Therefore, it is important to  
 1449 include the coincidence trigger in the baseline design of the SIDIS DAQ system.

### 1450 3.3 SIDIS-proton Experiment

1451 The E12-11-108 [293] is designed to measure the single/double spin asymmetries through the semi-  
 1452 inclusive deep-inelastic scattering (SIDIS) ( $e, e'\pi^\pm$ ) with the SoLID spectrometer and a transversely  
 1453 polarized proton target. The layout of the experiment is same as  $^3\text{He}$  program except the target as  
 1454 shown in Fig. 37. The entire detector system consists of two parts: the forward-angle detectors and  
 1455 the large-angle detectors. The overall luminosity in this case is smaller compared to that of using  
 1456 the polarized  $^3\text{He}$  target.

1457 An improved version of JLab/UVa/SLAC polarized  $\text{NH}_3$  target (shown in Fig. 38) will be used.

1458 The main upgrade is to replace the aging Helmholtz-coil magnet with a new magnet and to have a  
 1459 fast spin-flip capability with the AFP technique to minimize the systematic uncertainty in the single  
 1460 spin asymmetry measurement. In order to satisfy the requirements of phase space coverage, the  
 1461 new design will further allow both transverse and longitudinal direction to have a nominal forward  
 1462 opening of more than  $\pm 25^\circ$ , while maintaining the same maximum field (5 Tesla) and a uniform  
 1463 field region in the center. The target polarization is required to be higher than 70% with the spin flip  
 1464 every few hours.

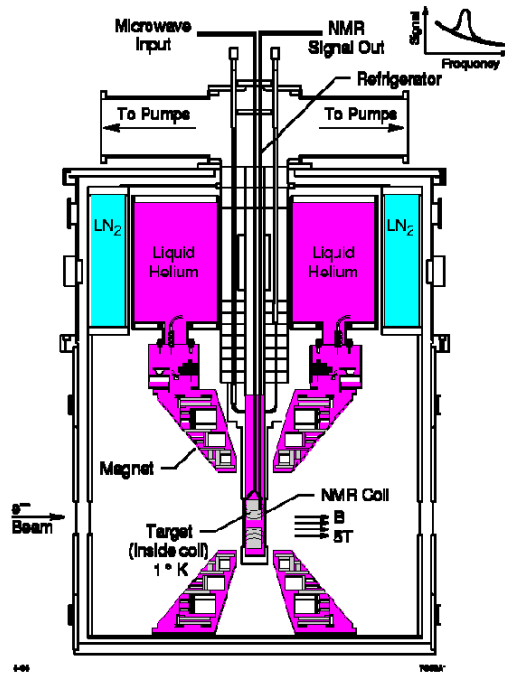


Figure 38: Polarized target system.

1465 Due to the large magnetic field in the transverse direction, this experiment suffers from a dif-  
 1466 ferent kind of background compared to the low field polarized  $^3\text{He}$  experiment, known as *sheet-*  
 1467 *of-flame*. The main feature of such a background is that a very high rate of charged particles with  
 1468 momentum range between 1-2 GeV will be localized in a very narrow region of the acceptance.  
 1469 Fig 39 shows this background on all six GEM planes in the SoLID. The GEM chambers in regions  
 1470 outside of the *sheet-of-flame* location see a background rate of less than 1.0 KHz/mm<sup>2</sup> on, whereas  
 1471 the regions inside have much higher rates. In order to handle this background and avoid damage to  
 1472 the apparatus, detector sectors in the direct line-of-sight of this *sheet of flame* will be removed or  
 1473 turned off during the proton experiment.

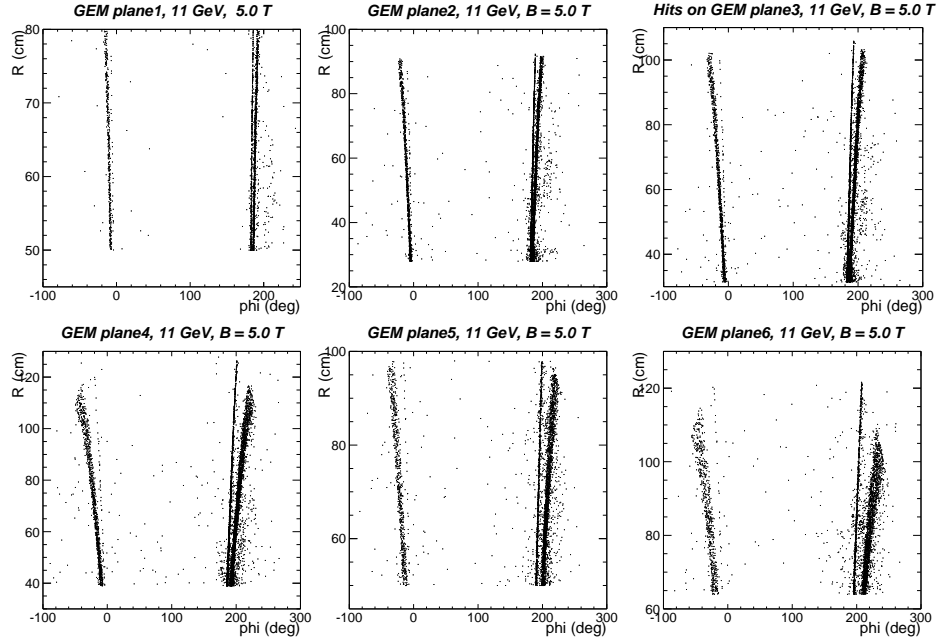


Figure 39: GEANT3 simulation results of background with  $\text{NH}_3$  target field ON. The  $x$ -axis is the azimuthal angle in lab frame. The  $y$ -axis is the radius of GEM chambers (1-6). Narrow regions of high rate (compared to rest of the acceptance) are clearly seen as a function of azimuthal angle  $\phi$ .

### 1474 3.4 PVDIS Experiment

1475 Experiment E12-10-007 [180] is designed to measure the parity violating asymmetries ( $A_{PV}$ )  
 1476 through the inclusive deep-inelastic scattering (DIS)  $p(\vec{e}, e')X$  with the SoLID spectrometer. The  
 1477 layout of the experiment is shown in Fig. 40 and Fig. 41. In order to eliminate high energy ( $\sim\text{GeV}$ )  
 1478 photons, a lead baffle will be placed downstream of the target to block direct lines of sight to the  
 1479 detector system. The detector system consists of four layers of GEM chambers for particle tracking,  
 1480 a 1 m long light gas Cherenkov counter for electron/pion separation, and a “shashlyk”-type elec-  
 1481 tromagnetic calorimeter system for the trigger and additional electron/pion separation. The GEM  
 1482 chambers will be divided into two groups, with one group placed in front of the gas Cherenkov  
 1483 counter and the other group behind it. This configuration will maximize the detector resolution,  
 1484 leading to about 2% momentum and 1 mr polar angle resolutions. The entire detector system will  
 1485 be divided into 30 independent sectors in the azimuthal angle.

1486 The polar angle and momentum coverages of the detector system are from  $22^\circ$  to  $35^\circ$  on an  
 1487 extended (40 cm) target and from 2 GeV/c to 6 GeV/c, respectively. These coverages transform into  
 1488 kinematic coverages of  $0.2 < x < 0.8$  and  $2 (\text{GeV}/c)^2 < Q^2 < 12 (\text{GeV}/c)^2$ . The overall luminosity  
 1489 is required to be larger than  $5 \times 10^{38} \text{ N cm}^{-2} \text{ s}^{-1}$  in order to reach about 0.5% relative statistical  
 1490 uncertainties on the parity violating asymmetries  $A_{PV}$  in each of the kinematic bins (see. Fig. 28).  
 1491 Such a high luminosity places specific requirements on the radiation hardness of the detector system.

1492 To leading order, the physics asymmetry  $A_{PV}^{phys}$  is related to the measured asymmetry  $A_{PV}^{measured}$

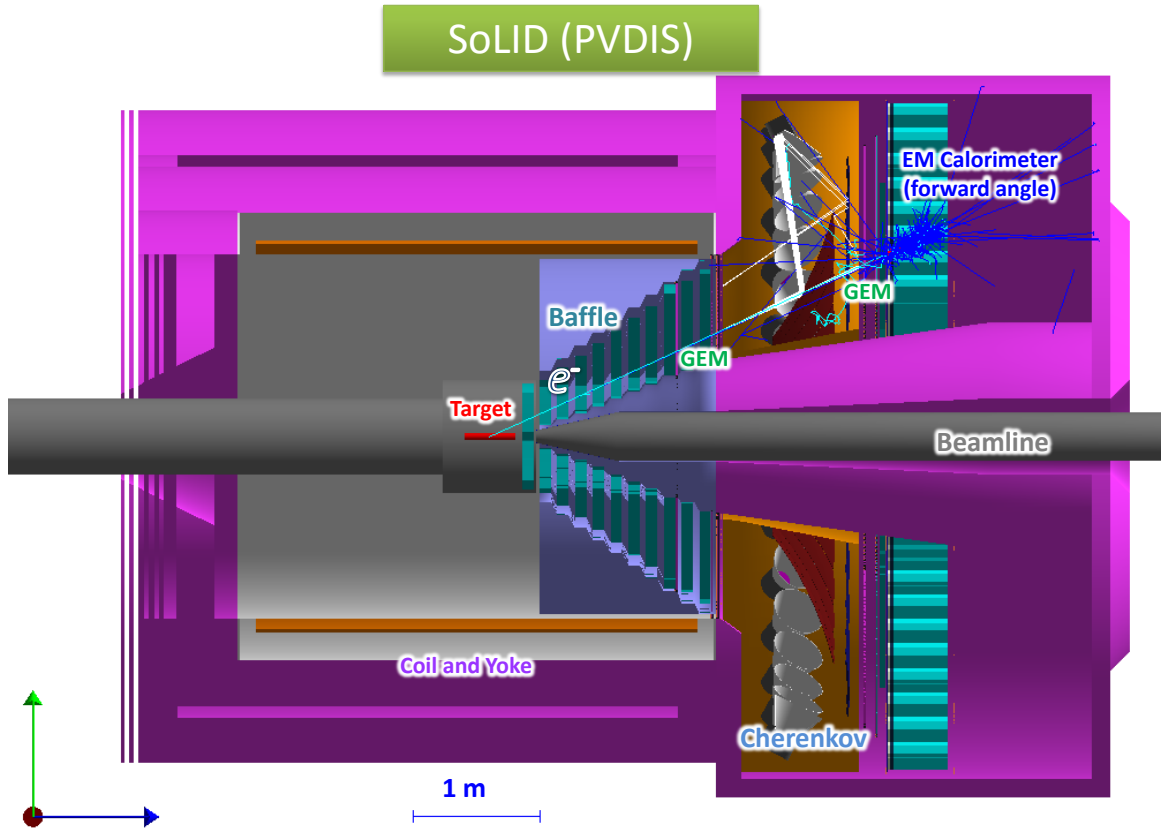


Figure 40: The experimental layout of SoLID PVDIS setup based on the CLEO magnet.

1493 by

$$A_{PV}^{phys} \sim \frac{1}{Q^2 \cdot P_{beam}} \cdot \frac{A_{PV}^{measured} - f \cdot A_{PV}^{\pi^-}}{1 - f} \quad (12)$$

1494 where  $P_{beam}$  is the polarization of the electron beam, and  $f$  and  $A_{PV}^{\pi^-}$  are the pion contamination and  
 1495 the parity violating asymmetry of pions, respectively. The proposed high precision measurement of  
 1496  $A_{PV}$  (about 0.5% in each kinematic bin) requires high accuracy. The uncertainty of the electron  
 1497 beam polarization is required to be smaller than 0.4%. Since  $A_{PV}$  for produced pions is expected to  
 1498 be similar to that of scattered electrons, the contamination of negative pions in the electron sample  
 1499 needs to be determined to about a  $10^{-3}$  level. Furthermore, the uncertainty in  $Q^2$  also must be  
 1500 controlled to below 0.1% using a precise and comprehensive optics calibration program.

1501 Since only the scattered electrons are detected in this experiment, each sector of the detector  
 1502 system can employ an independent DAQ system. Thus the requirement on the DAQ system for this  
 1503 experiment is modest. The average trigger rate for each sector is estimated to be less than 20 kHz,  
 1504 leading to a total trigger rate less than 600 kHz.

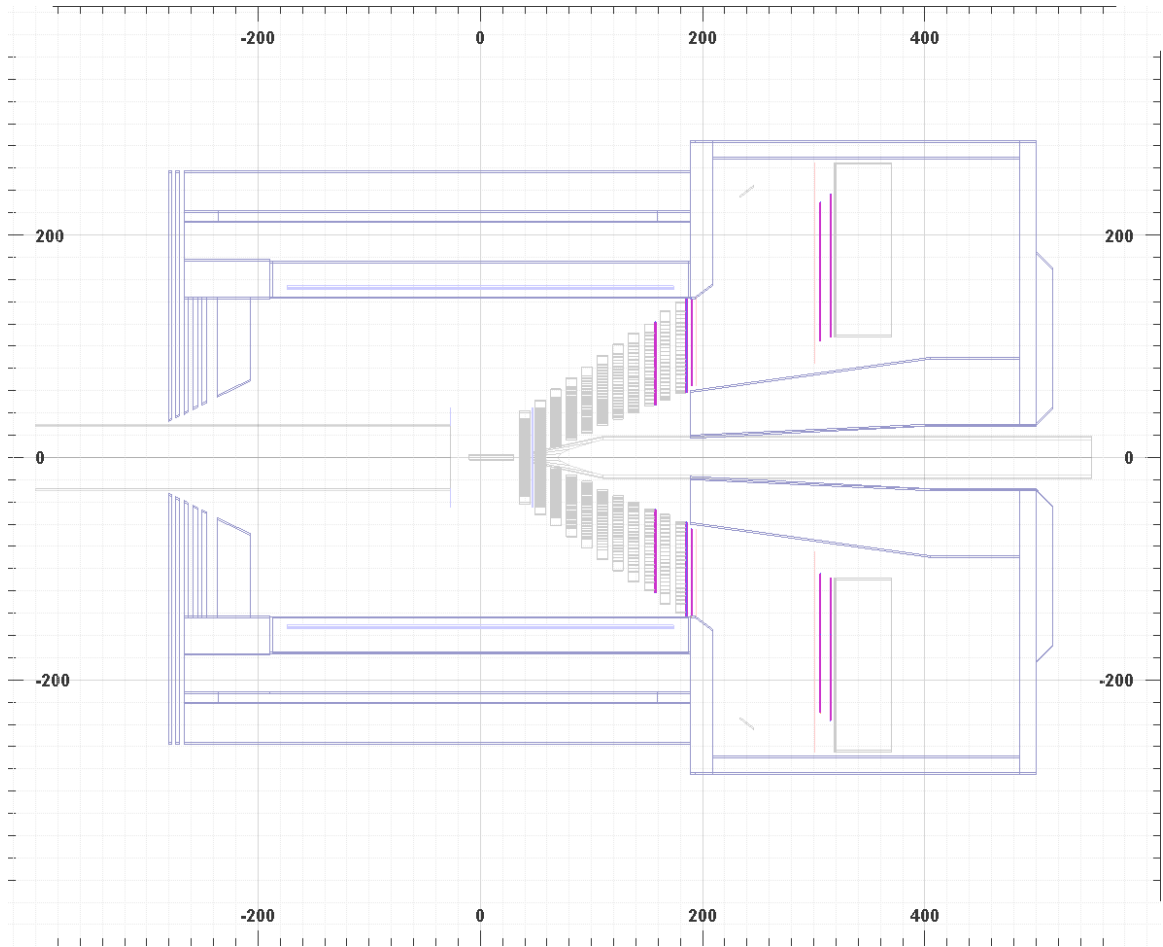


Figure 41: A 2D representation of the experimental layout of SoLID PVDIS.

### 1505 3.5 $J/\psi$ Experiment

1506 The E12-12-006 experiment [195] is designed to measure the cross section of  $J/\psi$  electroproduction  
 1507 near threshold. The reaction of interest is  $e + p \rightarrow e' + J/\Psi(e^-, e^+) + p$  where  $J/\psi$  is detected  
 1508 through its decay in a lepton pair ( $e^+, e^-$ ) with 5.94% branching ratio. Primary detection channels  
 1509 include a 4-fold coincidence, which consists of a detection of the scattered electron, the recoil  
 1510 proton, and the leptonic pair ( $e^+e^-$ ) from the  $J/\psi$  decay, a 3-fold coincidence, which is similar  
 1511 to the 4-fold coincidence but without the either scattered electron or the proton detection, and a  
 1512 2-fold coincidence of the leptonic pair ( $e^+e^-$ ) from the  $J/\psi$  decay only. In the 3-fold coincidence  
 1513 channel, the full kinematics of the recoil proton can be reconstructed through energy and momentum  
 1514 conservation. Since the recoil proton is not detected, the total number of events and the kinematic  
 1515 coverage are greatly enhanced compared to the 4-fold coincidence channel. Possible background in  
 1516 the 3-fold coincidence channel can be investigated fully with the 4-fold coincidence channel which  
 1517 offers a better signal to noise ratio. Because the electrons, positrons, as well as protons are required  
 1518 to be detected in coincidence, the configuration of SoLID will be similar to that of SIDIS. Fig. 42  
 1519 and Fig. 43 illustrates the layout of the experiment. The scattered electron and the recoil proton  
 1520 will be detected mostly by the forward angle detector, while the electron-positron pair from  $J/\psi$   
 1521 decay will be mostly detected by the large-angle detector. Compared to the SoLID-SIDIS setup,



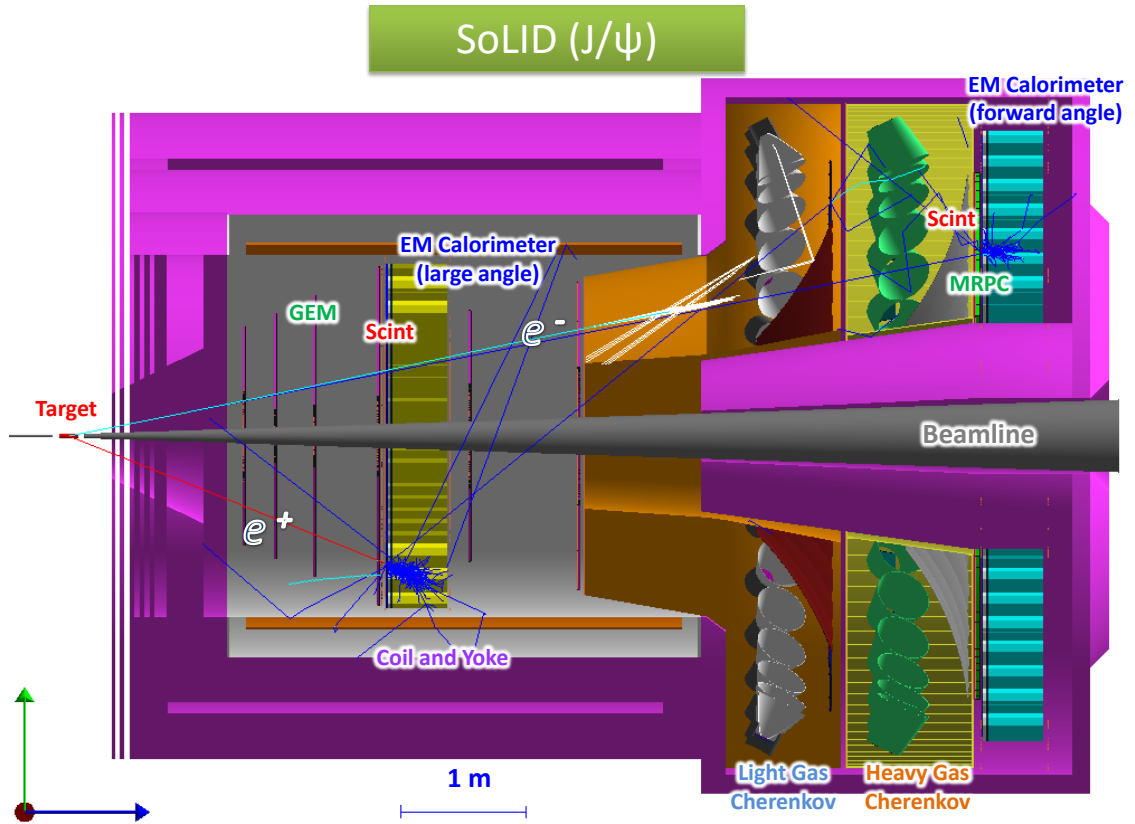


Figure 42: The experimental layout for the SoLID  $J/\psi$  setup based on the CLEO magnet. It's the same like SIDIS- $^3\text{He}$  setup, except the  $^3\text{He}$  target is replaced by the standard Hall A 15 cm liquid Hydrogen target upstream in front of the spectrometer entrance.

1522 the polarized target will be replaced by the standard Hall A 15 cm liquid Hydrogen target, but its  
 1523 position will be located about 35 cm more downstream relative to the target center of the SIDIS  
 1524 setup to improve the acceptance.

1525 The approved beam time for this experiment is 60 PAC days at an unpolarized luminosity of  $10^{37}$   
 1526  $\text{N cm}^{-2} \text{s}^{-1}$ . The kinematic coverage will be  $4.05 \text{ GeV} < W < 4.45 \text{ GeV}$  and  $|t - t_{min}| < 2.5$   
 1527  $\text{GeV}^2$ . Depending on the cross section model, the expected physics counts with 50 days production  
 1528 data for 4-fold (3-fold) coincidence range from  $\sim 0.7\text{k}$  ( $2.1\text{k}$ ) to  $\sim 2.9\text{k}$  ( $8.1\text{k}$ ) at the proposed lumi-  
 1529 nosity. Since this measurement is limited by statistics due to the rare nature of the  $J/\psi$  production  
 1530 near threshold process, a higher luminosity ( $> 10^{37} \text{ N cm}^{-2} \text{ s}^{-1}$ ) is strongly desired.

1531 The primary trigger is a triple coincidence of scattered electron,  $J/\psi$  decay electron, and  $J/\psi$   
 1532 decay positron. With a 100 ns coincidence window, the trigger rate would be dominated by the  
 1533 random coincidence events with a rate of about 3 kHz, which is far below the required  $\sim 100$  kHz  
 1534 trigger rate of SoLID-SIDIS. Therefore, the main requirement of SoLID- $J/\psi$  is the capability of  
 1535 forming hardware coincidence trigger.

1536 Since we are interested in the exclusive electroproduction of  $J/\psi$ , the resolution of the  $J/\psi$   
 1537 setup is important in rejecting different backgrounds. Currently the expected resolutions are similar  
 1538 between SIDIS and  $J/\psi$  setups and it would satisfy the requirement of this experiment. We are  
 1539 working on improving the  $J/\psi$  resolution further.



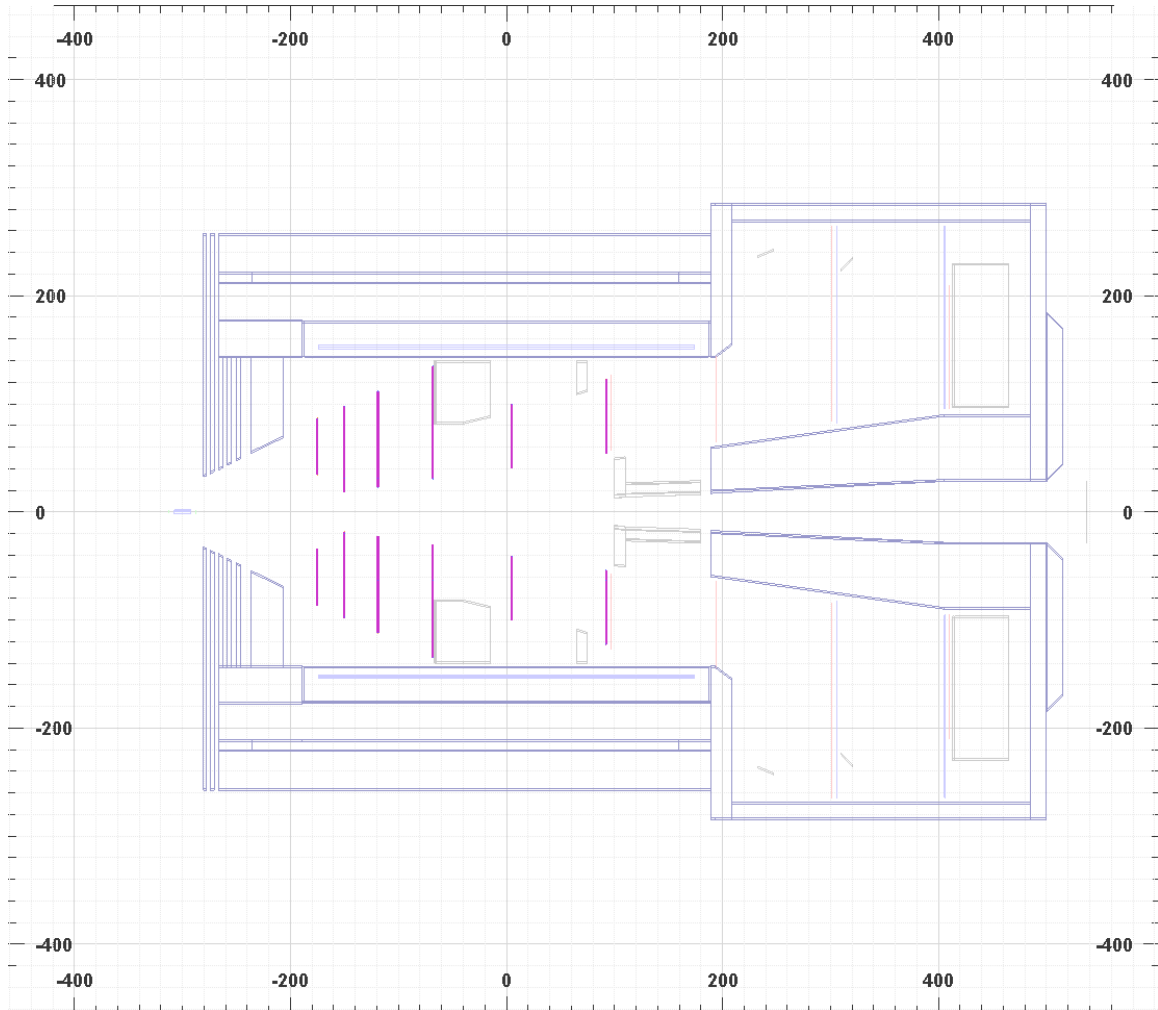


Figure 43: A 2D representation of the experimental layout of SoLID  $J/\psi$  setup.

1540 The particle identification of the recoil proton for the 4-fold coincidence relies on the time-  
 1541 of-flight (TOF) from the MRPC. The highest momentum of the recoil proton is about 3 GeV/c.  
 1542 With the designed 100 ps resolution in TOF, protons can be separated from kaons at 2 standard  
 1543 deviations (4 standard deviations from peak to peak). In addition, protons can be separated from  
 1544 pions at 6 standard deviations (12 standard deviations from peak to peak). The requirement on the  
 1545 exclusive kinematics in the off-line data analysis would further strengthen the particle identification  
 1546 of protons.

1547 There are two major types of backgrounds. The main physics background originates from the  
 1548 Bethe-Heitler (BH) process. At the proposed kinematics, the BH background is expected to be  
 1549 smaller than the physics  $J/\psi$  events by 1-2 order of magnitude in average <sup>2</sup>. The cross section  
 1550 associated with the BH background can be directly measured by choosing the invariant mass of the  
 1551 electron-positron pair to be away from the  $J/\psi$  peak. The other major background is the random  
 1552 coincidence of a  $J/\psi$  (normally photo-produced) and a scattered electron. The random coinci-

<sup>2</sup>Due to the rapid decrease of the cross section near threshold for the physics  $J/\psi$  events, the BH background becomes comparable at low W.

1553 dence background is expected to be 1-2 orders of magnitude smaller than the physics events with  
1554 the proposed setup. In addition, the random coincidence backgrounds can also be directly mea-  
1555 sured/subtracted through the commonly used off-window method.

## 1556 4 Magnet

### 1557 4.1 Requirements

1558 The SoLID spectrometer is designed to have large acceptance in polar angle, azimuthal angle, and  
1559 momentum acceptance, and also operate at high luminosity. A solenoid magnet is a natural choice in  
1560 this case. The magnetic field is symmetric around the beamline, confining the copious low energy  
1561 charged background particles to the beam pipe region. The detectors are placed symmetrically  
1562 around the beamline, both within the solenoid and in the end cap region. The approved experiments  
1563 all have some requirements on the magnet. They are summarized below:

1564 • The PVDIS experiment requires polar angle coverage for the center of the target from  $22^\circ$  to  
1565  $35^\circ$ . Its hydrogen and deuterium targets can operate in the magnetic field. To operate the detectors  
1566 at the design luminosity of  $10^{39}/\text{cm}^2/\text{s}$ , a set of baffles is required to block unwanted photons and  
1567 hadrons originating in the target. The magnetic field must then be strong enough to spiral the several  
1568 GeV DIS electrons through the gaps in the baffles and also provide sufficient curvature in the tracks  
1569 so that their momentum can be reconstructed. Both requirements can be met with a field integral  
1570 along the flight path on order of 2.5 T-m.

1571 • Both SIDIS proton and neutron experiments need polar angle coverage from  $8^\circ$  to  $24^\circ$ . The  
1572  $^3\text{He}$  and  $\text{NH}_3$  targets must be located just upstream of the solenoid where the fringe fields before  
1573 additional shielding are on the order of 5 G. The  $\text{NH}_3$  targets require a uniform 5 T field and the  
1574  $^3\text{He}$  targets require uniform fields on the order of a 25 Gauss. There are two sets of detectors. The  
1575 forward detectors, located in the end cap, cover particles with angles below  $15^\circ$ . This requires the  
1576 solenoid to be on the order of 3-4 m long. The large angle detectors are located near the center of  
1577 the magnet, requiring a diameter on the order of 3 m. The field integral needs to be on the order of  
1578 5 T-m in order to provide sufficient momentum resolution from the GEM tracking system.

1579 • The  $J/\psi$  experiment must detect the electron-positron pair from the  $J/\Psi$  decay as well as the  
1580 scattered electron. With a liquid hydrogen target placed upstream of the magnet, the configuration  
1581 for the SIDIS experiment meets the requirements.

1582 Overall, the ideal SoLID solenoid needs to have an outer radius  $< 3$  m to fit in the experimental  
1583 hall, an inner radius  $> 1$  m, a length of 3–4 m, and a field integral on the order of 5 T-m.

### 1584 4.2 SoLID magnet

1585 We have chosen the CLEO II magnet for the SoLID spectrometer. It is a solenoidal magnet with a  
1586 uniform axial central field of 1.5 T, a large inner space with a clear bore diameter of 2.9 m and a  
1587 coil of 3.1 m diameter. With a coil length of 3.5 m, its magnetic field uniformity is  $\pm 0.2\%$ . It was  
1588 built in the 1980s by Oxford in England and installed for CLEO II in 1989 [197, 198].

1589 The coil is made of  $5 \times 16 \text{ mm}^2$  aluminum stabilized superconductor and run at 3266 A with an  
1590 average current density of 1.2 MA/m. The large conductor size provides simpler construction and  
1591 ease of protection. A 3.8 m long cryostat encloses the coil and cools it with a thermosyphon system.  
1592 The return yoke has 3 layers with 36 cm thickness each and is octagonally divided. There are 2  
1593 collars 60 cm thick supporting not only the return yokes, but also the coil with 4 rods. The magnet  
1594 has good stability, low cryogenic heat load, passive cooling, and passive protection. This gave it the  
1595 flexibility to be frequently de-energized for maintenance and accelerator studies. It has been kept in  
1596 good condition since stopping beam. The coils and cryostat of the CLEO-II magnet have arrived at  
1597 JLab in 2016 and [preparations are being made to transport the return steel](#). To use the CLEO magnet  
1598 for SoLID, we will reuse the coil and cryogenic system, but the downstream collar and return yoke  
1599 will be modified to allow the PVDIS acceptance up to  $35^\circ$ . New endcap and front pieces will be

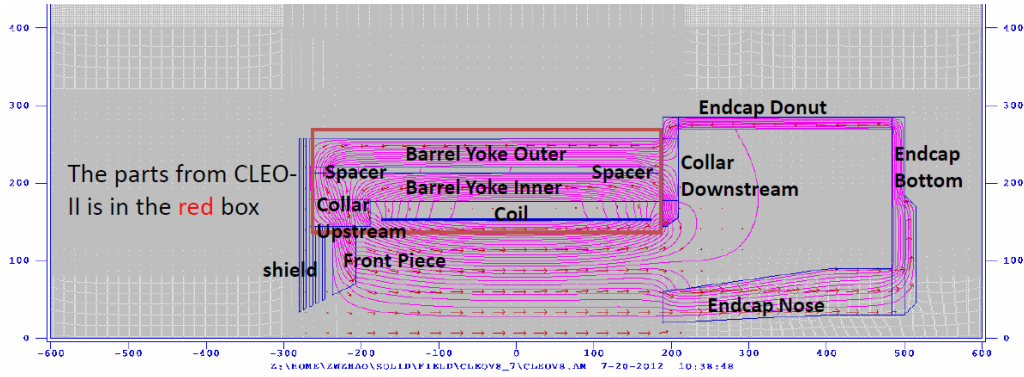


Figure 44: Design of the CLEO II magnet yoke for SoLID.

1600 fabricated.

1601 The design of the yoke for SoLID with the CLEO II magnet is shown in Figure 44. There are  
 1602 two layers of barrel flux return and an upstream collar which are kept from the original CLEO-II  
 1603 magnet. The simulation has shown that the original third layer of barrel flux return is not needed  
 1604 for SoLID and the field in the rest of two layers is well below saturation. The downstream collar  
 1605 is either modified or a new part. All other parts including the endcap, the front piece and the target  
 1606 shielding need to be built.

1607 The  $B$  field for the CLEO II magnet with the SoLID yoke is shown in Figure 45. The strongest  
 1608 field is within the solenoid and drops sharply in the endcap and upstream opening. The magnetic  
 1609 field was calculated using the 2D Poisson Superfish program.

1610 The  $B_z$  and  $B_r$  fields along the beamline are shown in Figure 46. The  $B_z$  field at the center is  
 1611 about 1.4 T, dropping to 0.8 T at the exit of the coil.

1612 The axial force for the 3 section of coils and all parts of yoke are shown in Figure 47. There are  
 1613 two strong forces compressing the coil. These forces can be balanced so that the net force on the  
 1614 coil is small. It can be adjusted by moving the location of the front piece, where the force varies by  
 1615 3–5 t/cm.

### 1616 4.3 Planned Modifications

1617 The CLEO magnet will require some modifications to its design for use in the SoLID experiments.  
 1618 Much of the CLEO magnet will be reused in its original condition. However, SoLID will not use  
 1619 the outermost muon ring. It will use the inner two rings, each consisting of 8 slabs of iron to make  
 1620 up the 8-sided ring. Each of these slabs will have to be shortened to allow the proper position of  
 1621 the endcap. The original upstream coil collar will be reused. Spacers between the slabs will also be  
 1622 reused. The downstream coil collar will be modified if an economical way of reducing its thickness  
 1623 can be found without wasting a majority of its unwanted material. If a solution is not found then a  
 1624 new downstream coil collar will be created. Additional pieces of iron will need to be fabricated to  
 1625 allow for the proper mating of the endcap with the barrel yoke. The existing outer and inner shower  
 1626 counters that mount inside of the coil collars do not appear to be reusable as the upstream coil cup  
 1627 that will reside inside the upstream coil collar. All supporting structure for the magnet barrel yoke  
 1628 and detector endcap will be new fabrications. Please refer to the study in Ref. [196].

1629 The endcap, which consists of the outer cylindrical ring, the backplate, and endcap nose, will  
 1630 all be made from new material. The endcap is designed to be part of the magnetic flux return yoke  
 1631 and house the downstream forward angle detector package. The endcap will be split vertically into

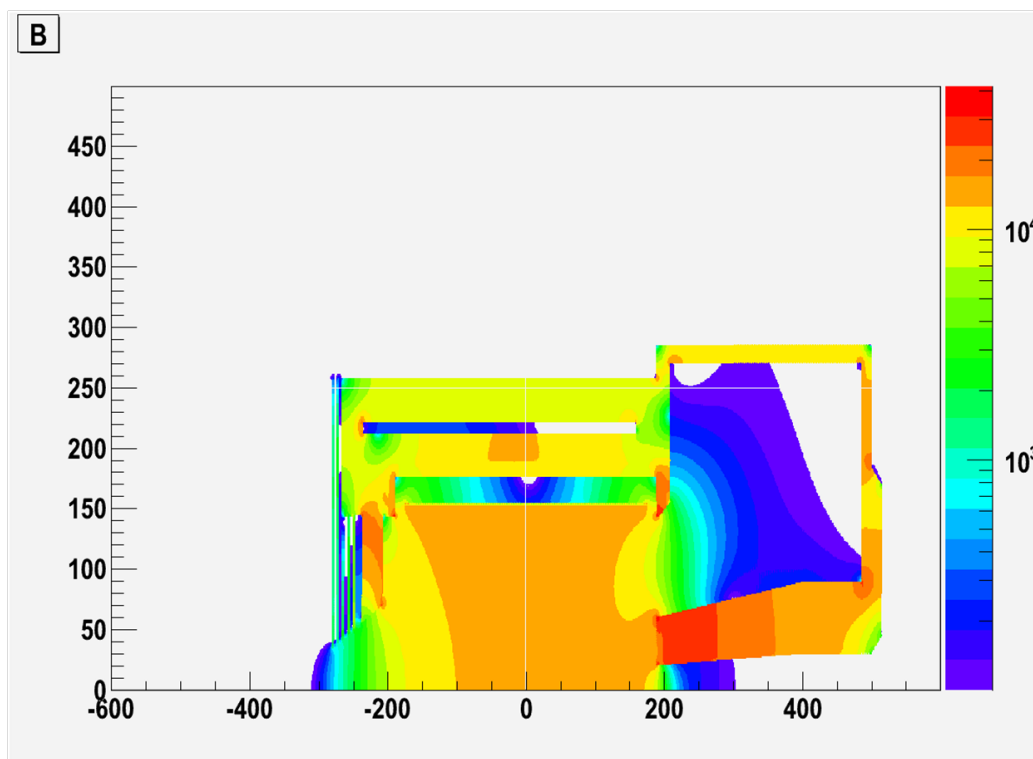


Figure 45: SoLID CLEO magnet field  $B > 100\text{G}$ .

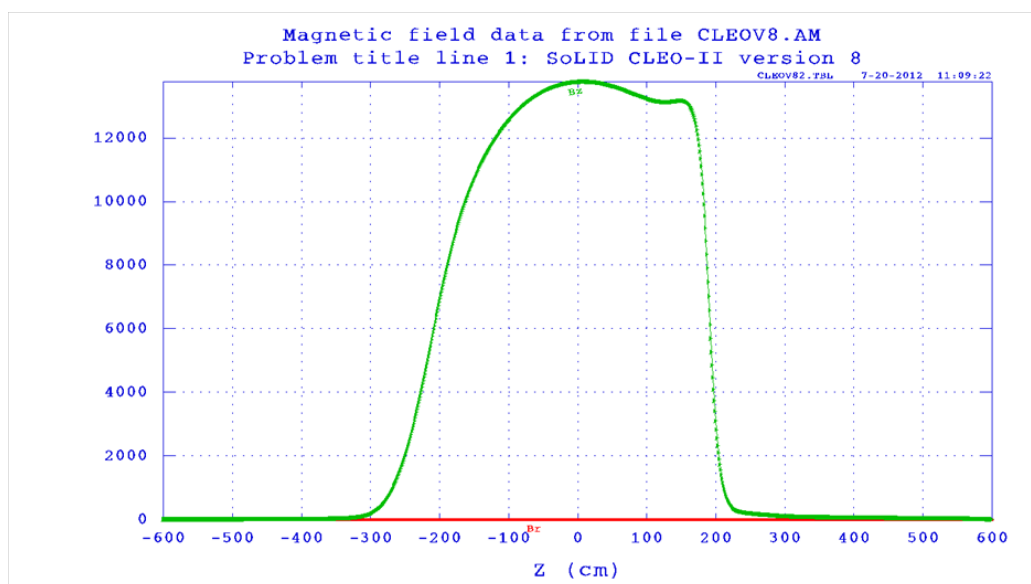


Figure 46: SoLID CLEO magnet field along beamline.

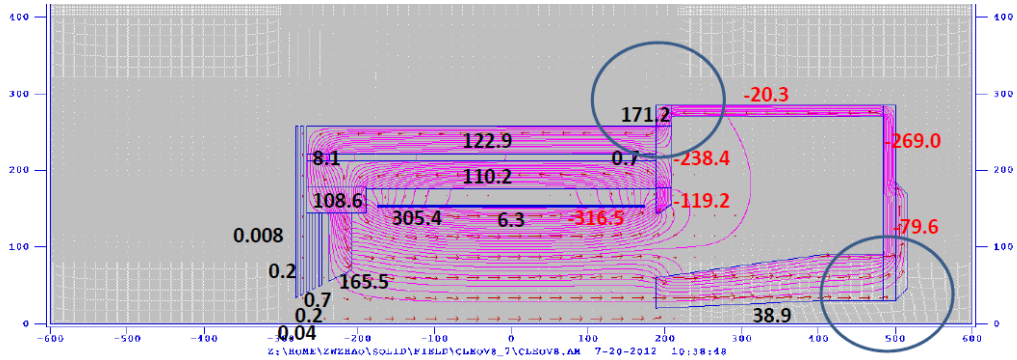


Figure 47: SoLID CLEO axial force in metric t. The two circles show where the force changes direction.

1632 halves and capable of separation to allow for access to the detector package, see Figure 48. The  
 1633 endcap nose with a secondary backing plate will be a cast two piece design to allow for separation.  
 1634 Each section of the nose will bolt to the main backplate which consists of a two piece round disk.  
 1635 The two halves of the cylindrical outer ring will bolt to the corresponding backplate. The structural  
 1636 support and motion mechanism for the endcap will be discussed in Section 18.

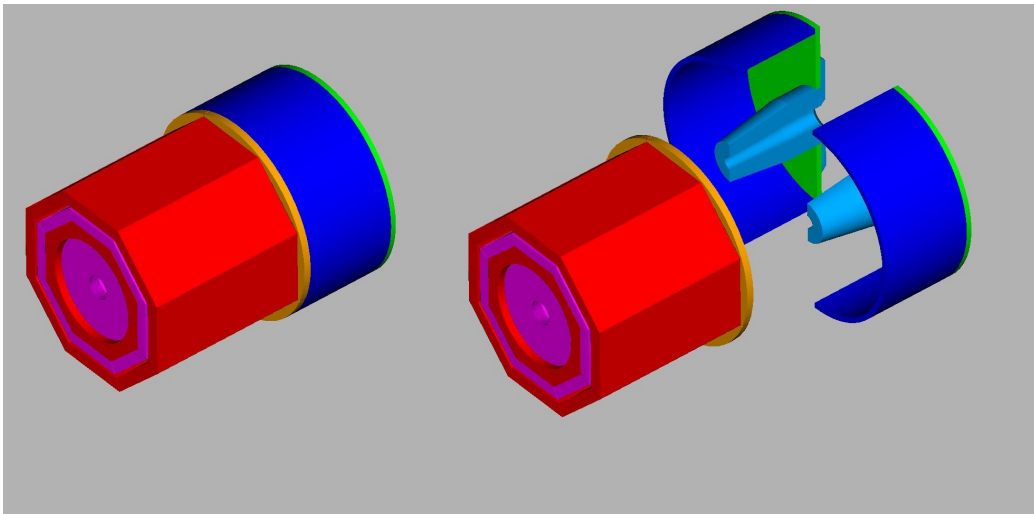


Figure 48: The endcap will be split vertically and also have the capability of separating in the lateral direction

1637 **4.4 Current Status and Planned Test**

1638 Jefferson Lab will develop a cold test requirements document and implementation plan prior to  
 1639 installing the magnet in Hall A. The cold test will be done without the iron yoke and thus at reduced  
 1640 operating parameters.

1641 A new magnet power supply cost has been added to the SoLID costs. Cost basis is from recent  
 1642 purchases.

1643 Mapping the magnetic field and evaluating the data will require an additional 4–6 weeks in

1644 schedule with use of 2 technicians and 1 scientist/engineer for the duration. Additional funding will  
1645 be required for the mapping apparatus, \$200k.

1646 Scheduling of the SoLID experiments will allow 1 year prior to installation for testing of the  
1647 magnet.

1648 We have included the cost for new power supply, transfer lines and supports. The only reuse  
1649 will be some magnet yoke steel and the cryostat.

1650 Work on the dismantling of the CLEO II magnet was started by Cornell University in the sum-  
1651 mer of 2015 with the disconnection of power, cryogen and control lines for the magnet from the  
1652 building infrastructure. Several of the large return iron blocks were also removed to provide practi-  
1653 cal experience for the Cornell rigging crew and the project management team to develop a compre-  
1654 hensive schedule for the 2016 removal.

1655 The 2016 summer down period started with the removal of the 700 liter helium dewar and outer  
1656 steel cladding. The leads, cooling supply and return lines as well as instrumentation cables needed  
1657 to be severed at the top of the service turret to allow the dewar to be lifted away. Next, the beamline  
1658 and detectors that resided in the bore of the magnet were uninstalled and the return iron was removed  
1659 layer by layer.

1660 Upon completion of the iron removal, including the coil collars, the axial transport brackets  
1661 were installed to protect the coils during movement. The cryostat housing the coils could then be  
1662 moved to the transport frame. The service turret and neck could then be removed from the top of the  
1663 cryostat. The neck required disassembly to separate the continuous leads from the thermal shielding  
1664 and cooling lines. The above mentioned disassembly steps adhered to the recommendations of the  
1665 Oxford Operating Manual for the CLEO II Magnet. The leads were packaged for protection and  
1666 secured to the side of the cryostat for safe transport. A stainless steel cover was fabricated and  
1667 attached to the flange on the top of the cryostat providing protection for the ends and the cryo lines  
1668 and leads. Any remaining openings were sealed to prevent contaminants from entering the vacuum  
1669 space. Prior to loading on a flatbed truck the entire cryostat was wrapped in fire retardant marine  
1670 grade shrink wrap to keep the unit weathertight for the trip to JLAB.

1671 After arrival at JLAB the cryostat was rolled into the high bay area of the Test Lab for climate  
1672 controlled storage until future use. Inspection indicated the cryostat remained sealed through trans-  
1673 port. Loads on the magnet were monitored during transport using (2) three-axis accelerometers and  
1674 remained under the maximum safe threshold indicated in the Oxford Manual. The two coil collars  
1675 accompanied the cryostat in the November 2016 delivery and were stored in the Test Lab, as shown  
1676 in Figure 49. The Test Plan for characterizing the magnet and integrating it into the JLAB systems  
1677 remains to be developed.



Figure 49: CLEO II magnet at JLab.



## 1678 **5 Targets**

1679 There are five approved SoLID experiments. Two semi-inclusive DIS experiments (E12-10-006  
1680 and E12-11-007) use a polarized  $^3\text{He}$  target with the achieved performance. One SIDIS experi-  
1681 ment (E12-11-108) uses a transversely polarized proton ( $\text{NH}_3$ ) target. The parity-violating DIS  
1682 experiment (E12-10-007) uses a 40-cm cryogenic liquid deuterium (hydrogen) target system. The  
1683 J/Psi experiment uses the standard cryogenic liquid hydrogen target. The following subsections will  
1684 describe the polarized  $^3\text{He}$  target, the polarized proton ( $\text{NH}_3$ ) target and the PVDIS cryotargets.

### 1685 **5.1 Polarized $^3\text{He}$ Target**

1686 The polarized  $^3\text{He}$  target is based on the technique of spin-exchange optical pumping of hybrid  
1687 Rb-K alkali atoms. Such a target was used successfully in the recently completed SIDIS experi-  
1688 ment [199] with a 6-GeV electron beam at JLab. Three sets of Helmholtz coils provide a 25 Gauss  
1689 holding field for any direction, supporting polarization in transverse (for E12-10-006) or longitu-  
1690 dinal (for E12-11-007) direction. Target cells were 40-cm long with density of about 10 amg (10  
1691 atm at  $0^\circ$ ). The luminosity was about  $10^{36}$  nuclei/s/cm with a beam current of  $15 \mu\text{A}$ . An in-beam  
1692 polarization of up to 60% was achieved. Both achieved luminosity and figure-of-merit are the  
1693 world-best so far. Two kinds of polarimetry, NMR and EPR (paramagnetic-Resonance), were used  
1694 to measure the polarization of the target. The precision for each method was about 5% (relative) and  
1695 the methods agreed well within uncertainties. It is expected to be able to reach 3% with the planned  
1696 improvements.

1697 Frequent target polarization direction reversal is needed to minimize target-spin-correlated sys-  
1698 tematic uncertainties. The fast target spin reversal was achieved in a few seconds for the 6 GeV  
1699 SIDIS experiment by using RF AFP technique. The frequency of the spin reversal was kept to 20  
1700 minutes to minimize the polarization loss due to AFP. The additional polarization loss due to fre-  
1701 quent spin reversal was kept at  $< 10\%$  (relative). The above quoted maximum in-beam polarization  
1702 achieved for the 6 GeV experiment (up to 60%) included the loss due to spin reversal. A new method  
1703 using field rotation for spin reversal was tested and a nearly no polarization-loss result was achieved  
1704 and will result in an improved performance. It will allow to have more frequent (a few minutes  
1705 instead of 20 minutes) spin reversal to help further improve the target-spin-correlated systematics.

1706 The upstream endcap plate will keep the magnetic field and its gradients under control in the  
1707 target region. In this design, the absolute magnetic field strength in the target region is about a few  
1708 Gauss with field gradients 50 mG/cm. Correction coils around the target will further reduce field  
1709 gradients to the desired level of 30 mG/cm.

1710 A collimator, similar to the one used in 6 GeV experiment, will be placed next to the target cell  
1711 window to minimize the target cell contribution to the total events.

1712 In addition to the polarized  $^3\text{He}$  target, the current target system has a multi-foil  $^{12}\text{C}$  target for  
1713 spectrometer optics study, a BeO target for beam tuning and a reference target cell system, which  
1714 allows to have different target gases, hydrogen, deuterium,  $^3\text{He}$  and nitrogen, be used to measure  
1715 unpolarized cross sections, for calibration and dilution study.

1716 Upgrades are planned for other polarized  $^3\text{He}$  experiments before the SoLID experiments. These  
1717 upgrades are not required for the SoLID experiments but will benefit them.

### 1718 **5.2 Transversely Polarized Proton Target**

1719 The SoLID collaboration proposes to measure single spin asymmetries in the semi-inclusive, deep-  
1720 inelastic ( $e, e'\pi^\pm$ ) reaction using a transversely polarized proton target. The target to be used is the

1721 dynamically polarized ammonia target that has been used at SLAC and at Jefferson on numerous  
1722 occasions [200]. Its last use was in 2012 for the g2p/Gep experiments, which took place in Hall  
1723 A [201]. Proton luminosities of  $10^{35} \text{ cm}^{-2}\text{s}^{-1}$  have been achieved with this target, in conjunction  
1724 with electron beam currents up to 100 nA. In order to meet requirements of the SoLID measurements  
1725 however, a new superconducting magnet must be procured, as discussed below.

1726 Dynamic nuclear polarization (DNP) has been used to polarize solid targets for nuclear and  
1727 particle experiments for more than four decades. To realize DNP, a paramagnetic species is im-  
1728 planted into the target material, either by dissolving a stable radical into the material (if the latter  
1729 is liquid at room temperature), or by producing radicals directly within the material using ionizing  
1730 radiation. The unpaired electrons are highly polarized by cooling the sample to a low temperature  
1731 and exposing it to a high magnetic field. For example, at the 1 K and 5 T operating conditions of  
1732 the JLab target, the electron polarization is -99.8%. Off-center microwave saturation of the radicals  
1733 Electron Spin Resonance (ESR) frequency is used to transfer this polarization to nearby nuclear  
1734 spins, with one or more mechanisms, such as the solid effect, thermal mixing or the cross effect, be-  
1735 ing responsible for the polarization transfer. Spin diffusion then transports the nuclear polarization  
1736 throughout the bulk of the sample. The polarization may be positive or negative, depending upon  
1737 whether the microwave frequency is below or above the ESR frequency. In well-designed systems,  
1738 proton polarizations exceeding 95% [202] and deuteron polarizations approaching 90% [203] have  
1739 been achieved.

1740 Frozen ammonia ( $\text{NH}_3$ ) has been the target material of choice for electron beam experiments at  
1741 Jefferson Lab. Proton polarizations in excess of 90% are routinely achieved in ammonia, and it has  
1742 a relatively high ratio of polarizable-to-nonpolarizable nucleons (17.6%). Additionally, ammonia  
1743 displays a very high resistance to radiation damage, and simply warming the material to about  
1744 100 K for a few minutes can largely repair the damage that does occur. Prior to the experiment,  
1745 paramagnetic radicals (chiefly  $\text{NH}_2$ ) are created within the ammonia by irradiating the material  
1746 (under liquid argon) with an electron beam. For convenience, this irradiation is typically done off  
1747 site, and the material is then stored under liquid nitrogen until required for the experiment. The JLab  
1748 target system, as utilized in Hall A, is shown in Fig 50. It consists of a 5 T split-coil superconducting  
1749 magnet, a  $^4\text{He}$  evaporation refrigerator with a cooling power of about 1 W at 1 K, and a target  
1750 insert containing two samples of frozen ammonia along with additional targets for background and  
1751 dilution studies. These reside in a purpose-built, evacuated scattering chamber with thin windows  
1752 around its perimeter for beam entrance and exit. Equipment outside the chamber includes a large set  
1753 of vacuum pumps for the evaporation refrigerator, microwave electronics for polarizing the target  
1754 sample, and a NMR system for measuring its polarization. Liquid helium is provided to the target  
1755 from a nearby 500 L dewar.

1756 Before its use in the g2p/Gep experiments, numerous upgrades were made to the polarized target  
1757 in order to improve its performance, reliability, and safety:

- 1758 • An entirely new refrigerator was constructed at JLab according to the safety regulations dic-  
1759 tated by 10 CFR 851;
- 1760 • The quench-relief piping system for the superconducting magnet was upgraded to replace  
1761 leaking rubber seals with copper gaskets, and also made compliant to 10 CFR 851;
- 1762 • The pumping system and controls were overhauled;
- 1763 • A more robust sample insert and motion mechanism were constructed to address problems  
1764 that were encountered in previous experiments;

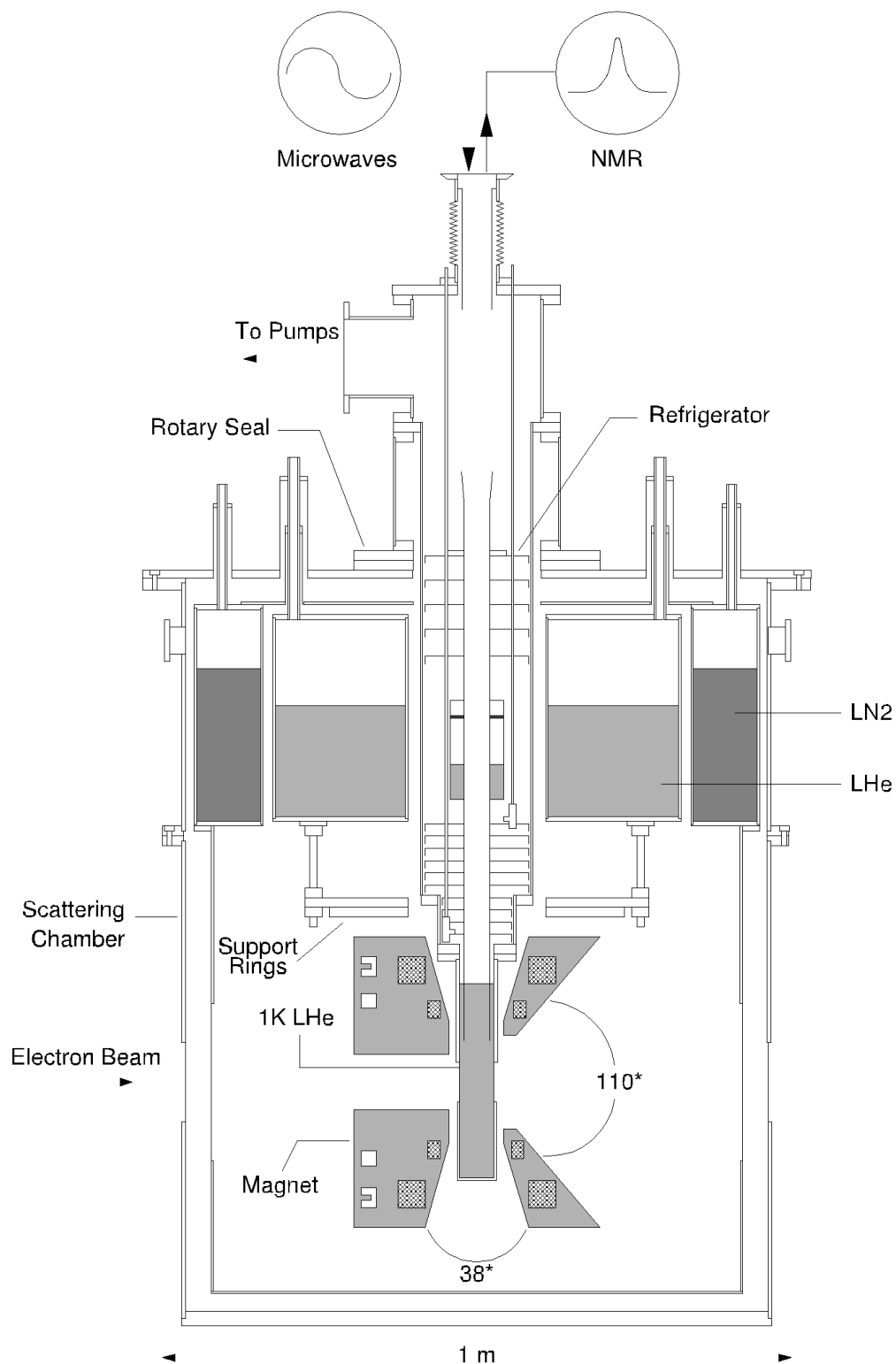


Figure 50: The dynamically polarized target, as utilized in Hall A. The cryostat can rotate  $90^\circ$  about the vertical axis, thus providing either longitudinal or transverse polarization with respect to the electron beam. The longitudinal orientation is shown.

- 1765 • A new rotary vacuum seal was implemented that significantly reduces the time required to  
1766 rotate the magnet between its longitudinal and transverse orientations. With the new seal,  
1767 there is no longer a need to disconnect the refrigerator pumping line, nor remove and replace  
1768 the sample insert;
- 1769 • The 5 T magnet suffered irreparable damage during the final systems tests, and was replaced  
1770 with a similar magnet removed from the Hall B polarized target [204].

1771 It should be noted that both the original and Hall B magnets were primarily designed to provide  
1772 longitudinal polarization, while still permitting limited use for transverse polarization. As such,  
1773 each magnet possesses an opening angle of  $110^\circ$  ( $\pm 55^\circ$ ) in the direction parallel to the magnetic  
1774 field, compared to only  $\pm 17^\circ$  perpendicular to it (see Fig. 50). Because the SoLID proposal requests  
1775 transverse polarization with an opening angle  $\pm 25^\circ$  or greater, a new magnet will be necessary.

1776 Oxford Instruments (manufacturer of both the Hall B and original magnet) has performed a  
1777 detailed feasibility study and concludes that they can build a 5 T split-coil magnet with both a  $\pm 25^\circ$   
1778 split angle and the homogeneity required for DNP [205]. The SoLID collaboration and JLab Target  
1779 Group will work alongside the eventual vendor to ensure the magnet can be easily incorporated into  
1780 the existing JLab cryostat. This will greatly reduce the time and cost required to field a transversely  
1781 polarized target for SoLID.

### 1782 **5.3 Cryogenic Target for PVDIS**

1783 The proposed target consists of 40 cm liquid hydrogen/deuterium cell. This cell will be filled with  
1784 either hydrogen or deuterium as needed. The heat load on this target will be much more modest  
1785 than the Qweak target that was employed from 2010 to 2012 at JLAB. A conceptual design of the  
1786 target is shown in the figure. The current concept allows for remote placement of a single cryogenic  
1787 cell and a dummy cell with several solid targets necessary for calibrations. Such a target has the  
1788 following basic elements:

- 1789 1. Heat exchanger (HX)
- 1790 2. Insulating vacuum chamber (IVC)
- 1791 3. Target stack
  - 1792 (a) Cell
  - 1793 (b) Dummy target
  - 1794 (c) Solid targets
- 1795 4. Recirculating pump
- 1796 5. Cryostat
- 1797 6. Temperature stabilizing heater
- 1798 7. Positioning system
- 1799 8. Gas handling system and gas storage
- 1800 9. Instrumentation
- 1801 10. Depolarizer

1802 All components in the system must comply with 10 CFR 851 with regard to pressure, electrical,  
1803 and fire safety. The majority of these components will remain outside the high magnetic field of the  
1804 solenoid. The cell and connecting piping together with the rest of the target stack are necessarily  
1805 placed in the magnetic field of the solenoid. Selection of materials for these components shall  
1806 consider this.

1807 The insulating vacuum chamber will consist of two main sections. One section will be inside  
1808 the bore of the solenoid and a section similar to the IVC for the standard Hall A cryogenic target  
1809 will be upstream of the magnet. This later section will contain the motion system, heat exchanger,  
1810 etc. The section in the magnet will only contain the target stack and connecting piping. Materials  
1811 for the chamber section inside the solenoid must be compatible with the magnetic field inside the  
1812 solenoid. The exit of the chamber will be compatible with the acceptance of the detector.

1813 Careful attention must be given to the design of the cell. While the requirements of this target  
1814 regarding density fluctuations are much less stringent than those imposed on either the Qweak or G0  
1815 targets, it is of some concern. Analysis of the cell design using computational fluid dynamics (CFD)  
1816 will be employed to ensure an acceptable cell design. Based on experience with previous targets  
1817 at JLAB, noise associated with density fluctuations is not expected to be significant compared to  
1818 counting statistics. To reduce the background from Al-e- asymmetries, the sections of the cell upon  
1819 which the beam impinges will be thin. Thicknesses of 120  $\mu\text{m}$  are commonly available and are  
1820 adequate for the needs of the experiment. The remainder of the cell will be designed to optimize  
1821 boiling performance, detector acceptance, and pressure safety. High strength aluminum alloys such  
1822 as AL-7075 and AL-2219 (used on welded components) shall be used on critical parts of the cell.  
1823 Through extensive experience it has been shown that cell and cell block assemblies are much more  
1824 reliable when welds and mechanical joints such as conflat (CF) are employed. This avoids the  
1825 issues with solder and other sealing techniques. This approach also accelerates the design and  
1826 prototyping phase and simplifies testing and assembly.

1827 To avoid interference between the exiting particles at maximum scattering angle of  $35^\circ$  and the  
1828 upper and lower target components, the cell and dummy target must be separated by a minimum of  
1829 28 cm plus half the width of the cell and dummy target. Similarly the dummy and the solid targets  
1830 (positioned at  $Z = 0$ ) will require 14 cm of separation plus half the width of the dummy target and  
1831 first solid target frame. A total stack height of more than 70 cm is expected. The motion system  
1832 must accommodate this height and allow for some alignment adjustments. The standard Hall A  
1833 cryogenic target has over 70 cm of travel, thus a similar mechanism will be suitable.

1834 Dummy and solid targets can be selected and installed as needed. The thickness of the dummy  
1835 target will be chosen to match the radiation length of the liquid cell. Solid targets required for optics  
1836 studies, background measurements and alignment checks will also be installed.

1837 The cryogenic liquid hydrogen and deuterium target must accommodate a beam current of  
1838 50  $\mu\text{A}$  on a 40 cm long cell. The estimated beam heat load for this is  $\sim 800\text{W}$ . The pump, heater  
1839 overhead, transfer line and other losses require an additional estimated  $\sim 250\text{W}$ . During the Qweak  
1840 experiment, more than 3 kW of power at 20K was dissipated by the heat exchanger. This design  
1841 made use of both 15K and 4K refrigerant from the End Station Refrigerator (ESR) and the Central  
1842 Helium Liquefier (CHL). A careful study of the target heat load and ESR/CHL refrigerators will  
1843 be necessary to design the heat exchanger. However, it is expected that the heat exchanger will not  
1844 need to dissipate more than 1500 W which includes a comfortable operating margin. Operationally,  
1845 only  $\sim 1\text{kW}$  of refrigeration will be required by one or more refrigerator.

1846 The hydrogen and deuterium target fluids may become slightly polarized in the magnetic field  
1847 of the solenoid. This would result in an asymmetry unrelated to the physics of interest. This effect  
1848 can be mitigated in the case of deuterium with an RF-depolarizer. In the case of hydrogen, pure  
1849 para-hydrogen would reduce this effect. A catalyst (such as an iron oxide bed) would enhance the

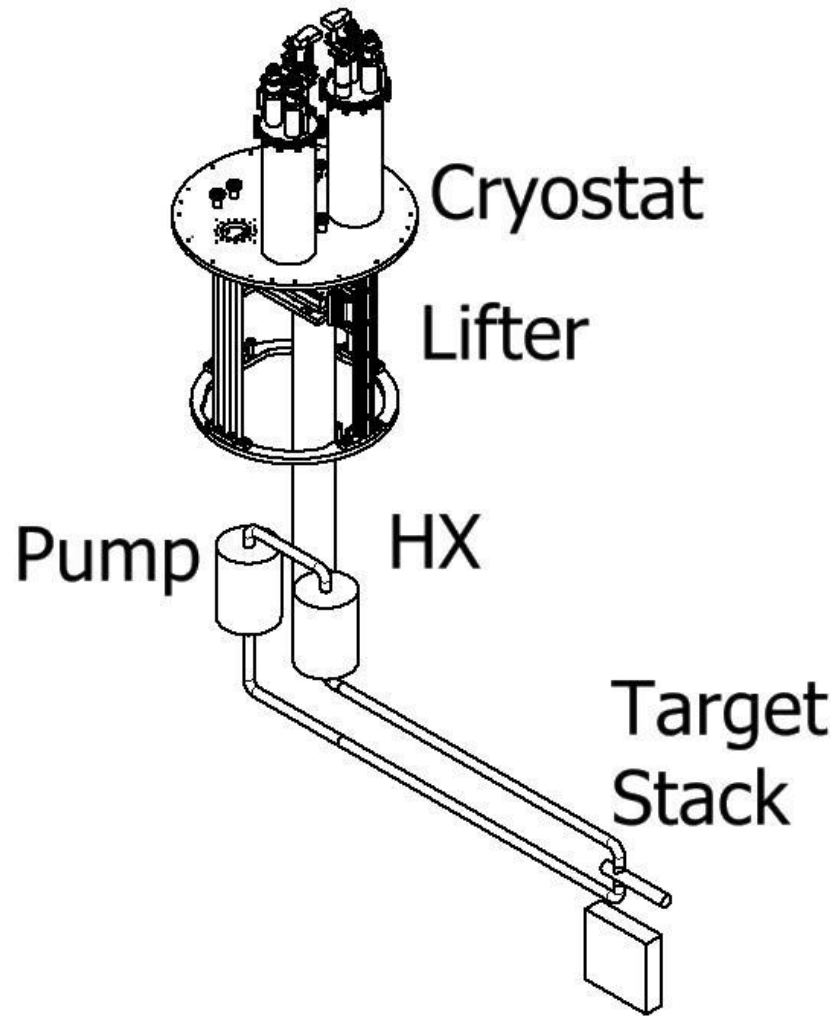


Figure 51: Cryogenic Target for PVDIS

1850 para to ortho fraction.

## 1851 6 Baffles

1852 In order for the detectors in the PVDIS experiment to operate at the design luminosity, a set of  
1853 baffles is required that passes a reasonable fraction of the DIS electrons while blocking as much of  
1854 the background as possible. The baffles provide curved channels through which only the spiraling  
1855 high energy negative particles can pass. Most line-of sight photons and positively charged hadrons  
1856 are blocked.

1857 The design of the baffles requires careful optimization since there are many sources of back-  
1858 ground and the different detectors respond differently to the different backgrounds. The dominant  
1859 background in the GEM's is soft photons, especially those between 1 and 2 MeV. The GEM's are rel-  
1860 atively inefficient for lower energy photons. Sources of these photons include beam bremsstrahlung,  
1861 forward radiation from wide-angle 30-100 MeV Møller electrons generated in the target, and pho-  
1862 tons from showers in the baffles induced by neutral pions. The light gas Cerenkov is sensitive to pair  
1863 production from photons above 20 MeV or so which can come from neutral pions produced in the  
1864 target to bremsstrahlung from the wide-angle Møller electrons. The ECal is sensitive the positive  
1865 hadron punch-through and high energy photons from neutral pion decay.

1866 To design the baffles for a specific magnetic field and detector configuration, ray-tracing of  
1867 simulated DIS electrons is performed for the desired momentum range. For a uniform solenoidal  
1868 field, high momentum electrons have a trajectory in  $\phi - z$  space that is linear and the  $\theta - z$  trajectory  
1869 is independent of the field. The design process takes simulated electrons in a realistic field and  
1870 exploits this approximate behavior to define pathways for ranges of electron momenta. This allows  
1871 for a relatively simple design process involving an extended target where one considers radial rings  
1872 of restricted scattering angle and places blocking material to only allow these trajectories. The  
1873 number of sectors to be used for this experiment is driven by the azimuthal angle  $\phi$  traversed by the  
1874 minimum momentum particles, which for these kinematics is about  $12^\circ$ , hence 30 sectors.

1875 To block line-of-sight photons, there must be sufficient material to block line particles that have  
1876 a constant trajectory in  $\phi$ . Due to the fact that the target is extended, the simple model does not  
1877 completely hold, allowing some fraction to leak through.

1878 We recently have undertaken studies of our baffle design including evaluation of materials, ac-  
1879 ceptance, and background reduction. While our baseline baffle design uses lead, other possibilities  
1880 include copper or tungsten. These materials vary by a factor of four in radiation length. The varia-  
1881 tion in nuclear interaction length is smaller, as shown in Table 9. Tungsten's high density and short  
1882 interaction length is advantageous, however its cost is higher, and solid tungsten is difficult to ma-  
1883 chine. An easier approach to construction would be to use powdered tungsten which can be easily  
1884 molded and glued.

1885 We have performed studies of trigger rates in the EC, rates of neutrons entering the EC, and rates  
1886 of photons striking the last GEM with baffles constructed of different materials, but with the same  
1887 geometry. All show fairly small differences, seen in Table 9. Lead provides a slightly lower photon  
1888 rate than copper, while copper's hadron rates are slightly better. Powdered tungsten has a density  
1889 only about 60% of solid tungsten, and consequently provides little or no performance advantage  
1890 over lead.

1891 An important background is photons from  $\pi^0$  decay interacting in the baffles. When photons  
1892 strike the baffles close to the "hot" edge of a slit, shower products can escape into the slit and from  
1893 there thread through the slits in the remaining baffle plates. A modification we have considered is to  
1894 remove material amounting to  $0.6^\circ$  in angular width from the hot edges on baffle plates 2, 4, 6, 8 and  
1895 10, allowing photons that would have hit near these slits to strike instead further from the hot edges  
1896 on the next plate. Our simulations show a 16% reduction in photon rates above  $p = 1 \text{ GeV}/c$ , and  
1897 26% reduction for  $p > 10 \text{ GeV}/c$ . Removal of this material would increase the pion background,

	Copper	Lead	Tungsten powder	Solid tungsten
Radiation length (cm)	1.436	0.5612	0.583	0.3504
Nuclear interaction length (cm)	15.32	17.59	16.58	9.946
Machinability	Easy	Soft, needs support	Easy to mold and glue	Hard
Cost	Low	Low	High	High
EC trigger rate (kHz)	$4.78 \times 10^3$	$5.45 \times 10^3$	$5.25 \times 10^3$	$4.59 \times 10^3$
Neutron rate in EC (kHz)	$3.35 \times 10^7$	$4.7 \times 10^7$	$4.0 \times 10^7$	$2.9 \times 10^7$
Photon rate in last GEM (GHz/sector)	2.98	2.59	—	—

Table 9: Properties and performance of copper, lead, tungsten powder and solid tungsten as baffle materials.



1898 but by less than 10%.

1899 We have performed detailed studies of track trajectories through the baffles to identify places  
1900 where improvements in the baffle geometry can be made. One finding was that, for the upstream  
1901 baffle plates, the solid ring at the inner radius and an angular constriction at small radius interfere  
1902 with the acceptance for electrons produced at the downstream end of the target. For vertices at the  
1903 upstream end of the target, acceptance was being lost due to the too-small outer radii of the upstream  
1904 baffle plates.

1905 Based on these studies we have developed an improved baffle design, shown in in Fig. 52.  
1906 Inner rings and angular constrictions on the first few plates have been removed, and outer radii  
1907 of these plates have been increased. Shapes of the slits in all the plates were optimized, keeping  
1908 the overall aperture in polar angle unchanged, but tightening up slits that were slightly too wide.  
1909 The outcome of this program was a geometrical design, having modest acceptance improvements  
1910 over our previous baffles while not significantly affecting photon rejection, which we believe to be  
1911 optimal; see Figures 53 and 54.

1912 A detailed study of the activation of different materials suitable for the baffle has been carried  
1913 out. Radiation levels for each material were studied for three different durations of beam exposure,  
1914 and possible shielding configurations were evaluated. The final selection of the baffle material will  
1915 likely be driven less by performance and more by activation and ease of construction.

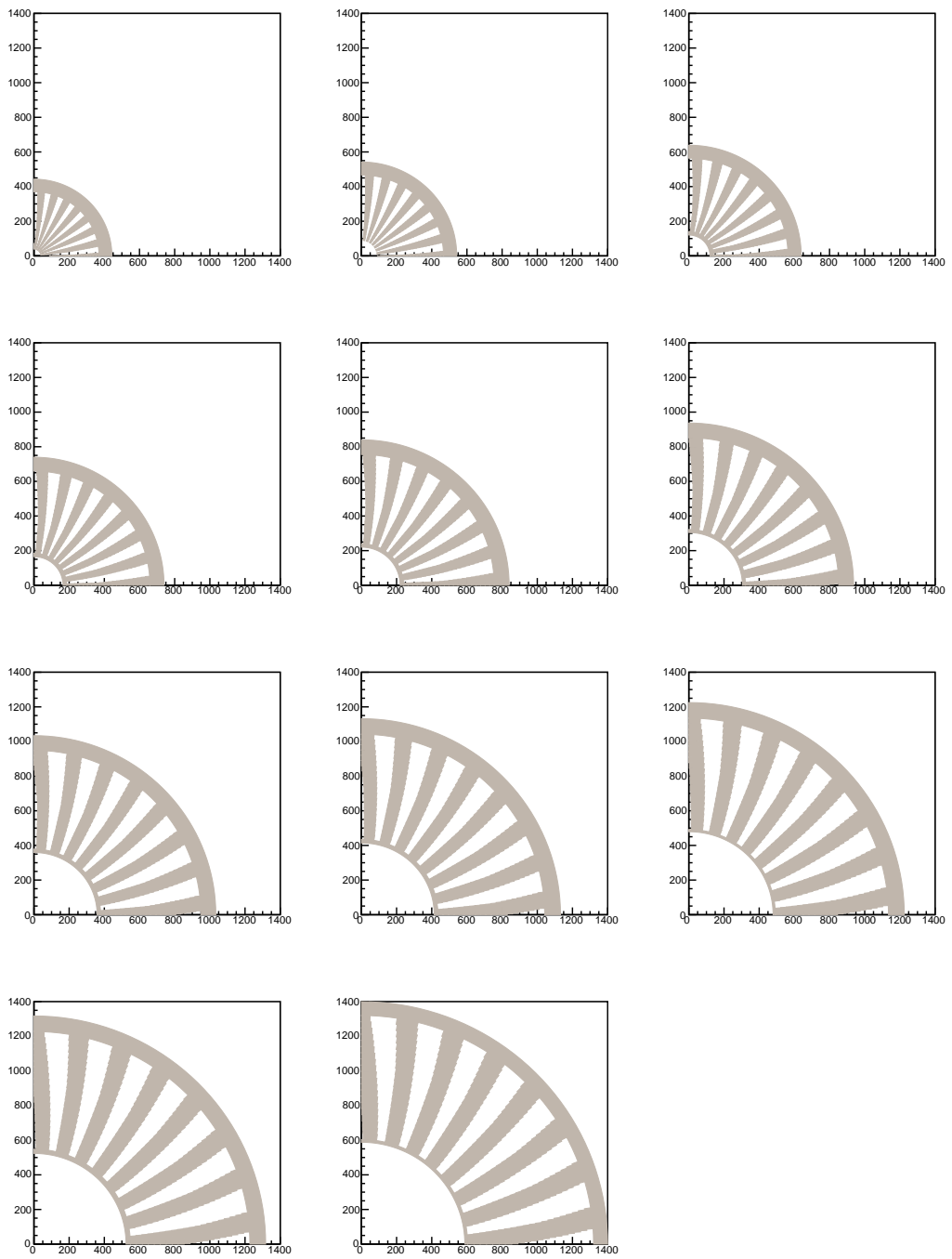


Figure 52: Face on views (first quadrant only) of the 11 plates in the PVDIS baffle system.

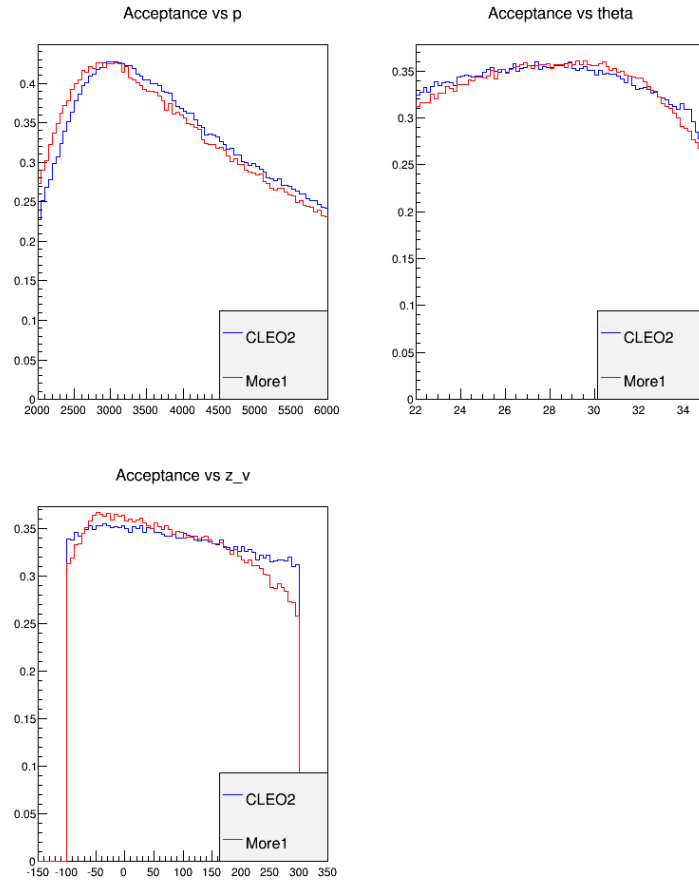


Figure 53: Geometric acceptance of the PVDIS baffles for DIS electrons with  $Q^2 > 6 \text{ GeV}^2$ ,  $W > 2 \text{ GeV}$ , and  $x_{bj} > 0.55$  versus momentum (top left), scattering angle (top right), and vertex position (bottom left). Blue (red) lines are acceptance for the optimized (previous) baffle design.

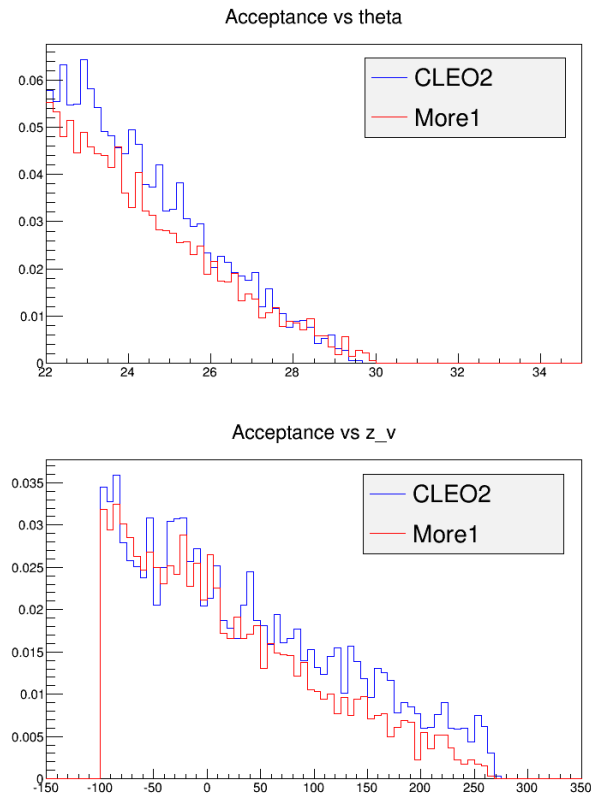


Figure 54: Geometric acceptance of the PVDIS baffles for photons versus scattering angle (top), and vertex position (bottom). Blue (red) lines are acceptance for the optimized (previous) baffle design.

## 1916 7 GEM Tracker

### 1917 7.1 Design

1918 The SoLID spectrometer requires high resolution track reconstruction under high rate conditions  
1919 over a large area. A cost effective solution for such requirements is provided by the Gas Elec-  
1920 tron Multiplier (GEM) technology invented by F. Sauli [206] in 1997. The GEM is based on gas  
1921 avalanche multiplication within small holes (on a scale of  $100\ \mu\text{m}$ ), etched in a Kapton foil with a  
1922 thin layer of copper on both sides. The avalanche is confined in the hole resulting in fast (about 10  
1923 ns rise time) signals. Several GEM foils (amplification stages) can be cascaded to achieve high gain  
1924 and stability in operation. The relatively small transparency of GEM foils reduces the occurrence  
1925 of secondary avalanches in cascaded GEM chambers. All these properties result in very high rate  
1926 capabilities of up to  $100\ \text{MHz per cm}^2$  and an excellent position resolution of  $70\ \mu\text{m}$ . Fig. 56 illus-  
1927 trates the principle of operation of a triple (three foil) GEM chamber. Triple GEM chambers were  
successfully used in the COMPASS experiment at CERN [207].

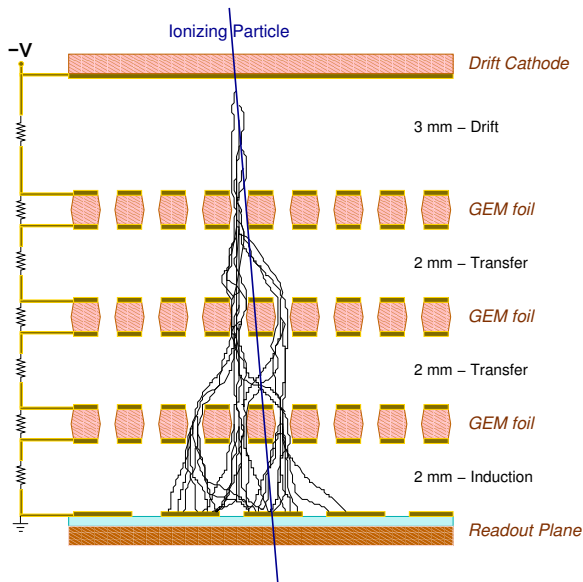


Figure 55: Principle of triple GEM operation.

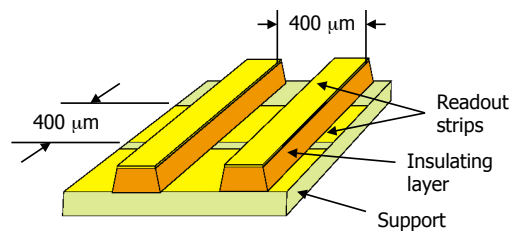


Figure 56: 3D view of the readout board.

1928  
1929 For the PVDIS configuration of SoLID, detector locations 1, 2, 3, 4, and 5 will be instrumented  
1930 with GEM chambers. Table 10 summarizes the parameters of the SoLID PVDIS GEM chambers.  
1931 At each detector location there will be 30 trapezoidal GEM chamber modules, one for each sector  
1932 defined by the baffles. The GEM modules will have an angular width of  $12^\circ$  with the readout stripes  
1933 parallel to the two edges of the sector, so that the stripes from the two readout layers are at a  $12^\circ$   
1934 stereo angle. The readout pitch for locations 1, 2 and 3 will be  $0.4\ \text{mm}$  while the pitch for locations  
1935 4 and 5 will be  $0.6\ \text{mm}$ . Figure 57 shows the GEM module arrangement for one of the detector  
1936 locations of the PVDIS configuration. Figures 58 and 59 show the details of the GEM module  
1937 edges and mounting at the inner and outer radii of the SoLID detector wheel.

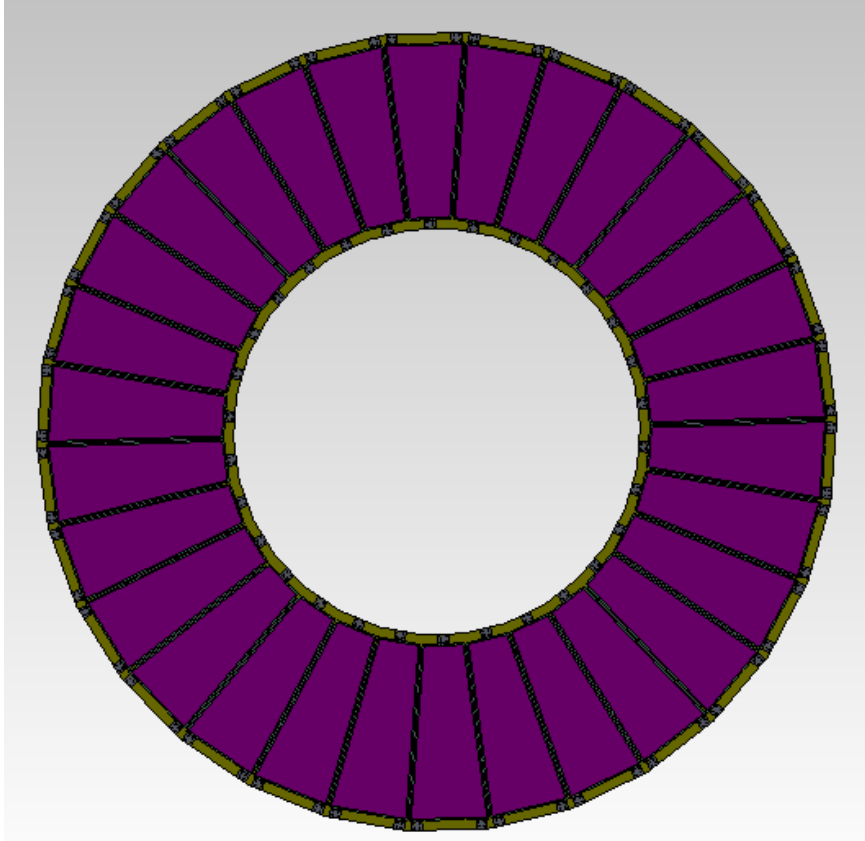


Figure 57: The GEM module arrangement at one of the detector locations of the SoLID PVDIS configuration

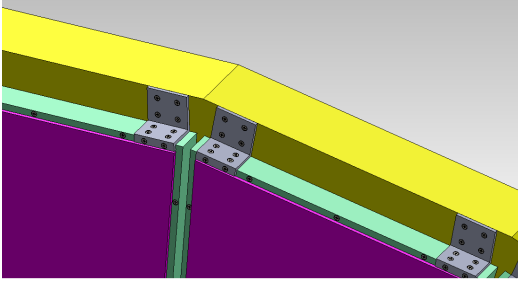


Figure 58: GEM module mounting at the outer edge of a GEM ring in the PVDIS configuration.

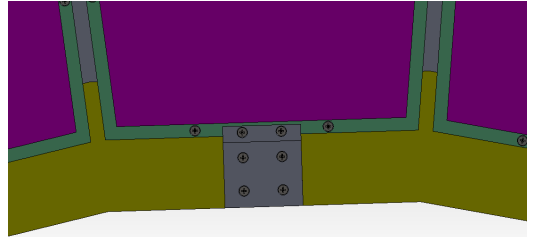


Figure 59: GEM module mounting at the inner edge.

Location	$Z$ (cm)	$R_{min}$ (cm)	$R_{max}$ (cm)	Surface (m <sup>2</sup> )	# chan
1	157.5	51	118	3.6	24 k
2	185.5	62	136	4.6	30 k
3	190	65	140	4.8	36 k
4	306	111	221	11.5	35 k
5	315	115	228	12.2	38 k
Total				≈ 36.6	≈ 164 k

Table 10: The locations, sizes and number of readout channels of GEM detectors for the SoLID PVDIS configuration

1938 The SIDIS configuration of SoLID calls for detector locations 1, 2, 3, 4, 5, and 6 instrumented  
 1939 with GEM modules. Table 11 summarizes the parameters of the SIDIS GEM chambers. While  
 1940 the number of detector stations is higher in the SIDIS configuration, the inner and outer radii of  
 1941 the detector wheels are significantly smaller compared to the PVDIS configuration. Furthermore,  
 1942 since there are no baffles in the SIDIS configuration, the active detection area has to cover the  
 1943 the entire surface area of each detector wheel. In order to meet these requirements, the SIDIS  
 1944 detector configuration will be set up by arranging the GEM modules from the PVDIS configuration  
 1945 in an overlapping two-wheel arrangement at each detector station as indicated in Figure 60. In this  
 1946 arrangement, 20 modules cover the entire active area of each detector station.

Location	Z (cm)	$R_{min}$ (cm)	$R_{max}$ (cm)	Surface (m <sup>2</sup> )	# chan
1	-175	36	87	2.0	24 k
2	-150	21	98	2.9	30 k
3	-119	25	112	3.7	33 k
4	-68	32	135	5.4	28 k
5	5	42	100	2.6	20 k
6	92	55	123	3.8	26 k
Total				$\approx 20.4$	$\approx 161$ k

Table 11: The locations, sizes and number of readout channels of GEM detectors for the SoLID SIDIS configuration

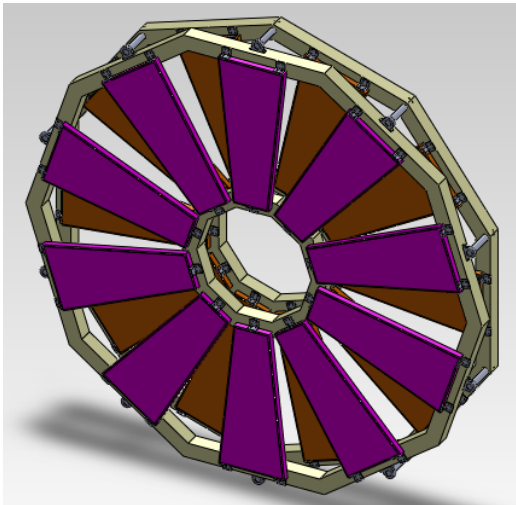


Figure 60: The GEM module arrangement at one of the detector locations of the SoLID SIDIS configuration

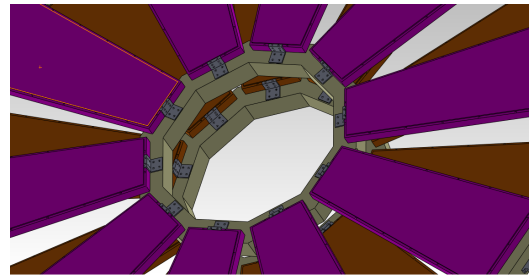


Figure 61: GEM module mounting at the inner edge of the ring in the SIDIS configuration

1947 Figure 62 shows the detailed design for a GEM module of the size proposed for SoLID. The  
 1948 “wings” shown in the frames are to support the frames during chamber assembly; they will be  
 1949 removed once the chamber is completed. The 2D readout plane will be glued on the bottom plate  
 1950 (shown in cyan). This plate, made out of a 3 mm thick honeycomb structure material, also provides

1951 structural rigidity to the GEM chamber. All other frames are made out of Permaglass<sup>3</sup> with 8 mm  
 1952 wide sides. The spacers shown within the active area are for keeping the GEM foils from touching  
 1953 each other; these spacers are approximately 300  $\mu\text{m}$  wide and contribute only about 1% reduction  
 1954 to the active area of the chamber. The GEM foils are mounted on the 3 light green frames, while the  
 1955 drift cathode is glued on the red frame. A thin gas window is glued on the orange frame.

1956 Figure 63 shows the concept for the 2D readout frame. Strips for one direction (shown in blue)  
 1957 continue across the readout plane, while the short segments of the strips for the other direc-  
 1958 tion (shown in red) are connected via through holes to readout lines running along the back of the  
 1959 plane. Large area readout planes of similar design have been tested in prototype GEM chambers for  
 KLOE2 at Frascati.

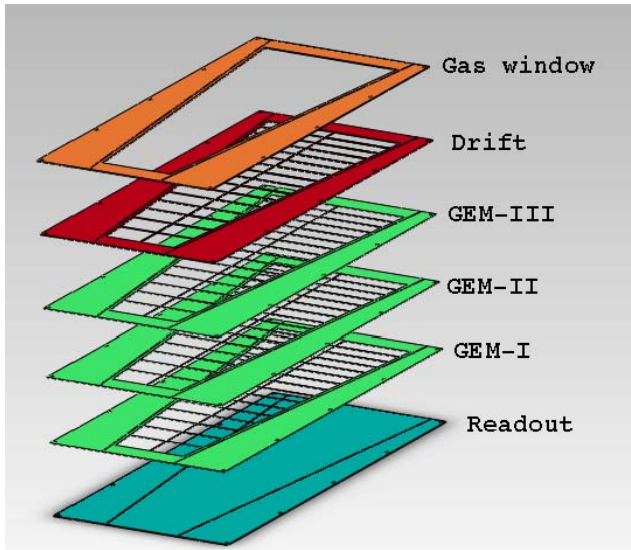


Figure 62: The frame assembly for a GEM module prototype of the size proposed for the largest SoLID GEMs

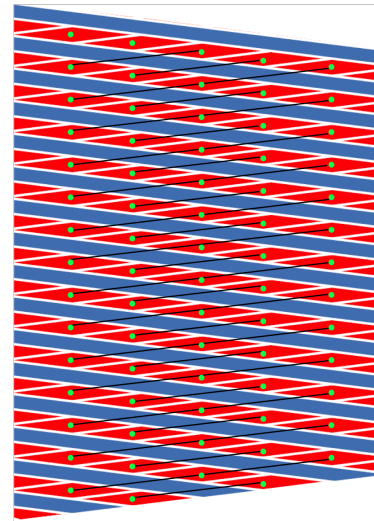


Figure 63: The schematics of the 2D readout plane proposed for SoLID

1960

1961 One challenge we are facing for the GEM trackers of SoLID is the large active area required;  
 1962 the active area of the largest GEM modules needed will be approximately  $113 \times (21-44) \text{ cm}^2$ . Un-  
 1963 til recently, the maximum GEM foil area had been limited to  $45 \times 50 \text{ cm}^2$ . However, over the last  
 1964 few years the Micro Pattern Gas Detector (MPGD) group at CERN, in collaboration with INFN,  
 1965 has perfected two techniques to produce large area GEM foils: single mask GEM etching and  
 1966 GEM splicing [208, 209]. The single mask technique allows for the fabrication of foils as large  
 1967 as  $100 \times 200 \text{ cm}^2$ . The splicing technique allows for two such foils to be combined with only a  
 1968 3 mm wide dead zone between the two foils. Recently several large prototype GEM chambers  
 1969 were constructed and tested at CERN using the large area GEM foils fabricated using the new tech-  
 1970 niques [210]. These new prototype chambers, constructed under the CMS upgrade GEM project,  
 1971 have trapezoidal shapes with an active areas of  $99 \times (25-45.5) \text{ cm}^2$ ; these dimensions are close to  
 1972 the dimensions of the largest GEM chamber modules planned for SoLID.

1973 Furthermore, there have been significant advances in the GEM chamber readout systems in the  
 1974 recent years. The RD-51 collaboration funded Scalable Readout System (SRS) project at CERN

<sup>3</sup>Permaglass is a glass fiber material with randomly oriented fibers that can be machined with very high precision.



1975 has already developed and tested a low cost APV-25 based readout. The APV25-S1 analog readout  
1976 chip [211] is currently in use for the COMPASS GEM trackers and the CMS silicon strip detec-  
1977 tors. A mid-size prototype system consisting of 15,000 channels was successfully tested and was  
1978 shown to work very well. The SRS group is continuing the development and is also working with  
1979 a commercial vendor to fabricate the SRS modules. The cost of the APV-25 based SRS readout is  
1980 expected to be approximately \$ 3 per channel.

## 1981 7.2 GEM tracker R&D

1982 Research and development towards the SoLID GEM tracker is currently being conducted in the  
1983 United States at the University of Virginia (UVa) and in China at five institutions: China Institute of  
1984 Atomic Energy (CIAE), Lanzhou University (LZU), Tsinghua University (THU), the University of  
1985 Science and Technology of China (USTC) and the Institute of Modern Physics (IMP). According  
1986 to the current plan, the UVa group, which has an ongoing large area GEM module production  
1987 program, will do the initial designs and prototyping of the SoLID GEM chambers, while the Chinese  
1988 institutions get their large area GEM production programs set up. At the same time CIAE has  
1989 been working with CERN and Chinese manufacturers to develop large area GEM foil production  
1990 capabilities in China.

### 1991 7.2.1 GEM chamber R&D program in UVa

1992 The Istituto Nazionale di Fisica Nucleare (INFN)-Roma group and the University of Virginia group  
1993 are currently leading an aggressive R&D program to develop large area GEM chambers for the  
1994 Hall A Super Bigbite apparatus (SBS). The active area of large tracking chambers of SBS will be  
1995  $50 \times 200 \text{ cm}^2$ . These large GEM trackers will be assembled by combining  $40 \times 50 \text{ cm}^2$  and  $50 \times 50$   
1996  $\text{cm}^2$  “chamber modules” with narrow edges. The UVa group has already constructed several  $40 \times 50$   
1997  $\text{cm}^2$  and  $50 \times 50 \text{ cm}^2$  GEM chamber modules. The expertise gained with these GEM modules will  
1998 be applied to the design of GEM modules for SoLID.

1999 The UVa group operates a well-equipped GEM R&D facility that includes the following:

- 2000 • **UVa Detector development lab:** This  $10 \times 10 \text{ m}^2$ , well-equipped nuclear physics detector lab  
2001 has been used for the development, construction and testing of many large detector systems.  
2002 The detector lab consists of two  $3 \times 3 \text{ m}^2$  level 1,000 clean rooms located within a  $4 \times 10 \text{ m}^2$   
2003 semi-clean area. So far seven large area GEM chambers have been successfully constructed in  
2004 this clean room. The specialized GEM construction equipment in the lab includes large area  
2005 GEM foil stretchers, GEM foil testing high-voltage boxes, a large volume ultra-sonic cleaner  
2006 for GEM frame cleaning, a Keithley 6485 picoammeter for GEM foil testing, and a GEM foil  
2007 storage dry  $\text{N}_2$  box.
- 2008 • **GEM readout systems based on APV25-S1 electronics:** The UVa group has two APV25  
2009 based readout systems: a 10,000 channel SRS system from CERN and a 3,500 channel system  
2010 developed by the INFN group. Both systems are fully operational and are used for testing  
2011 prototype GEM chambers.
- 2012 • **Wiener-Iseg multi-channel high voltage system** The UVa detector group owns a brand new  
2013 Wiener-Iseg multi-channel high voltage system that is especially suited to provide high volt-  
2014 age to sensitive tracking chambers. This system currently has 24 channels and can be ex-  
2015 panded to 160 channels.

2016 The  $50 \times 50 \text{ cm}^2$  GEM chambers built at UVa are currently being tested with radioactive sources  
 2017 and cosmic rays. Figures 64 and 65 show results obtained from these test data. Figure 64 is the  
 2018 absolute efficiency measured at several locations using electrons from a beta source, as a function  
 2019 of the high voltage. An efficiency of  $\approx 97\%$  is achieved. Figure 65 is the ratio of cluster charge for  
 2020 x and y hits.

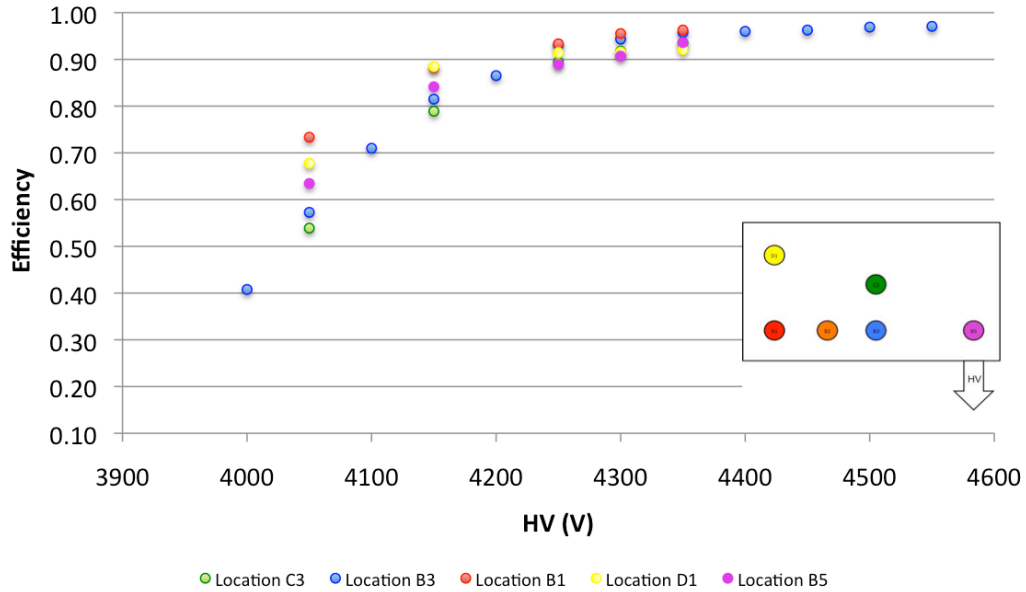


Figure 64: Efficiency of the  $40 \times 50 \text{ cm}^2$  GEM chamber

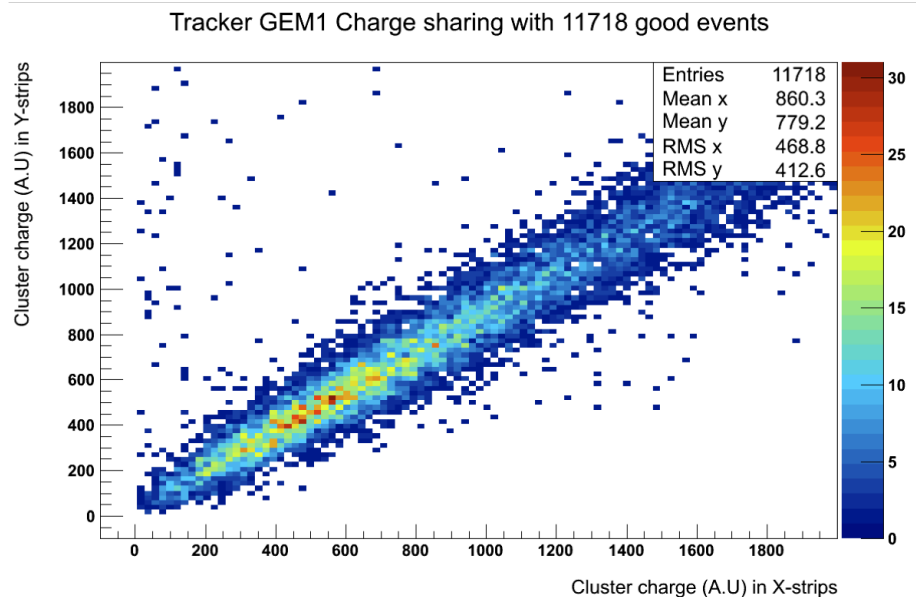


Figure 65: The charge division between x and y strips for the  $40 \times 50 \text{ cm}^2$  GEM chamber.

2021 The UVa group recently completed the fabrication of a large prototype GEM module with di-  
2022 mensions of  $100 \times (21-38)$  cm<sup>2</sup>, approaching the proposed size of the largest SoLID GEM sectors  
2023 (Figure 66). This prototype was constructed under the Electron Ion Collider (EIC) detector R&D  
2024 program. This chamber is the largest GEM chamber ever built with a 2-D readout. Its readout  
2025 consists of stripes from the two readout layers at a 12° stereo angle. The chamber is currently pre-  
2026 pared for a beam test at Fermilab scheduled for October 2013. The development and testing of this  
2027 large prototype is used to gain expertise and understand the mechanical, electrical and electronic  
properties of very large area GEM chambers.

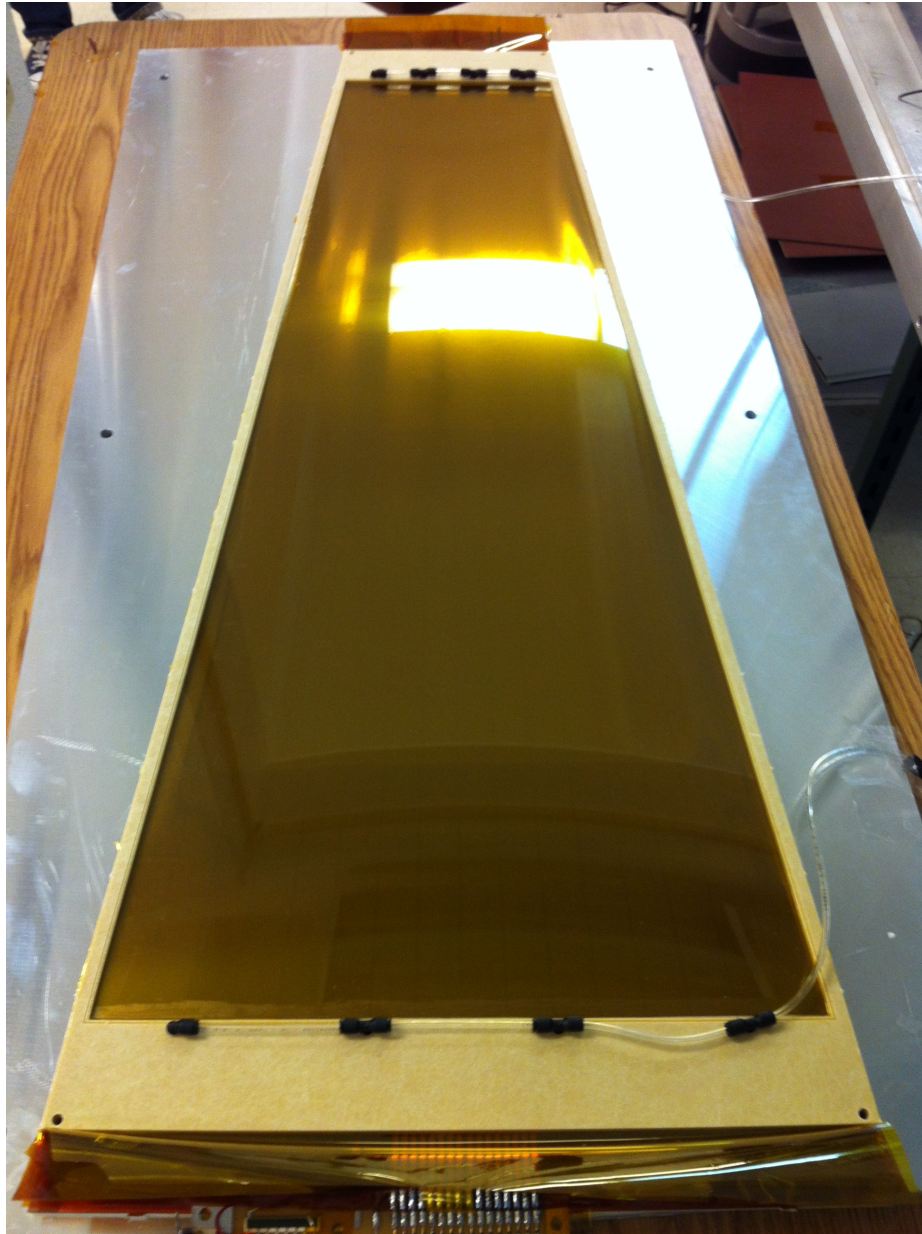


Figure 66: The 100 cm x (21 - 38) cm prototype GEM chamber at UVa being prepared for a beam test.

2028

## 2029 **7.2.2 GEM chamber R&D programs in China**

2030 The five institutions of the Chinese collaboration for SoLID GEM detectors all have worked on gas  
2031 detectors for many years, including R&D work on MWPC, MRPC, GEM, Micromegas, THGEM,  
2032 and TPC, and applications of these detectors. These institutions have well-equipped GEM R&D  
2033 facilities that include:

- 2034 • Clean rooms for GEM detector assembling
- 2035 • Front-end readout electronics based on APV25-S1 (developed by the INFN group)
- 2036 • Multi-channel HV power supply systems and DAQ systems

2037 CIAE, which has over 20 years of experience in nuclear pore foil production and Kapton etching,  
2038 just signed a license agreement for manufacturing and commercialization of GEM foils and GEM  
2039 based products with CERN, and received technical assistance from CERN. The base material of  
2040 GEM foil is ultrathin, non-adhesive copper on a polyimide substrate, which can be purchased from  
2041 CERN and other vendors. Several printed circuit board (PCB) technologies are applied during the  
2042 manufacture of GEM foil. Recently, CIAE has started working on:

- 2043 • Production of photo-masks, a component for the manufacturing of PCBs which is transferred  
2044 onto a light-sensitive chemical resist covering the surface of copper layer in the production of  
2045 GEMs.
- 2046 • Lamination and exposure of dry film photoresist: Using a hot roll lamination (HRL) machine,  
2047 both sides of the GEM substrate are laminated simultaneously by photoresist. The exposure  
2048 system consists of an exposure unit, vacuum exposure frame, light source cooling, and an  
2049 exposure control unit. This treatment transfers the photo-mask pattern onto the photoresist,  
2050 forming an exact copy.
- 2051 • Copper etching.
- 2052 • Polyimide film etching.
- 2053 • Final cleaning and chrome coating.

2054 Figure 67 shows the film etching device at CIAE. In the beginning of 2013, a physicist from  
2055 CIAE completed a training in GEM foil manufacturing at CERN.

2056 LZU has been building a Micromegas+AFTER chip system for fast neutron (14 MeV) imaging  
2057 in the past few years. The experience gained from this R&D work is useful to their GEM project.  
2058 For instance, several designs of neutron converters with different parameters were tried in a simu-  
2059 lation based on MCNP4 and GEANT4 (for both Micromegas and GEM), and different conversion  
2060 efficiencies were compared. Other studies based on Garfield to improve the spatial and time resolu-  
2061 tion (as shown in Figure 68) were also performed and were proved to be helpful for the experimental  
2062 study. The first version of the detector frame was designed and manufactured. 4 sets of GEM foils  
2063 with the standard frame were purchased from CERN. Currently, a PhD student and a staff member  
2064 are working together on the APV25-VME system. In the summer of 2013, an engineer visited JLab  
2065 to gain experience about the SoLID DAQ.

2066 THU has experience with GEM detectors by developing the electronics, such as a GEM-based  
2067 TPC readout, a 16-channel CSA and shaping amplifier for GEM. Recently, a planar GEM tracking  
2068 detector prototype was assembled for a spatial resolution test. In this test, THU used the event rate



Figure 67: Film etching device at China Institute of Atomic Energy

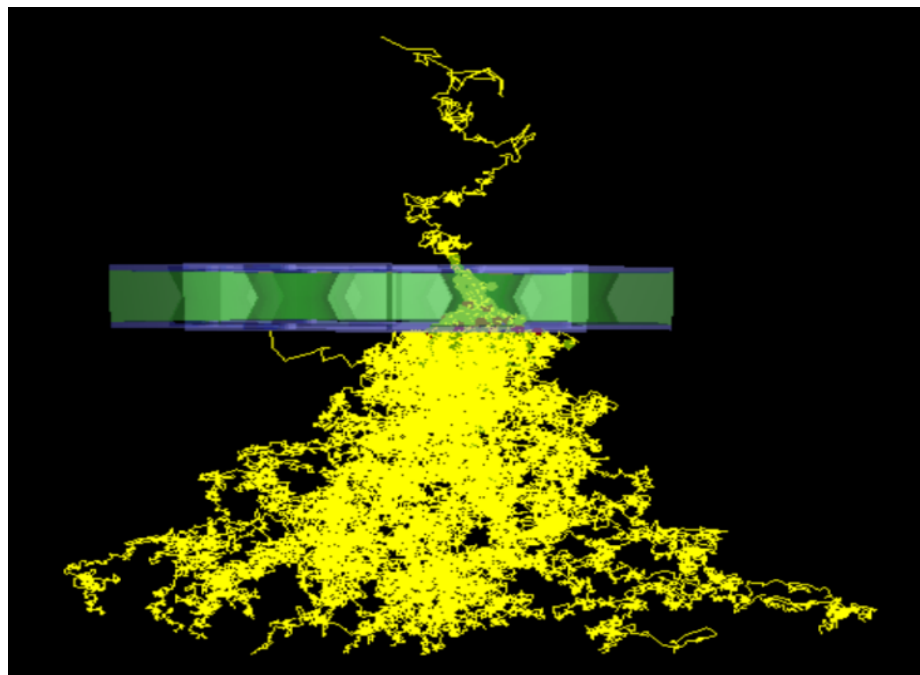


Figure 68: Avalanche process of an electron in a hole of GEM



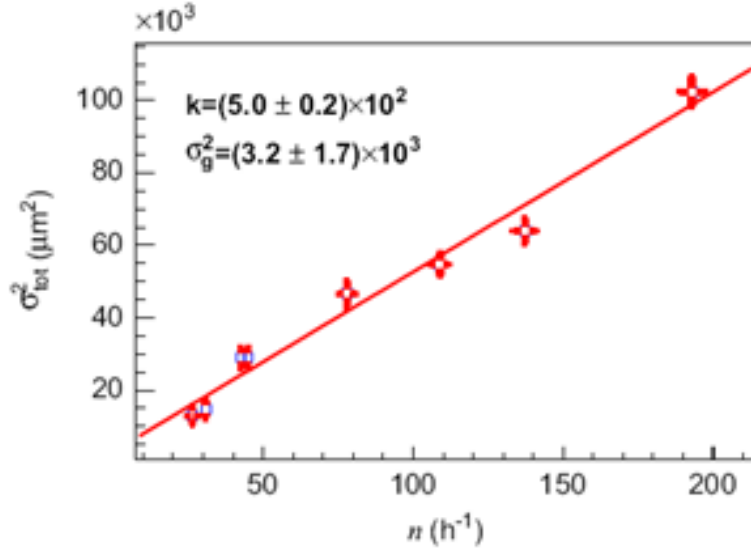


Figure 69: Linear fit of  $\sigma_{tot}^2$  versus  $n$

2069 to substitute for the square of the slit width to overcome the magnified uncertainty of the spatial  
 2070 resolution which arises from the uncertainty of the slit width. The test demonstrated that the total  
 2071 position variance of the incident particles exhibits a linear dependence on the event rate or square of  
 2072 the slit width. The next step was to extend the measurement to zero slit width which is not directly  
 2073 achievable, and it was practically implemented by a linear fit to data points on the  $\sigma_{tot}^2 - n$  plane.  
 2074 Figure 69 shows the linear fitting of  $\sigma_{tot}^2$  versus  $n$  and the spatial resolution of the prototype is  
 2075  $56 \pm 14 \mu\text{m}$ . Currently, THU is focusing on the inter-foil and inter-strip distance effects of the GEM  
 2076 detector. An APV based DAQ system will be built in the near future.

2077 USTC started the GEM R&D work in 2000. After working on the 3D electric field simulation of  
 2078 GEM, USTC carried out a detailed gain performance test for the  $10 \times 10 \text{ cm}^2$  triple GEM detector,  
 2079 then made a GEM X-ray imaging prototype. Both Center-of-Gravity (COG) and delay-line readout  
 2080 methods were used on this imaging prototype and a very good spatial resolution ( $\sim 80 \mu\text{m}$ ) was  
 2081 obtained. Currently, USTC is focusing on the R&D of the large area GEM detector. Due to the  
 2082 fact that large area GEMs built by the glue technology have some disadvantages (e.g. very long  
 2083 assembling period; parts of GEM detector are not replaceable; dead regions in the effective area;  
 2084 aging problems of the glue and so on), USTC decided to use the NS2 (No Stretch, No Stress)  
 2085 technology for the construction of a  $30 \times 30 \text{ cm}^2$  GEM detector. NS2, which was developed at  
 2086 CERN recently, is a totally new technology especially used for large area GEM detectors. The idea  
 2087 of NS2 is to use screws and a stable main frame to achieve self-stretching of the GEM foils. The  
 2088 advantages of NS2 are:

- 2089 • The whole construction process involves mainly tightening the screws, so it is easy and fast  
 2090 and we can assemble a detector in half a day.
- 2091 • Because all the GEM foils are self-stretched, the detector does not need support frames. There  
 2092 is no glue aging problem or dead area inside the detector.
- 2093 • All the screws can be loosened and tightened again, so that any part of the detector is replace-  
 2094 able. This also means that the cost of the project can be greatly reduced.

2095 USTC just finished the design of the new  $30 \times 30 \text{ cm}^2$  NS2 GEM and purchased six  $30 \times 30 \text{ cm}^2$   
2096 GEM foils from CERN. The HV dividers and screws are ready. The frames, drift electrode and  
2097 readout PCB are in manufacturing. The readout electronics and instruments are ready. Figure 70  
2098 shows a model of the  $30 \text{ cm} \times 30 \text{ cm}$  NS2 GEM detector (without readout PCB). This detector has  
2099 been assembled and tested in Summer 2013.

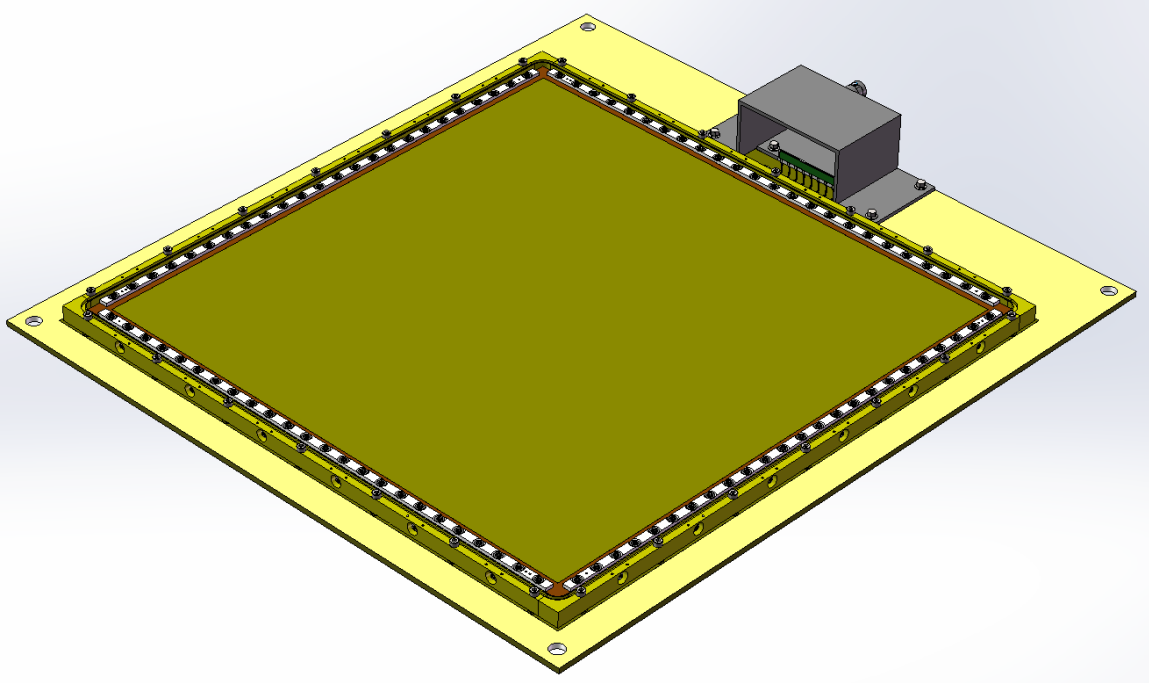


Figure 70: Design of the  $30 \times 30 \text{ cm}^2$  NS2 GEM detector

### 2100 7.3 Collaboration Status and Construction Outlook

2101 The close collaboration between the CIAE group in China developing GEM foil fabrication capabil-  
2102 ities and the US groups (UVa and Temple) is essential as the project moves forward. The ongoing  
2103 China-USA SoLID GEM collaboration activities have included monthly phone meetings, discus-  
2104 sion during SoLID collaboration meetings and hosting of Chinese visiting researchers at the GEM  
2105 lab at UVa.

2106 A timetable is worked out with the CIAE group to lay out milestones for the fabrication of GEM  
2107 foils with increasing active areas up to the full size of the largest SoLID modules. This timetable will  
2108 also include goals for providing specific numbers of GEM foils produced in China to the Temple  
2109 group for hole inspections and to the UVa and Temple groups for construction of test modules with  
2110 these foils. The Chinese foils will be subjected to all acceptance criteria used for CERN GEM foils.  
2111 The test modules will be evaluated under high luminosity conditions at the UVa x-ray test-stand  
2112 as well as in beam tests at Jefferson lab. The two US groups will be closely interacting with the  
2113 Chinese groups and giving them feedback during these evaluations. As part of the proposed SoLID  
2114 pre-R&D program, funds have been requested for covering the cost of these Chinese GEM foils as  
2115 well as for the fabrication of test modules.

2116 The current plan for SoLID calls for approximately 400 GEM foils. In the event the CIAE group  
2117 is unable to meet the GEM foil production goals, the backup option is purchasing the required

2118 number of foils from CERN. The estimated cost of purchasing all 400 SoLID GEM foils from  
2119 CERN will be approximately \$ 650 k

2120 The CERN workshop has demonstrated the capability to produce the largest size GEM foils  
2121 (113 cm x 44 cm) needed for SoLID. In fact, the UVa group recently used 123 cm x 55 cm GEM  
2122 foils produced at CERN to build two large area GEM detectors; these detectors were successfully  
2123 used for Jefferson Lab PRad experiment. Furthermore, CERN has the production capacity to deliver  
2124 large orders of GEM foils in a timely manner. Over the last two years the CERN workshop produced  
2125 and delivered approximately 140 large area GEM foils to UVa for SBS and PRad GEM modules;  
2126 these foils were of high quality with about 90% of the foils passing the acceptance criteria. The  
2127 manager of the CERN GEM workshop, Rui De Oliveira, has indicated that they have the capacity  
2128 to deliver the required number of GEM foils for SoLID and with an order to produce the required  
2129 number of foils they will hire the needed technicians to deliver the order in a timely manner.

2130 While the R&D to produce large area single mask GEM foils has been suspended for the mo-  
2131 ment at Tech-Etch due to lack of large orders for such foils, Tech-Etch has indicated that in the event  
2132 they receive a firm order for a large GEM production, they will be able to commit the resources for  
2133 the required R&D and production.

2134 Given these two backup options, the schedule risk due to a delay in Chinese GEM foils fabrica-  
2135 tion schedule will be rather low.

#### 2136 **7.4 GEM with Baseline and Enhanced Baseline Configurations**

2137 The SoLID GEM planes are arranged strategically to optimize the resolution and efficiency of the  
2138 tracking. The SIDIS setup is more complex because both forward and large angle kinematics must  
2139 be covered with the detectors. For the baseline configuration, there are 3 tracking planes covering  
2140 the large-angle kinematic range and 4 tracking planes covering the forward-angle region, where the  
2141 last 2 tracking planes of the large-angle and the first 2 tracking planes of the forward-angle kine-  
2142 matics are the same physical GEM planes. The SoLID tracking efficiency with the GEM's depends  
2143 strongly on the background rates, which are mainly produced from low energy particles created  
2144 by the electron beam hitting on the target. The background rate is almost linearly proportional to  
2145 the luminosity. The main purpose of multiple GEM planes used is to suppress background and  
2146 improve tracking efficiency. For the enhanced baseline configuration, we plan to add one more  
2147 physical GEM plane to cover both the forward and large angular ranges. We use simulations with a  
2148 complete SIDIS  $^3\text{He}$  target geometry and materials to obtain the designed luminosity with nominal  
2149 100% background to perform tracking studies in order to understand how single particle tracking  
2150 efficiency is affected by different ways of having one fewer GEM planes in the baseline configura-  
2151 tion compared with the enhanced baseline configuration in which all planes are present. The results  
2152 in Figure 71 shows that if we choose to not use the 2nd plane (GEM2) at the baseline configuration,  
2153 we can still achieve 95% efficiency at the forward-angle and 83% at the large-angle kinematics. At  
2154 the enhanced baseline configuration, the efficiency at the forward angle will be improved slightly to  
2155 96%, while the large angle result will be improved greatly to 93%. We also varied the background  
2156 to 85%, 70%, 50%, and 0% levels to study the tracking efficiency dependence on background levels  
2157 for the baseline configuration. The behavior of increasing efficiency with decreasing background is  
2158 expected.



### Tracking efficiency vs. background ratio

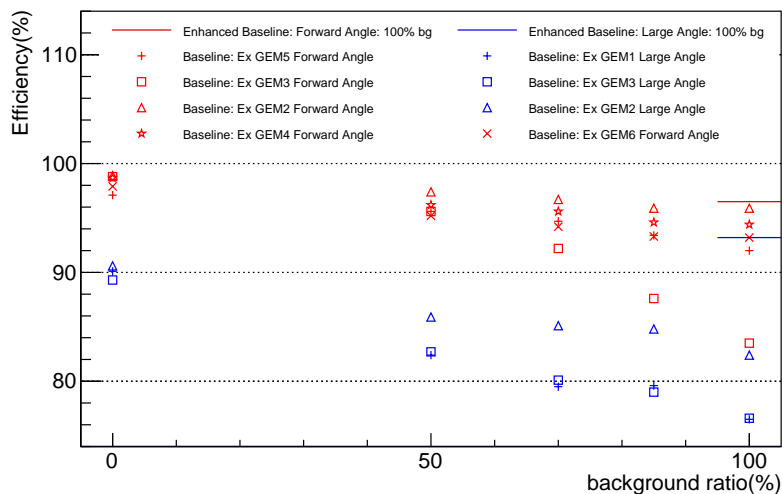


Figure 71: Single particle tracking efficiency of the SIDIS He3 setup is tested with the baseline configuration by removing one GEM plane for different background levels. As comparison, the enhanced baseline configuration result is shown with the designed luminosity at the 100% background level.

## 2159 8 Light Gas Cherenkov

### 2160 8.1 Design

2161 The light gas Cherenkov detector for SoLID is divided into 30 identical sectors to match the 30  
2162 sector symmetry of the PVDIS baffle system. Many elements of the light gas Cherenkov remain  
2163 identical between the PVDIS and SIDIS /  $J/\Psi$  experimental configurations, but some elements are  
2164 adjusted or added / removed. Beyond the criteria dictated by the experimental physics requirements,  
2165 the design of the Cherenkov detector was optimized with the goal of reducing the costs of construc-  
2166 tion and maintenance over the detector's lifetime including the switch over between experiments.  
2167 The specifications of the tank and each major element per sector for each configuration are described  
2168 below:

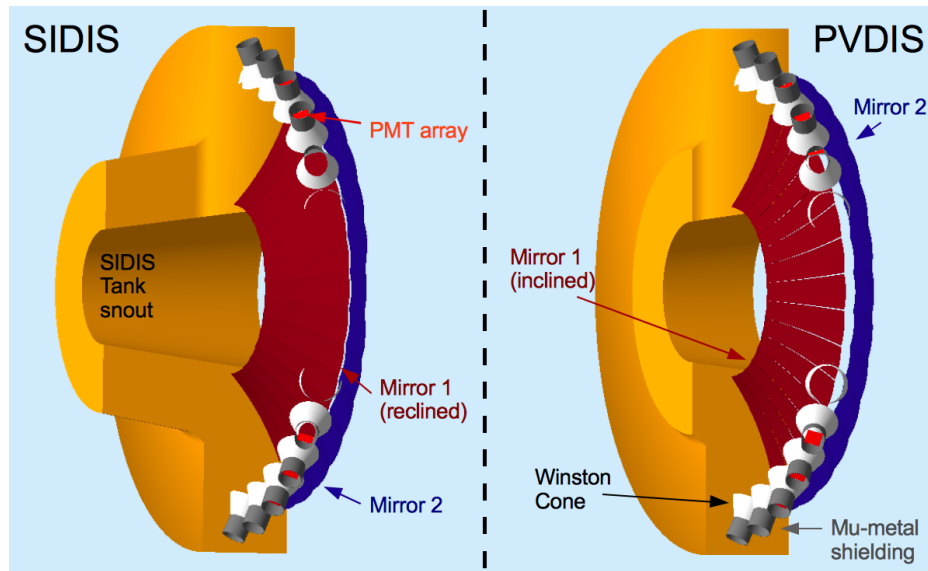


Figure 72: A side by side cross-section comparison of the light gas Cherenkov detector for both the SIDIS and PVDIS configuration with all major components labeled.

#### 2169 8.1.1 Tank and Cherenkov Gas

2170 The main body of the tank remains identical between PVDIS and SIDIS configurations, and has a  
2171 length roughly 105 cm with an inner radius of 71 to 85 cm, and an outer radius of 265 cm. With the  
2172 PVDIS baffles removed for SIDIS, an additional tank ‘snout’ is attached upstream of the main tank  
2173 inside the additional space evacuated by the baffle system. This tank snout adds an additional 107  
2174 cm of length to the tank with an inner radius of 58 to 71 cm, and an outer radius of 127 to 144 cm.  
2175 In both configurations, the windows will be constructed from polyvinyl fluoride (PVF or Tedlar) at  
2176 a thickness of 0.05 mm and 0.1 mm for the entrance and exit windows respectively. PVF provides  
2177 a strong and gas-tight seal at minimal density ( $1.45 \text{ g/cm}^3$ ). The radiator gas in both configurations  
2178 will be  $\text{CO}_2$  pressurized at slightly over atmospheric pressure to maintain gas purity.

#### 2179 8.1.2 Mirrors

2180 Each sector will consist of two spherical mirror segments with dimensions listed in Tab. 12. Radially  
2181 outward from the beam line, the inner most segment we will refer to as mirror 1 (red in Fig. 72) and

2182 the outermost segment as mirror 2 (blue in Fig. 72). In order to accommodate two different incident  
 2183 particle angles between PVDIS ( $22^\circ$  to  $35^\circ$  from a central Z-vertex 270 cm away) and SIDIS ( $8.0^\circ$   
 2184 to  $15.0^\circ$  from a vertex 520 cm away), mirror 1 must be adjusted between experiments such that  
 2185 the reflected Cherenkov light in both configurations falls into the PMT detector acceptance. This is  
 2186 achieved by rotating mirror 1 by an angle of approximately  $8^\circ$  inward about the mirror’s inner-most  
 2187 edge (or edge closest to the beam-line). In Fig. 72 we see a cross section of the light gas Cherenkov,  
 2188 sliced along the beam or Z-direction, with the mirrors in both the reclined and inclined positions.  
 2189 Mirror 2 is fixed in position and rotation and non-contributing to the SIDIS configuration; however,  
 2190 mirror 2 is necessary to cover the larger angular range in the PVDIS configuration. **The mirrors will  
 2191 be crafted to minimize areal density while maintaining good rigidity and keeping fabrication costs  
 2192 reasonable. A fine surface smoothness is required to reach good reflectivity below 200 nm. The  
 2193 spot size requirement of the spherical mirror is less than 5 mm.** Mirror coating will be performed  
 2194 by our collaborators at Stony Brook, and will consist of high reflectance ( $\geq 85\%$  for  $\lambda = 200$  nm  
 2195 to 620 nm) aluminum with a protective coating of  $\text{MgF}_2$ .

Mirror	inner-edge W (cm)	outer-edge W (cm)	L (cm)	R of curv. (cm)
Mirror 1	16.26	36.03	114.53	277.51
Mirror 2	37.06	45.95	59.26	157.99

Table 12: The dimensions of the two mirror segments in the light gas Cherenkov.

### 2196 8.1.3 PMTs

2197 The light gas Cherenkov will use Hamamatsu flat panel multianode photomultiplier tube assem-  
 2198 blies: H12700C [221]. These PMT assemblies are an  $8 \times 8$  pixel square array with a total active  
 2199 surface area of  $49 \text{ mm} \times 49 \text{ mm}$  with a UV-glass window, Bi-alkali photocathode material produc-  
 2200 ing an average quantum efficiency around 15%, and a 12-stage dynode structure allowing resolution  
 2201 down to a single photoelectron. A  $3 \times 3$  array of these PMT assemblies will be mounted in each  
 2202 sector, as shown in the PMT mounting prototype in Fig. 73. The position and orientation of the  
 2203 PMT array will remain fixed between PVDIS and SIDIS configurations. The PMTs will be coated  
 2204 with a wave-length shifting p-Terphenyl coating. This coating is a cost effective method to boost  
 2205 the PMT response of Cherenkov radiation in the UV range. The expected effective increase in pho-  
 2206 toelectron gain is shown in Fig. 74. Every pixel in the H12700C will be wired together to produce  
 2207 one signal per PMT; a trigger will then be constructed by requiring two PMT assemblies in the same  
 2208 array to fire in the same time window, with a minimum photoelectron discrimination. Simulations  
 2209 show a  $>90\%$  average electron detection efficiency, integrated over all angles and momenta, when  
 2210 requiring 2 separate PMTs assemblies in an array to each generate 2 or more photoelectrons in either  
 2211 the PVDIS or SIDIS configurations. This trigger configuration would result in 36 possible coinci-  
 2212 dences per sector, consequently reducing the single photoelectron rate due to dark current or other  
 2213 backgrounds by at least a factor of 10. Specific filtering of the PMT signals will be tested while  
 2214 prototyping the PMT array and electronics. Additionally, we plan on improving the resolution of  
 2215 the PMT sum signal through matrix gain balancing of the PMT pixel-array patented by Vladimir  
 2216 Popov to Jefferson Lab.

### 2217 8.1.4 Magnetic Shielding and Winston Cones

2218 The PMTs will be shielded by a mu-metal cylinder / cone construction that doubles as support for a  
 2219 reflective aluminum inner glass cone to direct light onto the PMT array. The cylinders will measure

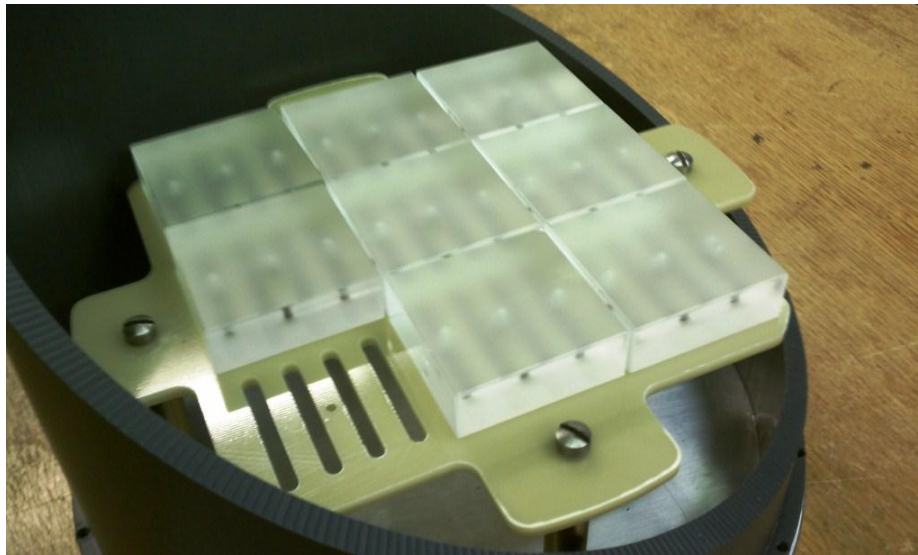


Figure 73: PMT assembly mounting prototype showing  $3 \times 3$  array of dummy PMTs inside the space restricted by magnetic shielding.

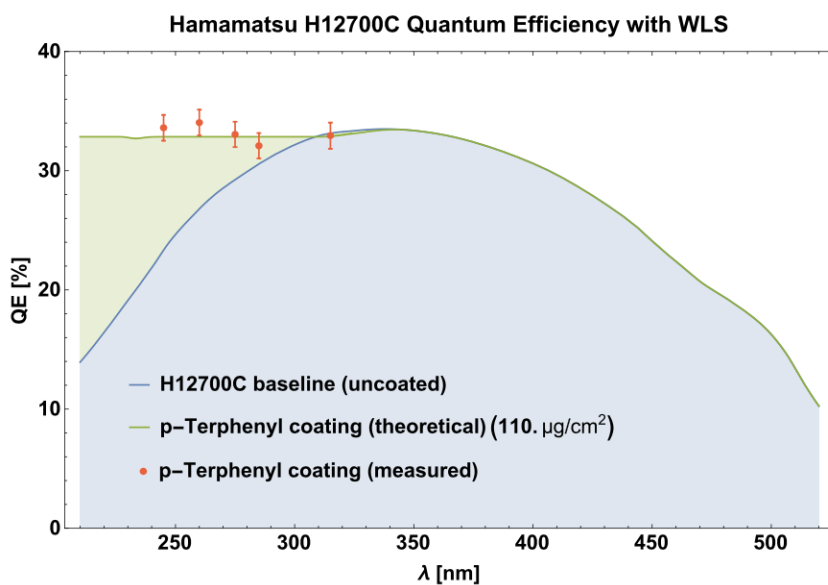


Figure 74: The increase in effective gain resulting from p-Terphenyl coating on H12700C PMTs. Red points are measurements done at Temple University. The curves show the current H12700C quantum efficiency, and the expected effective gain in the quantum efficiency from p-Terphenyl coating as a function of optical photon wavelength.

2220 30 cm in length with an inner radius of 11.28 cm, the cone will have a height of 30 cm with an inner  
 2221 radius of 7.8 cm at the narrow end and an inner radius of 21 cm at the wide end. The mu-metal  
 2222 shielding will be 0.04 inch thick reinforced by 0.125 inch thick 1008 carbon steel and manufactured  
 2223 by Amuneal Manufacturing Corp [222]. The PMTs are most sensitive to the magnitude of the  
 2224 magnetic field parallel to the photon collection face (transverse direction). We require a reduction  
 2225 of 95 gauss to <50 gauss in the transverse direction, and a reduction of 135 gauss to <50 gauss in

2226 the longitudinal direction, to where we expect an output loss  $<10\%$  as seen in Figure 86

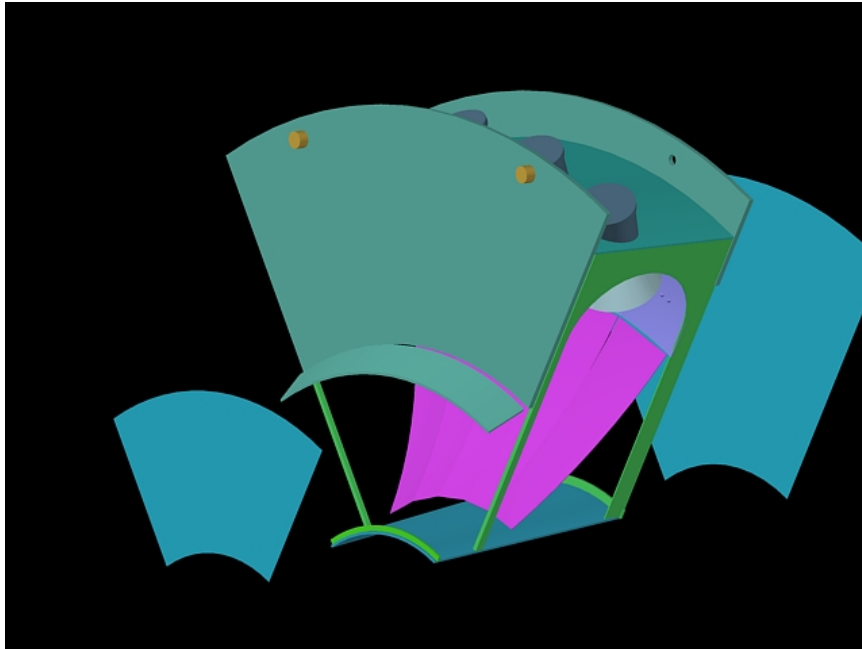


Figure 75: The support frame for one subsection of the light gas Cherenkov. The front and back acceptance windows (blue) are exploded to show the mirrors (pink and purple) and the support frame (green). The mounting points of the tank to the magnet housing are shown in orange.

## 2227 8.2 Tank Support

2228 The Cherenkov tank front and back windows will be divided into six radial sections. Between  
2229 each pair of sections will be two thin rectangular aluminum support spokes, one to support and  
2230 frame the upstream side of the tank and another to support and frame the downstream side (see Fig.  
2231 75). Both spokes are positioned and aligned to minimize the probability of tracks passing through  
2232 the support material. Additionally, both spokes are interconnected at the outer radius of the tank,  
2233 outside of the desired physics acceptance, by a solid arc-shaped plane to increase the rigidity of the  
2234 frame and provide additional support for mounting the focusing cones and PMT assemblies. The  
2235 space between the upstream and downstream spokes will remain open to maximize Cherenkov light  
2236 collection. The combined frame itself will be mounted to the back wall of the downstream magnet  
2237 housing, to support the full weight of the Cherenkov detector. This alleviates placing additional  
2238 stress on the end-cap nose, which other additional downstream detectors will use to support their  
2239 weight. Each PMT array will be accessible from the outer radial wall of the tank for alignment or  
2240 maintenance purposes.

## 2241 8.3 Simulations

2242 All simulations were done with a slightly modified version of the GEMC [223] software developed  
2243 at Jefferson Lab. GEMC uses a GEANT4.95 [224] backend to simulate all particle tracking through  
2244 and interaction with materials and geometries. All plots shown in the light gas Cherenkov section  
2245 of this document use the same simulation dataset. Event generation was performed by the eicRate

2246 DIS event generation tool authored by Seamus Riordan. The simulations also have the following  
2247 features:

- 2248 • Acceptance through the PVDIS baffle system (PVDIS events only).
- 2249 • Cherenkov radiation process for creation of optical photons.
- 2250 • Expected delta ray and pair creation from  $e^-$  and  $\pi^-$  particles interacting with the Cherenkov  
2251 front window using the standard and low energy EM packages for GEANT4.
- 2252 • Expanded mirror reflection properties in GEMC to be more in line with the latest functionality  
2253 from GEANT4.
- 2254 • PMT photoelectron signal simulation which includes the PMT dead area, quantum efficiency  
2255 pixel-by-pixel, and optical properties of the PMT UV glass window.

### 2256 8.3.1 Collection Efficiencies

2257 The collection efficiencies for electrons in both the PVDIS and SIDIS configuration can be seen  
2258 in Figs. 76 and 77. The slight jump in photoelectrons around  $32^\circ$  in the PVDIS figure is a result  
2259 of the inclined inner mirror, which moderately reduces the number of optical photons produced by  
2260 reducing the particle's path length through the gas before crossing the mirror.

### 2261 8.3.2 Background Rates

2262 A low energy inclusive background simulation was performed using GEMC by generating an elec-  
2263 tron beam on target, including all expected materials between the beam entrance to the Cherenkov  
2264 back window. Secondaries produced anywhere in the SoLID detector and above the Cherenkov radi-  
2265 ation momentum threshold while passing through the Cherenkov gas were considered as a possible  
2266 source of background. For the PVDIS configuration, lepton production from initial  $\pi^0$  production  
2267 at small angle produced the majority of accidental backgrounds. This background was calculated  
2268 using the same methodology as the modified Hall D generator, which uses a modified version of  
2269 PYTHIA and SAID input to match known world data. More information on the pion generator can  
2270 be found in Sec. 12.2.3. The combined background rate is estimated to be  $\approx 0.8$  MHz per sector for  
2271 a trigger requiring at least 2 photoelectrons in 2 separate PMTs in the same sector. For the SIDIS  
2272 configuration, the expected background rate is less than 100 KHz in the same trigger configuration  
2273 above.

### 2274 8.3.3 Pion Rejection

2275 The expected pion rejection is shown in Figs. 78 through 81. All pion signal below the pion  
2276 Cherenkov radiation threshold (3.2 GeV/c for the PVDIS gas) is produced by knock-ons or ( $e^+$ ,  
2277  $e^-$ ) pair creation. The photoelectron signal itself is a poisson distribution convoluted with a gaussian  
2278 to simulate the PMT 1 photoelectron resolution. The pion-electron photoelectron cut is determined  
2279 by taking the intersection of the two signal distributions, simultaneously maximizing the electron  
2280 selection probability while maximizing the pion rejection probability. Additional calculations are  
2281 shown in Figs. 78 and 80 with a stricter cut on the pion signal, which consequently reduces the  
2282 electron efficiency (by 10% for the red points and 20% for the blue points). An example of these  
2283 photoelectron cuts are shown in table for one bin in momentum in the PVDIS configuration.

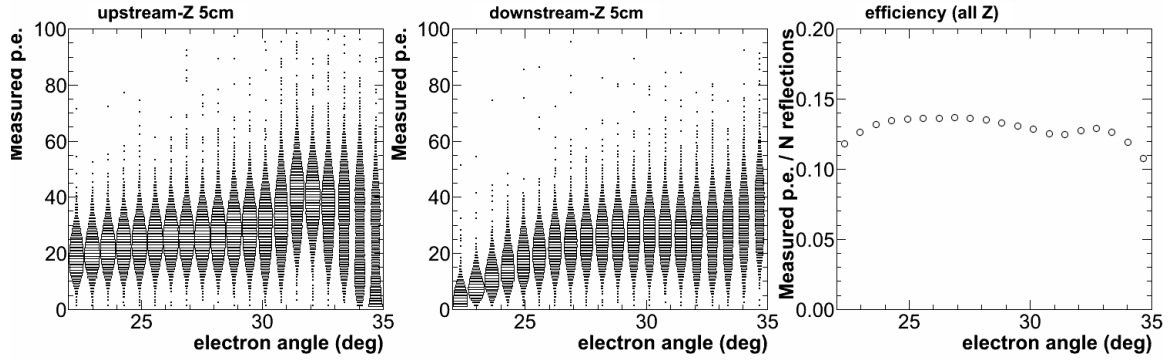


Figure 76: PVDIS configuration: The number of surviving photoelectrons versus theta after losses due to quantum efficiency of the PMTs, PMT dead area, or secondary reflections / absorptions off of the cones or PMT UV-glass window for events in the 5 cm of target most upstream (left) and 5 cm of target most downstream (middle). The right plot shows the corresponding collection efficiency versus theta for all 40 cm of the target Z-vertex.

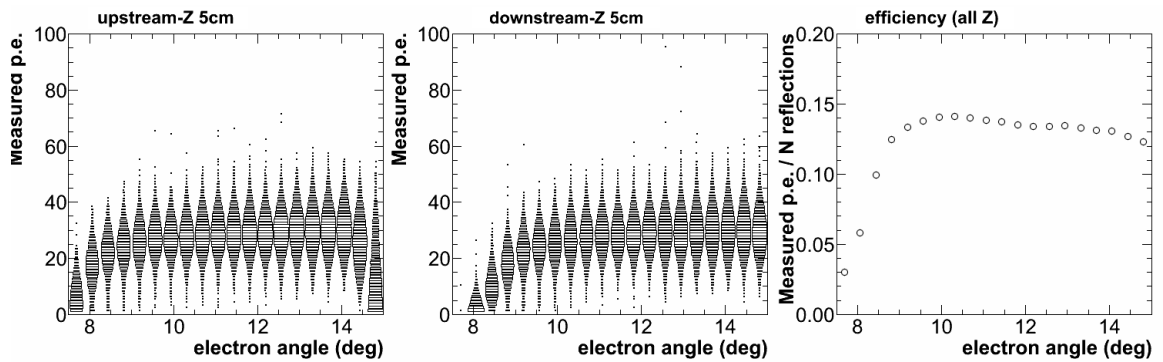


Figure 77: SIDIS configuration: Same as in Fig. 76 but with the SIDIS configuration.

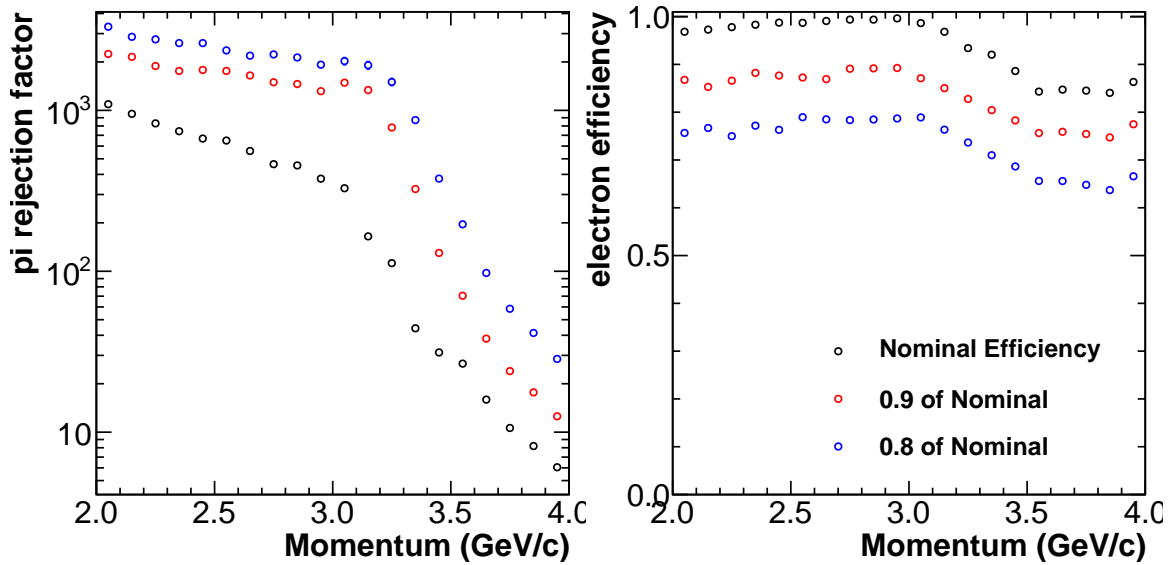


Figure 78: PVDIS configuration: The pion rejection factor versus momentum for 3 electron selection efficiencies: The nominal efficiency maximizes the pion rejection while minimizing loss of electrons, the red points correspond to a stricter pion cut with up to 10% additional loss of electrons, and the blue points allow an additional 20% loss of electrons.

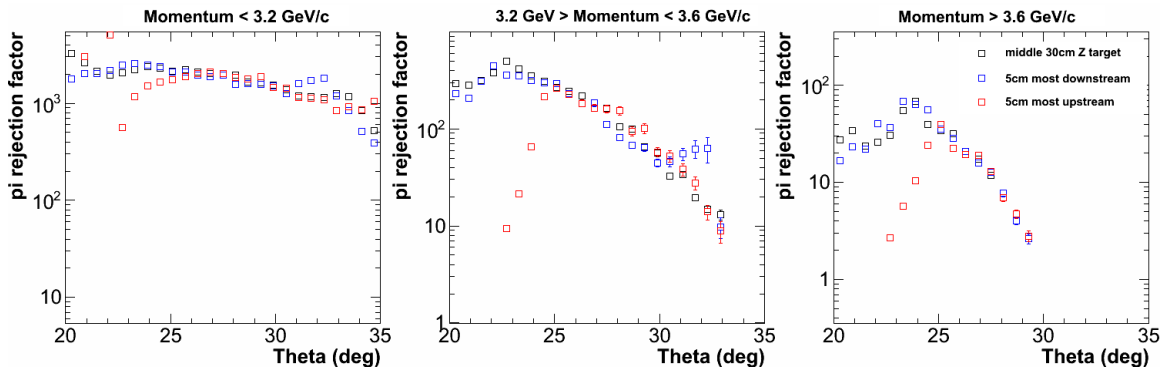


Figure 79: PVDIS configuration: The pion rejection factor versus the electron scattering angle theta over 3 momentum and Z-vertex ranges.



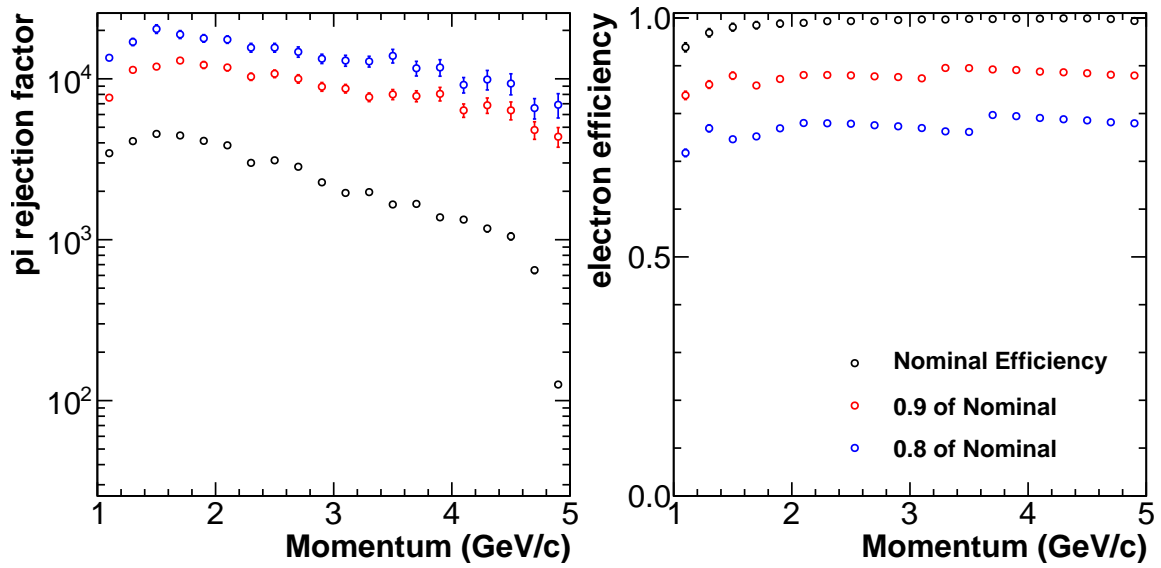


Figure 80: SIDIS configuration: Same as in Fig. 78 but with the SIDIS configuration.

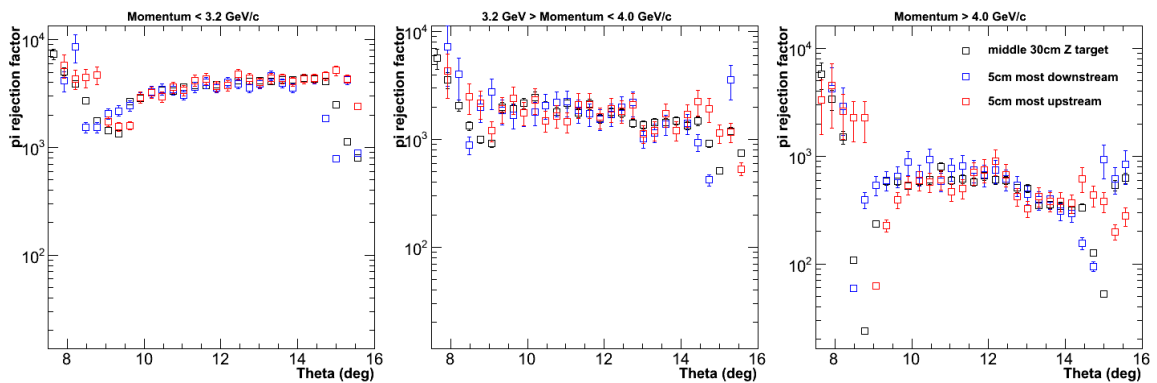


Figure 81: SIDIS configuration: Same as in Fig. 79 but with the SIDIS configuration.

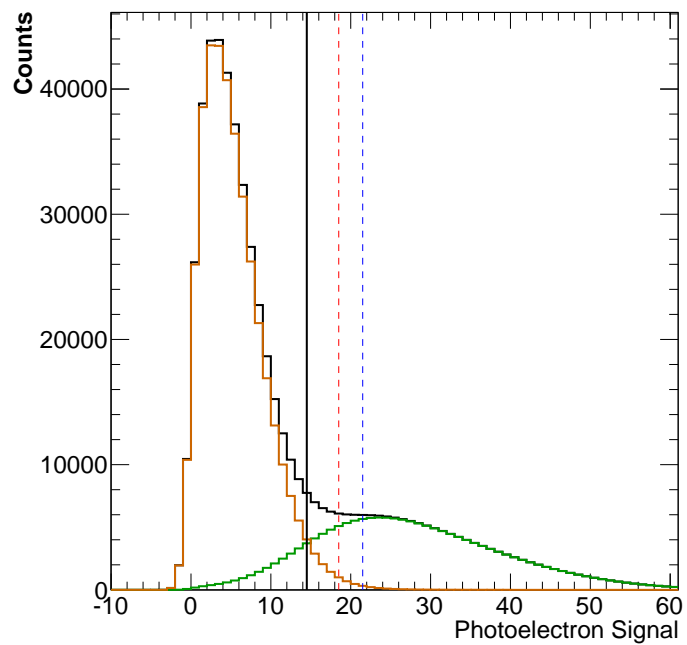


Figure 82: An example of the pion rejection cut made for one arbitrary bin in momentum for the PVDIS configuration. The pion signal is shown in orange and the electron signal is shown in green. The nominal efficiency cut is shown as a solid black line. The 90% and 80% electron efficiency cuts are shown as dashed red and blue lines respectively.

## 2284 9 Heavy Gas Cherenkov

### 2285 9.1 Optical System Design

2286 A hadron Cherenkov detector is required to help with the identification of both positive and negative  
2287 pions. A clear distinction between pion and kaon Cherenkov signals is mostly required in the mid  
2288 to high momentum range, namely from 2.5 to 7 GeV. The  $C_4F_8O/C_4F_{10}$  gas at 1.5 atm and a tem-  
2289 perature of  $20^\circ C$  gives a momentum threshold of 2.2 and 7.5 GeV for pions and kaons, respectively.  
2290 Due to geometrical acceptance constraints the gas length available for Cherenkov light production  
2291 is about 1 m. Requirements on the design are full azimuthal angular coverage and a good detector  
2292 performance in a magnetic field with strength as high as 150 Gauss. The optical system for the  
2293 Cherenkov light collection has been optimized using a GEANT4 simulation package taking into  
2294 account the expected SoLID magnetic field configuration with the CLEO-II magnet. The system  
2295 consists of a ring of 30 spherical mirrors of 1.2 m length each and inner and outer widths of 0.2 and  
2296 0.4 m, respectively. The mirrors will focus the light onto 30 photodetector as shown in Fig.83. The  
2297 size of each photodetector could be reduced to 8x8 inches (i.e. 16 of 2-inch PMTs per array) by  
2298 use of straight cones as an additional optical element to mirrors. The PMTs of choice are similar  
2299 to those used for the light gas Cherenkov namely the multi-anode 2 inch H8500-03/H12700-03 de-  
2300 vices from Hamamatsu: they perform well in relatively high magnetic field, are square shaped, and  
2301 have good photocathode coverage (89% of total area), making them ideal for tiling.

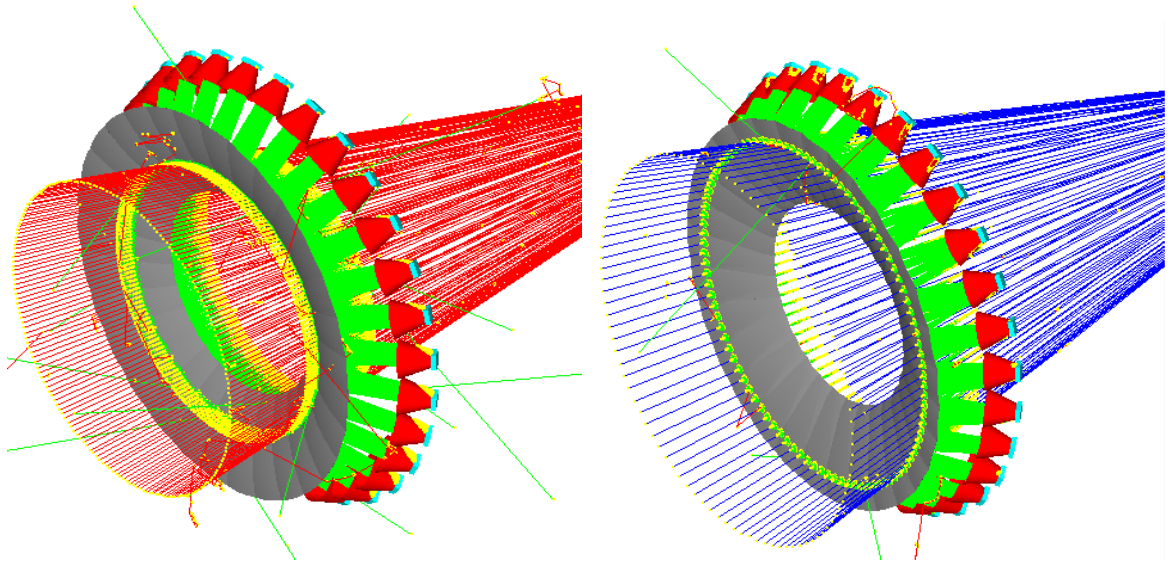


Figure 83: Optical system for the heavy-gas Cherenkov: a ring of 30 spherical mirrors (grey) will focus the Cherenkov photons created by the passage of negative (left panel) and positive (right panel) pions through the  $C_4F_8O/C_4F_{10}$  radiator gas onto PMT (cyan) arrays with the aid of straight cones (red).

## 2302 9.2 Simulation

### 2303 9.2.1 Photoelectron Yield

2304 Due to the SoLID geometrical acceptance with respect to the target and to the constraints on the  
2305 photon detector positioning inside the Cherenkov tank, the particles with large polar angle entering  
2306 the detector will travel a larger gas length compared to those with a low polar angle. Thus, the  
2307 optimization was done favoring the low angle kinematics whenever possible and by keeping the  
2308 number of maximum reflections to 2: one on the mirrors and one possibly on the cones (not all  
2309 photons need the extra bounce on the cones to be collected by the PMT arrays). As a consequence,  
2310 the loss of photons through absorption on the reflective surfaces is kept to a minimum.

2311 Our simulation of the expected number of photoelectrons shown in Fig.84, takes into account  
2312 realistic parameters for the gas index of refraction, gas transparency, mirror and cone reflectivities  
2313 and the quantum efficiency of the H8500-03 PMTs to account for the photon to photoelectron con-  
2314 version. We scaled down the number of photoelectrons obtained from the GEANT4 simulation by  
2315 a conservative factor of 0.5 mostly to account for the dead zones on the PMT tiles due to incom-  
2316 plete photocathode coverage. The index of refraction of  $C_4F_8O$  has been measured at Syracuse  
2317 University [225] between 400 and 650 nm, while below 400 nm we used an extrapolation based  
2318 on a parametrization from HERA/DELPHI of this index[226]. We studied the impact on the ex-  
2319 pected number of photoelectrons on the large uncertainty in the  $C_4F_8O$  refractivity by assuming a  
2320 refractivity 20% smaller than the nominal value extracted from the Syracuse and HERA/DELPHI  
2321 measurements. We found that the yield of photoelectrons would still be sufficient, though marginal,  
2322 at the lowest momentum of 2.5 GeV. The  $C_4F_8O$  transmittance has been measured at Jefferson Lab  
2323 in Hall B with great accuracy in a photon wavelength range of 200 to 500 nm. We used these data  
2324 in our simulation to account for Cherenkov photon absorption in the gas. For the mirrors, we plan  
2325 to use some light material with honeycomb structure for base to minimize the material budget and  
2326 coated them with Aluminum. For the reflection cones, we plan to use the Aluminum coated Lexan  
2327 film and attach it its base which sever as the magnetic fielding cone also. The film is also used by  
2328 CLAS12 Low Threshold Cerenkov as their mirror reflection surface and has good performance.

2329 The photoelectron yield dependence on polar angle and momentum is shown in Fig.84. For a  
2330 fixed polar angle the number of photoelectrons increases with increasing momentum as we move  
2331 away from the pion firing threshold of 2.2 GeV and then saturates. There is also an increase of yield  
2332 with increasing polar angle due to the detector geometry which allows pions with larger angle to  
2333 traverse more gas than those with low polar angle.

2334 The mirrors will be made using the same material and technique as those of the Light Gas  
2335 Cerenkov mirrors. The PMTs will also be the same and be coated with a wave-length shifting  
2336 p-Terphenyl coating to enhance the PMT response in the UV range. The readout system will be  
2337 similar with the exception that the Heavy Gas Cerenkov signal will not be in the trigger.

### 2338 9.2.2 Pion Detection Efficiency and Kaon Rejection Factor

2339 The expected performance of the detector has been further studied by estimating the pion detection  
2340 efficiency and kaon rejection factor for a given cut on the number of photoelectrons with no input  
2341 from other particle identification detectors. Background studies have shown [228] that the expected  
2342 pion to kaon ratio is 10 to 1. The pion and kaon photoelectron distributions are simulated as con-  
2343 volutions of Poisson and Gauss distributions. The resolution of the PMT enters as the standard  
2344 deviation of the Gauss distribution while the mean of the Poisson distribution is the output of the  
2345 GEANT4 simulation shown in Fig.84. We measured the resolution of H8500C-03 to be 1 photoelec-  
2346 tron. We mapped the pion detection efficiency and kaon rejection factor for few kinematics where

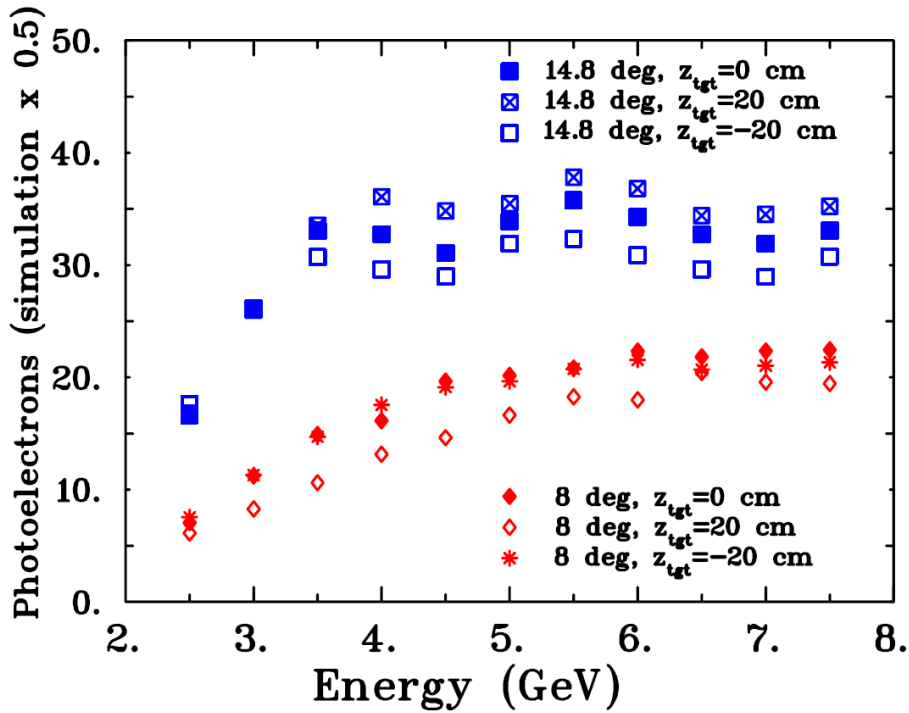


Figure 84: Simulated number of photoelectrons as a function of the pion polar angle and momentum. The results are shown for positive pions. A very similar output is obtained for negative pions.

2347 we expect the smallest number of photoelectrons, namely at 8.0 degrees and momentum between  
 2348 2.5 and 4.5 GeV and our results are shown in Fig.85. Assuming that kaons would produce at most 1  
 2349 photoelectron below the Cherenkov threshold, for a cut on the number of photoelectrons of 3, the a  
 2350 pion detection efficiency is 99.0% (99.6%) at 2.7 GeV (3.0 GeV) with the same kaon contamination  
 2351 as small as 0.8%. At 8 degrees and below 2.7 GeV, the pion efficiency starts to drop below 99%.  
 2352 For larger momenta, a cut placed at 4 photoelectrons would result in a pion detection efficiency  
 2353 larger than 99.7% with a kaon contamination below 0.3%. This would meet the requirements of the  
 2354 approved experiments with SoLID.

### 2355 9.3 Performance of the PMTs in Magnetic Field

2356 We performed extensive bench tests of the H8500-03 and H12700-03 PMT at Jefferson Lab to map  
 2357 its performance in a magnetic field and assessed its capability of resolving single photoelectron  
 2358 signals[229]. The single photoelectron resolution was measured to be 1 photoelectron or better.  
 2359 The magnetic field test results are summarized in Fig.86. The longitudinal field is perpendicular  
 2360 to the face of the PMT and is labeled as  $B_z$ . The transverse field orientations, perpendicular to the  
 2361 sides of the PMT are shown as  $B_x$  and  $B_y$ . The PMT relative output is reduced by at most 30% when  
 2362 exposed to a longitudinal magnetic field up to 400 Gauss. Our studies of the single photoelectron  
 2363 response in field indicated that these losses happen mostly at the amplification stage on the dynode  
 2364 chain making it possible to compensate for this effect with external amplification. These results are  
 2365 very encouraging as it suggests that the effect of the field component which is hardest to shield,  
 2366 the longitudinal one, could be compensated for by superficial shielding and additional external  
 2367 amplification. The degradation of the PMT output in transverse magnetic field is more pronounced,  
 2368 up to 90% at 180 Gauss but this field component is easier to shield.

2369 *The magnetic shield incorporating the cones used for focusing would reduce the SoLID mag-*

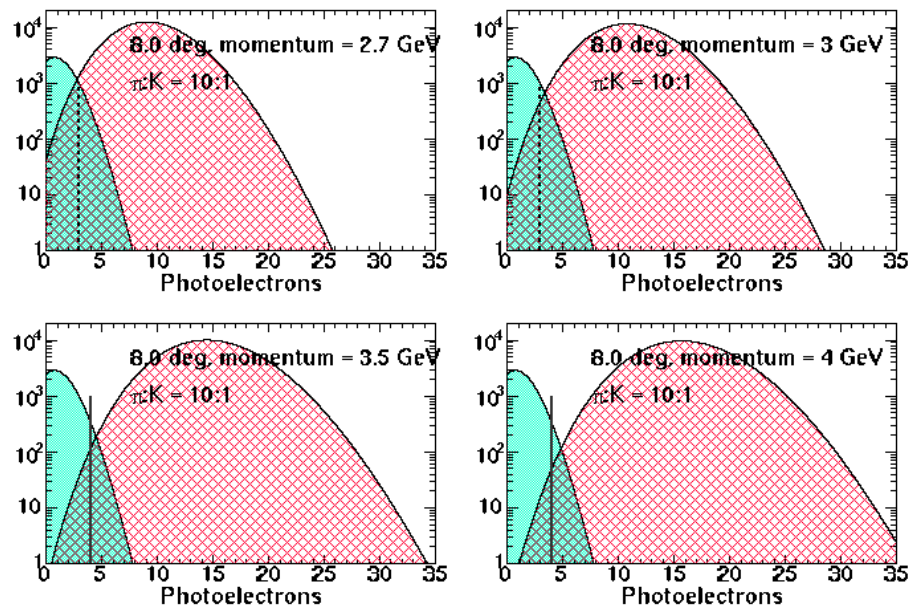


Figure 85: Simulated distributions of pions (red) and kaons (green) at with a polar angle of 8.0 degrees taking into account the photon detector resolution and the expected pion to kaon ratio.

2370 netic field at the PMT location to a few tens Gauss. The suggestion from shielding companies is  
 2371 that a 2-layer shield with a thin inner layer of mu-metal and a thin outer layer of carbon steel with  
 2372 mylar in between would meet our requirements. We are currently conducting tests and simulation  
 2373 to verify such ideas and to optimize the configuration.

#### 2374 9.4 Engineering Design

2375 The detector is separated into two halves and total 10 (36 deg) segments to facilitate fabrication and  
 2376 handling. An engineering design of one half of the pressure tank is given in Fig.87. The structure  
 2377 is mostly made of Aluminum. The outer shell parts will be fabricated as two sets of 5 modules  
 2378 each, individually assembled and sealed. One segment with PMTs, cones, and mirrors is shown in  
 2379 Fig.88. The PMT arrays are inserted from outside the tank into the cones. The cones are mounted  
 2380 inside the outer shell, with the possibility for fine position adjustment through the PMT mount tube.  
 2381 The spherical mirrors are fixed with mounts at their ends and attached to the tank. The detector is  
 2382 positioned in the magnet pole extension assembly, which is supported by individual rails mounted  
 2383 to the inner circumference of the cylindrical ring.

#### 2384 9.5 Gas and Gas System

2385 The detector uses  $C_4F_8O/C_4F_{10}$  gas as the radiator gas. The  $C_4F_8O$  gas is about 10 times heav-  
 2386 ier than air (9.19 g/L at 21°C), with a boiling point of  $-5^\circ C$  and a vapor pressure of 1.7 atm at  
 2387 21°C. The gas is stable, non-toxic, non-explosive and non-reactive except with alkali metal halides.  
 2388 However, due to its ability to pick up and transport oils, direct contact with organic materials needs  
 2389 to be avoided.  $C_4F_8O$  gas is not harmful to ozone but as being a perfluorocarbon compound, it is  
 2390 implicated as having a long atmospheric lifetime and high global warming potential. The  $C_4F_{10}$  gas  
 2391 has similar properties as the  $C_4F_8O$  gas, which is being considered as an alternative option for the  
 2392 radiator gas.

2393 The total volume of the Cherenkov tank is  $\sim 20 \text{ m}^3$  and it will be filled with  $\sim 300 \text{ kg C}_4\text{F}_8\text{O/C}_4\text{F}_{10}$   
2394 gas. The detector is hermetically sealed to allow containment of the radiator gas near the 1.5 atm  
2395 operation pressure at the temperature of  $20^\circ\text{C}$  which is the Hall A normal condition. The gas sys-  
2396 tem is similar to the Hall B heavy gas system During the filling process, the system will initially be  
2397 purged using the nitrogen gas to avoid the contamination of the oxygen and water vapor in the air.  
2398 Then the nitrogen gas will be purged by the radiator gas. The pressure of the gas will be monitored  
2399 by pressure gauge and a regulation system will be incorporated to maintain the tank at the desired  
2400 pressure. The gas will be collected back to tanks and purified to be used for refill.

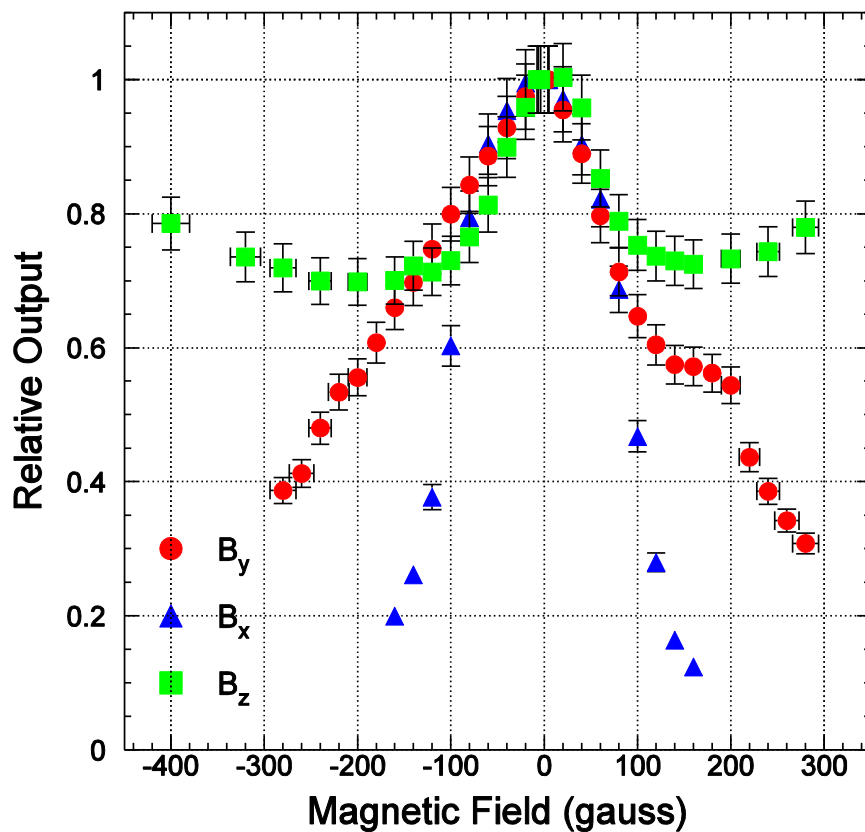


Figure 86: Relative output of the H8500-03 PMT in magnetic field. The PMT output normalized to the zero magnetic field configuration is shown for a longitudinal field orientation (i.e. perpendicular to the face of the PMT) in squares and for the transverse orientations (i.e. perpendicular to the sides of the PMT) in circles and triangles.



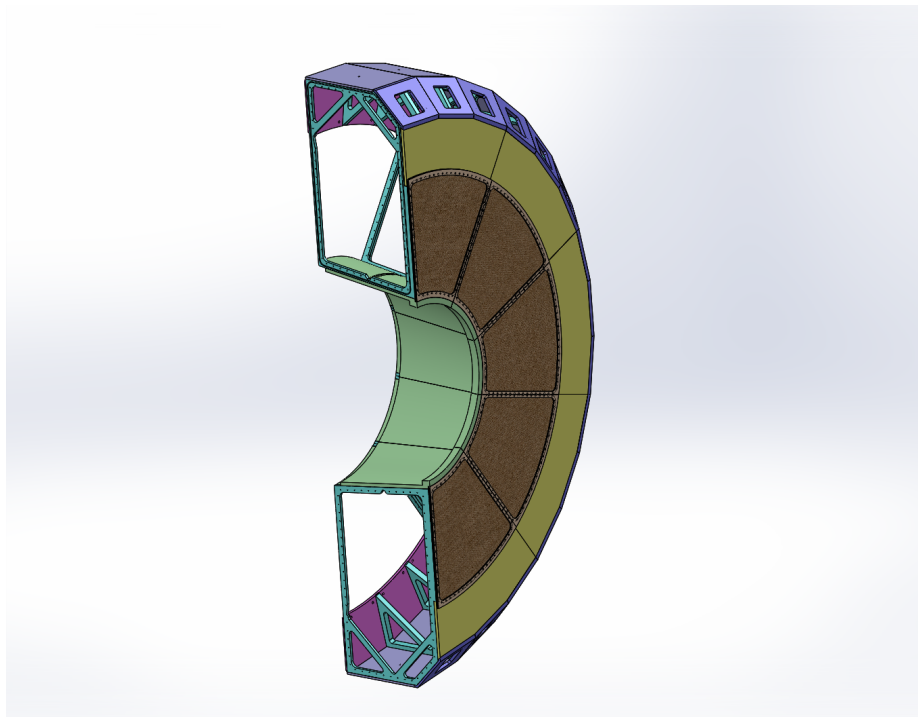


Figure 87: Conceptual design of the heavy gas Cherenkov detector

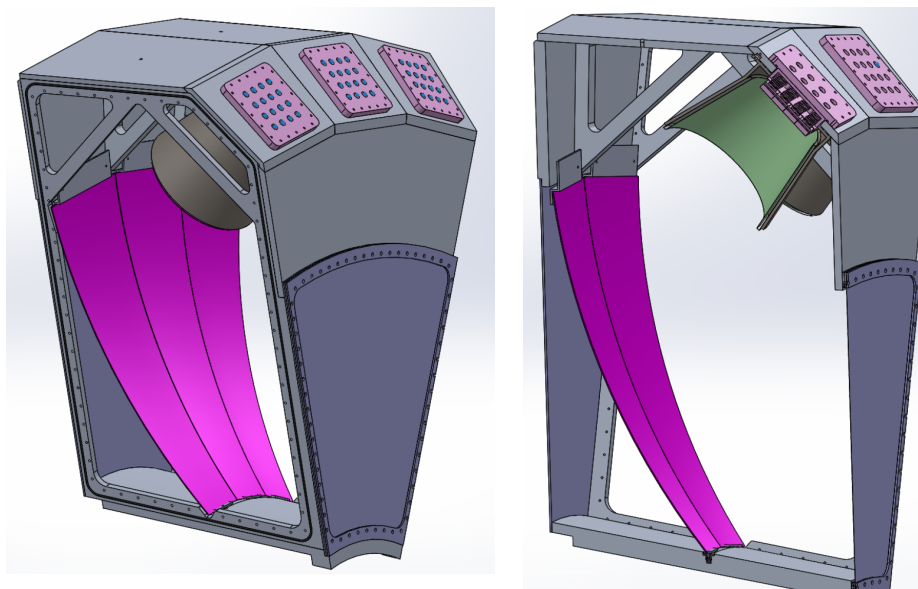


Figure 88: Conceptual design of the heavy gas Cherenkov detector (left) and PMT assembly (right)

## 2401 10 Electromagnetic Calorimeter

### 2402 10.1 Overview

2403 Electromagnetic calorimeters (EC) are used in the PVDIS, SIDIS and  $J/\psi$  experiments to mea-  
 2404 sure the energy deposition of electrons and hadrons, and to provide particle identification (PID).  
 2405 The SIDIS and  $J/\psi$  experiments share similar configurations and will be referred to as the SIDIS  
 2406 configuration hereafter. There are three calorimeters: the PVDIS experiment uses a forward angle  
 2407 calorimeter (FAEC) to detect the scattered electrons; the SIDIS experiments use a forward angle  
 2408 calorimeter (FAEC) and a large angle calorimeter (LAEC), both detect the scattered electrons while  
 2409 the FAEC also provides MIP triggers for pions. For electron detection, the dominant background  
 2410 comes from electro- and photo-produced pions. The desired performance is summarized in Table 13  
 2411 and the EC geometry in Table 14. Please note that the EC geometrical coverage is slightly larger  
 2412 than other detectors because the edges of the EC are expected to have degraded performance due to  
 2413 shower spreading. The total coverage area of the SIDIS FAEC and LAEC is less than that of the  
 2414 PVDIS FAEC. The plan is to share modules between the two configurations, thus all modules need  
 2415 to be rearranged when switching between the PVDIS and SIDIS configurations.

	Desired performance
$\pi^-$ rejection	$\gtrsim[50:1]$
$e^-$ efficiency	$\gtrsim 95\%$
Energy resolution	$< 10\%/\sqrt{E}$
Radiation resistance	$\gtrsim 400$ kRad
Position resolution	$\lesssim 1$ cm

Table 13: Overview of the SoLID calorimeter desired performance.

	PVDIS FAEC	SIDIS FAEC	SIDIS LAEC
$z$ (cm)	(320, 380)	(415, 475)	(-65, -5)
Polar angle (degrees)	(22,35)	(7.5,14.85)	(16.3, 24)
Azimuthal angle	Full coverage		
Radius (cm)	(110, 265)	(98, 230)	(83, 140)
Coverage area (m <sup>2</sup> )	18.3	13.6	4.0

Table 14: Geometrical coverage for the SoLID electromagnetic calorimeters. The  $z$  direction is along the electron beam and the origin is at the solenoid center.

2416 The design of the SoLID ECs is determined by both the physics goal and the expected running  
 2417 conditions. The design is challenging due to our unique constraints including high radiation back-  
 2418 ground ( $\approx 400$  kRad, as in Table 13), strong magnetic field (1.5 T on SIDIS LAEC), large coverage  
 2419 area, and the budget. These factors prevent the use of many traditional calorimeter technologies,  
 2420 including NaI (TI), CSI, BGO and lead glass because of the low radiation resistance;  $\text{PbWO}_4$ , LSO  
 2421 and  $\text{PbF}_2$  because of their high cost; and lead/scintillator fiber calorimeter because of the high cost  
 2422 and the large amount of light readout required.

2423 Due to the PID requirement, it is necessary to segment the EC longitudinally into a preshower  
 2424 and a shower detector. The following design that meets the experimental requirements was chosen:  
 2425 the shower calorimeter modules are based on the so-called Shashlyk design [230], a sampling-

2426 type design consisting of alternating layers of scintillator and lead (as an absorber); the preshower  
 2427 detector is made of a layer of lead as a passive radiator followed by scintillator pads [231, 232].  
 Details of the design are summarized in Tables 15 and 16.

Type	passive radiator + sensitive layer
Passive radiator	$2X_0$ , Pb
Sensitive layer	2 cm, plastic scintillator 100 cm <sup>2</sup> hexagon tile
Light transportation	WLS fiber embedded in the scintillator

Table 15: SoLID electromagnetic calorimeter, preshower design.

2428

Type	Shashlyk sampling calorimeter	
Each layer	Absorber	0.5 mm Pb
	Scintillator	1.5 mm STYRON 637 plastic scintillator
	Gap	Paper, 0.12 mm × 2 sheets
	Radiation Length	$0.093X_0$
Overall	Radiation length ( $X_0$ )	24 cm
	Molire radius	5 cm
	Length	$18 X_0$ , 43.4 cm
	Total number of layers	194
	Lateral granularity	100 cm <sup>2</sup> hexagon
	Light transportation	WLS fiber, 100 per module, penetrating layers longitudinally

Table 16: SoLID electromagnetic calorimeter, shower design.

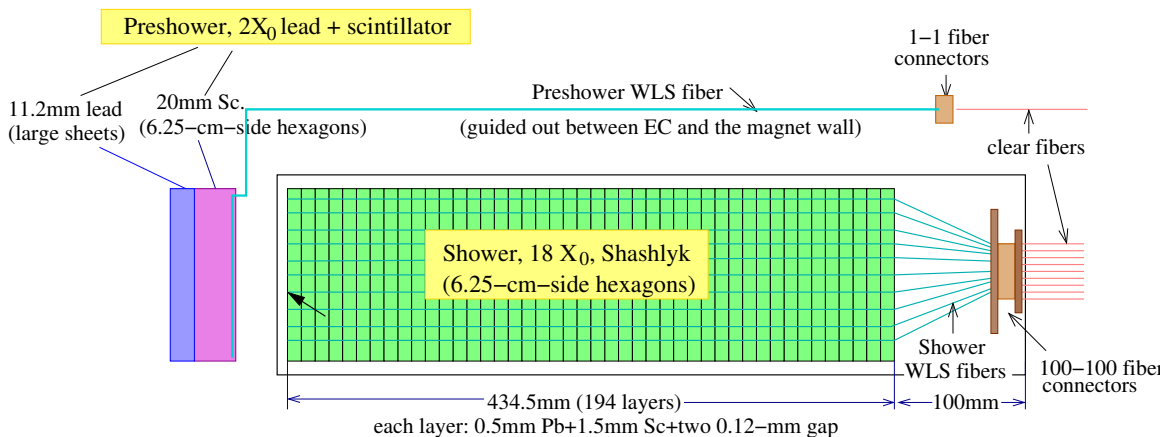


Figure 89: Design diagram of the SoLID electromagnetic calorimeter module. Spacing between the preshower and the shower detectors, and the spacing between the shower module and the 100-100 fiber connectors, need to be kept as small as possible yet still allow safe routing of the WLS fibers and positioning of the support structure.

2429 The structure of both the preshower and the shower detector is illustrated in Fig. 89. In the  
 2430 experiment, particles are incident close to perpendicular to the scintillator-lead layers. Scintillation

2431 light is absorbed, re-emitted and transported to the photon detector by wave-length shifting (WLS)  
 2432 optical fibers penetrating through the shower modules longitudinally, along the incident particle  
 2433 direction. The cross sectional area of the shower modules was optimized to be  $100\text{ cm}^2$  (see Sec-  
 2434 tion 10.2.3), with a hexagon shape determined for the convenience of the support structure design.  
 2435 The scintillator tile of preshower modules has the same  $100\text{ cm}^2$  hexagon shape to match the shower  
 2436 modules, which maximizes PID efficiencies, facilitates the design, and allows fast switch-over be-  
 2437 tween SIDIS and PVDIS. The lead absorber of the preshower can be made of large sheets.

2438 Geant4-based simulations are used to study the performance and optimize the design of the  
 2439 key specifications while minimizing the cost. Figure 90 shows the simulated shower of a 3 GeV  
 electron incident on the PVDIS EC. In the following we will present details of the shower and the

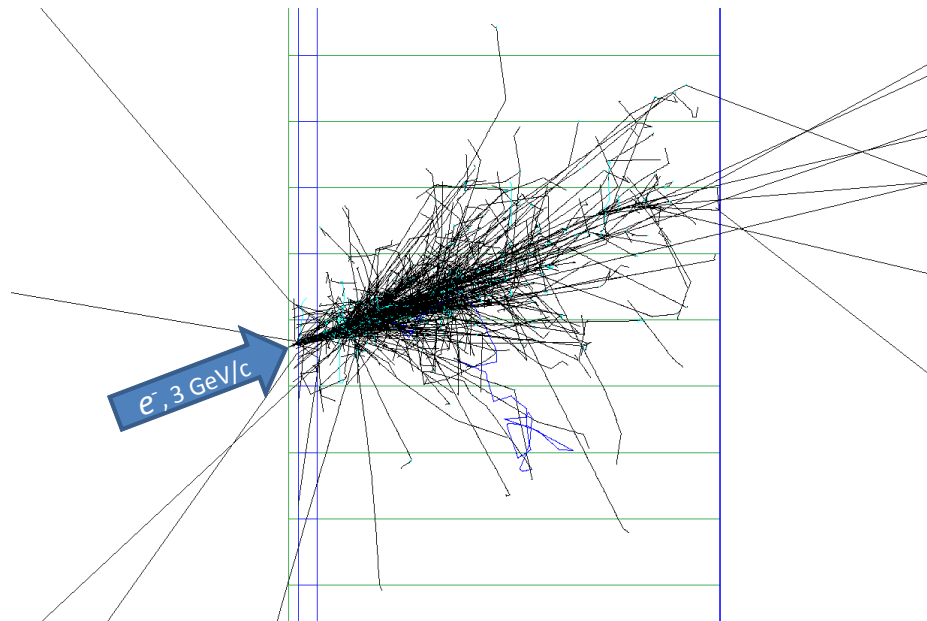


Figure 90: GEANT4 simulation of the shower generated by a 3-GeV electron incident on the PVDIS calorimeter. The black and green tracks are secondary photons and electrons respectively. The green horizontal lines are edges of calorimeter modules. The first two layers of materials are the preshower detector, consisting of  $2X_0$  of lead and 2 cm thick of scintillator.

2440

2441 preshower design, general layout and the support system, light readout, expected radiation dose,  
 2442 PID and trigger performance, and a cost estimate.

## 2443 10.2 Shower Detector Design Considerations

### 2444 10.2.1 Total Length of the Calorimeter

2445 The overall length of calorimeter should be long enough to enclose most of the electromagnetic  
 2446 shower and short enough to maximize the difference in energy deposition between electrons and  
 2447 pions. The fraction of energy leak out for electron showers, averaged inside the acceptance of  
 2448 the SIDIS-Forward calorimeter, was studied for different total lengths of calorimeter. As shown  
 2449 in Fig.91, a total length of 20 radiation lengths was found to be a good balance. Considering the  
 2450 2-radiation-length thickness of preshower, this leads to a shower detector length of 18 radiation  
 2451 lengths or 43.4 cm.

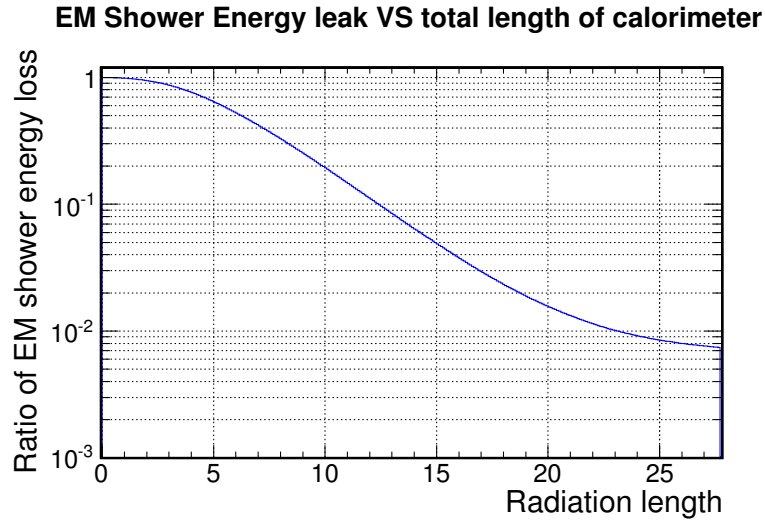


Figure 91: Fractional energy leak for an average SIDIS-Forward electron shower vs. different total length of the calorimeter.

2452 **10.2.2 Sampling Ratio of the Shower Detector**

2453 Each layer of the shower module consists of a 1.5 mm-thick scintillator plate and a 0.5-mm absorber  
 2454 plate made of lead. The Pb absorber thickness of 0.5 mm or less is favored to provide a fine sampling  
 2455 and therefore better energy resolution. The thickness of the scintillator plate should be thin enough  
 2456 to ensure fine longitudinal sampling, while thick enough to reduce light attenuation in the lateral  
 2457 direction. A thickness of 1.5 mm was chosen following the experience of previous Shashlyk designs  
 2458 used by the KOPIO experiment [230, 233], the PANDA experiment [234], and the COMPASS-II  
 2459 experiment. The COMPASS module is shown in Fig. 92. A gap of 120  $\mu\text{m}$  is kept between the lead  
 2460 and scintillator plates to accommodate a sheet of high-reflectivity paper, which reduces the loss of  
 2461 scintillation light.

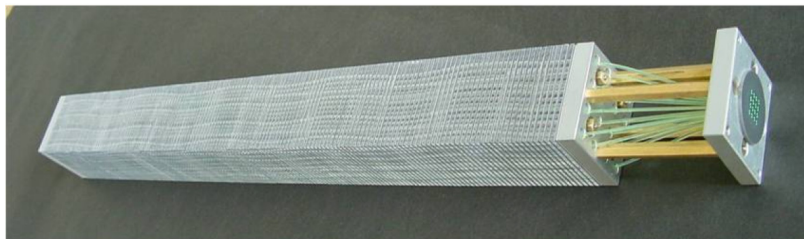


Figure 92: COMPASS-II Shashlyk calorimeter module. This illustrates the basic design of shashlyk modules: each module consists of alternating scintillator and lead (or other absorber material) layers, with WLS fibers penetrating across all layers to guide out the scintillation light signal. Four stainless steel rods are used to fix all layers together and support the whole module.

2462 Figure 93 shows the simulated energy resolution using the chosen configuration of 1.5 mm  
 2463 scintillator and 0.5 mm lead. A resolution of about  $4\%/\sqrt{E}$  is achieved.

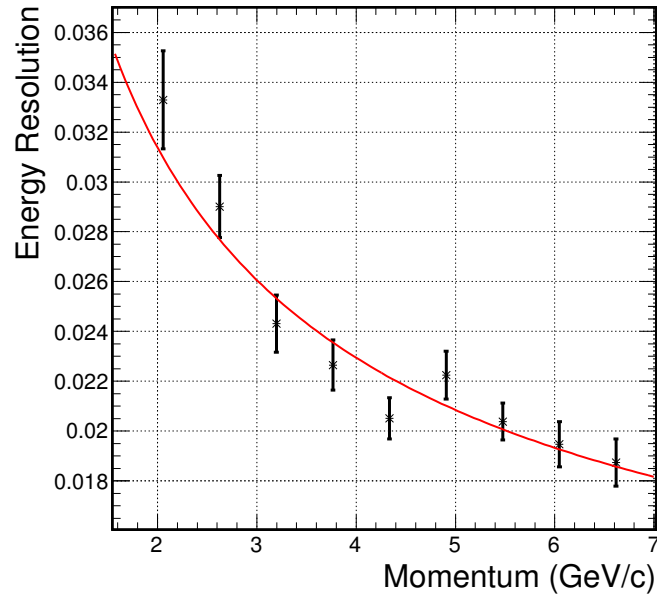


Figure 93: Simulated energy resolution of the SoLID calorimeter using both the Preshower and the Shower. The error bars are statistical error of the simulation. This simulation was performed without background to demonstrate the intrinsic PID performance of the EC. Simulation results including the background will be presented in section 10.7.

### 2464 10.2.3 Lateral Size of the Calorimeter Module

2465 A smaller lateral size for calorimeter modules leads to better position resolution and lower back-  
 2466 ground. However, it will also increase the total number of modules and readout channels, leading to  
 2467 higher overall cost. The study shows that a lateral size of about  $100 \text{ cm}^2$  will provide a good balance  
 2468 between position resolution, background and the overall cost as shown in Fig. 94. A hexagon lateral  
 2469 shape is favored by the layout and the support design.

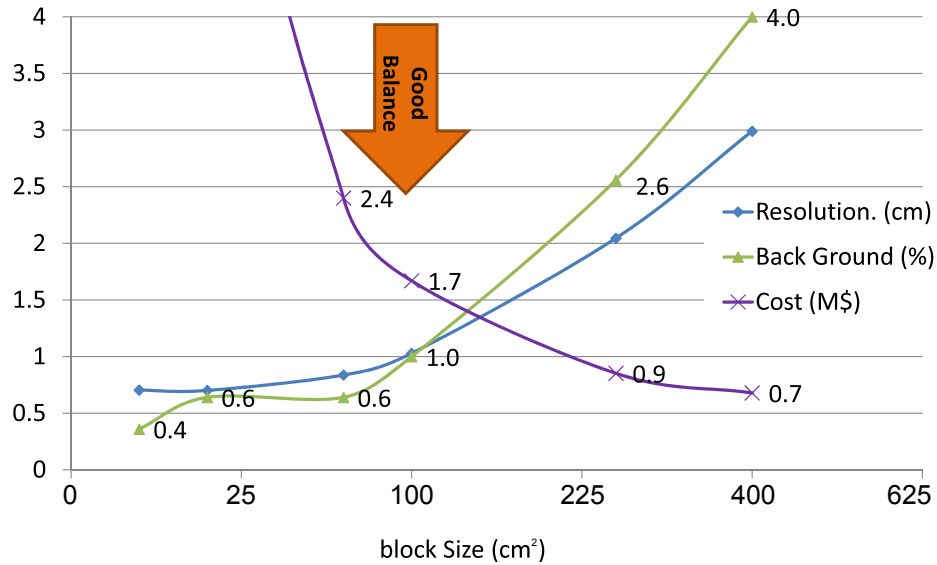


Figure 94: Position resolution and background level from simulation and the cost of the shower detector vs. lateral block size of the module.

### 2470 10.3 Preshower Detector

2471 Segmenting the EC longitudinally into a preshower and a shower part is essential to reaching the re-  
 2472 quired pion rejection. Two designs were considered for the preshower detector: a full Shashlyk-type  
 2473 design that is optically isolated from the shower detector, and a passive radiator/scintillator pad de-  
 2474 sign as used in the HERMES [231] and LHCb [232] experiments. Comparing to a Shashlyk-type  
 2475 preshower, the passive radiator/scintillator pad design has several advantages including increased  
 2476 radiation hardness, simplicity in construction, and fewer WLS fibers to read out. For a passive  
 2477 radiator of  $2X_0$ , the impact on overall energy resolution is less than  $0.5\%/\sqrt{E}$  for electrons with  
 2478 momentum larger than  $2 \text{ GeV}/c$ . Therefore, the passive radiator/scintillator pad design was adopted  
 2479 for the preshower detector. Details of the design are as follows:

- 2480 • The thickness of the preshower radiator was determined by optimizing the overall pion rejec-  
 2481 tion at the desired electron efficiency. As shown in Fig. 95 (top), the preshower-alone pion  
 2482 rejection improves as the radiator thickens up to  $3.5X_0$  due to immediate development of the  
 2483 electromagnetic shower. However, the impact on the overall energy resolution degrades with  
 2484 increased thickness of the absorber. A thickness of  $2X_0$  for the radiator was found to be an  
 2485 optimal choice for the SoLID application.
- 2486 • The scintillator and readout design is similar to that of the LHCb experiment [232]: WLS  
 2487 fibers are embedded in one 2 cm-thick scintillator pad to absorb, re-emit and conduct the  
 2488 photons for readout.

2489 With the above configuration and assuming a response of 100 photoelectrons per MIP (see next  
 2490 paragraph), the relation between pion rejection and electron efficiency for preshower alone can be  
 2491 plotted as a function of scintillator energy cuts, as shown in Fig. 95 (bottom right). One can see a  
 2492 pion rejection of better than 5 : 1 can be achieved at an electron efficiency of  $> 94\%$ .

2493 Figure 96 shows pictures of the LHCb preshower tile (left) compared to a SoLID preshower  
 2494 prototype made by IHEP (right). Preliminary cosmic tests show that we can achieve up to 50 photo-  
 2495 electrons per MIP by embedding two 1.5-m long, 1-mm diameter Kuraray Y11(200)S WLS fibers

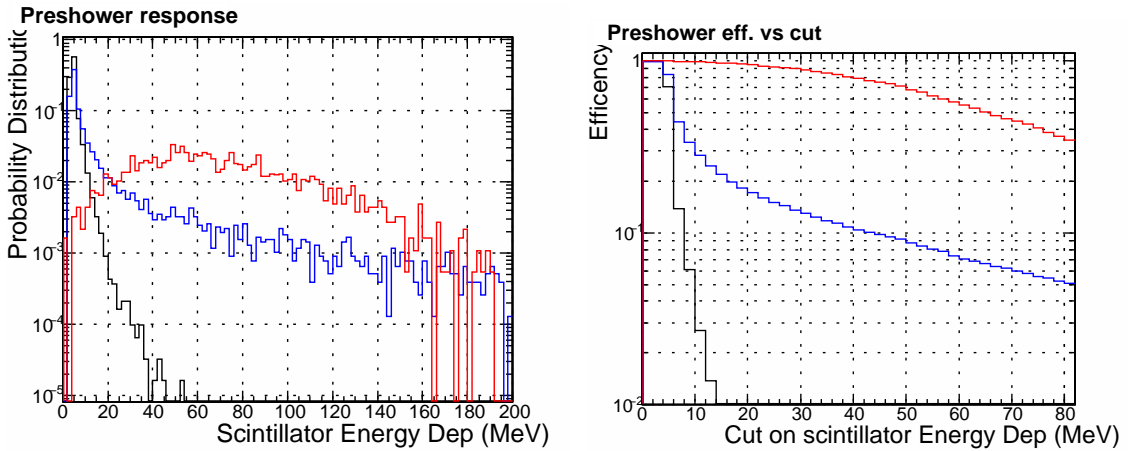
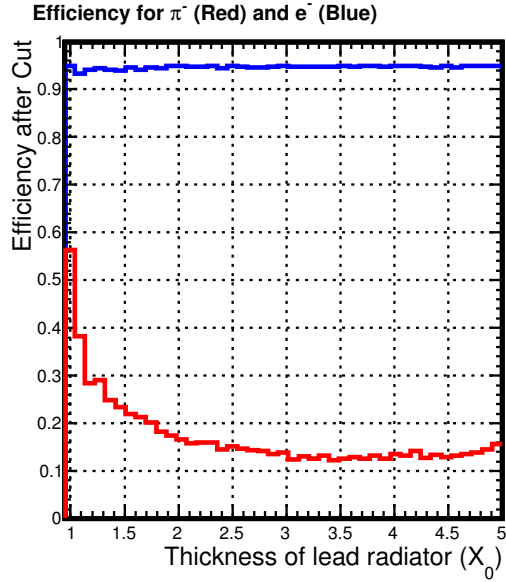


Figure 95: Simulated performance for the preshower detector. Top:  $1/(\pi^-$  rejection) (red curve) at a 95% electron efficiency (blue curve) vs. different thickness of the lead radiator. Bottom: Energy deposition in the scintillator (left) and detector efficiency vs. energy deposition cut (right), for electrons (red),  $\pi^-$  (blue) and  $\mu^-$  (black), for a preshower consisting of  $2X_0$  of lead radiator and 2 cm of scintillator.

2496 in the circular groove on the preshower scintillator. The use of multiple fibers allows minimizing  
 2497 the attenuation due to WLS fiber length. The final number of photoelectrons that reaches the PMT  
 2498 will depend further on loss in the fiber connector and the attenuation in the clear fiber. Current  
 2499 simulation assumes a preshower response of 100 photoelectrons per MIP, and studies of how the  
 2500 number of photoelectrons affects the PID performance are ongoing.



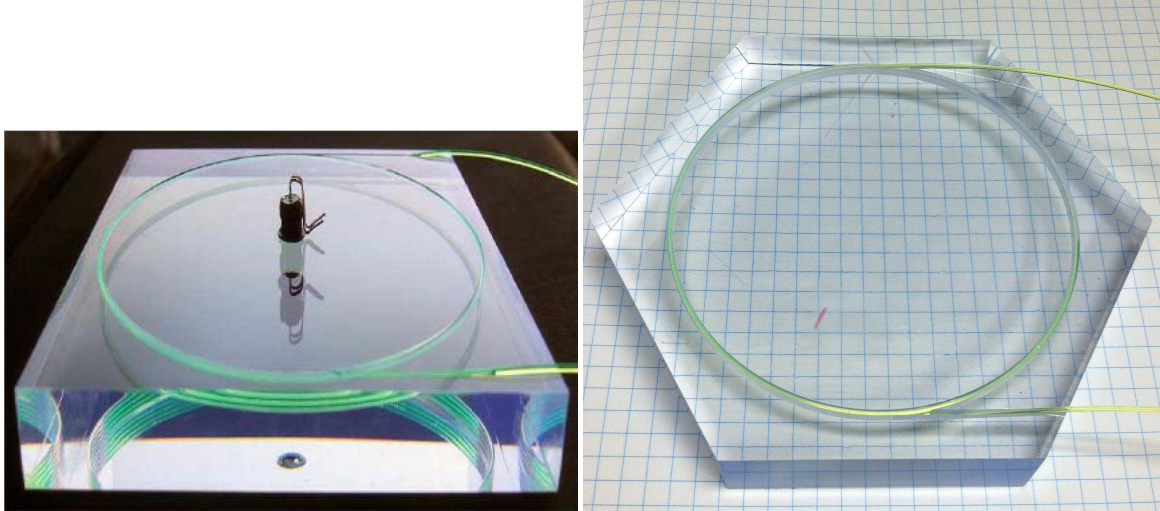


Figure 96: Preshower scintillators. Left: LHCb preshower tile ( $12 \times 12 \times 1.5$  cm) [232]. A single WLS fiber is embedded in a circular groove for 3.5 turns. In the middle of the tile is an LED for testing purposes. Right: SoLID preshower prototype made by IHEP. The SoLID prototype has a geometry of 6.25-cm-side hexagon and is 2 cm thick. Shown here are two 1-mm diameter WLS fibers embedded in a 9-cm diameter circular groove, each 2.5 turns.

#### 2501 10.4 Layout and Support

2502 The total area of the PVDIS EC is slightly larger than that of the SIDIS ECs. The modules will  
 2503 be re-arranged between the two configurations, where modules from the PVDIS FAEC will be split  
 2504 and re-arranged into the SIDIS FAEC and LAEC. The SIDIS EC layout must preserve the 2-fold  
 2505 rotation symmetry in the spectrometer, and it is convenient to have the same symmetry for the  
 2506 PVDIS configuration as well. The design layout that meets these requirements is shown in Fig.97  
 2507 for the PVDIS configuration. The forward angle support system is shared by PVDIS and SIDIS  
 2508 FAEC, and the SIDIS LAEC will have a separate support system.

2509 The scintillator tiles of the preshower modules will be mounted on a aluminum plate that simul-  
 2510 taneously supports also the  $2X_0$  lead. For shower modules, the lead and the scintillator layers in  
 2511 each Shashlyk module are held together by six stainless steel rods penetrating longitudinally through  
 2512 the module. The modules are terminated by two aluminum endplates. The six rods protrude from  
 2513 the endplates and are supported by two aluminum support structures, one 2 cm thick plate between  
 2514 preshower and shower, and one 4 cm thick plate behind the shower. The support structure also holds  
 2515 the optical fiber connectors (see next section).

#### 2516 10.5 Light Readout

2517 For both preshower and shower, the blue light from scintillators is converted into green light by  
 2518 WLS fibers embedded in or penetrating through the modules. Each preshower tile will use two  
 2519 WLS fibers with 1 mm diameter, each fiber arranged for two turns and embedded in a groove on  
 2520 the surface of the tile. The preshower WLS fibers will be routed using the space between preshower  
 2521 and shower to the space between EC and the solenoid wall. Each shower module will use 100  
 2522 1 mm diameter WLS fibers arranged along the direction of the particle trajectory, and the fibers  
 2523 will be guided directly towards the back of EC. To avoid light loss over long distances, WLS fibers  
 2524 will be connected immediately to clear fibers using one-to-one connectors for readout by PMTs.

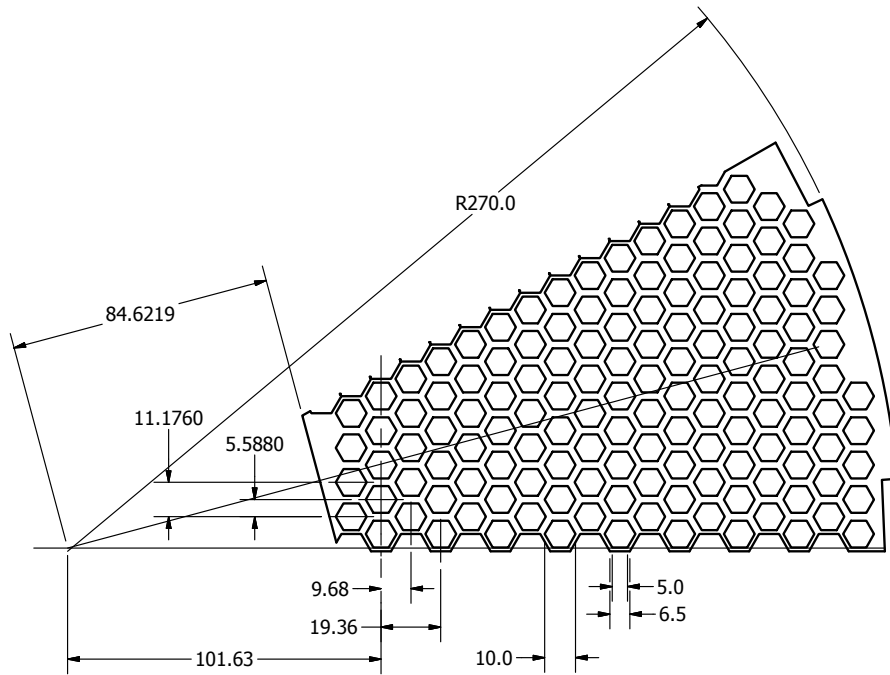


Figure 97: Layout of the hexagon-shaped modules with their support for a 30-degree wedge of the FAEC for the PVDIS configuration. The number of modules is 138 full modules plus 9 half-modules along the horizontal line. If counting 147 modules per 30-degree wedge, the total number of modules needed is 1764. We use 1800 modules for planning purposes at this stage.

2525 LHCb used homemade fiber connectors. For SoLID, homemade connectors is an option but we  
 2526 have tested fiber connectors from the Japanese Fujikura company and found they work well. The  
 2527 Fujikura connectors were used by the Minerva experiment and their tests indicate the light loss in  
 2528 the connector is in an acceptable range of (10-20)% [236].

2529 For the preshower it is essential to achieve a high photoelectron yield such that the best PID  
 2530 performance can be reached. We chose the Kuraray Y11(200) fiber because it has better mechanical  
 2531 properties and further a small minimal bending radius, as shown by the ATLAS Collaboration [235],  
 2532 which is crucial for us because our preshower fiber groove has a bending radius of 4.5cm. Our tests  
 2533 show the Bicon BCF91A fiber has similar light loss to Y11 but the light output is reduced by a factor  
 2534 of two when it is embedded in the preshower groove (compared to nearly zero loss for the Y11). The  
 2535 Y11 fiber has also been tested to higher radiation dose than Bicon BCF91A fibers by ATLAS [237].  
 2536 For shower modules, the fibers are straight and hence the Bicon BCF91A WLS fiber becomes a  
 2537 more economical choice while still satisfying the requirement on radiation hardness. Bicon BCF92  
 2538 fiber has faster decay time but gives less yield than BCF91A, and is not being considered for the  
 2539 SoLID ECs.

2540 The magnetic field reaches about 1.5 T behind the SIDIS LAEC and a few hundred gauss behind  
 2541 both the PVDIS and SIDIS FAECs. For other experiments such as those at JLab Hall D or at LHC,  
 2542 silicon photomultipliers (SiPMs) are used. However, our simulation shows the radiation background  
 2543 behind the calorimeter is at the level of  $10^{13} \text{ cm}^{-2}$  1 MeV equivalent neutrons. Studies done by the  
 2544 LHCb on their tracker upgrade [238] reported cooling the SiPM can overcome the radiation damage  
 2545 from a high neutron background. Still, projecting from the LHCb study tells us for SiPM to work

2546 for the shower detector, we need to cool to  $-70$  or  $-80$  °  $C$ . The space limitation alone imposed  
2547 by the SoLID magnet makes such cooling nearly impossible, let alone the necessary electronics for  
2548 temperature control. Therefore, our current default design is to use PMTs. Long clear fibers (about  
2549 1.5 m for the SIDIS FAEC and 3.5 m for the SIDIS LAEC) will be used to guide the light from the  
2550 WLS fibers to PMTs located outside the solenoid region.

2551 We will use one PMT per shower module to read out the 100 fibers. We plan to design custom  
2552 PMT bases so that preamplifiers with a  $\times(2-5)$  gain can be used and to minimize the aging of the  
2553 PMTs. For preshower modules we plan to use multi-anode PMT (MAPMTs), with all four fiber  
2554 ends from each module read out by one pixel of the MAPMT. For MAPMT, the high background of  
2555 the SoLID running condition constrains us to a relatively low gain in the range of  $5E3-2E4$ , due to  
2556 the fact that the total anode current needs to be kept at only a fraction of the maximum specification  
2557 to reduce the aging of the MAPMT. We plan to design pre-amplifiers with gain up to 50 and 16-  
2558 channel MAPMTs. Pre-R&D of MAPMT and its preamplification board is currently underway.  
2559 Note that LHCb used 64-ch MAPMTs at a gain of  $5E3$  combined with a front-end electronic board  
2560 that provided an intrinsic gain of about 10, and our current design is based on and is consistent with  
2561 the LHCb readout method.

## 2562 **10.6 Radiation Effects**

2563 The ECs for the SoLID spectrometer are designed for high luminosity experiments. The expected  
2564 luminosity and run time are 169 PAC-days at  $10^{39} N \cdot \text{cm}^{-2} \text{s}^{-1}$  in the PVDIS configuration, 245  
2565 PAC-days at  $10^{37} N \cdot \text{cm}^{-2} \text{s}^{-1}$  for the SIDIS experiments and 60 PAC-days for the  $J/\Psi$  experiment.  
2566 In the current design, the maximum radiation dose on the active material — scintillator and WLS  
2567 fibers — in the calorimeter is significantly reduced by the use of the  $2X_0$  lead plate in the preshower,  
2568 and the lead blocks described in section 6 for the PVDIS configuration. Because of the use of lead  
2569 blocks, the PVDIS configuration has been divided into higher and lower photon flux regions; each  
2570 consists of thirty 6-degree azimuthal regions.

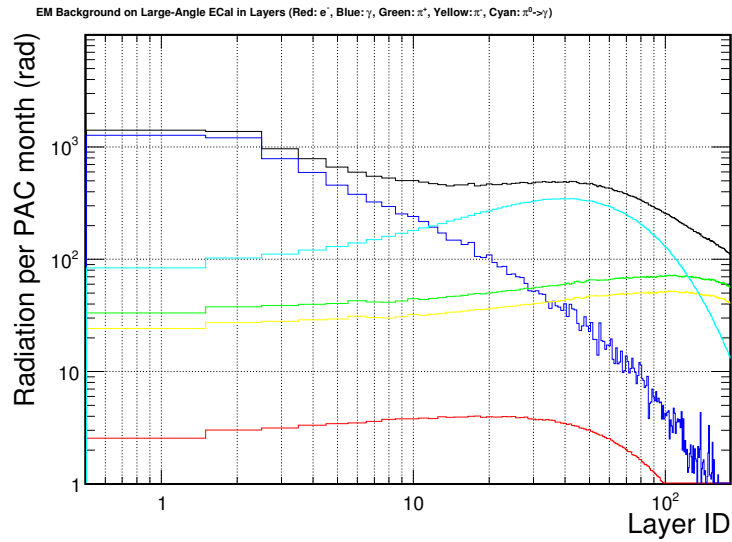
2571 The radiation dose inside the calorimeter was simulated using GEANT4 based simulations con-  
2572 sidering a wide range of energy and species for the background particles. The dose rates for the  
2573 active material (scintillators and fibers) are shown in Figs. 98 and 99. The highest radiation region  
2574 is at the front part of the calorimeter, including the preshower scintillator pad and the front scintil-  
2575 lators of the Shashlyk calorimeter modules. The maximum integrated radiation level for the active  
2576 material reaches 100 kRad for the PVDIS experiment and 20 kRad in the SIDIS and  $J/\Psi$  exper-  
2577 iments, which leads to a total radiation dose of less than 200 kRad for all approved experiments.  
2578 This dose level can be safely handled by the choice of scintillator and WLS fibers.

## 2579 **10.7 Performance**

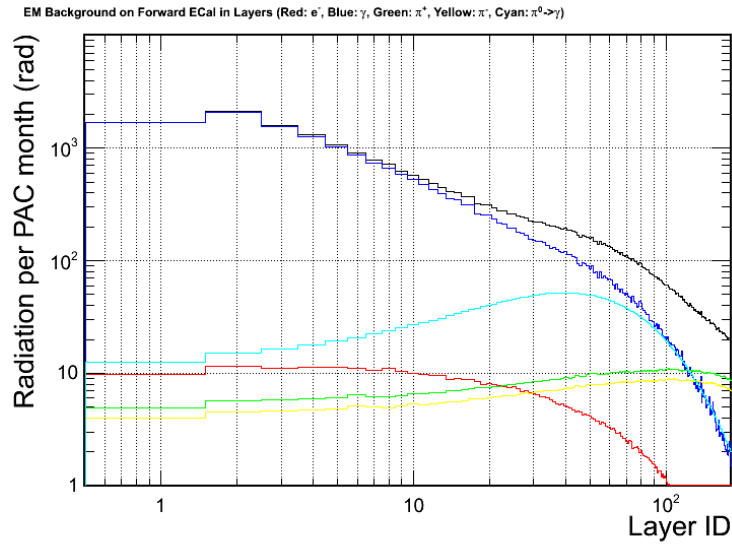
2580 The EC system plays multiple roles in the SoLID spectrometer. Its performance was evaluated in  
2581 the GEANT4 based simulation and discussed in this section, including PID performance, trigger  
2582 capability and shower position resolution. A realistic background simulation was set up to evaluate  
2583 the calorimeter considering a wide range of species and momenta of the background particles.

### 2584 **10.7.1 Intrinsic electron-pion separation**

2585 As a baseline, the PID performance was first evaluated without the background. The primary track  
2586 is propagated through the SoLID magnetic field in GEANT4, then enters the calorimeter. A lo-  
2587 cal cluster which consists of the central calorimeter module and six neighboring hexagon-shaped

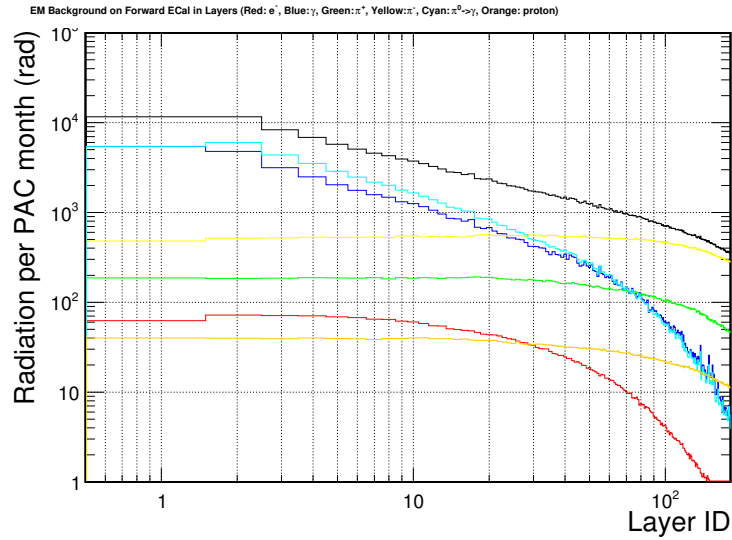


(a) SIDIS large-angle calorimeter

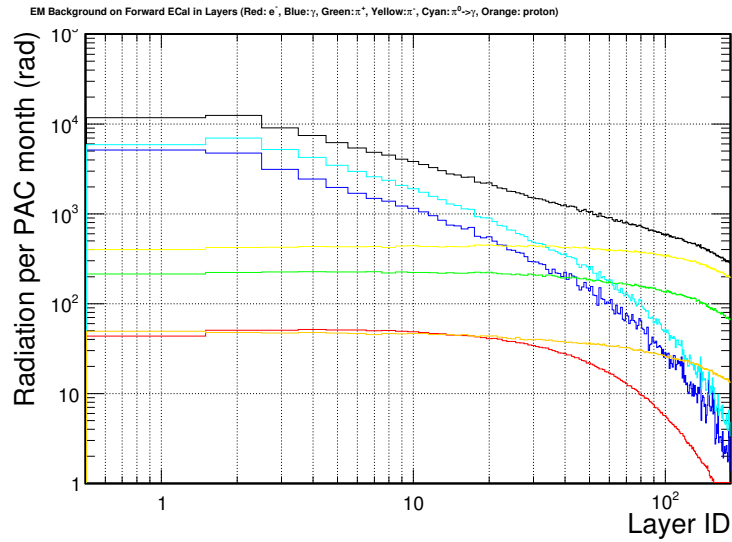


(b) SIDIS forward-angle calorimeter

Figure 98: SIDIS radiation dose rates per PAC month in each layer of the scintillator tiles in the calorimeter. Layer ID 1 is the preshower scintillator. The rest of IDs are assigned for each scintillator layer in the Shashlyk calorimeter in the order of increasing  $z$ . The color code stands for different contributions of various particle species at the front surface of the preshower: electrons (red), photons (blue), EM total (magenta),  $\pi^+$  (green),  $\pi^-$  (yellow). The overall dose is shown by the black curve.



(a) PVDIS calorimeter in higher-photon flux region



(b) PVDIS calorimeter in lower-photon flux region

Figure 99: PVDIS radiation dose rates per PAC month in each layer of the scintillator tiles in the calorimeter. Layer ID 1 is the preshower scintillator. The rest of IDs are assigned for each scintillator layer in the Shashlyk calorimeter in the order of increasing  $z$ . The color code stands for different contributions of various particle species at the front surface of the preshower: electrons (red), photons (blue), EM total (magenta),  $\pi^+$  (green),  $\pi^-$  (yellow), and protons (brown). The overall dose is shown by the black curve.

2588 modules is formed. With a multidimensional cut of the preshower and shower response within the  
 2589 cluster (see Sec. 10.7.5), the overall pion rejection averaged over the acceptance of each calorimeter  
 2590 is shown in Fig. 100. A 100 : 1 pion rejection at 95% electron efficiency is achieved for momentum  
 2591 bins of  $p > 2 \text{ GeV}/c$ . For the lowest momentum bin  $1 < p < 2 \text{ GeV}/c$ , which is only needed for  
 2592 the SIDIS FAEC, a better than 50 : 1 pion rejection at 90% electron efficiency is obtained.

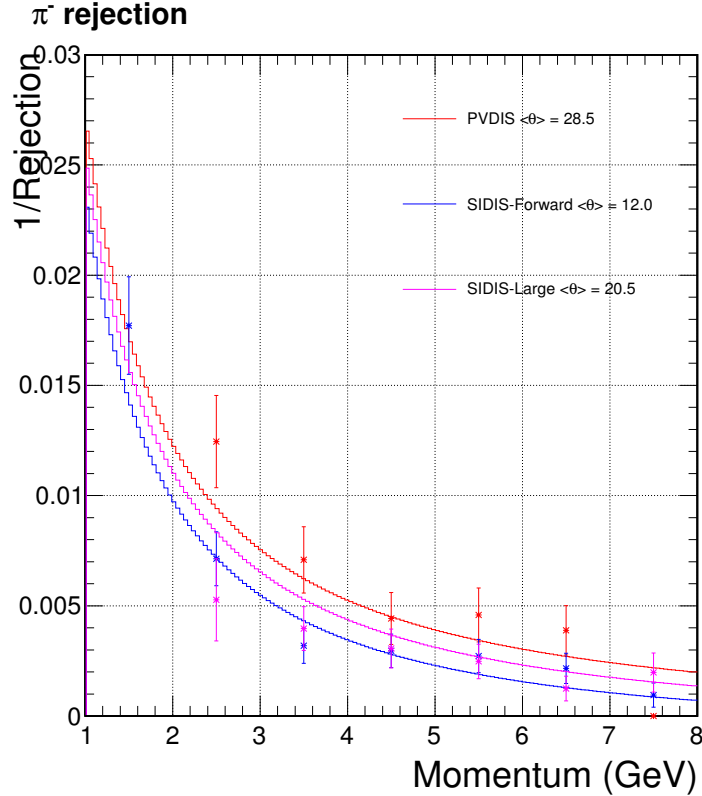


Figure 100: SoLID EC intrinsic (without background)  $\pi^-$  efficiency (1/rejection). From top to bottom: PVDIS with average track polar angle  $\langle\theta\rangle = 28.5^\circ$  (red), SIDIS LAEC with  $\langle\theta\rangle = 20.5^\circ$  (magenta) and SIDIS FAEC with  $\langle\theta\rangle = 12.0^\circ$  (blue). A constant 95% electron detector efficiency is maintained for  $p > 2 \text{ GeV}/c$ . A 90% electron efficiency is maintained for the lowest momentum bin  $1 < p < 2 \text{ GeV}/c$ , which is only required for the SIDIS FAEC. The  $\langle\theta\rangle$  value is different for the three calorimeter configurations, which leads to slight differences in the pion rejection curves.

### 2593 10.7.2 PID performance under realistic background simulation

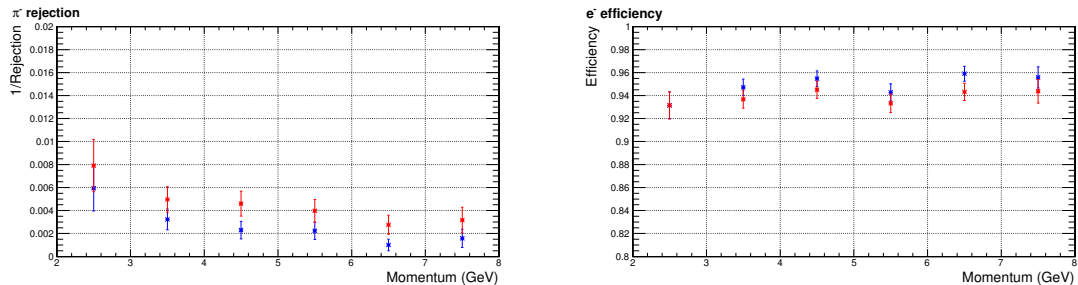
2594 For a large intensity device, background particles and their influence on the calorimeter perfor-  
 2595 mance have to be considered. A full background simulation was implemented to study calorimeter  
 2596 performance. The background simulation procedure is as follows:

- 2597 1. Particles are generated at the target including photons and electrons from the low energy  
 2598 EM processes (based on physics in GEANT4), DIS electrons (based on CTEQ6 PDF), and  
 2599 hadrons (based on the Wiser fit);

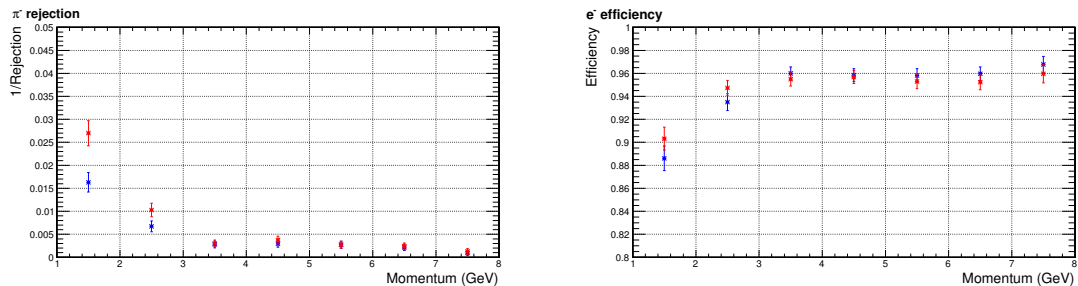


- 2600 2. Particles are propagated through a SoLID GEANT4 simulation to the front surface of the  
 2601 calorimeter;
- 2602 3. The EC response is simulated for a wide range of background particles — electrons, photons,  
 2603 pions, and protons — within the momentum range  $10 \text{ keV} < p < 11 \text{ GeV}$ . A statistical model  
 2604 is used for the correlation between preshower and shower responses;
- 2605 4. The background contribution to each event is produced by combining the background rate  
 2606 at the EC front surface and the EC response described above for a region of interest on the  
 2607 calorimeter, usually defined by a radius-azimuthal angular bin. A conservative 30 ns coinci-  
 2608 dence window between background particles and the primary event is assumed.
- 2609 5. The background contribution is embedded into the raw signal from the simulated primary  
 2610 particles (high energy electrons and pions). The background-embedded data are then analyzed  
 2611 as raw ADC signals. The energy response is calibrated and PID and trigger performance are  
 2612 analyzed.

2613 Typically, background rate is the highest in the inner radius region and drops by approximately  
 2614 one order of magnitude in the outer radius region. Figure 101 shows the EC performance for the  
 2615 SIDIS configuration in the inner radius region. For SIDIS experiments, effects from background  
 2616 particles are visible but not significant: for large-angle EC, the pion rejection remains better than  
 2617 100:1 for all momentum bins; for forward-angle EC, there is no noticeable change in the PID per-  
 2618 formance other than for the lowest momentum bin  $1 < p < 2 \text{ GeV}/c$  where the pion rejection is a  
 2619 half of the no-background case. However, the Cherenkov detector provides high PID performance  
 2620 in the low momentum range and the overall pion rejection is sufficient for the experiment.



(a) SIDIS large-angle calorimeter



(b) SIDIS forward calorimeter

Figure 101: Calorimeter pion and electron efficiency without (blue) and with (red) the consideration of background particles for the inner radius region (highest background) for the SIDIS configuration.

2621 In the PVDIS configuration, the background rate is significantly higher and the performance  
 2622 is affected. The 30-fold structure of the baffle system for the PVDIS experiment causes the back-  
 2623 ground to alternate between high- and low-rate 30 times in the azimuthal direction. Therefore,  
 2624 calorimeter performance is studied for the high- and the low-rate “slices” separately, with each  
 2625 fan-shaped slice covering 6 degrees. Background structure for the inner-radius, high-rate slice is  
 2626 shown in Fig. 102. The PID performance with the background is evaluated for different radius, see  
 2627 Fig. 103. Comparing to the intrinsic performance of Fig. 100, the pion rejection is up to 8 times  
 2628 worse: the pion rejection varies from 25–50 at  $p = 2.5$  GeV/ $c$  to 50–100 at  $p = 6$  GeV/ $c$ , while  
 2629 keeping the electron efficiency to be in the range (90–95)%. Particle identification for the experi-  
 2630 ment will need to rely on a full-waveform analysis of the EC, combined with information from the  
 2631 Cherenkov detector.

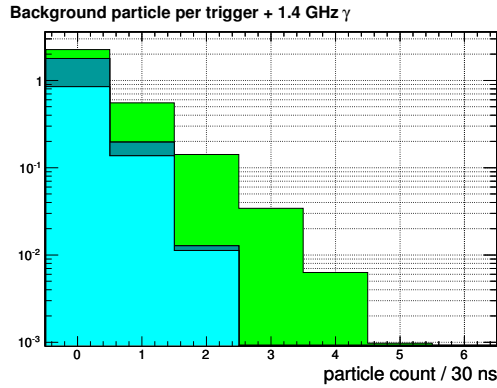
### 2632 10.7.3 Trigger capability

2633 Trigger capability is an important function of the EC. The calorimeter shower energy deposition  
 2634 in all combinations of local 6+1 clusters (central block plus six neighboring hexagon blocks) is  
 2635 first summed after digitization, forming local shower sums. Triggers are then formed by passing  
 2636 the local shower sums through a threshold cut. Electron triggers are formed with a targeted electron  
 2637 threshold, and the efficiency curves for both pions and electrons are studied with the full-background  
 2638 simulation. The following triggering specifications have been studied:

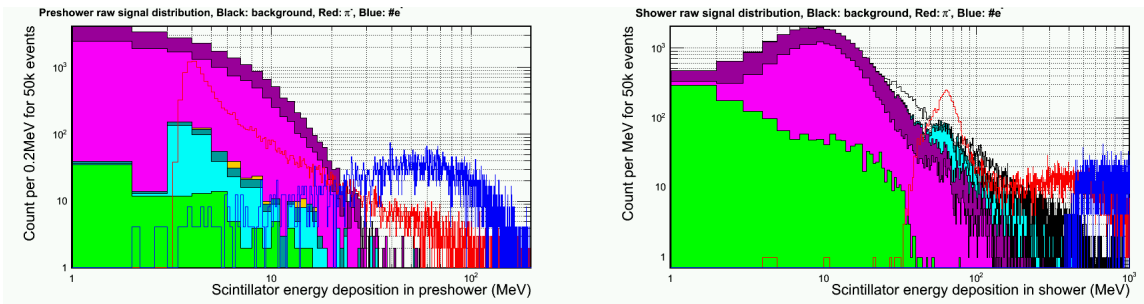
- 2639 • SIDIS large angle calorimeter: electron triggers of 3 GeV are formed by cutting on local  
 2640 shower sum larger than 2.6 GeV. The trigger turn-on curve is shown in Fig. 104. High elec-  
 2641 tron efficiency is observed for electrons above the threshold. The rejection on few-GeV pion  
 2642 background is high, in the range (20-100):1, which satisfies requirement of the SIDIS experi-  
 2643 ments.
- 2644 • SIDIS forward calorimeter: position dependent electron triggers provide high trigger effi-  
 2645 ciency for electrons of  $Q^2 > 1 \text{ GeV}^2$ . The pion rejections with 1 GeV threshold is shown on  
 2646 the left plot of Fig. 105. With higher thresholds, pion rejections are better.
- 2647 • SIDIS forward calorimeter: MIP triggers allow the calorimeter to trigger on hadrons for the  
 2648 SIDIS measurement. The threshold is determined by MIP peak - two sigma of the Landau  
 2649 fit of the distribution, which lead to a calibrated local shower sum energy of 220 MeV. The  
 2650 trigger efficiency for pions is high, as shown on the right plot of Fig. 105.
- 2651 • PVDIS forward calorimeter: electron triggers are formed with radius-dependent trigger thresh-  
 2652 olds. As shown in Fig. 106, the targeted electron threshold varies from 1.5 GeV at outer radius  
 2653 to 3.8 GeV at inner radius on the calorimeter, which produces high trigger efficiency for DIS  
 2654 electrons with  $x > 0.35$ . The trigger turn-on curves are evaluated for several regions on the  
 2655 calorimeter as shown in Fig. 106. The efficiency for both electrons and pions are lower for  
 2656 inner radius regions due to the use of high thresholds for background-suppression. Overall  
 2657 the pion rejection at the trigger level is  $> 2$  and varies with the radius.

2658 The PVDIS experiment will run with a luminosity up to  $10^{39} \text{ cm}^{-2}\text{s}^{-1}$ . A baffle system is  
 2659 used to reduce the very high background rate expected at this luminosity. To further reduce the rate  
 2660 from high energy photons from neutron pions and low energy backgrounds, fan-shape lead blocks,  
 2661 each covering 2.5 degrees azimuthally, will be placed in front of the EC. The trigger of PVDIS will  
 2662 be formed by taking the coincidence between the EC and the gas Cherenkov detector. Estimation

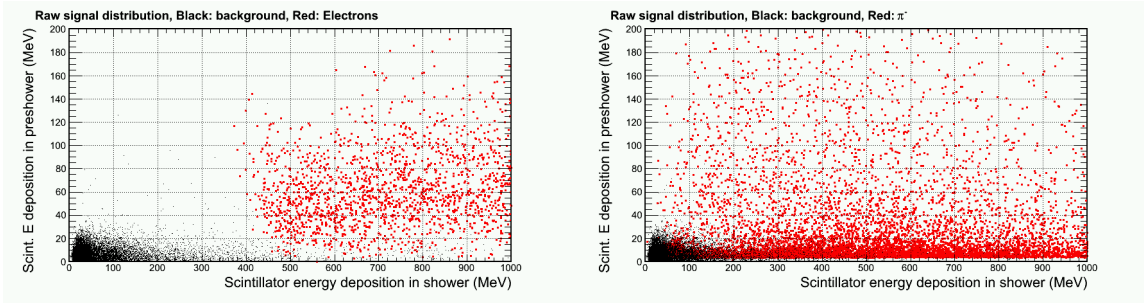




(a) Stacked probability to find the number of background  $\pi^-$  (light blue),  $\pi^+$  (dark blue) and electrons (green) at the front of the preshower. The photon rate is as high as  $\sim 1.4$  GHz, thus the photon count is off-scale and not shown in this figure.

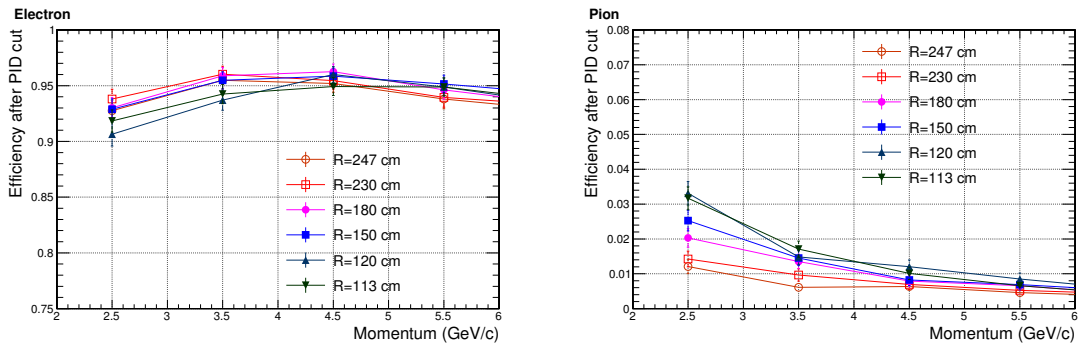


(b) Stacked probability (count per 50k events) vs. Preshower (left) and Shower (right) scintillator energy deposition for incoming background electrons (green),  $\pi^-$  (light blue),  $\pi^+$  (dark blue), protons (yellow), EM process-originated photons (magenta) and  $\pi^0$ -originated photons (dark magenta). For comparisons, energy deposition for high energy pion (red) and electrons (blue) are shown as non-filled curves.

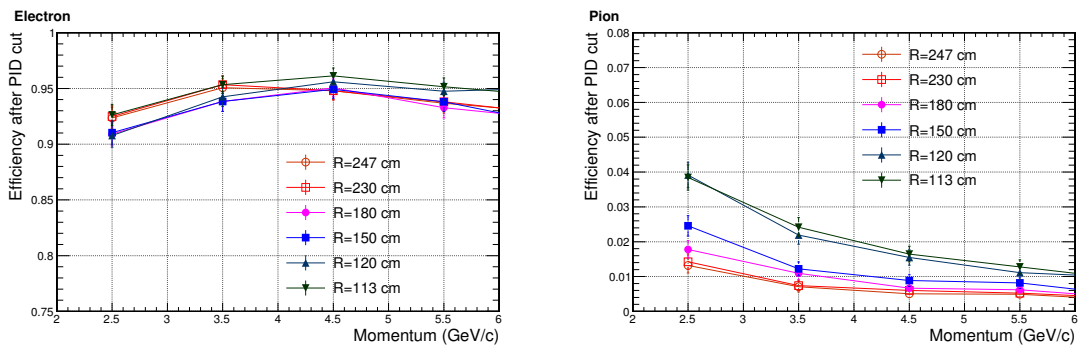


(c) Preshower-shower scintillator energy correlation for background particles (black), compared with high energy electrons (left, red) and pions (right, red)

Figure 102: Background distribution for the PVDIS forward calorimeter at the production luminosity of a liquid deuteron target. Background for the inner radius ( $R \sim 1.2$  m) and higher-radiation azimuthal region is shown. The energy deposition originated from background is compatible to that of high energy pions.

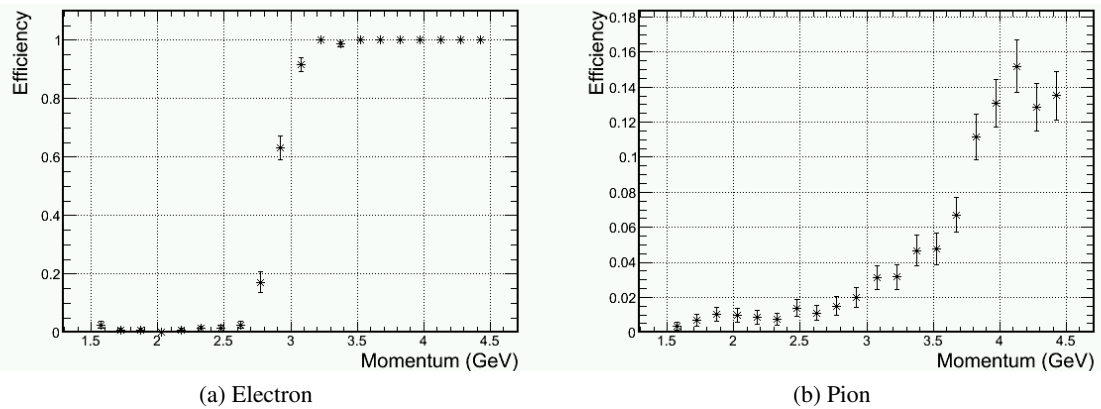


(a) lower-radiation azimuthal region



(b) higher-radiation azimuthal region

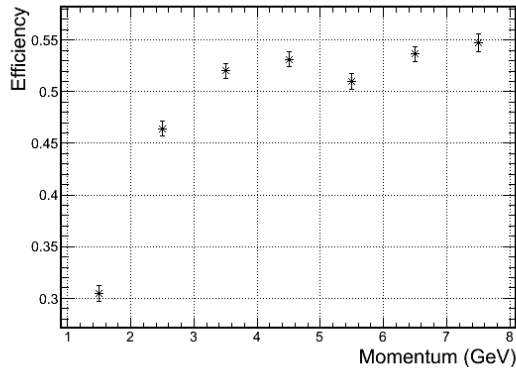
Figure 103: Calorimeter pion and electron efficiency for the PVDIS experiment, evaluated with the presence of background at eight typical regions on the calorimeter.



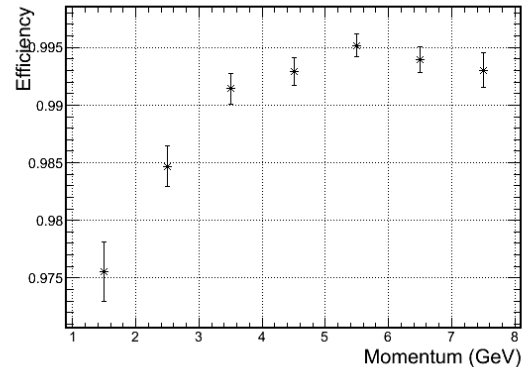
(a) Electron

(b) Pion

Figure 104: Trigger efficiency for electrons (a) and pions (b) for the SIDIS large angle calorimeter. The target trigger threshold is approximately  $P_e = 3 \text{ GeV}/c$ . Only the (high-background) inner-radius region is shown here.

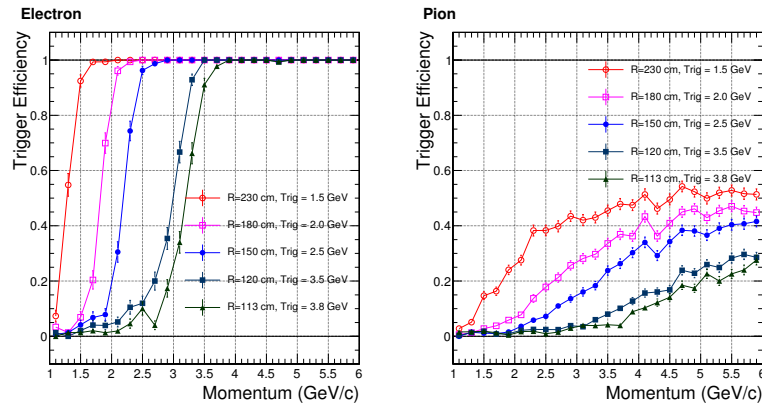


(a) Pion efficiency in electron trigger with a target trigger threshold of ( $P_e = 1 \text{ GeV}/c$ )

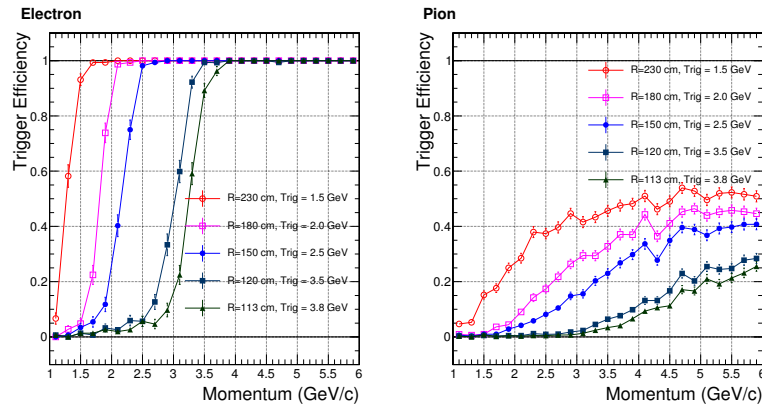


(b) Pion efficiency in the MIP trigger

Figure 105: Trigger efficiency for pions in the SIDIS forward calorimeter for electron triggers (a) and MIP triggers (b). Only the (high-background) inner-radius region is shown here.



(a) Higher-radiation azimuthal region



(b) Lower-radiation azimuthal region

Figure 106: Trigger efficiency curves for the PVDIS configuration.

2663 of the trigger rate from EC can be performed using the realistic background simulation (described  
 2664 previously in Section 10.7.2) combined with EC trigger capability results described above. The  
 2665 EC trigger rate will then be combined with gas Cherenkov trigger rate to obtain the expected DAQ  
 2666 trigger rates and to make sure they can be handled by the DAQ system. For SIDIS experiments  
 2667 on  ${}^3\text{He}$ , the luminosity will be up to  $3 \times 10^{36} \text{ cm}^{-2}\text{s}^{-1}$  on  ${}^3\text{He}$  target and additional about  $3.7 \times$   
 2668  $10^{36} \text{ cm}^{-2}\text{s}^{-1}$  on target glass windows. Target collimators (described previously in Section 10.7.2)  
 2669 will be used to reduce backgrounds from the glass windows. The SIDIS triggers are formed from  
 2670 EC in combination with Cherenkov, MRPC and SPD. The FAEC will also provide MIP trigger for  
 2671 hadron detection. Trigger rate estimation for SIDIS is carried out similar to the PVDIS case. Results  
 2672 for both PVDIS and SIDIS trigger rates will be presented in Section 14.

#### 2673 10.7.4 Shower Position Measurement

2674 Position resolution of the shower center was studied for different lateral sizes of the calorimeter  
 2675 modules, as shown in Fig. 107. The radial resolution is in general worse than the azimuthal resolu-  
 2676 tion because the tracks are not perpendicular to the radial direction. As can be seen from Fig. 107,  
 2677 with the use of proper algorithm, a position resolution of better than 1 cm is achieved for both  
 2678 directions at the designed lateral granularity of  $100 \text{ cm}^2$ .

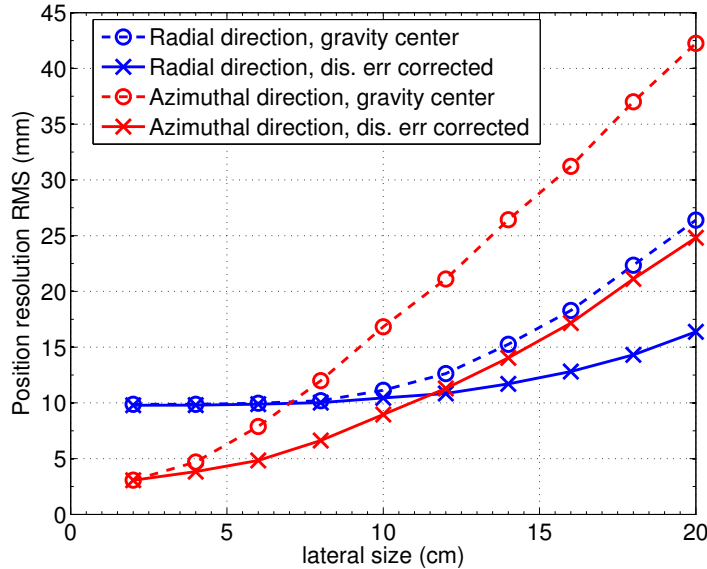


Figure 107: Position resolution for electron showers vs. different lateral size of the calorimeter module. Both azimuthal (red) and radial (blue) resolutions are shown, with the shower center calculated from a simple energy-weighted geometrical center (dashed curves), and those calculated with further corrections using the energy deposition distribution among neighboring modules (solid curves).

#### 2679 10.7.5 Supplemental Information: PID Selection Cuts

2680 A three dimensional PID cut was used to select the best electron samples with maximal  $\pi^-$  rejection  
 2681 as illustrated in Fig. 108. For each given momentum bin, the cut on  $E/P$  and preshower energy  
 2682 roughly follows the contour lines of the ratio of  $\pi^-$  efficiency to  $e^-$  efficiency, which is the optimal

2683 cut for the  $\pi^-/e^-$  separation. A momentum dependence is then introduced to the cut to maintain a  
 2684 constant 95% electron efficiency for most of the bins. Events passing the cut are highlighted in red  
 2685 in the plots.

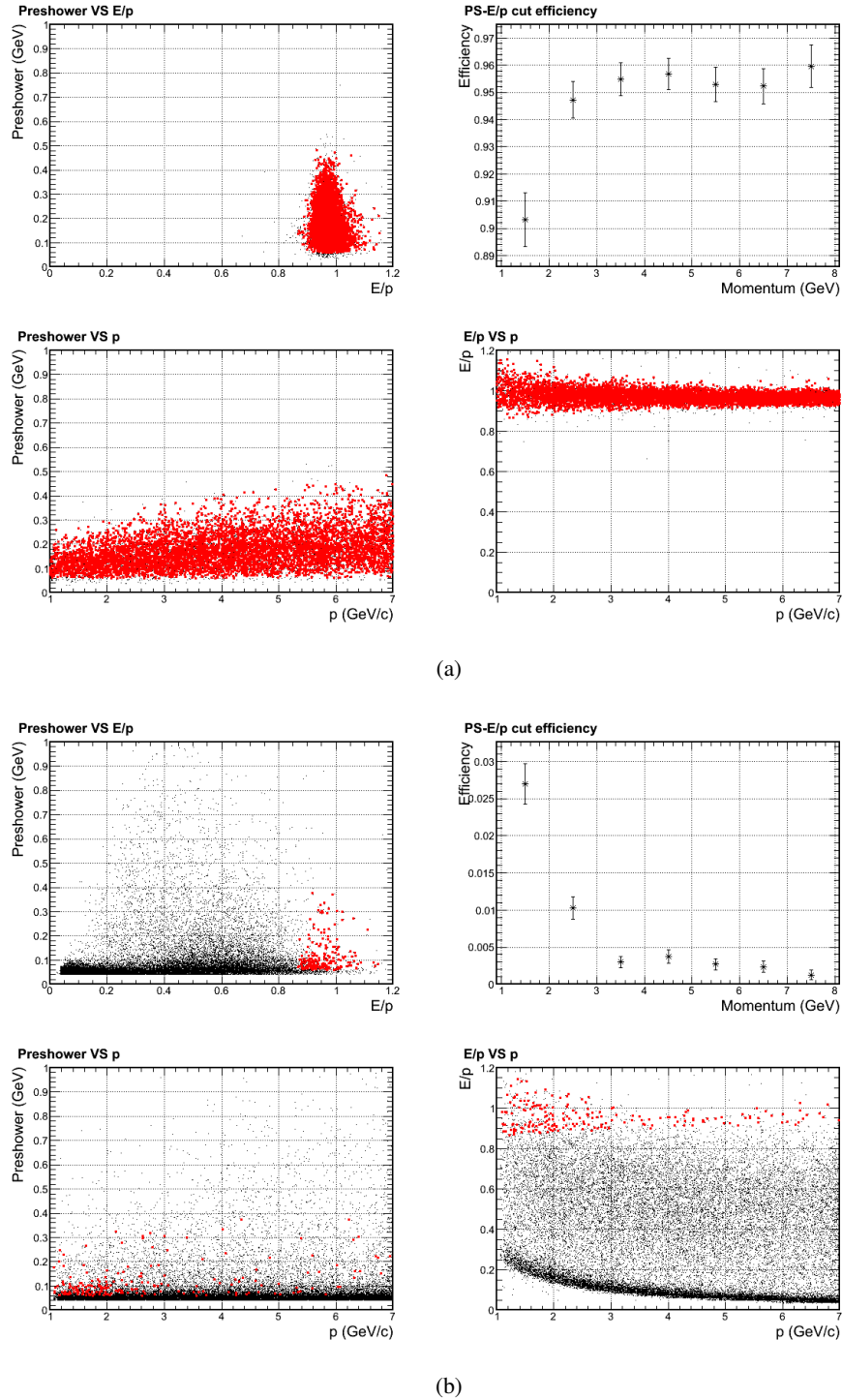


Figure 108: Illustration of electron sample cuts as highlighted in red dots, in comparison to simulated electron (a) and  $\pi^-$  (b) samples. The SIDIS forward calorimeter in the high background (small radius) region is studied in these plots.

## 2686 10.8 Scintillator Pad Detector for SIDIS Experiments

2687 The main purpose of the scintillator pad detector (SPD) is to reduce calorimeter-based trigger rates  
2688 for high-energy charged particles (see Section 10.7.3 for calorimeter trigger capability) by rejecting  
2689 photons through the coincidence between the SPD and the calorimeter. Two SPDs will be used: one  
2690 in the forward direction between the heavy gas Cherenkov detector and the MRPC, and the other  
2691 in the large-angle direction immediately before the large-angle calorimeter. Both SPDs consist of  
2692 fan-shaped scintillator pads arranged perpendicular to the beam direction. The LASPD will also  
2693 provide time-of-flight for particle identification with a timing resolution goal of 150 ps.

2694 The performance for the scintillator was studied in the GEANT4 simulation. For FASPD, we  
2695 plan to use 5 mm thickness scintillators based on a balance between the light yield and the radiation  
2696 length. The 5-mm thickness corresponds to a radiation length of  $\approx 0.013X_0$  which directly affect  
2697 the photon conversion rate. Typical responses of the FASPD to photons and charged particles are  
2698 shown in Fig. 109. Approximately 20% of the photon background leave energy in the scintillator  
2699 due to back splashing from the calorimeter front face. The trigger threshold was set at two standard  
deviations below the MIP peak to ensure a high efficiency for charged particles. Pile up effects

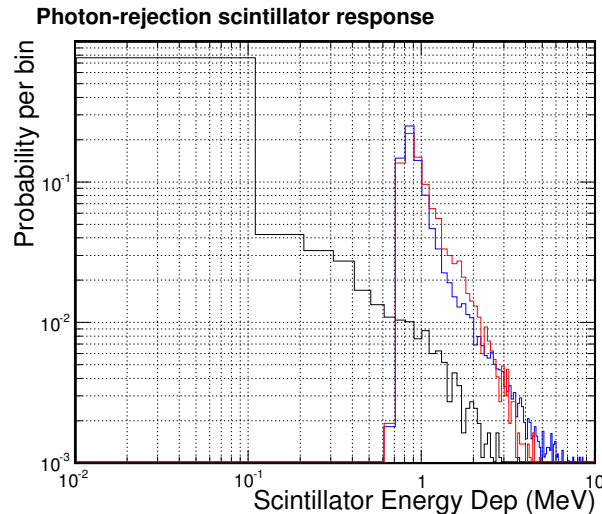


Figure 109: Typical probability for scintillator energy depositions in the SPD, for electron (blue), pion (red) and high energy photons (black).

2700 were studied for fixed ADC timing windows of 30 and 50 ns. The photon rejection depends not  
2701 only on the trigger rate per scintillator, but also the scintillator segmentation, see Fig. 110. In  
2702 addition, photons attenuates significantly in long scintillators and thus the length of the individual  
2703 segmentation needs to be minimized. The segmentation of FASPD is chosen to be 240 based on  
2704 Fig. 110 and a desired 5:1 photon rejection at the large angle, and is further divided into 60 in  
2705 the azimuthal direction and 4 in the radial direction. The readout of FASPD is by using WLS  
2706 fibers embedded on the surface of the scintillator, then connected to clear fibers and are readout by  
2707 MAPMTs. This is similar to the preshower. Because the threshold is below MIP and is much lower  
2708 than for preshower, a higher combined gain of PMT and the preamplifier is needed. We currently  
2709 plan to use preamplifiers with gain  $\approx 50$  because it's the maximum comfortable gain that can be  
2710 achieved on a pre-amplifier board. This will allow us to place the threshold around 20 mV, the  
2711 minimal threshold that is above the noise level.  
2712

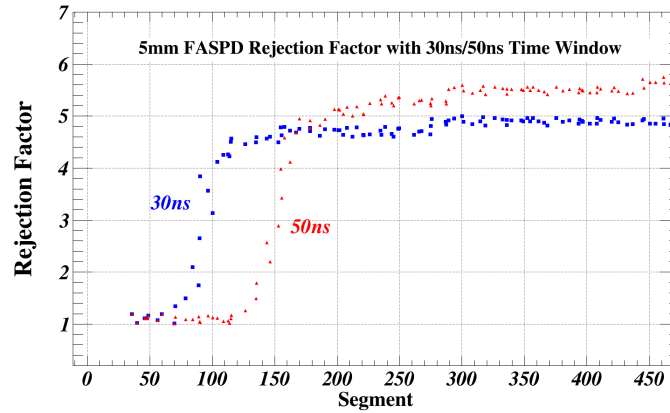


Figure 110: Photon rejection factor for 5-mm thick FASPD as a function of the segmentation, for DAQ windows of 30ns (blue) and 50ns (red), respectively. For the 30-ns timing window, a 240 segmentation is appropriate to reach a photon rejection of 5:1.

2713 For the LASPD, a 10:1 photon rejection is desired to bring the photon-induced calorimeter trig-  
 2714 ger rate down to below the electron-induced rate. Figure 111 shows the simulated photon rejection  
 2715 factor vs. segmentation. The 10:1 rejection can be achieved by 60 azimuthal segments. Because  
 2716 the radial coverage of the LASPD is small and because of the requirement of high photoelectron  
 2717 statistics to reach the TOF requirement, the LASPD has only azimuthal segmentation, with each  
 2718 covering 6 degrees. For readout, the use of WLS fiber is impossible, again because of high pho-  
 2719 toelectron statistics. We plan to use field-resistant fine-mesh PMTs on the outer radial edge of the  
 2720 LASPD to readout the scintillating light.

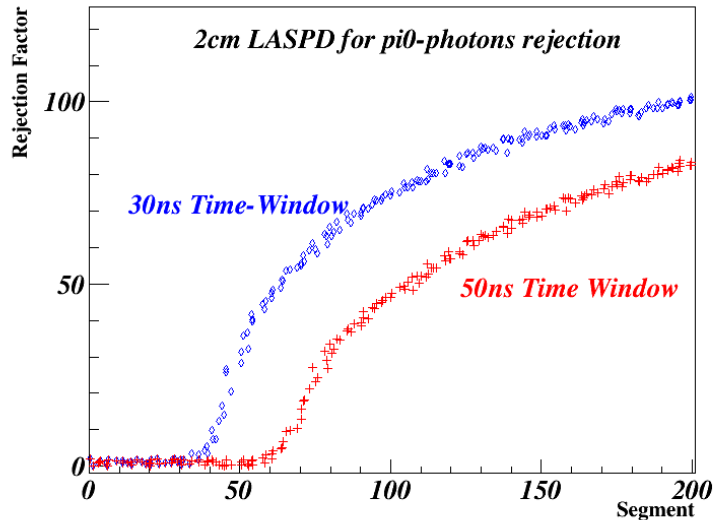


Figure 111: Photon rejection factor for 20-mm thick LASPD as a function of the segmentation, for DAQ windows of 30ns (blue) and 50ns (red), respectively. For the 30-ns timing window, a 60 segmentation is appropriate to reach a photon rejection above 10:1.



## 2721 **10.9 EC Collaboration Status and Construction Outlook**

2722 The shashlyk sampling technique adopted by SoLID EC has been used by many experiments, in-  
2723 cluding LHCb, ALICE and ATLAS at the LHC. The LHC/CMS experiment's calorimeter upgrade  
2724 will use a similar technique. In the R&D for SoLID EC, we studied extensively the calorimeter  
2725 design and technical details from these experiments. We also learned many useful facts from other  
2726 experiments and/or collaborations, including for example Minerva, MINOS, and JLab Hall D.

2727 Our general design for the SPD, the preshower, and the shashlyk shower modules is based heav-  
2728 ily on the LHCb's SPD and ECal design. The LHCb and other LHC experiment's detector TDR  
2729 and associated technical notes provide tremendous knowledge. This includes: readout design for  
2730 the preshower and the SPD (WLS fiber embedding in grooves on the scintillator surface and the  
2731 use of MAPMTs) (LHCb); wrapping of the scintillator (LHCb, ATLAS), relative light yield be-  
2732 tween different scintillator material and WLS fiber types (LHCb); the use of optical grease or glue  
2733 (LHCb); side treatment and painting of shashlyk modules (LHCb); adding mirror ends to WLS  
2734 fiber (LHCb); coupling between WLS fiber and MAPMTs (LHCb); Tests of light yield uniformity  
2735 (LHCb); radiation hardness of the preshower and shashlyk modules (LHCb ECal and HCal) and  
2736 plastic scintillating fibers (LHCb tracker upgrade, JLab Hall D GlueX barrel EMCAL); LED moni-  
2737 toring system (LHCb); WLS fiber bending light loss (simulation by LHCb; direct data from ATLAS  
2738 Tile ECal TDR); performance of SiPM under high neutron radiation background (mainly LHCb  
2739 tracker upgrade, but also JLab Hall D and CMS); EC commissioning and calibration procedure  
2740 (LHCb ECal and HCal); tolerance/quality control for the scintillators and fibers (LHCb).

2741 Once prototype modules are constructed, the light yield can be compared with that of LHCb,  
2742 ALICE, KOPIO, PHENIX, COMPASS, and COMPASS-II.

2743 Shashlyk-type calorimeter modules used by most previous experiments were produced by the  
2744 Russian IHEP group. For some experiments, the scintillators of shashlyk modules were produced  
2745 at Russian IHEP, and the modules were assembled elsewhere. For example, Wayne State Univer-  
2746 sity (WSU) and China Central Normal University (CCNU) both assembled modules for the ALICE  
2747 experiment (for CCNU, threading WLS fiber was done in Italy, separately from the initial assem-  
2748 bling). The collaboration contacted the WSU group about their equipment used for ALICE module  
2749 assembly, but unfortunately their assembly lab was dismantled a long time ago and most equipment  
2750 could not be recovered. We are also in contact with the U. of Iowa group (Prof. Onel) who is par-  
2751 ticipating in the CMS ECal upgrade, but the CMS Ecal utilizes crystal layers and is very different  
2752 from SoLID EC in the choice of material and the construction process.

2753 Overall, the collaboration could not gain substantial help from groups previously involved in  
2754 Shashlyk production and assembly, and complete production by the Russian IHEP group can be  
2755 sensitive to fluctuations in international relationship and economics. Given this status, currently the  
2756 collaboration is pursuing the possibility of manufacturing scintillators and assembling the Shashlyk  
2757 modules in China. Two groups, Shandong University (SDU) and Tsinghua University (THU), are  
2758 participating in the SoLID EC R&D, and they have developed local contact with the CCNU group  
2759 to learn their experience in module assembly. The SDU group has extensive experience with scin-  
2760 tillator production in China and cosmic ray testing of the scintillator's light yield, and is in a good  
2761 position to lead the prototype R&D for SoLID EC. If all Shashlyk modules are produced and pass  
2762 the initial cosmic-ray testing in China, they will be shipped to the US. Upon arrival the modules can  
2763 be sample-tested at JLab before installation. Construction of the preshower modules can be done in  
2764 the same manner.

2765 The scintillator pad detectors are planned to be manufactured in the US (Eljen) because their su-  
2766 perior scintillator quality can meet the high light yield requirement of SoLID. A total of 60 LASPD  
2767 and 240 FASPD modules will be assembled and cosmic-tested at the University of Virginia.



2768 **10.10 EC with Baseline and Enhanced Baseline Configurations**

2769 As described in earlier sections, the Shower part of the EC will be made of Shashlyk modules, each  
2770 with a  $100\text{ cm}^2$  lateral size in a hexagonal shape. Ideally each Shashlyk module is read out by one  
2771 PMT. In this section we present two configurations: (1) in the baseline configuration, three Shashlyk  
2772 modules will be grouped together into one single PMT and require one subsequent readout channel;  
2773 (2) in the enhanced baseline configuration, the shashlyk model be readout by one PMT per module.  
2774

2775 For baseline configuration, our EC trigger design will combine three readout channels from  
2776 nine modules as shown in the left panel of Figure 112. The area is large enough to cover the entire  
2777 EM shower when high energy electrons enter the modules, but not too large to have unnecessary  
2778 background. This will help us achieve excellent electron efficiency and good pion suppression to  
2779 maintain a trigger rate below the DAQ limit for our designed full luminosity. The offline analysis  
2780 can adjust the number and pattern of readout channels to maximize the electron detection efficiency  
2781 and energy resolution. When changing to the enhanced baseline configuration, we will connect one  
2782 shower module to one readout channel and thus triple the number of readout channels. The EC  
2783 trigger design will use seven readout channels from seven modules as shown in the right panel of  
2784 Figure 112. This will reduce the background by about 22% while keeping most EM shower energy  
2785 for better matching of its Moliere radius, and thus will achieve even better trigger efficiency. Our  
2786 studies for the SIDIS setup indicate that we can lower our trigger threshold for the large angle EC  
2787 from 3.4 GeV to 3 GeV while keeping the same electron detection efficiency and total trigger rate.  
2788 The increased number of readout channels will also improve EC position resolution to its best level  
2789 at about 1 cm, which is important for neutral particle detection possibly needed by future physics  
2790 programs.

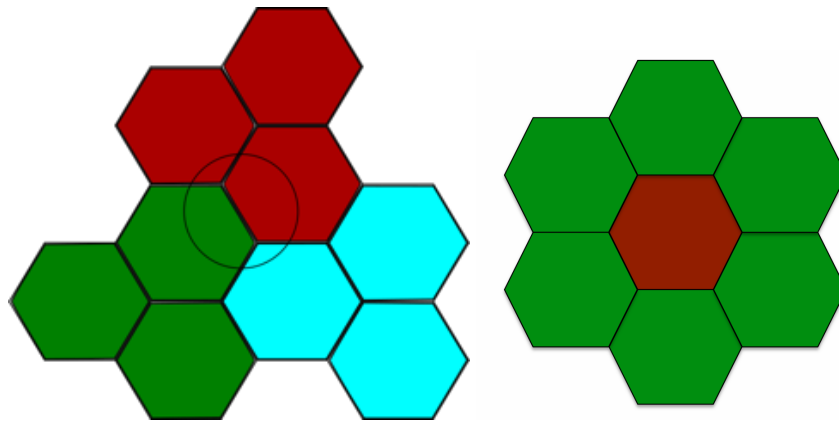


Figure 112: EC trigger pattern for the baseline configuration on the left and for the enhanced baseline configuration on the right.

## 2791 11 MRPC

### 2792 11.1 Overview

2793 The Multi-gap Resistive Plate Chamber (MRPC), which will be used as the time of flight (TOF)  
2794 system, is located in front of the forward-angle calorimeter. Several MRPCs have been recently used  
2795 in RHIC STAR and LHC ALICE as their TOF systems [239–242] and the typical time resolution for  
2796 these detectors is better than 80 ps. Most importantly, as a gas chamber, the MRPC does not need  
2797 PMTs for readout so it can work inside a magnetic field. For the SoLID-SIDIS configuration, the  
2798 total path length is around 8 meters from the target and the flight time is calculated by comparing the  
2799 timing signal to the beam RF signal. With a time resolution of 100 ps, we can identify pions from  
2800 kaons at a rejection factor of 20:1 with momenta up to 2.5 GeV/c. Compared with the MRPCs used  
2801 at STAR and ALICE, the MRPC for SoLID receives a higher flux rate, approximately 10 kHz/cm<sup>2</sup>.  
2802 Tsinghua University has developed a new type of low resistivity glass with a bulk resistivity on the  
2803 order of 10 Ωcm. The rate capability of the high rate MRPC assembled with this type of glass can  
2804 reach 50 kHz/cm<sup>2</sup> [243, 244]. We propose to construct the high rate SoLID-MRPCs with this low  
2805 resistive glass.

### 2806 11.2 Structure of the MRPC Prototype

2807 The layout of the MRPC is shown in Fig. 113. The inner diameter of the detector plane is about  
2808 1 meter and the outer diameter is 2 meters. The area of the disk is about 10 m<sup>2</sup>. The whole detector  
2809 consists of 50 super modules and each super module consists of 3 MRPC modules. There is overlap  
2810 between MRPC modules and super modules to avoid blind areas.

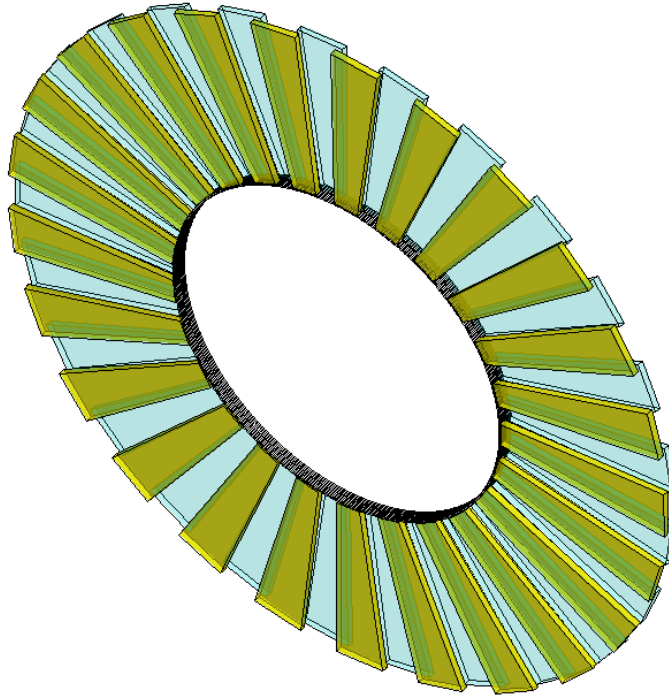


Figure 113: The layout of MRPC TOF

2811 A prototype of the MRPC has been assembled and its structure is shown in Fig. 114. This

2812 trapezoidal module is assembled with our low-resistivity glass. The module has ten gas gaps and  
 2813 the width of each gap is  $250\ \mu\text{m}$ . The outer glass is 1.1 mm thick and the inner glass is 0.7 mm  
 2814 thick. Colloidal graphite is sprayed on the surface of the outer glass and the surface resistivity is  
 2815 about  $5\text{M}\Omega\text{cm}$ . Fig. 115 shows the structure of the readout strips. Each module consists of 11 strips  
 2816 and the width of each strip is 25 mm with a 3 mm gap. The shortest strip is 13 cm and the longest  
 2817 is 17 cm. This prototype will be similar to the smallest module of the three modules in one super  
 2818 module. With this design, the whole detector will consist of 1650 strips, and the total number of  
 2819 readout channels is 3300 since each strip has readouts on both ends.

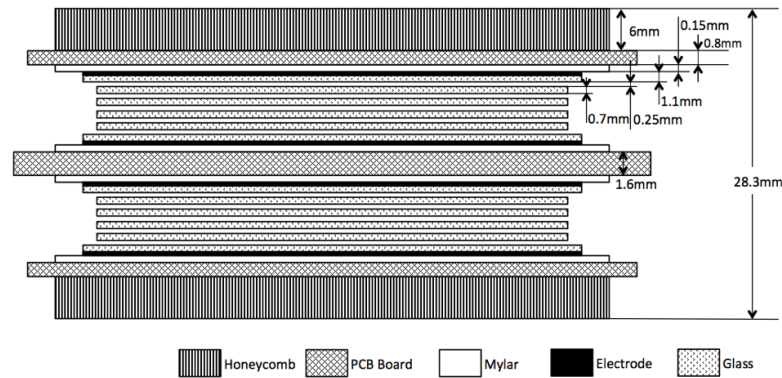


Figure 114: The structure of the MRPC prototype

### 2820 11.3 Gas system

2821 The MRPC uses a mix of Freon 90% R134 freon, 5% Isobutane and 5% SF6. The mix is in itself  
 2822 non flammable but since Freon and SF6 are green house gases we are planning for recycling system  
 2823 for the gas similar to what was used for PHENIX Hadron Blind Detector.

### 2824 11.4 Cosmic Ray Test

2825 The cosmic ray test system for the MRPC prototype consists of a cosmic ray telescope and a VME  
 2826 based DAQ system. The telescope consists of three  $20\ \text{cm} \times 5\ \text{cm} \times 5\ \text{cm}$  scintillators and two  
 2827  $4\ \text{cm} \times 2\ \text{cm} \times 1\ \text{cm}$  scintillators. These five scintillators were used to trigger on cosmic rays.  
 2828 The layout of the cosmic ray telescope and the prototype is shown in Fig. 116. Two of the larger  
 2829 scintillators and one of the smaller scintillators are above the module, and the rest are below the  
 2830 module. PMT0 through PMT4 were used for basic coincidence triggering and to provide the refer-  
 2831 ence time. The two small scintillators are used to measure the efficiency of the module. The width  
 2832 of the area subtended by the small scintillators is smaller than the width of a MRPC strip. Since  
 2833 this module would be tested with an electron beam at JLab (see later discussion), the cosmic test is  
 2834 only for checking primary performance parameters, such as dark current, noise, efficiency and time  
 2835 resolution. With a high voltage setting of 13.2 kV, the dark current is less than 10 nA and the noise  
 2836 rate is a few  $\text{Hz}/\text{cm}^2$ . Fig. 117 shows the efficiency plateau. It can be seen that the efficiency can  
 2837 reach 98% and the plateau region is larger than 600 V. Fig. 118 shows the relation between charge  
 2838 and time after slewing correction. The time spectrum after correction is shown in Fig. 119. The  
 2839 time jitter of four PMTs is 87 ps, so the resolution of the MRPC can reach 50 ps. All of these show  
 2840 that the MRPC module has good performance.

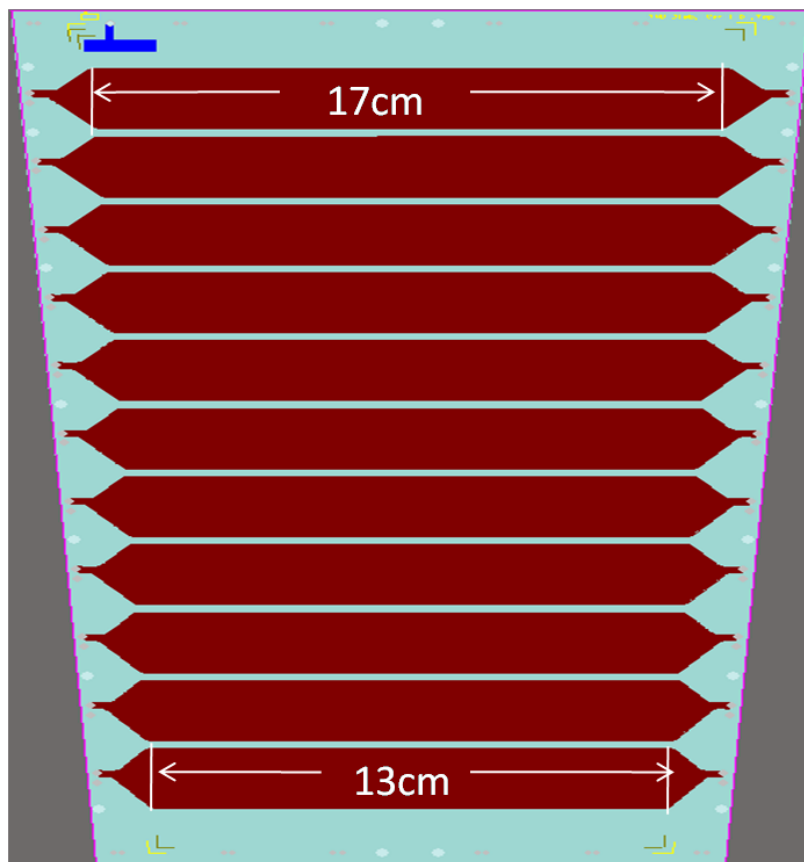


Figure 115: The structure of the readout strips

## 2841 11.5 Beam Test at Hall A

### 2842 11.5.1 Test Setup

2843 The setup of the beam test is shown in Fig. 120. The beam was mainly for the JLab g2p exper-  
 2844 iment [245]. Our test setup stood about 10 m to the side. There was an electron beam passing  
 2845 through our trigger system and the backgrounds were mainly soft photons, electrons and neutrons.  
 2846 The background intensity was stronger than the main electron beam. A thick concrete shield was  
 2847 used to suppress background particles striking the MRPC. A diagram of the DAQ is shown in  
 2848 Fig. 121. The trigger system was very similar to that of the cosmic test system. One small scintillator  
 2849 ( $5\text{ cm} \times 5\text{ cm} \times 1\text{ cm}$ ) was read out by PMT 0 and each of two long scintillators ( $10\text{ cm} \times 5\text{ cm} \times 1\text{ cm}$ )  
 2850 was read out on both ends (by PMTs 1–4). The coincidence of PMT0 and PMT4 provided the trig-  
 2851 ger signal of the system. The delayed coincident signal also acted as the gate signal of the flash  
 2852 ADC and the stop signal of the TDC. PMT1~PMT4 provided the reference time of the system.  
 2853 A CAEN V775 TDC was used to record the time signal and a flash ADC, JLAB FADC 250, was  
 2854 used to record the charge signals. A VME scaler was used to record the time interval between two  
 2855 triggers. From this time interval we can get the signal rate to study the rate capability of the detector.

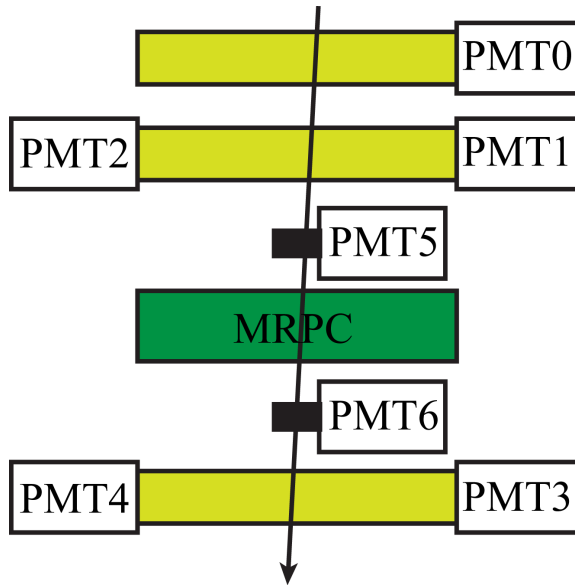


Figure 116: Layout of the test setup

2856 **11.5.2 HV Scan Result**

2857 MRPCs were conditioned under high voltage for a few hours in order to reach a stable, low dark rate  
 2858 working region. The electronics threshold was set to 30 mV. The dark current was less than 8 nA  
 2859 and the rate of the module was less than 10 Hz/cm<sup>2</sup> at 108 kV/cm. The coincidence of PMT1–PMT4  
 2860 provided the T0 of the test system, with a time jitter of about 100 ps. In order to find the optimum  
 2861 working voltage of the counters, the efficiency and time resolution were scanned as a function of  
 2862 the applied voltage for a ‘low’ flux of  $\bar{\phi} \sim 1\text{--}4$  kHz/cm<sup>2</sup>. The results are summarized in Fig. 122.  
 2863 The counters showed large efficiency plateaus above 600 V, and time resolutions were as good as  
 2864 75 ps. It can be seen that the time resolution obtained from cosmic rays is better than that from the  
 2865 electron beam test, because the time jitter of T0 in the beam test was larger than that in the cosmic  
 2866 test.

2867 **11.5.3 Rate Scan Result**

2868 The rate depended on background intensity. From the scaler we can get the signal rate of the MRPC.  
 2869 Fig. 123 shows the signal rate change with time in runs 188 and 193 respectively. The rate was not  
 2870 stable in each run. From these runs, we obtained different rates from 1 to 16 kHz/cm<sup>2</sup>. These two  
 2871 runs were combined to analyze the rate performance. The results are shown in Fig. 124. It can be  
 2872 seen even when the flux rate reaches 16 kHz/cm<sup>2</sup>, the efficiency is still higher than 94% and the  
 2873 time resolution is close to 80 ps. So this module meets the requirement of the SoLID TOF system.

2874 The evolution of the charge distribution can be seen in Fig. 125 for this MRPC. The charge is  
 2875 obtained from the sum of its two ends. It can be seen that, with increasing flux, the average charge  
 2876 decreases and the spectrum shifts down to lower charges as expected.

2877 **11.6 Radiation hardness and aging**

2878 Aging and radiation hardness tests were carried out. For the low conductivity glass, no change in  
 2879 resistivity were seen for neutron fluence up to 10<sup>14</sup>/cm<sup>2</sup> as show in Figure 126. The glass was

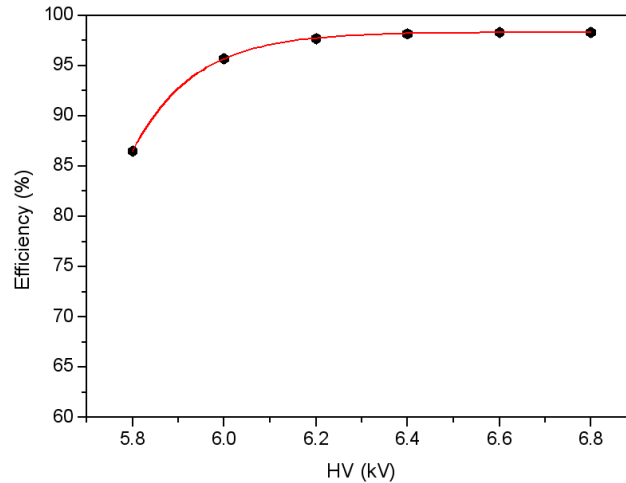


Figure 117: Efficiency plateau of the MRPC

2880 also applied with 1000V for about 32 days with integrated charge of  $1C/cm^2$  (about 2 years of  
 2881 continuous running in SIDIS conditions), and its resistivity remained stable. The module was tested  
 2882 using a X-ray source. the chamber was exposed to X-ray for 35 days which corresponded to about  
 2883  $0.1C/cm^2$ . No change in amplitude and efficiency were observed at the end of the test as show in  
 2884 Figure 127.

## 2885 11.7 Conclusions

2886 A high rate MRPC was planned to construct the time of flight system for the SoLID-SIDIS program,  
 2887 and a prototype has been designed and constructed. The trapezoidal prototype module assembled  
 2888 with low resistivity glass has  $10 \times 0.25$  mm gas gaps and 11 readout strips. The width of the strips  
 2889 is 2.5 cm with an interval of 3 mm. This module was tested using cosmic rays and also tested using  
 2890 electron beams in Hall A of JLab. The results show its rate capability of larger than  $16$  kHz/cm<sup>2</sup>.  
 2891 This module has a very promising time resolution. The time resolution can reach 50 ps in cosmic  
 2892 test and is about 75 ps in the beam test. The chambers behaved very stably during the test. A detailed  
 2893 aging study was performed to assure the stability over a long running time. The performance of the  
 2894 prototype meets the requirement of the SoLID-TOF system.

## 2895 11.8 R&D Plan for Better Time Resolution

2896 A R&D effort by the Chinese collaboration, jointly for SoLID, sPHENIX and EIC, for the next  
 2897 generation MRPC aims at 20 ps resolution. Tsinghua University is planning to develop a prototype  
 2898 in the next year. Beam test and finalization of detector and electronics will be done the following  
 2899 year.

2900 Obtaining good timing resolution also depends on the electronics, both preamplification of sig-  
 2901 nals and digitization:

2902 EIC R&D at BNL is using 7 GHz bandwidth TI LMH5401 [179] amplifiers for preamplifiers.  
 2903 Tsinghua University will also develop its own amplifier chip which could drive lower costs and give  
 2904 a more compact footprint for the electronics with a multichannel amplifier chip.

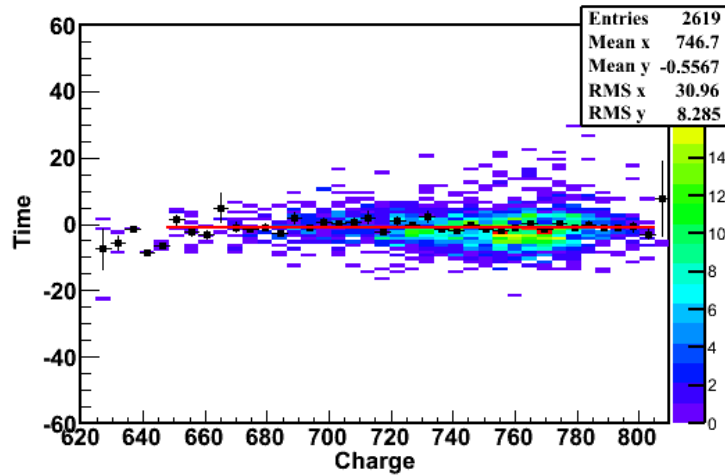


Figure 118: The relation between charge and time after slewing correction

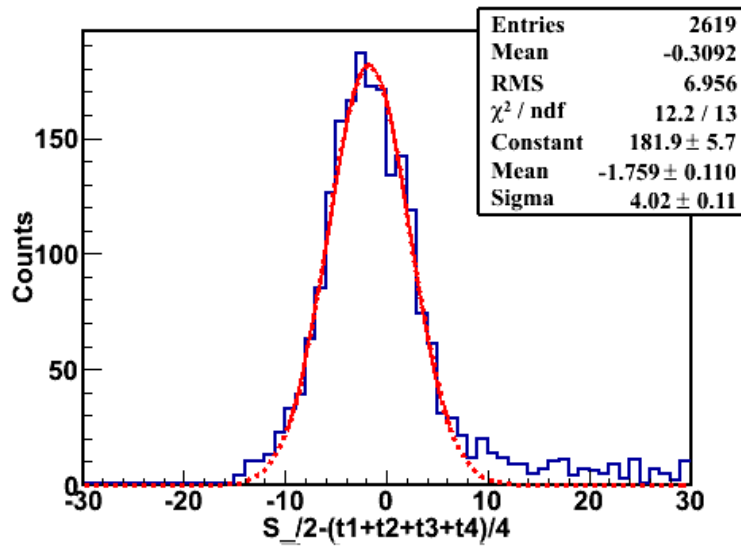


Figure 119: Time spectrum after correction

2905 New sampling electronics, development of which is being motivated by MCP PMTs, can reach  
 2906 picosecond level timing resolution for multi-photons. The system is based on Switched Capacitor  
 2907 Arrays (SCAs), which continuously sample the detector signal on a circular array of capacitors.  
 2908 Sampling frequencies up to 10 GSamples/s have been reached. With a good calibration, a timing  
 2909 resolution of 1 ps has been achieved. The following Table 17 summarizes the different available  
 2910 chips.

2911 One of the main drawbacks of the SCA is the inherent dead time to allow readout of all the  
 2912 samples for each trigger. A multi level array design will be implemented in the next generation of

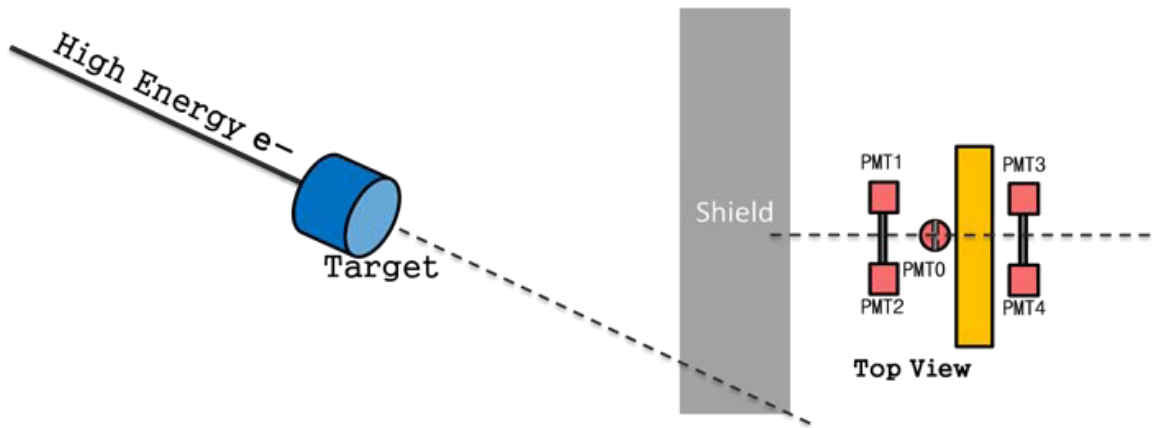


Figure 120: Setup of beam test in Hall A

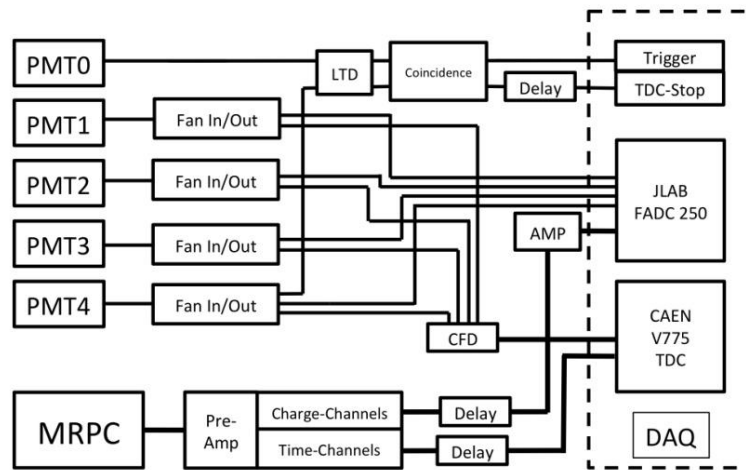


Figure 121: Diagram of the DAQ system

2913 chips such as the DRS5 or the successor of PSEC4 called AARDVARC. There is a joint effort from  
 2914 HEP/NP and the NALU commercial company to offer a commercial modular system based on the  
 2915 successor of PSEC4. This is currently the favored option with costs which could go as low as \$15  
 2916 per channel.



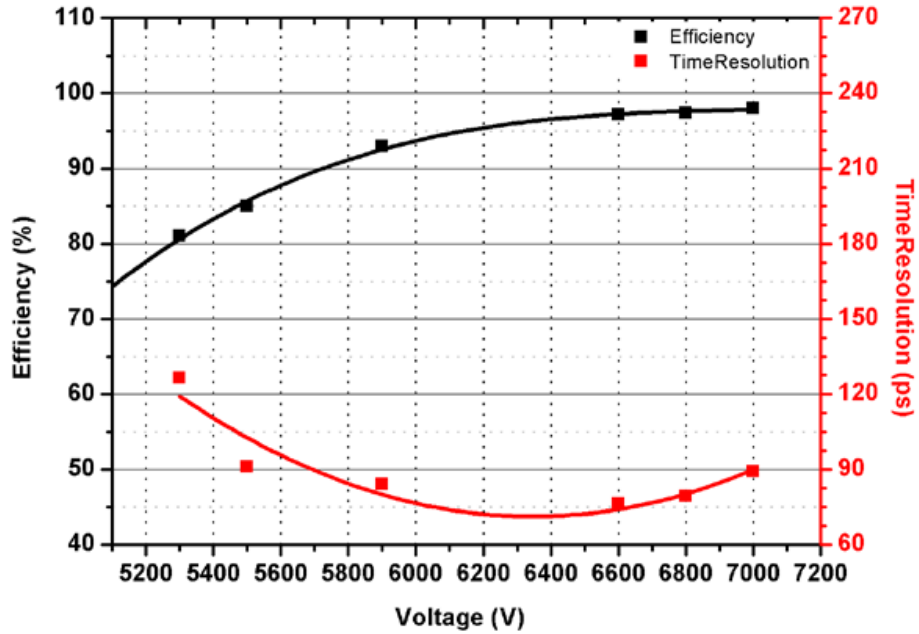


Figure 122: Time resolution and efficiency change versus applied voltage

Chip	Sample Frequency GHz	Bandwidth GHz	Samples	Channels	Readout MHz	Resolution ps
PSEC4	4 to 15	1.5	256	6	40 to 60	9
SAMPIC	3 to 8.2	1.6	64	16 or 8	80	5
DRS4	0.7 to 5 GHz	0.950	1024	9	33	1
DRS5	10	3	4096	32	300 ?	5 ?
PSEC5 (AARDVARC)	10 to 15	1.5 to 2	32768	6 to 8	500?	5?

Table 17: Table summarizing the characteristics of different sampling chips available and future generation ones for DRS5 and PSEC5 (AARDVARC)

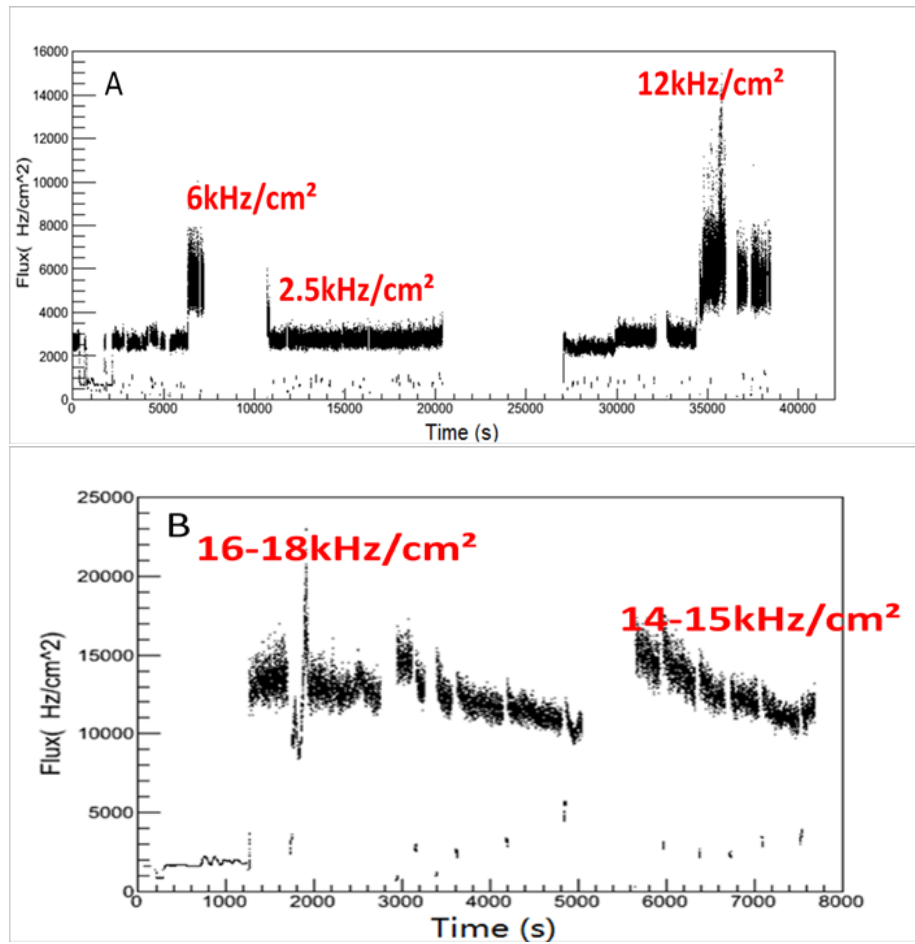


Figure 123: Signal rate changes with time. (A) shows run 188 and (B) shows run 193. The MRPC was located 5 meters from the target. There is shielding in front of the detector in (A), no shielding in front of the detector in (B).

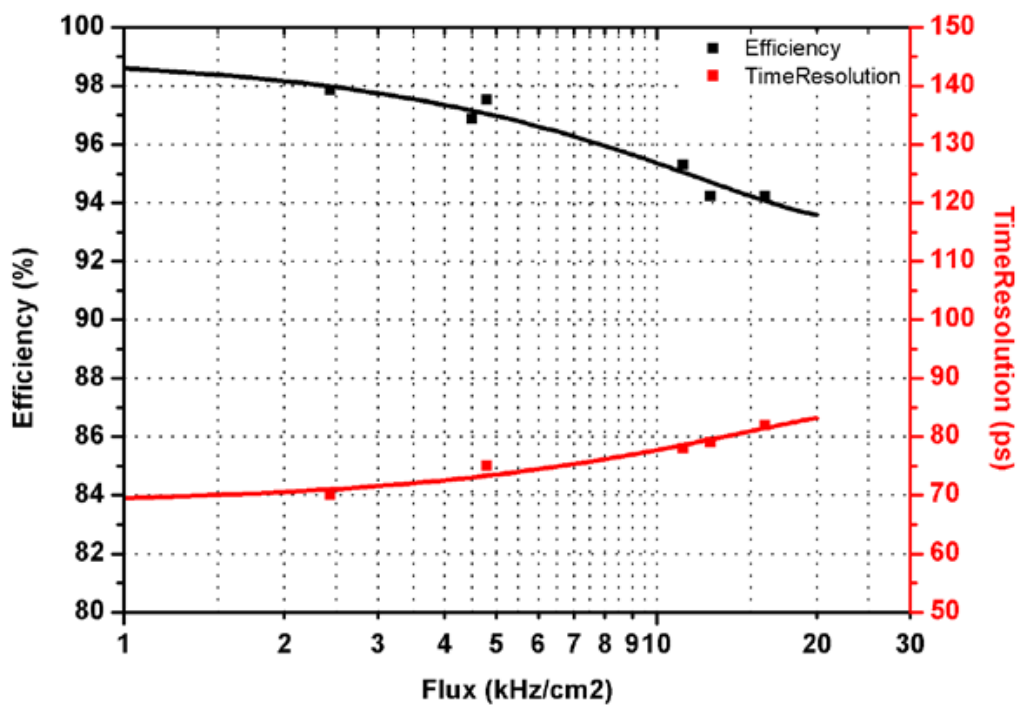


Figure 124: Measured efficiencies and time resolutions as a function of the particle flux.

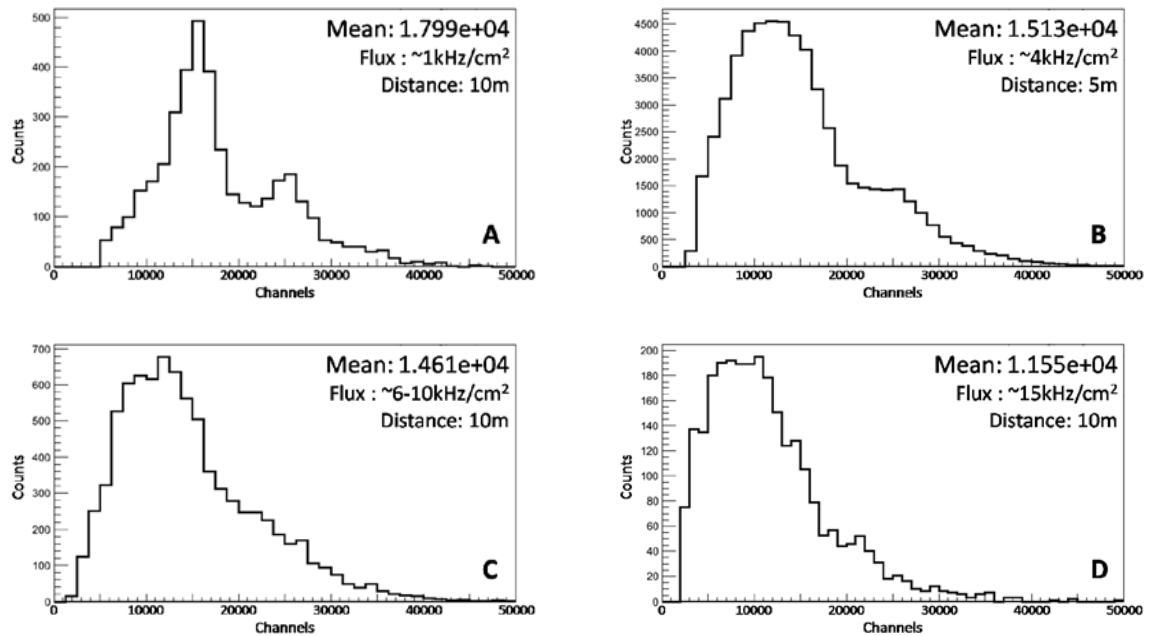


Figure 125: Charge distribution at various fluxes over one readout strip. Flux increases from figure A to D.

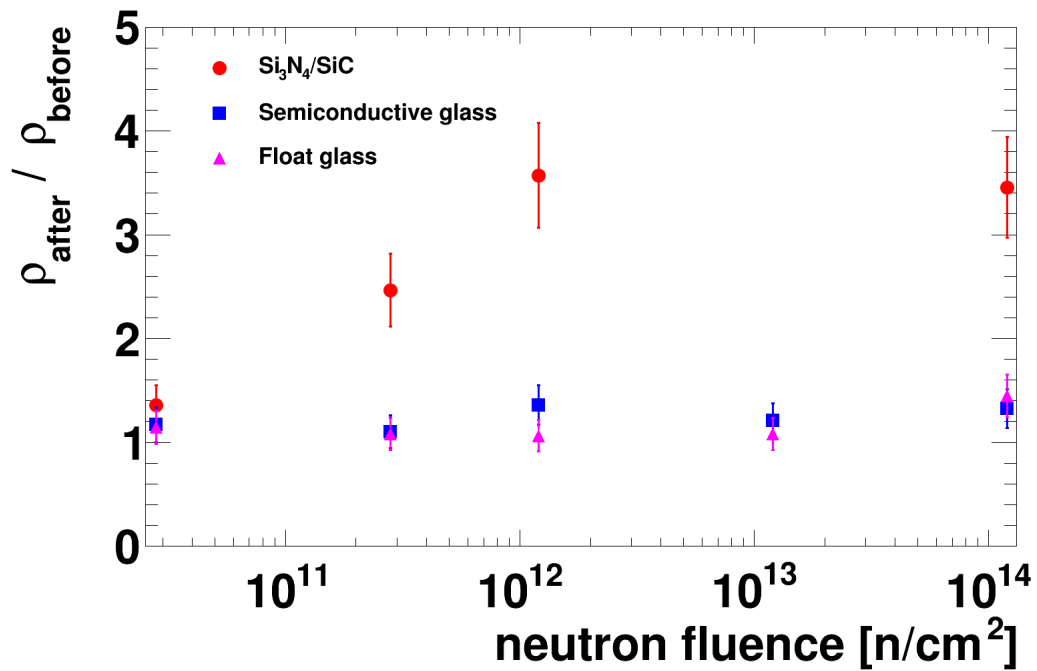


Figure 126: Change in glass resistivity as a function of neutron fluence, where the semiconductive glass is what we use.

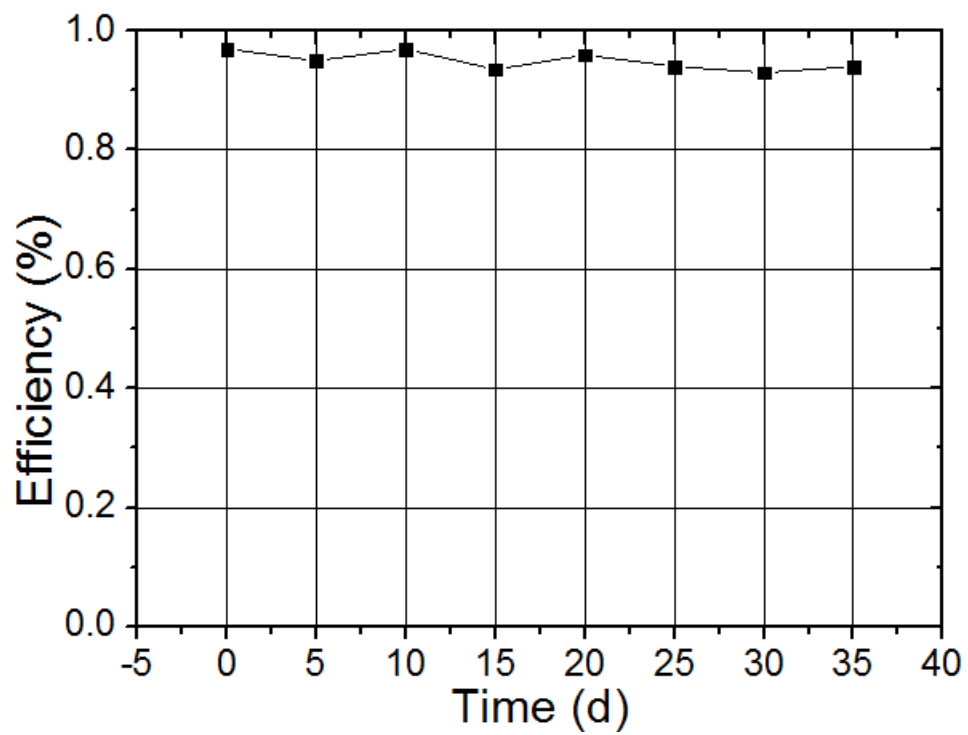


Figure 127: Chamber efficiency as a function of x-ray irradiation days

## 2917 12 Simulation and Reconstruction

### 2918 12.1 End-to-End Software Framework

2919 At the time of this writing, research is underway to identify a comprehensive software framework  
2920 for SoLID. A framework should be chosen early in the software development cycle, where SoLID  
2921 is now, to provide a common programming interface (API) for all software components. If chosen  
2922 well, the API will stay constant, or at least backward compatible, throughout the project’s life-  
2923 time so that early investments in code development will continue to pay off. Additionally, it is  
2924 important at this stage to identify software features and capabilities that will be needed for SoLID  
2925 data analysis, to the extent foreseeable now. Such feature requirements should be well matched to  
2926 the specifics of the SoLID experiments, such as data volumes, detector types and configurations,  
2927 and analysis methods. Retrofitting capabilities that were initially overlooked is often difficult and  
2928 wasteful because doing so may invalidate original design assumptions, requiring large parts of the  
2929 first-generation software to be re-written. Conversely, choosing a framework with too many fea-  
2930 tures typically results in overly complex, bloated software that is difficult to learn and faces user  
2931 resistance.

2932 With these goals in mind, we have developed the following requirements for the SoLID software  
2933 framework; it should

- 2934 1. support all major components of the physics data processing chain, *viz.* simulation, digi-  
2935 tization, reconstruction and physics analysis, within a *consistent* development and run-time  
2936 environment (“end-to-end framework”);
- 2937 2. allow multi-pass data processing, where the output of one analysis pass can be used as the  
2938 input for the next pass—an essential capability to minimize the need for reprocessing large  
2939 data sets;<sup>4</sup>
- 2940 3. allow multiple processing chains in a single job, for example to run different track fitting, PID  
2941 or physics analysis algorithms on the same data in a single processing pass;
- 2942 4. support interactive analysis of reconstructed quantities with ROOT, since ROOT will most  
2943 likely be the data analysis package best known to and preferred by future SoLID collaborators;
- 2944 5. save extensive metadata to its output, for example database parameters used in previous anal-  
2945 ysis stages (if practical) and detailed information about data provenance;
- 2946 6. support parallel computing, *i.e.* multi-threading and/or distributed processing;
- 2947 7. be written in C++, as most SoLID collaborators are well-versed in that language; and
- 2948 8. be readily available at this time, so that development can start without delay;

2949 Given limited manpower, the effort needed to develop a new framework from scratch that sat-  
2950 isfies the above set of requirements would be prohibitive. As experience in other collaborations  
2951 shows [246–249], frameworks with comparable capabilities are invariably complex and may take  
2952 the better part of a decade to mature. Therefore, it is practically unavoidable, and certainly wise, to  
2953 build the analysis software for a specific experiment on already existing packages, unless truly un-  
2954 usual or novel requirements arise. Of course, we are not the first to discover this. Motivated by the

---

<sup>4</sup>This is typically achieved in physics frameworks by a clear separation of data and algorithms, where the data objects are persistable and saved to intermediate files. Regarding object persistence, the ROOT streamer model represents the state of the art in the field.

2955 increasing complexity of software in the field, various collaborations worldwide have, over the past  
2956 decade or two, put considerable effort into developing high-quality, general-purpose frameworks  
2957 aimed at processing the event-type data prevalent in nuclear and particle physics experiments. The  
2958 present trend in HEP is a collaborative approach toward software, where already-developed, widely  
2959 tested frameworks are increasingly shared by similar experiments and re-used for new ones [250].  
2960 Practically no modern software in the field does without ROOT [251] in regard to interactive anal-  
2961 ysis, visualization and object persistency, while a number of choices exist for event processing  
2962 frameworks that support simulation and reconstruction.

2963 Obviously, we do not expect to find a perfect framework that satisfies all our criteria fully.  
2964 Generally, however, a good event processing framework should stand out by a superior technical  
2965 design and reliance on widely adopted, state-of-the-art technologies (*e.g.* support for C++11/14,  
2966 ROOT object persistency). To minimize development time and maximize user adoption, the right  
2967 mix of features, excellent documentation and a large body of available example code would clearly  
2968 be beneficial.

2969 At present, we are evaluating a number of different NP and HEP data analysis frameworks  
2970 that are popular and readily available. Specifically, we have been studying Podd (JLab Hall A/C)  
2971 [252], Clara (JLab Hall B) [246], JANA (JLab Hall D) [247], Fun4All (PHENIX/sPHENIX at BNL)  
2972 [253], FairRoot (GSI) [248], and *art* (FNAL) [249]. Of these, FairRoot, a package developed for the  
2973 heavy-ion program at the future FAIR facility at GSI in Darmstadt, Germany, and *art*, the framework  
2974 developed for and adopted by the Intensity Frontier experiments at Fermilab, appear to be the most  
2975 promising candidates for long-term use by SoLID. Both frameworks satisfy the majority of the  
2976 SoLID requirements listed above, are mature, sufficiently rich in features, sufficiently flexible for  
2977 general-purpose simulation and analysis tasks, well supported, and serve a large user community  
2978 that is unlikely to dissolve over the next decade.

2979 Both the FairRoot and *art* collaborations participate in the monthly ROOT planning meetings;  
2980 as stakeholders, they provide direct input to the ROOT team to help improve compatibility of the  
2981 respective frameworks with ROOT. We interpret this as an additional encouraging sign for the ex-  
2982 pected longevity of these two frameworks in particular.

2983 Currently, neither FairRoot nor *art* are multi-threaded, but as of 2017 a major effort is underway  
2984 by the core development team at Fermilab to implement multi-threading in *art* [254]. This feature  
2985 is expected to become available in 2018. The heavy dependence of FairRoot on ROOT, with its  
2986 many global variables, on the other hand, effectively rules out a future multi-threaded version of  
2987 FairRoot. Instead, the GSI FAIR experiments are considering moving to a new, concurrent and  
2988 distributed framework, ALFA [255], which will presumably be in the upgrade path of FairRoot.  
2989 This option may or may not materialize in time for SoLID. ALFA could also form the basis of an  
2990 extension of SoLID software to distributed computing.

2991 We are in the process of prototyping and testing simulation and analysis routines with several  
2992 frameworks to gain experience with the frameworks' relative benefits. A decision as to which  
2993 framework to adopt for SoLID, if any, will be made at an appropriate time.

2994 An estimate of the manpower required for implementing the complete SoLID simulation and  
2995 reconstruction software can be found in Appendix C.

## 2996 **12.2 Simulation**

### 2997 **12.2.1 Simulation Software**

2998 Development of the SoLID spectrometer requires the detailed evaluation of different solenoidal  
2999 fields, optics from those fields, backgrounds from multiple sources, possible detector and baffle

3000 geometries, detector responses, and tracking. Overall, a figure-of-merit must be calculated for dif-  
3001 ferent configurations for quantitative comparison. It is also necessary that such simulations be done  
3002 in a coherent fashion and validated as well as possible. Because details of the design have not been  
3003 finalized, it must also be flexible enough to be quickly adapted to different configurations.

3004 Initial simulations for SoLID were done using a combination of GEANT3 and COMGEANT.  
3005 However, these are FORTRAN based and GEANT3 is no longer actively maintained. The deci-  
3006 sion was made to offer a modern design based on Geant4 [257] to handle particle propagation and  
3007 interactions. This is a well-supported framework and offers a variety of physics packages, such  
3008 as simulation of low-energy electromagnetic backgrounds. However, the detector geometries, how  
3009 magnetic field maps are specified, input parameters, and output formats must all be developed on  
3010 top of this framework. Because this is being done with a new simulation package, it is necessary to  
3011 also compare and reconcile the output between GEANT3 and Geant4.

3012 To accomplish all these goals, we have adopted a simulation suite, GEMC, which was suc-  
3013 cessfully developed and employed for similar CLAS12 simulations [258]. It utilizes Geant4 and  
3014 includes facilities for external event generators, output to a compact style similar to that utilized by  
3015 JLab data acquisition systems, and a flexible framework to specify arbitrary detector geometries.  
3016 A framework for specifying sensitive detectors, processing particle hits, and generating output is  
3017 also included. The geometry and sensitive detector types are read in at run time allowing for easy  
3018 modification of designs. Advanced visualization abilities are available, which provides a useful  
3019 debugging tool.

3020 As described in Sec. 4, magnetic field maps for GEMC can be produced using the Poisson  
3021 Superfish package [259] developed at LANL or TOSCA [260]. The POISSON package allows for  
3022 the calculation of azimuthally symmetric magnetic fields (relevant for the solenoidal spectrometer).  
3023 Because both the optics and the fields in the detector regions are relevant, accurate optimization of  
3024 the iron yoke is important. More detailed field maps produced by TOSCA will be used for the next  
3025 stage of design.

3026 The overall software design is based on a modular philosophy which is general enough to allow  
3027 many different software components to interact with each other. This needs to encompass ideas  
3028 such as external event generators, ROOT analysis scripts, raw hit digitization, and tracking analysis.  
3029 A schematic is given in Fig. 128. Detailed discussions of the individual components follow in later  
3030 subsections and Sec. 12.1.

3031 GEMC and generally Geant4 provide the predominant simulation component in modeling sec-  
3032 ondary physics processes (such as multiple scattering) and propagation through a magnetic field.  
3033 Physics generators provide information on the initial particle type, position, and momentum to the  
3034 simulation for each event and are described in Sec. 12.2.3. These can take more than one form and  
3035 we allow for general text file input and internal generators within GEMC. Magnetic field maps are  
3036 described over a grid using text files. GEMC allows for various coordinate systems to be used in  
3037 the grids and handles all interpolation and lookup.

3038 Detector Description including geometries and materials are defined in a tabular structure which  
3039 can be store in text files or SQL database. GEMC is built as a library and linked to a code called  
3040 "solid\_gemc" to have detector responses and output file formats customized for SoLID simulation.  
3041 This gives access to all of the functionality within GEMC, but allows us to modify and add compo-  
3042 nents as we need them.

3043 Output from GEMC is through EVIO, which is a binary format developed at Jefferson Lab.  
3044 Libraries are available to provide decoding. These files can be converted to ROOT files through  
3045 available tools or used by higher level analysis packages, such as the detector digitization.



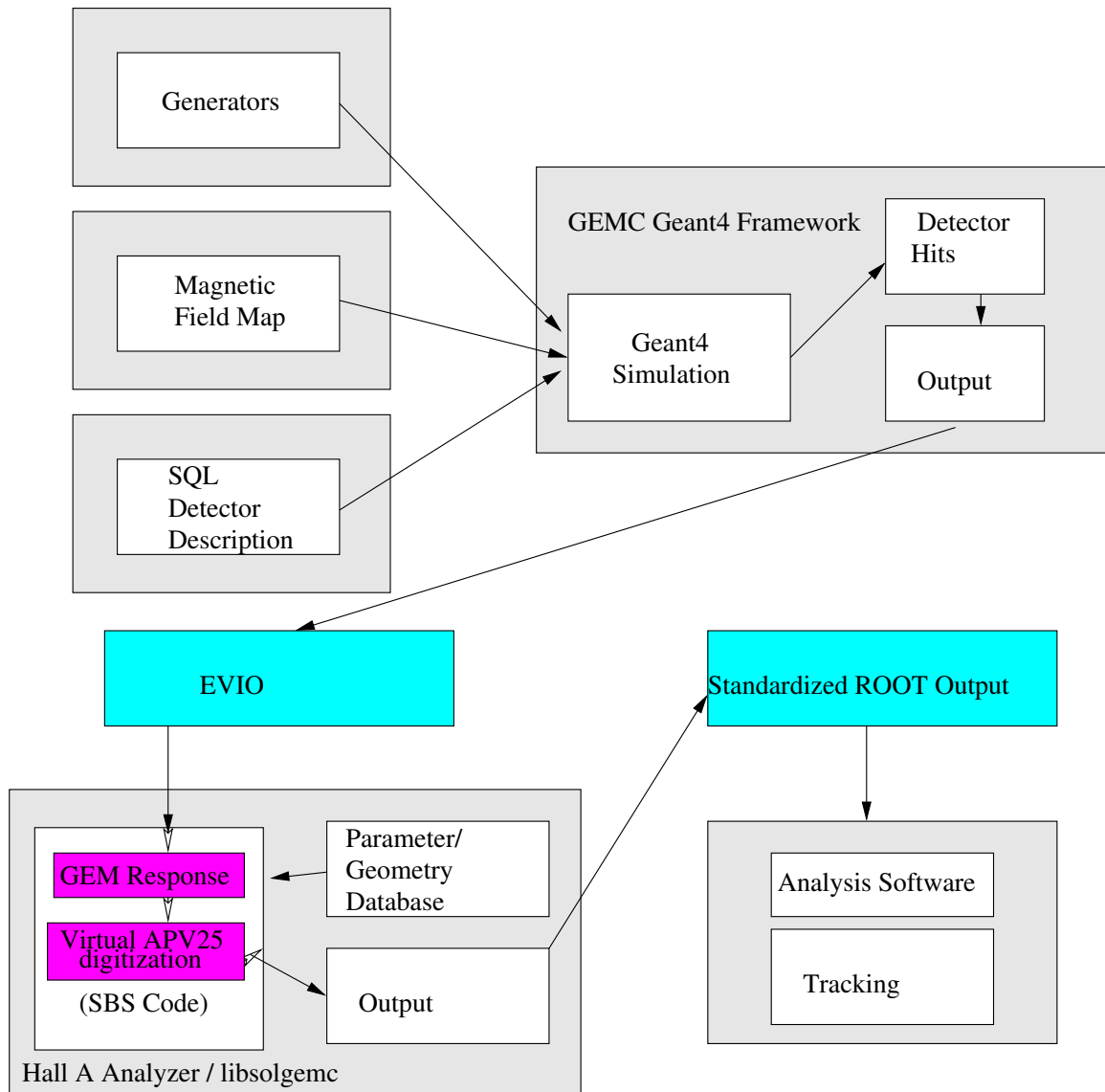


Figure 128: Schematic of the simulation and software framework.

### 3046 12.2.2 Simulation Status

3047 Significant progress has been made with the SoLID simulation, which has allowed realistic perfor-  
 3048 mance studies of the core measurements and other important issues. The SoLID simulation has been  
 3049 taking advantage of the new GEMC development. The simulation of each individual subsystem has  
 3050 been developed by different groups using the same framework, and then all subsystems are com-  
 3051 bined into the whole SoLID simulation without any code change at run time. We can also choose  
 3052 to turn off a subsystem or replace it with a different version in the whole simulation for testing. The  
 3053 entire code, including the production and development version, is kept in a version control system.

3054 The materials in non-detector subsystems have been implemented. Detector subsystems have  
 3055 materials and responses tailored to themselves. In addition to studies done by different groups for  
 3056 subsystems, we also produce the whole simulation output for various overall studies of characteris-  
 3057 tics such as acceptance, background rates and trigger performance to ensure consistent results.

3058 The simulation output is stored in ROOT trees. Each detector has a standalone tree, and different  
3059 trees are linked by the same tree index for one event. Then each tree is analyzed by a standalone  
3060 ROOT script. Combining the set of ROOT scripts, we can analyze all SoLID sub-detectors and  
3061 perform the overall studies mentioned above.

3062 In general, the SoLID simulation is an effort which will last the entire SoLID lifetime. We are  
3063 still at its early stage. The simulation code will evolve with the Geant4 and GEMC development.  
3064 SoLID's detector and engineering design will also evolve and they can be easily transferred into the  
3065 simulation by a CAD model. Detector prototyping and tests will give direct input to the simulations  
3066 and in turn improve the overall SoLID design.

3067 The SoLID collaboration may adopt the *art* event-processing framework as its software frame-  
3068 work. *art* currently uses generic Geant4 as its simulation engine and allows a flexible middle layer.  
3069 We are exploring the possibility of using GEMC for the simulation layer of *art*.

### 3070 12.2.3 Physics Event Generators

3071 Beyond the physics included in Geant4, several generators have been implemented to study specific  
3072 processes. The interface between the generator and GEMC is the LUND format (or an extension of  
3073 it), which is a text-based file containing event-by-event information of the initial particle configu-  
3074 ration. These generators allow for an extended target and randomly sampled position to simulate a  
3075 fast-rastering system. The generators implemented presently are

- 3076 • Deep inelastic scattering cross sections from the CTEQ6 parton distribution fits [262].
- 3077 • Charged and neutral pion production based on empirical fits to SLAC data [263] using the  
3078 Weizsäcker-Williams approximation.
- 3079 • Charged and neutral pion production based on the modified Hall D background generator
- 3080 • Elastic scattering from protons and neutrons based on dipole parameterizations.

3081 The modified Hall D background generator gives better pion background results matching exist-  
3082 ing data. The original Hall D photo-production generator uses various experimental data to generate  
3083 photo-production cross sections on a proton target for photon energies below 3 GeV [266, 267]. It  
3084 uses a modified version of PYTHIA to generate cross sections of photo-production for photon en-  
3085 ergies above 3 GeV [266, 267]. The Hall D generator is only a photo-production event generator.  
3086 SoLID requires an electro-production generator. Hadron production in electron scattering on a nu-  
3087 cleon target can originate either from real bremsstrahlung photons radiated in the target or from  
3088 the interaction of the virtual photon with the nucleons. The virtual contribution is calculated in  
3089 the Equivalent Photon Approximation [268]. The bremsstrahlung contribution is implemented fol-  
3090 lowing PDG-2012 [269, 270]. A more detailed overview of the hadron generators used for SoLID  
3091 simulation is available from [265].

3092 Additional generators are planned, which includes extending the present generators to include  
3093 initial radiative and multiple-scattering effects. Additionally, self-analyzing hyperon decay pro-  
3094 cesses are a potential systematic and must be evaluated as well. Background rates for processes  
3095 included in Geant4 can be evaluated by simulating sufficient numbers of individual electrons pass-  
3096 ing through the target.

3097 **12.2.4 GEM Digitization**

3098 GEM digitization is a crucial aspect in evaluating hit tracking under realistic conditions. The method  
 3099 implemented is based on an approach by the Super-BigBite collaboration, which takes the individual  
 3100 ionization events in the GEM drift region, and produces a charge signal across several readout strips  
 3101 based on a realistic model with parameters tuned to real data.

3102 A track passing through a GEM in Geant4 will record energy deposition events caused by ion-  
 3103 ization which are then amplified through the GEM foils, resulting in a detectable signal over several  
 3104 readout strips, Fig. 129. Within the simulation, the individual ionization events are written into the  
 3105 output and are post-processed through an independent library built upon the Hall A analyzer analy-  
 3106 sis software [252]. The digitization and track reconstruction can then be developed within a single  
 3107 framework similar to what could be used for analysis of real data.

3108 A full description of the digitization process can be found in Ref [273]. To summarize, from  
 3109 the individual ionization hits, an average number of hole/electron pairs are determined by sampling  
 3110 a Poisson distribution based on the ionization energy  $W$ , such that  $n_{\text{ion}} = \Delta E/W$ . The physical  
 3111 spread of the resulting charge cloud is described by a simple diffusion model assuming a constant  
 3112 drift velocity, where the Gaussian width of the cloud is given by

$$\sigma_s(t) = \sqrt{2Dt} \quad (13)$$

3113 where  $D$  is the diffusion constant and  $t$  is the time from ionization. Variation in the amplification of  
 3114 the GEM signal is described by a Furry distribution

$$f_{\text{Furry}} = \frac{1}{\bar{n}} \exp\left(-\frac{n}{\bar{n}}\right) \quad (14)$$

3115 where  $\bar{n}$  is the average number of ionization pairs. The previous formalism provides a realistic  
 3116 (unnormalized) charge distribution over an area which can then be associated with a set of GEM  
 3117 readout strips.

3118 The final component of the digitization is to reproduce the time-shaping of the electronics com-  
 3119 ponents. For this application, we have assumed the use of APV25 electronics developed at CERN  
 3120 (see Sec. 7). The time-dependent digitized signal  $S(t)$  is produced by convoluting the charge signal  
 3121 with the form

$$S(t) = A \frac{t}{T_p} \exp(-t/T_p) \quad (15)$$

3122 which provides a good parameterization of real data, Fig. 130. The parameters are chosen to repre-  
 3123 sent real data and the time constant  $T_p$  is roughly 50 ns, providing a full-width half-max of about  
 3124 100 ns.

3125 The advantage to using such a shaping signal is that three samples can be used to deconvolute  
 3126 the longer, shaped signal to suppress out-of-time background hits. Assuming the form given in  
 3127 Eq. 15, the signal in time sample  $k$  is given by

$$s_k = w_1 v_k + w_2 v_{k-1} + w_3 v_{k-2} \quad (16)$$

3128 where weights  $w_i$  are proportional to

$$w_1 \sim e^x/x, w_2 \sim 2/x, w_3 \sim e^{-x}/x. \quad (17)$$

3129 To obtain a more reliable result from the track reconstruction, it is crucial to simulate the res-  
 3130 sponses of GEM detectors and related electronics to a highly realistic level. Such an effort was

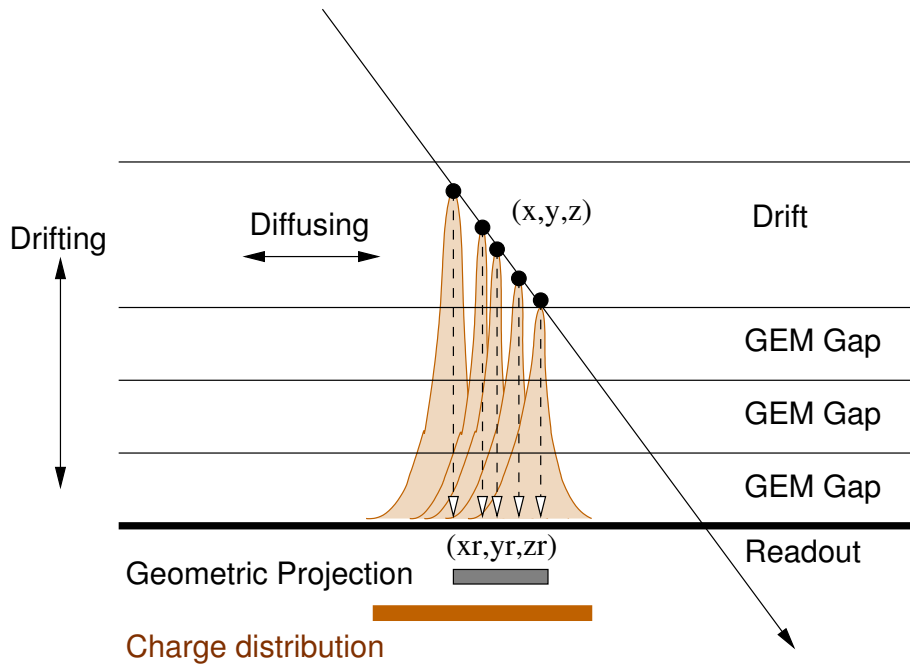


Figure 129: Diagram of the concept behind GEMs using electron avalanching and detection through a set of readout strips.

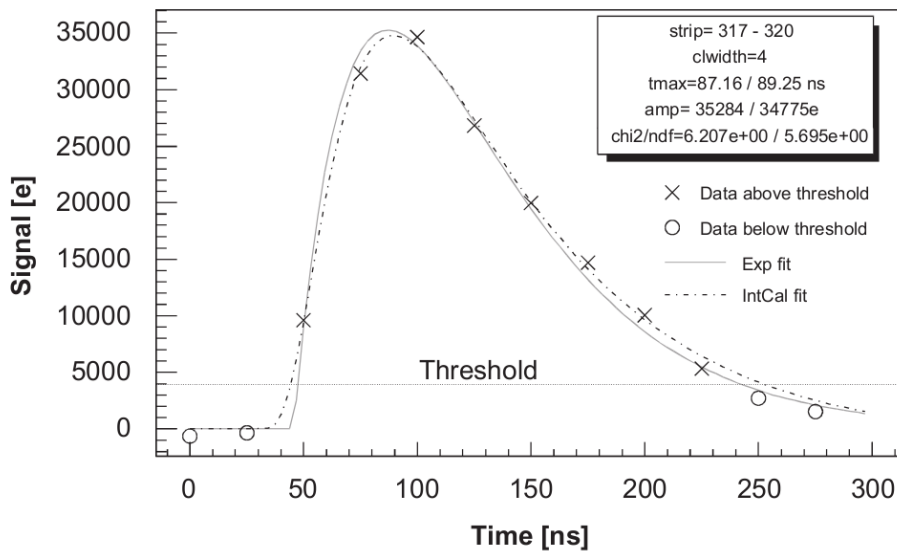


Figure 130: Representation of the signal vs. time response for an APV25 module.

PVDIS GEM occupancies			
Plane	Total strip number (u+v) per sector	Raw Occupancy (%)	Noise filtered Occupancy (%)
1	1156	21.17	9.97
2	1374	10.35	5.11
3	1374	8.81	4.42
4	2287	3.07	1.64
5	2350	2.79	1.50

Table 18: PVDIS GEM average occupancies with LD2 target estimated by digitizing its whole simulation data. The raw occupancy with only pedestal cut and the noise filtered occupancy with 3 samples are shown.

SIDIS $^3\text{He}$ GEM occupancies		
Plane	Total strip number (u+v) per sector	Raw Occupancy (%)
1	906	2.37
2	1020	7.98
3	1166	3.40
4	1404	2.24
5	1040	2.03
6	1280	1.52

Table 19: SIDIS  $^3\text{He}$  GEM average occupancies estimated by digitizing its whole simulation data. The raw occupancy with only pedestal cut is shown, Because only 1 sample is used, there is no noise filtering from multiple samples.

3131 recently carried out, based on the existing SoLID GEM digitization program, by comparing simu-  
3132 lated results with actual GEM detector experimental data from beam tests and highly ionizing x-ray  
3133 test at UVa. The digitization parameters were fine tuned based on this study to work for both highly  
3134 ionizing low energy photon signals and for MIP signals. This is critical for a reliable simulation of  
3135 SoLID conditions as much of the background hits in SoLID GEM detectors are due to low energy  
3136 photons.

3137 By using the tuned digitization code, we digitized the whole simulation for PVDIS setup with  
3138 LD2 target, SIDIS setup with  $^3\text{H3}$  target, and the  $J/\phi$  setup with LH2 target. The same set of  
3139 simulation data are used for acceptance and trigger study including all detector response. The GEM  
3140 geometry and material are modeled carefully in simulation the according to the latest design and  
3141 prototype. The things missing are dead areas by spacers and frames, and the possible overlap over  
3142 different sectors, which we plan to add in the next round of simulation. Both the simulation and our  
3143 test have shown that the dominant GEM background is caused by low energy photons which have  
3144 only a few percents probability to deposition energy and fire GEM, but a huge rate. The occupancy  
3145 is obtained as the average number of readout strips fired within 275 ns time window divided by total  
3146 number of strips in the readout plane in one of 30 sectors. Both u and v strips are counted. The  
3147 results are shown in Table 18, 19 and 20. The noise filtering from 3 samples is applied where it's  
3148 available.

$J/\psi$ GEM occupancies			
Plane	Total strip number (u+v) per sector	Raw Occupancy (%)	Noise filtered Occupancy (%)
1	906	7.68	4.65
2	1020	14.4	9.28
3	1166	8.82	5.49
4	1404	7.00	4.30
5	1040	5.92	3.78
6	1280	4.58	2.95

Table 20:  $J/\psi$  GEM average occupancies estimated by digitizing its whole simulation data. The raw occupancy with only pedestal cut and the noise filtered occupancy with 3 samples are shown.

## 3149 12.3 Reconstruction

### 3150 12.3.1 Tracking

3151 SoLID track reconstruction requires an accurate and efficient track finder able to identify signal  
3152 tracks in a high-noise environment and sufficiently fast for the level-3 trigger. In addition, an ac-  
3153 curate and robust track fitter is required in order to optimize the resolutions for the vertex variables  
3154 and other track-related variables.

3155 In order to satisfy the requirements, a Kalman Filter (KF)-based track finding and track fitting  
3156 algorithm is being developed and tested with digitized GEM simulation data. A Kalman Filter is a  
3157 recursive fitting algorithm [271]. In contrast to the well-known least-squares fit that provides only  
3158 one set of parameters after fitting, the track parameters of the KF can evolve along the trajectory.  
3159 There are three basic steps for the KF. First, it predicts the measurement on the next measurement  
3160 site by propagating the current track parameters. Second, the covariance matrices of current track  
3161 parameters are propagated along the trajectory. And last, it filters the next measurement in order to  
3162 improve the track parameters at the next measurement site. The local field information and errors  
3163 due to multiple scattering can be collected during the first two steps of the algorithm. Thus, given  
3164 that particle tracks in the SoLID detector will cross both fringe and uniform field regions, it is  
3165 expected to perform better than other algorithms that explicitly require a globally uniform magnetic  
3166 field.

3167 The KF can be easily extended into acting as a track finder as well, achieving concurrent track  
3168 finding and fitting. This is done by adding two steps to the standard KF algorithm. First, an algo-  
3169 rithm is needed to search for seeds, which are track segments that provide initial estimated track  
3170 parameters. These seeds are used to initialize the KF. Second, a set of arbitration rules need to be  
3171 applied before filtering to identify hits belonging to the track. A straightforward rule is to require  
3172 that the hit on the next measurement site fall within a window around the prediction. An alternative  
3173 rule is to cut on the  $\chi^2$  increment when a candidate hit is added [272].

3174 The whole simulation including all SoLID subsystems in their different respective configura-  
3175 tions is used for the tracking studies. Both signal tracks from various event generators and back-  
3176 ground produced by low energy particles, mostly photons, are included in the simulation data.

3177 At present, the track finding algorithm is being developed and tested for the different SoLID  
3178 configurations. For the SIDIS  $^3\text{He}$  configuration, using only one time-sample from the APV25  
3179 and GEM digitization, both the efficiency of the track finder and the probability of identifying all  
3180 correct hits of a track typically exceeds 90% for electron tracks in both the forward angle and the  
3181 large angle regions. For the PVDIS and  $J/\psi$  configurations, using three time-samples from the

3182 APV25 and GEM digitization, the efficiency is about 85% for electron tracks. The track finder  
 3183 also achieves a reasonable execution speed. We will study the possibility of using the current track  
 3184 finding algorithm with looser conditions to improve the reconstruction speed for the planned level-3  
 3185 data reduction farm.

3186 The track fitting algorithm is also being developed and tested for different SoLID configurations.  
 3187 The kinematic dependence of the reconstruction resolution of the track parameters for the SIDIS  $^3\text{He}$   
 3188 configuration is shown in Figure 131 as an example. Resolution values averaged over the kinematic  
 3189 ranges, obtained for the SIDIS  $^3\text{He}$  and PVDIS configurations, are summarized in Table 21.  $J/\psi$   
 3190 results are similar to SIDIS  $^3\text{He}$  results. In these studies, energy loss is included for all materials,  
 3191 except for materials in the dead areas of the GEM planes. Low energy photon background in the  
 3192 GEMs is also not included. Both of them could worsen the resolution. To make our current results  
 3193 conservative, we multiply all values by a safety factor of 1.5 when applying them to various physics  
 3194 studies. We will update the results with all effects included in near future.

3195 All SoLID physics programs are using these track resolutions in their studies by directly apply-  
 3196 ing the full kinematic dependent results.

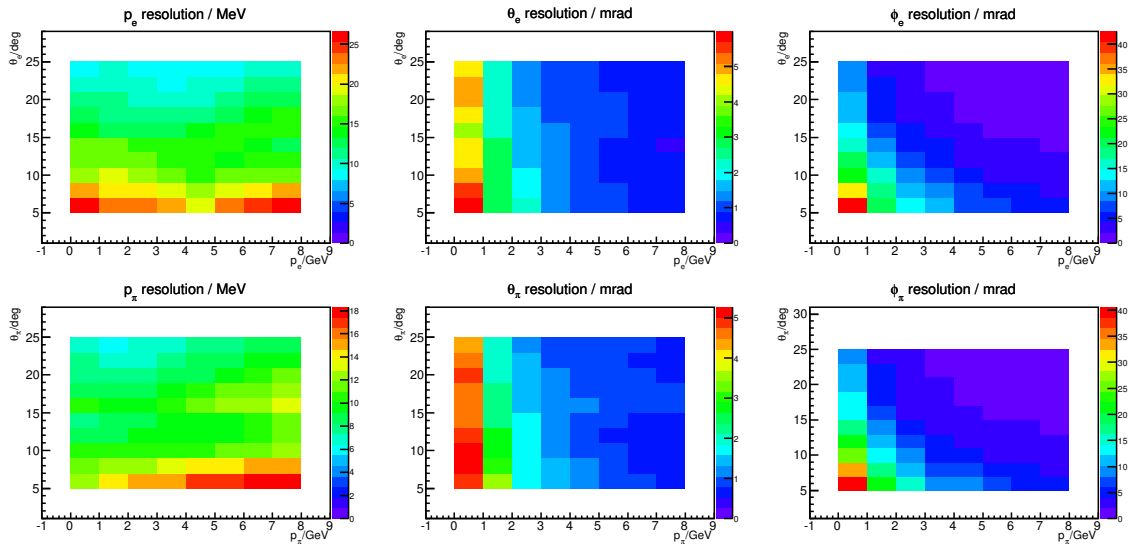


Figure 131: SIDIS  $^3\text{He}$  resolutions by track fitting studies with most of material energy loss and without background. The upper panels are the resolution of the electron kinematics. The lower panels are those of the pion kinematics. The variables are defined in lab frame with beam line as the  $z$ -axis.

	$\theta$ angle (mrad)	$\phi$ angle (mrad)	Vertex $z$ (cm)	$p$ (%)
SIDIS $^3\text{He}$ fwd angle ( $e$ )	1.3	5.7	0.9	1.7
SIDIS $^3\text{He}$ fwd angle ( $\pi$ )	1.2	5.2	0.9	1.1
SIDIS $^3\text{He}$ large angle ( $e$ )	1.0	1.7	0.5	1.2
PVDIS ( $e$ )	0.8	1.7	0.3	1.2

Table 21: Averaged resolutions by track fitting with most of material energy loss and without background

### 3197 **12.3.2 Additional Reconstruction Algorithms**

3198 Many existing detector reconstruction algorithms available in the Hall A analyzer [252] or in other  
3199 packages should be reusable for SoLID, for instance the Cherenkov photoelectron yield analysis and  
3200 the calorimeter clustering algorithm. While the basic physics algorithms can be adopted without  
3201 much change, code will have to be developed to support the cylindrical geometry of SoLID as well  
3202 as the individual local detector geometries. Furthermore, a likelihood-based particle identification  
3203 scheme or similar should be written. Development of calibration software tuned to the SoLID  
3204 detectors will be necessary as well.

3205 A high-level overview of the necessary algorithm development tasks can be found in Appendix  
3206 C, specifically in the spreadsheet referenced in that section [347].



## 3207 **13 Integration and Expected Performance**

### 3208 **13.1 Overview**

3209 System integration incorporates several tasks : 1) Quality control of the engineering of the appa-  
3210 ratus so that all the pieces fit and so that the system satisfies *all* of the experimental program with  
3211 minimal turnover between experiments; 2) Integration of the detectors so that they work together  
3212 and form efficient triggers, and so that we can predict the combined PID performance; 3) Control  
3213 of calibrations and systematic errors; and 4) Commissioning plans.

3214 In a preliminary engineering study done at Argonne National Lab by Paul Reimer, scenarios  
3215 for assembling and disassembling of the apparatus have been developed which allow for switching  
3216 rapidly between PVDIS and SIDIS, as well as for allowing other experiments to share Hall A during  
3217 the SoLID running era. We believe we can switch between running setups in approximately three  
3218 months.

3219 For the second topic, we have made a study of the combined particle ID using the gas Cherenkov  
3220 and the calorimeters, see Figure 132 where the resulting  $\pi/e$  ratios are shown. A similar PID perfor-  
3221 mance was achieved by the Hermes spectrometer [274]. Our study was performed by using the pion  
3222 rejection factor and electron efficiency as a function of the scattered angle and momentum for both  
3223 detectors for both the PVDIS and SIDIS configurations based on Geant simulations of the current  
3224 detector designs. The results here, shown for PVDIS, are preliminary since the detector designs  
3225 and the analysis strategies are still evolving. Nevertheless, the preliminary results are encouraging  
3226 and show that we can likely meet the requirements for the error in the pion contamination, which is  
3227  $10^{-3}$  for entire experimental program. We believe it may be possible to combine some information  
3228 with the shower shape in a multi-variable analysis to further improve the pion rejection. We are also  
3229 still considering the issues of rate dependence and pileup on the pion rejection factor.

3230 In the following sections, we will present the study of the acceptance, efficiency, systematics,  
3231 and calibration for various experiments.

### 3232 **13.2 SIDIS Program**

3233 The acceptance and efficiencies of the SIDIS configuration with a 40 cm long polarized  $^3\text{He}$  target  
3234 was studied using the whole simulation. The particles detected by the detectors were compared to  
3235 those of the original particles from a full-length target. We have good electron detection efficiency  
3236 from all sub-detectors. They vary slightly across the phase space and the average efficiency values  
3237 are shown in Table 22. The acceptance is  $\sim 0.7$  due to the two target window collimators. Fig-  
3238 ure 133 shows the combined effect of acceptance and efficiency (except tracking). We will continue  
3239 to fine-tune the design and the reconstruction algorithm to improve the efficiency.

Table 22: Average electron detection efficiencies of all SoLID sub-detectors and the total SoLID efficiency.

Detector	EC	Cerenkov	Scintillator pad and MRPC	GEM tracking	Total
average efficiency	95%	95%	98%	90%	80%

3240 We have conducted a careful study of the systematic uncertainties of the SIDIS experiments and  
3241 the results are presented below.

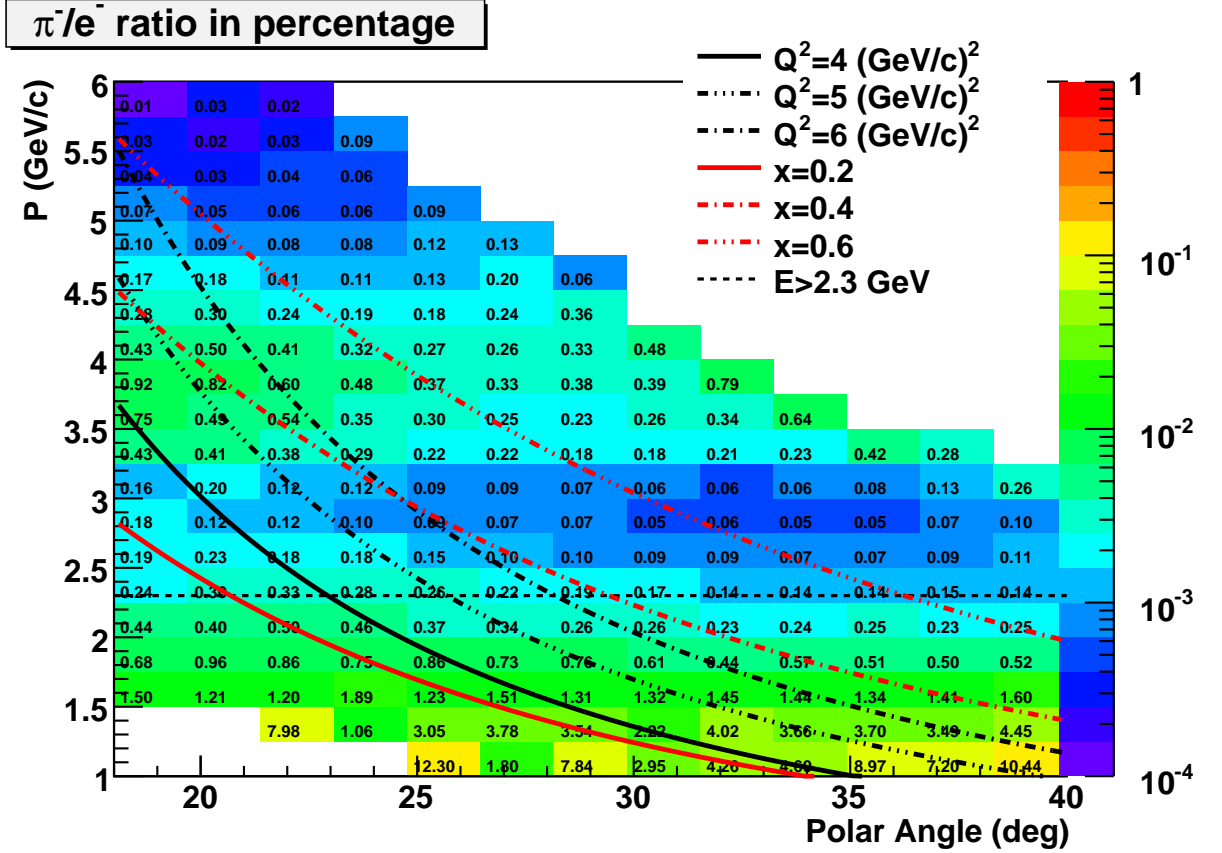


Figure 132: The  $\pi/e$  ratio from combined Cherenkov and Calorimeter detector performance as a function of the scattered momentum  $P$  and polar angle  $\theta$ . The numerical values are the ratios corresponding to that cell in  $(P, \theta)$ . The curves indicate various regions of  $Q^2$   $x$  or scattered energy  $E$ .

The SIDIS cross section is in general expressed as [275]

$$\frac{d\sigma}{dx dy dz dP_{h\perp}^2 d\phi_h d\phi_S} = \frac{\alpha^2}{xyQ^2} \frac{y^2}{2(1-\varepsilon)} \left(1 + \frac{\gamma^2}{2x}\right) [F_{UU}(x, z, Q^2, P_{h\perp}) + \text{asymmetric terms}]. \quad (18)$$

3242 In the simulation, we model the SIDIS cross section by assuming factorization to express the struc-  
3243 ture function as a convolution of TMD distribution and fragmentation functions

$$F_{UU}(x, z, Q^2, P_{h\perp}) = x \sum_a e_a^2 \int d^2k_{\perp} d^2p_{\perp} \delta^{(2)}(P_{h\perp} - p_{\perp} - zk_{\perp}) f_1^a(x, k_{\perp}) D_1^a(z, p_{\perp}). \quad (19)$$

The unpolarized TMD distribution function  $f_1(x, k_{\perp})$  and fragmentation function  $D_1(z, p_{\perp})$  are parameterized as

$$f_1(x, k_{\perp}) = f_1(x, Q^2) \frac{e^{-k_{\perp}^2/\langle k_{\perp}^2 \rangle}}{\pi \langle k_{\perp}^2 \rangle}, \quad (20)$$

$$D_1(z, p_{\perp}) = D_1(z, Q^2) \frac{e^{-p_{\perp}^2/\langle p_{\perp}^2 \rangle}}{\pi \langle p_{\perp}^2 \rangle}, \quad (21)$$

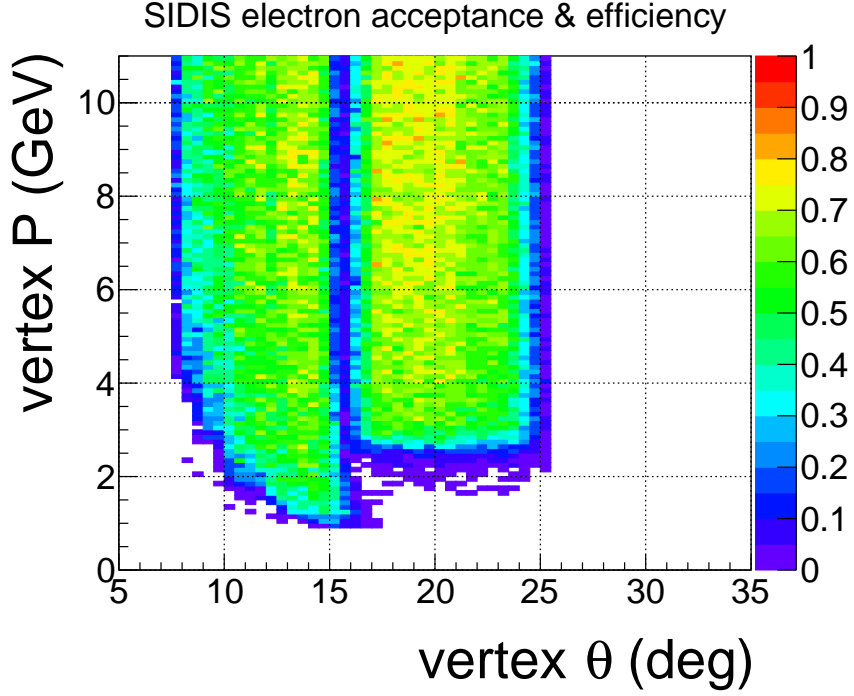


Figure 133: Electron acceptance and efficiency (except tracking) of SoLID SIDIS with the 40 cm  $^3\text{He}$  target and two target window collimators. The result for  $J/\psi$  has a similar shape, but higher values because it has a 15 cm long target and no collimator.

3244 where  $f_1(x, Q^2)$  and  $D_1(z, Q^2)$  are collinear distribution and fragmentation functions. In our simulation, we use CT14 leading order collinear PDF parameterization [276] and DSS leading order collinear FF parameterization [277]. The two parameters describing the transverse momentum dependence are chosen as  $\langle k_\perp^2 \rangle = 0.25$  and  $\langle p_\perp^2 \rangle = 0.20$  [278]. For the three leading twist single spin asymmetry (SSA) terms, the Sivers, the Collins, and the pretzelosity, we use the phenomenological models [279–281] as inputs to the simulation. To take into account the detector efficiency effect, we use 85% of the statistics for the estimation of the uncertainties.

Taking the advantage of the  $2\pi$  azimuthal coverage, we are able to reduce the systematic uncertainties associated with luminosity and detection efficiencies by defining the target single spin asymmetry as

$$A_{UT}(\phi_h, \phi_S) = \frac{2}{P_1 + P_2} \frac{\sqrt{N_1(\phi_h, \phi_S)N_2(\phi_h, \phi_S + \pi)} - \sqrt{N_1(\phi_h, \phi_S + \pi)N_2(\phi_h, \phi_S)}}{\sqrt{N_1(\phi_h, \phi_S)N_2(\phi_h, \phi_S + \pi)} + \sqrt{N_1(\phi_h, \phi_S + \pi)N_2(\phi_h, \phi_S)}}, \quad (22)$$

3251 where the subscripts 1, 2 represents a target spin flip pair.  $N_1(\phi_h, \phi_S)$  and  $N_1(\phi_h, \phi_S + \pi)$  are taken at the same time with target polarization  $P_1$ , while  $N_2(\phi_h, \phi_S)$  and  $N_2(\phi_h, \phi_S + \pi)$  are taken at the same time with target polarization  $P_2$ . Thus, the luminosity at different times will cancel. Since  $N_1(\phi_h, \phi_S)$  and  $N_2(\phi_h, \phi_S + \pi)$ ,  $N_1(\phi_h, \phi_S + \pi)$  and  $N_2(\phi_h, \phi_S)$  are taken in the same detector region, the acceptance and detector efficiency will also cancel to first order. The time-dependent detector efficiencies will be monitored with single electron and pion rates. With a  $^3\text{He}$  target spin flip rate of 1/(10 minutes) (20 minutes for each pair), we expect to control the time-dependent detector efficiency uncertainty to better than 1%. In 48 days with 11 GeV beam,

3259 we will have 3456 pairs, and in 21 days with 8.8 GeV beam, we will have 1512 pairs. Then, the  
 3260 systematic uncertainty of the raw asymmetry is estimated as  $1.0\%/\sqrt{3456} = 1.7 \times 10^{-4}$  for 11 GeV  
 3261 data, and  $1.0\%/\sqrt{1512} = 2.6 \times 10^{-4}$  for 8.8 GeV data. With a proton (ammonia) target spin flip  
 3262 rate of 1/hour (2 hours for each pair), we expect to control the time-dependent detector efficiency  
 3263 uncertainty to under 2%. In 55 days with 11 GeV beam, we will have 660 pairs giving an estimated  
 3264 systematic uncertainty of  $2.0\%/\sqrt{660} = 7.8 \times 10^{-4}$ . In 27.5 days with 8.8 GeV beam, will have  
 3265 330 pairs, and the systematic uncertainty is estimated as  $2.0\%/\sqrt{330} = 1.1 \times 10^{-3}$ . The derived  
 3266 absolute systematic uncertainties of the SSA data associated with the raw asymmetry are obtained  
 3267 by dividing these numbers by the target polarization and the dilution factor in each bin.

3268 The knowledge of the target polarization is at the 3% level. This translates to a 3% relative  
 3269 systematic uncertainty of the SSA data. The knowledge of the target polarization direction is about  
 3270 0.2 degree. The corresponding uncertainty of the target polar angle translates into  $6 \times 10^{-6}$  relative  
 3271 uncertainty of the SSA. The uncertainty of the target azimuthal angle is included in the uncertainty  
 3272 of the azimuthal angle  $\phi_S$  together with the detector resolution effect.

3273 The systematic uncertainties associated with detector resolutions are estimated based on the  
 3274 track fitting studies. The resolutions of the kinematic variables in the Trento convention for each  
 3275 bin are obtained by Monte Carlo sampling according to the resolutions of the lab frame variables  
 3276 shown in Figure 131. The resolutions of the kinematical variables in the Trento convention are  
 3277 summarized in Table 23. The systematic uncertainty associated with the resolution mostly come  
 3278 from the uncertainties of the azimuthal angles  $\phi_h$  and  $\phi_S$  which affect the separation of the SSA  
 3279 terms. It is estimated by smearing the pseudo-data according to the resolution, separating the SSA  
 3280 term with the smeared pseudo-data, and then comparing them to the model input of the simulation.  
 3281 The absolute systematic uncertainty of the SSA due to the resolution is less than  $1 \times 10^{-4}$ , which  
 3282 is negligible compared to the other uncertainties.

$E_{\text{beam}}$ (GeV)	$x$	$z$	$Q^2$ (GeV <sup>2</sup> )	$P_{h\perp}$ (GeV)	$\phi_h$ (rad)	$\phi_S$ (rad)
11	0.002	0.003	0.02	0.006	0.015	0.006
8.8	0.002	0.004	0.02	0.006	0.018	0.006

Table 23: Resolution of kinematical variables (in the Trento convention) with the <sup>3</sup>He target setup.

Nuclear effects contribute to the systematic uncertainty when we extract the SSA of the neutron from <sup>3</sup>He data. We derive the SSA of the neutron from that of <sup>3</sup>He as

$$A_n = \frac{A_{^3\text{He}} - 2P_p f_p A_p}{P_n f_n}, \quad (23)$$

3283 where the SSA of proton  $A_p$  will also be measured with SoLID in the same kinematic region. We  
 3284 assign 10% relative uncertainty of the knowledge of the proton SSA. The  $f_{p/n}$  are the dilution fac-  
 3285 tors associated with the hydrogen and the <sup>3</sup>He target, respectively. The light-front spectral function  
 3286 of <sup>3</sup>He including the final state interaction effect was recently developed [282]. With a theoret-  
 3287 ical calculation of the nuclear effect of the SSAs in the SoLID kinematic region [283], we estimate  
 3288 that the relative uncertainty in the extraction of the neutron SSAs due to the nuclear effect is about  
 3289 4~5%.

3290 The random coincidence background is estimated using single electron and single pion rates.  
 3291 By assuming a 1 ns time resolution, we choose a plus-minus three-sigma time window of 6 ns.  
 3292 For the <sup>3</sup>He target, we also apply a three-sigma vertex cut according to the track fitting results. As  
 3293 the SIDIS signal rate drops with increasing  $P_{h\perp}$ , we summarize the signal background ratio with

3294 respect to  $P_{h\perp}$  in Table 24. The relative systematic uncertainties due to the random coincidence  
 3295 background are estimated by varying the background rate by 20% for each bin.

$P_{h\perp}$ (GeV/c)	[0.0, 0.2]	[0.2, 0.4]	[0.4, 0.6]	[0.6, 0.8]	[0.8, 1.0]	[1.0, 1.2]
11 GeV beam ( $\pi^+$ )	110	160	150	105	75	40
11 GeV beam ( $\pi^-$ )	120	160	140	90	70	50
8.8 GeV beam ( $\pi^+$ )	75	95	80	50	45	
8.8 GeV beam ( $\pi^-$ )	65	95	75	50	45	

Table 24: The ratio of SIDIS signal and random coincidence background within 6 ns. These values are estimated with the  $^3\text{He}$  target. Similar results are obtained for the proton target.

3296 The radiative correction effect of SIDIS is simulated with HAPRAD, which was developed  
 3297 based on the QED calculation to one-loop level [284, 285]. The systematic uncertainties from the  
 3298 radiative corrections are estimated by varying the model parameters  $\langle k_{\perp}^2 \rangle$  and  $\langle p_{\perp}^2 \rangle$  of the SIDIS  
 3299 model in our simulation by a factor of 2 (multiplied and divided). This gives relative uncertainties  
 3300 of about 2.5% for the 11 GeV data and about 2% for the 8.8 GeV data. A summary of the systematic  
 3301 uncertainties is in table 25.

Table 25: The systematic uncertainties on the asymmetry measurements of SIDIS.

Systematic (abs.)		Systematic (rel.)	
Raw asymmetry	0.0014	Target polarization	3%
Detector resolution	< 0.0001	Nuclear effect	(4 – 5)%
		Random coincidence	0.2%
		Radiative correction	(2 – 3)%
		Diffraction meson	3%
Total	0.0014	Total	(6 – 7)%

### 3302 13.3 PVDIS Program

#### 3303 13.3.1 Acceptances, efficiencies, and systematic uncertainties for PVDIS

3304 We now have a full Monte Carlo simulation that includes all elements of the PVDIS apparatus, layer  
 3305 by layer energy deposition in the electromagnetic calorimeter (EC) and optical physics in the light  
 3306 gas Cherenkov (LGC). At present we have preliminary GEM responses and tracking under realistic  
 3307 backgrounds, both of which are under continued development. We now also have recent data from  
 3308 newly constructed GEMs which are being employed at Jefferson Lab to refine our simulations. For  
 3309 the present results, true values of track hit positions in the GEMs are used. Neither the GEMs nor  
 3310 the calorimeter are segmented in the simulation. However, since the GEM sector boundaries will be  
 3311 far from the baffle-defined signal regions and the tracks entering the EC will not be parallel to the  
 3312 module boundaries, the effects of GEM and EC segmentation on our acceptance are expected to be  
 3313 negligible.

3314 Input events to the Monte Carlo are electrons from a DIS generator using cross sections from  
 3315 CTEQ6 parton distribution fits [286]. Our analysis integrates primary electrons which reach the  
 3316 active area of the EC after passing through the active areas of all five GEMs and the front window  
 3317 of the LGC. The acceptance is shown in Figure 134 as a function of  $p$  and  $\theta$  (left panel) and as a

3318 function of  $Q^2$  and  $x_{bj}$  (right panel). Lines on these plots show the boundaries of the kinematic  
 3319 region of interest:  $Q^2 > 6 \text{ GeV}^2$ ,  $W > 2 \text{ GeV}$ , and  $x_{bj} > 0.55$ . Our acceptance in this region is  
 3320 typically 40%.

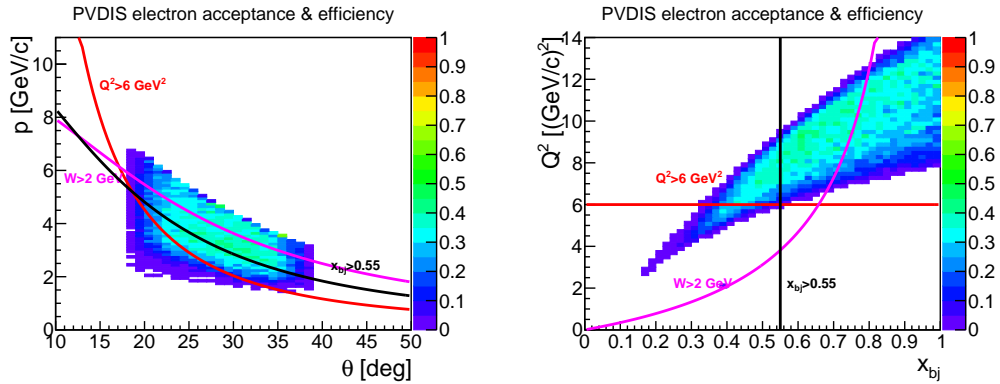


Figure 134: Left: PVDIS acceptance and efficiency as a function of  $p$  and  $\theta$ . Right: PVDIS acceptance and efficiency as a function of  $Q^2$  and  $x_{bj}$ . Curves show bounds of the kinematic range with  $Q^2 > 6 \text{ GeV}^2$ ,  $W > 2 \text{ GeV}$ , and  $x_{bj} > 0.55$ .

3321 Contributions to the efficiency are as follows:

3322 *Calorimeter:* Efficiency of  $\sim 95\%$  as reported in subsection 10.7.

3323 *LGC:* With the changes of the radiator gas and PMT quantum efficiency, new studies of the  
 3324 LGC efficiency need to be undertaken. Requiring  $\geq 2$  photoelectrons in each of  $\geq 2$  PMTs in the  
 3325 sector matching the EC yields 96% efficiency.

3326 *Tracking:* The GEM detection efficiency is 97% per plane. From our studies using a tree search  
 3327 algorithm with realistic and correlated superimposed backgrounds and our current model of digi-  
 3328 tization, a track finding efficiency of  $\sim 90\%$  appears to be achievable. Development of the track  
 3329 finding software is continuing.

3330 Combining the above contributions yields an estimate of 82% for our overall efficiency.

3331 The systematic errors on our measurement of the parity violating asymmetry are summarized in  
 3332 Table 26.

3333 The systematic error on the polarization of the beam  $\Delta P/P$  is required to be better than 0.4%  
 3334 [287]. The best achievable precision of such measurements is 0.6% at present, but 0.4% are consid-  
 3335 ered to be within reach [288]. The dominant systematic error in [287] is the laser polarization, which  
 3336 was estimated to be 0.3% but is given in [288] to be below 0.2%. The higher analyzing power and  
 3337 large-angle characteristics of the 11 GeV beam relative to the Qweak 1 GeV beam result in a better  
 3338 precision for SoLID. We also expect better to understand the systematic errors of the polarimetry  
 3339 by building on the experience of the MOLLER experiment, where polarimetry plays a particularly  
 3340 important role.

3341 The radiative corrections are similar to those computed for the HERA experiments [289]. Many  
 3342 of the important radiative corrections come from tails of events at larger  $x$ , which are small for the  
 3343 SoLID high- $x$  kinematics. We have assembled a team including A. Aleksejevs, S. Barkanova and  
 3344 W. Melnitchouk, who will assist in performing the necessary calculations. We estimate an error of  
 3345 0.2% from radiative corrections.

3346 Finally, systematics on the asymmetry due to reconstruction errors, including DAQ issues and  
 3347 particle identification, will be kept to the 0.2% level. The pion contamination is expected to be

3348 below 1% for most bins and the required corrections should be valid to at least 10% of that. Work  
 3349 on the DAQ is in progress to demonstrate that the pile-up and dead-time corrections can be kept to  
 3350 below 0.15%.

3351 The total systematic error is 0.6%, unchanged from the proposal value, allowing sufficient sen-  
 3352 sitivity to meet our physics goals.

Polarimetry	0.4
$Q^2$	0.2
Radiative corrections	0.2
Reconstruction errors	0.2
Total	0.6

Table 26: Summary of PVDIS systematic errors, in percent.

### 3353 13.3.2 Kinematics, Resolution and Calibration for PVDIS

3354 In this section, we describe the general method of measuring the momentum  $p$  and the scattering  
 3355 angle  $\theta$  of each track. In addition, we discuss the resolution of  $x$ , and  $Q^2$ , the relevant variables  
 3356 for the analysis. Finally, we discuss the calibration of the average value of  $Q^2$ . The most critical  
 3357 requirements are the the  $x$  resolution is on the order of 0.01 to avoid kinematic smearing and that  
 3358 the average  $Q^2$ , which is proportional to the asymmetry, is calibrated to 0.1%.

3359 The method that we use to reconstruct the tracks, determining the scattering angle and momen-  
 3360 tum, is easiest to understand in the approximation of a uniform field. Based on this method, we can  
 3361 explain our alignment tolerances and systematic errors. We then show how to make the corrections  
 3362 for the realistic case. These corrections do not alter most of the tolerances.

3363 First, we look at the track in the  $x$ - $y$  plane. This is given in Figure 135. All we require is hits  
 3364 in two GEM detectors. The one closest to the target is labeled GEM<sub>*i*</sub> and the other is GEM<sub>*j*</sub>. Since  
 3365 the beam is small (300  $\mu\text{m}$  by 250 $\mu\text{m}$ ), it provides a third point which is sufficient to determine the  
 3366 radius of curvature  $\rho$  of the helix. The transverse momentum of the electron is then  $\kappa/\rho$ , where  $\kappa$   
 3367 is a constant proportional to the magnetic field. The transverse distance between the beam and the  
 3368 first GEM is  $R$  and between the two GEM's is  $D$ . The angle between the line segments  $R$  and  $D$  is  
 3369  $(\psi + \delta)/2$ . From the diagram, we have

$$\frac{1}{\rho} = \frac{2(\sin(\psi/2) + \sin(\delta/2))}{(R + D)} \approx \frac{\psi + \delta}{R + D}, \quad (24)$$

3370 where the approximation is for small angles. Since

$$\frac{\sin(\psi/2)}{\sin(\delta/2)} = \frac{R}{D}$$

3371 and  $(\psi + \delta)/2$  is measured, Eq. 24 can be evaluated exactly.

3372 For the helix, the angle  $\theta$  between the trajectory and the  $z$ -direction is constant, and thus is the  
 3373 scattering angle. If  $\Delta z$  is the difference in the  $z$ -coordinates of the GEM's, then

$$\tan \theta = \frac{\rho}{\Delta z} \sin^{-1} \frac{D}{\rho} \approx \frac{D}{\Delta z}. \quad (25)$$

3374 From the approximation, we see that the error in  $\rho$  contributes little to the error in  $\theta$ .



3375

Finally, we note that

$$Q^2 = 4E^{\frac{\kappa}{\rho}} \tan(\theta/2).$$

3376

Thus the fractional error in  $Q^2$  is the sum in quadrature of the fractional errors in  $\rho$  and  $\theta$ .

3377

Thus with two GEM points and a narrow beam, we can reconstruct the important variables

3378

for DIS. In addition, the distance  $r$  from the first GEM to the beam line in the  $x$ - $y$  plane and

3379

the azimuthal angle of the first GEM hit are measured. The first can be used to determine the  $z$ -

3380

coordinate of the interaction, which can be used as a check that the track is valid and also determine

3381

if it came from the front or rear target windows.

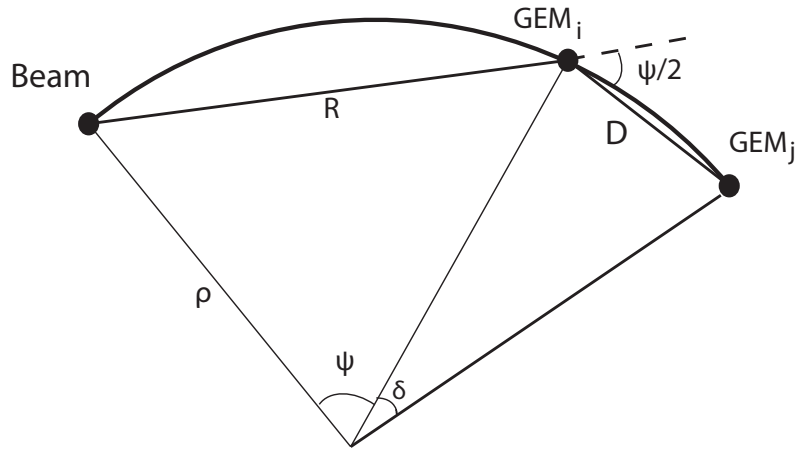


Figure 135: Projection of the track in the  $x - y$  plane. The projected radius of curvature is  $\rho$ .

3382

For realistic magnetic fields, we generated with our Monte Carlo many trajectories and deter-

3383

mined the discrepancies with Eqs. 24 and 25. These discrepancies could be parameterized in terms

3384

of the measured variables  $\psi + \delta$ ,  $D$ ,  $R$ , and  $r$  and used as corrections. With the corrections,  $\rho$  and

3385

$\theta$  can be determined from the GEM hits with a precision better than 0.1%.

3386

Rather than  $\psi + \delta$ , we used the angle  $\alpha$  between the line segment  $R$  and the line joining the

3387

beam with the hit in  $GEM_j$ . Then

$$\alpha \approx \frac{\psi + \delta}{2} \frac{D}{R + D},$$

3388

and

$$\frac{1}{\rho} = \frac{2\alpha}{D}.$$

3389

Thus our precise and realistic equation for  $\rho$  is

$$\frac{1}{\alpha\rho} = \frac{2}{D} + F_\rho(R, D, r, \Delta z). \quad (26)$$



3390 An important feature is that the angle  $\alpha$  only appears in the left side. This feature is useful for our  
 3391 momentum calibration method shown below. For  $\theta$ ,

$$\tan \theta = \frac{D}{\Delta z} + F_\theta(R, D, r, \Delta z, \alpha). \quad (27)$$

3392 There are two effects that contribute to  $F_\theta$ . The first is the approximation in Eq. 25. The second is  
 3393 the fact that radial components of the magnetic field change the angle that the trajectory makes with  
 3394 the  $z$ -axis. Thus  $F_\theta$  depends slightly on  $\alpha$ .

3395 Since  $F_\rho$  and  $F_\theta$  are small, the errors in their arguments do not contribute significantly to the  
 3396 errors in  $\rho$  or  $\theta$ . The requirements for calibration can be obtained from the leading approximations.

3397 The momentum resolution, which is dominated by multiple scattering, mostly in the air, is about  
 3398 1%, independent of momentum. The angular resolution, dominated by GEM resolution, is about  
 3399 0.5%. The resolution in  $Q^2$  is 1.5% and in  $x$  is 1%. The  $z$ -resolution is 7 mm. These numbers are  
 3400 obtained with our simulation with realistic GEM signals.

3401 The first step in momentum calibration is alignment of the GEM trackers. To make estimates  
 3402 of the systematic errors in track momentum reconstruction we use artificial displacements of GEM  
 3403 hits in our simulation. In the simple case of a uniform field and a thin target the minimum distance  
 3404 between the beam axis and the line through two GEM hits is linearly related to  $1/p$ . That distance  
 3405 is of order 10 cm, implying a need to calibrate the GEM transverse positions to  $\sim 100 \mu\text{m}$  in order  
 3406 to achieve a systematic error on the relative momentum  $\Delta p/p$  of order  $10^{-3}$ .

3407 For a more realistic estimate we use a Monte Carlo simulation incorporating a realistic field  
 3408 and a long target to study the effects on our momentum and angle reconstruction of all elementary  
 3409 displacements: lateral and transverse position shifts, and rotations in and perpendicular to the de-  
 3410 tector plane, of one or both GEMs. Results are shown in Table 27. Due to the symmetry of the  
 3411 apparatus,  $Q^2$  is insensitive to all these misalignments to first order except for single GEM angular  
 3412 displacement in-plane. We find that we need to understand transverse GEM positions relative to  
 3413 straight tracks to within about  $200 \mu\text{m}$ , and absolute positions parallel to the beam axis at the level  
 3414 of about 3 mm.

1/p and $\theta$ residuals for GEMs 1, 4					
transform	GEM(s)	$\delta p(\text{mean})$	$\delta p(\text{width})$	$\delta \theta(\text{mean})$	$\delta \theta(\text{width})$
transverse displacement	1, 4	-0.01%/mm	0.77%/mm	0.00%/mm	0.00%/mm
	4	0.00%/mm	0.76%/mm	0.00%/mm	0.08%/mm
longitudinal displacement	1, 4	0.05%/mm	0.00%/mm	0.00%/mm	0.00%/mm
	4	0.08%/mm	0.01%/mm	0.06%/mm	0.00%/mm
in-plane rotation	1, 4	0.00%/mrad	0.00%/mrad	0.00%/mm	0.00%/mm
	4	<b>1.61%/mrad</b>	0.15%/mrad	0.01%/mm	0.01%/mm
out-of-plane rotation	1, 4	0.00%/mrad	0.08%/mrad	0.00%/mm	0.03%/mm
	4	0.00%/mrad	0.09%/mrad	0.00%/mm	0.06%/mm

Table 27: Momentum and angle reconstruction sensitivities to various displacements of GEMs 1 and 4: transverse, longitudinal, and rotational (in and perpendicular to the detector plane) displacements of both GEMs or of GEM 4 only. “ $\delta p(\text{mean})$ ” and “ $\delta \theta(\text{mean})$ ” are the changes in the mean of the  $1/p$  and  $\theta$  residuals and “ $\delta p(\text{width})$ ” and “ $\delta \theta(\text{width})$ ” are the changes in those residuals’ width per unit displacement. Due to detector symmetry, the displacement to which we are most sensitive is single GEM in-plane rotation.

3415 Within a GEM, strip positions relative to one another will be known to within  $25 \mu\text{m}$ . With  
 3416 standard surveys, relative strip positions within a full GEM plane can be established to better than  
 3417  $500 \mu\text{m}$ . To achieve our resolution goal and to monitor possible motion of the tracking chambers,  
 3418 straight-through electrons with the magnetic field off and low energy photons with the field off and  
 3419 on will be used to calibrate the relative transverse positions of the GEMs with the required precision.  
 3420 A thin carbon target about 10 cm upstream of the LD<sub>2</sub> target has lines of sight to most of the area  
 3421 of the GEMs, as shown in Figure 136. For x-ray studies, an absorber ring with holes, or conversely  
 3422 a set of absorbing beads mounted on a ring of light material, will provide the fiducials.

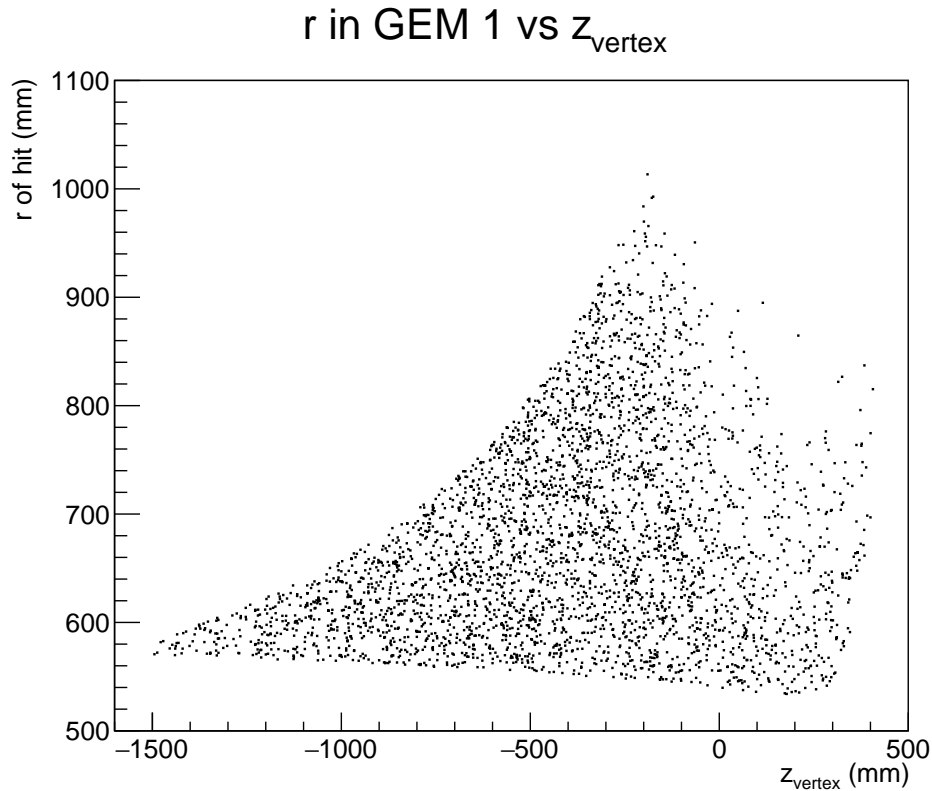


Figure 136: Radial coordinates of photon hits in GEM 1 versus vertex  $z$  position. Most of the detector area is covered for vertex at  $z = -200$  mm, corresponding to a position about 10 cm upstream of the LD<sub>2</sub> target. Similar results are seen in the other GEMs.

3423 Once the positions of the GEMs are known, the magnetic field is calibrated as follows. First  
 3424 a map is obtained with a precision of about 1%. With this map the radial fields are known well  
 3425 enough so that  $F_{\theta}$  can be precisely determined. To improve the calibration of the momentum to the  
 3426 0.1% level, we use electron hydrogen elastic scattering data at beam energies of 4.4 and 6.6 GeV as  
 3427 well as at different magnetic field settings. Since the beam energy is known to better than 0.1% and  
 3428 the angle can be measured to that precision, the location of the elastic peak provides a calibration  
 3429 of the magnetic field. One issue is that for one beam energy, there is only one track energy at each  
 3430 angle, whereas for DIS, the angle and energy are much less correlated. However, the correction  $F_{\rho}$   
 3431 in Eq. 26 is independent of  $\alpha$ , so a single momentum at each angle is sufficient. In other words, the  
 3432 importance difference between two similar fields is the value of  $\int B_z ds_{\perp}$  which is a scale factor for  
 3433 all momenta. Hence a single momentum from the elastic scattering is sufficient to make a precise

3434 correction.

3435 Clean separation of the elastic peak will be required. Figure 137 shows results from simulations  
3436 where the green histograms are elastics and the blue histograms are the inelastic background from a  
3437 Christy-Bosted parameterization [290]. Target and detector materials were included and momenta  
3438 were smeared by 1% to simulate detector resolution. At both energies the elastic peaks are cleanly  
3439 resolved. Rates are ample for calibration; see Figure 138. At 6.6 GeV, the integrated rate is about  
3440 150 Hz per  $\mu\text{A}$  of beam current. At 50  $\mu\text{A}$ , sufficient data can be collected in only a few minutes.

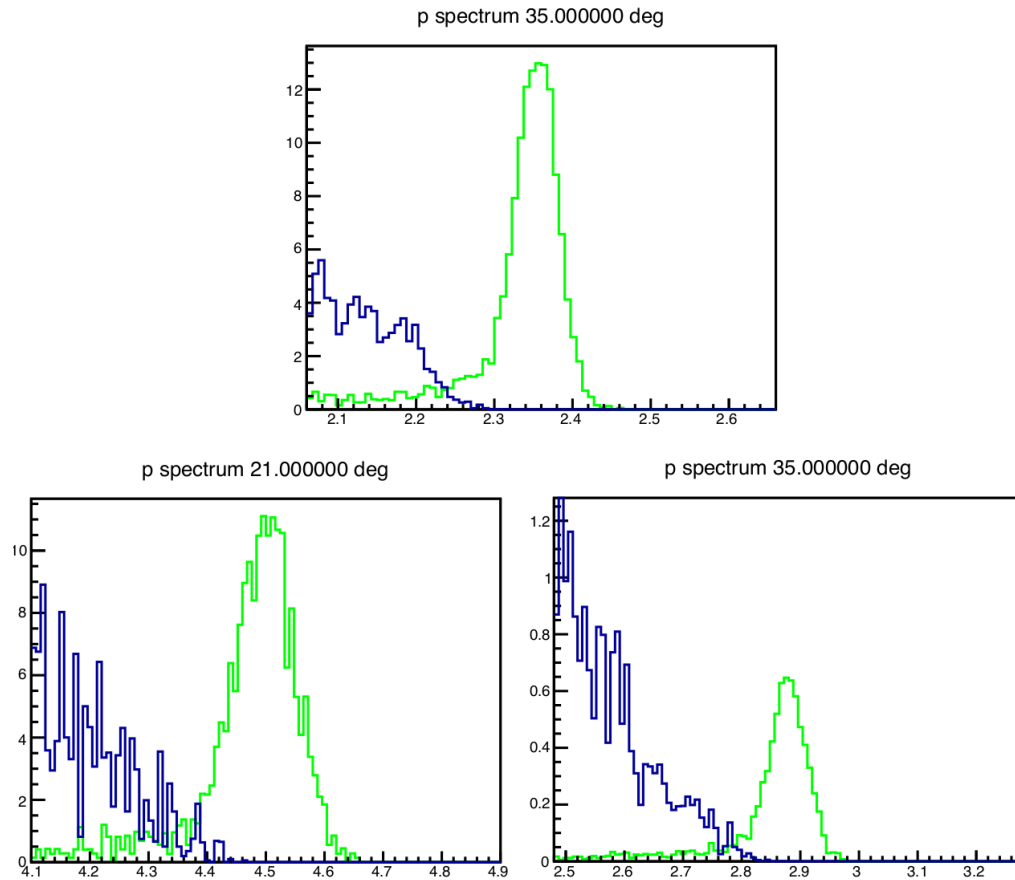


Figure 137: Elastic (green) and inelastic (blue) spectra for 4.4 GeV (top) and 6.6 GeV (bottom) electrons on a hydrogen target, at scattering angles of  $21^\circ$  (bottom left) and  $35^\circ$  (top and bottom right).

### 3441 13.4 $J/\psi$ Program

3442 Recent simulation studies of  $J/\psi$  production have been performed including approximate radiative  
3443 effects. External bremsstrahlung was applied to both the incident and scattered electrons. The inci-  
3444 dent electron radiation loss is calculated with the peaking approximation through the target material  
3445 up to the reaction vertex. The external radiative loss for the scattered electron is calculated within  
3446 the framework of Geant4/GEMC and folded into the total resolution smearing of the track. Internal  
3447 bremsstrahlung is calculated according to the  $Q^2$  dependent equivalent radiator method, and applied

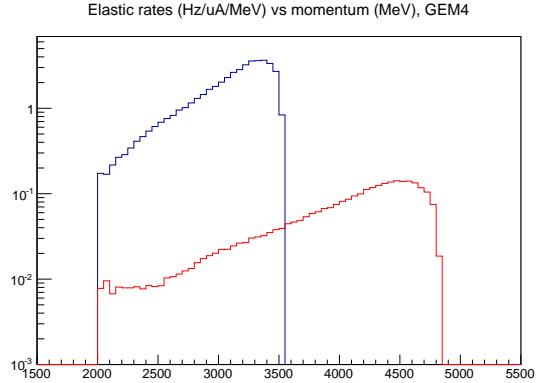


Figure 138: Elastic rates at GEM 4 for 4.4 GeV/c (blue line) and 6.6 GeV/c (red line) electrons on LH2, as a function of momentum in MeV/c. Rates are in Hz per  $\mu\text{A}$  per MeV/c. Target and detector materials are included.

3448 to both the incident and scattered electrons. These radiative calculations are well known and widely  
 3449 used and have historically described radiative losses with reasonable precision. A more robust and  
 3450 explicit calculation would allow for a more precise unfolding of the radiative losses, however such  
 3451 an endeavor is non-trivial and would require a significant investment of manpower. For the approxi-  
 3452 mate calculations, one can see in Figure 139 the effects of bin-migration along  $W$ , and the estimated  
 3453 correction needed to recover the unradiated cross-section. The plotted calculations were simulated  
 3454 with a 4-fold coincidence; the 3-fold coincidence has identical radiative losses (incident electron,  
 3455 scattered electron). Additionally, the internal radiative corrections in the equivalent radiator method  
 3456 are near zero when in the quasi-real photon kinematics of the 2-fold coincidence measurement. We  
 3457 plan to continue developing our radiative corrections procedure with exact calculations, accurate  
 3458 unfolding, and tests of model dependence.

3459 A physics generator which includes acceptance effects was developed for the experiment pro-  
 3460 posal and has since been extended to include resolution effects and the radiation effect approxima-  
 3461 tions outlined above.

3462 Because the  $J/\psi$  experimental configuration is very similar to the SIDIS setup: a target position  
 3463 offset by 35 cm being the only difference. the acceptance and efficiencies are in-line with the SIDIS  
 3464  $^3\text{He}$  program shown in Figure 133 and Table 22. The only difference is that the  $J/\psi$  setup has  
 3465 higher acceptance because its 15 cm long LH2 target requires no collimators as SIDIS  $^3\text{He}$

3466 As stated in the original proposal, we expect the systematic uncertainty to be dominated by the  
 3467 acceptance ( $<10\%$ ), with an additional contribution of a few percent from sub-detectors, luminosity,  
 3468 target windows and background contaminations. We take the total systematic uncertainty to be 11%.  
 3469 Without radiative corrections of the data, systematics due to bin migration can be estimated from  
 3470 Figure 139. However, much of these systematics can be corrected by accurately simulating and  
 3471 properly unfolding the radiative effects (see section above).

3472 An updated analysis of the  $J/\psi$  experiment's di-lepton trigger from the decay lepton pairs and  
 3473 triple lepton trigger with additional scattered electron were preformed, similar to what the PVDIS  
 3474 and SIDIS  $^3\text{He}$  programs have done. This simulated trigger study included the signal and combi-  
 3475 natorial background from leptons, pions, and additional hadrons over both forward and large angle  
 3476 acceptance including the most up-to-date EC, LGC, and SPD response. The resulting di-lepton  
 3477 trigger and triple lepton trigger are calculated to have a coincidence rate about 60 kHz and 30 kHz

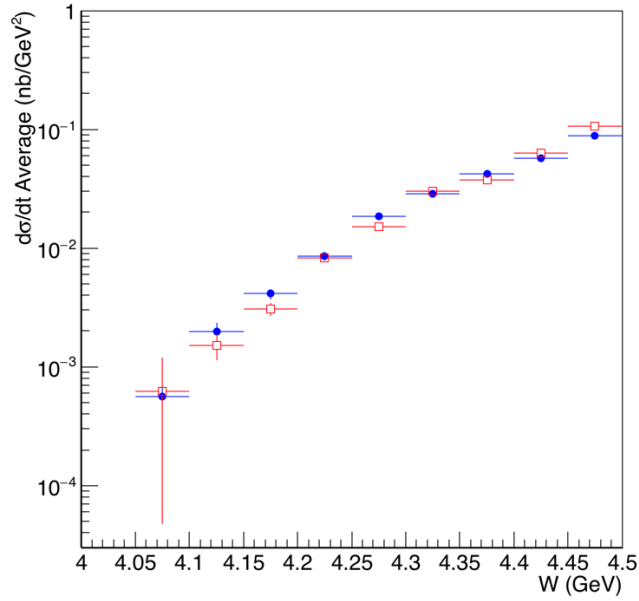


Figure 139: Simulation of cross-section including acceptance effects but no additional radiative losses (blue circles) for comparison with the expected cross-section measurement including acceptance smearing and all radiative effects listed in the text (red squares).

3478 respectively. The triple lepton trigger will be our main trigger and it's also possible to take some  
 3479 pre-scaled di-lepton trigger to preserve photoproduction data. We are working on improving the  
 3480 trigger rate estimation and fine tuning the trigger design to see what's the best way to maximize the  
 3481 physics program under reasonable trigger limit.

## 3482 14 Data Acquisition

### 3483 14.1 Introduction and Requirements

3484 The SoLID detector is a large acceptance detector designed to run at high luminosity. The detector  
3485 will operate in two basic configurations: the parity-violating electron scattering (PVDIS) config-  
3486 uration and the semi-inclusive deep inelastic scattering (SIDIS) configuration. The experiments  
3487 planned under these configurations have in common a large number of channels (over 160,000  
3488 GEM tracking channels and over 4,000 trigger/particle ID channels), high background rates, and  
3489 high trigger rates.

3490 We use the whole detector simulation with various experimental configurations to study the trig-  
3491 ger as mentioned in Section 12.2. The high energy primary particles are from event generators such  
3492 as a single electron generator, a SIDIS pion generator and the modified Hall D hadron generator.  
3493 All secondary particles are generated by Geant4. Low energy particles, primarily from electromag-  
3494 netic processes, are produced by Geant4 directly from beam electrons on the target. The response  
3495 in various detectors are examined event by event according to a given trigger configuration. Low  
3496 energy background and pile up effect are taken into account. The expected trigger rates are shown in  
3497 Table 28 for different experimental setups. (The trigger simulation will be updated as the simulation  
3498 tools are improved and additional information becomes available from JLab 12 GeV data and DAQ  
3499 tests.)

3500 The SIDIS configuration, with an expected trigger (coincidences and accidentals) rate of  $\sim 100$   
3501 kHz and total data rate of over 3 GB/s represents the greatest challenge for SoLID data acquisition.  
3502 For PVDIS, the DAQ requirement is more modest as the  $\sim 450$  kHz rate is divided among 30 parallel  
3503 DAQ systems, following the segmentation provided by the baffle system. However, there are addi-  
3504 tional challenges as the DAQ systems for adjacent sectors must communicate trigger information  
3505 and data for events where calorimeter showers extend into adjacent sectors.

3506 We present here a conceptual design for a DAQ system based on modest evolution of current  
3507 technology, much of which has been developed at JLab. Considering the large number of channels,  
3508 the rate requirements and the availability of new electronics developed for the Hall D GlueX de-  
3509 tector, a pipelined electronics approach has been chosen. These electronics continuously digitize  
3510 the detector signals, keeping the data in several microsecond deep buffers which can be retrieved  
3511 after a trigger is received. With these electronics, the First Level Trigger (L1) is generated primarily  
3512 from prompt data streams from Flash Analog to Digital Converters (FADC). This gives the ability  
3513 to reprogram trigger algorithms without the need for re-cabling.

Experiment	PVDIS	SIDIS $^3\text{He}$	$J/\psi$
Trigger rate (expected) (kHz)	$15 \times 30$	100	30
Data rate (GB/s)	$0.2 \times 30$	3.2	2.5
Running time (days)	169	125	60
Total data (PB)	175	70	25

Table 28: Rates, run times and data total estimates for the PVDIS, SIDIS  $^3\text{He}$  and  $J/\psi$  experiments. For PVDIS, there are 30 sectors each of which has a separate DAQ.

### 3514 **14.1.1 SIDIS Trigger and Rate Estimate**

3515 Three experiments, E12-10-006 [291], E12-11-007 [292], and E12-11-108 [293], have been ap-  
3516 proved to measure single and double asymmetries of semi-inclusive deep-inelastic scattering (SIDIS)  
3517 ( $e, e'\pi^\pm$ ) with SoLID. As these experiments have similar reaction channels, they can share the  
3518 same DAQ system design. The required overall luminosity of E12-10-006 and E12-11-007 is  
3519  $10^{37}/\text{cm}^2/\text{s}$ , which is an order of magnitude higher than that of E12-11-108. Therefore, we will use  
3520 E12-10-006 as an example to illustrate the requirements of the SIDIS DAQ. The goal of the SIDIS  
3521 DAQ is to satisfy the requirement of  $\sim 100$  kHz trigger rate, see Section 14.2.1 for more information  
3522 about the limit.

3523 The SIDIS process requires the detection of both the scattered electron and the leading pion.  
3524 Therefore, a single electron trigger or a coincidence trigger of the electron and the hadron would  
3525 satisfy this need. The electron trigger for the large angle detector will be provided by the E&M  
3526 calorimeter at a threshold of about 3 GeV. Such a trigger is sensitive to both high energy electrons  
3527 and high energy photons (mostly from the  $\pi^0$  decay). A set of scintillator paddles, added in front of  
3528 the calorimeter, are incorporated into the trigger in coincidence, significantly suppressing triggers  
3529 from high energy photons.

3530 The electron trigger at the forward angle detectors will be formed by a coincidence of the Gas  
3531 Cerenkov detector, the E&M calorimeter, the scintillator paddle detector (SPD) and the Multigap  
3532 Resistive Plate Chamber (MRPC). Considering the kinematics of the scattered electrons from the  
3533 DIS process (e.g.  $Q^2 > 1 \text{ GeV}^2$ ), a position dependent energy threshold with a lower limit of 1  
3534 GeV in the E&M calorimeter will be used.

3535 The single electron trigger rate was estimated from simulation to be 116 kHz for the forward  
3536 angle calorimeter in coincidence with the Gas Cerenkov, SPD and MRPC. Adding 32 kHz for the  
3537 large angle calorimeter in coincidence with the SPD gives a total single electron rate of 148 kHz.  
3538 In order to keep the Level-1 trigger rate below 100 kHz, we plan to form a coincidence trigger  
3539 between the electron trigger and the charged hadron trigger with a 20 ns time window. The charged  
3540 hadron trigger using the calorimeter with the SPD and the MRPC is 20 MHz. The SIDIS processes  
3541 including charge pions and misidentified neutral pions and protons, has a coincidence trigger rate of  
3542 27 kHz. Other multiple hadron process can also contribute to coincidence rate of 12 kHz. Excluding  
3543 the true coincidence from SIDIS and multiple hadron process, we estimate an accidental coincidence  
3544 rate of 46 kHz with a 20 ns time window. Some single electron triggers will also be acquired. These  
3545 will be prescaled to about 15 kHz such that the total trigger rate remains below 100 kHz.

### 3546 **14.1.2 $J/\psi$ Trigger and Rate Estimate**

3547 The E12-12-006 experiment is designed to measure the cross section of the  $p(e, e'J/\psi)p$  reaction  
3548 at an unpolarized luminosity of  $1.2 \times 10^{37} N/\text{cm}^2/\text{s}$  with a proton target. A coincidence trigger  
3549 between the electron and positron from  $J/\psi$  decay will allow both electroproduction and photopro-  
3550 duction reactions to be recorded. By using an electron trigger similar to the SIDIS configuration,  
3551 with a different radially dependent EC trigger threshold, a rate of 60 kHz is estimated. Adding the  
3552 scattered electron into trigger to form a triple coincidence will reduce the trigger rate by a factor of  
3553 2 to 30 kHz.

### 3554 **14.1.3 PVDIS Trigger and Rate Estimate**

3555 The PVDIS measurement is based on the asymmetry of inclusive electron scattering between inci-  
3556 dent electrons of opposite helicity states. To achieve the needed statistical accuracy of this parity  
3557 violating asymmetry, high rates will be required in the detector. The rate over the whole detector



3558 is expected to be of the order of 500 kHz, above the trigger rates that can be handled by the JLAB  
3559 electronics. As the measurement is of singles inclusive electrons, the detector electronics can be  
3560 divided into 30 sectors (corresponding to the baffle arrangement) each with a separate trigger, giv-  
3561 ing an acceptable rate for each sector. For each sector, the trigger will be a coincidence between  
3562 the gas Cerenkov and electromagnetic calorimeter. Based on our simulations of the inclusive elec-  
3563 tron rate and accidentals (with a 30 ns coincidence window) between singles in the electromagnetic  
3564 calorimeter and the Cerenkov counter, the estimated trigger rate is 15 kHz per sector.

## 3565 **14.2 DAQ Hardware and Trigger**

3566 The DAQ system for SoLID will use modules recently developed for Hall D by the JLab Physics Di-  
3567 vision Fast Electronics and Data Acquisition groups. These include flash ADCs (FADC250), VXS  
3568 Trigger Processors (VTP) and Global Trigger Processors (GTP), Sub-System Processors (SSP),  
3569 Trigger Supervisors (TS), Trigger Interface (TI), and Signal Distribution (SD) modules.

3570 Analog signals are digitized by the JLab FADC250, a 16-channel 12-bit flash analog to digital  
3571 converter sampling at 250 MHz. The input signals are continuously recorded into a memory with a  
3572 depth of up to 8  $\mu$ s with event data latched by a trigger. The system is dead-timeless as long as the  
3573 latched data can be readout as fast as it is generated.

3574 In addition to making data available for readout when triggered, the FADC250 is capable of  
3575 sending continuous digitized data over high speed VME switched Serial (VXS) lanes on the back-  
3576 plane connector. This data, a 16 bit word per module every 4 ns, could be a digital sum of the 16  
3577 channels of the ADC or more complex information.

3578 Each crate will have a VXS Trigger Processor (VTP) which receives a 16 bit word from each  
3579 FADC250 every 4 ns. The VTP processes the data stream from each module in the crate to generate  
3580 a 32-bit word every 4 ns. This word, which could be, for example, a sum of all the channels in the  
3581 crate or a bit pattern, is sent upstream via a 10 Gbps optical link to a Sub-System Processor (SSP)  
3582 board which gathers trigger data from multiple crates. All the SSP boards send their information to  
3583 the Global Trigger Processor (GTP) which generates the level one (L1) trigger.

3584 The GTP sends the trigger to the Trigger Supervisor (TS) which makes sure the system is ready  
3585 to accept a trigger and sends the accepted signal to Trigger Distribution boards which are linked to  
3586 the Trigger Interface (TI) boards in each crate via optical links as represented in Fig. 140. The trigger  
3587 and synchronization clock signals are then be sent back to individual crates and payload modules  
3588 through Trigger Distribution (TD) boards and Signal Distribution (SD) boards which distribute the  
3589 signals to electronics such as the FADCs. Once a trigger is generated, the full resolution data which  
3590 is still in the pipeline, is readout out using a serial VXS link at a data rate of 8 Gbit/s correspond to  
3591 1 GB/s. As this is a point to point connection, the aggregate full crate bandwidth is 16 GB/s, giving  
3592 plenty of headroom for FADC readout.

### 3593 **14.2.1 GEM readout**

The plan for readout of the GEM detectors is to use the CERN Scalable Readout System (SRS)  
[294] which is based on the APV25 [295] front end chip. The APV25 chip is a shaper amplifier  
circuit that samples 128 channels at 40 MHz, storing the most recent 192 samples of amplifier output  
in a switched capacitor analog memory array. When a trigger is issued the corresponding slice in  
time is frozen, allowing a look back in time of up to 4  $\mu$ s. With such a pipeline design, the system is  
deadtimeless as long as the trigger rate is well under the 40 MHz sample rate. Readout of the chip  
by the front end electronics is also done at 40 MHz. For each trigger, 128 channels are readout with  
additional control signals making a total of 141 signals to be transferred. The chip has the ability to



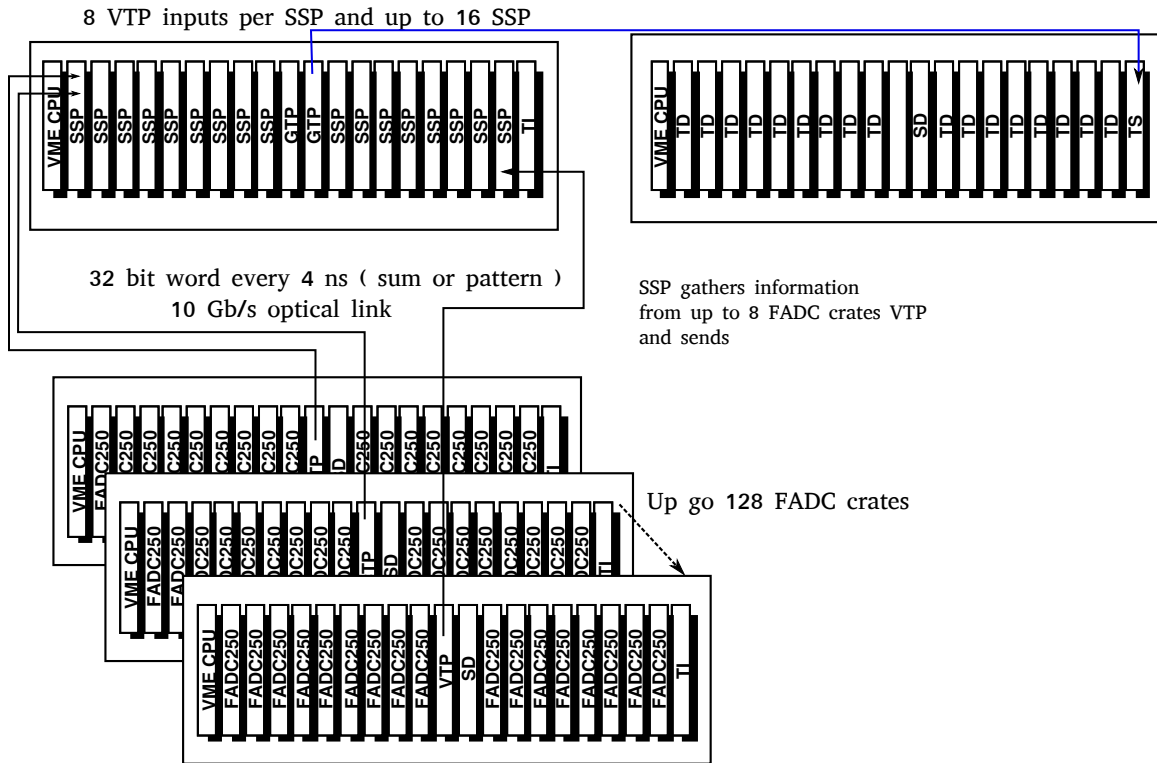


Figure 140: Standard Triggering scheme using the JLAB pipeline electronics

record 1 sample per trigger or 3 samples in case of high background. The signal is transferred in an analog form to the front end card where it is digitized by a flash ADC. In the case of one sample it will take :

$$141 * 25 = 3.6 \mu s$$

3594 to transfer the data from the chip. This time is tripled to 10.6 us for 3 sample readout. This data  
 3595 transfer rate is ultimately limiting the trigger rate capability of the chip to 91 kHz in 3 sample mode  
 3596 and 280 kHz in single sample mode. All the data is digitized on the front end board with pedestal  
 3597 subtraction and zero suppression.

3598 The SRS system, developed by the RD51 collaboration, gathers all the common high level  
 3599 digital functions of a typical readout system : triggering, buffering, data transfer and event building.  
 3600 To use the APV25, a chip specific adapter is needed. Such an adapter card is available which links to  
 3601 the the hybrid board that holds the APV25 using HDMI cables. This card has 8 FADCs reading out  
 3602 8 APVs chips, digitizing 2048 channels of detectors per board. These boards interface with the SRS  
 3603 Front-End Card (FEC). The FEC card process the digitized data and can transfer the data directly to  
 3604 a computer through Gigabit Ethernet. These FECs are mounted in Eurocrates which each can hold  
 3605 up to 8 FECs. For larger systems, a Scalable Readout Unit (SRU) can be used to gather data from  
 3606 multiple FECs. In this case data is transferred from the FEC to the SRU using a custom protocol  
 3607 over standard CAT6 ethernet cables. The data gathered by the SRU is sent to a computer over 10  
 3608 Gigabit Ethernet. As each FEC can communicate individually to a computer or a SRU, the system  
 3609 is highly scalable and modular. As many FECs can be added as need to readout all the detector  
 3610 channels.

3611 GEM readout systems based on the APV25 are currently in use at JLab (Heavy Photon Search,  
 3612 Proton Radius Experiment and the Super Bigbite Spectrometer). The experience with these exper-

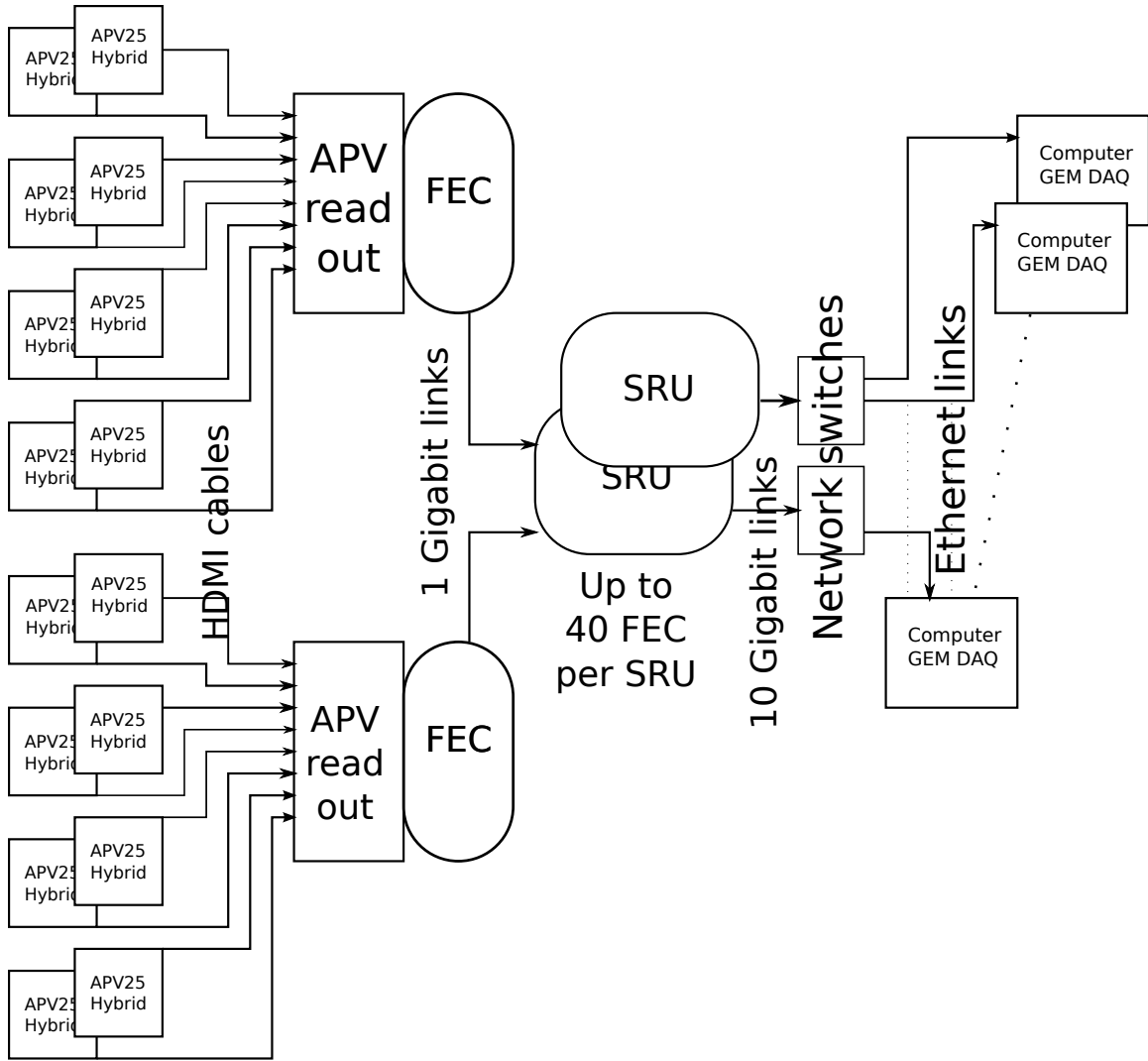


Figure 141: Standard SRS architecture which will be used for SIDIS experiment

3613 iments indicates that a readout system based on the APV25 can be built that supports the trigger  
 3614 and data rates required by SoLID. A variety of other GEM readout front end chips are under devel-  
 3615 opment. The collaboration will monitor these developments for improvements in cost, performance  
 3616 and DAQ rate.

#### 3617 **14.2.2 SIDIS Configuration**

3618 The SIDIS experiment will use a similar detector setup as the PVDIS experiment with the addition  
 3619 of more detectors. Scintillator planes will be used to reduce the photon background as the PVDIS  
 3620 baffles will be removed. A Heavy Gas Cerenkov and a MRPC will be added for  $\pi/K$  separation.  
 3621 The PVDIS crates will serve as the basis of the SIDIS DAQ, but the signals from the VTP will  
 3622 be sent to the SSP and GTP in an additional crate to make a coincidence trigger. The additional  
 3623 detectors will be instrumented with FADCs for the Heavy Gas Cerenkov and TDCs for the MRPC.

3624 Based on current simulations, the size of each event is expected to be about 31.1 kBytes includ-  
 3625 ing signals from all detectors. So for a SIDIS  $^3\text{He}$  rate of 100 kHz (coincidences plus prescaled

Detector	Channel
EC Shower	1800
EC Preshower	1800
SPD	300
Light Gas Cerenkov	270
Heavy Gas Cerenkov	480
MRPC	3300

Table 29: Detector channel counts for the SIDIS and  $J/\Psi$  experiments, excluding the GEMs.

3626 singles) a data rate of 3110 MB/s is expected.

3627 The SIDIS experiment trigger formula is

3628 **forward angle electron trigger** Forward Angle Calorimeter *AND* Light Gas Cherenkov *AND* SPD  
3629 *AND* MRPC

3630 **large angle electron trigger** Large Angle Calorimeter *AND* SPD

3631 **forward angle charged particle trigger** Forward Angle Calorimeter *AND* SPD *AND* MRPC

3632 **coincidence** electron trigger (large *OR* forward) *AND* forward angle charged particle trigger

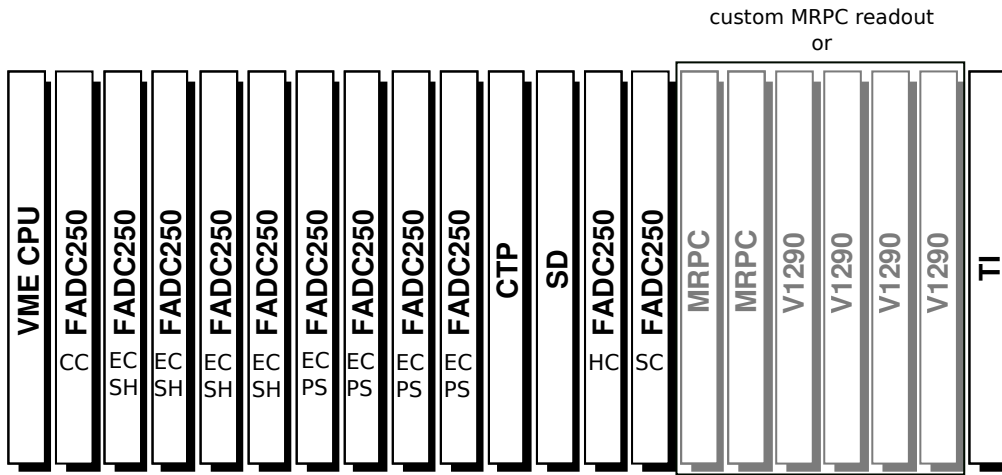
3633 The SIDIS experiment and  $J/\Psi$  will use the same detector configuration, cabling, DAQ and  
3634 trigger hardware. The only difference is that the DAQ will be configured to trigger on a high energy  
3635 electron and a pion for SIDIS while for  $J/\Psi$  it will trigger on 2 high energy leptons.

3636 **MRPC readout** The current plan for MRPC readout is to develop a custom electronics module for  
3637 the readout of the 1550 MRPC strips. It will be a custom designed TDC that digitizes 3300 channels  
3638 of MRPC. (Strips are readout at both ends.) The baseline solution will be to use a chip similar to the  
3639 NINO chip which is an amplifier discriminator chip. This chip generates a discriminated signal with  
3640 a time resolution on the order of 10 ps with a logic output width proportional to the time the pulse  
3641 is above threshold which allows amplitude information for time walk correction. In order to include  
3642 the MRPC in the trigger, a new module, the VETROC board, developed by the JLab electronics  
3643 group will be used.

3644 **SIDIS GEM rates** As the DAQ for the SIDIS experiments can not be segmented in to a separate  
3645 DAQ chain for each sector, the event size is an important factor in keeping the DAQ throughput  
3646 below limits to the overall data rate that can be recorded. The occupancy of the detector is fairly low  
3647 when using the on-board deconvolution which is the default running mode for SIDIS. By reading in  
3648 one sample mode, we expect the allowed trigger rate to be about 200 kHz. We are planning to use  
3649 several SRUs to concentrate the signal from the SRS front end cards. The SRU module gathers all  
3650 the FEC signals and sends the data to a 10 Gbit ( $\sim 1.2$  GB/s) Ethernet port. To have a safety margin,  
3651 4 SRUs will be used to handle the rate.

### 3652 14.2.3 PVDIS Configuration

3653 **Calorimeter trigger for PVDIS** There are currently two options to generate a Level-1 (L1) trig-  
3654 ger from the calorimeter. The standard option is to use the sum of the 16 FADC channels which is  
3655 computed and sent to the VTP every 4 ns. The VTP can add all the FADC sums, generating a global



Optical link 10 Gbps  
1250 MB/s

Figure 142: SIDIS FADC crate layout

Chamber	Occupancy	Hits per sector	Hits detector
1	2.37	21.5	644.2
2	7.98	81.4	2441.9
3	3.4	39.6	1189.3
4	2.24	31.5	943.5
5	2.03	21.1	633.4
6	1.52	19.4	583.7
Total hits		6435.9	193076.8
Event size 1 sample (Kbytes)		945.3	28408.4
Data rates 100 kHz (Mb/s)		94.5	2840

Table 30: SIDIS GEM occupancies and event size for GEM

Table 31: Channel counts of individual detectors for PVDIS for one sector

Detector	Module Type	Number of Channels	Number of Modules
Electromagnetic Calorimeter (EC)	FADC	122	8
Light Gas Cherenkov (GC)	FADC	9	1
GEM	SRS	4700	1

3656 sum for each crate and generating a trigger when that sum exceeds a threshold. Another scheme  
3657 was devised for the Heavy Photon Search experiment in Hall B. In this scheme 16 bits of data for  
3658 each of the 16 FADC channels is sent every 32 ns as in Fig. 145. These data contains both the signal  
3659 amplitude, and the timing (to a 4 ns resolution) of any threshold crossing. With the VTP receiving a  
3660 signal from all the calorimeter elements, it can compute the signal sum, in parallel, of every possible  
3661 cluster of one central and 6 surrounding blocks. This approach of triggering on the cluster sum can  
3662 reduce the number of triggers coming from background and improve online pion rejection.

3663 Particles near the edge of a sector will likely shower into calorimeter blocks in the adjacent  
3664 sector. In order to avoid inefficiencies near the edges of sectors, VTPs for neighboring sectors will  
3665 share information through bidirectional optical links as shown in Fig. 144. Once the VTP receives  
3666 all the FADC data from its own crate and the two adjacent crates, it either computes the total sum or  
3667 performs cluster searching to generate trigger. If the cluster trigger method is used, a 64 bit pattern  
3668 containing the FADC channels to be readout will be generated by the VTP and transferred to the  
3669 Flash ADC using the trigger data path. A new firmware for the FADC will be developed to take this  
3670 pattern into account allowing each FADC to only read the channels that are part of a cluster in order  
3671 reduce event sizes.

3672 **Gas Cerenkov trigger** Both Cerenkov detectors are divided into 30 sectors. The most straight-  
3673 forward way to generate a Cerenkov trigger is to put all the channels of a given sector (9 for the  
3674 light gas and 16 for the heavy gas) into one FADC board and generate the trigger in the VTP by  
3675 putting a threshold on the sum of the PMT signals. To improve efficiency at the interface between  
3676 two sectors one can include a threshold on the sum of the two adjacent sectors. If the combinatory  
3677 background is too large, a clustering scheme similar to that discussed for calorimeter could be used.  
3678 The efficiency and background of the different schemes has been evaluated in the full simulation of  
3679 the digitized background. This simulation shows that a simple trigger based on PMTs sums works  
3680 and has a sufficient efficiency.

3681 In order to estimate the per event size of data from the GEMs, the GEM signal and the APV25  
3682 digitization process were modeled in a simulation. This simulation is detailed in the simulation  
3683 section 12.2.4 of this document. The total number of GEM strips firing in a 25 ns window was  
3684 computed without and with deconvolution. The last column are the results coming from the GEM  
3685 digitization Section 18.

3686 **PVDIS GEM rates** For PVDIS, we are interested in the data rate per sector. The numbers in  
3687 Table 32 are evaluated for 20 kHz (15 kHz rate + 5 KHz of safety margin). Even though occupancies  
3688 are high, the data rates for PVDIS are reasonable (about 80 MB/s per sector) and simulations show  
3689 that tracks can be efficiently identified if 3 sample readout is used. The 3 sample readout will  
3690 allow for more effective offline rejection of pile up. The deconvolution and filtering are also able to  
3691 significantly reduce the occupancy and event size. Using the SRS system, each FEC can transfer up  
3692 to 1Gbps through its Ethernet link.

### 3693 14.3 Event size from FADC

3694 The FADC samples are 12 bits at 250 MHz. In the case of PVDIS, since pile up is going to be  
3695 significant, we plan to record the entire waveform. As pulses are 40 ns wide, we will record 10  
3696 samples for each detector channel. FADC events have a 4 byte block header, a 4 byte block trailer,  
3697 a 4 byte event header and pack 2 samples into each 4 byte word. For a 10 samples size, the event  
3698 size per module is thus  $(12 + 4 \times (10n/2))$  bytes where  $n$  is the number of channels firing.

Chamber	Occupancy (%)	Hits	Occupancy with noise cut (%)	Hits after noise cut
1	21.2	244.8	10.0	115.2
2	10.3	142.2	5.1	70.2
3	8.8	121.0	4.4	60.7
4	3.1	70.2	1.6	37.5
5	2.8	65.6	1.5	35.2
Total hits		643.8		159.8
Event size 3 samples (Kbytes)		7.9		3.9
Data rates 20 kHz 3 samples (Mb/s)		159.8		79.2

Table 32: PVDIS GEM occupancies and event size for GEM

Experiment	Event Size (kBytes)	L1 trig Rate (kHz)	Data Rate MByte/sec
PVDIS	146.4	20	110x30
SIDIS	31.2	100	3360
JPsi	133	30	3990

Table 33: Expected data rates to be sent to tape

3699 The FADC simulation with digitization is still being developed. Given the size of a sector,  
3700 the event size will be estimated with a maximum of 2 clusters of 7 for shower and 2 clusters of 7  
3701 preshower and assuming all 9 PMTs of the Cerenkov fire all the time. With this assumption the  
3702 event size is 1480 bytes per event.

3703 With a trigger rate of 20 kHz, this gives 29.6 MB/s data rate, well under the VME320 backplane  
3704 transfer rate limit of 200 MB/s.

3705 In the case of SIDIS, the occupancy on the detector is small enough that only pulse integrals  
3706 need to be recorded. The estimated event size using the occupancies from the simulation is 31.2  
3707 KBytes, which gives an aggregate data rate, including GEMs, of 3110 MB/s at 100 kHz for all 30  
3708 crates.

#### 3709 **14.4 Data rates, event size, and tape storage**

3710 A JLab network upgrade, completed in 2014, provided two 10 Gigabit Ethernet links between the  
3711 Hall A counting house and the computer center. Additionnal fibers are available making it possible  
3712 to upgrade the link up to 40 Gigabit/sec by using 4 fibers before SoLID running is planned. **Cur-**  
3713 **rently the JLab tape silo system can hold up to 11,240 tapes giving, with compression, a current**  
3714 **capacity of 47 PB using LTO6 drives. The computer center out year budgets include plans to add**  
3715 **a second silo, giving a storage capacity of 22,480 tapes and 48 drives. Assuming the evolution of**  
3716 **LTO technology (shown in table below), a fully upgraded silo would hold up to 919 PB of data using**  
3717 **LTO10 technology with a 13.2 GB/s data rate per drive frame or 26.4 GB/s for the whole silo. With**  
3718 **the planned second two frame silo system (24 drives) the total capacity would be 1840 PB with a**  
3719 **data transfer rate 13.2 GB x 4 = 52.8 GB/s, accommodating the needs of SoLID and the other halls.**

3720 LTO tape drive evolution.

LTO version	4	5	6	7	8	9	10
Availability	2008	2010	2012	2015	2018	2020	2023
Capacity/tape (TB)	0.8	1.5	2.5	6.25	12.8	25	48
Data rate/drive (MB/s)	120	140	200	300	472	708	1,100
Compression	2	2	2	2.5	2.5	2.5	2.5

3722 The total amount of data from all SoLID running will total to about 380 PB representing about  
3723 20 % of the future silo size.

3724

## 3725 **14.5 Hall DAQ installation**

3726 The DAQ for both the SIDIS and PVDIS configurations will be located in the hall. As is typically  
3727 done, a shielded bunker will be constructed to house the data acquisition electronics, protecting it  
3728 from beam induced radiation. This bunker will contain  $\sim 15$  racks containing 32 VXS crates and  
3729 the crates containing the GEM front-end cards.

3730 Approximately 4500 coaxial cables (RG58) will connect the PMT based detectors to the ADCs  
3731 in the bunker. Additionally,  $\sim 200$  ribbon cables will connect the on-detector MRPC discriminators  
3732 to TDCs in the bunker and HDMI cables will connect the detector mounted GEM chips to the front  
3733 end cards.

### 3734 **14.5.1 Experiment switch over**

3735 Switch over of the DAQ electronics between the PVDIS and SIDIS setups will be relatively straight-  
3736 forward. Changing to the PVDIS setup, the VTP module in each sector's crate will connect directly  
3737 to the TI module in that crate to give an L1 trigger signal for that crate and the corresponding GEM  
3738 electronics. The unused SSP, TD and TS, and VTP modules as well as ADC and TDC modules for  
3739 detectors not in PVDIS will be removed from the hall to avoid extra radiation dose.

## 3740 **14.6 Managing data rates**

3741 Managing total data rates for SoLID will require careful system design to avoid bottlenecks. While  
3742 the PVDIS configuration has the highest overall trigger and data rate, the segmentation of SoLID  
3743 into 30 nearly independent sectors allows for natural parallelization. The data rate per sector is a few  
3744 hundred MB/s. The parallel data paths can be preserved through the event builder (that combines  
3745 VME and GEM data), to temporary disk storage, through parallel network paths, and through an L3  
3746 farm before merging into a smaller number of paths for storage on tape.

3747 The SIDIS configuration is more challenging as the data for each event which is spread over 30  
3748 VME systems and 30 sectors of GEMs which must be combined to build events. It is presently not  
3749 feasible to build and events from these 60 sources into single data stream of over 3 GB/s. This can  
3750 be overcome with the option in CODA of multiplexing events to multiple event builders. A possible  
3751 architecture would have up to 60 ROCs pushing data to several primary event builders so that each  
3752 event builder handles a more modest data rate. (One event builder for the VME crates and several  
3753 event builders for the GEM data.) Each of these primary event builders, which contain a fraction of  
3754 each event, would feed, in round robin fashion, several secondary event builders. Each secondary  
3755 event builder would build complete events, but only have a fraction of a given run's events saved  
3756 to its disk cache. This architecture is scalable such that bottlenecks can be mitigated by using a  
3757 sufficient number of primary and secondary event builders.

3758 **14.7 Summary and Pre R&D plans**

3759 The conceptual design of the SoLID data acquisition system is based on hardware that has all ready  
3760 seen use with beam at JLab. While SoLID's trigger rate and total data rate exceed what has been  
3761 achieved by detectors such as GlueX and HPS, it expected that it is feasible to meet the requirements  
3762 with careful system design, hardware firmware improvements and upgrades to the CODA software.  
3763 The DAQ component of the SoLID Pre R&D will serve to understand the capability and limitations  
3764 of the conceptually designed system. Some of the specific items to address in Pre R&D include:

- 3765 • Test single VXS crate to acquire data at 100 kHz.
- 3766 • Test acquisition of GEM data from one sector at 100 kHz with data rate of 100 MB/sec.
- 3767 • Mockup 60 ROC system and multiple event builders and establish ability to handle throughput  
3768 of 4GB/sec at 100 kHz trigger rate.
- 3769 • Provide prototype small scale DAQ system for detector beam tests.
- 3770 • Test trigger and data sharing scheme between adjacent sector PVDIS DAQ systems.





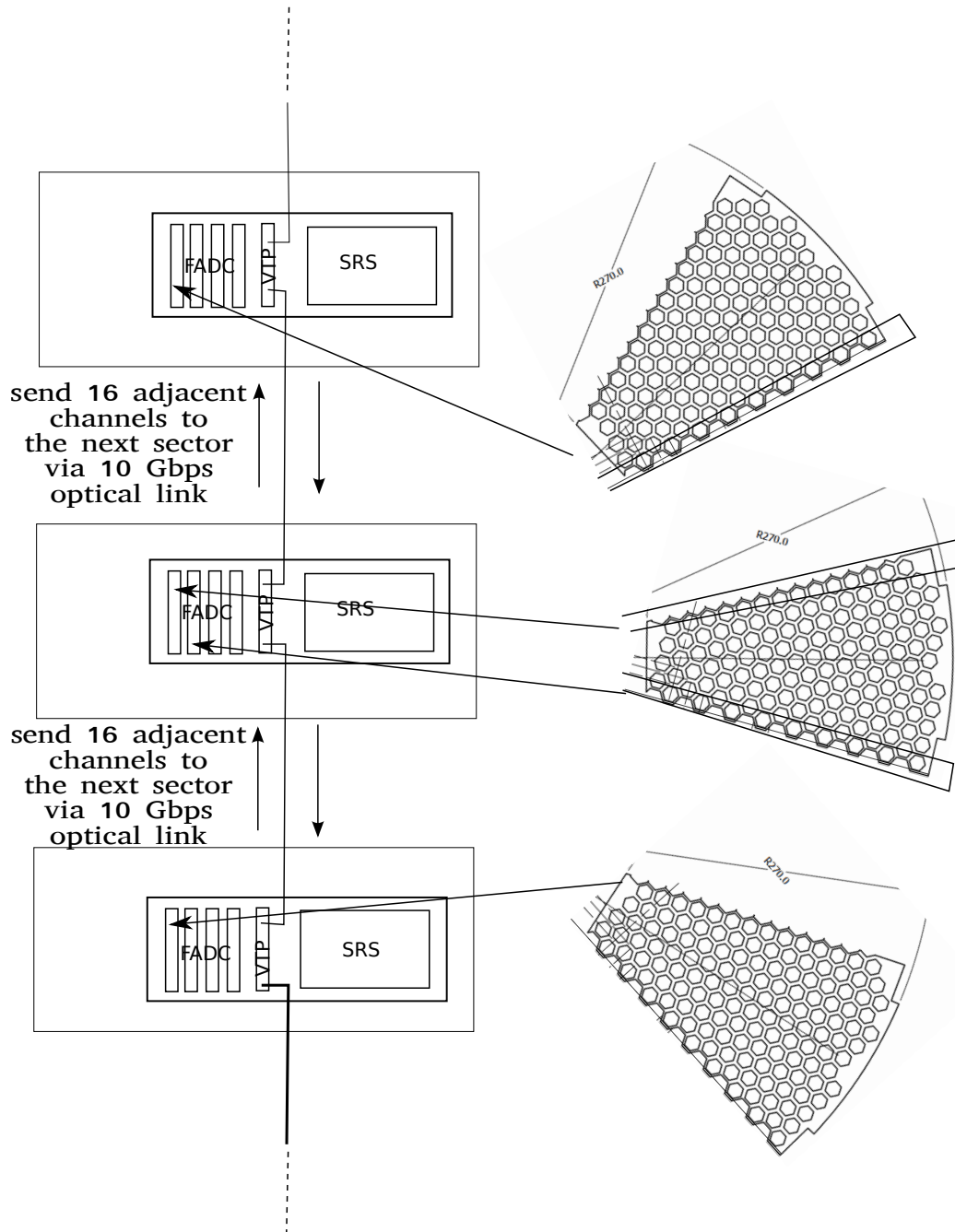


Figure 144: PVDIS specific electron trigger

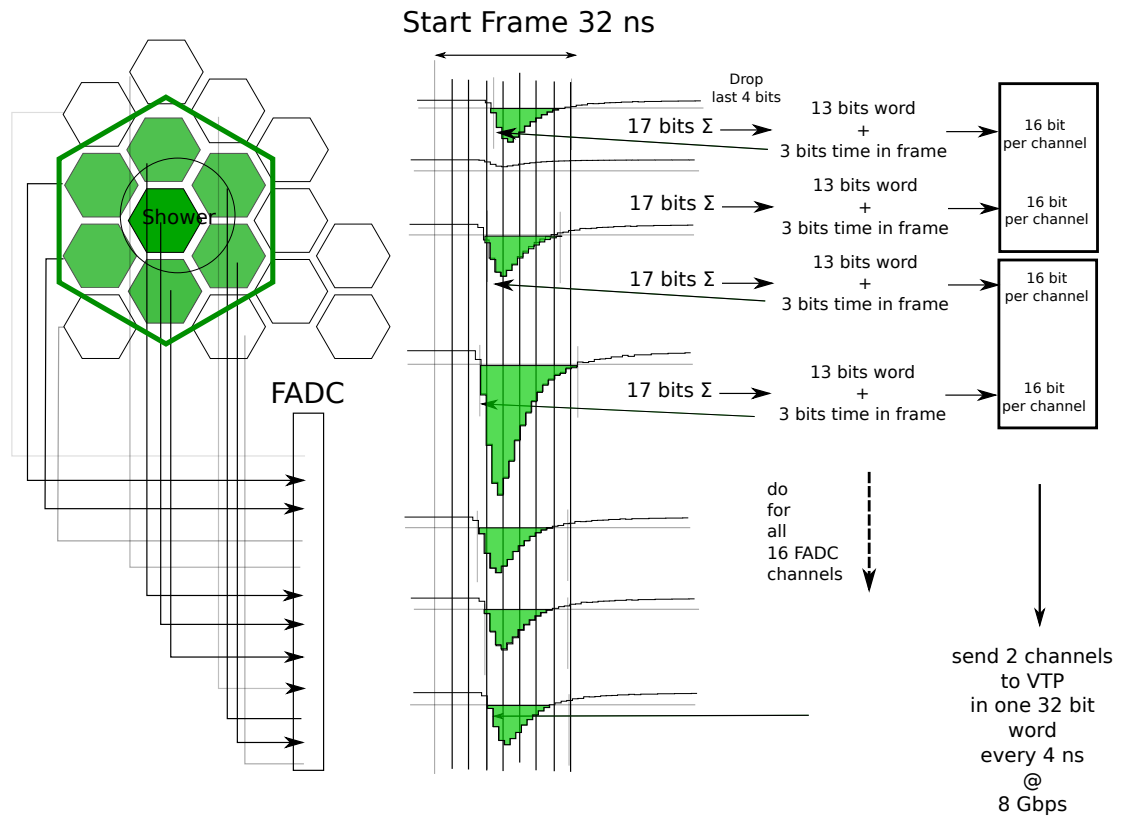


Figure 145: Calorimeter clustering scheme using the HPS algorithm. All calorimeter signals are sent to the FADC.

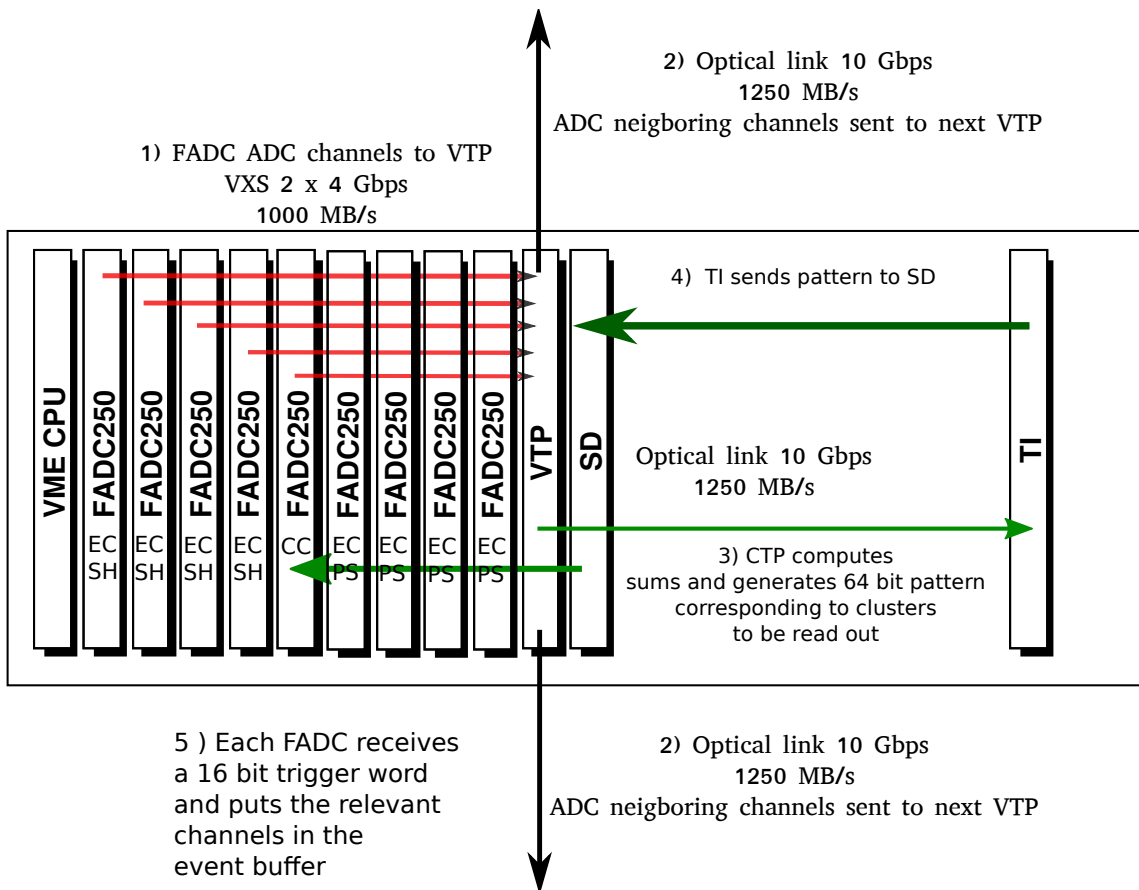
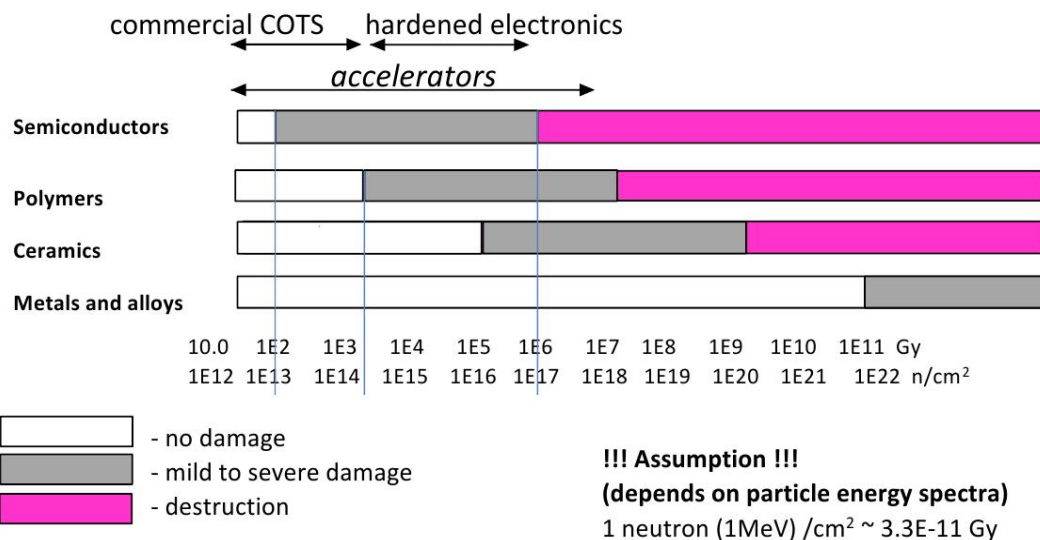


Figure 146: PVDIS FADC crate layout

3771 **15 Radiation damage estimates and Activation**

3772 The simulation and background calculation software for SoLID is using the two simulation packages  
 3773 with independent code base (Geant4 and FLUKA [298] [299]). This allows independent cross  
 3774 checks both in geometry and in physics modeling. At the same time the two codes each provide  
 3775 unique capabilities expanding the overall reach. FLUKA provides useful tools that simplify the  
 3776 study of radiation damage and estimates but the physics processes present in the simulation lack  
 3777 of direct electro-nuclear dissociation and fragmentation models. Such electro-nuclear reactions are  
 3778 dominant in the neutron production from the Liq.D target at high energies (see figure 152). If one  
 3779 just considers the neutron photo-production, both codes (GEANT4 and FLUKA) have really good  
 3780 agreement with experimental cross section, as shown in figure 150 and 151. A full simulation and  
 3781 tests are underway in order to construct a better and common target background generator for both  
 3782 simulation packages (see figure 152). To have a first idea of the tolerance of different material to  
 radiation damage, see figure 147. As a weighting factor to estimate the effect of radiation damage on



© Lockheed Martin

Figure 147: Estimate of the tolerance of different material to different level of radiation exposure given in Gy and  $\frac{neutron(1MeV)}{cm^2}$ . This is just a first order approximation and a detailed analysis of each equipment is needed in order to establish the correct radiation tolerance of each detector/material

3783 electronics I used, in parallel to the calculation of full Dose estimates, the Displacement damage in  
 3784 silicon, on-line compilation curves by A. Vasilescu (INPE Bucharest) and G. Lindstroem (University  
 3785 of Hamburg). This curves assume that the damage effects by energetic particles in the bulk of any  
 3786 material can be described as being proportional to the so called Non Ionizing Energy Loss and  
 3787 normalize the damage in Silicon to the one caused by a 1 MeV neutron (more details can be found  
 3788 here [301]).  
 3789

3790 **15.1 Radiation damage to GEM electronics**

3791 A simulation in order to test the radiation level on the GEM foils has been done. Comparison to  
 3792 estimated radiation level of the CMS experiment, which shares the part of the electronics most sus-

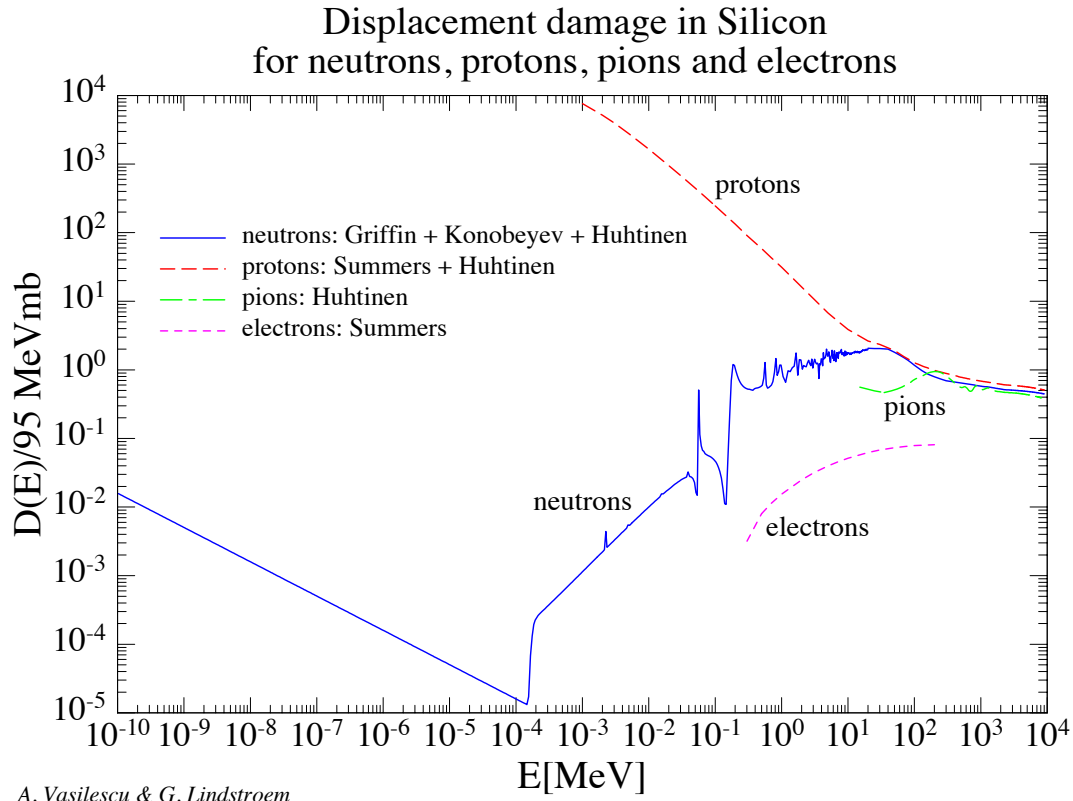


Figure 148: Not Ionizing Energy Loss curves to 1MeV equivalent damage in Silicon for electrons, pions, neutrons and protons

3793 ceptible to radiation damage for the GEM chambers detectors, permitted us to establish a radiation  
 3794 limit flux for our expected running time. Already with our first conceptual design of the shielding  
 3795 we are able to reach tolerable radiation levels also in the first layer of the GEM chambers (the one  
 3796 that is supposed to sustain the higher radiation fluxes). This result is show in figure 153

## 3797 15.2 Power deposited

3798 A detailed study of the power deposited in the SoLID spectrometer has been done in order to detect  
 3799 areas of possible activation. In these areas, in order to define possible activations, the FLUKA sim-  
 3800 ulation has been used as a tool, and particle fluxes were provided by GEANT4 for areas where was  
 3801 the particle fluxes estimated by FLUKA were known to be incorrect. FLUKA in fact provides many  
 3802 good tools for activation and radiation estimates, but lacks in direct electro-nuclear dissociation-  
 3803 fragmentation models and has limitations in producing more complex geometry, like the Baffle  
 3804 design for the PVDIS experiment in SoLID. In the following study of activation, GEANT4 has  
 3805 been used as a common input for an estimate of the background radiation in areas where direct  
 3806 electro-nuclear dissociation-fragmentation models are important.

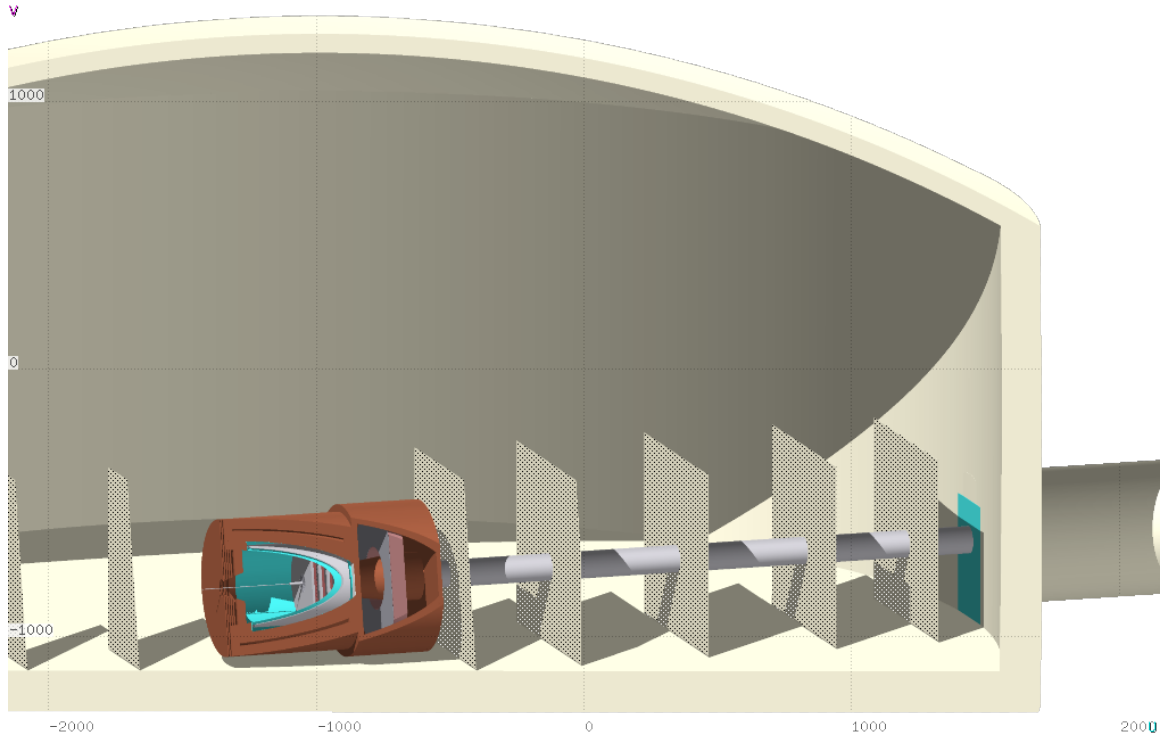


Figure 149: FLUKA simulation for the PVDIS experiment with SoLID.

### 3807 **15.2.1 Power in 1st baffle (due to Möllers), (Cooling, activation)**

3808 The first baffle, due to his proximity to the Deuterium target in the PVDIS configuration for SoLID,  
 3809 has a power deposition of  $\sim 8W$  for a beam current of  $50\mu A$  and an energy of  $6.6GeV$ . The high  
 3810 production of neutrons from the Deuterium target can be an ulterior source for activation in the  
 3811 baffle. For this reason an investigation of the possible activation has been done. In this study has  
 3812 been considered at the same time the radiation coming from the target and from the baffle itself  
 3813 that “self-irradiate” different parts of its structure. The impact of Activation due to the utilization  
 3814 of different materials have been directly studied (see 154 for the first baffle: In order to optimize  
 3815 the computing time and avoid issues of pixelization due to the detailed shape of the baffle, a single  
 3816 block of material was used in this study. Since the solid angle coverage seen by the main source of  
 3817 radiation (the target) of the baffle used in this study is not the same, the radiation calculated should  
 3818 be scaled accordingly or used as an extra safety factor due to our relying just on simulations.

3819 These results (see show the Dose equivalent radiation spatial distribution for 3 different cooling  
 3820 times. This study (see figure 154 ) shows, for example, that, in order to survey the area in proximity  
 3821 of the first baffle, one should wait around 1 day of cooling, in order to reach level of radiation  
 3822 tolerable. The Residual nuclei activated in the Lead baffle are shown for the same cooling time in  
 3823 the bottom plots of figure 155.

### 3824 **15.2.2 Power in exit hole in magnet (elastics) (Cooling, activation)**

3825 Another spot for possible activation will be the part close to the exit hole of the magnet. Further  
 3826 investigation will need to be done, after a final design of the magnet will be reached, but it is  
 3827 expected to be less important than the activation on the first baffle, due to the not proximity to the  
 3828 target and to the less intense and less localize radiation. This situation has been investigated and

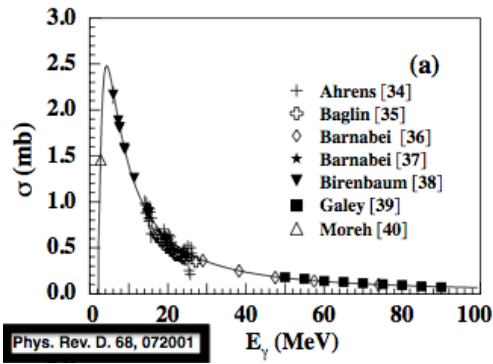


Figure 150: Neutron cross section for photo-production [300]

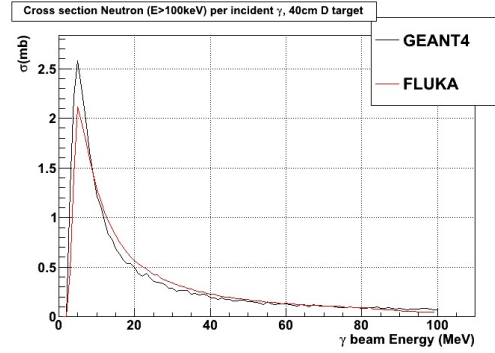


Figure 151: Test for Neutron cross section for photo-production with FLUKA and GEANT4

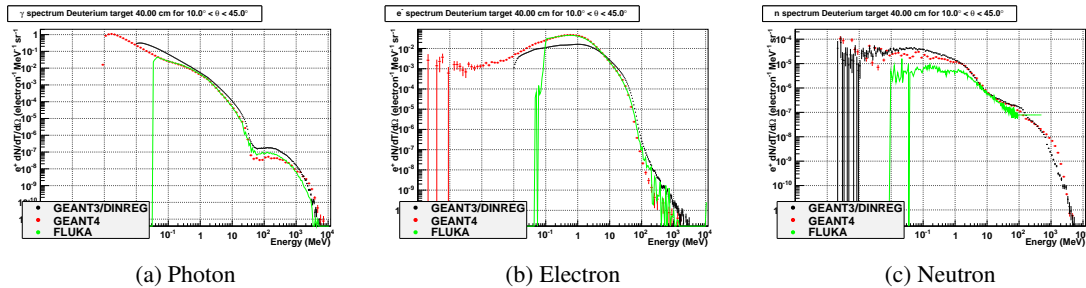


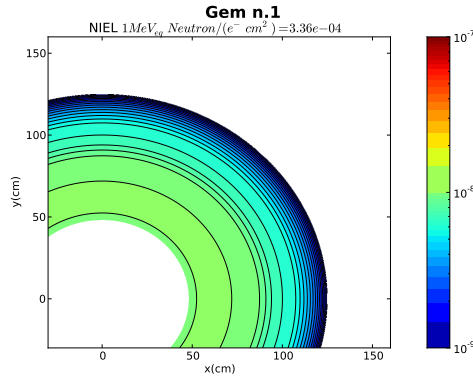
Figure 152: Background comparison produced from GEANT3(DINREG), GEANT4 and FLUKA with 40cm of Liquid Deuterium. Here is plotted the  $\frac{d^2N}{dT d\Omega}$  per incoming electron in the angle range of  $10^\circ < \theta < 45^\circ$  for  $\gamma$ (a),  $e^-$ (b) and  $n$ (c)

3829 compared to the PVDIS design, because it is the one with the expected higher activation of all the  
 3830 configuration with SoLID, with the proximity of the lead baffles to the target (see this section at  
 3831 page 189). This has been done in order to compare power deposition to have a first idea of possible  
 3832 activation areas. The levels of power deposited in the exit hole of the magnet are at least lower  
 3833 by one order of magnitude respect to the one expected in the first baffle, as shown in figure 156a  
 3834 and 156b. The integrated value (using the cylindrical symmetry) over the higher area of power  
 3835 deposition in the exit hole of the magnet has a maximum of  $\sim 0.9W$  per cm in the z direction  
 3836 over the full internal section of the exit hole with  $r_{xy} < 40cm$  (color scale of  $\sim 3E - 04$  in figure  
 3837 156a ). This compares to a full power deposition on the first baffle of  $\sim 20W$ , running in the same  
 3838 conditions. A power deposition estimate for the beam-line downstream is shown in figure 156b.  
 3839 As one can see in 157c, is considerably smaller the impact of the configurations like SIDIS to the  
 3840 activation in this area.

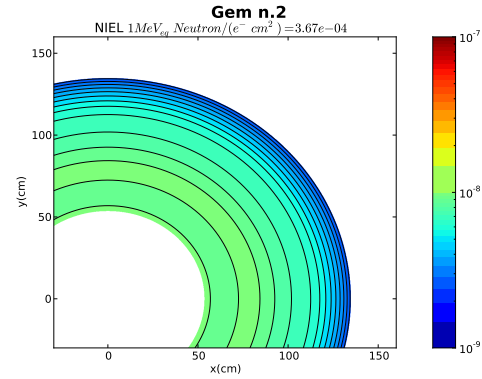
### 3841 15.2.3 Power in the entrance surface of the magnet (Cooling, activation) (external target 3842 configurations)

3843 With configuration like SIDIS that have the target positioned outside the magnet, there is a consistent  
 3844 power deposition in the front part of the magnet. Some simulation has been done in order to estimate  
 3845 the possible activation in this area. The results of these studies are presented in figure 157 and show  
 3846 the areas of power deposition in the magnet and in the front surface of the magnet. As expected

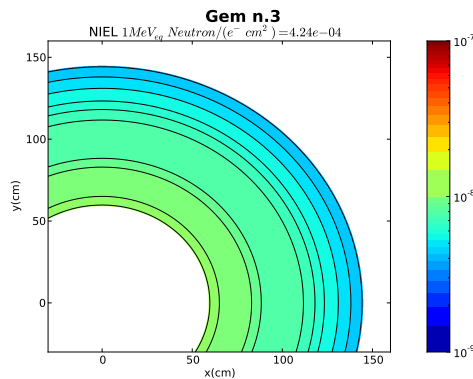




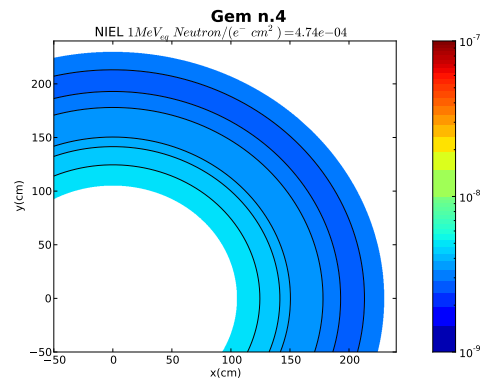
(a) NIEL weighted 1MeV equivalent neutron flux per  $cm^2$  per incident electron on the 1<sup>st</sup> GEM foil



(c) NIEL weighted 1MeV equivalent neutron flux per  $cm^2$  per incident electron on the 2<sup>nd</sup> GEM foil



(b) NIEL weighted 1MeV neutron equivalent neutron flux per  $cm^2$  per incident electron on the 3<sup>rd</sup> GEM foil



(d) NIEL weighted 1MeV equivalent neutron flux per  $cm^2$  per incident electron on the 4<sup>th</sup> GEM foil

Figure 153: The CMS experiment dose rates are expected to be of the order of 10 MRad( $SiO_2$ ) ( $5 \times 10^{13} \frac{n}{cm^2}$ ). This translate for us, assuming 2000 hours of beam at  $100\mu A$ , in a flux of  $\sim 1.1 \times 10^{-8} \frac{1MeVeqn}{e^-cm^2}$ . This put us on the same level of radiation that the APV25 chip was built to tolerate

3847 the areas of possible activation is the area more exposed to the target radiation and the collimator  
3848 positioned in front of the nose-cone of the magnet.

#### 3849 15.2.4 Heat load in magnet cryostat

3850 A detailed design of the Cryogenics and coils of the CLEO II solenoid has been obtained and was  
3851 constructed a detailed model that replicates key components of the magnet (see Fig.158). Particular  
3852 attention was put in well represent:

- 3853 1. the 3-5 mm of stainless steel which is the inner bore of the cryostat
- 3854 2. the 3-5 mm of aluminum thermal shield 3-5 cm beyond (1)
- 3855 3. the 6+ mm of stainless steel which is the helium vessel
- 3856 4. any winding forms left at the inner diameter of the coils

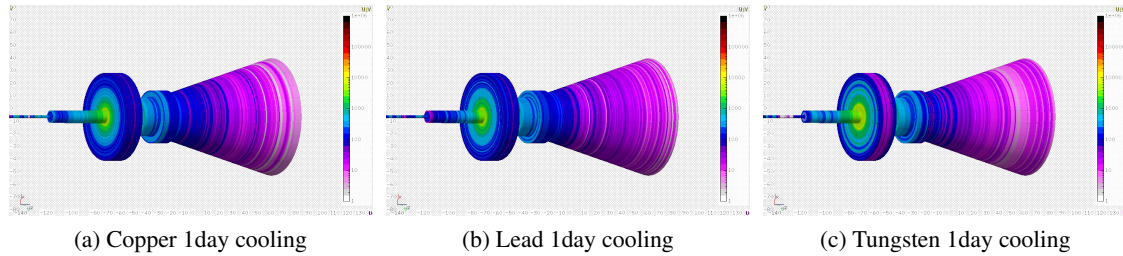


Figure 154: First Baffle: Activation study has been calculated for 3 different Cooling times (here is just shown after 1day), after an assumed exposure to the beam of 3 separate full weeks interleaved by a down time of 4 days. (154a, 154b,154c) The dose is expressed in  $mrem/h$  and here is shown their spatial distribution.

3857 5. the copper matrix in which the Nb-Ti is embedded. Typical conductors of the era were 66-  
3858 80% copper with balance Nb-Ti (2:1 to 4:1 Cu:SC).

3859 After updating the design, a detailed calculation was done with the PVDIS configuration with Deu-  
3860 terium as its target: This configuration, with the Deuterium target inside the magnet, is the one be-  
3861 tween the different SoLID configurations which presents the highest flux of neutrons on the Coils.  
3862 An integrated dose was calculated and determined using the cylindrical symmetry of the system  
3863 and the flux calculated per  $cm^2$  on the more susceptible parts of the magnet. An integrated dose  
3864 of  $10^{17} \frac{1MeV_{neutron}}{cm^2}$  is needed in order to start to see some modification on the Critical Current ( $I_c$ )  
3865 of the magnet. A map of the integrated dose for the PVDIS and  $D_2$  case was created and presents  
3866 peaks for the integrated fluxes around  $10^{14} \frac{1MeV_{neutron}}{cm^2}$ , well below the tolerance level of the mag-  
3867 net. As a consequence, also if it is not known what is the current level of exposure reached by the  
3868 CLEO-II solenoid, the full scientific outreach that is planned at this moment with SoLID does not  
3869 seem to be going to affect considerably the lifetime of the coils of the magnet (see Fig. 159).

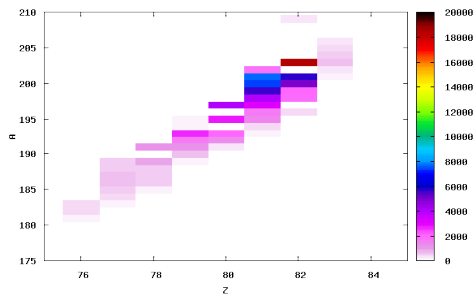
### 3870 15.3 Estimates for radiation damage in the Hall

3871 A study has been done in order to address possible radiation damage areas with the current SoLID  
3872 design with no further shielding in place. This work has been done in order to address and pinpoint  
3873 areas that will need to be further investigated when a final design for the magnet and electronics will  
3874 be reached.

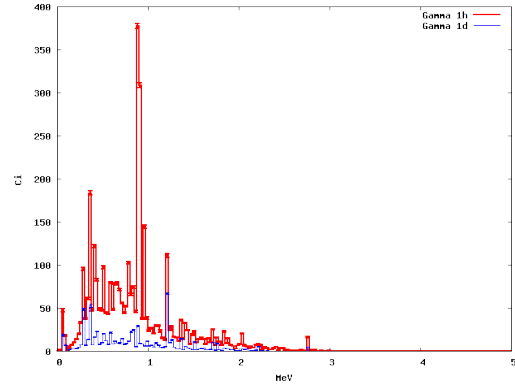
#### 3875 15.3.1 Radiation damage to electronics in Hall

3876 The results of the different simulations run suggest that the design of a shielding structure to min-  
3877 imize the radiation in the Hall seems not to be a priority. With the current different layouts of the  
3878 multiple configuration possible with the SoLID spectrometer. In this study the magnet has been  
3879 placed in a dome structure of concrete that mimics the presence of the Hall (It is important to con-  
3880 sider that the SoLID spectrometer will not be placed in an open environment, but in an Hall full  
3881 of equipments, with relative reflectivity that could cause an enhancement of the radiation present  
3882 in the Hall). Different features of these results are in common with the different configurations for  
3883 SoLID:

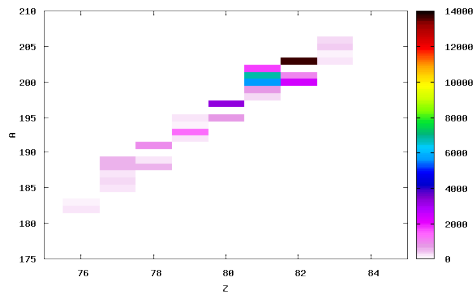
- 3884 • The radiation damage estimated with the simulation is, as expected, consistently lower in the  
3885 area outside the SoLID spectrometer respect to the one inside the magnet.



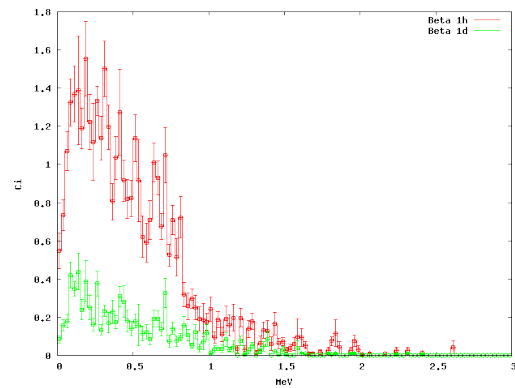
(a) Residual Nuclei for Lead Target after 1hour cooling (Z vs A)



(c) Photon Energy spectrum in Curie due to activation at 2 different cooling times



(b) Residual Nuclei for Lead Target after 1day cooling (Z vs A)



(d) Electron Energy spectrum in Curie due to activation at 2 different cooling time

Figure 155: (155a, 155b) The Residual decaying Nuclei are shown as a function of Z,A in the first baffle assumed constructed on Lead. The Gamma and Beta activity is also shown for the same decaying time (155c, 155d). Determining the activity permits in establishing different needs for shielding at different times of the experimental running (repair or decommissioning)

- 3886 • In the downstream part of the Hall, the predominant part of the radiation that escape the
- 3887 magnet is present in the last part of the beam-line, enhancing the choice of keeping in the
- 3888 upstream section of the Hall the existing left and right arm spectrometers existing in Hall-A.
- 3889 • The configurations that have the target area external to the solenoid have also an high radiation
- 3890 area in the proximity of the target

3891 The configuration that gives the higher radiation estimates in this simulation study, is the PVDIS  
 3892 configuration with Deuterium target. The radiation damage estimate in this configuration is investi-  
 3893 gated in detail in the next section.

### 3894 15.3.2 Radiation from beam pipe

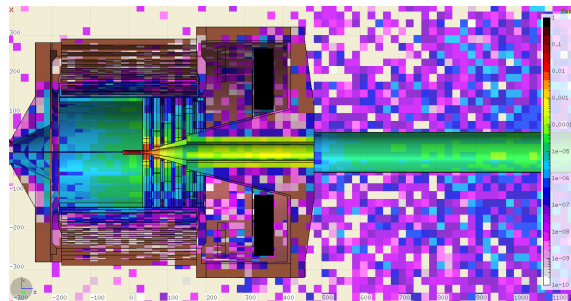
3895 The main source of radiation leaking from the magnet to the Hall is from the beam pipe downstream.  
 3896 In order to quantify the leaking with the different layouts with SoLID, different simulation have been  
 3897 carried out. The one that presents the biggest impact on possible damage to electronics is the PVDIS

3898 configuration with 40cm Liquid Deuterium target, but the localization of the leakage (close to the  
3899 beam-line, see figures [160b](#) ,[160c](#) and [160d](#)), and the low level of radiation present, suggest that a  
3900 shielding construction is not needed. A further factor of 10 reduction, if needed, can probably be  
3901 reached placing shielding material on the hot areas, around the beam-line, if this area, will be used  
3902 during the experiment, reaching levels of radiation compatible also to commercial electronics.

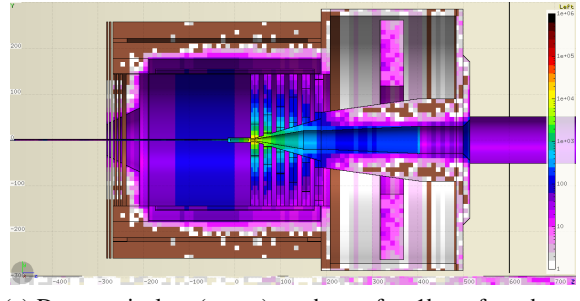
### 3903 **15.3.3 Radiation with external targets**

3904 Some of the configuration with the SoLID spectrometer, position their target in the proximity of  
3905 the entrance of the magnet. Simulations have been done in order to evaluate possible high radiation  
3906 areas for electronics. An example for the possible areas of high radiation with these layouts for  
3907 the experiments is shown in figure [161](#) (SIDIS configuration with  ${}^3\text{He}$  target) and figure [162](#) ( $J/\Psi$   
3908 configuration with  $H_2$  target).

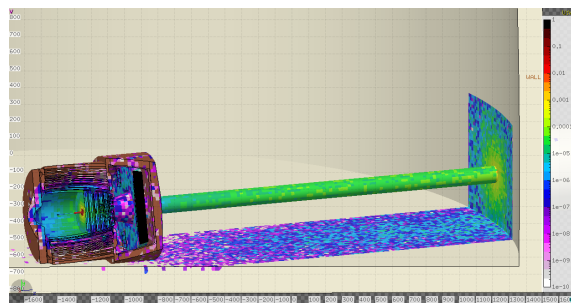
3909 More details and plots on the studies can be found in [[302](#)].



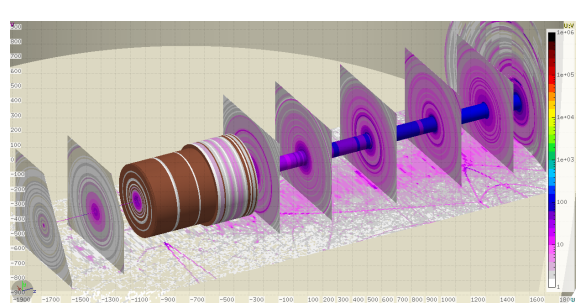
(a) Energy deposited (W) per  $cm^3$  for PVDIS configuration and Liquid Deuterium target



(c) Dose equivalent (mrem) per hour after 1 hour from beam exposure for PVDIS configuration and Liquid Deuterium target

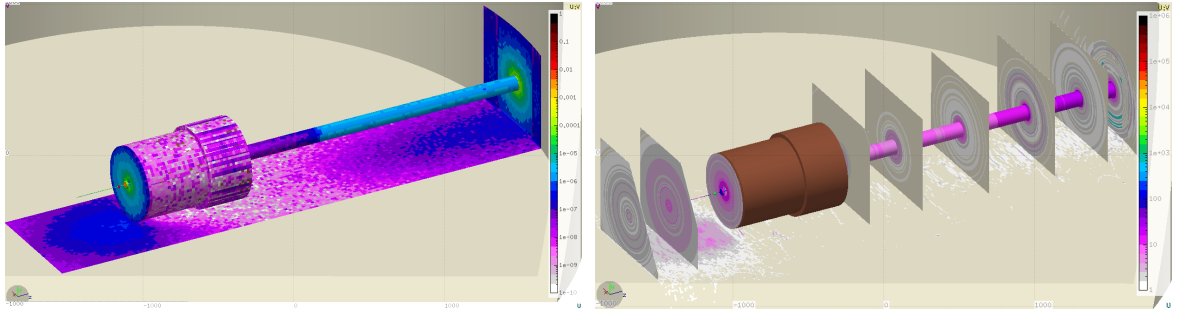


(b) Energy deposited (W) per  $cm^3$  for PVDIS configuration and Liquid Deuterium target (Hall view)

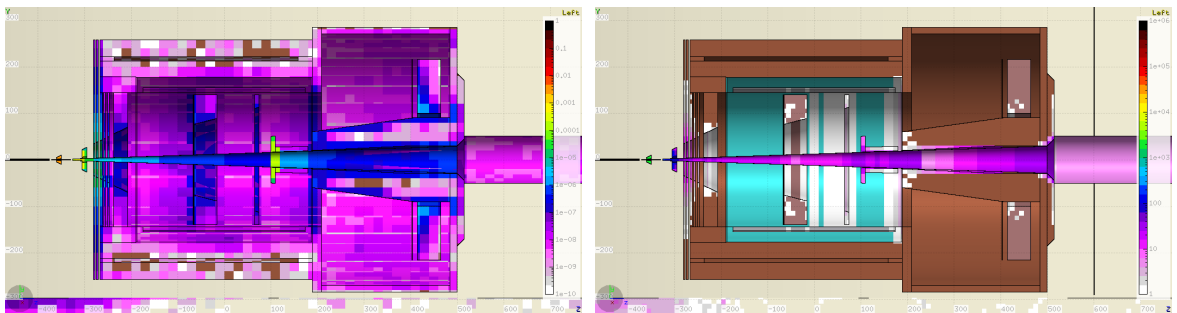


(d) Dose equivalent (mrem) per hour after 1 hour from beam exposure for PVDIS configuration and Liquid Deuterium target (Hall view)

Figure 156: Energy deposited (W) per  $cm^3$  (156a and 156b) considering running condition with Liquid Deuterium target and electron beam current of  $100\mu A$ . The spectrum is averaged in blocks of size of  $20cm \times 20cm \times 20cm$  in order to boost statistics, since this simulation with the complex SoLID design is very high demanding in CPU time. One can see how the power deposited in the first baffle region is considerably higher respect to the one expected in the exit hole of the magnet. In order to obtain the integrated power deposition for the expected beam time for the PVDIS configuration (2000h), multiply the values of the plots by  $7.2E+06$ . Activation dose equivalent (mrem) rate per hour (156c and 156d) expected with the same configuration after 1 hour from beam exposure (  $100\mu A$  for a month ). This study has been done in order to simulate condition in the Hall during running time. For a more accurate description of the activation expected in the baffle area, see figure 154



(a) Energy deposited (W) per  $cm^3$  considering SIDIS running (b) Dose equivalent (mrem) per hour after 1 hour from beam exposure for SIDIS configuration and  $^3He$  target (Hall view) (Hall view)



(c) Energy deposited (W) per  $cm^3$  considering SIDIS running (d) Dose equivalent (mrem) per hour after 1 hour from beam exposure for SIDIS configuration and  $^3He$  target (Inside the magnet) (Inside the magnet)

Figure 157: Energy deposited (W) per  $cm^3$  (157a 157c) considering running condition with  $^3He$  target and electron beam current of  $15\mu A$ . In order to obtain the integrated power deposition for the expected beam time for the SIDIS configuration (3000h), multiply the values of the plots by  $1.08E+07$ . The main part of the energy is deposited, as expected, in the target area and in the collimator positioned in front of the nose-cone part of the magnet. The energy deposited in the exit hole of the magnet is considerably lower than with the PVDIS configuration. Activation dose equivalent (mrem) rate per hour (157b and 157d) expected with the same configuration after 1 hour from beam exposure ( $15\mu A$  for a month). This study has been done in order to simulate condition in the Hall during running time.

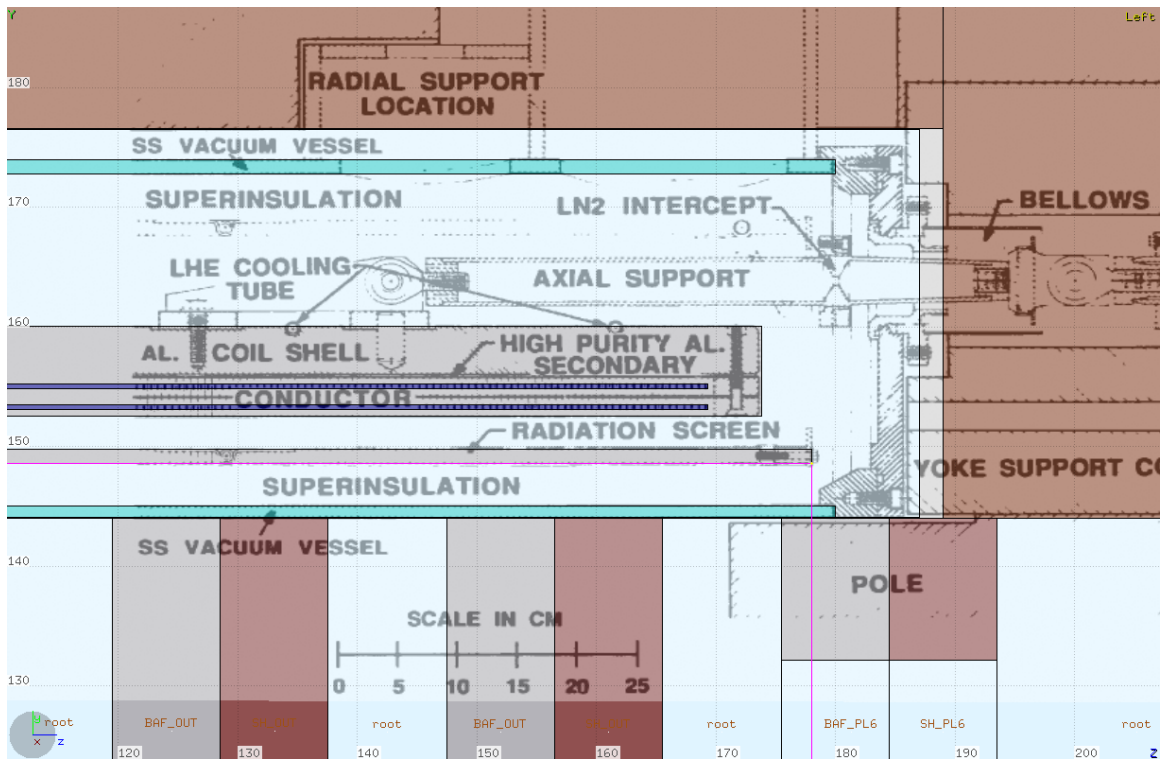
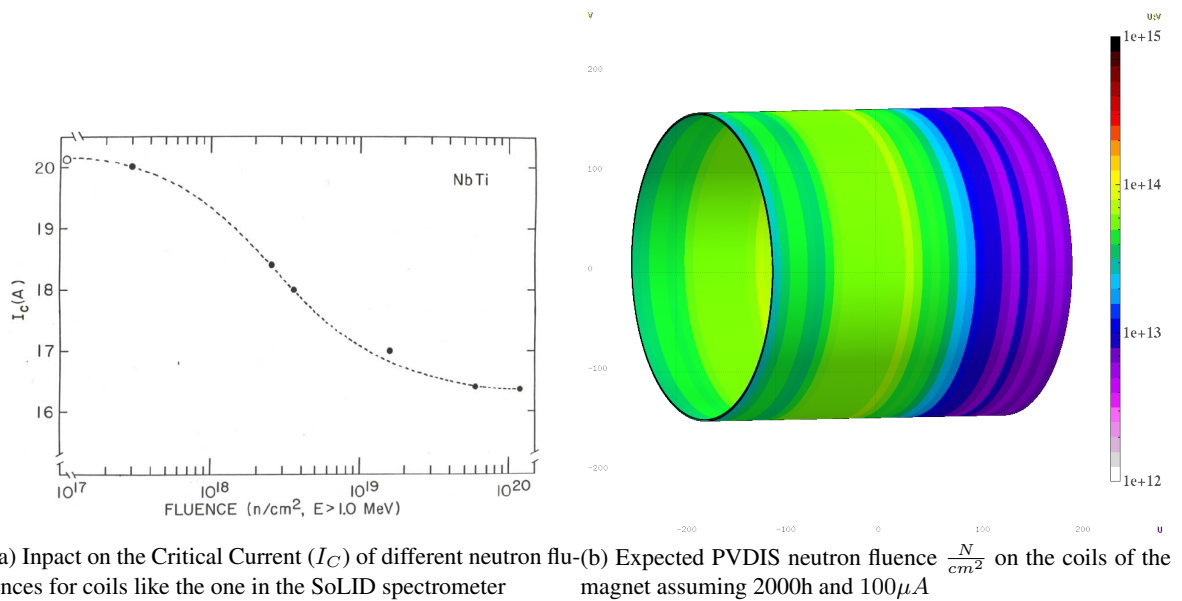


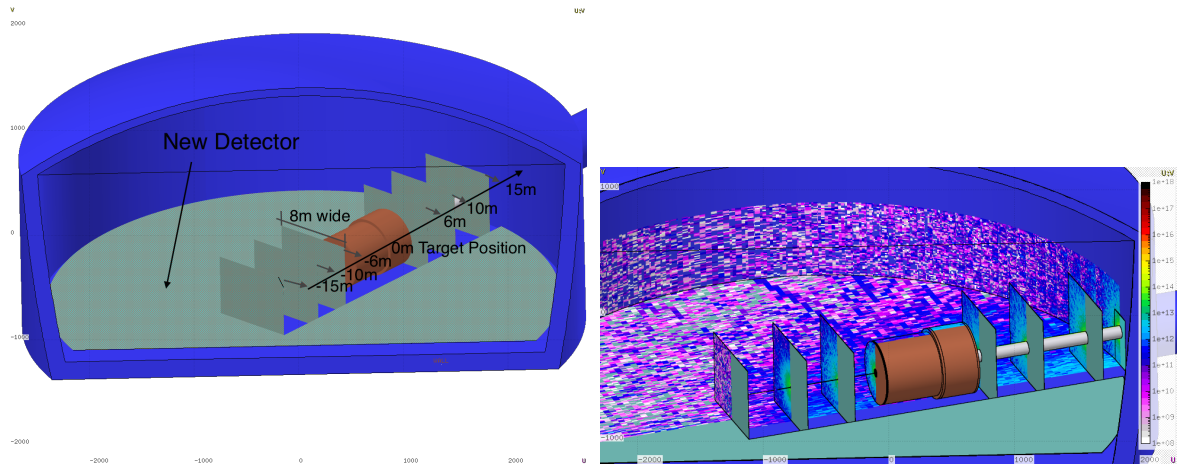
Figure 158: Existing engineering design for the CLEO magnet are put in comparison with the simulation design used for this study.



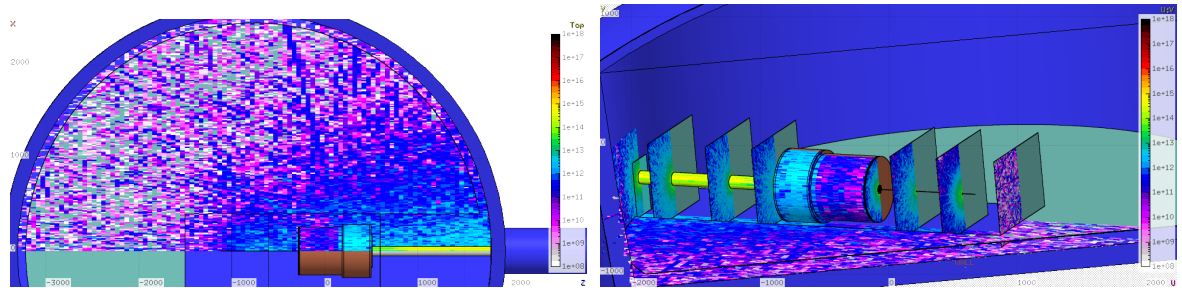
(a) Impact on the Critical Current ( $I_C$ ) of different neutron fluences for coils like the one in the SoLID spectrometer  
 (b) Expected PVDIS neutron fluence  $\frac{N}{cm^2}$  on the coils of the magnet assuming 2000h and  $100\mu A$

Figure 159: Expected exposure of the Solid magnet coil and expected impact of neutron fluence on Nb-Ti based coil for the Critical Current of the superconducting magnet.





(a) Position of the different planes where in the next plots (b) Estimate of radiation damage in the Hall with the SoLID spectrometer and the PVDIS configuration: A different view planes are put at different positions perpendicular to the beam-line; A plane is also put parallel to the floor at 1m of height



(c) Estimate of radiation damage in the Hall with the SoLID spectrometer and the PVDIS configuration: A different view (d) Estimate of radiation damage in the Hall with the SoLID spectrometer and the PVDIS configuration: A different view

Figure 160: Estimate of radiation damage in the Hall with the SoLID spectrometer and the PVDIS configuration. The leading part of radiation present in the Hall for the SoLID spectrometer is leaking through the downstream part of the beam-line assembly. In this plot is shown the 1MeV Neutron equivalent flux per  $cm^2$  on the volumes surfaces estimated for 2000h of continuous running with a beam current of  $100\mu A$  (This is the expected beam-time with the PVDIS configuration). In order to better show the behavior of the radiation leaking, different plane of observation have been inserted (at a distance from the target of  $\Delta z = -15m$ ,  $\Delta z = -10m$ ,  $\Delta z = -6m$ ,  $\Delta z = 6m$ ,  $\Delta z = 10m$ ,  $\Delta z = 15m$  (see Fig. 160a). The level of radiation leaking increases as one moves farther from the target, reaching a maximum  $\leq 10^{15} \frac{N_{1MeV}}{cm^2}$ . These levels of radiation is on the “mild to severe” damage range for commercial semiconductors ( as one can see comparing them with Estimate of the tolerance of different material plots 147). This area is not expected to carry any delicate equipment. On the upstream section of the beam-line, the level of radiation leaking is tolerable to also commercial equipment (not rad-hard). A comparable plot of this one, with a projection plane on the zy axis, is show in figure 160c



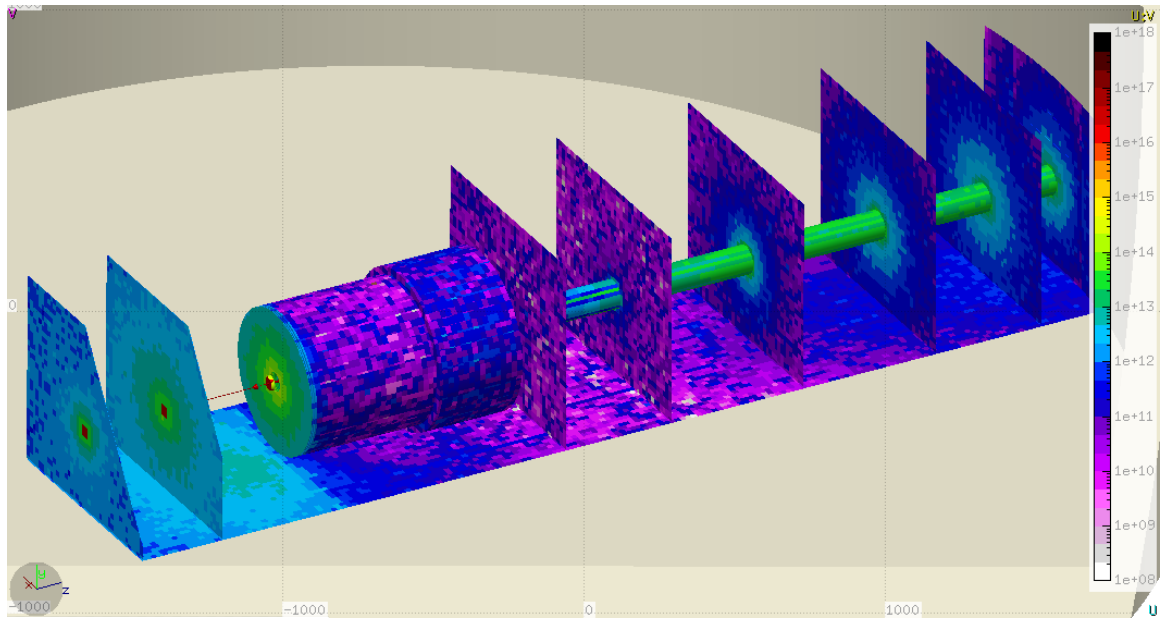


Figure 161: Estimate of radiation damage in the Hall with the SoLID spectrometer and the SIDIS  $^3\text{He}$  configuration. The leading part of radiation present in the Hall for the SoLID spectrometer is originating from the target area and the closer surface of the magnet. In this plot is shown the 1MeV Neutron equivalent flux per  $\text{cm}^2$  on the volumes surfaces estimated for 3000h of continuous running with a beam current of  $15\mu\text{A}$  (This is the expected beam-time with the SIDIS configuration). In order to better show the behavior of the radiation leaking, different planes of observation have been inserted (at a distance from the center of the Cryostat of the magnet of  $\Delta z = -10\text{m}$ ,  $\Delta z = -6\text{m}$ ,  $\Delta z = 6\text{m}$ ,  $\Delta z = 10\text{m}$ ,  $\Delta z = 15\text{m}$ ,  $\Delta z = 20\text{m}$ ,  $\Delta z = 24\text{m}$ ). The level of radiation leaking increases as one moves farther from the target, reaching a maximum  $< 10^{14} \frac{\text{N}_{1\text{MeV}}}{\text{cm}^2}$ . These levels of radiation is on the “mild to severe” damage range for commercial semiconductors ( as one can see comparing them with Estimate of the tolerance of different material plots 147). This area is not expected to carry any delicate equipment.

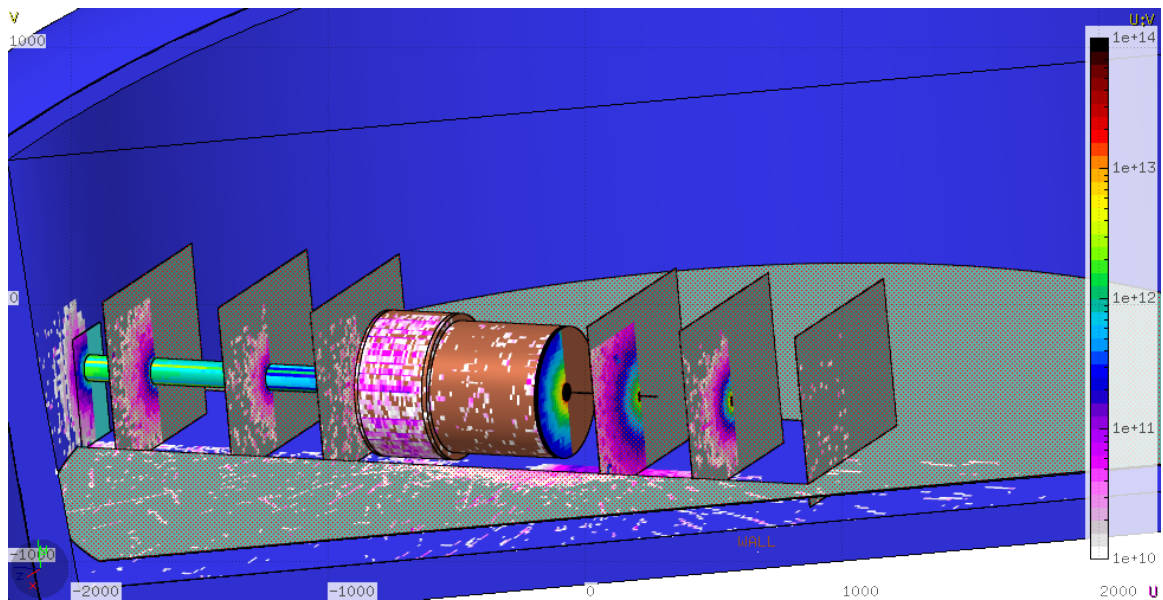


Figure 162: Estimate of radiation damage in the Hall with the SoLID spectrometer and the  $J/\Psi$  configuration with a 15cm Liquid Hydrogen target. The leading part of radiation present in the Hall for the SoLID spectrometer is originating from the target area and the closer surface of the magnet. In this plot is shown the 1MeV Neutron equivalent flux per  $cm^2$  on the volumes surfaces estimated for 60 days of continuous running with a beam current of  $3\mu A$  (This is the expected beam-time with the  $J/\Psi$  configuration). In order to better show the behavior of the radiation leaking, different planes of observation have been inserted (see Fig. 160a for reference of the position of each plane). The Color scale is different than in the previous cases in order to enhance the details in the desired region.

## 3910 **16 Slow Controls**

3911 Slow Controls typically covers the “infrastructure support” systems and logging for the detector  
3912 package as a whole. This includes real-time controls and status monitoring of power, vacuum, tem-  
3913 peratures, etc., in addition to integrated safety interlocks and alarm functions. Typical measurement  
3914 and response times for such systems are on the order of a 100s of milliseconds to seconds. More  
3915 rapid response times are also available if needed. Common examples of slow controls involve the  
3916 high- and low-voltage power supplies for all detector apparatuses, gas composition and flow regu-  
3917 lation, control of gain-monitoring systems, etc.

3918 This section *excludes* any discussion of slow controls for the target and solenoid magnet. Slow  
3919 controls for those systems will be designed and implemented by their respective working groups.  
3920 The systems covered here involve only the SoLID detector subsystems.

3921 Due to the obvious interdependence between the hardware and the software used to control it,  
3922 details of several slow control components will need to wait until the hardware design is better  
3923 developed (*eg.* gas systems). We will give an overview of some baseline requirements and expecta-  
3924 tions that the Collaboration will abide by to ensure slow controls development and implementation  
3925 will proceed smoothly.

3926 It is understood that any fast interlocks (*i.e.* millisecond level or faster) that cross system bound-  
3927 aries need to be identified at the design stage. Examples may include tripping high-voltage if the  
3928 gas flow is interrupted for the GEM system, disabling the flammable gas flows in the event of a fire  
3929 alarm, etc.

### 3930 **16.1 General Requirements**

3931 The Collaboration agrees that all components must be able to interface with the EPICS (Experi-  
3932 mental Physics and Industrial Control System) environment already present at Jefferson Lab. This  
3933 imposes a common mid-level API for inter-system communication and allows the systems to take  
3934 advantage of the well supported EPICS infrastructure at JLab. This includes local expert support  
3935 from other experimental Halls (particularly Halls B & D), and the Accelerator Division for any  
3936 necessary PLC, software and/or hardware IOC development, as well as taking advantage of JLab’s  
3937 EPICS data archiver “MYA”.

### 3938 **16.2 Frontend GUIs**

3939 The graphical interface employed for all systems is expected to be based on the Control Systems  
3940 Studio (CSS) environment. This is an Eclipse-based toolkit that is slowly replacing the legacy  
3941 EDM/MEDM GUIs developed during JLab’s 6 GeV period. Hall D and Hall B already make exten-  
3942 sive use of the CSS toolkit, and Hall C will be migrating its legacy M/EDM GUIs as time permits.

3943 The BEAST alarm handler, part of the CSS system, will be used to monitor EPICS variables  
3944 and alert shift crew and/or external experts of problems.

3945 Systems that require lower-latency response times than softIOCs and EPICS polling systems  
3946 can provide will investigate the CompactRIO (cRIO) standard successfully used in Halls B & D.

3947 The Hall B slow controls development experience, in particular, has been well documented by  
3948 those involved and will provide an excellent local repository of interface code and management  
3949 processes that SoLID can leverage.

### 3950 **16.3 High/Low Voltage Controls**

3951 High Voltage hardware will be standardized as much as possible. CAEN and Wiener systems are  
3952 both in use as JLab. They each come with integrated EPICS support and pre-existing software sup-  
3953 port on-site. Detector, sub-detector, and individual channel control and monitoring will be provided.  
3954 Legacy LeCroy HV systems will *not* be supported.

### 3955 **16.4 DAQ Crate Control**

3956 It is desired to have realtime monitoring of VME and other data acquisition crate power systems and  
3957 temperatures. All DAQ crates are expected to provide an integrated ethernet interface and EPICS  
3958 support. Examples of such hardware include the Wiener 60xx series in common use across JLab.

### 3959 **16.5 Gas Systems Requirements**

3960 In addition to the necessary EPICS interface, the Collaboration agrees that the various gas sub-  
3961 systems (Cerenkovs, GEMs, MRPC) will standardize any hardware that requires software support.  
3962 This includes items such as mass flow controllers (MFCs) and hardware process controllers, etc.  
3963 This will allow for a common spares inventory and simplify control software development and  
3964 maintenance.

### 3965 **16.6 Detector Systems**

3966 The following list runs through the various sub-detectors and summarizes the necessary slow con-  
3967 trols.

- 3968 • **EC:** HV control and monitoring.
- 3969 • **FA/LASPD:** HV control and monitoring.
- 3970 • **GEM Tracking:** HV/LV control and monitoring. The non-recirculating gas system will use  
3971 Ar/CO<sub>2</sub> at STP and will employ a basic gas mixer system with flow monitoring and control.
- 3972 • **LGC:** HV control and monitoring. The CO<sub>2</sub> gas employed operates at STP and will be served  
3973 by a simple non-recirculating “flow-through” system.
- 3974 • **HGC:** HV control and monitoring. The C<sub>4</sub>F<sub>10</sub> gas employed is expensive and used in large  
3975 quantities. Such a system will require a somewhat sophisticated recapture/purification/recirculation  
3976 infrastructure involving PLC/IOC controls that remain to be designed.
- 3977 • **MRPC:** HV/LV control and monitoring. The MRPC gas system employs a 5% SF<sub>6</sub> + 90%  
3978 R134 + 5% Isobutane mix that will likely require a recapture/recirculation infrastructure also  
3979 involving a PLC/IOC system. This is still to be designed.

3980 In addition to the above items, gain-monitoring systems have been discussed that would also require  
3981 some nominal controls. It is not expected that such systems would be a significant burden.

## 3982 **17 Electron Beam Polarimetry**

3983 The interpretation of the measurement of the parity-violating asymmetry relies on precise correc-  
3984 tion for finite beam polarization, with an accurate absolute normalization to 0.4% accuracy at both  
3985 11 GeV and 6.6 GeV. This will be achieved using two independent measurement techniques with  
3986 independent sources of calibration errors, which can be directly cross-checked to high precision.  
3987 This is an ambitious goal. The most precision electron beam polarimetry result to date in a physics  
3988 publication is the 0.5% Compton polarimetry result by the SLD collaboration [303]. Compton po-  
3989 larimetry is well-suited for the energy and intensity of the upgraded Jefferson Lab beam. Plans for  
3990 upgrading the existing Hall A Compton polarimeter to achieve 0.4% precision are described below.

3991 The best candidate for a second, high-precision, independent measurement is Møller polarime-  
3992 try. The use of iron foils in high magnetic fields can provide a precision well better than 1%, and  
3993 may prove to be more precise to the level of 0.5%.

### 3994 **17.1 Compton Polarimetry**

3995 Compton polarimetry is a very promising technique for high precision polarimetry at beam en-  
3996 ergies above a few GeV. Beam interactions with a photon target are non-disruptive, so Compton  
3997 polarimetry can be employed at high currents as a continuous polarization monitor. The photon  
3998 target polarization can be measured and monitored with a very high precision, and the scattering  
3999 between a real photon and free electron has no theoretical uncertainty, such as the atomic or nuclear  
4000 effects which can complicate other measurements. Radiative corrections to the scattering process  
4001 are at the level of 0.3% and are very precisely known. While the SLD collaboration result, with  
4002 a precision of 0.5%, demonstrates the feasibility of very high accuracy Compton polarimetry, that  
4003 measurement was ultimately limited by the inability to detect individual scattered particles (due to  
4004 the pulsed beam) and the high Bremsstrahlung background in the photon detector due to the prox-  
4005 imity to the interaction region. Conditions at JLab are favorable for both of these concerns. The  
4006 existing apparatus and plans for future improvements are described below.

### 4007 **17.2 The Hall A Compton Polarimeter Baseline Upgrade**

4008 As pictured in Fig. 163, the Hall A Compton polarimeter [304] is located in a chicane, about 15  
4009 meters long, just below the beamline. After modification of the bend angle to accommodate 11  
4010 GeV running with the existing chicane magnets, the electron-photon interaction point will be 21 cm  
4011 below the primary (straight-through) beamline. After passing the electron-photon interaction point,  
4012 the electron beam is bent about 3.5 degrees by the third chicane magnet and then restored to the  
4013 main beamline. The scattered electrons are separated from the primary beam and detected using  
4014 silicon microstrips, just before the fourth chicane magnet. Scattered photons pass through the bore  
4015 of the third chicane magnet to be detected in a calorimeter.

4016 The photon target is a 0.85 cm long Fabry-Perot cavity crossing the electron beam at an angle  
4017 of  $1.4^\circ$ . The laser system can be configured for infrared (1064 nm) or green (532 nm) light, and  
4018 has achieved power levels of 10 kW of green light for polarimetry measurements. The laser light is  
4019 polarized using a quarter-wave plate, and can be toggled between opposite polarizations of highly  
4020 circularly polarized light. The feedback loop which locks the laser to the cavity resonance can  
4021 be disabled to enable backgrounds from all non-Compton-scattering processes. To reduce overhead  
4022 from the time required to re-lock the cavity, the transition between laser states is typically performed  
4023 with a period of 1-2 minutes. The polarization of the transmitted light from the locked cavity and

4024 the reflected light from the unlocked cavity are each monitored and can be used to characterize the  
 4025 laser polarization at the interaction point.

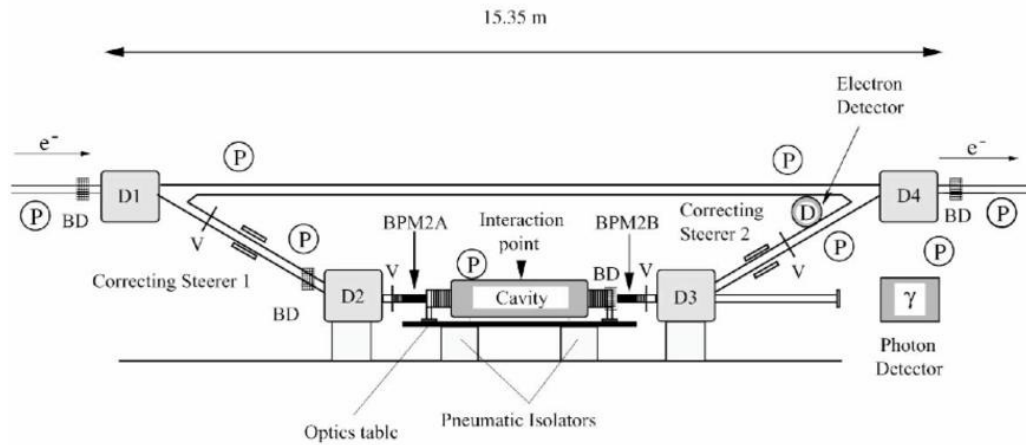


Figure 163: Schematic of the Hall A Compton polarimeter. Figure from [304].

4026 The vacuum in the interaction region is at the level of few  $\times 10^{-8}$  torr, implying a photon back-  
 4027 ground rate due to Bremsstrahlung scattering from residual gas of around  $5 \text{ Hz}/\mu\text{A}$ . The dominant  
 4028 source of background in the photon detector is thought to be tails of the beam halo distribution  
 4029 interacting with the apertures in the interaction region. In contrast, for the electron detector the  
 4030 background is thought to be dominated by energy tail or position halo of the primary beam since  
 4031 electrons from aperture scattering would presumably not cleanly transit the third dipole. When  
 4032 well-tuned, the background rates in the photon and electron detectors have been seen to be roughly  
 4033 similar: around  $<100 \text{ Hz}/\mu\text{A}$  in recent use. At 11 GeV, with a 10 kW IR cavity, the Compton-  
 4034 scattered rates would be approximately  $20 \text{ kHz}/\mu\text{A}$  and the asymmetry will range from 17.8% to  
 4035  $-4\%$  over the energy spectrum. At 6.6 GeV, a 10 kW green cavity will be used, which will provide a  
 4036 rate of  $13 \text{ kHz}/\mu\text{A}$  with an asymmetry ranging from 20.9% to  $-4.7\%$ . If backgrounds remain com-  
 4037 parable to recent operation, statistical precision of 0.4% would be possible in less than 5 minutes,  
 4038 depending on the specific detection and analysis approach which is considered.

4039 Electrons are detected in a set of 4 planes of silicon microstrips located just before the 4th  
 4040 dipole. Each microstrip instruments 192 strips with a pitch of  $240 \mu\text{m}$ . Custom readout electronics  
 4041 pre-amplify and discriminate signals from the microstrips, implement a simple tracking algorithm  
 4042 to reduce non-directional backgrounds, and count hits in each strip over specified integration gates  
 4043 corresponding to the helicity pattern of the electron beam. Presently, this system is operating at low  
 4044 efficiency with poor signal size for a minimum ionizing track compared to environmental noise on  
 4045 individual strips. The baseline upgrade would include an improvement in this system to achieve  
 4046 high efficiency and high signal-over-noise for the microstrip readout. The use of diamond mi-  
 4047 crostrips, such as were recently successfully used for the Hall C Compton polarimeter [305], is  
 4048 under consideration. Such diamond microstrips are more difficult to procure and in principle are  
 4049 more challenging to instrument than silicon strips, however, they are more radiation hard and less  
 4050 susceptible to low-energy photon backgrounds.

4051 The calorimeter for detecting scattered photons lies about 7 meters downstream of the interac-  
 4052 tion point. The strong forward boost of scattered photons leads to a tightly collimated photon beam  
 4053 ( $<1 \text{ mrad}$ ), so the calorimeter size is determined by consideration of energy resolution through

4054 shower loss. The photon calorimeter is a GSO crystal scintillator of 6 cm diameter and 15 cm  
4055 length, with a single photomultiplier tube. The PMT signal is split between two parallel data acqui-  
4056 sitions: one with a fast-counting, buffered ADC self-triggered on pulses from the photon detector,  
4057 and the other utilizing a 250MHz flash ADC (fADC) to integrate the total signal over periods corre-  
4058 sponding to the helicity pattern of the electron beam. The fADC system can also record a very low  
4059 rate of individual pulses for calibration. Each of these dual readouts can be analyzed independently.  
4060 The fast counting ADC readout and the sample pulses in the fADC system can both be triggered  
4061 using the electron detector, providing an electron-photon coincidence spectrum for calibration.

### 4062 **17.3 Upgrades Beyond the Baseline**

4063 There are several issues which must be addressed, related either to operation at the higher beam  
4064 energy or to the very high level of precision which is proposed.

- 4065 • The electron beam halo — a term meant to describe a long tail on the momentum or position  
4066 distribution of the beam — is expected to be larger at 11 GeV compared to 6 GeV operation,  
4067 due to synchrotron light emission in the recirculation arcs which will increase the momentum-  
4068 normalized beam emittance. For Compton polarimetry, a tail on the beam energy distribution  
4069 is directly responsible for the dominant backgrounds in electron detection, while scattering of  
4070 beam halo from narrow apertures in the interaction region is thought to dominate backgrounds  
4071 in photon detection.
- 4072 • The measurement of the laser polarization must be performed with very high precision.
- 4073 • The total power of synchrotron radiation emitted by the beam in the chicane arcs will be more  
4074 than an order of magnitude higher compared to Compton measurements in the 6 GeV era,  
4075 and this radiation spectrum will be significantly stiffer. Dilution from this radiation would  
4076 complicate photon and electron detection.
- 4077 • Photon detection must provide a well-characterized and linear response for photons in an  
4078 energy range from about 3 GeV to low energies and over a large variation in signal rate, while  
4079 being radiation hard and also insensitive or shielded from the synchrotron radiation power.

4080 These issues are addressed by several modifications which go beyond the baseline 11 GeV upgrade,  
4081 listed below and described in the following sections. These improvements are expected to allow us  
4082 to achieve the precision goals listed in Table 34.

- 4083 • **Laser system** A larger crossing angle for the photon and electron beams would allow larger  
4084 electron beam apertures, and reduce backgrounds in the photon detector. This increase in  
4085 crossing angle comes at the expense of lower luminosity, leading to a tradeoff in signal rate  
4086 and background rate. With the high cavity power that has been achieved with this laser system,  
4087 we do not expect to be limited by laser power even at increased crossing angle. The decision  
4088 on crossing angle can be made when more is known about beam conditions at 11 GeV. The  
4089 beamline through the chicane magnets is one inch inner diameter, which is about a factor of  
4090 three larger than the aperture required by the present laser crossing angle. The luminosity  
4091 would drop roughly linearly with crossing angle, and even with a factor of 1/3 the statistical  
4092 power of the signal rate for a 10 kW cavity would still be sufficient assuming a reduced  
4093 background fraction.

4094 In addition to the option to increase this crossing angle, a system for measuring laser po-  
4095 larization inside the resonant optical cavity (although not while locked to resonance) must

Relative error (%)	electron	photon
Position asymmetries*	-	-
$E_{Beam}$ and $\lambda_{Laser}$ *	0.03	0.03
Radiative Corrections*	0.05	0.05
Laser polarization*	0.20	0.20
Background / Deadtime / Pileup	0.20	0.20
Analyzing power Calibration / Detector Linearity	0.25	0.35
Total:	0.38	0.45

Table 34: Goals for systematic errors for the Hall A Compton polarimeter at 11 GeV. Topics marked \* are common systematic errors between the photon and electron analyses, while the others are largely independent between the detector systems.

4096 be developed and used, along with a thorough study of all optical components, to improve  
4097 knowledge of the photon polarization.

4098 • **Chicane Modification** The synchrotron light power on the photon detector will be signifi-  
4099 cantly reduced by installing shims to increase the fringe fields of the chicane dipole magnets  
4100 in the interaction region. This would also soften the synchrotron energy spectrum, making  
4101 shielding more effective. The effect of synchrotron light on the electron detector is being  
4102 investigated, with the possibility to add some baffling to limit reflection into the detector.

4103 • **Photon Detector** The photon detection system used for recent running will be replaced with  
4104 a detector better matched to the Compton photon energy spectrum for 11 GeV operation.

4105 These upgrades are described in more detail below.

### 4106 17.3.1 Laser System and Luminosity

4107 As described above, in the current configuration of the Hall A Compton, the electron beam interacts  
4108 with green (532 nm) light in a resonant optical cavity at a crossing angle of about  $1.4^\circ$ . After  
4109 accounting for the length of the optical cavity (about 85 cm) and the finite size of the cavity mirror,  
4110 it is necessary to enforce an aperture on the electron beam of  $\pm 5$  mm. It is thought that this narrow  
4111 aperture is the dominant source of background for 6 GeV running. At higher energies, synchrotron  
4112 light emission in the accelerator recirculation arcs will increase the beam emittance and presumably  
4113 lead to significantly larger backgrounds from this aperture scattering. In present use of the Compton  
4114 polarimeter, frequent beam tuning is required to maintain operation with the signal-over-background  
4115  $> 10$ . A large background signal is often associated with large fluctuations over the period of time in  
4116 the laser on/off cycle used to measure backgrounds. This reduces the measurement precision, and  
4117 potentially introduces a significant systematic error through instability in the phototube under large  
4118 variations in rate. For this reason, it is desirable to keep the signal-over-background ratio large.

4119 The aperture can be widened only by increasing the laser crossing angle which would also  
4120 lower the luminosity. Although the baseline upgrade plans do not make provision for changing this  
4121 crossing angle, operability at 11 GeV may require larger apertures. At a finite crossing angle  $\alpha$ , the  
4122 luminosity for a continuous-wave electron and photon beam, with intersecting electron and photon



4123 waists sizes  $\sigma_e$  and  $\sigma_\gamma$ , is given by:

$$\mathcal{L} \approx \frac{1 + \cos \alpha}{\sqrt{2\pi}} \frac{I_e P_\gamma}{ek_0 c} \frac{1}{\sqrt{\sigma_e^2 + \sigma_\gamma^2}} \frac{1}{\sin \alpha} \quad (28)$$

4124 Here  $P_\gamma$  is the power of the photon beam,  $I_e$  is the current in the electron beam, and  $k_0$  is the  
4125 photon energy scattered at the kinematic maximum limit of colinear backscattering. As an example:  
4126 at 10000 W stored power at 532 nm, the Compton scattering rate would be about 12 kHz/ $\mu$ A at  
4127  $1.4^\circ$  crossing angle and about 4.8 Hz/ $\mu$ A at  $3.5^\circ$ . At the expense of approximately a factor of  
4128 2.5 in luminosity, that larger crossing angle would allow a  $\pm 0.5$  inch aperture, comparable to the  
4129 maximum aperture allowed by the 1" beam pipe diameter in the bore of the existing dipole magnets  
4130 in the chicane.

4131 With an available laser power of 10 kW, the polarimeter is not expected to be limited by low  
4132 signal rates even at the larger crossing angles. However, the drop in luminosity with increasing  
4133 crossing angle suggests that any change must be optimized from the point of view of signal-over-  
4134 background. Until beam tests at higher beam energies are performed to form reliable estimates of  
4135 background levels, it is prudent to design for both large crossing angle and large luminosity.

4136 We propose the use of an infrared cavity storing 10 kW of optical power at 1064 nm for operation  
4137 at beam energy above 8.8 GeV, and a cavity storing 10 kW of optical power at 532 nm for beam  
4138 energies at 6.6 GeV and below. The primary disadvantages to the longer photon wavelength are  
4139 the reductions in analyzing power and softening of the energy spectrum (17% analyzing power and  
4140 1.8 GeV maximum photon energy for IR at 11 GeV, compared to 32% and 3 GeV for 532 nm).  
4141 The advantages for the IR system would be a greater available luminosity and system reliability.  
4142 While the cross-section is very similar between the two photon energies, at 1064 nm there are twice  
4143 as many photons per unit energy. At 10 kW, an IR cavity would provide a rate of 9 kHz/ $\mu$ A  
4144 at the increased crossing angle to allow the full  $\pm 0.5$ " electron beam aperture, or 23 kHz/ $\mu$ A at the  
4145 original design  $1.4^\circ$  crossing angle. The 532 nm system requires an additional stage to frequency-  
4146 double the original 1064 laser light. Without this doubling stage, the IR system can inject higher  
4147 power to the cavity, enabling higher cavity power or the same cavity power with reduced cavity  
4148 gain. A lower gain cavity will typically be more robust, and and less sensitive to radiation damage  
4149 of the cavity optics. At beam energies below 8.8 GeV, the improvement in analyzing power and  
4150 higher scattered photon energy endpoint are worth the possible trade-off in ease of operability.

4151 Precision electron beam polarimetry also requires precise determination of the polarization of  
4152 the photon target. This has proved to be the dominant systematic error contribution in recent Hall A  
4153 Compton polarimeter measurements, in part because the use of a high-gain resonant cavity signifi-  
4154 cantly complicates this determination. In a resonant cavity, the polarization state of the stored light  
4155 can not be directly measured without destroying the resonance. For the present Hall A polarimeter,  
4156 the laser polarization is inferred from measurements of the light that transmits through the cavity.  
4157 A transfer function, relating the polarization of light in the Compton Interaction Region (CIP) to  
4158 the polarization measured in the transmitted beam outside the vacuum vessel, is determined from  
4159 measurements with an un-locked cavity. The highly-reflective cavity mirrors must be removed for  
4160 these measurement, and the cavity must be open to air, which implies a relaxation of stress-induced  
4161 birefringence of the vacuum entrance and exit windows. Contributions from birefringence in the  
4162 cavity mirror substrate and stress on the vacuum windows can be characterized separately, but as  
4163 a practical matter these corrections are difficult to determine with high precision. For the Hall A  
4164 polarimeter, previous studies have quoted the uncertainty in beam polarization to be 0.35%, but in  
4165 recent operation the uncertainty could not be bounded to better than 0.7%.

4166 An improved technique has been used in Hall C to control the laser polarization uncertainty. The

4167 polarization of light arriving at the cavity entrance can be inferred from light reflected back from  
 4168 the cavity and analyzed with the same apparatus used to create the initial polarization state, mea-  
 4169 suring a single power level [306]. This technique was employed in Hall C to maximize the circular  
 4170 polarization of light injected in the cavity and to monitor the polarization during the run. It was  
 4171 verified to work by two methods. In the first, with the cavity under vacuum in running conditions,  
 4172 a scan over a broad range of initial polarization states was performed, and the recorded analyzed  
 4173 reflected power was shown to be well described by the simple hypothesis of optical reversibility. A  
 4174 more direct verification was made with the cavity opened, directly measuring the polarization of the  
 4175 injected light in the cavity and correlating this with the analysis of the reflected light. The correla-  
 4176 tion is shown over the full range of the scan, and zoomed in for measurements at maximum circular  
 4177 polarization, in Fig. 164. In operation, the Hall C Compton polarimeter ran with the reflected light  
 4178 very near minimum, with an implied uncertainty on the circular polarization within the cavity of  
 4179 0.1%.

4180 These studies demonstrate that this technique may provide knowledge and monitoring of the  
 4181 circular polarization in the cavity to the level of 0.1%. An *in situ* measure of the polarization would  
 4182 be a valuable confirmation of this procedure. Modifications to the interaction region will be made  
 4183 to allow an insertable, vacuum-compatible analysis assembly for measurements of the beam in the  
 4184 CIP. The power level for such measurements will necessarily be very low, as the highly reflective  
 4185 mirrors of the cavity will attenuate incident light, but such a direct measurement would include all  
 4186 effects of birefringence and depolarization in the injection of optical power into the cavity.

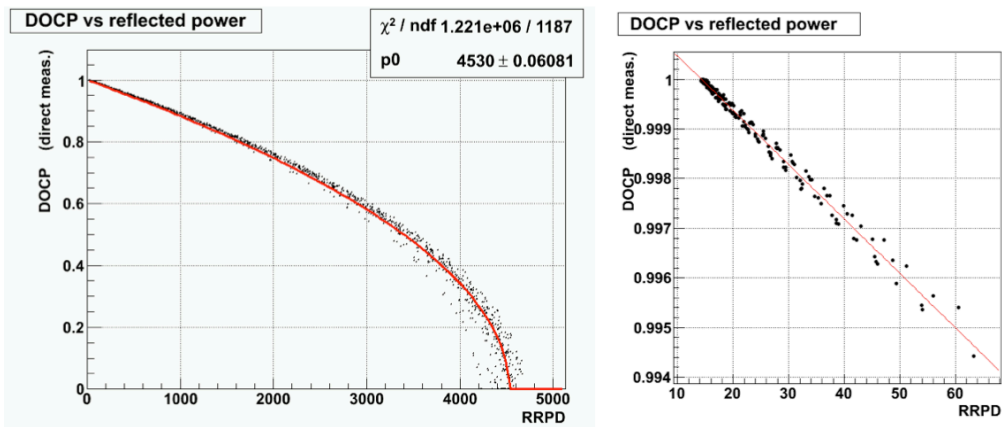


Figure 164: Measured degree of circular polarization in the Hall C Compton laser cavity vs. the polarization-analyzed reflected light, measured over a broad scan of initial polarization states. The figure on the right is zoomed in the region of maximum circular polarization.

### 4187 17.3.2 Alternative Laser System

4188 An alternative laser system has also been considered, based on the use of a short-pulse RF laser  
 4189 synchronized to the electron bunch frequency. Such a system would concentrate laser power on  
 4190 the electron bunches, in effect creating an electron-photon collider. For a laser with narrow pulse  
 4191 structure ( $\approx 10$  ps) and repetition frequency sub-harmonic to the electron beam ( $f_{laser} = 499$  MHz

4192 /  $n$  with integer  $n$ ), the the ratio of luminosity for the same average power goes as:

$$\frac{\mathcal{L}_{pulsed}}{\mathcal{L}_{CW}} \approx \frac{c}{f_{beam} \sqrt{2\pi}} \frac{1}{\sqrt{\sigma_{e,z}^2 + \sigma_{\gamma,z}^2 + \frac{1}{\sin^2 \alpha/2} (\sigma_e^2 + \sigma_\gamma^2)}}. \quad (29)$$

4193 Here  $f_{beam}$  is the electron repetition rate and  $\sigma_{e,z}$  ( $\sigma_{\gamma,z}$ ) is the longitudinal size of the electron (laser)  
 4194 pulse. For the parameters relevant to the proposed system, this corresponds to an enhancement of  
 4195 luminosity per unit power of between 20-50. Commercially available mode-locked laser systems  
 4196 has been identified providing 45 W at 1064 nm, with 100 MHz repetition rates and 10 ps pulse  
 4197 widths. Assuming an average injected power of 30 W at the  $3.6^\circ$  crossing angle, such a pulsed laser  
 4198 would provide 330 Hz/ $\mu$ A with a single-pass beam, that is, without the resonant optical cavity.

4199 Although the relatively low rates would be expected to be a disadvantage, it may turn out to  
 4200 be operable depending on the characteristics of the 11 GeV electron beam. The statistical preci-  
 4201 sion (0.4% in about 3 hours) would be sufficient for a high precision measurement. The primary  
 4202 advantage of such a system would be a more straightforward determination of the laser polarization,  
 4203 relative to a high-gain optical cavity. There are other advantages as well. Locking and unlocking  
 4204 a cavity takes time, so to maintain a high duty factor for a cavity system the locked and un-locked  
 4205 periods used to determine backgrounds are long ( $\approx 1$  minute) relative to the fluctuations in the back-  
 4206 ground. On the other hand, a laser can be turned off or deflected to a dump quickly, so background  
 4207 measurements for such a single pass system could take place quickly, potentially providing superior  
 4208 control of background fluctuations even if the signal-over-background ratio is smaller. Similarly,  
 4209 without the requirement to maintain the delicate balance of signal levels necessary to robustly lock  
 4210 a high-gain cavity, systematic studies varying laser power or position would be simplified.

4211 Should the rate from such a system be unmanageably small relative to backgrounds, it could be  
 4212 roughly doubled using a “butterfly” cavity to recirculate the exit beam through the interaction point.  
 4213 A more powerful option would be a hybrid system in which the RF pulses are stored in a resonant  
 4214 optical cavity. A moderate cavity gain  $\approx 20$  would double the Compton signal rate compared to the  
 4215 10 kW, gain  $\approx 3000$  CW default design. At such a low gain, the cavity lock would be relatively easy  
 4216 to acquire, potentially enabling more rapid background measurements than the high-gain system.  
 4217 The polarization measurement would also likely be simpler than for a high-gain cavity system, as the  
 4218 injection beam in the interaction region would still be similar to the beam stored through relatively  
 4219 few resonant reflections.

4220 Such a cavity would require the dual resonance condition of being both an integral number of  
 4221 optical and RF wavelengths. This is not a particularly difficult condition to maintain. The injec-  
 4222 tion laser must be mode-locked to ensure coherence between pulses. Locking mode-locked lasers  
 4223 to Fabry-Perot cavities has been actively pursued over the last decade in development studies for  
 4224 Compton-based X-ray sources [307, 308] and for a polarized positron source for the ILC [309, 310],  
 4225 with significant technical success beyond the requirements for this proposed system.

4226 The above discussion demonstrates the utility and technical feasibility of the alternative proposal  
 4227 for a 10 ps pulse length, 100 MHz, 1064 nm laser system operating either as an injection laser for a  
 4228 gain  $\approx 20$  resonant cavity or as a 30 W single-pass system. This alternative proposal would require  
 4229 new investment for acquisition of the injection laser and high-power optics. In addition, the pos-  
 4230 sibility of time-dependent polarization in the short RF laser pulse may additionally complicate the  
 4231 laser polarization determination. The alternative system remains as a backup should complications  
 4232 in determining the laser polarization inside the high-gain laser cavity prove to be insurmountable.

4233 **17.3.3 Chicane Magnet Modification**

4234 At 11 GeV, significant synchrotron radiation is emitted when the electron beam is bent in a magnetic  
 4235 field. The total radiated power rises as  $\beta^4$  for the same bend radius. At 11 GeV, this radiation load  
 4236 will be a significant background in the photon detector and may overwhelm the signal from Compton  
 4237 scattering. Figure 165 shows the energy spectrum of synchrotron light attenuated by lead shielding  
 4238 between 1–5 mm thick, depending on the beam energy. On the left, the spectrum for 11 GeV with  
 4239 unmodified magnets is compared to calculations for the recent runs of HAPPEX-III (3 GeV) and  
 4240 PV-DIS (6 GeV). On the right, the energy spectrum (“Fringe 2”) is shown when iron extensions,  
 4241 15 cm in length, are added to the dipole magnets in order to provide an extended region of reduced  
 4242 field. This reduced magnetic field produces synchrotron light with lower energy range and with  
 4243 reduced intensity, for the portion of the electron beam trajectory that projects to the photon detector.  
 4244 With this modification, the bending strength of the magnet remains the same but the synchrotron  
 4245 light radiated into the detector is reduced by a factor of  $10^4$ , to a level comparable to HAPPEX-  
 4246 III. The magnetic field extensions were modeled using TOSCA, and have been constructed. Field  
 4247 measurements have been taken to verify the magnetic model for both the integral  $Bdl$  and the shape  
 4248 of the fringe field with and without the field extensions. These field extension pieces have been built  
 4249 and will be ready for installation at the start of 11 GeV operations.

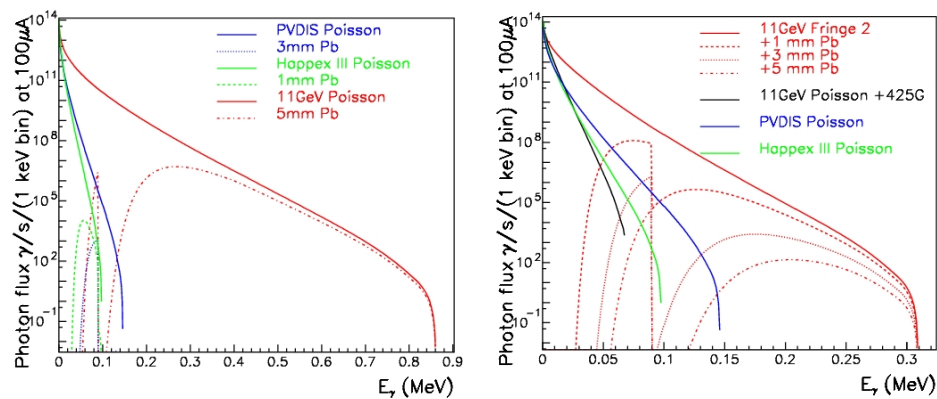


Figure 165: Energy spectrum of synchrotron radiation penetrating lead shielding of thickness listed. Plot on left shows unmodified chicane magnets, plot on right shows energy spectrum for proposed magnetic shims which reduce the field for the bend radiating into the Compton photon detector acceptance. Note the different horizontal scales between the plots.

4250 **17.3.4 Photon Detection**

4251 The specific calorimeter to be employed is not yet determined. The present calorimeter is a GSO  
 4252 crystal scintillator, which has excellent light yield suitable for measurements at low energies. The  
 4253 crystal is too small to contain most showers at higher energies, and a new calorimeter will be re-  
 4254 quired for precision measurements at 11 GeV. In the past, Hall A has used an undoped lead tungstate  
 4255 ( $\text{PbWO}_4$ ) array. This may be suitable for 11 GeV operation; the relatively low light yield for  $\text{PbWO}_4$   
 4256 is not an issue for higher photon energies of the proposed measurements or for the integrating mea-  
 4257 surements, and the high speed of this material reduces pile-up issues in counting measurements.  
 4258 Designs for multi-layer sampling calorimeters, using either scintillation or Cherenkov light, will  
 4259 also be considered.

## 4260 **17.4 Systematic Uncertainties**

4261 While the proposed system should assure operability and sufficient statistical precision at 11 GeV,  
4262 the challenge will be achieving an absolute measurement of beam polarization with a precision of  
4263 0.4%. Table 34 summarizes the goals for various contributions to systematic uncertainty. The first  
4264 four rows list sources of uncertainty which are highly or completely correlated between the electron  
4265 and photon analyses. Other potential systematic errors arise in detector readout or calibration and  
4266 are mostly or entirely decorrelated between the analyses. Each of these separate categories of po-  
4267 tential systematic uncertainty: correlated, electron-only, and photon-only, will be discussed in the  
4268 following sections.

### 4269 **17.4.1 Sources of Correlated Error**

4270 Any error associated with the Compton scattering process will be a common source of systematic  
4271 error between the electron- and photon-detector analyses. One example lies in the energy normaliza-  
4272 tion of the scattering process. The analyzing power is a function of both electron energy and photon  
4273 energy, so these must be precisely determined. The photon wavelength will be determined to better  
4274 than 0.1 nm and the electron energy to 0.05%, which leads to an uncertainty at the level of 0.03%.  
4275 A similarly small uncertainty will come from radiative corrections, which are calculable [311] with  
4276 high precision and will contribute at the level of  $10^{-3}$ .

4277 Helicity-correlated changes in luminosity of the laser/electron interaction point can introduce a  
4278 false asymmetry. Various causes of luminosity variation must be considered, such as electron beam  
4279 intensity, beam motion or spot-size variation. The control of helicity-correlated beam asymmetries  
4280 is now a standard technology at Jefferson Lab, and typically achievable results (few part per mil-  
4281 lion intensity, 10's of nanometers beam motion,  $<10^{-3}$  spot size changes) will suitably constrain  
4282 the electron-photon crossing luminosity variations. Another possible source of false asymmetry  
4283 would be electronics pickup of the helicity signal, which could potentially impact an integrating  
4284 photon analysis. However, the demands of the primary experiment for isolation of the helicity sig-  
4285 nal exceed those for polarimetry by several orders of magnitude. In addition, the laser polarization  
4286 reversal provides an additional cancellation for asymmetries correlated to the electron beam helicity.  
4287 For these reasons, beam asymmetries are expected to be a negligible source of uncertainty in this  
4288 measurement.

4289 A more significant potential source of error comes from the uncertainty in the photon polar-  
4290 ization. As described above, the determination of photon polarization will be improved with the  
4291 analysis of light reflected from the cavity input mirror, which will allow precise control and mea-  
4292 surement of the polarization state injected into the cavity. This will be supplemented by an insertable  
4293 stage to measure the polarization in the interaction region directly. The circular polarization of the  
4294 laser will be determined and cross-checked with a precision of 0.2%. If studies do not demonstrate  
4295 that this can be achieved within the high-gain cavity, the alternative laser system will need to be  
4296 developed.

### 4297 **17.4.2 Systematic Errors for the Electron Detector**

4298 The electron detector is composed of 4 planes of silicon microstrips normal to the electron beam  
4299 trajectory and positioned on the low-energy side of the beam trajectory in the dispersive chicane.  
4300 Electrons which have given up energy to a scattering process are separated from the primary beam  
4301 by the third chicane dipole, and the energy of a detected electron is implied by the distance of the  
4302 track from the primary beam with a dispersion of about 0.45% of the beam energy per millimeter.  
4303 Models of the chicane magnets are used to calculate the electron energy as a function of position

4304 in the detector. The effects of electronics noise and non-directional backgrounds are reduced by  
 4305 triggering on tracks which are restricted to very small angles relative to the beam. The trigger can  
 4306 be adjusted for the range of track angles and number of planes used in the track, including a single  
 4307 plane trigger. The efficiency of individual strips can also be measured using data from the multiple  
 4308 planes.

4309 The silicon detector may also be sensitive to synchrotron light, and while the detector is not  
 4310 in line-of-sight to synchrotron emission in dipole 3, synchrotron photons rescattered in the beam  
 4311 pipe may be a problem. The 11 GeV upgrade includes a gate valve installed on the straight-through  
 4312 beam pipe, to block synchrotron light from the first dipole of the chicane during operation of the  
 4313 polarimeter.

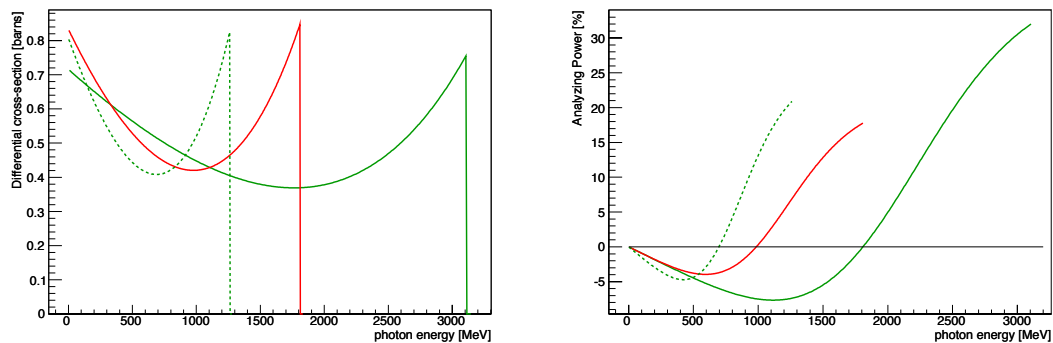


Figure 166: *The cross-section and asymmetry plotted versus Compton scattered photon energy for the Hall A polarimeter at 11 GeV for 532 nm (green solid line) and 1064 nm (red line) laser options, and at 6.6 GeV for the 532 nm laser (green dotted line).*

4314 The cross-section and asymmetry as a function of Compton scattered photon energy is plotted in  
 4315 Figure 166 for 11 GeV electron beam. The Compton edge (the kinematic endpoint of the Compton  
 4316 energy spectrum) is observed in the electron detector and used to calibrate the distance of the detec-  
 4317 tor from the primary beam. In addition, the asymmetry as a function of photon energy  $k$  exhibits a  
 4318 zero crossing. Determining the location of this asymmetry zero crossing (0xing) provides a second  
 4319 absolute energy calibration point, so together the Compton edge and 0xing can be used to calibrate  
 4320 two parameters: the detector location relative to the beam and the strength of the magnetic field  
 4321 in dipole 3. In this way, survey results and magnetic field maps serve as a cross-check to a beam-  
 4322 based self-calibration of the Compton energy spectrum. The precision of this calibration is limited  
 4323 by delta-ray production in the microstrips, which distorts the measured spectrum, and efficiency  
 4324 variations between the microstrips.

4325 In operation at low beam energies, the 0xing is close to the primary beam: for HAPPEX-II, the  
 4326 separation was approximately 5 mm. At this proximity, background rates were extremely sensitive  
 4327 to beam tuning in the injector and RF phase corrections in the linacs, presumably due to energy  
 4328 tails. At 11 GeV with the IR laser, the 0xing will be around 16mm from the primary beam, which  
 4329 should allow for robust operation. The analyzing power for the measured electron distribution can  
 4330 be very accurately determined with use of this self-calibration, with the systematic error dependent  
 4331 upon the specifics of the analysis approach.

4332 For an example of a specific analysis technique, consider an asymmetry measured from the  
 4333 Compton edge to some selected cut-off in the electron spectrum. This would need to be compared  
 4334 to the theoretically expected average asymmetry, which would be sensitive the the energy cut-off

4335 threshold. In an analysis that computed a single count-rate asymmetry from the integrated rate  
4336 from the Oxing to Compton edge, an error in determining the Oxing would act approximately as a  
4337 dilution effect (as the asymmetry is small in the neighborhood of the Oxing). While there may be  
4338 statistical variation in determining the Oxing, this would be merely a source of statistical noise. If the  
4339 systematic bias in determining the Oxing is estimated to be within  $1/10$   $\mu$ strip width (about  $25 \mu\text{m}$ ),  
4340 this would imply a systematic bias in the analyzing power of about 0.15%. While this is a useful  
4341 estimate of the error due to energy calibration, this analysis relies on integrating the rate-weighted  
4342 average asymmetry over the accepted energy range, and so would likely suffer a larger contribution  
4343 of systematic error due to efficiency variations in the  $\mu$ strips.

4344 Other analysis techniques which would be less sensitive to efficiency variations would rely on  
4345 averaging asymmetries over a range of strips, rather than averaging the count rate. In this case, both  
4346 energy calibration points are needed to determine the expected asymmetry at each  $\mu$ strip. Because  
4347 the Compton edge will be extracted from the rate spectrum, efficiency variation between the silicon  
4348 strips must be minimized and well-known to avoid biasing this determination. In addition, careful  
4349 study of the contribution of delta-ray production, which distorts the asymmetry spectrum at the  
4350 Oxing and the rate spectrum at the Compton edge, will also be important. Here also, a high strip  
4351 efficiency will be helpful, by providing a high-efficiency for vetoing events with multiple tracks.  
4352 Strip-by-strip efficiencies can be calculated by comparing track-hit efficiency between the multiple  
4353 planes of the  $\mu$ strip detector, and comparisons between planes can also help benchmark corrections  
4354 for delta-ray production. A uniform and high-efficiency detector will be an important component of  
4355 this system.

4356 It is worth noting a measurement using only the last, single silicon strip at the Compton edge  
4357 will be capable of 0.4% statistical precision on time-scales of around one hour. The rate of change  
4358 of the asymmetry in this region is only 0.5% / mm. Locating this strip, relative to Compton edge, to  
4359 a little better than half its own width should provide a robust accuracy on the analyzing power better  
4360 than 0.4%. This technique would be sensitive to determination of the location of the Compton edge,  
4361 but otherwise very insensitive to other calibration parameters.

4362 Similarly, if the electron detector can be moved close to the primary beam (about 9 mm from the  
4363 primary beam for the IR laser at 11 GeV) the asymmetry minimum could be detected. The statistical  
4364 power is much lower in this region, with a single strip requiring 20 hours to achieve 0.4% statistical  
4365 precision on the polarization (assuming signal-noise ratio of 10:1). However, here the asymmetry is  
4366 not changing with position, so there is minimal calibration error in selecting a strip in this minimum.  
4367 Beam position and angle may vary the asymmetry minimum over hundreds of microns during this  
4368 time span, but such changes can be tracked using beam position monitors or the Compton edge,  
4369 and the analyzing power varies by only about 0.4% of itself over a range of  $\pm 300 \mu\text{m}$ , suggesting  
4370 minimal corrections will be necessary .

4371 Cross-checks between calibrations and techniques should provide convincing evidence that the  
4372 system is well understood. Given these considerations, it seems likely that the calibration of the  
4373 electron detector will be understood at the level of 0.3% or better.

4374 Regardless of the analysis, contributions from deadtime and pileup will need to be understood.  
4375 The fast-counting DAQ can take very high rates with low deadtimes, and deterministic deadtime in-  
4376 tervals are enforced in readout and acquisition electronics stages. While the total Compton-scattered  
4377 data rates may as high as 1 MHz, rates in individual strips will be reduced by segmentation to  
4378  $< 15 \text{ kHz}$ , which will allow dead-time and pile-up systematic errors to be controlled at the level  
4379 of 0.2%. The high statistical power of the measurement is of significant use here; high precision  
4380 studies can be performed to benchmark models of the readout system against changes in the laser  
4381 power or the parameters of the triggering (preamp levels, logical gate lengths, coincidence levels,  
4382 etc).



4383 Backgrounds are also a potential but small source of systematic uncertainty. Backgrounds are  
4384 studied with the laser cavity unlocked, allowing both the background level and asymmetry to be  
4385 well determined. However, high backgrounds could impact the systematic error due to deadtime or  
4386 pile-up corrections. There is also the possibility of backgrounds from Compton-scattered electrons,  
4387 which can produce delta rays when scattering in the detector or in its shielding. These tracks can  
4388 themselves be sufficiently forward-going to pass the trigger, thus changing the analyzing power as a  
4389 function of energy. Simulation will be used to avoid such problems, and studies of track distribution  
4390 and electron-tagged photon energy spectra can be used to identify such effects in the data.

4391 Finally, it is perhaps obvious, but worth stating, that beam properties at 11 GeV will be important  
4392 for the precision of the electron detector analysis. If simulations reveal that halo backgrounds for  
4393 the electron detector are likely to be large in the region  $\sim 15$  mm from the primary beam, then the  
4394 green laser option would be required for high precision polarimetry. Using 532 nm light in a cavity  
4395 would put the zero-crossing about 33 mm from the primary beam. It is also worth noting that the  
4396 single-strip analyses would be also be improved with the higher resolution and larger asymmetries  
4397 (and larger distances from the primary beam) available from a green laser.

### 4398 **17.4.3 Systematic Errors for the Photon Detector**

4399 The precise determination of the analyzing power as a function of energy is more difficult for the  
4400 photon calorimeter than for the electron detector due to the width and shape of the detector response  
4401 function. In order to fit the asymmetry as a function of detected photon energy, the analyzing power  
4402 must be calculated as a convolution of the response function with the theoretical analyzing power  
4403 curve. The response function shape and energy calibration can be simulated, and studied using the  
4404 photon tagging through coincidence triggers with the electron detector.

4405 In general, determining the effect of a low-energy threshold on the analyzing power depends  
4406 sensitively on the shape of the response function; at low energies this is a major source of uncer-  
4407 tainty. At high energies, the improved resolution and consistency of the response function shape  
4408 over the range of interest should significantly reduce this problem. As noted above, the photon  
4409 calorimeter will be upgraded to better contain showers from high energy photons, with the primary  
4410 objective to provide a response function which scales linearly over a broad range of energy.

4411 The pulse-counting analysis in the photon detector is also sensitive to pile-up, which distorts  
4412 the asymmetry distribution. Background and rate distributions will serve as inputs to simulation for  
4413 corrections to the analyzing power. In the current Hall A analysis, pile-up corrections are estimated  
4414 at the level of 1%, and the effect can be controlled at a level better than 10% of itself. Deadtime  
4415 corrections, which can vary significantly with background conditions, will also represent a potential  
4416 systematic uncertainty.

4417 Uncertainties related to the threshold, response function shape, absolute energy calibration,  
4418 deadtime and pile-up can also be eliminated by integrating the photon calorimeter signal, with-  
4419 out threshold [312]. These previous problems are then replaced with a requirement on the linearity  
4420 of the average response to the photon energy. Because the analyzing power integral is energy-  
4421 weighted, the statistical figure-of-merit is not badly degraded by the negative asymmetry region at  
4422 low photon energies.

4423 The PREX experiment, with a beam energy near 1 GeV, relied on the integrating photon method  
4424 for polarimetry at the level of 1% precision. Simulations of the photon response function were  
4425 sufficient to control the analyzing power uncertainties for those measurements. The dominant un-  
4426 certainty in the asymmetry measurement arises from variation in the photomultiplier response with  
4427 changes in average rate which introduces a systematic error through background subtraction.

4428 At high energies, with the ability to study response function with the electron-detector-tagged



4429 photon beam over a large fraction of the energy range, the photon detector analyzing power nor-  
4430 malization uncertainty in the range of 0.3% should be achievable. Characterization of the pho-  
4431 totube response as a function of rate and pulse-size will also be important. As described above,  
4432 Bremsstrahlung scattering from apertures in the interaction region, coupled with the characteristics  
4433 of the 11 GeV electron beam, present a possible source of background.

## 4434 **17.5 Summary of Compton Polarimetry**

4435 The prospects for 0.4% Compton polarimetry are excellent. This ambitious goal will require vig-  
4436 orous and dedicated efforts to reduce sources of systematic uncertainty. It is expected that some  
4437 significant fraction of data production time will be used for studies of the Compton polarimeter sys-  
4438 tem which are not disruptive to the experiment, for example, scans of detector positions, laser power  
4439 and polarization, and data acquisition parameters. The scattering asymmetry at 11 GeV is relatively  
4440 large which, for some analysis approaches, will provide statistical precision at the level of  $\sim 0.5\%$  in  
4441 a few minutes of data collection. Given this high statistical power, these studies will be an effective  
4442 method for constraining many of the possible experimental systematic uncertainties.

4443 The future use of the Hall A polarimeter at 11 GeV will be a very different situation from  
4444 the recent operation. The dominant systematic errors in recent operation lay in the determination  
4445 of the analyzing power and laser polarization. Operating at lower energies the asymmetries were  
4446 significantly lower and therefore the statistical power was worse. In addition, the limits of systematic  
4447 uncertainty had not been pushed by demands of the experiment precision.

4448 The 0-Xing “self-calibration” of the electron detector was attempted for the first time for the  
4449 HAPPEX-II and HAPPEX-He measurements. The situation was complicated due to the low beam  
4450 energy of around 3 GeV, which not only reduced the average asymmetry but also reduced the ra-  
4451 tio of Compton-scattered photon energies and the electron energies. At 3 GeV, the zero-crossing  
4452 was about 5 mm from the primary beam, which was as close as the electron detector could get to  
4453 the beam. Geometric efficiencies at the edge were a significant complication in this approach. In  
4454 addition, the microstrip detector was damaged and displayed low and uneven efficiency, which com-  
4455 plicated the analysis. The estimated systematic errors for that analysis which were not associated  
4456 with these efficiency issues are consistent with Table 34. A similar technique has been successfully  
4457 employed in the Hall C Compton polarimeter at 1 GeV, where a larger chicane and green laser were  
4458 used to optimize for the low beam energy during the Qweak experiment. While analysis is ongoing,  
4459 the current status indicates that the ultimate precision will be significantly better than 1%.

4460 For the photon detector, the integration readout method has been successfully used in the HAP-  
4461 PEX-3 and PREX experiments, with the primary limitations being the characterization of the photo-  
4462 tube response over the range of signal levels. The rapid access to high statistical power expected for  
4463 11 GeV operation, which is so powerful for cross-checking potential sources of systematic uncer-  
4464 tainty, has never before been available to the Hall A Compton. Coincidence measurements between  
4465 the photon and electron detectors will also provide a significant cross-check to the response function  
4466 and energy calibrations. As described above, recent improvements in available laser power, analy-  
4467 sis techniques, laser polarization measurements, and the favorable kinematics of the higher electron  
4468 beam energy have opened the door to 0.4% precision Compton polarimetry for the SoLID program.

## 4469 **17.6 Møller Polarimetry**

4470 This section describes our plans for precision Møller polarimetry in Hall A. Møller polarimetry  
4471 will provide a useful cross check on beam polarization measurements performed with Compton  
4472 scattering, gathering high statistics in a short amount of time and with different attendant systematic

4473 errors. The principal challenge is to achieve high precision ( $\sim 0.5\%$  on the beam polarization)  
 4474 through careful control of the systematic effects.

4475 Electron-electron scattering, with arbitrary spin orientation for the beam and target, has been  
 4476 calculated in lowest order QED by many authors [313–316], and the basic formulas for (non parity-  
 4477 violating) polarized Møller scattering are given in many places. For example, following [317], the  
 4478 cross section at high energies in the center of mass frame can be written as

$$\frac{d\sigma}{d\Omega_{cm}} = \frac{\alpha^2}{s} \frac{(3 + \cos^2 \theta)^2}{\sin^4 \theta} [1 - P_{\text{long}}^{\text{B}} P_{\text{long}}^{\text{T}} A_{\text{long}}(\theta) - P_{\text{tran}}^{\text{B}} P_{\text{tran}}^{\text{T}} A_{\text{tran}}(\theta) \cos(2\phi - \phi_B - \phi_T)] \quad (30)$$

4479 Here,  $s = (2E)^2$  for electron energy  $E$ ,  $\theta$  is the scattering angle,  $P_{\text{long,tran}}^{\text{B,T}}$  are the longitudinal and  
 4480 transverse polarizations of the beam and target electrons,  $\phi$  is the azimuthal scattering angle, and  
 4481  $\phi_{\text{B,T}}$  are the azimuthal angles of the beam and target polarizations. The analyzing powers are

$$A_{\text{long}}(\theta) = \frac{(7 + \cos^2 \theta) \sin^2 \theta}{(3 + \cos^2 \theta)^2} \quad \text{and} \quad A_{\text{tran}}(\theta) = \frac{\sin^4 \theta}{(3 + \cos^2 \theta)^2} \quad (31)$$

4482 which are maximized at  $\theta = 90^\circ$  with  $A_{\text{long}}(90^\circ) = 7/9$  and  $A_{\text{tran}}(90^\circ) = 1/9$ . The electron  
 4483 laboratory scattering angle for  $\theta = 90^\circ$  is  $(2m/E)^{1/2}$ , rather small for GeV electron beams.

4484 A Møller polarimeter makes use of Eq. 30 to measure the beam polarization vector  $\vec{P}^{\text{B}} =$   
 4485  $(P_{\text{long}}^{\text{B}}, P_{\text{tran}}^{\text{B}})$  by incorporating a target with a known electron polarization vector  $\vec{P}^{\text{T}} = (P_{\text{long}}^{\text{T}}, P_{\text{tran}}^{\text{T}})$   
 4486 into a spectrometer to detect one or both of the scattered electrons. By reversing the beam polar-  
 4487 ization vector  $\vec{P}^{\text{B}} \rightarrow -\vec{P}^{\text{B}}$ , one can deduce its magnitude, and perhaps its direction, through the  
 4488 analyzing powers (31). The ideal Møller polarimeter, for determining longitudinal beam polariza-  
 4489 tion  $P_{\text{long}}^{\text{B}}$ , is set at  $\theta = 90^\circ$  with maximal (minimal) target longitudinal (transverse) polarization  
 4490  $P_{\text{long(tran)}}^{\text{T}}$ .

4491 We describe two techniques for getting as close as possible to the ideal Møller polarimeter.  
 4492 One is based on iron foil targets, in which the outer atomic electrons are polarized, and the other  
 4493 is based on an atomic hydrogen target. In the case of the iron foil target design, polarimeters at  
 4494 Jefferson Lab have already described control of systematic errors near the 0.5% level. We describe  
 4495 upgrades already in progress in Hall A in preparation the general 12 GeV program at Jefferson Lab  
 4496 which will enable that level of performance. While potentially very precise, such a polarimeter re-  
 4497 quires calibration from a body of magnetization studies with iron, and this normalization has never  
 4498 been cross-checked to the required precision. In addition, iron foil polarimeters require dedicated  
 4499 measurements at low current, and so measured polarization must be interpolated between spot mea-  
 4500 surements and extrapolated to the high currents used for production. Møller polarimetry with an  
 4501 atomic hydrogen target, in contrast, would be able to provide a continuous, non-invasive polariza-  
 4502 tion measurement and would not require external calibration for accuracy at the few  $10^{-3}$  level, but  
 4503 would be a new technology requiring significant technical R&D.

4504 The strategy for Møller polarimetry, therefore, is to complete the upgrade of the Hall A iron foil  
 4505 polarimeter and seek to maximize the accuracy of this device. A cross-calibration with the upgraded  
 4506 Compton polarimeter should demonstrate that normalization of the target foil polarization is under  
 4507 control. The atomic hydrogen polarimeter option could be pursued if it is needed to confirm results  
 4508 of those studies.

## 4509 17.7 The Hall A Upgrade: “High Field” Iron Foil Targets

4510 Nearly all high energy Møller polarimeters operated to date [321, 322, 325–330] make use of tilted  
 4511 ferromagnetic foil targets. High permeability alloys coupled with  $\sim$ few hundred gauss magnetic

Variable	Hall C	Hall A:	
		High Field Foil	Hydrogen
Target polarization	0.25%	0.25%	0.01%
Target angle	‡	‡	*
Analyzing power	0.24%	0.20%	0.10%
Levchuk effect	0.30%	0.20%	*
Target temperature	0.05%	0.05%	*
Dead time	‡	0.10%	0.10%
Background	‡	0.10%	0.10%
Others	0.10%	0.10%	0.30%
Total	0.47%	0.42%	0.35%

\*: Not applicable      ‡: not estimated

Table 35: Systematic error summary for Møller polarimeters at JLab, including anticipated uncertainties for future prospects. The Hall C polarimeter [318] uses a high field pure iron target [319, 320] with a simple two-quadrupole spectrometer. Uncertainties quoted for that system are taken from a publication detailing calibration of the analyzing power. The current Hall A Møller polarimeter [321, 322] uses a tilted ferromagnetic allow target, and a spectrometer with a dipole magnet following three quadrupoles. A high-field pure iron target upgrade is underway with plans for an additional quadrupole in the spectrometer for high energy operation. Uncertainties for this system are the expected performance after the upgrade. Research and development for a hydrogen gas target [323, 324] provides the basis for a second continuously-running high precision polarimeter to complement the Compton apparatus.

4512 fields preferentially polarize in the plane of the foil, so tilting the foil at a moderate angle gives  
4513 a substantial longitudinal target polarization. Calculating the effective polarization, however, is  
4514 typically the limiting systematic error, and such devices cannot ultimately do better than several  
4515 percent precision.

4516 A different approach [318], implemented in Hall C at Jefferson Lab, using a high magnetic field  
4517 perpendicular to the foil plane [319, 320], has reported 1% precision on the beam polarization. It is  
4518 this target design that we are adopting for SOLID, and indeed are already preparing to implement  
4519 in Hall A.

4520 Below we describe the principles of “high field” iron foil targets, the plans for redesign of  
4521 the scattering chamber, and modifications to the existing spectrometer including simulations for  
4522 operation at high energy.

### 4523 17.7.1 Ferromagnetic Foil Targets

4524 Materials respond to external magnetic fields because atomic electrons, with spin and orbital an-  
4525 gular momentum, align themselves to an applied field. However, with a Bohr magneton equal to  
4526  $5.8 \times 10^{-5}$  eV/tesla, the magnetic energy at several tesla is still much smaller than the thermal en-  
4527 ergy at room temperature, so the effects of magnetic fields in most materials (“diamagnetism” and  
4528 “paramagnetism”) are quite small.

4529 Ferromagnetism, on the other hand, is a quantum mechanical phenomenon in which a subset  
4530 of atomic electrons in some elements and alloys spontaneously align. These alignments happen in  
4531 localized domains, which themselves are randomly oriented. However, the application of relatively

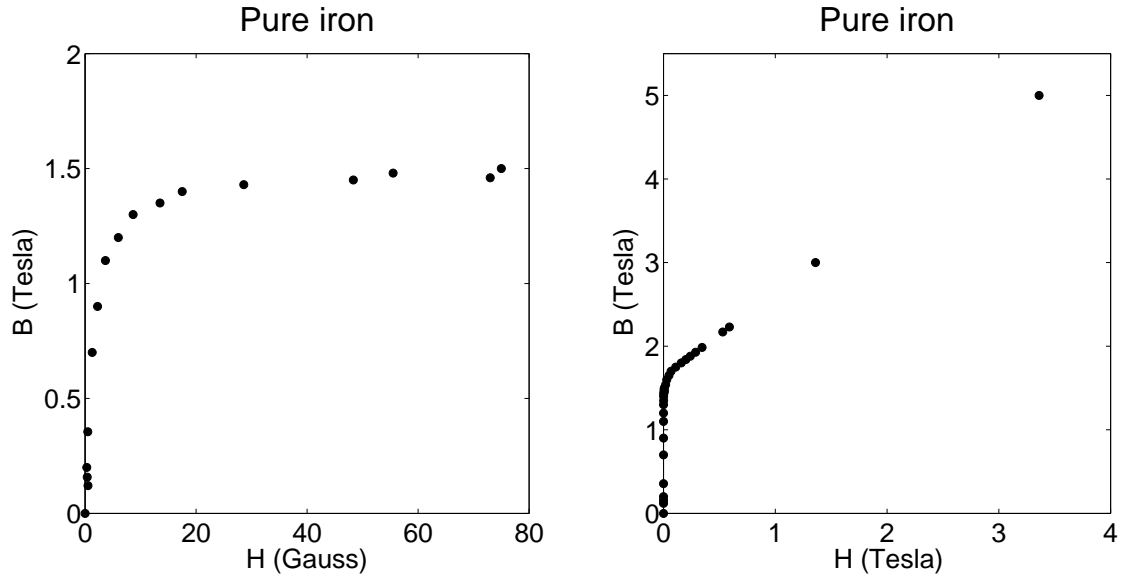


Figure 167: Magnetization curves for pure iron, from <http://www.fieldp.com/magneticproperties.html>. We use CGS units, so both  $B$  and  $H$  are properly measured in Gauss, but  $1 \text{ Tesla} = 10^4 \text{ Gauss}$ . Both plots are of the same data set, but the horizontal scale is much expanded on the right.

4532 small magnetic fields cause the domains themselves to line up, leading to large induced magnetic  
 4533 fields.

4534 Magnetostatics (in CGS units) is governed by the equations  $\vec{\nabla} \cdot \vec{B} = 0$  and  $\vec{\nabla} \times \vec{H} = 4\pi\vec{j}/c$   
 4535 where  $\vec{B}$  is the magnetic field,  $\vec{j}$  is the free current density, and  $\vec{H}$  absorbs the magnetic response  
 4536 of the medium. To be precise,  $\vec{H} \equiv \vec{B} - 4\pi\vec{M}$  where the magnetization  $\vec{M}$  is the magnetic dipole  
 4537 moment per unit volume. It is the magnetization  $\vec{M}$  that we interpret, ultimately, as the polarization  
 4538 of target electrons.

4539 For *linear* materials (which *do not* include ferromagnets), we define the magnetic permeability  
 4540  $\mu$  through  $\vec{B} = \mu\vec{H}$ . It is nevertheless a habit to speak of  $\mu$  for ferromagnetic materials in terms of  
 4541 vector magnitudes, that is  $B = \mu H$ . For most materials,  $\mu$  is a constant slightly larger than unity.  
 4542 In ferromagnets, however,  $\mu$  is a strong function of  $H$  and can be very large.

4543 Figure 167 shows magnetization data for pure iron. At several tens of gauss of “applied” field  
 4544  $H$ , the magnetic field  $B$  saturates at  $\sim 1.5$  tesla because the domains are aligned. The resulting  
 4545 magnetization corresponds to  $\sim 2$  Bohr magnetons per iron atom, that is, roughly two electrons  
 4546 worth of magnetic dipole moment in *each* iron atom. As  $H$  reaches and exceeds several tesla, the  
 4547 magnetization field simply adds directly to the applied field. The value of  $\mu$  rises to several thousand  
 4548 for a few gauss, and then decreases to unity for fields much greater than saturation.

4549 Møller polarimeters using “low field tilted” foil targets operate in the region where  $\mu \gg 1$ . In  
 4550 fact, they generally make use of special alloys that have exceptionally high values of  $\mu$ , that is,  
 4551 saturate at relatively low values of  $H$ . In this case  $\vec{B} = 4\pi\vec{M}$  to a very good approximation. Since  
 4552  $\vec{\nabla} \cdot \vec{B} = 0$  implies that perpendicular components of  $\vec{B}$  are continuous across the foil surface, and  
 4553 since  $B = H$  outside the foil is hundreds of times smaller than the magnetization, the only way to  
 4554 meet the boundary condition is for  $\vec{M}$  to point in the plane of the foil. (Of course, this argument  
 4555 breaks down if the foil is at right angles to the applied field.) Thus a target tilted at some angle, say  
 4556  $\sim 20^\circ$  provides a dominantly longitudinally polarized target for an incident electron beam in the

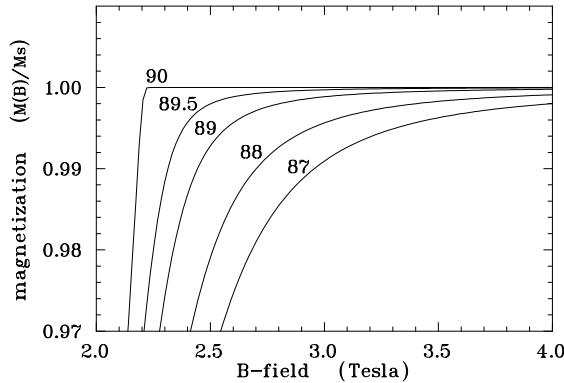


Figure 168: Simulations of foil magnetization for angles between the foil plane and the B-field direction close to 90 degrees. Errors due to imperfect alignment or a slight warp of the foil could produce such a result. Taken from [319, 320], which uses a calculation [335] of magnetization curves for uniformly magnetized prolate ellipsoidal domains.

4557 same direction as the applied field.

4558 The limiting precision of polarimeters using such targets, however, is extracting the target elec-  
 4559 tron spin polarization from the magnetization. The ratio of “spin” magnetization  $M_s$  to the total can  
 4560 be written as [331]  $M_s/M = 2(g' - 1)/g'$ , with  $g'$  close to, but somewhat less than 2. The attendant  
 4561 uncertainties in  $g'$  for the alloys used in tilted target applications, limit one’s knowledge of the target  
 4562 polarization to several percent.

4563 Measurements in *pure* iron or nickel, however, point to very precise knowledge of their magne-  
 4564 tization parameters [332, 333]. The approach used by the Basel/Hall C group [318–320] is to not  
 4565 only use pure iron foil targets, but to polarize them with a very high (several tesla) field, provided  
 4566 by superconducting coils. This overcomes limitations of a not-so-large value of  $\mu$  for pure iron.

4567 It is important to note that the magnetization of the foils in the strong longitudinal field has not  
 4568 been measured, but is taken from published data on the properties of bulk iron, which claims an ac-  
 4569 curacy of  $\sim 0.1\%$ . The orbital contributions to the magnetization of about 5% can be evaluated and  
 4570 subtracted using the magneto-mechanical factor, measured by other dedicated experiments [334].  
 4571 With strong external fields of 3-4 T several additional correction of about 0.5% have to be made to  
 4572 compensate for extra orbital momenta and other complex effects. These corrections are tempera-  
 4573 ture dependent. It will be important to carefully evaluate the literature on these measurements and  
 4574 their interpretation to verify that the uncertainty is not larger than a few  $10^{-3}$ . For example, it is  
 4575 apparent that the anomalous magnetic moment of the electron has not been accounted for in recent  
 4576 publications, amounting to a correction of more than 0.2% to the target electron spin polarization.

4577 Calculations of the longitudinal magnetization of a foil placed perpendicularly (or nearly so) to  
 4578 an applied field are quite difficult. Figure 168, taken from [319, 320], shows the magnetization  
 4579 (relative to its maximum value) of a pure iron foil as a function of applied magnetic field, for  
 4580 different angles between the field and the normal to the foil. To be sure, this calculation is in fact of  
 4581 a model of non-interacting prolate ellipsoidal domains [335], and the extent to which it applies to a  
 4582 pure iron foil is not clear.

4583 A polarimeter based on this “high field” target was constructed in Hall C at Jefferson Lab [318].  
 4584 The device has performed well, with experimenters claiming accuracy of 1% or better on the lon-  
 4585 gitudinal beam polarization. Much of the updated design of the Hall A Møller polarimeter is based  
 4586 on the Hall C experience.

### 4587 17.7.2 Simplified Møller Scattering Target Assembly

4588 Quite a number of small, systematic effects need to be considered in order to achieve 0.5% uncer-  
 4589 tainty on the longitudinal beam polarization. For example, Figure 168 gives an idea of the tolerance



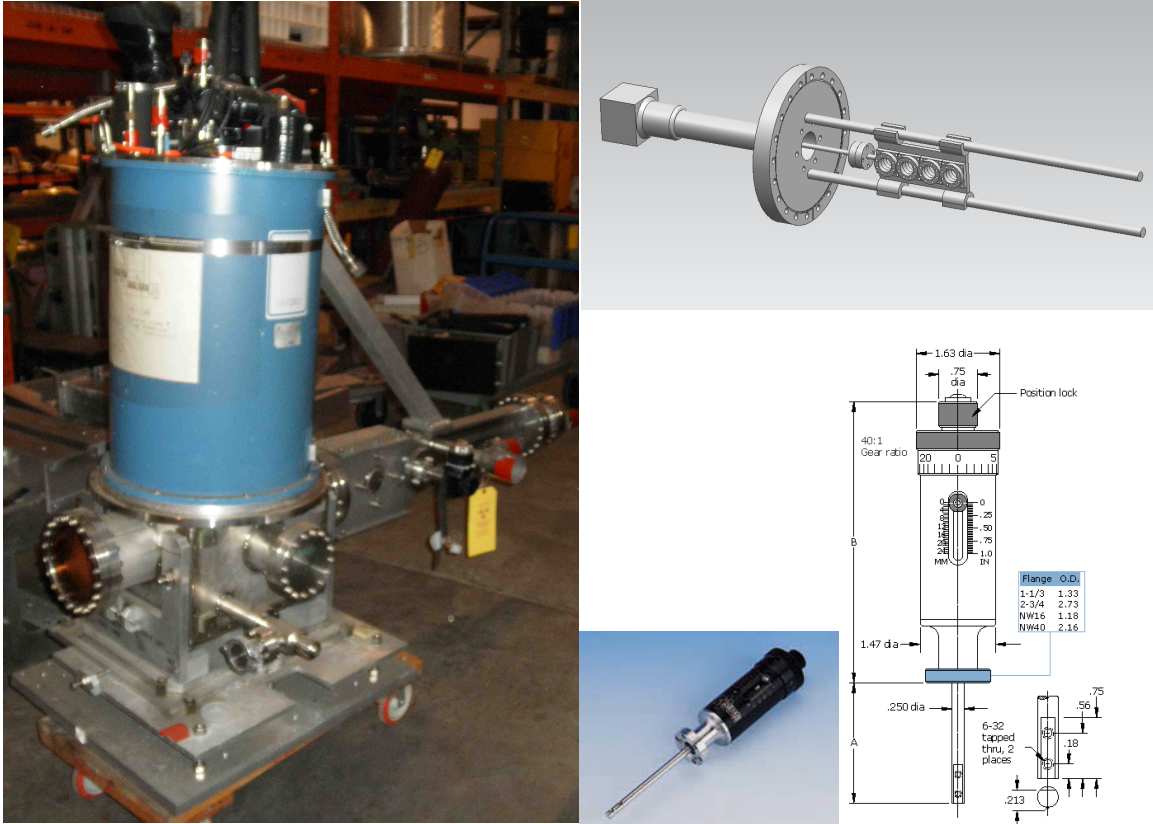


Figure 169: *Left:* Existing Hall A target chamber with ladder actuator extending off to the right. The magnet cryogenic system sits on top of the chamber. Our plan is to replace the actuator assembly, here shown supported by a boom attached to the cryo system. *Right:* Design concept for a new ladder actuator system, based on the Hall C design, along with a photo and schematic of the MDC660034 linear motion feedthrough.

4590 needed on iron target alignment. In order to be assured of at least 99.8% of the maximum target  
 4591 polarization for a field of  $\sim 3$  T, the tolerance on the foil angle misalignment is  $\sim 1^\circ$ .

4592 Figure 169 includes a photograph of the high-field foil target chamber previously in place in  
 4593 Hall A, and some details of our current plans for the upgrade. Our plan is to retain the cryogenic  
 4594 magnet system and the target chamber and overall adjustment mechanism, but to replace the target  
 4595 actuator assembly. Originally designed to provide adjustments in many degrees of freedom, the  
 4596 existing actuator assembly proved unwieldy for regular use. It was also very heavy, and required  
 4597 stabilization through a connection to the dewar for the cryogenes. The redesign relies on precision  
 4598 construction with fewer adjustable degrees of freedom, and will be much lighter.

4599 In order to interpret the target polarization to high precision, it is imperative that the foil be  
 4600 saturated. This can be confirmed by studying the Møller scattering asymmetry as a function of  
 4601 applied magnetic field. The cryogenic magnet is limited to fields less than 4 T, so according to  
 4602 Fig. 168 we need to have the target angle precise to about  $1^\circ$ . It would be useful to in fact confirm  
 4603 the behavior suggested by the figure, by making these measurements with the target arm rotated by  
 4604 various angles close to  $90^\circ$ .

## 4605 **18 Supports and Infrastructure**

### 4606 **18.1 Magnet Support**

4607 The initial plan used for estimating the cost is to build a stationary frame and distribute the approx-  
4608 imate 1000 ton load of the modified CLEO-II magnet section using eight 200 ton energpac jacks.  
4609 Steel plates and large steel blocks and/or large I-beams will be used to distribute the load out over a  
4610 safe area. The 200 ton jacks will be used for vertical alignment and have locking rings which allow  
4611 for a full mechanical connection and not rely on hydraulic pressure for stationary support.

### 4612 **18.2 Endcap Support Structure and Motion Mechanism**

4613 The endcap will have a support structure that cradles each half the cylindrical ring. The structure  
4614 will be integrated into a track system that is mounted to steel plates resting upon the concrete floor.  
4615 The initial design concept for the track system requires a set of longitudinal (downstream direction)  
4616 tracks for moving the endcap away from the magnet. A second set of tracks that would separate  
4617 the endcap halves in the lateral direction would ride on top of the longitudinal tracks. The endcap  
4618 support structure would then be attached to the top lateral track system. Motion can be achieved by  
4619 using hydraulic or electric cylinders to push and pull the entire system into position.

### 4620 **18.3 Support Structure for Equipment Located Inside Cryostat Bore**

4621 The magnet will be located adjacent to the existing Hall A center pivot/target mount area and will  
4622 have limited access to the front of the magnet. The insertion of the large angle detector packages  
4623 that will reside internal to the cryostat will be accomplished from the downstream side of the magnet  
4624 using a supporting framework to roll the packages in and out. This will require the detector hut to  
4625 be moved downstream to allow access to the cryostat.

4626 An internal frame system is needed to mount the lead baffles in the PVDIS experiment. See  
4627 Figure 170. The frame cannot come into contact with the inside bore of the cryostat. This requires  
4628 the frame to span the entire length of the cryostat and mount to the return yoke iron. *A stainless steel  
4629 cylinder will be mounted between the two coil collars to bridge across the length of the cryostat. Its  
4630 outside diameter will be 2" less than the diameter of the cryostat bore allowing a 1" gap of clearance  
4631 with the bore. The downstream end will be mounted directly to the coil collar through a spacer ring.  
4632 The upstream end will mount through an annular plate that attaches to the front piece. The front  
4633 piece resides inside the bore of the upstream coil collar. Since the front piece has to be movable  
4634 to balance the magnetic forces on the coils the annular plate will be attached to the front piece  
4635 with studs. This will allow the framework to remain stationary if the front piece has to be adjusted.  
4636 Individual rails similar to those used in the endcap will bolt directly to the stainless cylinder to allow  
4637 the internal detector packages to roll into place.* The same rail system can be used for the SIDIS  
4638 experiment for mounting the large angle calorimeter and GEMs.

### 4639 **18.4 Power Requirements**

4640 The projected electrical power load is 1.6MVA, maximum current for magnet at 3266A. The present  
4641 power consumption for Hall A is less than 1 MVA. So upgrade to the Hall substation to have 2 MVA  
4642 is required. (MOLLER Experiment has included the cost (\$300k) for this in their MIE).

4643 The CLEO-II magnet is designed to have a low cryogenic heat load with passive cooling. The  
4644 HRS arms will not be operational during SoLID, so it is expected that the refrigeration heat load

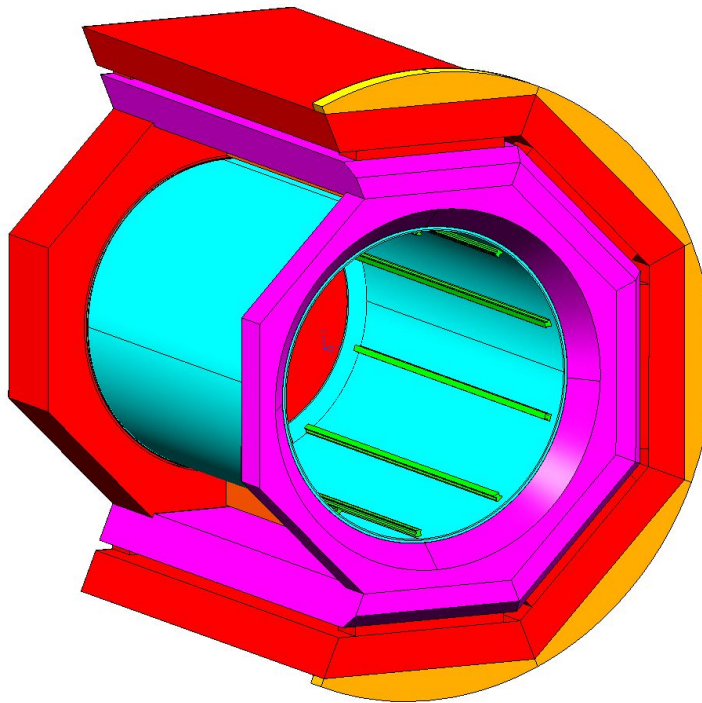


Figure 170: The internal rail system will be used to mount all parts inside the barrel, including PVDIS baffle, SIDIS large angle calorimeter and GEM's

4645 will be less than needed for HRS. The refrigeration need for the cryotarget is discussed in the target  
4646 section (Section 5).



## 4647 **19 Installation**

### 4648 **19.1 Experimental Layout**

4649 An initial check of the experimental equipment layout in Hall A has been done and no major ob-  
4650 structions have been found. The experiment layout puts the beam left HRS arm at 90 degrees to the  
4651 beamline and the beam right HRS arm at a forward angle of 145 degrees. The forward angle of the  
4652 BL arm allows a direct path from the wall opening at the bottom of the truck ramp to the assembly  
4653 area. The target is at the nominal pivot location with the center of the CLEO-II magnet 350 cm  
4654 downstream of the target center. The SoLID magnet and detectors encompass an area of 5.8 meters  
4655 in diameter and 7.3 meters long. With the magnet on beamline center, clearance to the Hall floor  
4656 ranges from 10 to 38 cm. This is sufficient area to support the load. The weight of the CLEO-II  
4657 magnet, detector hut and detectors is estimated to be 1300 tons. The floor in this installation region  
4658 is designed for 250 tons for a 12 square foot pad.

### 4659 **19.2 Magnet Moving and Placement**

4660 In evaluating the use of the CLEO magnet for SoLID consideration is given to how the CLEO  
4661 magnet can be transported into Hall A and how Hall A structurally meets the requirements of CLEO.  
4662 The footprint of SoLID utilizing the CLEO magnet will be approximately a 1000 ton load with  
4663 dimensions of 24 feet long by 19 feet in diameter. Hall A is 164 feet in diameter. In the area  
4664 required to install SoLID, the floor is constructed to carry 250 to 500 tons per 12 square feet.

4665 The existing Hall A equipment consists of the two High Resolution Spectrometers mounted at  
4666 the center pivot and all related infrastructure. To accommodate installation of SoLID, the SIDIS  
4667 target will need to be mounted 145 cm downstream from the existing support location in order for  
4668 the magnet to clear the HRS bearing assembly. Placing the CLEO magnet on beamline height gives  
4669 15 inches clearance to the floor for adequate support and alignment.

4670 The bird's eye view Figure 171 and the back side Figure 172 show SoLID in Hall A with  
4671 the two HRS arms in position. The SoLID detector hut is retracted backwards and a crane and  
4672 lowboy tractor-trailer are shown to indicate there is sufficient room to offload and assemble SoLID  
4673 components within Hall A.

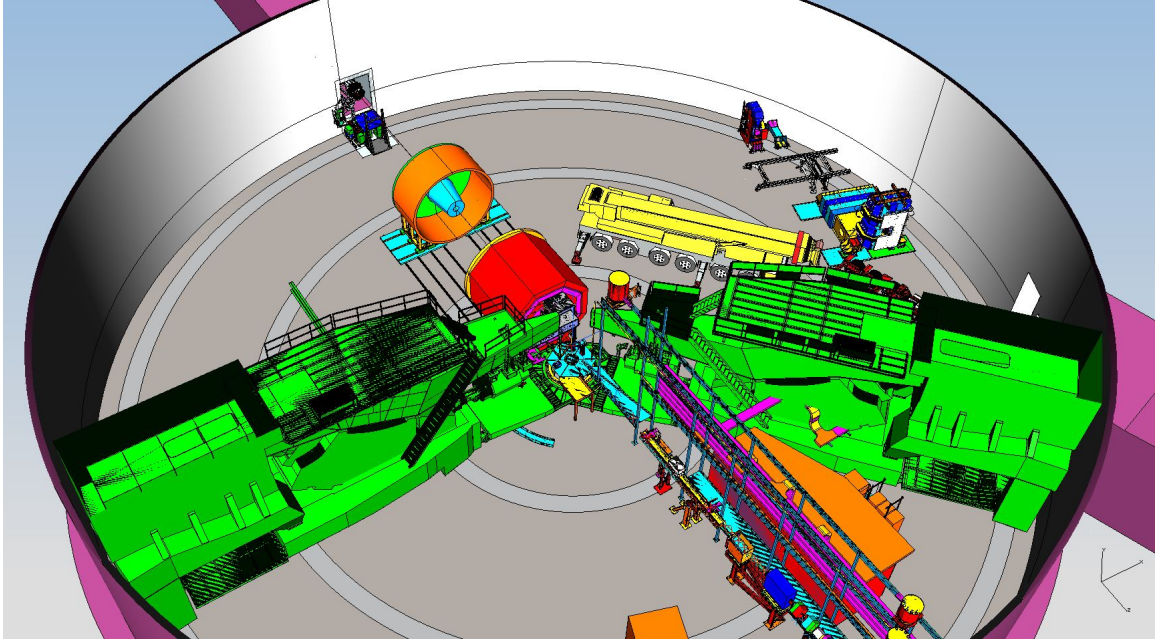


Figure 171: The bird's eye view of SoLID in Hall A

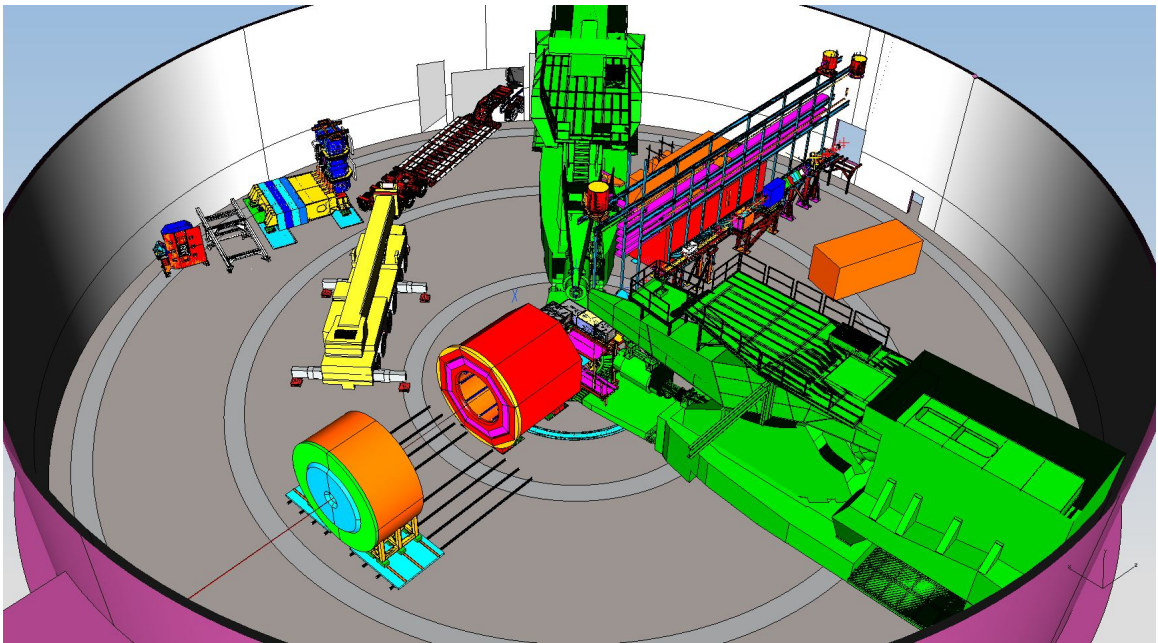


Figure 172: The back side view of SoLID in Hall A

4674 The CLEO-II magnet was disassembled and loaded on trucks for shipping by the Cornell per-  
 4675 sonnel with oversight by Jefferson Lab. The coils, coil collars and cryostat of the CLEO-II magnet  
 4676 have arrived at JLab in 2016.

4677 We have identified all of the parts of the CLEO magnet, with sizes and weights. We have  
 4678 identified specifically the parts to reuse in building the SoLID magnet. The cryostat (35k lbs)  
 4679 and power supply are stored in an environment-controlled area of approximately 400 square feet.  
 4680 Jefferson Lab projects the use of the CMSA site for storage of all parts.

4681 In developing the installation plan for SoLID, the largest part to transport is the cryostat. The  
 4682 cryostat is 12.3 feet long, 11.8 feet in diameter and weighs 22 tons. The height of the truck ramp  
 4683 into Hall A is limited to 17 feet in height. This will require the cryostat to be moved into the Hall on  
 4684 a roller structure rather than a flatbed type truck. This type of procedure has been completed several  
 4685 times at Jefferson Lab. See Figure 173, Figure 174, and Figure 175.

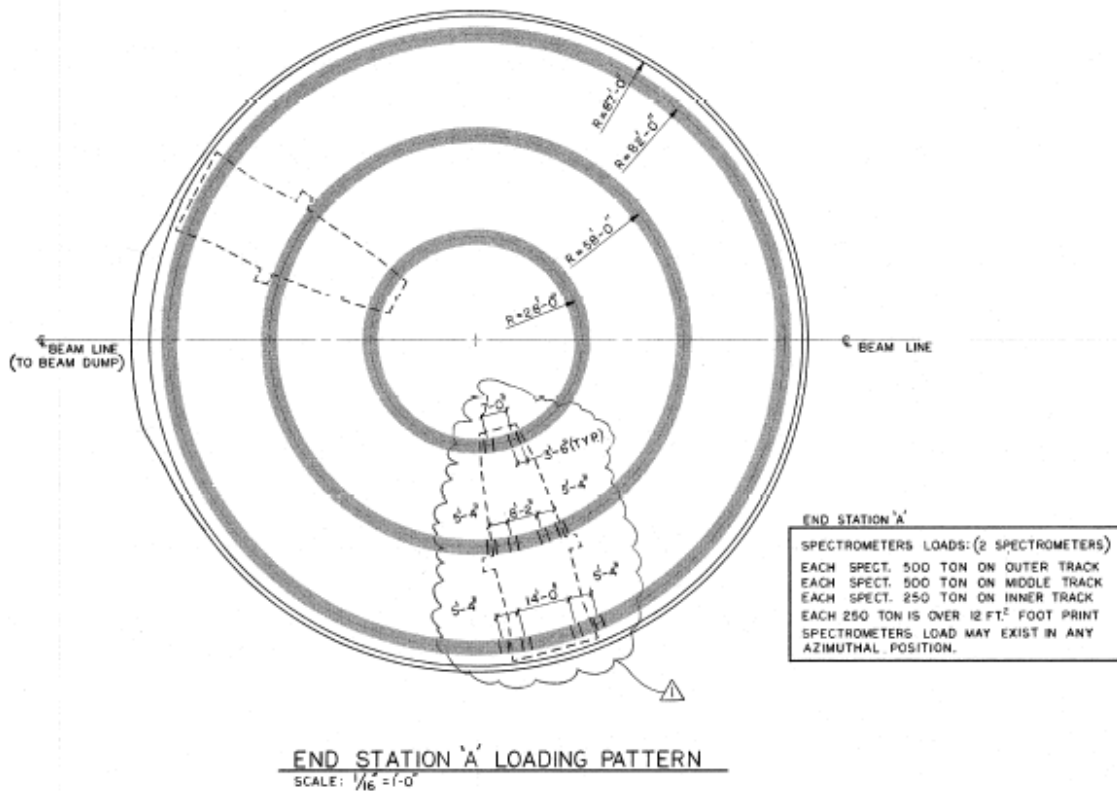


Figure 173: Hall A loading pattern.

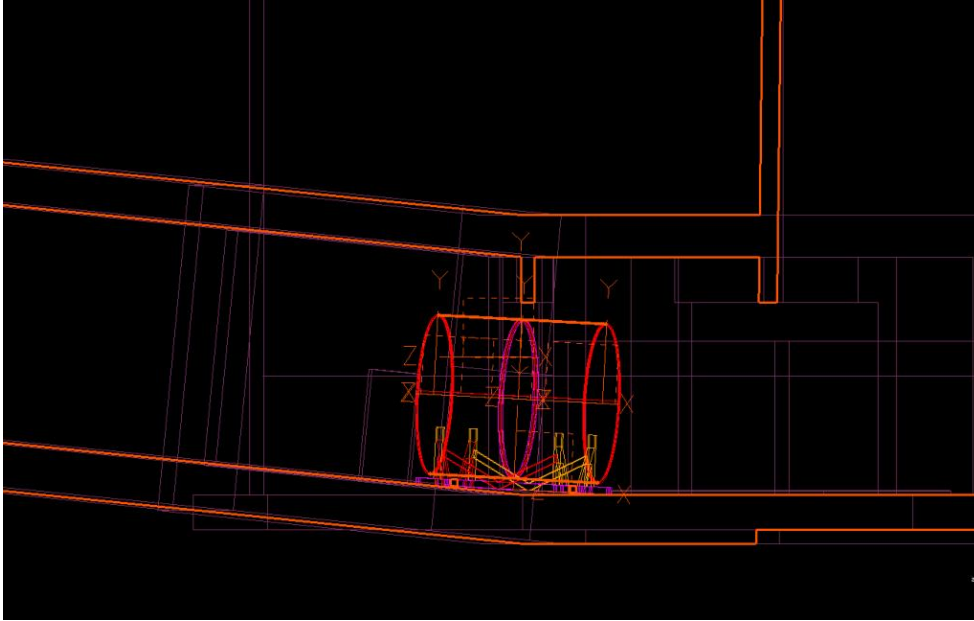


Figure 174: The plan of moving CLEO cryostat through Hall A ramp.

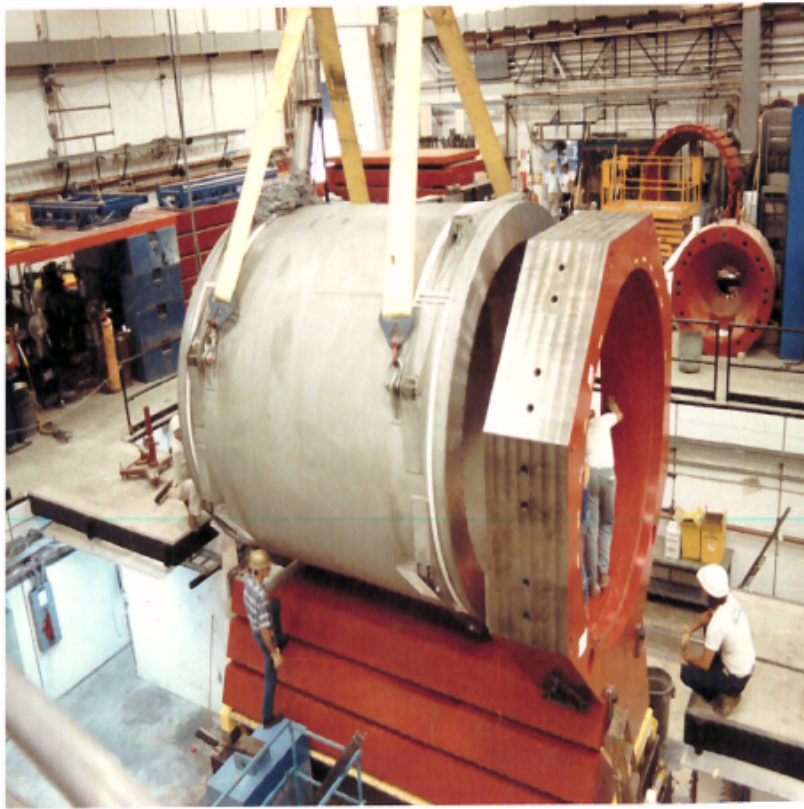


Figure 175: CLEO cryostat lifted during the installation at Cornell.



4686 **19.3 Helium Dewar Support and Upper Access Platform**

4687 An upper personnel access platform that is capable of supporting the helium dewar will be mounted  
4688 to the top of the magnet. A similar platform was used for the CLEO II experiments. See Figure  
4689 176.

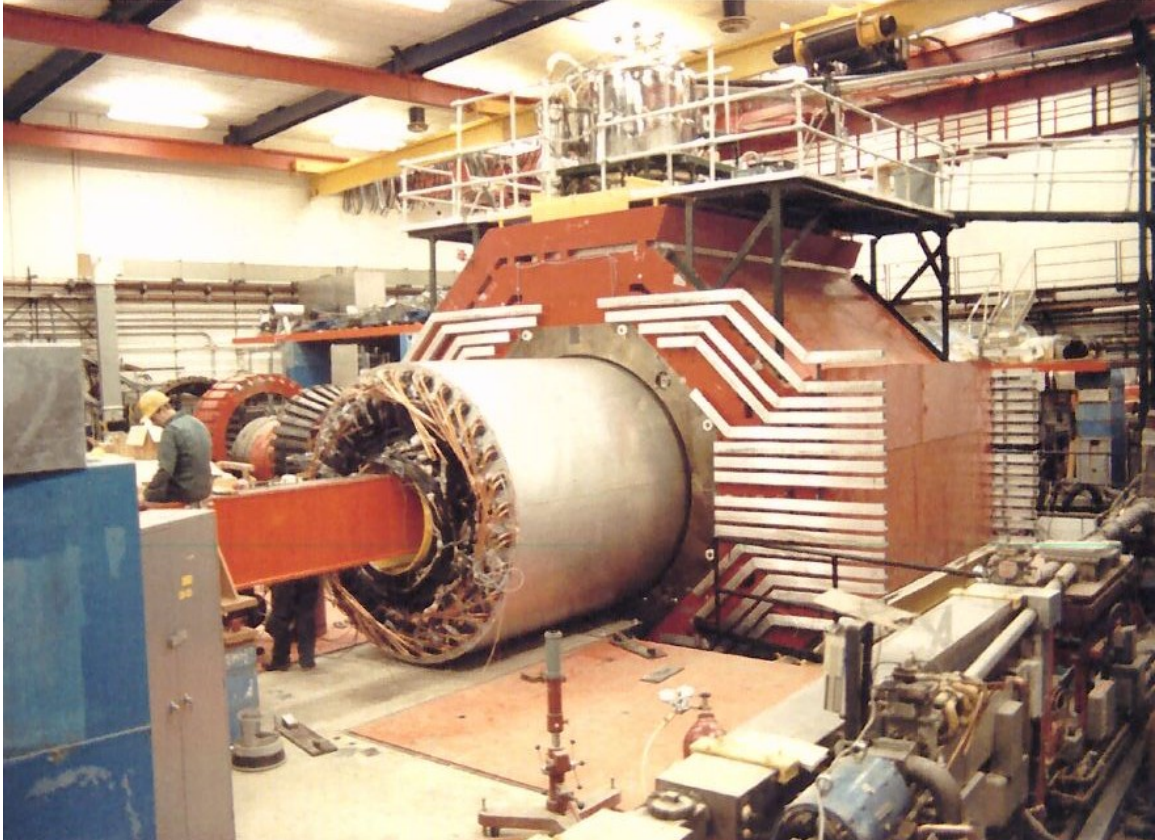


Figure 176: Helium dewar support upper access platform and detector loading inside of cryostat.

4690 **19.4 Endcap Forward Angle Detector Package Installation Structure**

4691 The basic design concept for the detectors mounted inside the endcap will have them supported by  
4692 individual rails mounted to the inner circumference of the cylindrical ring and on rails attached to the  
4693 outer horizontal circumferential surface of the nose if needed. A large universal installation fixture  
4694 is envisioned to load each of the detector packages onto the endcap rails. The framework design  
4695 is intended to accommodate the various endcap detectors with interchangeable fixturing specific to  
4696 each group. Personnel access to the endcap will be through man lifts and/or a specialized scaffolding  
4697 as needed.

4698 **19.5 Large Angle Detector and Baffle Installation Mechanism**

4699 An installation mechanism is needed to load the large angle detector packages and baffle system into  
4700 the internal support structure mentioned in the last section. This mechanism will likely be mounted  
4701 to the longitudinal track system used for the endcap movement and can utilize the tracks for rolling  
4702 the detectors and baffles into the cryostat and transferring the load to the internal frame. Depending

4703 on the final design of the detectors and baffle system the support could be a simple beam that runs  
4704 through the middle of the detectors and baffles. See Figure 176 for similar approach at BNL

## 4705 **19.6 Light Gas Cherenkov Installation Structure**

4706 The light gas Cherenkov will mount to the external downstream end of the magnet and will not  
4707 traverse with endcap. When the endcap is in the operational position the light gas Cherenkov will  
4708 be enclosed within the cylindrical ring along with the rest of the forward angle detectors. The light  
4709 gas Cherenkov detector will be made up of six pie shaped sections that will need to be bolted to  
4710 the downstream side of the magnet. A space frame similar to a scaffolding system would hold  
4711 and position each section while being attached to magnet. The space frame would attach to the  
4712 rail system and could be movable along the rails if needed. The space frame will be suitable for  
4713 personnel access to allow workers to perform the installation and maintenance of the detectors.

## 4714 **20 Project Status and Proposed Management Organization**

4715 The SoLID spectrometer was initially proposed in 2009 for two experiments: SIDIS experiment  
4716 (PR12-09-014, later became E12-10-006) and the PVDIS experiment (PR12-09-012, later became  
4717 E12-10-007). Both experiments aim to achieve high precision which require very high statistics.  
4718 A spectrometer/detector system with a large acceptance and also able to handle high luminosity is  
4719 needed. Therefore SoLID is designed to have a large solid angle and broad momentum acceptance  
4720 and can handle luminosity up to  $10^{39}\text{s}^{-1}\text{cm}^{-2}$  with a baffle system in the PVDIS configuration  
4721 and  $10^{37}\text{s}^{-1}\text{cm}^{-2}$  without a baffle system in the SIDIS configuration. With these unique features,  
4722 SoLID is ideal for inclusive and semi-inclusive DIS experiments and is also good for measurements  
4723 of certain exclusive reactions. The SoLID base equipment consists of a solenoid magnet (CLEO-II  
4724 magnet), tracking detectors (GEMs), electron PID detectors (electromagnetic calorimeter and light  
4725 gas Cherenkov detector) and hadron PID detectors (MRPC, heavy gas Cherenkov and EC), DAQ  
4726 system, supporting structure and infrastructure needed for the spectrometer. Leveraging the unique  
4727 capabilities of SoLID, currently, there are five high impact (four “A” rating and one “A<sup>-</sup>”) experi-  
4728 ments approved using SoLID, including a near threshold  $J/\psi$  production experiment in addition to  
4729 three SIDIS and one PVDIS experiments. Three more run-group proposals were also approved.

4730 The pre-conceptual design has gone through many iterations, including careful studies, detailed  
4731 simulations, pre-R&D testings and a number of internal reviews. Among the various internal re-  
4732 views, it is worth mentioning the two brainstorming sessions in September 2011 and January 2012,  
4733 organized by the JLab physics division, and the dry run review in June 2012 with external experts  
4734 (outside SoLID collaboration, including people from outside JLab). A formal pre-conceptual de-  
4735 sign report was submitted to the JLab management in July 2014. A Director’s Review was help in  
4736 February 2015. These reviews helped greatly in optimizing, improving and finalizing the concep-  
4737 tual design. Detailed simulations with realistic background (including neutron backgrounds) and  
4738 pre-R&D activities focusing on the major challenges have significantly improved the reliability of  
4739 the conceptual design.

### 4740 **20.1 Collaboration and Organization**

4741 The SoLID collaboration has more than 250 members from over 70 institutions over 13 countries.  
4742 SoLID has attracted international attention with many groups committed to make significant con-  
4743 tributions, including noticeably the contributions to the R& D efforts for large detector projects  
4744 (GEMs, MRPC and EC) from several Chinese groups and Heavy Gas Cherenkov detector from the  
4745 Regina group in Canada.

4746 The proposed SoLID Organization Chart is shown in Figure 177.

#### 4747 **Project Manager**

4748 Function: The Project Manager (PM) will be in charge of executing the project and report  
4749 to JLab management. The collaboration will provide advice and oversight, and members of the  
4750 collaboration will work under the PM in various roles to execute the project. For example, all  
4751 subsystems coordinators will report to the PM. The PM has the authority and responsibility to  
4752 manage the SoLID project.

4753 Jian-ping Chen is the initial PM.

#### 4754 **Executive Board**

4755 Function: The Executive Board (EB) makes decisions on scientific and organizational choices,  
4756 and provides high level oversight on all matter pertaining to preparation and operation of the SoLID  
4757 project.

4758 The Chair of EB is the science leader, and is the principle contact between the collaboration

4759 and the lab management/DOE. The Chair will provide oversight and input to the PM for the SoLID  
 4760 project. The Chair, together with the PM, is responsible for the performance and assessment of all  
 4761 subsystems.

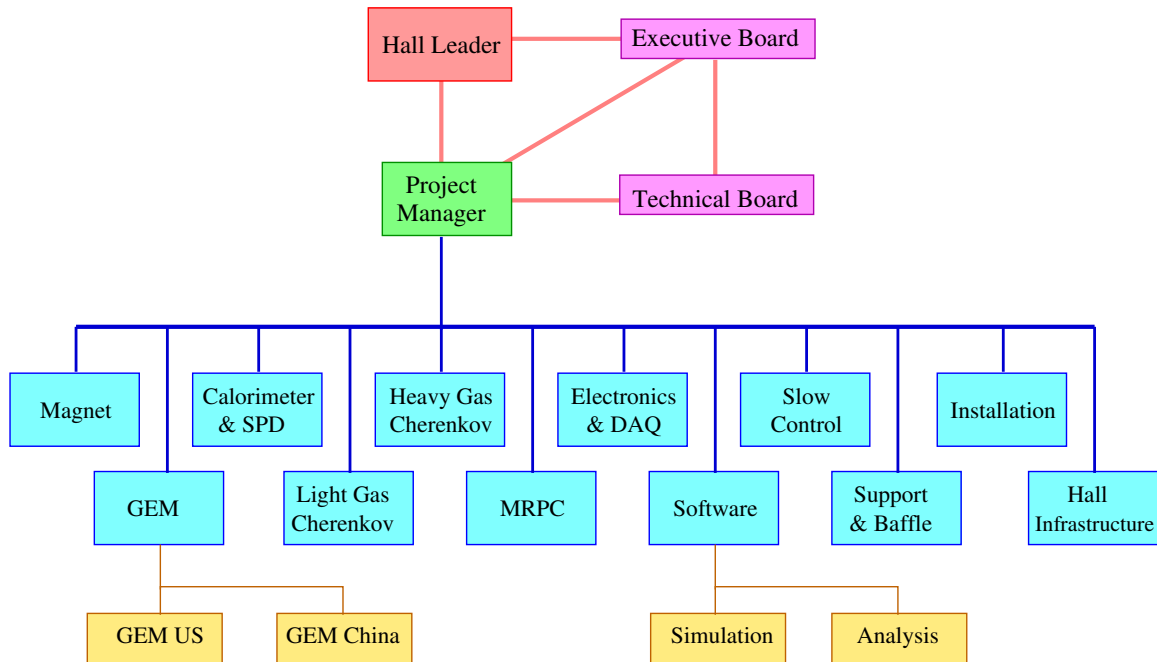


Figure 177: SoLID Organization Chart

4762 Initial members are the senior spokespeople plus the Hall Leader (ex-officio) and the PM (ex-  
 4763 officio): Paul Souder (PVDIS), Haiyan Gao (SIDIS), Zein-Eddine Meziani ( $J/\psi$ ), Thia Keppel  
 4764 (Hall Leader, ex-officio) and Jian-ping Chen (PM, ex-officio).

4765 Paul Souder is the 1st Chair. It is expected that the Chair position will rotate.

4766 **Technical Board**

4767 Function: The technical Board (TB) advises the PM on all aspects of the Project, including any  
 4768 changes in cost, scope or schedule.

4769 The TB will have a group of (usually senior) collaborators who represent the full range of  
 4770 required technical expertise and usually a representative from each subsystem is expected to be on  
 4771 this board. This group will be appointed by the EB. In addition, the TB will include the PM and also  
 4772 project engineers when they are appointed. The membership of the TB can be periodically adjusted  
 4773 by the EB as the situation warrants.

4774 The chair of the TB will be the PM. All EB members who are not already in the TB are ex-officio  
 4775 members, along with the Hall leader.

4776 Initial members: Jian-ping Chen (Chair), Paul Souder, Haiyan Gao, Zein-Eddine Meziani, Thia  
 4777 Keppel (ex-officio); Alexandre Camsonne, Eugene Chudakov, Tom Hemmick, Xiaodong Jiang,  
 4778 Nilanga Liyanage, Bob Michaels, Xin Qian, Paul Reimer, Yi Wang, Zhengguo Zhao, Xiaochao  
 4779 Zheng

4780 **Sub-System Lead Coordinators and Institutions**

4781 • **Magnet:** Robin Wines / Paul Reimer; JLab, Argonne

4782 • **GEM-US:** Nilanga Liyanage / Bernd Surrow ; UVa, Temple



- 4783 • **GEM-China:** Zhengguo Zhao / Xiaomei Li; USTC, CIAE, Lanzhou, Tsinghua, IMP
- 4784 • **Calorimeter:** Xiaochao Zheng / Wouter Deconick / Chufeng Feng; UVa, W&M, Shandong  
4785 (China), Argonne
- 4786 • **Light Gas Cherenkov:** Zein-Eddine Meziani / Michael Paolone; Temple
- 4787 • **Heavy Gas Cherenkov:** Haiyan Gao / Zhiwen Zhao / Garth Huber; Duke, Regina (Canada)
- 4788 • **MRPC:** Yi Wang / Alexandre Camsonne; Tsinghua (China), JLab, Duke, Rutgers
- 4789 • **DAQ/Electronics:** Alexandre Camsonne / Ron Gilman; JLab, Stony Brook, Rutgers
- 4790 • **Simulation:** Seamus Riordan / Zhiwen Zhao ; Argonne, Duke, UVa, Syracuse, Stony Brook,  
4791 Temple
- 4792 • **Reconstruction and Analysis:** Ole Hansen; JLab
- 4793 • **Slow Control:** Brad Sawatzky; JLab
- 4794 • **Supporting Structure and Baffle:** Robin Wines / Seamus Riordan; JLab, Argonne
- 4795 • **Hall Infrastructure Modification:** Robin Wines / Jessie Butler; JLab
- 4796 • **Installation:** Jessie Butler / Robin Wines; JLab, all user groups.

4797 The names listed are the coordinators for sub-systems. Institutions working on and responsible  
4798 for the sub-systems are also listed. Details of the responsibilities are described in the summary for  
4799 each sub-system. The list reflects the current situation and it is expected to be modified as more  
4800 groups join the effort as the SoLID project moves forward.

## 4801 **20.2 Cost estimation**

4802 Cost estimation has gone through many iterations in the last a few years. Procurement cost and  
4803 manpower estimations were first performed by the coordinators of subsystems. There are variations  
4804 in assumptions, including the number of years to complete the project. The final estimation made  
4805 adjustments to keep consistency for all subsystems in the assumptions. The length of the project  
4806 is assumed to be 5 years. Most of the procurement costs were estimated based on quotations from  
4807 vendors. Manpower were estimated from comparison with similar projects. JLab manpower was  
4808 estimated initially based on the estimation of similar projects from other halls. They were revised  
4809 later using the actual manpower used at the end of project completion in Hall D. The JLab budget  
4810 office provided valuable assistance in the cost estimation.

## 4811 **Bibliography**

- 4812 [1] Z. B. Kang, A. Prokudin, P. Sun and F. Yuan, Phys. Rev. D **93**, 014009 (2016).
- 4813 [2] Z. Ye, N. Sato, K. Allada, T. Liu, J.P. Chen, H. Gao, Z. B. Kang, A. Prokudin, P. Sun, and F.  
4814 Yuan, Phys. Lett. B. **767**, 91-98 (2017).
- 4815 [3] D. Wang *et al.* (PVDIS Collaboration), Nature **506**, 67 (2014).
- 4816 [4] E. Eichten, K. D. Lane and M. E. Peskin, Phys. Rev. Lett. **50**, 811 (1983).
- 4817 [5] J. Erler, C. J. Horowitz, S. Mantry and P. A. Souder, Ann. Rev. Nucl. Part. Sci. **64**, 269 (2014).
- 4818 [6] S. Durr *et al.*, Science **322**, 1224 (2008).
- 4819 [7] Wang, Qian, Liu, Xiao-Hai and Zhao, Qiang, Phys. Rev. D **92**, 034022 (2015).
- 4820 [8] S. An et al, NIM A **594**, 39 (2008).
- 4821 [9] Mickey Chiu et al, Progress Report of (Sub) 10 Picosecond Timing Detectors for Generic  
4822 Detector R&D for an Electron Ion Collider, [https://wiki.bnl.gov/conferences/  
4823 images/c/c8/ERD10\\_Report\\_2015-06.pdf](https://wiki.bnl.gov/conferences/images/c/c8/ERD10_Report_2015-06.pdf).
- 4824 [10] M. Boggione, L. Gamberg, J. O. Gonzalez-Hernandez, T. C. Rogers and N. Sato, Phys. Lett. B  
4825 **766**, 245 (2017).
- 4826 [11] European Muon, J. Ashman *et al.*, Phys. Lett. **B206**, 364 (1988).
- 4827 [12] B. W. Filippone and X.-D. Ji, Adv. Nucl. Phys. **26**, 1 (2001), hep-ph/0101224.
- 4828 [13] S. E. Kuhn, J. P. Chen, and E. Leader, Prog. Part. Nucl. Phys. **63**, 1 (2009), 0812.3535.
- 4829 [14] X. Artru and M. Mekhfi, Z. Phys. **C45**, 669 (1990).
- 4830 [15] P. J. Mulders and R. D. Tangerman, Nucl. Phys. **B461**, 197 (1996), hep-ph/9510301.
- 4831 [16] D. Boer and P. J. Mulders, Phys. Rev. **D57**, 5780 (1998), hep-ph/9711485.
- 4832 [17] X.-d. Ji, J.-P. Ma, and F. Yuan, Phys. Lett. **B597**, 299 (2004), hep-ph/0405085.
- 4833 [18] K. Hidaka, E. Monsay, and D. W. Sivers, Phys. Rev. **D19**, 1503 (1979).
- 4834 [19] J. P. Ralston and D. E. Soper, Nucl. Phys. **B152**, 109 (1979).
- 4835 [20] R. L. Jaffe and X.-D. Ji, Phys. Rev. Lett. **67**, 552 (1991).
- 4836 [21] V. Barone, Phys. Lett. **B409**, 499 (1997), hep-ph/9703343.
- 4837 [22] C. Bourrely, J. Soffer, and O. V. Teryaev, Phys. Lett. **B420**, 375 (1998), hep-ph/9710224.
- 4838 [23] J. Soffer, Phys. Rev. Lett. **74**, 1292 (1995), hep-ph/9409254.
- 4839 [24] W. Vogelsang, Phys. Rev. **D57**, 1886 (1998), hep-ph/9706511.
- 4840 [25] G. R. Goldstein, R. L. Jaffe, and X.-D. Ji, Phys. Rev. **D52**, 5006 (1995), hep-ph/9501297.
- 4841 [26] J. Ralston, private communications.

- 4842 [27] QCDSF, M. Gockeler *et al.*, Phys. Lett. **B627**, 113 (2005), hep-lat/0507001.
- 4843 [28] H.-X. He and X.-D. Ji, Phys. Rev. **D52**, 2960 (1995), hep-ph/9412235.
- 4844 [29] B. Q. Ma, I. Schmidt, and J. Soffer, Phys. Lett. **B441**, 461 (1998).
- 4845 [30] L. P. Gamberg and G. R. Goldstein, Phys. Rev. Lett. **87**, 242001 (2001), hep-ph/0107176.
- 4846 [31] I. C. Cloet, W. Bentz, and A. W. Thomas, Phys. Lett. **B659**, 214 (2008), 0708.3246.
- 4847 [32] M. Wakamatsu, Phys. Lett. **B653**, 398 (2007), 0705.2917.
- 4848 [33] B. Pasquini, M. Pincetti, and S. Boffi, Phys. Rev. **D72**, 094029 (2005), hep-ph/0510376.
- 4849 [34] J. C. Collins, Nucl. Phys. **B396**, 161 (1993), hep-ph/9208213.
- 4850 [35] Belle, K. Abe *et al.*, Phys. Rev. Lett. **96**, 232002 (2006), hep-ex/0507063.
- 4851 [36] HERMES, A. Airapetian *et al.*, (2010), hep-ex/1006.4221.
- 4852 [37] HERMES, A. Airapetian *et al.*, Phys. Rev. Lett. **103**, 152002 (2009), 0906.3918.
- 4853 [38] HERMES, A. Airapetian *et al.*, Phys. Rev. Lett. **94**, 012002 (2005), hep-ex/0408013.
- 4854 [39] COMPASS, M. G. Alekseev *et al.*, (2010), 1005.5609.
- 4855 [40] COMPASS, V. Y. Alexakhin *et al.*, Phys. Rev. Lett. **94**, 202002 (2005), hep-ex/0503002.
- 4856 [41] D. W. Sivers, Phys. Rev. **D41**, 83 (1990).
- 4857 [42] X. Qian *et al.*, Phys. Rev. Lett. **107**, 072003 (2011).
- 4858 [43] G. L. Kane, J. Pumplin, and W. Repko, Phys. Rev. Lett. **41**, 1689 (1978).
- 4859 [44] M. Anselmino, M. Boglione, and F. Murgia, Phys. Lett. **B362**, 164 (1995), hep-ph/9503290.
- 4860 [45] J. C. Collins, Phys. Lett. **B536**, 43 (2002), hep-ph/0204004.
- 4861 [46] A. V. Belitsky, X. Ji, and F. Yuan, Nucl. Phys. **B656**, 165 (2003), hep-ph/0208038.
- 4862 [47] D. Boer, P. J. Mulders, and F. Pijlman, Nucl. Phys. **B667**, 201 (2003), hep-ph/0303034.
- 4863 [48] S. J. Brodsky, D. S. Hwang, and I. Schmidt, Phys. Lett. **B530**, 99 (2002), hep-ph/0201296.
- 4864 [49] X.-d. Ji and F. Yuan, Phys. Lett. **B543**, 66 (2002), hep-ph/0206057.
- 4865 [50] L. P. Gamberg, G. R. Goldstein, and K. A. Oganessyan, Phys. Rev. **D67**, 071504 (2003),  
4866 hep-ph/0301018.
- 4867 [51] M. Burkardt, Phys. Rev. **D69**, 057501 (2004), hep-ph/0311013.
- 4868 [52] M. Burkardt, Phys. Rev. **D72**, 094020 (2005), hep-ph/0505189.
- 4869 [53] S. J. Brodsky and S. Gardner, Phys. Lett. **B643**, 22 (2006), hep-ph/0608219.
- 4870 [54] J. Huang *et al.*, Phys. Rev. Lett. **108**, 052001 (2012).
- 4871 [55] T.-C. Meng, J.-C. Pan, Q.-b. Xie, and W. Zhu, Phys. Rev. **D40**, 769 (1989).

- 4872 [56] M. Anselmino, M. Boglione, and F. Murgia, Phys. Rev. **D60**, 054027 (1999), hep-ph/9901442.
- 4873 [57] A. Bacchetta, A. Schaefer, and J.-J. Yang, Phys. Lett. **B578**, 109 (2004), hep-ph/0309246.
- 4874 [58] Z. Lu and B.-Q. Ma, Nucl. Phys. **A741**, 200 (2004), hep-ph/0406171.
- 4875 [59] L. P. Gamberg, G. R. Goldstein, and M. Schlegel, (2007), 0708.2580.
- 4876 [60] A. Bacchetta, F. Conti, and M. Radici, Phys. Rev. **D78**, 074010 (2008), 0807.0323.
- 4877 [61] B. Pasquini and F. Yuan, Phys. Rev. D **81**, 114013 (2010).
- 4878 [62] F. Yuan, Phys. Lett. **B575**, 45 (2003), hep-ph/0308157.
- 4879 [63] D. Amrath, A. Bacchetta, and A. Metz, Phys. Rev. **D71**, 114018 (2005), hep-ph/0504124.
- 4880 [64] A. Bacchetta, L. P. Gamberg, G. R. Goldstein, and A. Mukherjee, Phys. Lett. **B659**, 234  
4881 (2008), arXiv:0707.3372 [hep-ph].
- 4882 [65] H. H. Matevosyan, A. W. Thomas, W. Bentz, Phys. Rev. D **86**, 034025 (2012),  
4883 arXiv:1205.5813 [hep-ph].
- 4884 [66] A. Kotzinian, H. H. Matevosyan and A. W. Thomas, arXiv:1403.5562 [hep-ph].
- 4885 [67] A. Metz, Phys. Lett. **B549**, 139 (2002).
- 4886 [68] J. C. Collins and A. Metz, Phys. Rev. Lett. **93**, 252001 (2004), hep-ph/0408249.
- 4887 [69] L. P. Gamberg, A. Mukherjee, and P. J. Mulders, Phys. Rev. **D77**, 114026 (2008), 0803.2632.
- 4888 [70] G. R. Goldstein and L. Gamberg, (2002), Transversity and meson photoproduction Proceed-  
4889 ings of ICHEP 2002; North Holland Amsterdam, p. 452 (2003), hep-ph/0209085, Published in  
4890 Amsterdam ICHEP 452-454.
- 4891 [71] Z. Lu and B.-Q. Ma, Phys. Rev. **D70**, 094044 (2004), hep-ph/0411043.
- 4892 [72] H. Avakian *et al.*, Phys. Rev. D **78**, 114024 (2008).
- 4893 [73] J. She, J. Zhu, and B.-Q. Ma, Phys. Rev. D **79**, 054008 (2009).
- 4894 [74] B. Pasquini, S. Cazzaniga, and F. Yuan, Phys. Rev. D **78**, 034025 (2008).
- 4895 [75] S. Boffi, A. V. Efremov, B. Pasquini, and P. Schweitzer, Phys. Rev. **D79**, 094012 (2009),  
4896 0903.1271.
- 4897 [76] V. Barone, Z. Lu, and B.-Q. Ma, Phys. Lett. **B632**, 277 (2006), hep-ph/0512145.
- 4898 [77] V. Barone, A. Prokudin, and B.-Q. Ma, Phys. Rev. **D78**, 045022 (2008), 0804.3024.
- 4899 [78] M. Anselmino *et al.*, Phys. Rev. **D75**, 054032 (2007), hep-ph/0701006.
- 4900 [79] COMPASS, E. S. Ageev *et al.*, Nucl. Phys. **B765**, 31 (2007), hep-ex/0610068.
- 4901 [80] COMPASS, M. Alekseev *et al.*, Phys. Lett. **B673**, 127 (2009), 0802.2160.
- 4902 [81] M. Anselmino *et al.*, Eur. Phys. J. **A39**, 89 (2009), 0805.2677.

- 4903 [82] M. Anselmino *et al.*, Phys. Rev. **D72**, 094007 (2005), hep-ph/0507181.
- 4904 [83] M. Anselmino *et al.*, (2005), hep-ph/0511017.
- 4905 [84] M. Anselmino *et al.*, Phys. Rev. **D71**, 074006 (2005), hep-ph/0501196.
- 4906 [85] J. C. Collins *et al.*, Phys. Rev. **D73**, 014021 (2006), hep-ph/0509076.
- 4907 [86] V. Barone, A. Drago, and P. G. Ratcliffe, Phys. Rept. **359**, 1 (2002), hep-ph/0104283.
- 4908 [87] Jefferson Lab Experiment E12-10-006, Spokespersons: Chen, Gao (contact), Jiang, Peng, and  
4909 Qian.
- 4910 [88] Jefferson Lab Experiment E12-10-006, Spokespersons: Chen, Huang (contact), Qiang, and  
4911 Yan.
- 4912 [89] Jefferson Lab Experiment E12-11-108, Spokespersons: Allada, Chen, Gao (contact), Li, and  
4913 Meziani.
- 4914 [90] D. Crabb *et al.*, Phys. Rev. Letts. **64**, 2627 (2008).
- 4915 [91] C. Keith *et al.*, Nucl. Inst. Meth. **A501**, 327 (2003).
- 4916 [92] G. S. Atoian *et al.*, Nucl. Inst. Meth. **A531**, 467 (2004).
- 4917 [93] G. S. Atoian *et al.*, Nucl. Inst. Meth. **A584**, 291 (2008).
- 4918 [94] M. Anselmino and A. Prokudin, private communications.
- 4919 [95] J. Huang and Y. Qiang, *Maximum likelihood estimation of asymmetry and angular modulation*  
4920 *for transversity (2010)*, URL <http://www.jlab.org/jinhuang/Transversity/MLE.pdf>.
- 4921 [96] Z. Ye *et al.*, Phys. Lett. B **767**, 91 (2017).
- 4922 [97] T. Hobbs and W. Melnitchouk, Phys. Rev. D **77**, 114023 (2008) [arXiv:0801.4791 [hep-ph]].
- 4923 [98] D. Wang *et al.* [PVDIS Collaboration], Nature **506**, no. 7486, 67 (2014).
- 4924 [99] S. Mantry, M. J. Ramsey-Musolf and G. F. Sacco, Phys. Rev. C **82**, 065205 (2010)  
4925 [arXiv:1004.3307 [hep-ph]].
- 4926 [100] M. R. Buckley and M. J. Ramsey-Musolf, Phys. Lett. B **712**, 261 (2012) [arXiv:1203.1102  
4927 [hep-ph]].
- 4928 [101] E. Eichten, K. D. Lane and M. E. Peskin, Phys. Rev. Lett. **50**, 811 (1983).
- 4929 [102] F. E. Close and A. W. Thomas, Phys. Lett. B **212**, 227 (1988).
- 4930 [103] E. Sather, Phys. Lett. B **274**, 433 (1992).
- 4931 [104] E. N. Rodionov, A. W. Thomas and J. T. Londergan, Mod. Phys. Lett. A **9**, 1799 (1994).
- 4932 [105] G. P. Zeller *et al.* [NuTeV Collaboration], Phys. Rev. Lett. **88**, 091802 (2002) [Erratum-ibid.  
4933 **90** 239902 (2003)].
- 4934 [106] J. T. Londergan and A. W. Thomas, Phys. Lett. B **558** 132 (2003).

- 4935 [107] J. T. Londergan and A. W. Thomas, *J. Phys. G* **31** 1151 (2005).
- 4936 [108] M. Gluck, P. Jimenez-Delgado and E. Reya, *Phys. Rev. Lett.* **95** 022002 (2005).
- 4937 [109] I. C. Cloet, W. Bentz and A. W. Thomas, *Phys. Rev. Lett.* **102**, 252301 (2009)  
4938 [arXiv:0901.3559 [nucl-th]].
- 4939 [110] W. Melnitchouk, I. R. Afnan, F. Bissey and A. W. Thomas, *Phys. Rev. Lett.* **84** 5455 (2000).
- 4940 [111] W. Melnitchouk and A. W. Thomas, *Phys. Lett. B* **377** 11 (1996).
- 4941 [112] S. I. Alekhin, *Phys. Rev. D* **63** 094022 (2001).
- 4942 [113] S. Kuhlmann *et al.*, *Phys. Lett. B* 476 297 (2000).
- 4943 [114] S. J. Brodsky and G. A. Miller, *Phys. Lett. B* **412**, 125 (1997).
- 4944 [115] S. J. Brodsky, I. A. Schmidt, and G. F. de Téramond, *Phys. Rev. Lett.*, **64**, 1011 (1990).
- 4945 [116] M. E. Luke, A. V. Manohar, and M. J. Savage. *Phys. Lett. B* **288**, 355 (1992).
- 4946 [117] A. B. Kaidalov and P. E. Volkovitsky, *Phys. Rev. Lett.*, **69**, 3155 (1992).
- 4947 [118] G. F. de Téramond, R. Espinoza, and M. Ortega-Rodriguez. *Phys. Rev. D* **58**, 034012 (1998).
- 4948 [119] V. I. Shevchenko, *Phys. Lett. B* **392**, 457 (1997).
- 4949 [120] A. Hayashigaki, *Prog. Theor. Phys.*, **101**, 923 (1999).
- 4950 [121] K. Yokokawa, S. Sasaki, T. Hatsuda, and A. Hayashigaki, *Phys. Rev. D* **74**, 034504 (2006).
- 4951 [122] T. Kawanai and S. Sasaki, *Phys. Rev. D* **82**, 091501 (2010).
- 4952 [123] K. Tsushima, D. H. Lu, G. Krein, and A. W. Thomas, *Phys. Rev. C* **83**, 065208 (2011).
- 4953 [124] K. Tsushima, D. H. Lu, G. Krein, and A. W. Thomas, *AIP Conf. Proc.* **1354**, 39 (2011).
- 4954 [125] M. Binkeley *et al.*, *Phys. Rev. Lett.* **48**, 73 (1982).
- 4955 [126] B. H. Denby *et al.*, *Phys. Rev. Lett.* **52**, 795 (1984).
- 4956 [127] M. D. Sokoloff *et al.*, *Phys. Rev. Lett.* **57**, 3003 (1986).
- 4957 [128] R. Barate *et al.*, *Z. Phys. C* **33**, 505 (1987).
- 4958 [129] P. L. Frabetti *et al.*, *Phys. Lett. B* **316**, 197 (1993).
- 4959 [130] S. Aid *et al.*, *Nucl. Phys. B* **472**, 3 (1996).
- 4960 [131] J. Breitweg *et al.*, *Z. Phys. C* **76**, 599 (1997).
- 4961 [132] S. Aid *et al.*, *Nucl. Phys. B* **472**, 2 (1996).
- 4962 [133] U. Camerini *et al.*, *Phys. Rev. Lett.* **35**, 483 (1975).
- 4963 [134] B. Gittelman *et al.*, *Phys. Rev. Lett.* **35**, 1616 (1975).
- 4964 [135] B. Knapp *et al.*, *Phys. Rev. Lett.* **34**, 1040 (1975).

- 4965 [136] R. L. Anderson, *Excess Muons and New Results in  $\Psi$  Photoproduction*, SLAC-PUB-1471.
- 4966 [137] D. Kharzeev, nucl-th/9601029.
- 4967 [138] D. Kharzeev, H. Satz, A. Syamtomov, and G. Zinovjev, *Eur. Phys. J. C* **9**, 459 (1999).
- 4968 [139] S. J. Brodsky, E. Chudakov, P. Hoyer, and J.M. Laget, *Phys. Lett. B* **498**, 23 (2001).
- 4969 [140] A. Sibirtsev, S. Krewald, and A. W. Thomas, *J. Phys. G* **30**, 1427 (2004).
- 4970 [141] M. A. Shifman, A. I. Vainshtein, and V. I. Zakharov, *Phys. Lett. B* **65**, 255 (1976).
- 4971 [142] V. A. Novikov, M. A. Shifman, A. I. Vainshtein, and V. I. Zakharov, *Nucl. Phys.* **B136**, 125  
4972 (1978).
- 4973 [143] . A. Shifman, A. I. Vainshtein, and V. I. Zakharov, *Nucl. Phys.* **B136**, 157 (1978).
- 4974 [144] A. Sibirtsev and M. B. Voloshin, *Phys. Rev. D* **71**, 076005 (2005).
- 4975 [145] R. B. Baldini, S. Pacetti and A. Zallo, arXiv:0812.3283 [hep-ph].
- 4976 [146] M. Ablikim *et al.* (BESIII Collaboration), *Phys. Rev. Lett.* **108**, 112003 (2012).
- 4977 [147] Gryniuk, Oleksii and Vanderhaeghen, Marc”, *Phys. Rev. D* **94**, 074001 (2016).
- 4978 [148] J. J. Wu, R. Molina, E. Oset, and B.-S. Zou, *Phys. Rev. Lett.* **105**, 232001 (2010).
- 4979 [149] P. Bosted *et al.*, *Phys. Rev. C* **79**, 015209 (2009).
- 4980 [150] Contact Person: E. Chudakov, PAC32 PR12-07-106 The A-dependence of  $J/\Psi$  Photopro-  
4981 duction near Threshold.
- 4982 [151] Contact Person: Z.-E. Meziani, PAC39 [https://www.jlab.org/exp\\_prog/  
4983 proposals/12/PR12-12-006.pdf](https://www.jlab.org/exp_prog/proposals/12/PR12-12-006.pdf).
- 4984 [152] Contact Person: P. Souder, PAC34 [http://hallaweb.jlab.org/collab/PAC/  
4985 PAC34/PR-09-012-pvdis.pdf](http://hallaweb.jlab.org/collab/PAC/PAC34/PR-09-012-pvdis.pdf).
- 4986 [153] Contact Person: H. Gao, PAC34 [http://hallaweb.jlab.org/collab/PAC/  
4987 PAC34/PR-09-014-transversity.pdf](http://hallaweb.jlab.org/collab/PAC/PAC34/PR-09-014-transversity.pdf).
- 4988 [154] Contact Person: J. Huang, PAC37 [http://www.jlab.org/exp\\$\\$\\_prog/PACpage/  
4989 PAC37/proposals/Proposals/NewProposals/PR-11-007.pdf](http://www.jlab.org/exp$$_prog/PACpage/PAC37/proposals/Proposals/NewProposals/PR-11-007.pdf).
- 4990 [155] Contact Person: H. Gao, PAC38 [http://wwwold.jlab.org/exp\\$\\$\\_prog/  
4991 proposals/11/PR12-11-108.pdf](http://wwwold.jlab.org/exp$$_prog/proposals/11/PR12-11-108.pdf).
- 4992 [156] X. Qian et al., *Phys. Rev. C* **81**, 055209 (2010).
- 4993 [157] S. J. Brodsky et al., *Phys. Lett. B* **498**, 23 (2001).
- 4994 [158] K. Schilling and G. Wolf, *Nucl. Phys.* **B61**, 381 (1973).
- 4995 [159] R. Fiore et al., *Phys. Rev. D* **80**, 116001 (2009).
- 4996 [160] Aaij, Roel et al. (LHCb Collaboration), *Phys. Rev. Lett.*, **115**, 072001 (2015).

- 4997 [161] C. Adloff et al., Eur. Phys. J. C **13**, 371 (2000).
- 4998 [162] L. W. Whitlow, Ph. D. thesis, Stanford University, SLAC-Report-357 (1990).
- 4999 [163] Developed by J. W. Lightbody and J. S. O’Connell in 1988.
- 5000 [164] D. E. Wiser, Ph. D. thesis, Univ. of Wisconsin (1977).
- 5001 [165] X. Qian, Ph. D. thesis, Duke University.
- 5002 [166] T. Abe, Computer Physics Communications **136**, 126 (2001).
- 5003 [167] PYTHIA, <http://projects.hepforge.org/pythia6/>, 2006.
- 5004 [168] Y. Kubota et al., Nucl. Instr. and Meth. A **320** (1992).
- 5005 [169] Poisson Superfish, [http://laacg1.lanl.gov/laacg/services/download\\_sfp.html](http://laacg1.lanl.gov/laacg/services/download_sfp.html).
- 5006
- 5007 [170] G. Atoian et al., Nucl. Instr. and Meth. A **584**, 291 (2008).
- 5008 [171] W. Anderson et al., arXiv:1103.4277 [physics.ins-det].
- 5009 [172] B. Azmoun et al., IEEE Trans. Nucl. Sci. **56-3**, 1544 (2009).
- 5010 [173] C. Lu and K. T. McDonald, Nucl. Instr. and Meth. A **343**, 135 (1994).
- 5011 [174] Y. Wang et al., Chin. Phys. C **33**, 374 (2009).
- 5012 [175] S. J. Brodsky, P. Hoyer, C. Peterson, and N. Sakai, Phys. Lett. **93B**, 451 (1980).
- 5013 [176] S. J. Brodsky, C. Peterson and N. Sakai, Phys. Rev. D **23**, 2745 (1981).
- 5014 [177] W. C. Chang and J. C. Peng, Phys. Lett. B **704**, 197 (2011).
- 5015 [178] B. W. Adams *et al.*, “A Brief Technical History of the Large-Area Picosecond Photodetector (LAPPD) Collaboration,” arXiv:1603.01843.
- 5016
- 5017 [179] “eRD14: PID Consortium for an integrated program for Particle Identification (PID) at  
5018 a future Electron Ion Collider,” [https://wiki.bnl.gov/conferences/images/6/6f/  
5019 ERD14\\_progress\\_report\\_Dec\\_2015.pdf](https://wiki.bnl.gov/conferences/images/6/6f/ERD14_progress_report_Dec_2015.pdf).
- 5020 [180] E12-10-007 “Precision Measurement of Parity-violation in Deep Inelastic Scattering Over a  
5021 Broad Kinematic Range” Contact person: P. Souder.
- 5022 [181] E12-10-006, “Target Single Spin Asymmetry in Semi-Inclusive Deep-Inelastic ( $e, e'\pi^\pm$ ) on  
5023 a Transversely Polarized  $^3\text{He}$  Target at 8.8 and 11 GeV”, Spokesperson: J.-P. Chen, H. Gao  
5024 (contact), X. Jiang, J.-C. Peng, and X. Qian.
- 5025 [182] E12-11-007, “Asymmetries in Semi-Inclusive Deep-Inelastic ( $e, e'\pi^\pm$ ) Reactions on a Longi-  
5026 tudinally Polarized  $^3\text{He}$  Target at 8.8 and 11 GeV”, Spokesperson: J.-P. Chen, J. Huang (contact),  
5027 Y. Qiang, and W.-B. Yan.
- 5028 [183] E12-11-108 “Target Single Spin Asymmetry in Semi-Inclusive Deep-Inelastic ( $e, e'\pi^\pm$ ) on a  
5029 Transversely Polarized Proton Target”, Spokespersons: K. Allada, J.-P. Chen, H. Gao (contact),  
5030 Z.-E. Meziani, and X.-M. Li.



- 5031 [184] M. Anselmino and A. Prokudin, *private communications*. Predictions are based on the ex-  
5032 tractions of Ref. [185].
- 5033 [185] M. Anselmino *et al.*, proceedings of the XVI International Workshop on Deep Inelastic Scat-  
5034 tering and Related Subjects, DIS 2008, London, U.K. 2009. e-Print: arXiv:0807.0173.
- 5035 [186] W. Vogelsang and F. Yuan, *private communications*.
- 5036 [187] B. Pasquini, *private communication*.  
5037 S. Boffi, A. V. Efremov, B. Pasquini and P. Schweitzer, Phys. Rev. **D79**, 094012 (2009)  
5038 arXiv:0903.1271.
- 5039 [188] X. Qian *et al.* (JLab Hall A Collaboration) Phys. Rev. Lett. **107**, 072003 (2011).
- 5040 [189] J. Huang *et al.* (JLab Hall A Collaboration) Phys. Rev. Lett. **108**, 052001 (2012).
- 5041 [190] X. Qian, Modern Phys. Lett. **A27**, 1230021 (2012).
- 5042 [191] Y. Zhang *et al.* Chinese Physics **C36**, 610 (2012).
- 5043 [192] L. W. Whitlow, SLAC-Report-357 (1990).
- 5044 [193] J. W. Lightbody and J. S. O’Connell, Computers in Physics 2, 57 (1988).
- 5045 [194] D. E. Wiser, Ph. D. thesis, Univ. of Wisconsin (1977).
- 5046 [195] E12-12-006, “Near-Threshold Electroproduction of  $J/\psi$  with a 11 GeV Beam”, Spokesper-  
5047 sons: K. Hafidi, Z.-E. Meziani (contact), X. Qian, N. Sparveris, and Z.-W. Zhao.
- 5048 [196] Study of modifying CLEO II magnet for SoLID, E.Chudakov  
5049 ([https://userweb.jlab.org/~gen/jlab12gev/cleo\\_mag/](https://userweb.jlab.org/~gen/jlab12gev/cleo_mag/))
- 5050 [197] Y. Kubota *et al.*, Nucl. Instr. and Meth., **A320** 66 (1992)
- 5051 [198] D. M. Coffman *et al.*, IEEE Transactions on Nuclear Science, **37** 1172 (1990)
- 5052 [199] X. Qian *et al.*, Phys. Rev. Lett. 107, (2012) 072003. J. Huang *et al.*, Phys. Rev. Lett. 108  
5053 (2012) 052001.
- 5054 [200] T.D. Averett, *et al.*, Nucl. Instr. and Meth. A 427 (1999) 440.
- 5055 [201] J. Maxwell *et al.*, to be submitted to Nucl. Instr. and Meth. A.
- 5056 [202] D.G. Crabb, C.B. Higley, A.D. Krisch, R.S. Raymond, T. Roser, and J.A. Stewart, Phys. Rev.  
5057 Lett. 64, (1990) 2627.
- 5058 [203] C.D. Keith, *et al.*, Nucl. Instr. and Meth. A 684 (2012) 27.
- 5059 [204] C.D. Keith, *et al.*, Nucl. Instr. and Meth. A 501 (2003) 327.
- 5060 [205] Design Report rfq 14231, Oxford Instruments Nanotechnology Tools Ltd.
- 5061 [206] F. Sauli, Nucl. Instr. and Meth. **A 386**, 531 (1997).
- 5062 [207] B. Ketzer *et al.*, Nucl. Phys. B (Proc. Suppl.) **125**, 368 (2003).

- 5063 [208] M. Villa, *et al.*, Nucl. Inst. and Meth. **A 628** 182 (2011).
- 5064 [209] M. Alfonsi *et al.*, Nucl. Inst. and Meth. **A 617**, 151 (2010).
- 5065 [210] D. Abbaneo *et al.*, Nucl. Inst. and Meth. **A** (2010).
- 5066 [211] M.J. French *et al.*, Nucl. Instr. and Meth. **A 466** 359 (2001).
- 5067 [212] F.Sauli, RD51-NOTE-2012-007 REVISED 21.09.2012.
- 5068 [213] D. Abbaneo *et al.*, RD51-NOTE-2012-012 16.11.2012.
- 5069 [214] William Whyte, “Cleanroom Technology: Fundamentals of Design, Testing and Operation”  
5070 (2001) ISBN 978-0-470-74806-0
- 5071 [215] P. Walker, V. Weber, *et al.*, Journal of Photographic Science, **18** 150 (1970).
- 5072 [216] J. M. Shaw, J. D. Gelorme, *et al.*, IBM Journal of Research and Development. **41** 81 (1997)  
5073 ISSN: 0018-8646
- 5074 [217] Rensheng Wang, Yan Huang, Zhigang Xiao *et al.*, Nucl. Inst. and Meth. **A701** 54 (2013)
- 5075 [218] S. P. Malace, B. D. Sawatzky and H. Gao, “Studies of single-photoelectron response and  
5076 of performance in magnetic field of a H8500C-03 photomultiplier tube,” JINST **1309**, P09004  
5077 (2013) [arXiv:1306.6277 ].
- 5078 [219] Composite Mirror Applications, Inc. 1638 S. Research Loop, Suite 100 Tucson, Arizona  
5079 85710. <http://www.compositemirrors.com>
- 5080 [220] LHCb RICH Technical Design Report, The LHCb Colaboration: [lhcb-rich.web.cern.ch/lhcb-rich/richtdr/tdr.pdf](http://lhcb-rich.web.cern.ch/lhcb-rich/richtdr/tdr.pdf)
- 5081
- 5082 [221] Hamamatsu flat panel type multianode photomultiplier tube assembly H8500 series specifi-  
5083 cations are found at [http://jp.hamamatsu.com/products/sensor-eta/pd002/  
5084 pd394/H8500C/index\\_en.html](http://jp.hamamatsu.com/products/sensor-eta/pd002/pd394/H8500C/index_en.html)
- 5085 [222] Amuneal Manufacturing Corporation. 4737 Darrah Street Philadelphia, PA 19124, USA.  
5086 [www.amuneal.com](http://www.amuneal.com)
- 5087 [223] GEMC: a GEant4 Monte Carlo. <https://gemc.jlab.org/>
- 5088 [224] GEANT4: a toolkit for the simulation of the passage of particles through matter: [http:  
5089 //geant4.cern.ch/](http://geant4.cern.ch/)
- 5090 [225] M. Artuso *et al.*, Nuclear Instruments and Methods A, 558 373-387 (2006).
- 5091 [226] A. Bulla, Ph.D. thesis (1997); E. Foktitis *et al.*, Nuclear Instruments and Methods A 371 255  
5092 (1996).
- 5093 [227] G.J. Barber *et al.*, Nuclear Instruments and Methods A 593 624-637 (2008).
- 5094 [228] JLab approved experiments E-12-09-014 and E-12-10-006  
5095 [http://www.jlab.org/exp\\_prog/proposals/09/PR12-09-014.pdf](http://www.jlab.org/exp_prog/proposals/09/PR12-09-014.pdf)  
5096 [http://www.jlab.org/exp\\_prog/proposals/10/PR12-10-006.pdf](http://www.jlab.org/exp_prog/proposals/10/PR12-10-006.pdf)  
5097

- 5098 [229] S. P. Malace, B. D. Sawatzky and H. Gao, “Studies of single-photoelectron response and  
5099 of performance in magnetic field of a H8500C-03 photomultiplier tube,” JINST **1309**, P09004  
5100 (2013) [arXiv:1306.6277 ].
- 5101 [230] G. S. Atoian *et al.*, Nucl. Instrum. Meth. A **584**, 291 (2008).
- 5102 [231] H. Avakian *et al.*, Nucl. Instrum. Meth. A **417**, 69 (1998).
- 5103 [232] E. Picatoste Olloqui [LHCb Collaboration], J. Phys. Conf. Ser. **160**, 012046 (2009).
- 5104 [233] Y. V. Kharlov *et al.*, Nucl. Instrum. Meth. A **606**, 432 (2009).
- 5105 [234] D. A. Morozov *et al.*, J. Phys. Conf. Ser. **160**, 012021 (2009).
- 5106 [235] ATLAS Tile Calorimeter Technical Design Report (1996).
- 5107 [236] L. Aliaga *et al.* [MINERvA Collaboration], Nucl. Instrum. Meth. A **743**, 130 (2014)  
5108 doi:10.1016/j.nima.2013.12.053 [arXiv:1305.5199 [physics.ins-det]].
- 5109 [237] M. J. Varanda, M. David, A. Gomes and A. Maio, Nucl. Instrum. Meth. A **453**, 255 (2000).  
5110 doi:10.1016/S0168-9002(00)00642-2
- 5111 [238] LHCb Tracker Upgrade Technical Design Report.
- 5112 [239] Y. Wang, *et al.*, Nucl. Instr. and Meth. A 538 (2005) 425.
- 5113 [240] Y. Wang, *et al.*, Nucl. Instr. and Meth. A 537 (2005) 698.
- 5114 [241] A. Akhondov, *et al.*, Nucl. Instr. and Meth. A 602 (2009) 709.
- 5115 [242] A. Akhondov, *et al.*, Nucl. Instr. and Meth. A 533 (2004) 74.
- 5116 [243] Y. Wang, *et al.*, Chinese Physics C. 33 (2009) 374.
- 5117 [244] J.B. Wang, *et al.*, 2012 JINST 7 P10004.
- 5118 [245] JLab E-08-027, A. Camsonne, J. P. Chen, D. Crabb and K Slifer, spokespersons;  
5119 [http://www.jlab.org/exp\\_prog/proposals/08/PR-08-027.pdf](http://www.jlab.org/exp_prog/proposals/08/PR-08-027.pdf)
- 5120 [246] V. Gyurjyan *et al.*, J. Phys. Conf. Ser. **331**, 032013 (2011). [https://claraweb.jlab.](https://claraweb.jlab.org/docs/claraweb)  
5121 [org/docs/claraweb](https://claraweb.jlab.org/docs/claraweb)
- 5122 [247] D. Lawrence, J. Phys. Conf. Ser. **119**, 042018 (2008). <https://www.jlab.org/JANA>
- 5123 [248] M. Al-Turany *et al.*, J. Phys. Conf. Ser. **396**, 022001 (2012). [https://fairroot.gsi.](https://fairroot.gsi.de)  
5124 [de](https://fairroot.gsi.de)
- 5125 [249] C. Green *et al.*, J. Phys. Conf. Ser. **396**, 022020 (2012). <http://art.fnal.gov>
- 5126 [250] See for example E. Sexton-Kennedy, *A Review of Event Processing Frameworks used in HEP*,  
5127 Talk at CHEP 2015, [http://indico.cern.ch/event/304944/contributions/](http://indico.cern.ch/event/304944/contributions/1672690/)  
5128 [1672690/](http://indico.cern.ch/event/304944/contributions/1672690/)
- 5129 [251] R. Brun and F. Rademakers, Nucl. Instr. Meth. Phys. Res. A **389**, 81 (1997). [http://](http://root.cern/)  
5130 [root.cern/](http://root.cern/)

- 5131 [252] ROOT/C++ Analyzer for JLab Hall A, <https://hallaweb.jlab.org/podd>. Code  
5132 repository <https://github.com/JeffersonLab/analyzer>
- 5133 [253] <https://github.com/sPHENIX-Collaboration/coresoftware>
- 5134 [254] <https://cdcv.s.fnal.gov/redmine/issues/15372>
- 5135 [255] M. Al-Turany *et al.*, J. Phys. Conf. Ser. **664**, 072001 (2015).
- 5136 [256] Fluka, <http://www.fluka.org>
- 5137 [257] Geant4, <http://geant4.cern.ch/>
- 5138 [258] GEMC, <https://gemc.jlab.org/>
- 5139 [259] Poisson superfish, [http://laacg1.lanl.gov/laacg/services/download\\_](http://laacg1.lanl.gov/laacg/services/download_sf.shtml)  
5140 [sf.shtml](http://laacg1.lanl.gov/laacg/services/download_sf.shtml)
- 5141 [260] Tosca, [http://www.chilton-computing.org.uk/inf/eng/](http://www.chilton-computing.org.uk/inf/eng/electromagnetics/p001.htm)  
5142 [electromagnetics/p001.htm](http://www.chilton-computing.org.uk/inf/eng/electromagnetics/p001.htm)
- 5143 [261] C. Altunbas *et al.*, Nucl. Inst. Meth. A **490**, 177 (2002).
- 5144 [262] J. Huston, H.L. Lai, P. Nadolsky, W.K. Tung, J. Pumplin, and D.R. Stump, JHEP 07 (2002)  
5145 012.
- 5146 [263] David E. Wisner, and Pions at SLAC Energies,” PhD thesis, Wisconsin University Madison,  
5147 1977, <http://wwwlib.umi.com/dissertations/fullcit?p7719743>
- 5148 [264] S. Riordan, X. Zheng, Z. W. Zhao and N. Ton, unpublished (2014).
- 5149 [265] R. Beminiwattha, [https://hallaweb.jlab.org/DocDB/0002/000212/001/](https://hallaweb.jlab.org/DocDB/0002/000212/001/HallD_Gen_Summary.pdf)  
5150 [HallD\\_Gen\\_Summary.pdf](https://hallaweb.jlab.org/DocDB/0002/000212/001/HallD_Gen_Summary.pdf)
- 5151 [266] Mark Ito, private communication (2014).
- 5152 [267] Eugene Chudakov, private communication (2014).
- 5153 [268] V. M. Budnev, I. F. Ginzburg, G. V. Meledin and V. G. Serbo, Phys. Rep. **15**, 181 (1975).
- 5154 [269] J. Beringer *et al.* (Particle Data Group), Phys. Rev. D **86**, 010001 (2012).
- 5155 [270] Yung-Su Tsai, Rev. Mod. Phys. **46**, 815 (1974).
- 5156 [271] R. E. Kalman, Transactions of ASME Journ. Basic Engineering **82**, 35 (1960).
- 5157 [272] R. Mankel, Rept. Prog. Phys. **67**, 553 (2004).
- 5158 [273] M. Capogni, E. Cisbani, G.M. Urciuli, *Note on GEM digitization modeling*, [http://www.](http://www.iss.infn.it/cisbani/atmp/sbs/ft/gemc/diginote_0.2.pdf)  
5159 [iss.infn.it/cisbani/atmp/sbs/ft/gemc/diginote\\_0.2.pdf](http://www.iss.infn.it/cisbani/atmp/sbs/ft/gemc/diginote_0.2.pdf).
- 5160 [274] H. Avakian *et.al* Nucl. Instrum. Meth. A**417**, 69 (1998).
- 5161 [275] A. Bacchetta, M. Diehl, K. Goeke, A. Metz, P. J. Mulders, and M. Schlegel, JHEP **0702**, 093  
5162 (2007).

- 5163 [276] S. Dulat *et al.*, Phys. Rev. D **93**, 033006 (2016).
- 5164 [277] D. de Florian, R. Sassot and M. Stratmann, Phys. Rev. D **75**, 114010 (2007).
- 5165 [278] M. Anselmino, M. Boglione, U. D’Alesio, A. Kotzinian, F. Murgia and A. Prokudin, Phys.  
5166 Rev. D **71**, 074006 (2005).
- 5167 [279] M. Anselmino, M. Boglione, U. D’Alesio, A. Kotzinian, S. Melis, F. Murgia, A. Prokudin  
5168 and C. Turk, Eur. Phys. J. A **39**, 89 (2009).
- 5169 [280] M. Anselmino, M. Boglione, U. D’Alesio, S. Melis, F. Murgia and A. Prokudin, Phys. Rev.  
5170 D **87**, 094019 (2013).
- 5171 [281] C. Lefky and A. Prokudin, Phys. Rev. D **91**, 034010 (2015).
- 5172 [282] L. P. Kaptari, A. Del Dotto, E. Pace, G. Salmè and S. Scopetta, Phys. Rev. C **89**, 035206  
5173 (2014).
- 5174 [283] A. Del Dotto, private communication
- 5175 [284] I. Akushevich, N. Shumeiko and A. Soroko, Eur. Phys. J. C **10**, 681 (1999).
- 5176 [285] I. Akushevich, A. Ilyichev and M. Osipenko, Phys. Lett. B **672**, 35 (2009).
- 5177 [286] J. Pumplin, D. R. Stump, J. Huston, H. L. Lai, P. M. Nadolsky and W. K. Tung, JHEP **0207**,  
5178 012 (2002).
- 5179 [287] “SoLID Preliminary Conceptual Design Report”, The SoLID Collaboration, unpublished  
5180 (2014).
- 5181 [288] A. Narayan *et al.*, Phys. Rev. X **6**, no. 1, 011013 (2016).
- 5182 [289] H. Spiesberger, Phys. Rev. D **52**, 4936 (1995).
- 5183 [290] M. E. Christy and P. E. Bosted, Phys. Rev. C **81**, 055213 (2010).
- 5184 [291] E12-10-006, “Target Single Spin Asymmetry in Semi-Inclusive Deep-Inelastic ( $e, e'\pi^\pm$ ) on  
5185 a Transversely Polarized  $^3\text{He}$  Target at 8.8 and 11 GeV”, Spokesperson: J.-P. Chen, H. Gao (con-  
5186 tact), X. Jiang, J.-C. Peng, and X. Qian.
- 5187 [292] E12-11-007, “Asymmetries in Semi-Inclusive Deep-Inelastic ( $e, e'\pi^\pm$ ) Reactions on a Longi-  
5188 tudinally Polarized  $^3\text{He}$  Target at 8.8 and 11 GeV”, Spokesperson: J.-P. Chen, J. Huang (contact),  
5189 Y. Qiang, and W.-B. Yan.
- 5190 [293] E12-11-108 “Target Single Spin Asymmetry in Semi-Inclusive Deep-Inelastic ( $e, e'\pi^\pm$ ) on a  
5191 Transversely Polarized Proton Target”, Spokespersons: K. Allada, J.-P. Chen, H. Gao (contact),  
5192 Z.-E. Meziani, and X.-M. Li.
- 5193 [294] S. Martoiu, H. Muller and J. Toledo, Conference Proceedings: 2011 IEEE Nuclear Science  
5194 Symposium Conference Record, 2036 (2011).
- 5195 [295] M.J. French *et al.*, Nucl. Instr. and Meth. A **466** 359 (2001).
- 5196 [296] A. Neiser *et al.*, Journal of Instrumentation **8**, C12043 (2013).

- 5197 [297] E12-12-006, “Near-threshold Electroproduction of  $J/\psi$  with a 11 GeV Beam”, Spokesper-  
5198 sons: K. Hafidi, Z.-E. Meziani (contact), X. Qian, N. Sparveris, and Z.-W. Zhao.
- 5199 [298] *The FLUKA code: Description and benchmarking* G. Battistoni, S. Muraro, P.R. Sala, F.  
5200 Cerutti, A. Ferrari, S. Roesler, A. Fassio, J. Ranft, Proceedings of the Hadronic Shower Simu-  
5201 lation Workshop 2006, Fermilab 6–8 September 2006, M.Albrow, R. Raja eds., AIP Conference  
5202 Proceeding 896, 31-49, (2007)
- 5203 [299] *FLUKA: a multi-particle transport code* A. Ferrari, P.R. Sala, A. Fassio, and J. Ranft, CERN-  
5204 2005-10 (2005), INFN/TC\_05/11, SLAC-R-773
- 5205 [300] *Photodisintegration of deuterium and big bang nucleosynthesis* K.Y.Hare and others, *Phys.*  
5206 *Rev. D* **68**, 072001 (2003)
- 5207 [301] *Displacement damage in silicon, on-line compilation* A. Vasilescu and G. Lindstroem  
5208 available at [http://hepweb03.phys.sinica.edu.tw/opto/Irradiation/](http://hepweb03.phys.sinica.edu.tw/opto/Irradiation/Documents/NIEL_scaling/gunnar.htm)  
5209 [Documents/NIEL\\_scaling/gunnar.htm](http://hepweb03.phys.sinica.edu.tw/opto/Irradiation/Documents/NIEL_scaling/gunnar.htm)
- 5210 [302] [https://solid.jlab.org/DocDB/0000/000025/001/zana\\_solid\\_radiation\\_](https://solid.jlab.org/DocDB/0000/000025/001/zana_solid_radiation_and_activation_mar_2017.pdf)  
5211 [and\\_activation\\_mar\\_2017.pdf](https://solid.jlab.org/DocDB/0000/000025/001/zana_solid_radiation_and_activation_mar_2017.pdf)
- 5212 [303] K. Abe *et al.* [SLD Collaboration], *Phys. Rev. Lett.* **84**, 5945 (2000) [arXiv:hep-ex/0004026].
- 5213 [304] N. Falletto *et al.*, “Compton scattering off polarized electrons with a high finesse Fabry-Perot  
5214 cavity at JLab,” *Nucl. Instrum. Meth.*, A459, 212-425, 2001.
- 5215 [305] A. Narayan, D. Dutta, V. Tvaskis and J. W. Martin, *Nuovo Cim. C* **035N04**, 134 (2012).
- 5216 [306] N. Vansteenkise, P. Vignolo, and A. Aspect, “Optical Reversibility Theorems for Polariza-  
5217 tion: Application to Remote Control of Polarization”, *J. Opt. Soc. Am. A*, Vol. 10, No. 10, (1993)  
5218 2240.
- 5219 [307] R.J. Loewen, “A compact light source: Design and technical feasibility study of a laser-  
5220 electron storage ring X-ray source,” SLAC-R-0632 (2003).
- 5221 [308] S. Miyoshi *et al.*, Photon generation by laser-Compton scattering at the KEK-ATF, NIM  
5222 A623 (2010) 576.
- 5223 [309] A. Variola *et al.*, The LAL Compton Program,, NIM A608 (2009) S83.
- 5224 [310] V. Brisson *et al.*, High finesse Fabry-Perot cavities in the picosecond regime, NIM A608  
5225 (2009) S75.
- 5226 [311] A. Denner and S. Dittmaier, “Complete  $O(\alpha)$  QED corrections to polarized Compton scatter-  
5227 ing”, *Nucl. Phys. B* **540** 58 (1999).
- 5228 [312] M. Friend *et al.*, “Upgraded photon calorimeter with integrating readout for Hall A Compton  
5229 Polarimeter at Jefferson Lab”, [arXiv:1108.3116 [physics.ins-det]].
- 5230 [313] G. W. Ford and C. J. Mullin, “Scattering of Polarized Dirac Particles on Electrons,” *Phys.*  
5231 *Rev.* **108**, 477 (1957); Erratum, *Phys. Rev.* **110**, 1485(E) (1958).
- 5232 [314] A. M. Bincer, “Scattering of Longitudinally Polarized Fermions,” *Phys. Rev.* **107**, 1434  
5233 (1957).

- 5234 [315] P. Stehle, “Calculation of Electron-Electron Scattering,” *Phys. Rev.* **110**, 1458 (1958).
- 5235 [316] A. Raçzka and R. Raçzka, “Møller Scattering of Arbitrarily Polarized Electrons,” Erratum,  
5236 *Phys. Rev.* **110**, 1469 (1958).
- 5237 [317] G. Alexander and I. Cohen, “Møller scattering polarimetry for high-energy  $e^+e^-$  linear col-  
5238 liders,” *Nucl. Instrum. Meth. A* **486**, 552 (2002) [hep-ex/0006007]. This paper contains the basic  
5239 formulas for Møller polarimetry, as well as references to calculations of higher order QED cor-  
5240 rections.
- 5241 [318] M. Hauger *et al.*, “A high-precision polarimeter,” *Nucl. Instrum. Meth.*, vol. A462, pp. 382–  
5242 392, 2001, nucl-ex/9910013.
- 5243 [319] Matthias Loppacher, “Møller Polarimetry for CEBAF Hall C”, Inaugural Dissertation, Uni-  
5244 versität Basel (1996).
- 5245 [320] L. V. de Bever, J. Jourdan, M. Loppacher, S. Robinson, I. Sick, J. Zhao, “A Target for Precise  
5246 Møller Polarimetry”, *Nucl. Instrum. Meth. A* **400**, 379 (1997).
- 5247 [321] A. V. Glamazdin, V. G. Gorbenko, L. G. Levchuk, R. I. Pomatsalyuk, A. L. Rubashkin,  
5248 P. V. Sorokin, D. S. Dale and B. Doyle *et al.*, “Electron beam Møller polarimeter at JLab Hall  
5249 A,” *Fizika B* **8**, 91 (1999) [hep-ex/9912063].
- 5250 [322] E. A. Chudakov, A. V. Glamazdin, V. G. Gorbenko, L. G. Levchuk, R. I. Pomatsalyuk,  
5251 P. V. Sorokin, “Electron beam Møller polarimeter at Hall A, JLab”, *Prob.Atom.Sci.Tech.* **40**,  
5252 43 (2002)
- 5253 [323] E. Chudakov and V. Luppov, “Møller polarimetry with atomic hydrogen targets,” *IEEE Trans.*  
5254 *Nucl. Sci.*, vol. 51, pp. 1533–1540, 2004.
- 5255 [324] E. Chudakov and V. Luppov, “Moeller polarimetry with atomic hydrogen targets,” *Eur. Phys.*  
5256 *J.*, vol. A24S2, pp. 123–126, 2005.
- 5257 [325] P. S. Cooper, M. J. Alguard, R. D. Ehrlich, V. W. Hughes, H. Kobayakawa, J. S. Ladish,  
5258 M. S. Lubell and N. Sasao *et al.*, “Polarized electron Electron Scattering at GeV Energies,” *Phys.*  
5259 *Rev. Lett.* **34**, 1589 (1975).
- 5260 [326] B. Wagner, H. G. Andresen, K. H. Steffens, W. Hartmann, W. Heil and E. Reichert, “A Møller  
5261 polarimeter for CW and pulsed intermediate-energy electron beams,” *Nucl. Instrum. Meth. A*  
5262 **294**, 541 (1990).
- 5263 [327] J. Arrington, E. J. Beise, B. W. Filippone, T. G. O’Neill, W. R. Dodge, G. W. Dodson,  
5264 K. A. Dow and J. D. Zumbro, “A Variable energy Møller polarimeter at the MIT Bates Linear  
5265 Accelerator Center,” *Nucl. Instrum. Meth. A* **311**, 39 (1992).
- 5266 [328] K. B. Beard, R. Madey, W. M. Zhang, D. M. Manley, B. D. Anderson, A. R. Baldwin,  
5267 J. M. Cameron and C. C. Chang *et al.*, “Measurement of the polarization of a pulsed elec-  
5268 tron beam with a Møller polarimeter in the coincidence mode,” *Nucl. Instrum. Meth. A* **361**,  
5269 46 (1995).
- 5270 [329] H. R. Band, G. Mitchell, R. Prepost and T. Wright, “A Møller polarimeter for high-energy  
5271 electron beams,” *Nucl. Instrum. Meth. A* **400**, 24 (1997).

- 5272 [330] P. Steiner, A. Feltham, I. Sick, M. Zeier and B. Zihlmann, “A high-rate coincidence Moller  
5273 polarimeter,” *Nucl. Instrum. Meth. A* **419**, 105 (1998).
- 5274 [331] G. G. Scott and H. W. Sturmer, “Magnetomechanical Ratios for Fe-Co Alloys,” *Phys. Rev.*  
5275 **184**, 490 (1969).
- 5276 [332] J. Crangle and G. M. Goodman, “The Magnetization of Pure Iron and Nickel,” Proceedings  
5277 of the Royal Society of London, Series A, **321**, 477 (1971).
- 5278 [333] C. D. Graham, Jr., “Iron and Nickel as Magnetization Standards,” *J. Appl. Phys.* **53**, 2032  
5279 (1982).
- 5280 [334] G. G. Scott, “Review of gyromagnetic ratio experiments,” *Rev. Mod. Phys.*, vol. 34, pp. 102–  
5281 109, Jan 1962.
- 5282 [335] E. C. Stoner and E. P. Wohlfarth, “A Mechanism of Magnetic Hysteresis in Heterogeneous  
5283 Alloys,” *Phil. Trans. Royal Soc. London, Series A* **240**, 599 (1948).
- 5284 [336] L. G. Levchuk, “The Intraatomic motion of bound electrons as a possible source of a system-  
5285 atic error in electron beam polarization measurements by means of a Møller polarimeter,” *Nucl.*  
5286 *Instrum. Meth.*, vol. A345, pp. 496–499, 1994.
- 5287 [337] M. Swartz, H. R. Band, F. J. Decker, P. Emma, M. J. Fero, R. Frey, R. King and A. Lath *et*  
5288 *al.*, “Observation of target electron momentum effects in single arm Møller polarimetry,” *Nucl.*  
5289 *Instrum. Meth. A* **363**, 526 (1995) [hep-ex/9412006].
- 5290 [338] D. Gaskell, D. G. Meekins, and C. Yan, “New methods for precision Møller polarimetry,”  
5291 *Eur. Phys. J.*, vol. A32, pp. 561–564, 2007.
- 5292 [339] E. Chudakov and V. Luppov, “Møller polarimetry with atomic hydrogen targets,” tech. rep.,  
5293 JLab, 2005. [http://www.jlab.org/~gen/hyd/loi\\_3.pdf](http://www.jlab.org/~gen/hyd/loi_3.pdf).
- 5294 [340] I. F. Silvera, “Ultimate fate of a gas of atomic hydrogen in a liquid-helium chamber: Recom-  
5295 bination and burial,” *Phys. Rev. B*, vol. 29, pp. 3899–3904, Apr 1984.
- 5296 [341] I. F. Silvera and J. T. M. Walraven, “Stabilization of atomic hydrogen at low temperature,”  
5297 *Phys. Rev. Lett.*, vol. 44, pp. 164–168, Jan 1980.
- 5298 [342] I. F. Silvera and J. T. M. Walraven, “Spin polarized atomic hydrogen,” *Progress in Low*  
5299 *Temperature Physics*, vol. X, pp. 139–370, 1986.
- 5300 [343] T. Roser *et al.*, “Microwave driven extraction of stabilized spin polarized atomic hydrogen,”  
5301 *Nucl. Instrum. Meth.*, vol. A301, pp. 42–46, 1991.
- 5302 [344] M. Mertig, V. G. Luppov, T. Roser, and B. Vuaridel, “Continuous density measurement of  
5303 atomic hydrogen by means of a bolometer,” *Rev. Sci. Instrum.*, vol. 62, pp. 251–252, 1991.
- 5304 [345] M. D. Miller and L. H. Nosanow, “Possible ”new” quantum systems. ii. properties of the  
5305 isotopes of spin-aligned hydrogen,” *Phys. Rev. B*, vol. 15, pp. 4376–4385, May 1977.
- 5306 [346] M. Poelker, J. Grames, J. Hansknecht, R. Kazimi, J. Musson, *Phys. Rev. ST Accel. Beams*  
5307 **10**, 053502 (2007).



5308 [347] [https://hallaweb.jlab.org/12GeV/SoLID/download/doc/Estimated\\_](https://hallaweb.jlab.org/12GeV/SoLID/download/doc/Estimated_)  
5309 [SoLID\\_Offline\\_Effort-v4.ods](https://hallaweb.jlab.org/12GeV/SoLID/download/doc/Estimated_SoLID_Offline_Effort-v4.ods)

5310 [348] [https://halldsvn.jlab.org/repos/trunk/docs/offline/](https://halldsvn.jlab.org/repos/trunk/docs/offline/ProjectProgress/OfflineComputingActivities2013.xlsx)  
5311 [ProjectProgress/OfflineComputingActivities2013.xlsx](https://halldsvn.jlab.org/repos/trunk/docs/offline/ProjectProgress/OfflineComputingActivities2013.xlsx)

5312 [349] EventDisplay3D project in the *art* workbook, available from [https://cdcvs.](https://cdcvs.fnal.gov/redmine/projects/art-workbook)  
5313 [fnal.gov/redmine/projects/art-workbook](https://cdcvs.fnal.gov/redmine/projects/art-workbook)

## 5315 **Appendix A Summary of Recommendations from the 2015 SoLID Di-** 5316 **rector’s Review and the Responses**

5317 The SoLID Director’s Review was held at JLab on 23-24 February 2015. The committee con-  
 5318 sisted of: Paul Brindza (JLab), Marcel Demarteau (ANL), Nancy Grossman (ANL), David Mack  
 5319 (JLab), Richard Majka (Yale), Naomi Makins (UIUC), Curtis Meyer (CMU)(chair), Ernest Sicht-  
 5320 mann (LBL), William Wisniewski (SLAC) and Bolek Wyslouch (MIT).

5321 A summary of all recommendations made by the committee is provided below, with each rec-  
 5322 ommendation ordered by number to improve readability. [We also note briefly below each recom-](#)  
 5323 [mendation what has been done.”](#)

### 5324 **A.1 On the physics relevance and risks**

#### 5325 **On the completeness and credibility of the discussion of the experimental reach, including** 5326 **statistical, systematic and theoretical uncertainties**

5327 **Recommendation 1: End-to-end simulations with realistic subsystem responses and mate-**  
 5328 **rial budgets, and complete track finding and reconstruction should be developed.**

5329 The simulations of all SoLID subsystems are unified in the GEANT4 based simulation frame-  
 5330 work, GEMC, with realistic setup and simple responses for all detectors. Digitization for GEM and  
 5331 tracking with field effects are conducted after simulation.

5332 **Recommendation 2: Acceptances, efficiencies, and systematic uncertainties should be sim-**  
 5333 **ulated for each of the core measurements.**

5334 Acceptances, efficiencies, and systematic uncertainties for each of the core measurements have  
 5335 been performed with the aforementioned simulation.

5336 **Recommendation 3: For the PVDIS measurements, the viability of the elastic scattering**  
 5337 **calibration procedure, to determine absolute  $Q^2$  should be demonstrated by simulations for**  
 5338 **similar scattering angles to those probed in DIS, and with realistic misalignments.**

5339 A study was performed with simulation which demonstrated that absolute  $Q^2$  can be determined  
 5340 to the required precision with elastic scattering calibration assuming realistic misalignments.

5341 **Recommendation 4: Bin migration effects should be simulated for the measurements of**  
 5342 **the sharply rising  $J/\psi$  production cross section near threshold.**

5343 Bin migration effects were simulated combining radiative effects and track resolution.

#### 5344 **On the ability to handle the desired luminosities and backgrounds including impacts on both** 5345 **the apparatus and the beam line downstream of the target**

5346 **Recommendation 5: The signal and background trigger rates should be simulated for the**  
 5347  **$J/\psi$  measurements.**

5348 We have performed a simulation for both signal and background trigger rates for  $J/\psi$  using the  
 5349 full SoLID simulation similar to what we did for PVDIS and SIDIS.

5350 **Recommendation 6: The dead-time(s) in the DAQ chain should be modeled.**

5351 We have continued to develop the deadtime analysis in the context of experimental impact and  
 5352 verification is ongoing based on experience with the hardware modules.

5353 **Recommendation 7: The development of a simulation framework with realistic recon-**  
 5354 **struction and analysis should be pursued with high priority and increased resources.**

5355 The development of a full simulation package with realistic reconstruction and analysis has  
 5356 continued to be a high priority and focus for the collaboration. We have been progressing to develop

5357 a full end-to-end simulation of all SoLID experiments and have been soliciting increased resources  
5358 to fully realize this.

5359 **On the implications for the relevance of the physics results in the context of possibly competing**  
5360 **experiments at both Jefferson Lab and internationally.**

5361 **Recommendation 8: Better comparisons with the expected results on programs such as**  
5362 **SBS and particularly CLAS12 are needed to clarify the need for the SoLID SIDIS program.**  
5363 **Crisp demonstrations of the improvements possible with SoLID should be developed.**

5364 With the help of theory group, a new method was developed to properly evaluate the impact of  
5365 future SIDIS measurements on TMDs. Comparisons of SoLID projections with SBS and CLAS12  
5366 were performed, which demonstrated significant improvement of SoLID over SBS and CLAS12.

5367 **Recommendation 9: The SoLID Collaboration should investigate the possibility of kaon**  
5368 **identification, especially given their high luminosity.**

5369 We have explored different options for kaon identification, and are pursuing the path of upgrad-  
5370 ing the MRPC time of flight to reach resolution of 20ps. R&D on the MRPC upgrade is underway.

5371 **Recommendation 10: The SoLID collaboration should investigate the feasibility of carry-**  
5372 **ing out a competitive GPD program. Such a program would seem particularly well suited to**  
5373 **their open geometry and high luminosity. If SoLID's luminosity is sufficiently high to permit**  
5374 **a program of precise Double Deeply Virtual Compton Scattering (DDVCS) measurements, it**  
5375 **would make a groundbreaking contribution to GPD studies.**

5376 A GPD program has been initiated, including an approved timelike Compton scattering pro-  
5377 posal, an approved deep exclusive meson production proposal, a letter of intent for DDVCS, and a  
5378 polarized DVCS measurement under study.

## 5379 **A.2 On the viability of approach and the experimental technique**

5380 **On any R&D required to meet the technical challenges of the experiment**

5381 **Recommendation 11: Develop an overall R&D plan for the project with a timeline.**

5382 We have developed a pre-R&D plan which was submitted to the DOE medium energy nuclear  
5383 physics program manager in Summer 2016, which received feedback with encouragement. The full  
5384 R&D plan and project timeline is under development.

5385 **Recommendation 12: Close interaction between the US and Chinese groups in the devel-**  
5386 **opment of GEM foils to assure good quality control is highly recommended.**

5387 We have continued to work closely with the Chinese groups for GEM foil production through  
5388 regular meetings and discussions, as well as hosting visiting Chinese researchers at the UVA GEM  
5389 laboratory. Plans have been developed to ensure produced GEM quality at multiple levels including  
5390 by sample inspection by the UVA and Temple groups.

5391 **Recommendation 13: Investigate the schedule risk when GEM foils are not produced in a**  
5392 **timely way and continue to pursue Tech-Etch as a potential supplier for the foils.**

5393 We have contacted Tech-Etch as a potential backup option and they have indicated they would  
5394 be able to commit the resources to produce a large order of GEMs in such an event. The CERN  
5395 workshop also presents an option with the capability to be able to fulfill a large order of necessary  
5396 GEMs.

5397 **Recommendation 14: The calorimeter group is encouraged to contact other groups (AL-**  
5398 **ICE, LHCb SiPMs and possibly CMS) to understand the detector design choices these groups**  
5399 **have made and resources needed for construction.**

5400 Beyond the initial LHCb contact at the beginning of R&D, the calorimeter group has been  
5401 in contact with the University of Iowa CMS group and Central China Normal University group  
5402 which assembled modules for the ALICE experiment. We have also acquired relevant technical  
5403 documents from LHCb and other CERN experiments which have been beneficial in detailing design  
5404 choices. The design was refined, prototyping modules were constructed by two newly joined groups  
5405 (Shandong University and Tsinghua University from China) and cosmic and beam tests are on-  
5406 going.

5407 **Recommendation 15: The stability tests of the conductivity of the glass for the MRPCs**  
5408 **should be extended for a much longer period and the risk associated with the R&D needs to**  
5409 **be identified.**

5410 Conductivities of the glass were tested for extended period with large radiation dose of neutron  
5411 and xray, showed no aging or stability issues.

5412 **Recommendation 16: The collaboration is strongly encouraged to develop an end-to-end**  
5413 **realistic simulation and reconstruction to further optimize cost and physics reach and derive**  
5414 **clear performance requirements for the individual subdetectors.**

5415 All subsystems simulations have been unified into the same simulation framework with simple  
5416 reconstruction. We have continued to iterate the designs within the simulation, especially as more  
5417 engineering resources have become available. For example, studies evolving the detector layouts  
5418 are being performed as internal mounting and field constraint specifications are developed.

5419 **Recommendation 17: The collaboration is encouraged to explore the power of extended**  
5420 **kaon identification (through Cherenkov or TOF).**

5421 The collaboration has identified that the MRPC time of flight option for kaon identification will  
5422 be the most promising approach. We have initiated R&D on the 20ps MRPC upgrade. (Section  
5423 [2.5.2](#) and [11.8](#)).

5424 **On the proposed magnet concept and choice, including magnet configuration modifications (if**  
5425 **any), magnet cool-down and infrastructure requirements**

5426 **Recommendation 18: The Committee strongly recommends testing the CLEO magnet**  
5427 **coils (cold test), power supply and controls, before installation in Hall A.**

5428 A cold test is planned at reduced operating parameters by Jefferson Lab engineering which will  
5429 be carried out prior to installation in Hall A.

5430 **Recommendation 19: A new magnet power supply should be included in the total cost of**  
5431 **SoLID.**

5432 The collaboration is planning for a new power supply for the solenoid and has now included the  
5433 cost in the budget.

5434 **Recommendation 20: Evaluate the schedule impact of mapping the magnetic field in situ**  
5435 **in Hall A.**

5436 Field mapping and analysis has been estimated by Jefferson Lab engineering and estimates of  
5437 necessary workforce and cost have also been evaluated and included.

5438 **On the proposed detector concept and associated electronics and data acquisition**

5439 **Recommendation 21: The plans for the High Level Trigger and the needs for slow control**  
5440 **need to be worked out in detail and the implications for resources need to be evaluated.**

5441 Development of the hardware trigger in particular for the complicated SIDIS trigger has contin-  
5442 ued and further details are included.

5443 Slow controls have now been integrated into the experiment design and budget and a responsible  
5444 subsystem coordinator has been assigned.

5445 **Recommendation 22: The implications of the need for these resources in the context of**  
5446 **availability of resources at the laboratory need to be understood.**

5447 Consideration of further details of lab resources are presented in Section 14 and Appendix C.  
5448 The collaboration has been in active communication with the JLab computing center about the needs  
5449 for SoLID including data volumes and analysis.

5450 **Recommendation 23: Closer communication with the other JLab experiments and the**  
5451 **JLab computing center is strongly encouraged.**

5452 We have closer communication with other JLab groups and the computing center. Software and  
5453 computing resource needs have been further evaluated, especially related to larger JLab 12 GeV  
5454 projects.

5455 **Recommendation 24: Having a functional simulation and reconstruction routines as soon**  
5456 **as possible should be a high priority in the software effort. Such software will pay off many**  
5457 **times over in experimental design and avoiding pitfalls.**

5458 Development of the simulation and using that to develop and test reconstruction algorithms has  
5459 been a high priority of the collaboration. We have had postdocs and students dedicated to these  
5460 efforts and have been requesting further resources to meet short term goals.

5461 **On the beam line design, including collimation and shielding**

5462 **Recommendation 25: Complete radiation calculations to determine activation and ab-**  
5463 **sorbed dose on components of concern and mitigate as appropriate.**

5464 We have completed initial radiation calculations for all the experiments in Geant4 as well neu-  
5465 tron dose and activation studies in FLUKA. These continue to be iterated as design details become  
5466 available.

5467 **Recommendation 26: It should be confirmed that the baffle design, including the sup-**  
5468 **port structure, is optimized for background rejection and signal acceptance. Furthermore the**  
5469 **baffle design should minimize generation of secondary backgrounds.**

5470 Optimization studies and baffle refinement have been completed with material, acceptance,  
5471 background, and secondary production in the figure of merit. Detailed evaluation of baffle sup-  
5472 ports are ongoing with engineering.

5473 **On the cryogenic and polarized target system concepts and integration**

5474 No recommendation was presented in the report.

5475 **On the beam polarimetry requirements.**

5476 No recommendation was presented in the report.

5477 **A.3 On the understanding, completeness, and credibility of the resources needed for**  
5478 **the SoLID project.**

5479 **On the experience, expertise and quantity of the scientific and technical manpower for the**  
5480 **project**

5481 **Recommendation 27: Compare the resource levels you have assumed in some key areas**  
5482 **(particularly in software, data acquisition and project management) to make sure the esti-**  
5483 **mates align with other similar projects or there is a good reason they do not.**

5484 Further details in required software resources based on other large scale experiments at Jefferson  
5485 Lab and outside of the lab have been considered. Communicating with JLab fast electronics, DAQ  
5486 and IT groups to have a better estimation of resource level for DAQ. (Section 14 and Appendix C).

5487 **Recommendation 28: Redo the cost estimate using an average cost per type of resource.**

5488 A new full cost estimate is anticipated to be performed after a DOE science review.

5489 **Recommendation 29: Create a high level resource loaded schedule to get a more realistic**  
5490 **schedule, funding and resource profile. This will also allow JLab to better determine their**  
5491 **ability to support the FTE needs.**

5492 A high level resource loaded schedule is anticipated to be performed after a DOE science review.

5493 **Recommendation 30: Revisit the comments of the 2012 Internal Review Report in con-**  
5494 **junction with the recommendations from this report.**

5495 We revisited those comments and they are addressed in multiple sections of this document.

5496 **On utilities (power, cabling, LCW, cryogenics) requirements for the project**

5497 **Recommendation 31: A cost benefit analysis for any systems being reused should be car-**  
5498 **ried out, including the magnet power supply.**

5499 A cost-benefit analysis was performed and the only reused components will be the iron yoke  
5500 and cryostat. Cost for a new power supply, controls, transfer lines, and supports have been included  
5501 in the budget. (Section 4.4).

5502 **Recommendation 32: Appoint a small team to facilitate the integration planning for SoLID.**

5503 Integration has been a consideration in the development of the subsystems. A full team will be  
5504 assigned after a DOE science review.

5505 **On requirements from Jefferson Lab on for instance engineering needs, electron beam, polar-**  
5506 **ized source, and cryogenic target requirements**

5507 **Recommendation 33: We strongly recommend tests at JLab of the CLEOII magnet coils**  
5508 **(cold test), ideally with the new power supply and controls, before installation into the hall.**

5509 A cold test is planned at reduced operating parameters by Jefferson Lab engineering which will  
5510 be carried out prior to installation in Hall A.

5511 **Recommendation 34: An effort should be made to clearly specify resources required from**  
5512 **JLab that are not explicitly in the project (effort, non-effort, equipment, building space, etc.).**

5513 Many of these resources have been identified and it is an ongoing process within the collabora-  
5514 tion.

5515 **On general experiment installation and alignment issues, including potential interaction with**  
5516 **other Hall A programs and operations**

5517 **Recommendation 35: The project should develop a preliminary resource loaded schedule**  
5518 **for the installation and the corresponding space-management plan for the hall floor.**

5519 A preliminary plan has been outlined for installation of the magnet and major subsystems.

5520 **Recommendation 36: The project should start planning the process of how to change from**  
5521 **one SoLID configuration to another in order to better understand the time and effort involved**  
5522 **and if there are any potential issues such as radiation levels.**

5523 Based on the initial radiation studies, a preliminary plan is made and details will continue to be  
5524 refined.

## 5525 **Appendix B Summary of Subsystems**

5526 In responding to the recommendations from JLab physics division, we add this section, aiming to  
5527 provide a brief description of the key assumptions for each subsystem, namely where the subsystem  
5528 will be built, which groups will build it, where the fund comes from, how long it will take and what  
5529 is needed from JLab to support it. Anything unique to the system which drives the project will also  
5530 be listed.

### 5531 **B.1 Magnet**

5532 The solenoid magnet provides the magnetic field required for measuring the momentum of the track  
5533 in the experiment. The detectors for SoLID will be mounted on the magnet yoke. The collaboration  
5534 has identified the CLEO-II magnet as the one to be used for SoLID after modifications. The JLab  
5535 Hall A engineering team, with assistance from JLab Engineering Division and also from the SoLID  
5536 collaboration, is responsible for the transportation and modification of the magnet.

5537 The coils and cryostat of the magnet have arrived at JLab and the exterior steel is being shipped.  
5538 The transportation (disassembling and shipping) the magnet from Cornell to JLab and initial refurbishing  
5539 to verify the magnet is in good state for specific modifications for physics experiments is  
5540 covered from the JLab Physics Division (operation fund). The cost for refurbishing and modifica-  
5541 tions specific to SoLID is to be part of the SoLID MIE to DOE.

5542 The refurbishing and modification specific to SoLID will take 2.5 years. JLab will perform most  
5543 of the work. Space will be needed at JLab for refurbishing, modification and storage. We will also  
5544 need JLab support for the cryogenic and control systems.

### 5545 **B.2 GEM**

5546 • **Where the system will be built and who will build it:** It is assumed that the SoLID GEM  
5547 tracker will be built in China by the five member institutions of the Chinese SoLID GEM  
5548 collaboration: CIAE, LZU, THU,USTC and IMP. The GEM module development, design  
5549 prototyping and benchmarking would be done in collaboration with the GEM detector groups  
5550 at the University of Virginia (Liyanage) and Temple University (Sarrow). The GEM module  
5551 and Electronics fabrication activities would be divided among the Chinese collaboration as  
5552 follows:

5553 – USTC: The main institution for GEM module fabrication, readout electronics develop-  
5554 ment and fabrication.

5555 – CIAE: GEM foil fabrication and GEM module fabrication.

5556 – LZU: GEM module fabrication

5557 – THU and IMP: GEM module fabrication and testing.

5558 • **Who will fund it ?**

5559 The funding for the SoLID GEM tracker will be sought from the Chinese funding agencies.  
5560 Only the pre R&D funds and R&D funds (of the order of \$ 400 k) for the activities conducted  
5561 at the University of Virginia and Temple University will be requested from the US DoE.

5562 • **How long will it take ?**

5563 The pre-R&D phase of the project would take at least 2 years. This would be especially true  
5564 if the GEM foils fabricated in China are to be used for the project as assumed. A well focused

5565 and intense pre-R&D program in China is required to ensure that the manufacturing capabil-  
5566 ities and capacities for full size GEM foils, and that GEM module assembly facilities setup  
5567 and several full size prototype module constructed and tested at each of the five institutions.

5568 After the successful conclusion of the pre-R&D program, it would take at least two more  
5569 years for the R&D, construction, testing, installation and the commissioning phase.

5570 • **what is needed from JLab to support it ?**

5571 Jlab engineering support will be needed for the design of the GEM module mounting struc-  
5572 ture, and DAQ support will be needed to integrate the GEM readout into the hall A DAQ  
5573 framework.

5574 **B.3 Light Gas Cherenkov**

5575 The light gas Cherenkov prototyping and construction will be done by the Temple University Nu-  
5576 clear Physics Group. All of the construction will be done at Temple, with the possible exception of  
5577 any specific materials needed to adapt and integrate the subsystem into the larger SoLID detector.  
5578 Funds for the project will be requested by the group from DOE and/or NSF. The light gas Cherenkov  
5579 detector will also be designed at Temple University with the expectation that communication with  
5580 the SoLID project engineers at Jefferson Lab, as well as access to schematics and documentation,  
5581 will be made available concerning interfacing the sub-detector design with the larger SoLID design.

5582 **B.4 Heavy Gas Cherenkov**

5583 The Heavy Gas Cherenkov (HGC) will provide the required particle identification of pions in a  
5584 background of kaons and protons. It will be built by Prof. Haiyan Gao's Medium Energy Physics  
5585 group from Duke University with engineering and technical help from the Triangle Universities  
5586 Nuclear Laboratory (TUNL), and by Prof. Garth Huber's group from the University of Regina in  
5587 Canada.

5588 **B.5 Electromagnetic Calorimeter and Scintillator-Pad Detector**

5589 The Electromagnetic Calorimeter (EC), in combination with other detectors, provides the main  
5590 trigger and the particle identification for the SoLID experiments. The EC consists of a Preshower  
5591 and a Shower portion. The technologies that we chose for the EC – WLS-fiber-embedded scintillator  
5592 for the Preshower with MAPMT readout and the Shashlyk-type modules for the Shower with regular  
5593 PMT readout – have both been used in experiments at the LHC. The main goal of the pre-R&D is  
5594 thus to adopt such technology and to optimize the design configuration of the EC to meet the physics  
5595 requirement of SoLID, and to determine the best construction institution/site.

5596 The Scintillator Pad Detector (SPD) is needed only by the SIDIS program of SoLID. It consists  
5597 of a forward- (FA) and a large-angle (LA) parts. Both FASPD and LASPD will serve as a photon  
5598 veto in order to reduce the photon background to a manageable level. Design of the FASPD is  
5599 very similar to the Preshower detector of the EC, with WLS fibers embedded in thin scintillators.  
5600 The LASPD will also provide time-of-flight information and a 150-ps timing resolution is required.  
5601 The LASPD will thus consists of thick scintillators with direct readout by field-resistant fine-mesh  
5602 PMTs inside the solenoid.

5603 The pre-R&D stage of EC and SPD will likely take up to two years. The lead institutions on  
5604 the EC includes University of Virginia (UVa), and the Chinese Shandong University (SDU) and Ts-  
5605 inghua University (THU). The SDU group has extensive experience with scintillator manufacturing



5606 in China, and have produced preshower modules with similar light yield as those produced by the  
5607 Russian IHEP (the sole manufacturer of EC for nearly all LHC experiments). For Shashlyk mod-  
5608 ules, both THU and SDU groups have already constructed prototypes and are currently working on  
5609 improving their light yield. The pre-R&D will focus on increasing the light yield, conducting beam  
5610 tests to determine their PID performance, and to design an effective mass-quantity construction  
5611 method.

5612 The SPD will be manufactured by the US Eljen company and further constructed at UVa. Pro-  
5613 totype modules have already been made and tested with cosmic rays and their light yield has been  
5614 characterized. The pre-R&D goal will be to determine the light yield uniformity for the FASPD,  
5615 and to determine the timing resolution of the LASPD under SoLID-like running conditions.

## 5616 **B.6 MRPC**

5617 The Multi Gap Resistive Plate Chamber (MRPC) will be used by the SIDIS experiment for parti-  
5618 cle identification by means of time of flight. A MRPC can achieve a timing resolution of 50 ps.  
5619 Under more realistic conditions with large background rates, timing resolution of 80 ps has been  
5620 demonstrated.

- 5621 • Who will build it :  
5622 Tsinghua University
- 5623 • Where the system will be built:  
5624 In Tsinghua University, Beijing
- 5625 • Rutgers university will take care of the readout electronics.
- 5626 • Who will fund it :  
5627 NSFC (China) for the detector; the front end electronics will be funded by the DOE, and also  
5628 the NSF through Rutgers University.
- 5629 • How long will it take :  
5630 Two and half years
- 5631 • What is needed from JLab to support it:  
5632 Beam tests will be needed at JLab including electronics and DAQ system in order to test the  
5633 detector and optimize it under realistic beam conditions. Since it is planned to include the  
5634 MRPC in the trigger to reduce the background, a special board from JLab will be required to  
5635 send the logic signals to the L1 trigger.
- 5636 • Anything unique to that system that's a project driver : This is the first high rate TOF system  
5637 in hadron physics experiments and is need for the particle identification.

## 5638 **B.7 DAQ**

5639 The SoLID experiment is a large acceptance detector designed to run at high luminosities. The  
5640 trigger rates expected for PVDIS are of the order of 600 KHz and for SIDIS up to 100 KHz. This  
5641 pipelined electronics is crucial to generate a selective trigger in the very large background present  
5642 in the detector.

- 5643 • Where the system will be built and who will build :  
5644 The Rutgers University with the group of Prof. Ronald Gilman group will be in charge of  
5645 the high resolution timing measurement aspects of the development and production for the  
5646 electronics and help in the testing of the Flash ADCs similar to what was done for Hall D.
  
- 5647 • Who will fund it ?  
5648 The electronics will be funded by the DOE request.
  
- 5649 • How long it will take  
5650 The project will take 2 years of preRD, 4 years of R%D, production and testing, and installa-  
5651 tion.
  
- 5652 • What is needed from JLAB to support it  
5653 Since SoLID will be using the Jefferson Laboratory Pipelined Electronics, the JLAB Fast  
5654 electronics group will be largely involved in the development, tests and deployment of the  
5655 electronics. An estimate of the electronics and DAQ group is summarized in the table in  
5656 addition of the JLab physics staff person.

## 5657 **Appendix C Software Development Effort Estimate**

5658 The software development effort for SoLID is considered a dependency and will be funded ex-  
5659 ternally from the project largely through contributions from collaborating institutions. However,  
5660 simulations to the extent that they are necessary to inform the design of hardware components are  
5661 included in the project cost. In the following, we present an estimate of the overall effort expected  
5662 to be spent on developing all SoLID software for reference. Section C.3 discusses the simulation  
5663 component included in the project.

### 5664 **C.1 Effort Estimate**

5665 A preliminary assessment of the effort required to carry out all SoLID offline computing-related  
5666 tasks, assuming adoption of the *art* framework [249] as an example, yields approximately 570 FTE-  
5667 weeks. With contingency and overhead, explained below, this number increases to a total of 950  
5668 FTE-weeks, or about 22 FTE-years, assuming 44 work weeks per year per developer. A spreadsheet  
5669 with this calculation can be found online [347].

5670 This estimate covers simulations, reconstruction, calibrations and alignment, data challenges,  
5671 production and analysis, where “analysis” represents a baseline set of replay configurations (PVDIS,  
5672 SIDIS-<sup>3</sup>He, SIDIS-*p*, *J/ψ*), data quality checks, plots, production output variables, corrections,  
5673 cuts and histograms. Not included in the estimate are DAQ software (firmware, front-end and  
5674 trigger programming, run control etc.), online analysis and monitoring, and the intellectual effort to  
5675 understand and interpret the results of the simulations and experimental data analysis. The latter is  
5676 excluded because it is largely an open-ended creative process.

5677 For each covered area, we have counted the work required to develop the actual software, test  
5678 the code and validate results, coordinate efforts (meetings, wikis and similar), write and generate  
5679 user and developer-level documentation, and to configure and monitor offline computing operations  
5680 (simulation and production passes, data challenges). The time estimates at this point are subjective  
5681 best guesses, based on our experience with similar efforts. They assume expert developers who are  
5682 fully familiar with all task requirements, programming languages, framework paradigms, library  
5683 APIs, tools etc. This yields a sum of 570 FTE-weeks. A contingency of 25% is added to this total  
5684 to account for missed tasks, time overruns, etc. Furthermore, since developers are never the ideal  
5685 experts assumed above, we estimated an average “developer efficiency” of 75%, *i.e.* on average  
5686 each developer is assumed to spend an extra 1/3 of the estimated task time on preparations such as  
5687 collecting requirements and learning. A more precise estimate of this efficiency factor would have  
5688 to be made on a task-by-task basis under consideration of the personnel assigned to the task, infor-  
5689 mation which is incomplete at this time. With contingency and overhead, the total effort estimate is  
5690 950 FTE-weeks.

### 5691 **C.2 Comparison with GlueX**

5692 In comparison to a similar project, GlueX have estimated their offline computing effort at 1866  
5693 FTE-weeks [348]. (This number excludes 110 FTE-weeks that GlueX allocate for “online” tasks  
5694 (beamline commissioning and monitoring), which is outside of our scope.) It is unclear if the GlueX  
5695 numbers include developer overhead, *i.e.* the time spent on task preparations and learning discussed  
5696 above, but given the generous allowances made generally, we assume that they do.

5697 The offline computing manpower requirements estimated by GlueX and SoLID are summarized  
5698 in Table 36. To make the GlueX estimates comparable to ours, we combined certain line items of  
5699 the GlueX offline computing effort document [348] as follows:

- 5700 • The quoted “Simulation” effort includes “Geant3 simulation”, “Geant4 simulation” plus 1/4  
5701 of “Integration/QC” and “Coordination” (total of 16.5 FTE-weeks) from the Miscellaneous  
5702 section.
- 5703 • “Reconstruction” counts all of “Reconstruction” plus “DAQ Translation”, “Event Viewer”,  
5704 “Documentation”, “Integration of Slow Controls”, 1/2 of “Recon/analysis code Q/A” and  
5705 again 16.5 FTE-weeks for integration and coordination.
- 5706 • “Calibration” is taken as the total of “Calibrations” plus 1/4 of “Integration/QC” (11 FTE-  
5707 weeks).
- 5708 • “Production” comprises “DST Generation”, “MC Studies for Detector Optimization” and  
5709 again 11 FTE-weeks of “Integration/QC”.
- 5710 • “Analysis” takes all of “Analysis” less 1/2 of “Recon/analysis code Q/A” already counted  
5711 under “Reconstruction” plus 1/2 of “Coordination”.
- 5712 • The “Data Challenges” estimate is taken as is.

5713 These allocations make the top-level categories approximately comparable.

Task Group	Labor estimate (FTE-weeks)		Main reasons for difference (see text)
	GlueX [348]	SoLID [347]	
Simulation	192	240	Simulation to be integrated into frame- work.
Reconstruction	787	335	Adoption of existing framework. Re-use of algorithms. Smaller number of subsys- tems.
Calibration	275	103	Smaller number of subsystems.
Production	275	155	Standard data format. Re-use of workflow tools.
Analysis	275	94	No PWA analysis and no grid implemen- tation of analysis.
Data Challenges	62	23	No PWA data challenge.
Totals	1866	950	

Table 36: Offline computing manpower requirements estimated by SoLID and GlueX

5714 SoLID estimates a larger simulation effort than GlueX, possibly because GlueX make approxi-  
5715 mate estimates of time already spent on finished work, while SoLID is using a detailed breakdown  
5716 of anticipated future tasks. Also, SoLID plans to integrate simulations into the overall software  
5717 framework, while GlueX’s simulations are standalone.

5718 The estimated SoLID effort for reconstruction is significantly lower than GlueX’s. The differ-  
5719 ence is to a great extent due to the fact that SoLID proposes to adopt an existing framework rather  
5720 than write a new one and that SoLID anticipates to reuse well-tested existing algorithms for stan-  
5721 dard tasks such as track fitting, *e.g.* from the `genfit` library, and calorimeter cluster reconstruction.

5722 Documentation effort is reduced in SoLID's case also due to the already very good user-level doc-  
5723 umentation of the proposed *art* framework. Furthermore, the difference can be attributed to the  
5724 smaller number of detector subsystems in SoLID than in GlueX, 5 vs. 7, the lower complexity  
5725 of these systems (one vs. two tracker systems, Cherenkovs vs. multiple calorimeter systems), and  
5726 the more challenging multi-particle final state reconstruction and PID in GlueX. Lastly, a SoLID  
5727 event viewer can be readily assembled from an existing MC geometry with minimal effort (days vs.  
5728 months) using ROOT's `TEve` framework within *art*, as demonstrated by *art* example code [349].

5729 Calibration effort for SoLID is also estimated lower than in GlueX, again in part due to fewer  
5730 main detector systems, smaller channel counts and easier calibration of SoLID's GEMs vs. GlueX's  
5731 drift chambers.

5732 The lower estimated time for Production (DST generation) is attributable to the fact that we do  
5733 not anticipate spending time on developing and maintaining a custom file format (it is defined by  
5734 *art*) and expect to be able to reuse the job control and workflow tools currently under development  
5735 for GlueX and CLAS12.

5736 Finally, SoLID estimates much lower analysis effort than GlueX because no kinematic fitting  
5737 and PWA analysis is foreseen for SoLID nor is SoLID planning a grid implementation at this point  
5738 as the JLab compute farm resources are expected to be sufficient for us. For similar reasons, our  
5739 estimate for data challenges is lower.

### 5740 **C.3 Simulations Required for Project Goals**

5741 Selecting from the detailed task list provided in [347] only those software-related tasks with direct  
5742 bearing on hardware design (detectors, shielding, DAQ and trigger, etc.), we arrive at a base effort  
5743 of 68 FTE-weeks to carry out design-relevant simulation work. Adding contingency and developer  
5744 efficiency, described above, this yields an estimated realistic effort of 113 FTE-weeks. Ideally,  
5745 this effort would be spent early in the project's lifetime, say during the first two years, since it is  
5746 intended to guide later R&D. Hence, 57 FTE-weeks/year can be expected to be spent in the first two  
5747 years. Assuming effectively 44 work weeks per year, the project thus requires 1.3 FTE to work on  
5748 design-related simulations for two years. This number enters Table 181 and Section ??.

5749 **Appendix D Cost Estimations 2018**

5750 **D.1 Summary of SoLID overall cost estimation 2018**

5751 This is outdated. It's currently being edited somewhere else and will be merged back into here once  
5752 finished. Zhiwen

**SoLID Cost Estimate  
Costs are in FY18\$K**

FY18 \$k (Direct)	Yr 1	Yr 2	Yr 3	Yr 4	Yr 5	Total	Contribute	Request
<b>Ecal</b>	1,401.4	2,048.5	2,053.5	2,058.5	1,184.9	8,746.8	1,817.4	6,929.4
Labor \$	402.5	402.5	402.5	402.5	517.5	2,127.5	1,150.0	977.5
Proc \$	998.9	1,646.0	1,651.0	1,656.0	667.4	6,619.3	667.4	5,951.9
FTEs	3.5	3.5	3.5	3.5	4.5	18.5	10.0	8.5
Jlab	1.5	1.5	1.5	1.5	2.5	8.5	-	8.5
Other	2.0	2.0	2.0	2.0	2.0	10.0	10.0	-
University	0.5	0.5	0.5	0.5	0.5	2.5	-	-
<b>e Cherenkov</b>	987.0	1,344.0	1,270.5	376.5		3,978.0	-	3,978.0
Labor \$	345.0	345.0	345.0	345.0		1,380.0	-	1,380.0
Proc \$	642.0	999.0	925.5	31.5		2,598.0	-	2,598.0
FTEs	3.0	3.0	3.0	3.0		12.0	-	12.0
Jlab	3.0	3.0	3.0	3.0		12.0	-	12.0
Other						-	-	-
University	0.2	0.2	0.7	0.7		1.8	-	-
<b>h Cherenkov</b>	1,195.5	1,195.5	1,195.5	1,050.5	195.5	4,832.5	-	4,832.5
Labor \$	195.5	195.5	195.5	195.5	195.5	977.5	-	977.5
Proc \$	1,000.0	1,000.0	1,000.0	855.0		3,855.0	-	3,855.0
FTEs	1.7	1.7	1.7	1.7	1.7	8.5	-	8.5
Jlab	1.7	1.7	1.7	1.7	1.7	8.5	-	8.5
Other						-	-	-
University	0.3	0.3	0.3	0.3	0.3	1.5	-	-
<b>GEM-US</b>	1,773.5	1,712.5	912.5	857.5		5,256.0	-	5,256.0
Labor \$	632.5	632.5	632.5	632.5		2,530.0	-	2,530.0
Proc \$	1,141.0	1,080.0	280.0	225.0		2,726.0	-	2,726.0
FTEs	5.5	5.5	5.5	5.5	-	22.0	-	22.0
Jlab	5.5	5.5	5.5	5.5		22.0	-	22.0
Other	-	-	-	-		-	-	-
University	0.2	0.2	0.2	0.2	0.2	1.0	-	-
<b>GEM-China</b>	369.0	350.0	385.0	385.0		1,489.0	1,489.0	-
Labor \$	230.0	230.0	230.0	230.0		920.0	920.0	-
Proc \$	139.0	120.0	155.0	155.0		569.0	569.0	-
FTEs	2.0	2.0	2.0	2.0		8.0	8.0	-
Jlab	-	-	-	-		-	-	-
Other	2.0	2.0	2.0	2.0		8.0	8.0	-
University						-	-	-
<b>MRPC-US</b>	145.4	145.4	145.4	145.4	30.0	611.5	-	611.5
Labor \$	115.4	115.4	115.4	115.4		461.5	-	461.5
Proc \$	30.0	30.0	30.0	30.0	30.0	150.0	-	150.0
FTEs	1.0	1.0	1.0	1.0		4.0	-	4.0
Jlab	1.0	1.0	1.0	1.0		4.0	-	4.0
Other	-	-	-	-		-	-	-
University	0.1	0.1	0.1	0.1		0.5	-	-
<b>MRPC-China</b>	1,589.5	1,189.0	979.5	187.5		3,945.5	3,945.5	-
Labor \$	187.5	187.5	187.5	187.5		750.0	750.0	-
Proc \$	1,402.0	1,001.5	792.0	-		3,195.5	3,195.5	-
FTEs	1.9	1.9	1.9	1.9		7.5	7.5	-
Jlab	-	-	-	-		-	-	-
Other	1.9	1.9	1.9	1.9		7.5	7.5	-
University						-	-	-
<b>DAQ / Electronics</b>	710.5	1,225.5	1,010.5	510.5	522.0	3,979.0	1,165.0	2,814.0
Labor \$	310.5	310.5	310.5	310.5	322.0	1,564.0	-	1,564.0
Proc \$	400.0	915.0	700.0	200.0	200.0	2,415.0	1,165.0	1,250.0
FTEs	2.7	2.7	2.7	2.7	2.8	13.6	-	13.6

Figure 178: Estimation of SoLID Overall Cost 2018, page 1

<b>FY18 \$k (Direct)</b>	<b>Yr 1</b>	<b>Yr 2</b>	<b>Yr 3</b>	<b>Yr 4</b>	<b>Yr 5</b>	<b>Total</b>	<b>Contribute</b>	<b>Request</b>
Jlab	2.7	2.7	2.7	2.7	2.8	13.6		13.6
Other						-	-	
University	0.5	0.5	0.5	0.5	0.5	2.5		
<b>Magnet</b>	<b>3,024.0</b>	<b>2,184.0</b>	<b>1,902.0</b>	<b>627.0</b>	<b>505.0</b>	<b>8,242.0</b>	<b>-</b>	<b>8,242.0</b>
Labor \$	322.0	448.5	299.0	276.0	333.5	1,679.0	-	1,679.0
Proc \$	2,702.0	1,735.5	1,603.0	351.0	171.5	6,563.0	-	6,563.0
<b>FTEs</b>	<b>2.8</b>	<b>3.9</b>	<b>2.6</b>	<b>2.4</b>	<b>2.9</b>	<b>14.6</b>	<b>-</b>	<b>14.6</b>
Jlab	2.8	3.9	2.6	2.4	2.9	14.6		14.6
Other	-	-	-	-	-	-	-	
University	-	-	-	-	-	-	-	
<b>Support</b>	<b>607.0</b>	<b>2,197.0</b>	<b>1,457.7</b>	<b>967.7</b>		<b>5,229.3</b>	<b>-</b>	<b>5,229.3</b>
Labor \$	437.0	690.0	807.7	807.7		2,742.3	-	2,742.3
Proc \$	170.0	1,507.0	650.0	160.0		2,487.0	-	2,487.0
<b>FTEs</b>	<b>3.8</b>	<b>6.0</b>	<b>7.0</b>	<b>7.0</b>		<b>23.8</b>	<b>-</b>	<b>23.8</b>
Jlab	3.8	6.0	7.0	7.0		23.8		23.8
Other	-	-	-	-		-	-	
University	-	-	-	-		-	-	
<b>Software</b>	<b>165.4</b>	<b>165.4</b>	<b>165.4</b>	<b>165.4</b>	<b>172.5</b>	<b>834.0</b>	<b>-</b>	<b>834.0</b>
Labor \$	165.4	165.4	165.4	165.4	172.5	834.0	-	834.0
Proc \$	-	-	-	-	-	-	-	
<b>FTEs</b>	<b>1.5</b>	<b>1.5</b>	<b>1.5</b>	<b>1.5</b>	<b>1.5</b>	<b>7.5</b>	<b>-</b>	<b>7.5</b>
Jlab	1.5	1.5	1.5	1.5	1.5	7.5		7.5
Other	-	-	-	-	-	-	-	
University	-	-	-	-	-	-	-	
<b>Oversight</b>	<b>150.0</b>	<b>150.0</b>	<b>150.0</b>	<b>150.0</b>	<b>150.0</b>	<b>750.1</b>	<b>-</b>	<b>750.1</b>
Labor \$	150.0	150.0	150.0	150.0	150.0	750.1	-	750.1
Proc \$	-	-	-	-	-	-	-	
<b>FTEs</b>	<b>1.3</b>	<b>1.3</b>	<b>1.3</b>	<b>1.3</b>	<b>1.3</b>	<b>6.5</b>	<b>-</b>	<b>6.5</b>
Jlab	1.3	1.3	1.3	1.3	1.3	6.5		6.5
Other	-	-	-	-	-	-	-	
University	-	-	-	-	-	-	-	
<b>Net Total \$k</b>	<b>12,118</b>	<b>13,907</b>	<b>11,627</b>	<b>7,481</b>	<b>2,760</b>	<b>47,894</b>	<b>8,417</b>	<b>39,477</b>
<b>FTEs</b>	<b>30.7</b>	<b>34.0</b>	<b>33.7</b>	<b>33.5</b>	<b>14.7</b>	<b>146.5</b>	<b>25.5</b>	<b>121.0</b>
<b>JLab FTEs</b>	<b>24.8</b>	<b>28.1</b>	<b>27.8</b>	<b>27.6</b>	<b>12.7</b>	<b>121.0</b>	<b>-</b>	<b>121.0</b>
Overhead	1,939	2,225	1,860	1,197	442	7,663	1,347	6,316
Subtotal w/ Overhead	14,057	16,132	13,488	8,678	3,202	55,557	9,764	45,793
Contingency @ 35%	4,920	5,646	4,721	3,037	1,121	19,445	3,417	16,028
<b>Grand Total</b>	<b>18,977</b>	<b>21,778</b>	<b>18,209</b>	<b>11,716</b>	<b>4,322</b>	<b>75,002</b>	<b>13,181</b>	<b>61,821</b>

Figure 179: Estimation of SoLID Overall Cost 2018, page 2



5753 **Appendix E Cost Estimations**

5754 **E.1 Summary of SoLID overall cost estimation**

5755 The cost estimation for each subsystem is listed in Figures 180 and 181. The costs are assumed  
5756 to be spread in four years. The 5th column is the sum of the 4 years. The next column is the  
5757 contributions from other sources, including the anticipated contributions from China for the GEM  
5758 and MRPC detectors and contributions from other groups, and the last column is the amount to be  
5759 requested from DOE (as an MIE). For each major item, there are 7 rows: the first row is the total  
5760 for this item, the next two row split it into labor and procurement. Then the labor part is listed  
5761 as FTEs and divided further into the JLab FTEs, other contributed FTEs and the University FTEs  
5762 (which are the FTEs subcontracted to the University groups). Net total is the sum of all the direct  
5763 cost, including both procurement and labor. JLab overhead is listed, including the overhead for both  
5764 procurement and JLab FTEs.

5765 The total request to DOE is \$47.7M. The total cost for SoLID, including contributions of  
5766 \$11.4M from other sources, is estimated to be \$59.1M. (Note: The total contribution from other  
5767 sources is expected to be higher, given that the \$11.4M estimate has a lower cost basis for FTE and  
5768 no overhead included.)

**SoLID Cost Estimate**  
**Costs are in FY14\$K**

FY14 \$k (Direct)	Yr 1	Yr 2	Yr 3	Yr 4	Total	Contribute	Request
<b>Ecal</b>	1,278.1	3,278.1	1,473.1	565.1	6,594.3	400.0	6,194.3
Labor \$	273.1	273.1	273.1	273.1	1,092.3	400.0	692.3
Proc \$	1,005.0	3,005.0	1,200.0	292.0	5,502.0	-	5,502.0
<b>FTEs</b>	4.0	4.0	4.0	4.0	16.0	4.0	12.0
Jlab	1.5	1.5	1.5	1.5	6.0	-	6.0
Other	1.0	1.0	1.0	1.0	4.0	4.0	-
University	1.5	1.5	1.5	1.5	6.0	-	6.0
<b>e Cherenkov</b>	504.3	1,176.3	822.7	142.7	2,645.9	148.7	2,497.2
Labor \$	184.3	136.3	122.7	122.7	565.9	148.7	417.2
Proc \$	320.0	1,040.0	700.0	20.0	2,080.0	-	2,080.0
<b>FTEs</b>	3.0	3.0	2.0	2.0	10.0	1.5	8.5
Jlab	1.2	1.2	0.8	0.8	4.0	-	4.0
Other	0.5	0.5	0.3	0.3	1.5	1.5	-
University	1.3	1.3	0.9	0.9	4.5	-	4.5
<b>h Cherenkov</b>	952.9	952.9	952.9	325.9	3,184.5	150.0	3,034.5
Labor \$	152.9	152.9	152.9	152.9	611.5	150.0	461.5
Proc \$	800.0	800.0	800.0	173.0	2,573.0	-	2,573.0
<b>FTEs</b>	2.0	2.0	2.0	2.0	8.0	1.5	6.5
Jlab	1.0	1.0	1.0	1.0	4.0	-	4.0
Other	0.4	0.4	0.4	0.4	1.5	1.5	-
University	0.6	0.6	0.6	0.6	2.5	-	2.5
<b>GEM-US</b>	113.7	183.7	250.0	171.3	718.6	-	718.6
Labor \$	83.7	83.7	150.0	141.3	458.6	-	458.6
Proc \$	30.0	100.0	100.0	30.0	260.0	-	260.0
<b>FTEs</b>	0.9	0.9	1.4	1.4	4.5	-	4.5
Jlab	0.7	0.7	1.3	1.2	4.0	-	4.0
Other	-	-	-	-	-	-	-
University	0.1	0.1	0.1	0.1	0.5	-	0.5
<b>GEM-China</b>	1,737.5	1,737.5	1,137.5	832.5	5,445.0	5,445.0	-
Labor \$	637.5	637.5	537.5	537.5	2,350.0	2,350.0	-
Proc \$	1,100.0	1,100.0	600.0	295.0	3,095.0	3,095.0	-
<b>FTEs</b>	6.4	6.4	5.4	5.4	23.5	23.5	-
Jlab	-	-	-	-	-	-	-
Other	6.4	6.4	5.4	5.4	23.5	23.5	-
University	-	-	-	-	-	-	-
<b>MRPC-US</b>	265.4	325.4	215.4	155.4	961.5	-	961.5
Labor \$	115.4	115.4	115.4	115.4	461.5	-	461.5
Proc \$	150.0	210.0	100.0	40.0	500.0	-	500.0
<b>FTEs</b>	1.1	1.1	1.1	1.1	4.5	-	4.5
Jlab	1.0	1.0	1.0	1.0	4.0	-	4.0
Other	-	-	-	-	-	-	-
University	0.1	0.1	0.1	0.1	0.5	-	0.5
<b>MRPC-China</b>	687.5	587.5	377.5	187.5	1,840.0	1,840.0	-
Labor \$	187.5	187.5	187.5	187.5	750.0	750.0	-
Proc \$	500.0	400.0	190.0	-	1,090.0	1,090.0	-

Figure 180: Estimation of SoLID Overall Cost, page 1

FY14 \$k (Direct)	Yr 1	Yr 2	Yr 3	Yr 4	Total	Contribute	Request
FTEs	1.9	1.9	1.9	1.9	7.5	7.5	-
Jlab	-	-	-	-	-	-	-
Other	1.9	1.9	1.9	1.9	7.5	7.5	-
University	-	-	-	-	-	-	-
<b>DAQ/ Electronics</b>	<b>1,146.3</b>	<b>1,056.3</b>	<b>915.3</b>	<b>952.3</b>	<b>4,070.2</b>	<b>238.0</b>	<b>3,832.2</b>
Labor \$	446.3	456.3	452.3	452.3	1,807.2	238.0	1,569.2
Proc \$	700.0	600.0	463.0	500.0	2,263.0	-	2,263.0
FTEs	3.9	4.0	4.0	4.0	16.0	2.4	13.6
Jlab	3.4	3.4	3.4	3.4	13.6	-	13.6
Other	0.5	0.6	0.6	0.6	2.4	2.4	-
University	-	-	-	-	-	-	-
<b>Magnet</b>	<b>2,232.7</b>	<b>2,354.7</b>	<b>950.0</b>	<b>411.5</b>	<b>5,948.9</b>	<b>-</b>	<b>5,948.9</b>
Labor \$	507.7	507.7	300.0	311.5	1,626.9	-	1,626.9
Proc \$	1,725.0	1,847.0	650.0	100.0	4,322.0	-	4,322.0
FTEs	4.4	4.4	2.6	2.7	14.1	-	14.1
Jlab	4.4	4.4	2.6	2.7	14.1	-	14.1
Other	-	-	-	-	-	-	-
University	-	-	-	-	-	-	-
<b>Support</b>	<b>465.4</b>	<b>2,014.2</b>	<b>1,457.7</b>	<b>967.7</b>	<b>4,904.9</b>	<b>-</b>	<b>4,904.9</b>
Labor \$	415.4	669.2	807.7	807.7	2,699.9	-	2,699.9
Proc \$	50.0	1,345.0	650.0	160.0	2,205.0	-	2,205.0
FTEs	3.6	5.8	7.0	7.0	23.4	-	23.4
Jlab	3.6	5.8	7.0	7.0	23.4	-	23.4
Other	-	-	-	-	-	-	-
University	-	-	-	-	-	-	-
<b>Software</b>	<b>165.4</b>	<b>165.4</b>	<b>165.4</b>	<b>165.4</b>	<b>661.5</b>	<b>200.4</b>	<b>461.1</b>
Labor \$	165.4	165.4	165.4	165.4	661.5	200.4	461.1
Proc \$	-	-	-	-	-	-	-
FTEs	1.5	1.5	1.5	1.5	6.0	2.0	4.0
Jlab	1.0	1.0	1.0	1.0	4.0	-	4.0
Other	0.5	0.5	0.5	0.5	2.0	2.0	-
University	-	-	-	-	-	-	-
<b>Oversight</b>	<b>173.1</b>	<b>173.1</b>	<b>173.1</b>	<b>173.1</b>	<b>692.3</b>	<b>-</b>	<b>692.3</b>
Labor \$	173.1	173.1	173.1	173.1	692.3	-	692.3
Proc \$	-	-	-	-	-	-	-
FTEs	1.5	1.5	1.5	1.5	6.0	-	6.0
Jlab	1.5	1.5	1.5	1.5	6.0	-	6.0
Other	-	-	-	-	-	-	-
University	-	-	-	-	-	-	-
<b>Net Total \$k</b>	<b>9,722</b>	<b>14,005</b>	<b>8,890</b>	<b>5,050</b>	<b>37,668</b>	<b>8,422</b>	<b>29,245</b>
<b>FTEs</b>	<b>34.2</b>	<b>36.4</b>	<b>34.4</b>	<b>34.4</b>	<b>139.4</b>	<b>42.4</b>	<b>97.0</b>
<b>Jlab FTEs</b>	<b>19.3</b>	<b>21.5</b>	<b>21.1</b>	<b>21.1</b>	<b>83.1</b>	<b>-</b>	<b>83.1</b>
Overhead	1,626	1,933	1,924	1,732	7,215	-	7,215
Subtotal w/ Overhead	11,348	15,938	10,815	6,782	44,883	8,422	36,461
Contingency @ 35%	3,583	5,185	3,435	2,023	14,226	2,948	11,278
<b>Grand Total</b>	<b>14,931</b>	<b>21,124</b>	<b>14,249</b>	<b>8,805</b>	<b>59,109</b>	<b>11,370</b>	<b>47,739</b>

Figure 181: Estimation of SoLID Overall Cost, page 2

5769 **E.2 Estimation of Cost Request for Subsystems**

5770 **E.2.1 Cost of Electromagnetic Calorimeters**

Table 37: EM Calorimeter (SH/PS/SPD) Request Cost Breakdown

	Year-1	Year-2	Year-3	Year-4	Sum	Contrib	Request
Shower Modules	315	1870	655	132	2972		2972
PreShower Modules	80	180	100	30	390		390
SPD Modules	30	30	5		65		65
WLS Fiber	80	100	39		219		219
Clear Fiber	150	250	126		526		526
Fiber Connectors	100	175	86		361		361
Shower PMTs	100	200	104	50	454		454
PS MAPMTs	80	120	34	30	264		264
SPD MAPMTs	30	30	6		66		66
Assembling and Testing	30	30	35	40	135		135
FTE	4	4	4	4	16	4	12
Shipping	10	20	10	10	50		50
Total-EC-cost	1005	3005	1200	292	5502		5502
Total-EC-FTE	4	4	4	4	16	4	12

5771 **E.2.2 Cost of the Light-Gas Cherenkov Counters**

Table 38: Light Gas Cherenkov Request Cost Breakdown

	Year-1	Year-2	Year-3	Year-4	Sum		Contrib	Request
Engineering Design FTE	1	1	0.5	0.5	3		0.5	2.5
Physics Oversight FTE	1	1	0.5	0.5	3		0.5	2.5
Technical Work FTE	1	1	1	1	4		0.5	3.5
H8500C-03 PMTs	126	122.5	700		948.5			948.5
Mu-metal Shields	6	37.5			43.5			43.5
Aluminized Cones	25	125			150			152
Mirror Blanks	58	290			348			348
Mirror Coating	35	165			200			200
Gas System	50				50			50
Tank	20	300			320			320
Transport				20	20			20
Total-LG	320	1040	700	20	2080			2080
Total-LG FTE	3	3	2	2	10		1.5	8.5

5772 **E.2.3 Cost of Heavy-Gas Cherenkov Detectors**

Table 39: Heavy Gas Cherenkov Request Cost Breakdown

	Year-1	Year-2	Year-3	Year-4	Sum		Contrib	Request
Design, Assembly	2	2	2	2	8		1.5	6.5
Full Tank		300			300			300
Mirror		290			290			290
Cone		116			116			116
PMTs	800	94	734		1628			1628
Gas System			66	19	85			85
Gas				154	154			154
Total-HG	800	800	800	173	2573			2573
Total-HG FTE	2	2	2	2	8		1.5	6.5

5773 **E.2.4 Cost of GEM detectors**

Table 40: GEM Cost Breakdown

	Year-1	Year-2	Year-3	Year-4	Sum	Contrib	Request
GEM-China	1100	1100	600	295	3095	3095	0
GEM-China FTE	6	6	5	5	22	22	
Design and Prototyping FTE	0.5	0.5	0.5	0.5	2	0.5	1.5
Hosting Chinese Collaborators	10				10		10
Installation /tesing	20	100	100	30	250		250
Installation /testing FTE			0.5	0.5	1		1
DAQ FTE	0.25	0.25	0.25	0.25	1	0.5	0.5
Management FTE	0.5	0.5	0.5	0.5	2	0.5	1.5
<b>Total-GEM</b>	<b>1130</b>	<b>1200</b>	<b>700</b>	<b>325</b>	<b>3355</b>	<b>3095</b>	<b>260</b>
<b>Total-GEM FTE</b>	<b>7.5</b>	<b>7.5</b>	<b>6.5</b>	<b>6.5</b>	<b>28</b>	<b>23.5</b>	<b>4.5</b>

5774 The other source contributions include the anticipated funding from Chinese groups.

5775 **E.2.5 Cost of MRPC**

Table 41: MRPC Cost Breakdown

	Year-1	Year-2	Year-3	Year-4	Sum	Contrib	Request
MRPC-China	500	400	190		1090	1090	0
MRPC-China FTE	1.5	1.5	1.5	1.5	6	6	0
Read-out Electronics	110	190	70		370		370
Gas System	20				20		20
Testing and Installation	20	20	30	40	110		110
FTE	1.5	1.5	1.5	1.5	6	1.5	4.5
<b>Total-MRPC</b>	<b>650</b>	<b>610</b>	<b>290</b>	<b>40</b>	<b>1590</b>	<b>1090</b>	<b>500</b>
<b>Total-MRPC FTE</b>	<b>3</b>	<b>3</b>	<b>3</b>	<b>3</b>	<b>12</b>	<b>7.5</b>	<b>4.5</b>

5776 The other source contributions include the anticipated funding from Chinese groups.

5777 **E.2.6 Cost of DAQ Electronics and High Voltage Power Supplies**

Table 42: DAQ Cost Breakdown

	Year-1	Year-2	Year-3	Year-4	Sum		Contrib	Request
DAQ Elec- tronics	700	600	400	200	1900		0	1900
HV power supply			63	300	363		0	363
DAQ FTE	3.6	4	4	4	16		2.4	13.6
Total- DAQ	700	600	463	500	2263		0	2263
Total- DAQ FTE	3.6	4	4	4	16		2.4	13.6

5778 **E.2.7 Cost of Magnet Modification and Refurbishing**

Table 43: Magnet Cost Breakdown

	Year-1	Year-2	Year-3	Year-4	Sum	Contrib	Request
Yoke	360				360		360
FTE	0.3	0.3	0.2		0.6		0.6
Upstream Endcap	335	342			677		677
FTE	0.5	0.5	0.2		0.8		0.3
Downstream endcap	450	425			875		875
FTE	0.7	0.5	0.2		1.4		1.4
Nose Extension	330	330			660		660
FTE	0.3	0.3	0.1		0.7		0.7
Downstream coil collar	250	250			500		500
FTE	0.8	0.6	0.1		1.5		1.5
Magnet support, alignment		100	250		350		350
FTE	1	0.4	0.4	0.2	2		2
Control		100	200	100	400		400
FTE	0.5	0.5	1	1	3		3
Cryogenic		300	200		500		500
FTE	0.3	0.3	0.4	0.5	1.5		1.5
Magnet Testing					100		100
FTE		1		1	2		2
Total- magnet	1725	1847	650	100	4322		4322
Total-FTE	4.4	4.4	2.6	2.7	14.1		14.1



5779 **E.2.8 Cost of Detector Support, Hall Infrastructure Upgrade and Installation**

Table 44: Engineering, Detector Support Structure, Hall Infrastructure Upgrade and Installation

	Year-1	Year-2	Year-3	Year-4	Sum	Contrib	Request
Detector Engineer FTE	2	2.5	2.5	0.5	7.5		7.5
Detector Support		250	250		500		500
FEC Support		125			125		125
FTE	0.1	0.1			0.2		0.2
LAEC Supp.		80			80		80
FTE	0.1	0.1			0.2		0.2
Baffle		300			300		300
FTE	0.1	0.1			0.2		0.2
Baffle Supp.		220			220		220
FTE	0.1	0.1			0.2		0.2
Access		170			170		170
FTE		0.1	0.1		0.2		0.2
Power		100	100		200		200
FTE	0.1	0.1	0.1		0.3		0.3
Beamline/ Chambers			200	60	260		260
FTE			0.2	0.2	0.4		0.4
Ramp		50			50		50
FTE		0.1			0.1		0.1
Hall	50	50	50		150		150
FTE	0.5	0.5	0.5		1.5		2
Layout FTE	0.1	0.1	0.1	0.1	0.4		0.4
Assembly and Installation			50	100	150		150
FTE	0.5	2	5.5	6.2	14.2		14.2
Total-Structure	50	1225	650	160	2205		2205
FTE	3.6	5.8	7.0	7	23.4		23.4

5780 **Appendix F Basis for Cost Estimates**

5781 The cost and manpower estimations in the subsections for each subsystem were provided by the  
 5782 coordinators of the subsystems. They form the basis for the cost estimation of each subsystem.  
 5783 The manpower parts of the estimations were adjusted based on JLab Hall D experience with similar  
 5784 subsystems. The spending profiles were also adjusted to be 4 years. Additional JLab technical and  
 5785 oversight supporting manpower was added to the estimation for each subsystem. JLab overhead  
 5786 was estimated in a separate section and was included in the total.

5787 The follow are the original estimations for each subsystem. (Note: Pre-R&D costs were not  
 5788 used in the final cost estimation, but kept here for references). The 1st iteration refers to the cost  
 5789 estimation in the December 2013 version. The 2nd iteration refers to the cost estimation by June  
 5790 2014.

5791 **F.1 Cost of Electromagnetic Calorimeters**

5792 **F.1.1 Cost Estimation: 1st iteration**

5793 The estimated cost for the SoLID calorimeters is summarized in Table 45. It is based on 1800 shower  
 5794 and 1800 preshower modules. All IHEP cost includes 30% of overhead. Shipping cost is an esti-  
 5795 mate. Cost for prototyping is estimated to be 0.3M\$. Two supporting FTEs from JLab are included  
 5796 in the manpower estimation. Cost of the SPD is estimated and also included in the table. If produced  
 5797 at IHEP, the total cost including 30% of IHEP overhead and the supporting structure will be in the  
 5798 range \$(70-120)K.

Table 45: Cost estimation for the SoLID calorimeters.

Component	cost (K\$)
IHEP Preshower material+production	113-122
IHEP Shower material+production	570-678
IHEP Structure + assembly	540-720
IHEP Fiber cutting + mirrors	108-117
WLS fibers	234
clear fibers	564
Fiber connector+tubing	300
PMTs (with bases)	2,430
shipping	50
prototyping	300
SPD	70-120
SubTotal	5,280-5,640
Labor (7 tech FTE + 2 postdoc FTE + 5 student-years)	1,150

5799 **F.1.2 Cost Estimation: 2nd iteration, breakdown by the year**

5800 Overhead rate for each group is listed below:

- 5801 • UVa: 56% on-campus rate on salary, wages, material and supplies; 0% on equipment funds  
 5802 above \$5k;

Pre-R&D year 1		Pre-R&D year 2	
cost	manpower	cost	manpower
\$30k	1 undergrad, 2.5 grad student, 1.3 postdoc, 0.3 technician, 0.1 physicist, 0.1 engineer	\$30k	1 undergrad, 2.5 grad student, 1.3 postdoc, 0.3 technician, 0.1 physicist, 0.1 engineer

Table 46: Pre R&D cost for EC and SPD. Cost includes prototyping, travel, material and supply.

Item	Sub-item	sub-item cost	Item cost
Modules	Shower	\$2,972k	\$3,427k
	Preshower	\$390k	
	SPD	\$65k	
Fiber and connectors	WLS fiber	\$219k	\$1,106k
	clear fiber	\$526k	
	fiber connectors	\$361k	
PMT	Shower	\$454k	\$784k
	Preshower (MAPMT)	\$264k	
	SPD	\$66k	
support structure			\$50k
shipping			\$50k

Table 47: EC and SPD production cost breakdown. Direct cost only, except for module production (IHEP) which includes 30% indirect cost. Total cost for production is \$5.367M, to be divided evenly between year 1 and year 2 of construction. This cost does not include HV power supply or HV and signal cables.

Year 1		Year 2		Year 3	
cost	manpower	cost	manpower	cost	manpower
\$45k	1 undergrad, 3 grad students, 1.5 postdoc, 0.5 technician, 0.2 physicist, 0.25 engineer	\$45k	1 undergrad, 3 grad students, 1.5 postdoc, 0.5 technician, 0.4 physicist, 0.3 engineer	\$45k	1 undergrad, 3 grad students, 1.5 postdoc, 0.5 technician, 0.4 physicist, 0.15 engineer

Table 48: EC and SPD construction cost breakdown. Cost includes travel, material and supply.

- 5803 • WM: 47% on salary, wages, material and supplies, and equipment below \$5k; 0% on equip-
- 5804 • ment funds above \$5k;
- 5805 • ANL: 51% on salary and wages; 13% on material, supplies and equipment;
- 5806 • SDU: 20% on all types;

5807 **F.2 Cost of the Light-Gas Cherenkov Counters**

5808 **F.2.1 Cost Estimation: 1st iteration**

5809 The total expected budget is presented in Tab. 49. Most numbers are from recent manufacturing  
 5810 quotes. Minimizing cost while maintaining high levels of  $\pi/e$  separation and efficiency was a pri-  
 5811 mary goal of the current design; some significant cost saving was achieved by using the same mirrors  
 5812 in both PVDIS and SIDIS configurations, as well as the same set of PMTs and Winston Cones.

Table 49: Cost for the light-gas Cherenkov detectors.

Item	Cost (K\$)
60 Mirror blanks + tooling	348
60 Mirrors coating	200
30 × 9 + 10 spares H8500C-03 PMTs (\$3.5K each)	980
30 Mu-metal cylinder	45
30 Aluminized glass cones	60
Tank	300
Gas system	50
SubTotal	1,983
2 tech FTEs + 1 postdoc + 2 students	400

5813 **F.2.2 Cost Estimation: 2nd iteration, breakdown by the year**

5814 Completion time from the start of funding is expected to take 3 years:

- 5815 • Year 1: Ordering and procurement of materials, basic electronics testing, finalization of pro-  
 5816 totype design.
- 5817 • Year 2: Construction of 1 prototype sub-section (which consists of 5 of the 30 SoLID sectors,  
 5818 equivalent to 1/6 the total Cherenkov detector) for testing and design refinement.
- 5819 • Year 3: Production of all 6 sub-sections, continued testing and optimization. Some materials  
 5820 from the prototype will be stripped and used in the final detector.

5821 Following the 3rd year, the Cherenkov will be shipped to Jefferson Lab and approximately 3  
 5822 months will be needed for installation and integration.

5823 Additional personnel that is requested from Jefferson Lab is as follows:

- 5824 • Year 1: Engineering support – 1/3 FTE
- 5825 • Year 2: Engineering support – 1/3 FTE
- 5826 • Year 3: Engineering support – 1/3 FTE, Technician assistance for installation – 1/3 FTE,  
 5827 Scientist assistance for hardware integration, testing, and calibration – 1/3 FTE.

	Pre-R&D		Year-1		Year-2		Year-3	
	cost	FTE	cost	FTE	cost	FTE	cost	FTE
Design	-	0.5 Eng	-	1.0 Eng	-	1.0 Eng	-	1.0 Eng
Oversight	-	0.5 Sci	-	1.0 Sci	-	1.0 Sci	-	1.0 Sci
Assembly	-	0.5 Stu	-	2.0 Stu	-	2.0 Stu	-	4.0 Stu
PMTs	31.5	-	126	-	822.5	-	-	-
Shields	4	-	6	-	37.5	-	-	-
Cones	2	-	10	-	50	-	-	-
Mirrors	10	-	58	-	290	-	-	-
Coating	-	-	33.3	-	166.5	-	-	-
Gas system	-	-	50	-	-	-	-	-
Prototype	-	-	20	-	-	-	-	-
Tank	-	-	-	-	300	-	-	-
Transport	-	-	-	-	-	-	20	-

Table 50: Light Gas Cherenkov Cost Breakdown. Cost is in \$K and manpower is in FTE.

Item	Ind. Cost (K\$)	Quantity	Sum (K\$)
H8500C-03 PMTs	3.5	9	31.5
Mu-metal cylinder	4	1 (plus tooling)	4
Mirror blanks	10	1 (plus tooling)	10
Aluminized glass cones	2	1	2
Equipment Subtotal			47.5
Continued Design and Oversight	1/2 FTE	1 Research Scientist	50
Technician Workers	1/2 FTE	1 Student Researchers	15
Preliminary Design	1/2 FTE	1 Engineer	50
Personnel Subtotal			115
Total			162.5

Table 51: Current pre-R&D operating budget for the LGC

5828 **F.3 Cost of Heavy-Gas Cherenkov Detectors**

5829 **F.3.1 Cost Estimation: 1st iteration**

5830 The cost estimate of the full detector package including the mirrors, the PMTs the Winstone cones,  
5831 the Cherenkov tank and the gas system is given in table 56. The 3/4 technician year represents the  
5832 amount of work for two technicians and one welder needed for a period of three months to build the  
5833 gas system.

5834 **F.3.2 Cost Estimation: 2nd iteration, breakdown by the year**

5835 We anticipate the funding for the construction of the full HGC detector will come through the MRE  
5836 program of DOE. For prototyping, we plan to request funds from DOE through the Duke Medium  
5837 Energy Group's DOE grant. The Pre-R&D work will be funded by Duke University.

5838 The time estimate for completing the project is 4 years with 2 years for pre-R&D and prototyping  
5839 and testing, and two years for the construction of the full detector. The HGC project requires  
5840 support from JLab in the areas of thin-Window expertise as the these windows need to meet Jlab's

Item	Ind. Cost (K\$)	Quantity	Sum (K\$)
Mirror blanks	5.8	10	58
Mirror coating	3.33	10	33.3
H8500C-03 PMTs	3.5	36	126
Mu-metal cylinders	1.5	4	6
Aluminized glass cones	2.0	5	10
Prototype Tank Section	20	1	20
Gas system	50	1	50
Equipment Subtotal			253.3
Oversight and Project Lead	1 FTE	1 Research Scientist	100
Technician Workers	1/2 FTE	2 Student Researchers	30
Design and Engineering	1 FTE	1 Engineer	100
Personnel Subtotal			230
Total			483.3

Table 52: First Year Budget for the LGC

Item	Ind. Cost (K\$)	Quantity	Sum (K\$)
Mirror blanks	5.8	50	290
Mirror coating	3.33	50	166.5
H8500C-03 PMTs	3.5	235	822.5
Mu-metal cylinders	1.5	25	37.5
Aluminized glass cones	2.0	25	50
Tank	300	1	300
Equipment Subtotal			1666.5
Oversight and Project Lead	1 FTE	1 Research Scientist	100
Technician Workers	1/2 FTE	2 Student Researchers	30
Design and Engineering	1 FTE	1 Engineer	100
Personnel Subtotal			230
Total			1896.5

Table 53: Second Year Budget for the LGC

Item	Ind. Cost (K\$)	Quantity	Sum (K\$)
Transport	20	1	20
Equipment Subtotal			20
Oversight and Project Lead	1 FTE	1 Research Scientist	100
Technician Workers	1/2 FTE	4 Student Researchers	60
Design and Engineering	1 FTE	1 Engineer	100
Personnel Subtotal			260
Total			280

Table 54: Third Year Budget for the LGC

5841 pressure vessel requirements, and the gas handling system for the detector. Large spherical mirrors  
5842 are important components of the HGC and the procurement of these mirrors will drive the timeline  
5843 of the project.

Year	Material (K\$)	Personnel (K\$)	Sum (K\$)
1	253.3	230	483.3
2	1666.5	230	1896.5
3	20	260	280
Total	1939.8	740	2679.8

Table 55: Total budget breakdown for the LGC (NOT including pre-R&D and requested Jefferson Lab personnel)

	Cost (K\$)
Mirrors	277
PMTs	1,488
Winstone Cones	62
Tank Material	50
Assembly hardware	15
Shop work	100
Gas System: Sensor, piping	50
Recovering System	35
SubTotal	\$2.10M
2 tech FTEs + 1 postdoc +1 student	350

Table 56: Cost estimate of the heavy-gas Cherenkov detectors.

5844 Breakdown of the cost as in the table (cost in \$K and manpower in FTE, Tech. and Grad. Stud stand  
5845 for Technician and and Graduate Student respectively). The total manpower cost is \$K590

	Pre-R&D		Year-1		Year-2		Year-3	
	cost	FTE	cost	FTE	cost	FTE	cost	FTE
Prototype	50	1/2 Postdoc 1/2 Eng		1/2 Postdoc 1/2 Eng 1/2 Tech.				
Full tank					300	1/2 Postdoc 1 Eng 1/2 Tech. 1 Stud.		1/2 Postdoc  1 Stud.
Mirror	10				290			
Cone	4				116			
PMT	52.5		1627.5					
Gas					154			
Gas system			85	1/2 JLab				
Total	116.5		1712.5		860			

Table 57: Heavy Gas Cerenkov Cost Breakdown

5846 **F.4 Cost of GEM Detectors**

5847 **F.4.1 Cost Estimation: 1st iteration**

5848 The GEM cost estimation is summarized in Table 40. A funding proposal to the Chinese funding  
5849 agency is being prepared by the Chinese groups (USTC, CIAE, Tsinghua, Lanzhou, IMP, Peking,  
5850 Shangdong and Huazhong Tech) to cover the main part of the GEM cost (dependency). Only the  
5851 prototyping and supporting cost (\$400K) is included in the total request here. One supporting FTE  
5852 from JLab is also included.

5853 **F.4.2 Cost Estimation: 2nd iteration, breakdown by the year**

5854 **Budget breakdown by the year**

5855 A significant portion of the pre-R&D and R&D funds (of the order of \$ 400 k) from the US DoE  
5856 will have to be spent during the first 2 year pre-R&D phase of the project. It is also anticipated that  
5857 the focused pre-R&D activities at each Chinese institute might cost approximately \$ 100 k during  
5858 the pre-R&D phase of the project, with an additional \$ 150 k to support the GEM foil fabrication  
5859 effort.

5860 The main GEM module system budget of approximately \$ 5 M will have to be spent roughly  
5861 equally over the 2 year construction period.

5862 **Extra manpower needs**

5863 Given the complexity and the magnitude of the project, the SoLID GEM construction may  
5864 require a knowledgeable project manager (~ 1 FTEY over the duration of the project) for the co-  
5865 ordination and management of this part of the project. Funds will also be required for site visits in  
5866 China. The DAQ expert manpower needed might be of the order 0.5 FTEY.

5867 **Installation costs**

5868 A very rough estimate is approximately \$ 200 k - \$ 250 k for the installation of the SoLID GEM  
5869 modules, in addition to the estimated 0.5 FTEY of design and engineering manpower.

5870 **Budget breakdown table for expected US funds.**



Item	Number	Unit Cost (\$)	Cost (\$)
tooling	5	10,000	50,000
Modules 1,2,3(foil Length 75cm)			
GEM foils	270	1,103	357,210
Drift Foils	90	525	56,700
Readout Boards	90	1,890	204,120
Honeycomb	90	473	51,030
Panasonic connectors	1080	3	4,082
Assembly of connectors	1080	20	25,515
Chamber frame sets (RESARM)	90	2,000	216,000
Modules 4,5(foil length 115cm)			
GEM foils	180	1,890	408,240
Drift Foils	60	788	56,700
Readout Boards	60	3,150	226,800
Honeycomb	60	735	52,920
Panasonic connectors	900	3	3,402
Assembly of connectors	900	20	21,263
Chamber frame sets (RESARM)	60	2,000	144,000
For all modules			
Chamber supplies	5	10,000	50,000
Gas system plumbing	5	10,000	50,000
HV distribution	5	10,000	50,000
HV power mainframes	2	7,000	14,000
8-channel HV modules	20	3,500	70,000
HV cabling	150	100	16,500
Readout electronics			
SRS APV-25 Channels	170000	4	816,000
Equipment total			<i>2,944,482</i>
Technician (FTE years)	16	100,000	1,600,000
Graduate Students (FTE years)	6	50,000	300,000
Manpower total			<i>1,900,000</i>
Travel costs (to CERN and Jlab)	1	150,000	<i>150,000</i>
<b>Total for GEM Production</b>			<b>4,994,482</b>
design and prototyping			
Prototype electronic systems	10000	5	50,000
Material for 5 prototypes	5	20,000	100,000
Research Scientist	2	125,000	250,000
<b>Prototyping Total</b>			<b>400,000</b>
<b>Total for GEM</b>			<b>5,394,482</b>

Table 58: GEM Cost Estimation

	Pre-R&D		Year-1		Year-2		Year-3	
	cost	FTEY	cost	FTEY	cost	FTEY	cost	FTEY
Design and Prototyping	100	2.0		0.25		0.25		0.25
Hosting Chinese collaborators	40		10					
Installation				0.25	125		125	0.25
DAQ		0.1				0.2		0.2
Project management		0.25		0.25		0.25		0.25

Table 59: GEM US Cost Breakdown: the costs are given in k\$

5871 **F.5 Cost of MRPC**

5872 **F.5.1 Cost Estimation: 1st iteration**

5873 The cost of the MRPC detector is summarized in Table 60. A funding proposal to the National  
5874 Science Foundation of China by the Chinese collaboration (Tsinghua and Huangshan University) is  
5875 in progress to cover the detector and manpower (dependency) (except one FTE from JLab side is  
5876 needed for assisting, installation and testing). The electronics is planned to be jointly funded by the  
5877 Chinese side (dependency) and US side. About half of the electronics cost (US \$500K) is included  
5878 here in the request, which helps to leverage in the full MRPC funding application.

Item	Cost (K\$)
Detector Modules ( $12m^2$ )	460
Mechanical structure, mainframe	30
Service (HV, LV, cooling )	40
Gas system	20
Others (installation, cables and tools)	100
Front-end and readout electronics	1,020
SubTotal	1,670
SubTotal-req	500
1 tech FTE + 1 postdoc + 2 students	300

Table 60: MRPC Cost

5879 **F.5.2 Cost Estimation: 2nd iteration, breakdown by the year**

Year	Cost
PreRD	30 K
Year 1	280k
Year 2	130k
Year 3	50k

Table 61: MRPC budget breakdown for detector

5880 Electronics cost include 120 K\$ for development and build of input register to add MRPC in  
5881 the trigger, 300 K\$ to build the gas box with the integrated readout circuit board and 600 K\$ for the  
5882 readout electronics.

Year	1	2	3	Total
Mechanical	10	10	10	30
HV,LV,Cooling	10	10	20	40
Gas system	20	0	0	20
Cables, tools	30	30	40	100
Electronics	700	530	440	1020
Total	420	400	390	1210

Table 62: MRPC budget breakdown for the rest of the system

	Pre-R&D manpower	Year-1 manpower	Year-2 manpower	Year-3 Installation manpower	Year-4 Installation manpower
Ele eng	0	0.3	0.2	0	0
DAQ staff	0	0.2	0.1	0.1	0.1
Postdoc	0.2	0.3	0.3	0.2	0.2
Student	0.2	0.8	0.7	0.5	0.5
Physicist	0.1	0.2	0.1	0.1	0.1
Technician	0.05	0.3	0.3	0.2	0.2

Table 63: MRPC Manpower

5883        The student and postdoc will be funded by the collaborating Universities, there rest will Jeffer-  
5884        son Laboratory staff people.

Table 64: Total DAQ electronics required

Module	Unit price (K\$)	Number	Total price (K\$)
FADC 250	4.5	282	1 269.5
TD	3	12	36
CTP	7	30	210
SSP	5	4	20
GTP	5	1	5
TS	3.5	1	3.5
TID	3	61	183
SD	2.5	31	77.5
VXS crate	15	32	480
VME CPU	3.4	32	108.8
Total electronics			2,393
SRS computers	3	30	90
Prototyping			100
Electronics shielding			50
BNC cable	0.057	4030	230
Ribbon cable	0.130	160	21
SubTotal			2,884
SubTotal-Req			1,854

Table 65: Estimated man power for DAQ

Year	2014	2015	2016	2017	2018	2019	Sum
DAQ/Scientist	0.3	0.3	0.3	0.3	0.3	0.3	1.8
Electronics	0.5	0.5	0.5	0.3	0.3	0.3	2.4
Postdoc	0.3	0.5	0.5	0.5	0.5	0.5	2.8
Student	0.5	0.5	0.5	0.5	0.5	0.5	3.0/2
Technician	0.1	0.1	0.1	0.1	0.5	1.0	1.9
Design	0.05	0.05	0.05	0.05	0.05	0.05	0.3
Total FTEs							10.7

5885 **F.6 Cost of DAQ Electronics and High Voltage Power Supplies**

5886 **F.6.1 Cost Estimation: 1st iteration**

5887 Price including spares, this price assumes the GEM electronics and the MRPC electronics are paid  
5888 by their respective responsible university.

5889 Total price for DAQ electronics is 2,884 M\$. With 230 FADC available from the JLab Physics  
5890 Division shared electronics pool (dependency), the total cost of 1,854 M\$ is needed.

5891 The man power includes development and test of the CTP firmware for the trigger, development  
5892 of new SD and TD boards to allow to FADC to readout only specific channels. Total manpower  
5893 needed is 9.2 FTEs + 3 student-years.

5894 **F.6.2 Cost Estimation: 2nd iteration, breakdown by the year**

5895 Some PreRD work is needed to make sure the electronics achieve the performances required by  
5896 SoLID experiment. This work will include getting the electronics to provide the trigger and readout

5897 for a small subset of detectors. This will allow testing the trigger logic and rate capabilities of the  
 5898 system and to gather data with test beam to be closer from the actual background of the experi-  
 5899 ment. This PreRD would also include the development and testing of the high resolution timing  
 5900 measurements, the goal being to develop an affordable but high performance readout system for the  
 5901 MRPC. About 2 years of preRD will be needed. When the project starts, hardware and firmware  
 5902 development for individual channel readout will start, in addition to trigger firmware development.  
 5903 This step will take about 1 year. The hardware will then be ordered and tested the following two  
 5904 years. Installation of the electronics will be done in parallel with detector installation during the  
 5905 next two years.

5906 **Installation costs** A budget of 50 K\$ is added for setup of the racks, cable trays and shielding.

Year	Material (K\$)	Man power (FTE)
PreRD	140	1.9
Year 1	745.5	3.4
Year 2	655.8	3.9
Year 3	498	2.5
Total	2039.3	11.7
Total-excPreRD	1899.3	9.8

	Pre-R&D manpower	Year-1 manpower	Year-2 manpower	Year-3 manpower
Electronics engineer	0.2	0.6	0.6	0.3
DAQ staff	0.2	0.4	0.4	0.2
Postdoc	0.2	1	1	1
Student	0.6	1	1	0.5
Physics staff	0.4	1	1	1

Table 66: DAQ Manpower

5908 The student and postdoc will be funded by the collaborating Universities, the rest will be mem-  
 5909 bers of the JLab staff.

5910 **High Voltage for PMTs**

Detector	Number of channels
EC	1830 + 1830/16
SPD	300 / 16
Light Gas Cerenkov	270
Heavy Gas Cerenkov	480
Total	2714

5912 We got price estimate for 24 channels board, each crate can host up to 7 boards and one con-  
 5913 troller.

Item	Number	Unit price	Total
Cables	2714	0.15	407.1
Boards	114	6.6	752.4
Controller	17	2.5	42.5
Mainframes	17	9	153
Total			1355

5915 We assume we can reuse 2000 HV channels from SuperBigBite GEp5 experiment.

Item	Number	Unit price	Total
Cables	714	0.15	107.1
Boards	30	6.6	198
5916 Controller	5	2.5	12.5
Mainframes	5	9	45
Total			362.6

5917 The HV for the GEM and MRPC are included in their costs table.

5918 **F.7 Cost of Magnet Modification and Refurbishing**

5919 **F.7.1 Cost Estimation: 1st iteration**

5920 Cost of magnet modification and refurbishing was estimated by the Hall A engineering group with  
5921 inputs from CLEO.

Table 67: Cost Estimation for Magnet Modification and Refurbishing

Item	Cost (\$K)	FTE (\$K)	Sum
Disassemble		500	500
Shipping	240		240
Modifications	860	120	980
Upstream Endcap	677	50	727
Downstream Endcap	875	80	955
Nose Extension	660	20	680
Magnet Support	350	40	390
Control	300	30	330
Cryo Modification	500	200	700
Total	4462	1040	5502
Total-Req (excl disassemble/shipping)	4222	540	4762

5922 Total cost for disassemble and transporting the magnet to JLab is estimated to be \$240K plus 5  
5923 FTEs, which is listed as a dependency. Total cost for the magnet modification and refurbishing is  
5924 \$4222K. Engineering and technician manpower needed is 5.4 FTEs.

5925 **F.7.2 Cost Estimation: 2nd iteration, breakdown by the year**

5926 refer to Table [43](#)

5927 **F.8 Cost of Detector Support, Hall Infrastructure Upgrade and Installation**

5928 **F.8.1 Cost Estimation: 1st iteration**

5929 Cost of the general detector support was estimated by the Hall A engineering group which includes  
5930 the support for all detectors except the electromagnetic calorimeters. Estimation for the support  
5931 for the baffles is also done by the Hall A engineering group. The support for the forward EC  
5932 was estimated by the Argonne group and the large-angle EC was estimated based on scaling the  
5933 estimation cost for the forward EC. Overhead is included. The total cost is \$725K and 1.65 FTEs  
manpower.

Table 68: Cost Estimation for Detector Support

Item	Cost (\$K)	FTE (\$K)	Sum
General detector support	500	100	600
Baffle support	220	20	320
Forward EC support	125	25	150
LAEC support	80	20	100
Total	725	165	890

5934

5935 The cost for hall infrastructure upgrade was estimated by the Hall A engineering group. It  
5936 includes the hall floor enhancement, the power supply connections, LCW, supports, cabling, beam  
5937 line, Thompson slides and the ramp modifications. Total cost of \$1550K and 2.1 FTEs are needed.

5938 **F.8.2 Cost Estimation of Baffles: 1st iteration**

5939 The total cost of the baffles needs to be evaluated by engineers. The cost of lead material is approx-  
5940 imately \$2200 per metric ton, or about a total of \$37k for the 17 ton baffles as presented. In overall  
5941 construction costs, it should contribute less than \$300k including 0.2 FTE to the cost of the project.

5942 **F.8.3 Cost Estimation: 2nd iteration, breakdown by the year**

5943 refer to Table 44

5944 **F.9 Oversight Manpower**

5945 **F.9.1 Cost Estimation: 1st iteration**

5946 Oversight manpower is estimated to be 2 FTEs (over the full period), including 1.0 FTE manage-  
5947 ment, 0.5 FTE engineer and 0.5 scientist.

5948 **F.9.2 Cost Estimation: 2nd iteration, breakdown by the year**

5949 Oversight manpower estimation is increased to be 6 FTEs (over 4 years), refer to Figure 181

5950 **F.10 JLab Overhead**

5951 **F.10.1 Cost Estimation: 1st iteration**

5952 Overheads from the collaborating university groups have been included in each sub-system. Over-  
5953 head from JLab side is estimated and listed in Table 69. The overhead rate is assumed to be 51%,



5954 which applies to all JLab manpower and small procurements. For large procurements, a cap of \$25K  
 5955 is used. In the estimation, For the magnet, 7 large procurements were assumed. For the detec-  
 5956 tors, it is planned to have the collaborating university groups to undertake the responsibility. Large  
 5957 contracts with university groups to construct major detector subsystems were assumed. Ten large  
 5958 procurements (two groups for five years) were assumed for the Calorimeter and the SPD. Five large  
 5959 procurements (one group for 5 years) were assumed for the light gas Cherenkov, five (one group  
 5960 for five years) for the heavy gas Cherenkov and five (one group for five years for prototyping and  
 5961 supporting) for the GEMs. One JLab FTE (total over the during of construction) for each of the  
 5962 detectors (Calorimeter, SPD, LC, HC, GEMs and MRPC) was assumed and corresponding 51%  
 5963 overhead was included. For DAQ electronics, each item in the DAQ electronics table was taken  
 5964 as one procurement and all manpower was assumed to be JLab with 51% overhead. For the Hall  
 5965 infrastructure and detector supports, Fifteen large procurements were assumed and all manpower  
 assumed to be JLab. The total overhead is \$2.88M.

Table 69: Cost Estimation for JLab Overhead

Item	Overhead on Procurement (\$K)	Overhead on FTE (\$K)	Sum
Magnet	175	275	450
Calorimeters	250	102	227
e Cherenkov	125	51	101
h Cherenkov	125	51	101
GEMs	125	51	101
MRPC		51	51
Detector Subtotal	625	306	931
Electronics	278	546	824
Infrastructure	375	201	576
Oversight		102	102
Total Overhead	1453	1430	2883

5966

5967 **F.10.2 Cost Estimation: 2nd iteration, breakdown by the year**

5968 The updated JLab overhead cost breakdown by the year is in Table 70.

Table 70: JLab Overhead Cost Breakdown, overhead for manpower (MP) is also in units of \$K

	Year-1 cost/MP	Year-2 cost/MP	Year-3 cost/MP	Year-4 cost/MP	Sum cost/MP		Contrib cost/MP	Request cost/MP
ECal	75/ 75	75/ 75	50/ 75	50/ 75	250/ 300		0/0	250/ 300
e Ch	50/ 50	25/ 50	25/ 50	25/ 50	125/ 200		0/0	125/ 200
h Ch	50/ 50	25/ 50	25/ 50	25/ 50	125/ 200		0/0	125/ 200
GEMs	20/ 50	15/ 50	20/ 50	20/ 50	75/ 200		0/0	75/ 200
MRPC	15/ 50	15/ 50	10/ 50	10/ 50	50/ 200		0/0	50/ 200
DAQ	100/150	100/170	100/170	50/170	350/ 660		0/0	350/ 660
Magnet	75/220	75/220	25/130	25/135	200/ 705		0/0	200/ 705
Struc.	25/220	250/290	50/350	25/350	350/1170		0/0	350/1170
Software	/ 50	/ 50	/ 50	/ 50	/ 200		0/0	/ 200
Oversight	/ 75	/ 75	/ 75	/ 75	/ 300		0/0	/ 300
Total- overhead	480/ 900	710/1080	335/1050	335/1055	1525/3935		0/0	1525/3935